

Colloids and Surfaces in Reprographic Technology

Colloids and Surfaces in Reprographic Technology

Michael Hair, EDITOR

Xerox Research Centre of Canada

Melvin D. Croucher, EDITOR

Xerox Research Centre of Canada

Based on a symposium
sponsored by the ACS Division
of Colloid and Surface Chemistry
at the 182nd Meeting
of the American Chemical Society,
New York, New York,
August 23–28, 1981.

A C S S Y M P O S I U M S E R I E S **200**

AMERICAN CHEMICAL SOCIETY
WASHINGTON, D. C. 1982



Library of Congress Cataloging in Publication Data

Colloids and surfaces in reprographic technology.
(ACS symposium series, ISSN 0097-6156; 200)

Includes bibliographies and index.

1. Copying processes—Congresses. 2. Colloids—
Congresses. 3. Surface chemistry—Congresses.

I. Hair, Michael L. II. Croucher, Melvin D., 1945—
III. American Chemical Society. Division of
Colloid and Surface Chemistry. IV. Series.

Z48.C64 1982 686.4 82-13931
ISBN 0-8412-0737-2 ACSMC8 200 1-595 1982

Copyright © 1982

American Chemical Society

All Rights Reserved. The appearance of the code at the bottom of the first page of each article in this volume indicates the copyright owner's consent that reprographic copies of the article may be made for personal or internal use or for the personal or internal use of specific clients. This consent is given on the condition, however, that the copier pay the stated per copy fee through the Copyright Clearance Center, Inc. for copying beyond that permitted by Sections 107 or 108 of the U.S. Copyright Law. This consent does not extend to copying or transmission by any means—graphic or electronic—for any other purpose, such as for general distribution, for advertising or promotional purposes, for creating new collective work, for resale, or for information storage and retrieval systems. The copying fee for each chapter is indicated in the code at the bottom of the first page of the chapter.

The citation of trade names and/or names of manufacturers in this publication is not to be construed as an endorsement or as approval by ACS of the commercial products or services referenced herein; nor should the mere reference herein to any drawing, specification, chemical process, or other data be regarded as a license or as a conveyance of any right or permission, to the holder, reader, or any other person or corporation, to manufacture, reproduce, use, or sell any patented invention or copyrighted work that may in any way be related thereto.

PRINTED IN THE UNITED STATES OF AMERICA

**American Chemical
Society Library**

1155 16th St., N.W.

In Colloids and Surfaces in Reprographic Technology; Hair, M., et al.;
ACS Symposium Series 200, American Chemical Society, Washington, DC, 1982.

Washington, D.C. 20036

ACS Symposium Series

M. Joan Comstock, *Series Editor*

Advisory Board

David L. Allara

Robert Baker

Donald D. Dollberg

Robert E. Feeney

Brian M. Harney

W. Jeffrey Howe

James D. Idol, Jr.

Herbert D. Kaesz

Marvin Margoshes

Robert Ory

Leon Petrakis

Theodore Provder

Charles N. Satterfield

Dennis Schuetzle

Davis L. Temple, Jr.

Gunter Zweig

FOREWORD

The ACS SYMPOSIUM SERIES was founded in 1974 to provide a medium for publishing symposia quickly in book form. The format of the Series parallels that of the continuing ADVANCES IN CHEMISTRY SERIES except that in order to save time the papers are not typeset but are reproduced as they are submitted by the authors in camera-ready form. Papers are reviewed under the supervision of the Editors with the assistance of the Series Advisory Board and are selected to maintain the integrity of the symposia; however, verbatim reproductions of previously published papers are not accepted. Both reviews and reports of research are acceptable since symposia may embrace both types of presentation.

PREFACE

THE PRODUCTION AND REPRODUCTION OF GRAPHIC MATERIAL has occupied the attention of mankind since human evolution. Indeed, this desire to create, store, and communicate information sets us apart from lesser animals. Colloids and surfaces have always played a major role in the development of this technology—some of our earliest inventions being polymer stabilized suspensions (inks) and porous substrates (paper). The discovery of photon activated processes led to reprographic technology as it is known today.

Beginning a new decade, the reprographics industry awaits the next major revolution—the arrival of electronic information and the certain revolution that will occur in electronic printing. One of the most exciting developments will be the advent of ink jet printing. The desire to translate directly from an electronic signal to a mark on paper brings its own set of marking technologies and problems.

The scope of this volume is broad, with topics ranging from surface physics and chemistry to aqueous and nonaqueous colloid science. The subject matter chosen illustrates both the breadth and depth of scientific knowledge needed to advance these important technologies, and emphasizes the common scientific threads which run through these apparently differing subjects.

In assembling this collection of papers, covering such a wide area of science, we recognize an apparent lack of coherence due to the nonappearance of one over-riding discipline. That, however, is the message. The nature of the technologies orients both theoretical and practical questions toward surface science in the broadest aspects of the definition. In putting these particular remarks on this particular piece of paper, much of the information discussed in these contributions will have been utilized. From the illegible pen and ink scribble most of us use to document our first drafts, through the mechanical typewriting, to the xerographic printer and the final photographic reproduction, we will mirror several thousand years of human development. As we become more automated and move into

the electronic world of the next decade more printing problems will arise. Many will involve surface science in all its forms, and this book represents a contribution towards this progress and understanding.

MICHAEL HAIR

MELVIN D. CROUCHER

Xerox Research Centre of Canada

Mississauga, Ontario, Canada

May 1982

Surface Effects in Silver Halide Photography

GEORGE R. BIRD

Rutgers University, Department of Chemistry, New Brunswick, NJ 08903

Model systems of photographic sensitizing dyes and silver halide crystals lend themselves to basic studies of adsorption and ordering on surfaces. One of the goals of this paper is to make available to surface scientists at large the techniques for determining the size and structure of surface aggregates. These methods include the direct optical observation of monolayers of dyes on silver halide crystals, the diagnostic calculation of the large spectral shifts which occur when large dye aggregates form, the examination of polarized light absorption by dyes on orienting faces or facets, and the determination of surface concentration from conservation of integrated absorption.

The structure and electrochemistry of surface aggregates of silver atoms on silver halides are also topics open for basic surface studies. Here the surface scientist will seek simple model systems and avoid the plethora of surface additives so essential in forming the photographic latent image. Examples will be given.

The most remarkable feature of the silver halide photographic process is its extreme light sensitivity. This sensitivity reaches a level at which some 10 absorbed photons create one 3 atom silver cluster at a favorable site on the individual microcrystal, and this cluster acts as a catalyst for the reduction (development) of an entire crystal containing some $3 \cdot 10^{10}$ silver atoms. The mere fact that one takes a film to the local drug store to have it developed effectively conceals the astonishing performance of the multitude of microscopic amplifiers inside the film.

Not only is the "grain" of AgBr a remarkable amplifier, it has to function as a coincidence counter. If grains responded to the generation of single thermal conduction electrons, false development of unexposed grains would quickly follow (1). The action of a single photon (or a thermal event) produces one elec-

0097-6156/82/0200-0003\$13.95/0

© 1982 American Chemical Society

tron and one hole, and these both trap and de-trap repeatedly over a period on the order of one second before one of the two meets the other at a trap, and recombination (annihilation) occurs. This is the process which closes the gate unless additional photons arrive during the "open" period and produce additional electrons to facilitate the nucleation of a silver cluster, usually on the surface of the grain. Once this cluster is formed, it must be protected against attack by holes (bromine atoms) and atmospheric oxygen for a storage period of months in the camera. This protection process is assisted by the sensitizing dyes and by a variety of other special additives. This paper will not stress the field of surface additives, since this field is so specialized, proprietary, and dependent on access to experimental film coatings. Residence in a large photographic laboratory is all but essential to pursue the field of additives. By contrast, the field of sensitizing dyes and their surface effects can be open to those living outside the "silver curtain". Similarly, there are essential basic experiments to be done on the properties of small silver clusters, and many helpful experiments have already been done far from any coating alley. Some of these will be described, and some avenues for new work will be indicated.

This will not be a review paper. Herz has given a thorough discussion of dye adsorption phenomena (2), and the chapters which bracket his work in "The Theory of the Photographic Process" give a broad overview of the interactions of sensitizing dyes with silver halide microcrystals in photographic films (3,4). Similarly, Hamilton has treated the formation of the latent image in great detail (5). Here we shall concentrate on the availability of new tools for surface studies, and on the need for new surface studies to remove the last shortcomings in the silver halide photographic process.

The Materials

Silver bromide, silver chloride, and the mixed halide compounds (AgBr·I and AgCl·Br) are used in preference to the pure halides in photography) are an accessible and versatile experimental system. Both AgCl and AgBr can be grown as large single crystals (f.c.c.), and are obtainable commercially. The materials are very soft (Moh hardness of 1, the bottom of the scale), and must be sliced and oriented with care, cleavage being impossible. Orientation can be done visually by depositing visibly ordered microcrystals of NaCl on the silver halide boule by growth from a saturated salt solution. The silver halides must not be allowed to come in contact with metals other than silver, gold, and the platinum metals. Crystal surfaces can be cleaned by a very brief stripping etch in water solutions of ordinary photographic hypo.

Two aspects of AgBr behavior must be emphasized (Figure 1). the production of practical photographic "emulsions" or film coat-

ings the material usually crystallizes in the (111) facial form (6), giving the familiar tabular crystal which is the emblem of the Society of Photographic Scientists and Engineers. Madelung calculations suggest that this face ought to be unstable with respect to the (100) and (110) faces, but of course these calculations take the face in vacuum as the reference point of energy. The formal (111) face is a sheet of like ions, either all Ag^+ or all Br^- , an electrostatic monstrosity. Berry has commented that the face should be considered as a full sheet of one ion (Br^-) overlaid with a random half sheet of the other (Ag^+). This view suggests that the random half layer might be reorganized to accommodate ordered arrays of adsorbing molecules (7). Neglect of this possibility of reorganization has produced arguments that certain dye structures cannot possibly form on tabular AgBr (8).

Very closely related to the stability of the (111) face is the occurrence of a structural coincidence between the inorganic host and the organic guest adsorbate (9). Insofar as one does consider the planar face at all, the parallel lines of atoms ([110] intercepts) are separated by 3.535\AA on AgBr and 3.399\AA on AgCl . Both of these are within acceptable coincidence with the "graphitic distance" of 3.4\AA , the normal separation of parallel aromatic planes in graphite and in crystals of large aromatic or heterocyclic compounds. It is hardly surprising that the cubic silver halides have an affinity for planar aromatic and heterocyclic compounds, and one can anticipate that ordered, close-packed monolayers of adsorbed molecules will frequently form. This is the case with the cyanine sensitizing dyes.

The surface silver ions of AgBr also represent an opportunity for chemical interactions. When a clean crystal is exposed to a potential reactant such as a mercaptan in solution, the crystal quickly acquires a surface layer of the silver mercaptide. The photographic development "restrainer", 1-phenyl-1-H-tetrazole-5-thiol (alias phenylmercaptotetrazole or PMT) (10) is a good example of this behavior, giving multilayers of Ag^+PMT^- thick enough to yield a clear infrared spectrum on observation of a plate of AgBr or AgCl so dipped. With small molecules of this sort, characterized by insoluble silver salts, adsorption passes easily into actual metathetical reaction, with formation of AgPMT , for example, as a separate solid phase. We do well to remember that both AgCl and AgBr have been used as infrared optical materials for windows and even prisms. Thus, with either scale expansion on a good quality conventional IR spectrometer or high sensitivity observation on a Fourier transform (FTIR) instrument, one can observe even monolayers of adsorbed material on two sides of a disc, which may be either single crystal or polycrystalline material. This provides an unusual and much-neglected opportunity to surface chemists. Short of outright reaction by mercaptans, heterocyclic compounds carrying exposed, cyclized nitrogen or sulfur functions can form multiple ligand bonds to adjacent silver ions.

This appears to be the case with the tetraazaindene "stabilizers" (11) and also with some of the thiocarbocyanine sensitizers. Strong adsorption can occur without any such ligand bonding, but one ought not to neglect this additional force, especially as an origin of ordering in the attached layer, since it is a short range force of appreciable strength.

The cyanine dyes are among the strongest light absorbers known to man (12). Some representative structures and spectra are shown in Figure (2). Oddly, although these dyes have a cationic aromatic structure, they function with high quantum efficiency as injectors of electrons from the excited states of the dyes to the silver halide host. Further, the dyes can also accept holes from the host, so the final transient state which follows either direct absorption by the host (blue or UV light) or dye absorption (green, red, or IR light) is a conduction electron in the host crystal and a trapped hole in the dye layer. We have come to the end of an era of debate on "THE" mechanism of spectral (dye) sensitization, and it is now apparent that the dominant mechanism is one of electron injection (4). However, careful experiments by Kuhn and Möbius with insulated monolayers have shown that direct energy transfer from dye to host is a possible minority mechanism (13). The predominance of the electronic mechanism is underscored by the extensive correlations between redox potentials of isolated dye molecules in solution and the crossover potentials for transitions from sensitization to non-sensitization and on to image destruction by hole injection. Gilman and coworkers have calibrated the solution electrochemical scale against the solid state (vacuum = 0.0) scale (14), and so fixed the electrochemical thresholds for a number of processes. Since this is primarily an electrochemical problem, and a problem well in hand, we pass on to the critical surface phenomena involved in the interactions between AgBr and dyes.

Tools for Surface Science

In principle, one ought to be able to use the modern surface techniques such as low energy electron diffraction (LEED) to determine the structures of dye layers on single crystals of the silver halides. Results to date have been a disappointment (15). Instead of absolute structure determinations being made, a series of techniques has been developed to gain some partial information on the packing of ordered, monolayer dye structures on the silver halides. These techniques are primarily optical in nature, and rely on the simple fact that a single monolayer of a cyanine dye has sufficient optical absorption to be easily observed by a modern spectrophotometer. This is hardly surprising, as Kuhn and Möbius have long measured the absorption of surfactant cyanine dyes lifted from close-packed state on a water surface onto a prepared glass slide (16). A single monolayer of a cyanine dye may give from 4% to 40% peak absorption of light, depending on the

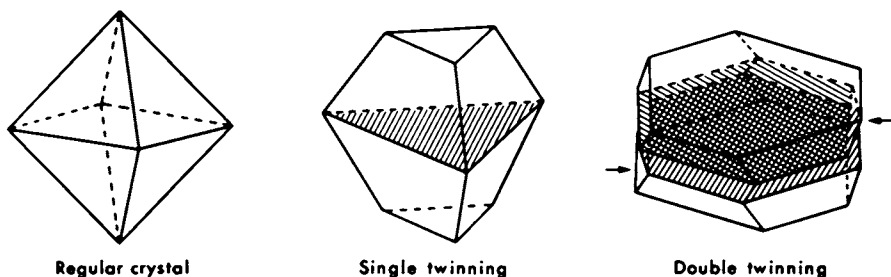


Figure 1. Complexity of silver bromide crystal growth without imperfections, with a single twin plane, and with a pair of twin planes.

The doubly twinned form, commonly encountered in the production of commercial photographic films, has a recessed (re-entrant) line at one of the twin planes. This is probably an active area for collection of the latent image for the action of special photographic additives. (Reproduced, with permission, from Ref. 6. Copyright 1963, *Photographische korrespondenz*.)

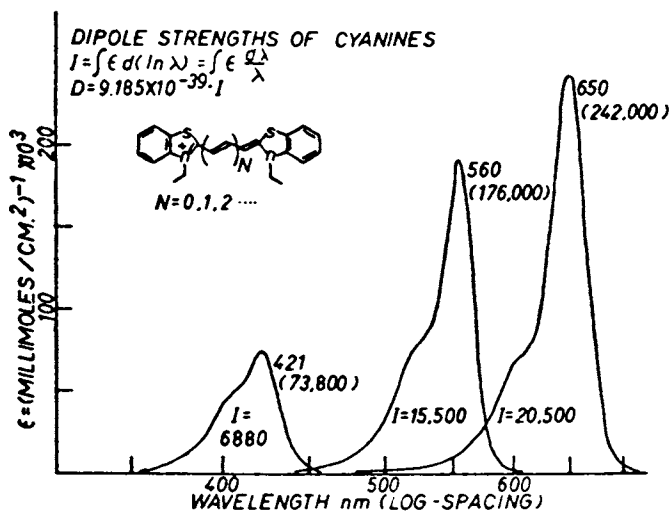


Figure 2. Absorption spectra of three cyanine sensitizing dyes: thiacyanine⁺ (CH), thiacyanocyanine⁺ (CH)₂, and thiadicyanocyanine⁺ (CH)₃, and illustrates the progression of cyanine absorption bands by ~100nm for each addition of (CH)₂, a carbo group.

This figure has been constructed with logarithmic spacing of the wavelength scale, so that the relative dipole strengths of the absorption bands of the dyes are represented by the areas under the absorption curves. Dipole strength rises with the addition of carbo groups. (Reproduced, with permission, from Ref. 12. Copyright 1980, Society of Photographic Scientists and Engineers.)

sharpness of the absorption band(s) of the dye on the crystal. Consequently we have a monolayer system which presents itself for convenient observation. We shall see that the absorption spectrum of a monolayer is quite different from the spectrum of a true solution of the same dye. This was once considered a paradox: Sensitizing dyes (on AgBr) produce action at wavelengths where the dyes (in solution) are not absorbing. Yesterday's paradox becomes today's advantage, as much can be determined about the packing structure of a monolayer from the wavelength shift and shape of the monolayer absorption band.

The reader will begin to sense a certain preoccupation with close-packed monolayers of dye. This has at least three origins. Most important, the quantum efficiency of the sensitization process declines as dye coverage reaches and exceeds one close-packed monolayer (17). The mechanism(s) underlying this failure of photographic and photoconductive sensitization are not well understood. This monolayer limitation stands as the largest performance gap of the silver halides, and removal of the limitation would open a route to new films of greatly enhanced resolution and increased sensitivity (12). Some limited progress has been recorded in this direction (18).

A second origin of the preoccupation with monolayers lies in the mordanting power of gelatin for sensitizing dyes. The silver halide surface readily picks up the first monolayer, but selected sites of opposite charge in the gelatin of a photographic emulsion have affinities* for the cyanine dyes which might otherwise bind weakly as a second monolayer. It is generally observed that the concentration of "free" monomeric dye rises abruptly in the water-gelatin medium just as soon as monolayer coverage is reached.

*Gelatin can bind even aggregates of substantial size. Some years ago, Mr. Hector A. Rodriguez and the writer thermally cycled a cyanine dye in water between monomer and dimer at high temperatures and the high polymeric J-aggregate at low temperatures. This cycling is reproducible, and there is a highest temperature for the existence of the J-aggregate for each particular dye concentration. On the down-cycle there was a delay of variable length before the J-aggregate nucleated. With 0.1% to 1% of gelatin added to the water, the ceiling temperature of the J-aggregate rose considerably, and it was obvious from small blue shifts that the gelatin was stabilizing aggregates of small size (N-10). It is difficult to explain this sort of stabilization at high gelatin dilution without invoking specific sites (charged amino acid sequences) in the gelatin. Regrettably, we did not characterize the net charge on the gelatin in these experiments, and thus are unable to give a completely satisfying answer to a question asked by Dr. A.H. Herz. However, we do have to note that all of the appropriate sites do not disappear as soon as the average charge of the gelatin begins to match the charge on the dye near the isoelectric point.

Third and finally, few cyanines have a molecular structure suitable for the formation of stable multilayers. The dyes adsorb with one molecular long edge in contact with the silver halide surface, and this long edge must be free from bulky groups which might interfere with adsorption. The opposite long edge can bear a wide variety of projecting groups, such as N,N'-diethyl-, N,N'-disulfobutyl, or N,N'-dimethyl-, without any significant change in either the surface coverage or the shift of absorption wavelength. One comes naturally to a mental picture of the extended N,N'- substituents as projecting upward and away from the silver halide surface and presenting a disordered contact at the outside surface of the dye monolayer.

A close-packed monolayer of long, planar molecules must necessarily contain at least "islands" of local order in which molecules are packed plane-to-plane. One notices that crystals of these dyes tend to pack in sheets, within which the molecules have their long axes parallel to one another and parallel to the plane of the sheet. The molecular short axes are nearly perpendicular to the plane of the sheet, and the intermolecular contacts within the sheet tend to occur at the graphitic distance, except for molecules which are bent or twisted out of planarity. Twisted molecules ("overcrowded" in Brooker's classification) generally make poor sensitizers, probably because they have a fast route of deexcitation directly from the excited singlet state to the ground state opened by the existence of the twisted, stressed structure.

Given all this ordering in a monolayer sheet, one has to ask whether an epitaxial contact - a kind of lock and key fitting - may not occur between the sheet of dye and the silver halide surface (9). Apparently this happens frequently, and seems to be a characteristic of the best sensitizing dyes. If one can be reasonably certain that epitaxial contact is occurring, the problem of analyzing surface structures is simplified to the consideration of a very small number of alternate possibilities. Much of the behavior of state-of-the-art sensitizers can be explained by the hypothesis of epitaxial attachment. However, efficient sensitization can occur without epitaxial contact. In particular, the surfactant dyes (N,N'-dioctadecyl substituted cyanines) of Kuhn and Möbius (16) tend not to form epitaxial contacts on AgBr. There is one well documented case of such a dye which attaches epitaxially on single crystal AgBr but not on evaporated, polycrystalline AgBr (19); and there are numerous examples of non-epitaxial contact. The forces of stacking the parallel octadecyl chains apparently override the ordering forces at the surface, except for molecules having structural backbones especially favorable to epitaxial contact. We shall shortly examine some of the evidence for epitaxial contacts.

Now let us consider the kinds of optical observations which can be made on various systems of dye and silver halide:

1. As a classical method for observation of isotherms, the silver halide crystals in a suspension (a melted gelatin "emulsion") can be centrifuged out, leaving the clear supernatant liquid available for quantitative spectroscopic analysis.
2. The total reflectance of an optically thick layer of dyed particles of AgBr can be measured with a spectrophotometer equipped with an integrating sphere. One then interprets the reflectance spectrum with the aid of Kubelka-Munk functions (20), as is commonly done with paints and pigments.
3. Using a spectrometer with integrating sphere, the total reflectance and total transmittance spectra may be obtained from a simple emulsion coating (21) (A photographic emulsion). This type of measurement must be done on a negative which has no secondary absorber, such as the familiar antihalo coating. On many films this coating lies on the opposite side of the film base from the silver halide, and can be removed by local swabbing with hypo or sulfite solution. Once the spectra $\%R(\lambda)$ and $\%T(\lambda)$ have been obtained, baseline corrections are made, and the absorption of the layer is calculated as $\%A = 100\% - \%R - \%T$. This technique is essential for studying the photochemical efficiency and quantum yields of silver halide films, but is less successful than (2.) above in determining the properties of a surface layer of dye.
4. The transmission and reflection spectra of a dyed single crystal can be determined (22). Unless monolayer coverage is substantially exceeded, there is very little change in the reflection spectrum on application of the dye. There is a certain antagonism between creating a freshly etched surface for adsorption of the dye and maintaining a quality of optical polish on the surface for ordinary transmission measurements. We find it best to concentrate on the dye-surface contact, and to measure the somewhat diffusing surface of the crystal with an integrating sphere as in (3.), obtaining both transmission and reflection (23). It is most helpful to have a computerized spectrometer to manipulate and correct the data, and especially to expand the relatively small absorption obtained with just two monolayers.
5. The single crystal method of (4.) can be repeated with other host crystals which are transparent in the visible or infrared. Since NaCl is isomorphous with AgBr and AgCl and has a lattice parameter intermediate between the two silver halides, it is a model host of choice for studies on the (100) face (22). It must, of course, be dyed out of nonaqueous media. Gypsum ($\text{CaSO}_4 \cdot 2\text{H}_2\text{O}$) has also been

used for special purposes (24), and many other ionic compounds could presumably be tried. CdS has also been used as a model for photoconductivity sensitization (25) by cyanines, and could presumably be used for surface studies. Like AgBr, it is yellow (blue absorbing) and an infrared window material.

6. Following Kuhn and Möbius (16), either prepared microscope slides or cleaved single crystals can be used to lift compressed monolayers of surfactant-dyes off a water surface. The spectrometer developed at Marburg and Göttingen is of special interest for this work. In it, a half-dyed slide is oscillated across a single beam of monochromatic light. The phase-detected signal carrying the information (undyed area - dyed area) is ratioed against the absolute intensity of the beam transmitted through the undyed area. This differential spectrometer has the special capability of measuring films in which the dye is heavily diluted with non-absorbing film-formers such as arachidic acid.
7. In cases (4.), (5.), and (6.), the crystal face may be selected to be anisotropic and to have a capability of aligning the long axes of dye molecules in a single direction in the plane (24). Alternately, a non-directing face (111) or (100) can be cut off-axis so that etching produces long, narrow terraces. The terrace edges can then serve as lines of nucleation for aligned aggregates (25). In either case, polarization spectra can be obtained and analyzed. One caveat here is that grating spectrometers have an internal polarization (mostly from the diffraction grating) which is both strong and highly variable with wavelength. This puts a premium on having a very good polarizer and aligning it parallel to the preferred polarization of the monochromator. The only proper optical sequence is monochromator-polarizer-sample.

Examples of all of the above modes of observation will be presented in the discussion below.

Spectroscopic observations on adsorbed dyes would be quite incomplete without a set of structural models and equations to process and interpret the data. Classical adsorption isotherms (1.) are of value, but tell nothing about the detailed structure of the adsorbed dye. Figure (3.) shows the adsorption of a variety of cyanine (+) and merocyanine (uncharged) dyes (26). Although the silver halide surface area is not given for this figure, dyes 1, 2, and 4 are familiar sensitizing materials, and can be seen to be occupying similar areas on the available surface. Dye 4 definitely does not give a Langmuir isotherm, as it shows a clear inflection point. If we infer that the silver iodobromide dispersion used here had predominately the octahedral (111) habit

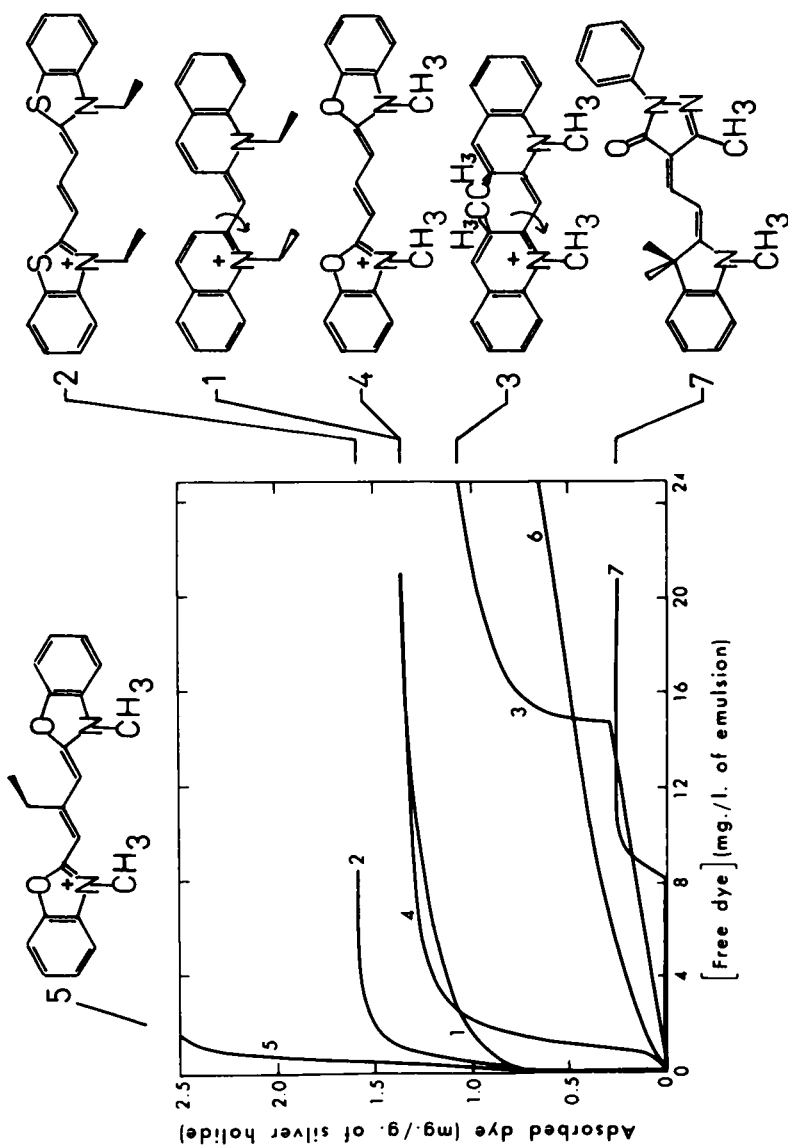


Figure 3. Adsorption isotherms for some cyanine and merocyanine sensitizing dyes.

The inflection on the isotherm of dye 4 and the phase transitions of dyes 3 and 7 show that Langmuir isotherms are not applicable to the higher surface coverages of these dyes. Dye 5 establishes a coverage equivalent to two close-packed monolayers on the surfaces of the $\text{AgBr} \cdot 1$ microcrystals in the gelatin suspension. (Reproduced from Ref. 26. Copyright 1952, American Chemical Society.)

and a halide concentration close to pure AgBr, then the three dyes cited (1,2,4) can be presumed to be adsorbed long edge-on with graphitic packing. Herz *et al.* arrived at a coverage of $57\text{\AA}^2/\text{molecule}$ for dye #1 in the edge-on configuration (20), and this compares remarkably with four lattice repeats on the (111) surface giving an area of $4 \times 4.083 \times 3.535\text{\AA}^2$ or 57.73\AA^2 . If their calibration area of 57\AA^2 holds, then the surface area of this particular iodobromide dispersion is determined from the saturation coverage of 1.38mg. dye/gm. AgBr·I to be $1.04 \cdot 10^4 \text{cm}^2/\text{gm}$. Unfortunately, area estimates of this sort are often omitted in surface studies published from photographic laboratories. Dye #2 is expected to occupy $5 \times 4.083 \times 3.535\text{\AA}^2 = 72.2\text{\AA}^2$ per molecule (9), and from it one would calculate an emulsion area of $1.41 \cdot 10^4 \text{cm}^2/\text{gm}$. If one has to choose between these estimates, it should be noted that dye 2 is a planar molecule, while dye 1 has recently been determined to be a severely twisted molecule, having the two quinoline rings inclined at an angle of 50.6° to each other (27). Thus it is expected to fail to fit into the simple graphitic packing scheme, and the idealized figure of $57.7\text{\AA}^2/\text{molecule}$ is rendered somewhat doubtful.

Dyes 2 and 4 have closely similar structures, and would be expected to occupy the same areas on the (111) face. In fact, the surface coverage of dye 2 is only 1.6% higher in moles / (wt. of substrate) than the coverage of dye 4. One can note that the rapidly rising portions of the plots indicate that dye 2 is much more strongly adsorbed than dye 4, a change which might well be attributed to the extra adsorption forces generated by formation of a pair of $\text{S} \cdots \text{Ag}^+$ ligand bonds when dye 2 is adsorbed edge-on. The upward curvature corresponding to the transition from flat-on monomeric dye to edge-on dye is visible for the oxacarbocyanine (4) but is obscured against the y-axis for the thiocarbocyanine as seen in Figure (3.).

Dye #3 is a pathological case of a really severely twisted molecule. It cannot make a favorable monomeric contact with AgBr nor a favorable intermolecular aggregate contact. This gives us a clear view of the initial rise of adsorption corresponding to the binding of isolated molecules on the surface. Even after the sharp break into some kind of aggregate structure, the approach to saturation coverage in the aggregated structure is very slow. One might expect the weight-saturation coverage of dye 3 to lie slightly above that for dye 1.

Dye #5 is an especially interesting case. It differs only trivially from dye 4 in molecular length and weight, and both dyes are planar or nearly so. One wishes that we had a better understanding of the clear formation of a double sheet of close-packed molecules by dye 5. It would be a really striking improvement in the whole art of dye sensitization if we could even get efficient sensitization from a close-packed bilayer. But here we confront the deficiencies of classical surface measurements. We

are literally working in the dark, and do not know the structures of the obviously close-packed aggregates of dyes 1-5. If, for example, the bilayer of dye 5 has such a structure that its optical absorption is blue-shifted so far that it falls under the existing blue absorption and sensitivity of AgBr, then this remarkable structure is of no immediate use at all. But before we move to the examination of optical results from methods 2-7, it will be necessary to develop the conceptual models for evaluating the data.

Conceptual Models:

1. The strength of absorption of a monomeric dye, measured as dipole strength, is conserved to a good approximation upon going into an aggregated monolayer structure. The shape and the peak extinction of an absorption band of a dye will change completely on aggregation, but the dipole strength will not. This leads to a kind of integral variant of Beer's Law(22):

$$\int A(\lambda) \frac{d\lambda}{\lambda} = p C_s \int \epsilon \frac{d\lambda}{\lambda} \quad (1)$$

Here $A(\lambda)$ is the measured absorbance of a film of dye on a surface, λ is the wavelength in any convenient dimensional unit, C_s is the concentration of dye on the surface given in millimoles/cm² (This is the correct unit of surface concentration to use with the ordinary solution extinction coefficient with units of (moles/liter)⁻¹cm¹ or (millimoles/cm³)⁻¹cm.⁻¹). $\epsilon(\lambda)$ is, of course, the measured solution extinction coefficient. The factor p is an orientation factor, taking account of the selective arrangement of molecules on the surface. For a film having complete parallel orientation of all molecular long axes, $p = 3$ for one sense of polarized light and $p = 0$ for the other. For plano-orientation, the arrangement most commonly found, in which there are islands of aggregates oriented in several directions in the surface plane, $p = 3/2$. The dipole strength does not appear in this equation,

but the right hand (solution) integral $I = \int \epsilon \frac{d\lambda}{\lambda}$ need only be multiplied by the constant $9.185 \cdot 10^{-39}$ to give the dipole strength in esu²cm.² As may be seen in figure (2) it is often convenient to give the value of the simple solution integral I in units of molar extinction coefficient. This permits convenient comparisons between the peak extinction coefficients of dyes and their integrated extinctions. This solution integral can be approximated satisfactorily by a sum

$$I = \Delta\lambda \sum \frac{\epsilon}{\lambda} \quad (2)$$

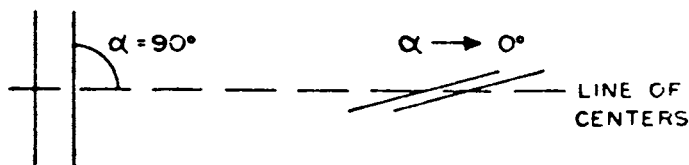
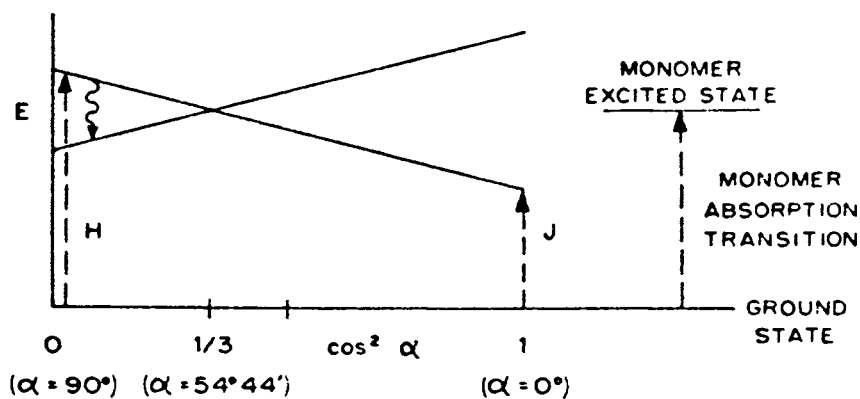
done with a computerized spectrophotometer or simply by hand calculator from an existing spectrum.

2. An aggregate structure does not have A single spectrum, but rather a size-dependent array of spectra. For simple linear column aggregates, an approximate equation for the large spectral shifts is $\Delta\nu_N = \Delta\nu_\infty(N-1)/N$ where N = number of molecules (28). For the two-dimensional aggregates more commonly seen, the observed spectral shift depends on both the length and the width of the aggregate. The general method of calculating size-dependent spectral shifts will be given below. Even so, one routinely observes spectral shifting with size, and the equation just given is a qualitative conceptual aid. This is certainly a simpler and more direct method for analyzing the sizes of aggregate islands than full scale electron diffraction methods.
3. The direction of the absorption dipoles of individual molecules is also conserved as the molecules become incorporated into an aggregate (9). The aggregate has a two-dimensional unit cell, and the number and arrangement of molecules in this cell determine the number of electronic transitions which will be seen. When there is only a single molecule in the cell, we observe the single sharp absorption of an H- (hypsochromic or blue-shifted) aggregate or a J-aggregate (red shifted). When two or more molecules lie in the cell with their long axes parallel, multiple absorption bands will be seen, all having the same sense of linear polarization on a directing substrate. When the multiple molecules in the cell are non-parallel (herringbone, V- or X-packing), the multiple absorption bands will have two perpendicular senses of polarization (29). In the simplest case of herringbone packing of two molecules in the unit cell, the ratio of intensities of the two perpendicularly polarized absorption bands will be given simply by $I_\perp/I_\parallel = \tan^2\theta$, where θ is the angle between the line of advance of the herringbone and the individual molecular long axes. The spectrum of a herringbone structure and the corresponding hypothetical structure are shown in Figures (8a,c). Note, however, the above simple intensity equation refers ONLY to the integrated band intensities and not to the peaks. Since the two bands usually overlap, it may require a bit of imagination to extract an accurate value of θ . This is certainly the simplest possible route to a structural parameter that one can imagine.
4. There is a reliable method of calculating the spectral shifts of aggregates of known structure. The oversimplified point-dipole approach to this problem fails quanti-

tatively (9), but the point-dipole expression for a single column of aggregated molecules is instructive:

$$\Delta E(N) = \frac{2D}{hr^3} (1 - 3\cos^2\alpha)(N-1)/N \quad (3)$$

Here D is the dipole strength, h is Planck's constant, r is the separation between centers of adjacent molecules, α is the angle between the line of centers of molecules and the long axis of any molecule, and N is the size of the aggregate. Figure (4.) represents the prediction of (3.) for a dimer aggregate. We see from this simple equation that the spectral shift will be to the blue for a perpendicular stack of molecules (deck-of-cards in the box) but to the red if the molecules rotate sufficiently about the line of centers (slipped deck-of-cards). This can explain the spectral shifts of +100nm from the solution monomer peak seen with H- and J̄-aggregates. What must be substituted for the point-dipole theory is a general quantum mechanical perturbation theory of spectral shifting in ordered clusters of molecules. This treatment has been given by Norland, Ames, and Taylor (30), and has been elaborated by Reich (29,31). To calculate the spectral shifting of an aggregate, one must first produce the ground state and first excited singlet state wavefunctions of an isolated cyanine dye molecule. This can be done with increasing levels of sophistication by Hückel LCAO-MO, Pariser-Parr-Pople, or CNDO methods. The transition dipole for the $S_0 \rightarrow S_1$ absorption is calculated and compared with the observed dipole strength. The discrepancy is usually only a few percent when working with cyanine chromophores, and is used to refine the result of the next step. Using the calculated wavefunctions, the total transition dipole is divided into transition densities localized on the atoms of the molecule. Physically, these transition densities represent the fractional electronic charges which flow to and then away from particular atoms during successive half cycles of the radiation field which drives the absorption process. The interacting molecules are now arranged in the aggregate geometry, and an instantaneous Coulombic interaction energy is calculated. Figure (5) shows the two possible excited state interactions between a pair of stick-molecules, and Figure (6) shows the transition densities calculated for a model thiocarbocyanine. The calculation of interaction energies is accomplished by treating the transition densities as though they were static Coulombic charges and allowing all possible atom-to-atom interactions to occur between molecules according to the Coulombic interaction between point charges. The matrix of interaction energies is diagonalized, giving



ALIGNMENT OF TRANSITION DIPOLES
(OR MOLECULAR LONG AXES)
RELATIVE TO LINE-OF-CENTERS

Figure 4. Qualitative predictions from the point-dipole expression (Equation 3) for spectral shifting of dimers. Dimer formation splits the excited state into two levels, one which allows transition to the ground state, and one which is silent for the case of parallel molecules in the dimer. The spectral shift depends on the stacking angle of the pair of molecules. The slipped structure is the precursor of the red shifted J-aggregate, a desirable structure for photographic sensitization. (Reproduced, with permission, from Ref. 9. Copyright 1968, Society of Photographic Scientists and Engineers.)

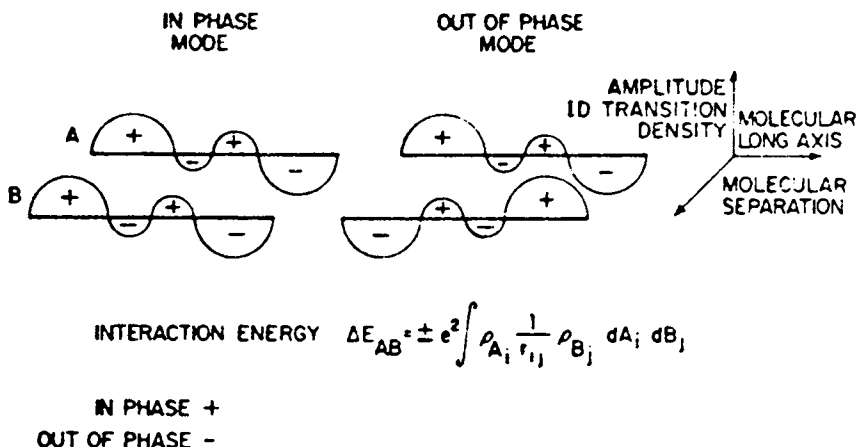


Figure 5. "Stick" molecules in the possible modes of interaction during an optical transition, with transition density represented by vertical displacement from the horizontal sticks. Right, the transition densities cancel each other and are silent, and left, the transition densities add so that the dimer becomes a supermolecule with a single allowed optical transition having the combined dipole strength of the two participating molecules. (Reproduced, with permission, from Ref. 30. Copyright 1973, Society of Photographic Scientists and Engineers.)

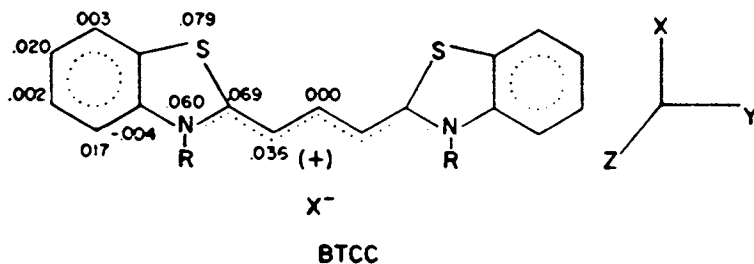


Figure 6. Transition density values calculated for a thiocarbocyanine sensitizer by the Hückel LCAO MO method. Transition densities are localized on the conjugated atoms of the chromophore. The numbers represent the values in units of electron charge. The transition densities on the opposite side of the molecule differ only by a change of sign, and have not been reproduced. The transition densities alternate small, large, small, large, etc. along the chromophore; one of the values is actually being negative and cancelling some of the overall dipole strength of the transition. (Reproduced, with permission, from Ref. 30. Copyright 1973, Society of Photographic Scientists and Engineers.)

the set of N excited singlet energies for an aggregate of N molecules. As shown by Norland *et al.* this diagonalized matrix also supplies the coefficients which give the contributions (+ or -) of the individual molecules to the transition dipole of the whole array. Thus the calculation gives the energy shifts (wavelength shifts) and the individual dipole strengths of the array of N possible $S_0 \rightarrow S_1$ transitions belonging to the N -molecule aggregate.

The transition density of a large aggregate will often concentrate in one or a few of the N transitions. When this happens, the aggregate is behaving as a kind of super-molecule. We note, for example, that the radiative lifetime for such an aggregate transition may be shorter by a factor nearly N^{-1} than the radiative lifetime of a single molecule for aggregates of modest size. This calculation of energy shifts and intensities gives surprisingly good results, relatively independent of the details of the molecular orbitals used to generate the wavefunctions. This seems to be a kind of theoretical reward for concentrating on truly allowed transitions of simple, non-degenerate molecules- the precise situation in which perturbation calculations ought to work well. A program for executing this kind of aggregate calculation may be found in the appendix of Reich's thesis (32). This work requires a large digital computer, but the cost of computation need not be high unless one insists on doing large aggregates.

5. The epitaxial hypothesis becomes interlocked with transition density calculations when one considers the cost and the practical difficulties of "fishing" for an unknown aggregate structure by doing an extended series of calculations on different structures. If epitaxial attachment of a dye has occurred, there will be only a handful of possible structures (just 3 for a primitive unit cell aligned along [110] intercepts on the (111) face of AgBr, where the graphitic coincidence favors a particular orientation of molecular axes). In this situation, one does a limited number of transition density calculations for the alternate possibilities. However, this is no guarantee that epitaxial attachment actually has occurred. It does seem to be a common occurrence, and some of the confirmatory indications of epitaxial attachment are:
 - a. The dye spectrum shifts or splits when dye is adsorbed on a new face of a familiar host. (AgBr (100)) (29,31).

- b. The dye spectrum shifts in a predictable way when the host lattice parameter is changed, as in comparison spectra on the (100) faces of AgCl and AgBr (33).
- c. The dye tends to be attached more firmly in the epitaxial mode, and it becomes more difficult to reorganize small islands into large sheet aggregates. Consequently, small spectral shifts are observed when steps such as incubation at slightly elevated temperature are taken (21).
- d. Phase transitions are sometimes observed, corresponding to gliding movements of the close-packed molecules (21). These movements produce striking changes in the absorption spectrum, but give no change at all in surface coverage and little change in the strength of attachment. When these phase transitions do occur on well-characterized faces, the spectral shift observed in the phase transition is predicted by the transition density calculations and the epitaxial hypothesis (31).
- e. Once one begins to understand the nature of these gliding phase transitions, it becomes possible to understand the critical role of "indexing" groups. These are minor chemical substituents which protrude out of the molecular plane and so prevent the formation of one or more of the epitaxial structures.

In the discussions below, we shall see numerous examples of the results of epitaxial attachment.

Figure (7) shows the reflection spectra of thick, nontransmitting layers of AgBr-gelatin dispersions containing the same amounts of AgBr and increasing amounts of dye (2,20). The reflectance spectra (here given as $-\text{Log}_{10}R_{\infty}$) may be converted back to R_{∞} and processed according to the Kubelka-Munk equation (4).

$$\frac{K}{S} = \frac{(1-R_{\infty})^2}{2R_{\infty}} = \frac{\epsilon}{cS} \quad (4)$$

Here R_{∞} is the reflectance (at wavelength λ) from an optically thick layer of a pigment coated with the sensitizing dye, c is a volume concentration of dye in the suspension, K and S are the absorption and scatter coefficients of the suspension (as determined by observation of R_{∞}). Thus, at a given wavelength, R_{∞} is measured, giving K/S , and S may be determined for the same emulsion by adding a non-adsorbing dye of known ϵ . A study of this equation shows that it does lead to determination of reasonable values of ϵ_{agg} for aggregate species. Certain absorption bands

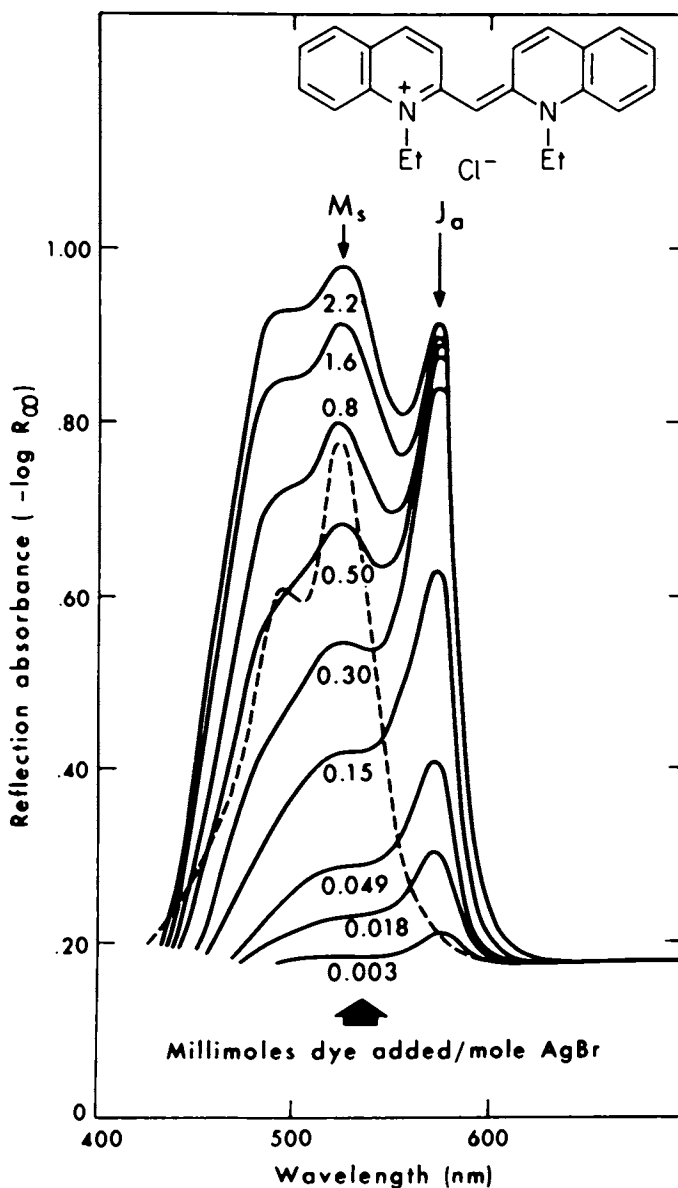


Figure 7a. Optical data of microcrystalline suspensions with added dye.

AgBr is dispersed in gelatin at constant concentration, and the dyes are added as shown. Reflectance is measured from a dispersion layer so thick that no radiation emerges from the far side giving R_{∞} . The red-shifted aggregate is the dominant species until a saturation coverage is approached. Beyond this saturated and close-packed monolayer, additional dye simply dissolves in the suspending medium. (Reproduced, with permission, from Ref. 2. Copyright 1977, MacMillan Publishing Co., Inc.)

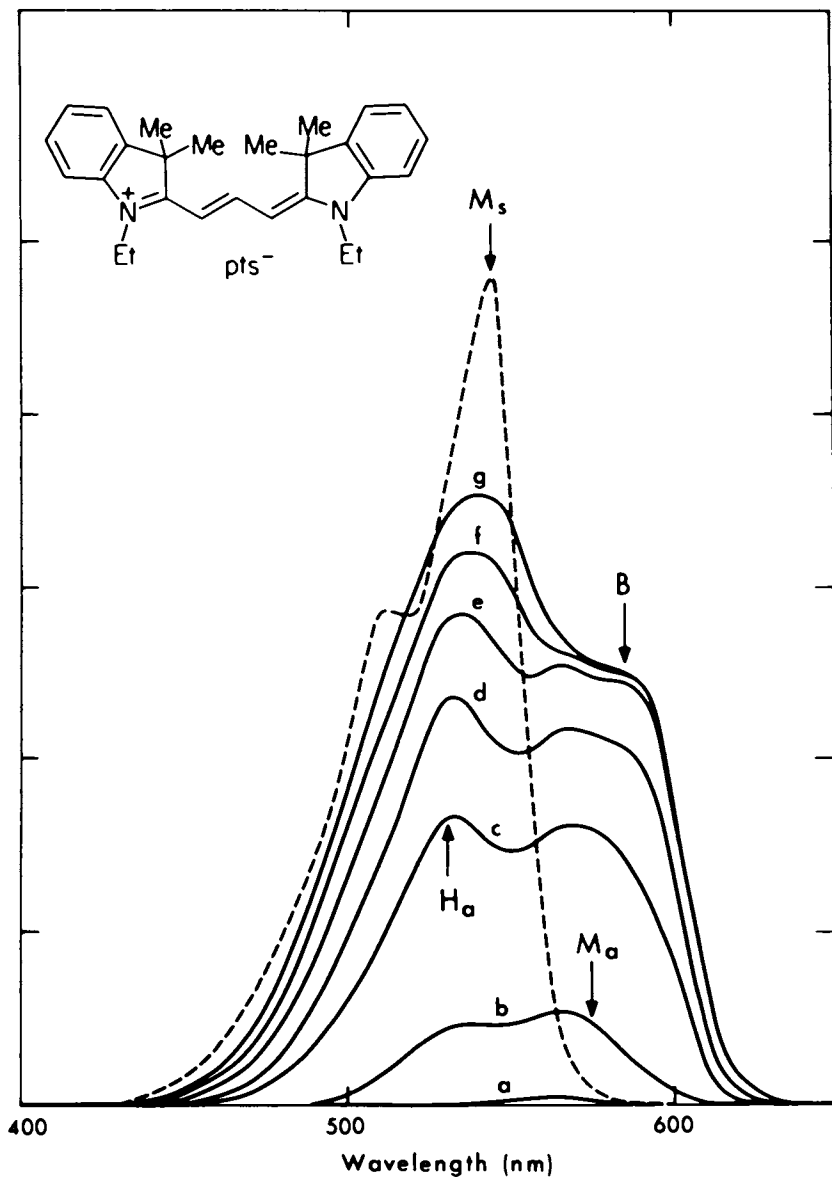


Figure 7b. Optical data of microcrystalline suspensions with added dye.

AgBr is dispersed in gelatin at constant concentration, and the dyes are added as shown. Reflectance is measured from a dispersion layer so thick that no radiation emerges from the far side, giving R_{∞} . This dye, with six methyl groups projecting out of the chromophoric plane, absorbs first as isolated monomer molecules (M_s), and then forms an aggregate with red- and blue-shifted bands at higher total dye concentrations. (Reproduced, with permission, from Ref. 2. Copyright 1977, MacMillan Publishing Co., Inc.)

(especially the red-shifted "J" band) do level off or saturate in intensity at some ratio of millimoles of dye per mole of substrate. In this way optical adsorption isotherms can be determined, and used to show the saturation coverage and the surface area per molecule, as for the red shifted "J" aggregate of 1,1'-diethyl-2,2'-cyanine⁺iodide⁻ in figure 7a.

The pseudoindole carbocyanine of figure (7b) is a good example of a dye having too many non-planar groups to be able to pack well in a graphitic aggregate. It thus shows a surface monomer band (flat-on adsorbed dye on AgBr, with a modest red shift from the solution monomer. This red shift is caused by interaction of the isolated molecules with the optical dielectric constant (34) of the silver bromide adsorbent). At much higher concentrations it then shows a multiple banded aggregate which is not a simple H- or J- structure.

Figure (8) shows absorption spectra of AgBr dispersions as obtained from measuring the reflection and transmission of actual photographic coatings (method 3). The most striking difference between the adsorption of this dye on cubic and on octahedral faces is that the ratio of intensities of the two absorption bands is constant on the cubic face but varies markedly on the octahedral face (35). This suggests that a single aggregate is forming on the cube face, whereas the familiar "J" aggregate with red-shifted absorption is forming on the octahedral face at higher dye concentrations. Simpson has confirmed by detailed luminescence measurements that the cubic absorption peaks at 590nm and 525nm match a pair of excitation peaks which give a common output spectrum and identical luminescence decay curves. Transition density calculations by Reich have shown that these double absorption bands can be described in detail by assuming V-packed "herringbone" structures for epitaxially attached aggregates (29). His results for a related dye, 3,3'-dicarboxyethyl-5,5'-dichlorothiacarbocyanine, are shown in Table I. The fact that a class of thiacyanobocyanine dyes shows this common sensitivity to the particular crystal face of the AgBr substrate has always seemed to us to be a proof of epitaxial attachment. Reich's finding of a particular dye which gives double-banded absorption spectra on both cubic and octahedral faces, but with a large shift in absorption maxima (Table I) strengthens this conclusion.

The probable presence of more than one aggregate structure in epitaxial attachment on the (111) face of AgBr lays open the possibility that monolayer phase transitions might occur. The three most obvious structures available to a 5,5'-disubstituted dye on this face are shown in Figure (9). These are characterized by slip angles of 60°, 30°, and 19°06' and by predicted absorption maxima of 477nm, 643nm, and 653nm as calculated by the transition density method (31) relative to a monomer absorption peak at 579nm (in a hypothetical medium of optical dielectric constant matching

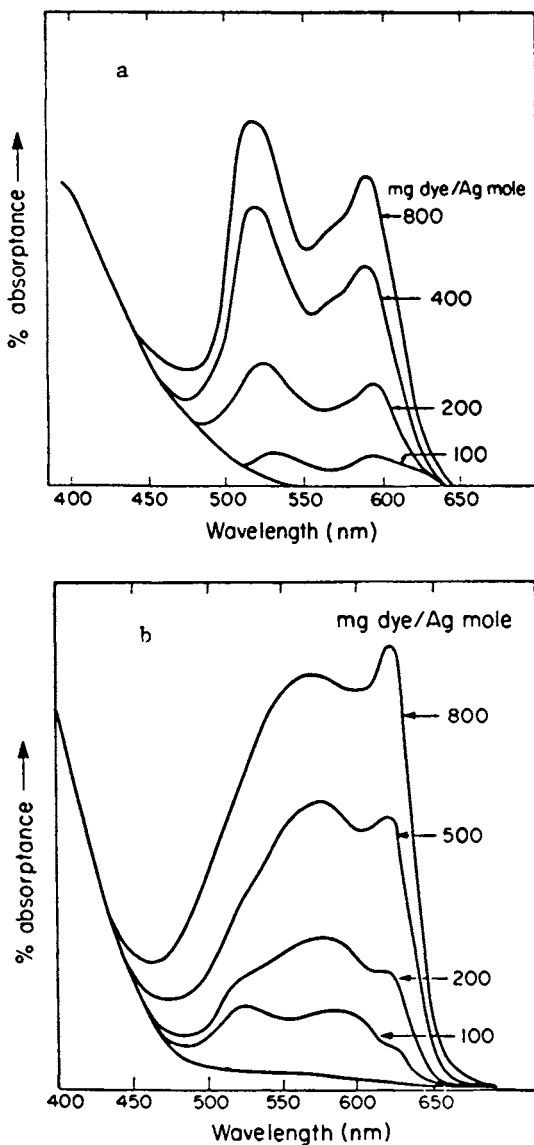


Figure 8. Wavelength vs. absorbance for a normal photographic coating of a thiocarbocyanine dye on cubic crystals (a), and on octahedral crystals of $\text{AgBr} \cdot \text{I}$ (2.5% I) (b). The rising absorption to the left of each plot is the intrinsic absorption of the silver halide. (Reproduced, with permission, from Ref. 35. Copyright 1974, Society of Photographic Scientists and Engineers.)

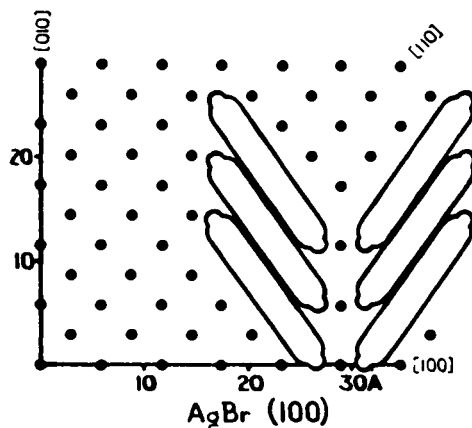


Figure 8c. A cubic herringbone structure for a thiocarbocyanine dye unsubstituted in the 5,6,5',6' positions. (Reproduced, with permission, from Ref. 29. Copyright 1974, Society of Photographic Scientists and Engineers.)

Table I

Calculated and Observed Spectra of Herringbone Aggregates
on Various Faces of AgBr

Crystal Face	Slip Angle	Molecular Length in Lattice Repeats	λ_{\max} (calc)	Rel. Int. (calc)	λ_{\max} (obs)	Rel. Int.
(111)	30°	5	582 669	3.09 1		
(111)	30°	6	593 649	2.9 1	600 645	3 1
(111)	60°	5	433 485	1 3.04		
(111)	60°	6	441 473	1 3		
(100)	35°50'	5	550(avg.) 598	2.15 1	525 590	
(100)	35°50'	6	560(avg.) 592	2.05 1		

Table I is computed from the results of references 29,32, and 35. The term "(avg.)" indicates that the original calculation produced a cluster of closed spaced absorptions. Since this cluster is an artifact of the particular aggregate geometry calculated (2 columns of herringbones of size 2x10 molecules on the (100) face), a weighted average wavelength is given.

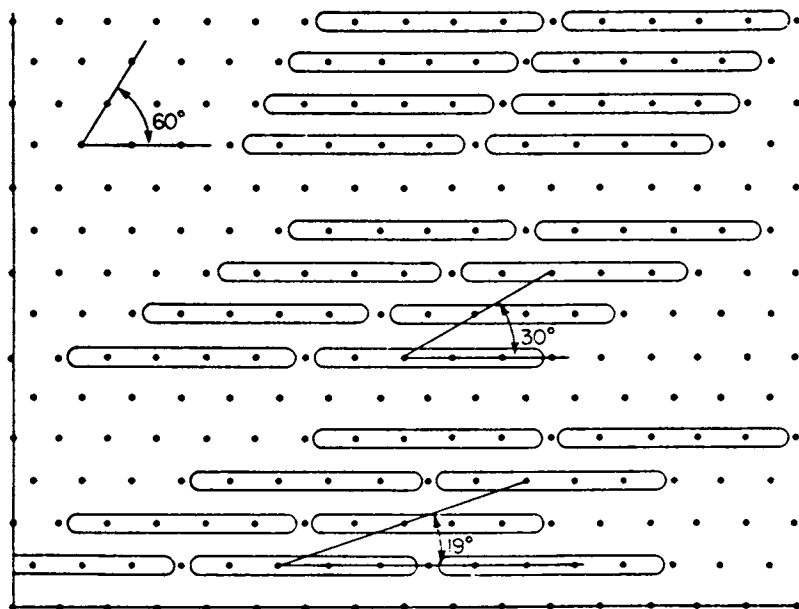


Figure 9. The octahedral (111) face of AgBr covered with three possible ordered, epitaxial monolayers of adsorbed dye.

The dots represent Ag⁺ ions in lattice positions, with nearest neighbors being separated by 4.083 Å. The lines of Ag⁺ ions are separated by 3.535 Å, a distance very close to the normal packing distance of 3.4 Å between aromatic planes in crystals, including graphite. Thus, planar molecules can form any of these structures while preserving their optimal packing dimension. The top structure is predicted to give a blue shift of absorption, the middle structure to give a red shift, and the bottom structure a larger red shift. The molecular length shown is appropriate to a 5,6-unsubstituted thiocarbocyanine dye, which covers $5 \times 4.083 \times 3.535 \text{ \AA}^2 = 72.2 \text{ \AA}^2$. These structures can explain many of the observations on thiocarbocyanine red sensitizers on octahedral surfaces, including the observation of gliding phase transitions among the structures. (Reproduced, with permission, from Ref. 8. Copyright 1974, Society of Photographic Scientists and Engineers.)

the interior of an aggregate). Rosenoff *et al.* have described a set of observations on a pair of dyes which differ from Reich's herringbone-forming dye only by the addition of 9-ethyl or 9-methyl groups (21). As observed by combined reflectance and transmittance measurements on photographic coatings, the 9-ethyl dye was seen to be a well behaved red sensitizer, always giving the red-shifted J-aggregate at 648-650nm, as seen in Fig. (10). In total contrast, the 9-methyl dye had gained a certain notoriety by giving irreproducible results which came to be known as "the day of the week effect". This peculiar behavior was shown to be due to a gliding phase transition from small blue-shifted 60° aggregates to red-shifted aggregates, now assigned to the more strongly shifted 19° structure. It was also shown that the growth of the 19° aggregates followed autocatalytic kinetics, giving initial growth curves which were concave upward. Since the intermolecular contacts between the first two members of a 19° J-aggregate form only a fragmentary contact between halves of the molecules, one might expect that the small aggregates would be unstable with respect to both the 60° aggregate and the large, nested multicolumn 19° J-aggregate.

It's interesting to note that this sort of gliding phase transition occurs with no change in the surface area occupied by the dye. Thus little or no change would be seen on an isotherm as in Fig. (3). The 5,5'-dichloro substituted dyes have molecular lengths of 21.1Å (including the 1.8Å van der Waals radii of the terminal chlorines) and so must occupy $6 \times 4.083\text{Å}$ along the [110] edge on the (111) face of AgBr (7). Given an edge separation of 3.535Å, the predicted surface coverage on (111) AgBr is 86.60Å^2 for any of the structures shown. Reich *et al.* have surveyed the available structures on the (111) and (100) faces of AgBr and have assigned the octahedral absorptions at 620nm and 648nm as the 30° and 19°06' structures for 6 unit dyes respectively (31). The longest observed absorption wavelength (660nm) is assigned to the cube face. Here it is amusing to note that two hypothetical aggregate structures on the cube face predict almost exactly the same aggregate absorption wavelength and the same surface coverage. One of these is a structure propagating along the [310] edge proposed by Smith (36), the other is propagating along the [110] edge as proposed by the writer (37). One ought not to be too dogmatic as to which epitaxial structure may be occurring, even though the facts strongly support epitaxial attachment in a particular case. The two cube structures are predicted to occupy exactly the same area of $3a_0^2 = 95.4\text{Å}^2$ per molecule. Both structures may one day be established as occurring for particular dyes. At the moment we have no means for differentiating between them.

The molecular details of the surface contacts between AgBr and these same carbocyanine dyes have been explored through the use of a crystal structure determination by Potenza and Mastro-

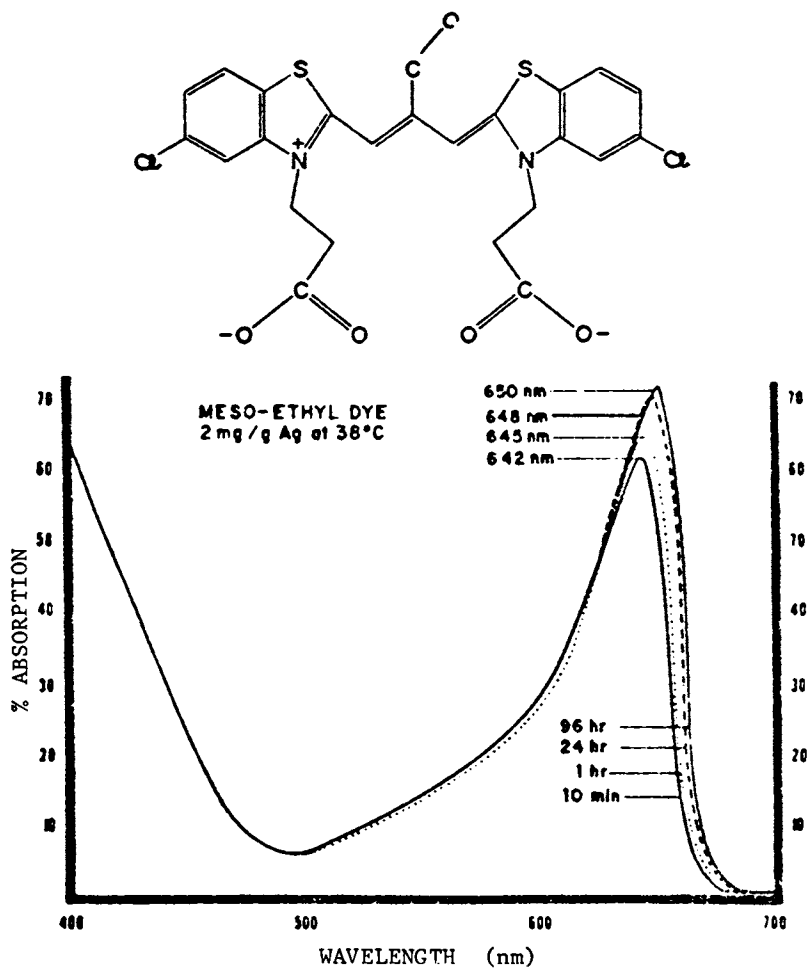


Figure 10a. Results of coating matching octahedral $\text{AgBr} \cdot \text{I}$ (1% I) emulsions on clear acetate film base and measuring %R, %T. On incubation at 38°C, the red-shifted aggregates are simply ordered increasingly with time, and a modest red shift occurs. The central ethyl group prevents formation of the 60° structure. (Re-produced, with permission, from Ref. 21. Copyright 1970, Society of Photographic Scientists and Engineers.)

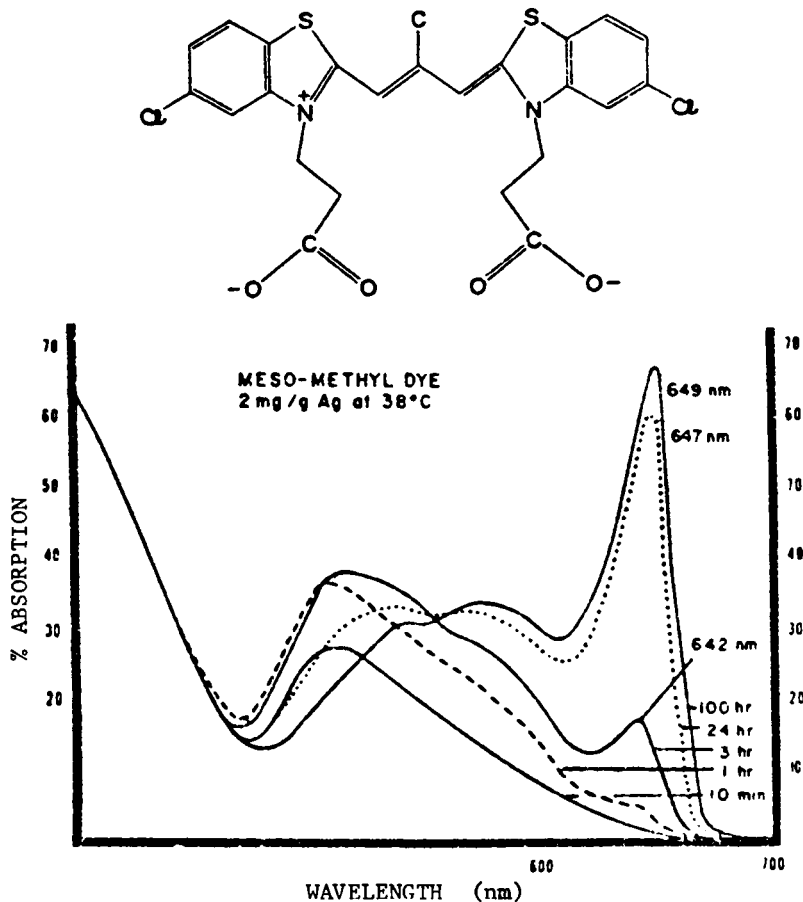


Figure 10b. Results of coating matching octahedral $\text{AgBr} \cdot 1$ (1% 1) emulsions on clear acetate film base and measuring %R, %T, which undergoes a gliding phase transition presumed to be from the 60° structure to the 19° structure. Figure 10b differs from Figure 10a by the central 9-ethyl group found on the structure of Figure 10a. (Reproduced, with permission, from Ref. 21. Copyright 1970, Society of Photographic Scientists and Engineers.)

paolo (38). Given the partially random atomic configuration of this surface, contact structures can be proposed which accommodate a variety of differently charged dyes and restore the electrical neutrality of the combined AgBr-dye surface (7), as shown in Fig. (11).

The use of the hypothesis of epitaxial attachment has been criticized on the grounds that seemingly continuous absorption shifts occur as the host or the dye is changed (2). This is particularly likely to occur when a host is taken through a domain of facial instability (62). One can, indeed, observe continuous spectral shifts under these circumstances, but the continuous shifts can be explained in terms of a confusing superposition of size shifts $(N-1)/N$ and of the actual facial transformation shift. In a poorly characterized facial system it is essentially impossible to prove or disprove epitaxial attachment. It is also incorrect to argue for continuous spectral shifting from observations of thiocarbocyanines on the (111) face when the cyanines are of such molecular length that different members of the set occupy different numbers of lattice positions. In general, the epitaxial hypothesis is a very economical explanation of a large set of phenomena. However, these are very real exceptions to the action of the hypothesis and many of these are discussed in this paper.

The use of single crystals of the silver halides as model systems for the study of adsorption and surface ordering has already been suggested. With crystals which have been carefully prepared to maximize the displacement of conduction electrons (schubweg), the dye-sensitized photoconductivity of the crystals can be measured, and relative quantum yields for charge carrier generation can be determined (39). The yields are relative in the sense that absolute quantum yields can be determined for direct absorption of blue and UV light in the body of the crystal, and then the dye absorption spectrum and carrier generation can be compared to the intrinsic yields. Figure (12) shows the results of Piechowski on two dyeings at quite different coverages with a well known dye, 1,1',3,3'-tetraethyl-5,5',6,6'-tetrachlorobenzimidazolocarbo-cyanine⁺ iodide⁻ (40). The first of these is dyed to a coverage of a single close-packed monolayer, and shows substantially perfect parallelism between the absorption spectrum and the current yield (actually measured as a charge-displacement signal in a capacitor). This is clearly an epitaxial monolayer, as this dye tends to form a J-aggregate with somewhat different absorption maximum (594nm) on less directing surfaces.

The second dyeing is equivalent to about four monolayers, and the shift of absorption maximum toward 594nm can be noted. Gardner and Herz have noted that multilayer formation with this dye is strongly favored by the presence of I⁻ (40b). The mechanism of assistance of multilayering is not clear. It could be a

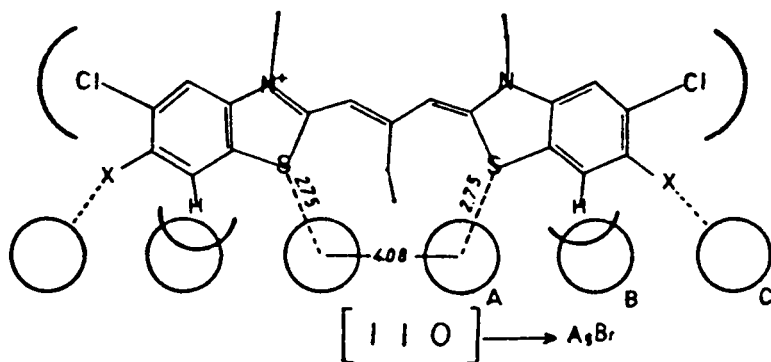


Figure 11. Hypothetical packing arrangement for a thiocarbocyanine dye on a $[110]$ edge on the (111) face of AgBr from a crystal structure determination.

The circles represent surface positions for Ag^+ ions. In the absence of the dye, half of the Ag^+ positions are filled randomly. When an attractive ligand interaction is established between the heterocyclic sulfurs of the dye and two Ag^+ ions, position, A,A' are filled, and B,B' must be emptied to remove a repulsive interaction between the $7,7'$ protons of the dye and the Ag^+ ions. Positions C,C' will be emptied to maintain local electrical near-neutrality if the dye is a cationic carbocyanine. If a charge-compensated betaine dye (e.g. monosulfopropyl) is added, one of the C,C' positions may be filled, or if an anionic dye ($\text{N,N}'$ -disulfopropyl) is added, both may be filled. (Reproduced, with permission, from Ref. 7. Copyright 1974, Society of Photographic Scientists and Engineers.)

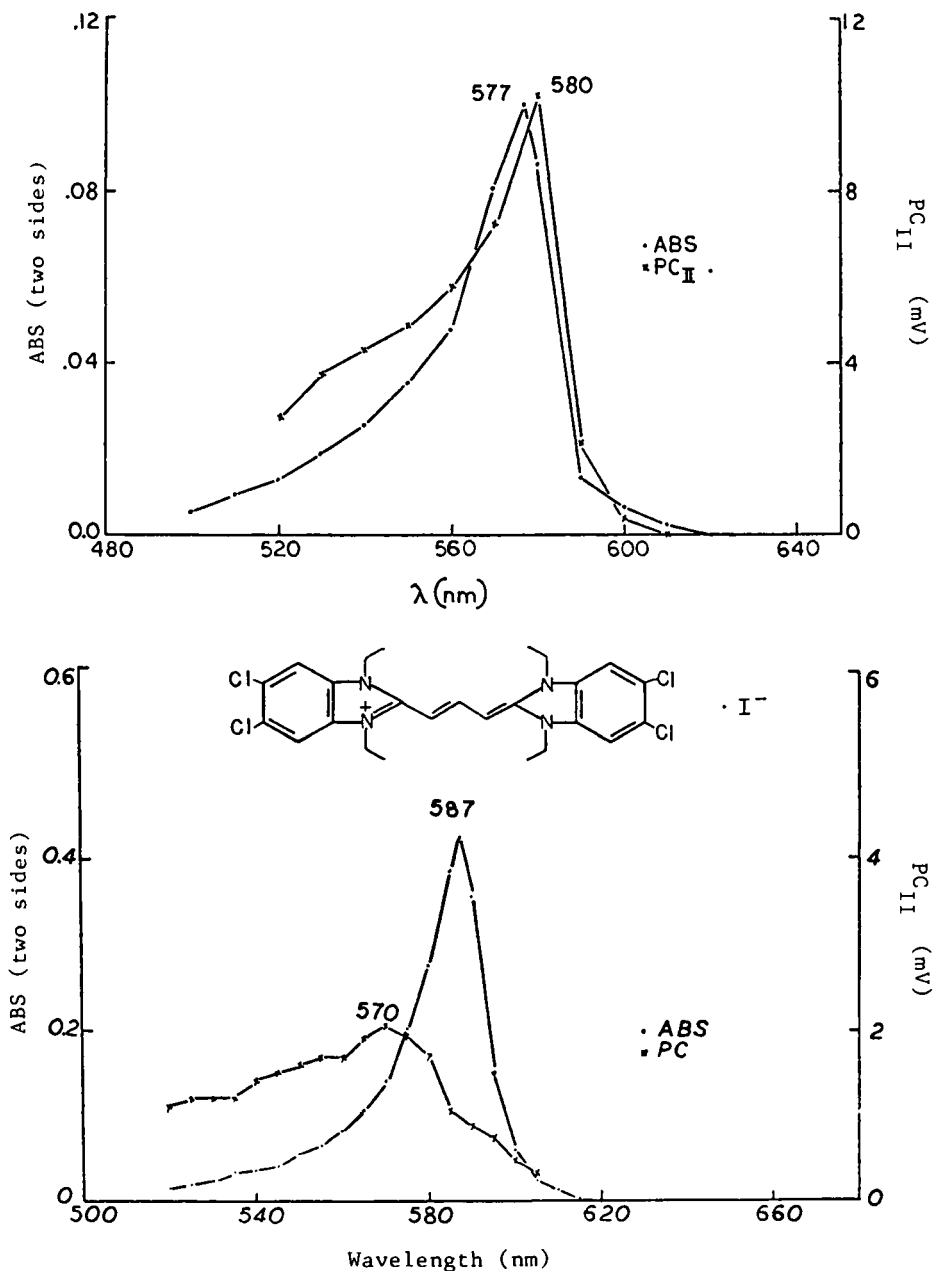


Figure 12. Absorption and photoconducance of a nominal (110) AgCl crystal dyed on both sides with the benzimidazolocarboyanine dye shown (top), and the same dye on a (111) AgBr crystal (bottom).

The PC_{II} values are photoconductivities corrected to equal photon flux at each wavelength of observation. The ratio PC_{II}(λ)/A(λ) is the relative quantum yield of photoelectrons. Note the change in the absorption scales. (Reproduced, with permission, from Ref. 40. Copyright 1978, Society of Photographic Scientists and Engineers.)

pitting of the AgBr surface or an actual AgI overgrowth. However, we should note that multilayer formation soon requires the incorporation of counterions to avoid huge electrostatic effects. Thus a multilayer, like an actual crystalline phase, is expected to be specific to the incorporated counterion. Monolayers and small aggregates are demonstrably independent of the identity of the counterions.

Multilayer coverage has degraded the response of the dye, but not completely destroyed sensitization at the aggregate absorption peak. As multilayer dyeings go, this is an unusually good photoconductive response. The quantum yield is still high at shorter wavelengths, corresponding to small islands of aggregated molecules, if one assumes that the surface is not uniformly covered with multilayers of dye. The long wavelength results make a very simple illustration that not all of the trouble with multilayer sensitization enters at the latent image-forming stage. Instead of an onset of latent image attack by mobile holes, we have here a breakdown of the efficiency of formation and injection of photoelectrons into the AgBr phase. The experimental results are simple to present, but this simplicity conceals a need for painstaking conditioning of the AgBr crystal prior to dyeing and the measurement of photoconductivity. As indicated, the optical measurement of dye absorption is greatly facilitated by use of an integrating sphere attachment with the spectrophotometer (A Cary model 17 in our case).

The use of NaCl as a mock-silver halide substrate has produced some of the most precise and striking surface determinations ever made, and has done so with a set of procedures remarkably free from criticality or difficulty (22). Historically, the use of NaCl was taken up in the hope of obtaining interpretable LEED patterns from dyed NaCl surfaces as an alternative to unsuccessful experiments on AgBr, where it appeared that the dye was decomposed by the combination of electron impact and the presence of a potentially oxidizing substrate (15). A clear diffraction pattern was obtained from the dyed NaCl; however, since epitaxial dye islands were oriented in all possible directions on the crystal surface, the diffraction pattern of the host crystal was simply duplicated - though with an intensity much superior to undyed NaCl. In other words, the LEED experiment indicated only that an epitaxial attachment of dye had occurred. This we already felt we knew.

NaCl is one of the easiest of single crystal materials to obtain and handle. We purchased a 1" x 6" cylindrical rod of the stock commonly sold for making IR sample plates. The rod was stored over a desiccant, and fresh discs were cleaved with hammer and single-edge razor blade as needed. A good cleavage produces a (100) face with a minimum number of terrace steps and an optical quality good enough for direct transmission measurements without

an integrating sphere. Another advantage of NaCl is that it binds cyanine dyes only weakly, so that highly ordered dye layers can be obtained. In general, the J-aggregate absorption bands on NaCl were considerably sharper than the comparison bands on (100) AgCl. Aside from band width considerations, there was no significant difference between the absorption spectra on the two hosts.

Figure (13) shows one of the most remarkable results on NaCl, a systematic spectral shift with increasing surface coverage of dye. As coverage was increased from 22% to 45% to 88% to 100% the absorption peak of the aggregates shifted from 643nm to 648nm to 653nm to 657nm. If we interpret this shift on the basis of the oversimplified point-dipole expression for single column aggregates, the average aggregate lengths are 7, 11, 22, and ∞ molecules per column. But of course the formula is oversimplified, and the aggregates are two-dimensional islands rather than columns. One must either make some simplifying assumption or do an independent determination of the shapes of aggregate islands, before transition density calculations for the actual sizes and shapes of islands can be done. Still, the writer knows of no simpler physical indication of the sizes and shapes of aggregates on a fresh surface of a single crystal. This is a remarkably simple determination, and ought to be of use in basic studies of adsorption effects.

The determination of the adsorption isotherm of the red sensitizing dye 3,3'-sulfoethyl-5,5'-dichloro-9-ethylthiacarbocyanine⁺ gave highly reproducible results. Unlike most of the "isotherms" obtained with dyes strongly bound to silver halides, this weakly bound system was truly reversible, as shown by rapid approach to equilibrium with crystals either overdyed or underdyed before insertion in the final dye bath. The puzzling result is that the isotherms fit the Langmuir equation within experimental error. We do not understand this result at all, since the Langmuir expression is derived for the case of completely independent adsorption sites, whereas this dye is adsorbing in highly ordered, close-packed islands. The fit to the Langmuir expression can only be described as accidental in the sense that some cancellation of forces is occurring. On AgCl a much more sensible cooperative isotherm is obtained, as shown in Figure (14). This result is consistent with the isotherms derived by Hill or by Ross, both containing terms to describe the cooperative interaction between adjacent filled sites (60,61).

Whatever the form of the isotherm, this dye gives a plateau at close-packed monolayer coverage over a wide range of concentrations. The surface occupancy determined from this plateau is $91.7 \pm .9 \text{ \AA}^2$ per molecule. As already indicated, this dye should occupy three unit cell cube surfaces, or 95.4 \AA^2 , a disagreement of 3.9%. The difference is explainable in terms of the excess dye bound at the terrace steps (excess dye = lower apparent area

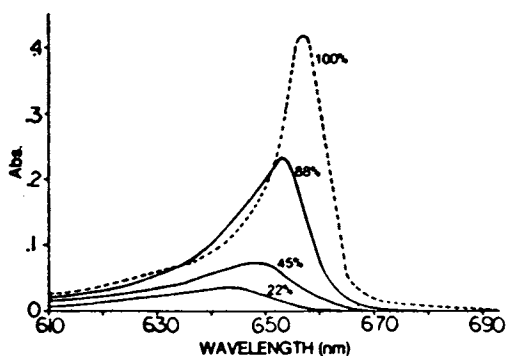


Figure 13. Absorption spectra of a cleaved single crystal of NaCl dyed on both (100) faces with increasing coverages of the dye 3,3'-sulfoethyl-5,5'-dimethyl-9-ethylthiacarbocyanine out of 40% CH_2Cl_2 (dye solvent) and 60% CCl_4 (non-solvent). Wavelengths, coverages, and approximate aggregate sizes are given in the text. (Reproduced, with permission, from Ref. 22. Copyright 1974, Society of Photographic Scientists and Engineers.)

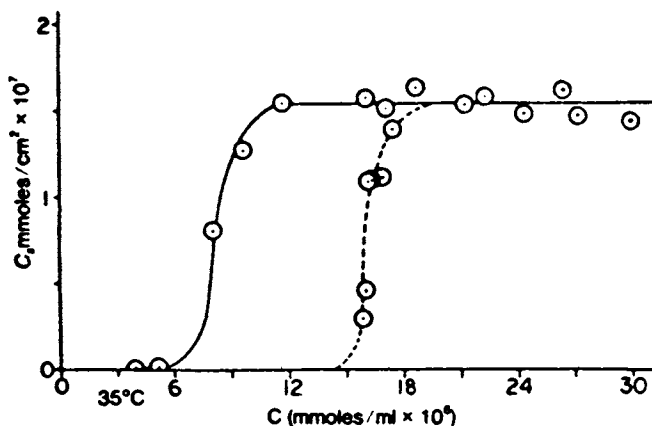


Figure 14. Plots of the isotherms at 35°C on (100) AgCl.

Key: —, 40% CH_2Cl_2 :60% CCl_4 dyeing solution or ---, 30% CH_2Cl_2 :70% CCl_4 solution. The two solvent systems give different isotherms, but the 50% coverage midpoint occurs at the same dye activity, $25\% \pm 2\%$ of saturation in the two solvents. No significant adsorption of monomeric dye has been detected in this system. (Reproduced, with permission, from Ref. 22. Copyright 1974, Society of Photographic Scientists and Engineers.)

occupancy). This is about as precise a determination as one can expect in surface chemistry.

These determinations were made by dyeing discs, cleaving off all of the edges to produce a crystal dyed only on two opposing faces, measuring the absorption spectrum, then stripping off all of the dye with a strong solvent for spectroscopic measurement of the dye concentration in a known volume of stripping solution. Since the cyanine dyes are subject to slow (dark) oxidation reactions in solution, it is important to deaerate the solvents immediately before use for the best quantitative work. Elegant deoxygenation techniques are not required.

These measurements of dyed crystals and stripped dye also allowed the test of conservation of dipole strength as molecules are transported from the solution monomer to the close-packed J-aggregate. Dipole strength is conserved within about 16%, and the shift is in the direction of increasing absorption and dipole strength in the aggregate. There is no hypochromism in the aggregate, though this had been suggested on the basis of UV hypochromism in the spectrum of DNA in the coiled form. This approximate conservation of dipole strength allows the use of the integral form of Beers' Law given in equation (1), and one can do rapid, convenient surface studies through the use of this equation, as applied to single crystals. It should be noted that if a dye system is ever found to adsorb end-on to one of the silver halides on a particular face, the optical absorption of this system will vanish for measurements made with rays propagating perpendicular to that face. One would like to find systems of this sort for other useful purposes, but none have been found.

The surface coverage of this same red sensitizer is found to be about 15% lower on AgCl than on NaCl. This difference can best be attributed to the much stronger adsorption on AgCl, leading to the "parking lot effect". When growing aggregates meet in this situation, there are apt to be numerous sites partially covered by molecules. Extended time of dyeing and increased temperature can ultimately reduce the deviation of the parking lot effect, but the surface ordering process is likely to be slow indeed.

An extension of the studies of packing and light absorption on single crystals is the observation of polarized visible and infrared absorption on selected crystal faces (41,25,42). This gives direct information about the alignment of molecular long axes. Ideally, there should be no polarization when dye is adsorbed to a face of high symmetry such as the octahedral face of AgBr with three-fold symmetry or the cube face with four-fold symmetry. However, when a soft crystal of AgBr is necessarily cut rather than cleaved, the misalignment is usually sufficient to bring on appreciable polarization. It can be inferred that a failure of alignment of ca. 1° can hardly produce some exotic

facial structure - rather, it will tend to produce a non-face which will be immediately attacked by the stripping solvent to produce long, narrow terraces of a stable face. On this basis, Gray et al. prepared a test crystal which was very close to (111) on one side and wedge-finished to be 5° out of (111) on the other side. This one crystal was then single-side dyed successively on the two faces and measured for infrared and visible dichroism. The results are shown in figures (15) and (16). With the crystal dyed with a multilayer coating of the highly symmetric benzimidazolocarbo-cyanine already discussed, it was possible to observe the polarized infrared spectrum using only x10 scale expansion on a modern grating spectrometer. The infrared results were a bit less spectacular than hoped, in that all of the observed IR bands were long axis polarized in the dye molecule and showed the same sense of polarization. The out-of-plane vibrations would be expected to occur at long wavelengths in the region obscured by the IR absorption of AgBr. However, there was one vibration at 1475 cm.^{-1} which disappeared in the change from KBr powder pellet to AgBr face, and this transition was assigned to a short axis polarized band.

The production of dichroic ratios as high as 10 in this experiment was no accident. The off-axis cut was aligned to leave one of the three [110] intercepts (one of the lines of Ag^+ ions in the (111) face) intact. Some of these lines are then expected to become the edges of long, narrow (111) terraces as the face is etched with hypo (25). From the work of Rosenoff et al. the need to nucleate the red-shifted J-aggregates was clear (21), and this lead us to the hypothesis that nucleation would occur, producing polarized absorption in the direction of the preserved [110] edge. This occurred, and the high dichroic ratio was predictable on the basis of the 30° or 19° (111) structures. Spectroscopic observations on a monolayer of a thiocarbo-cyanine dye would indicate that it was in the 19° structure.

There is a second type of adsorption which produces polarization; this is assignable to adsorption on a host face of two-fold or lower symmetry. The (110) face of AgCl is such an aligning face, having alternating parallel lines of Ag^+ and Cl^- ions. Unfortunately, this face is not one of the stable faces of the crystal; one has to assume that etching will produce a corrugated texture of exposed (100) faces, not fundamentally different from the terraces produced by off-axis cutting from the (111) face of AgBr. Pandolfe has explored the alternate possibilities of (100) terraces in the form of troughs in the [100] direction or of actual (110) facial exposure with molecular orientation along the [100] direction in this face (15a). The one fact which became painfully clear from Pandolfe's study was that many alternate epitaxial structures could be conceived to satisfy the conditions of ligand bonding and graphitic stacking of nearest neighbor

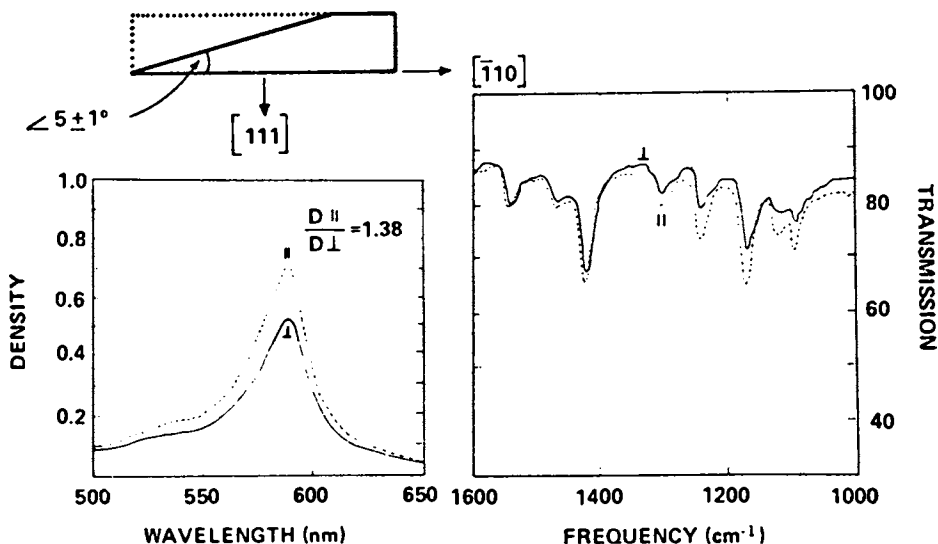


Figure 15. Results of dyeing one side of a single crystal of AgBr with the dye benzimidazolocarboyanine shown in Figure 12.

The face giving the visible and infrared absorption data was polished as close to (111) as possible, and then etched with thiosulfate. The residual dichroism is a consequence of failing to obtain perfect (111) alignment. The opposite side of the crystal was finished 5° off (111) alignment, deliberately inclined to preserve one of the three [110] edges along the line of intersection of the cut with the (111) plane. On etching in hypo, this face is expected to develop long, narrow (111) facets. The high visible and infrared dichroism is consistent with the direction of the preserved [110] intercept. (Reproduced, with permission, from Ref. 25. Copyright 1970, Society of Photographic Scientists and Engineers.)

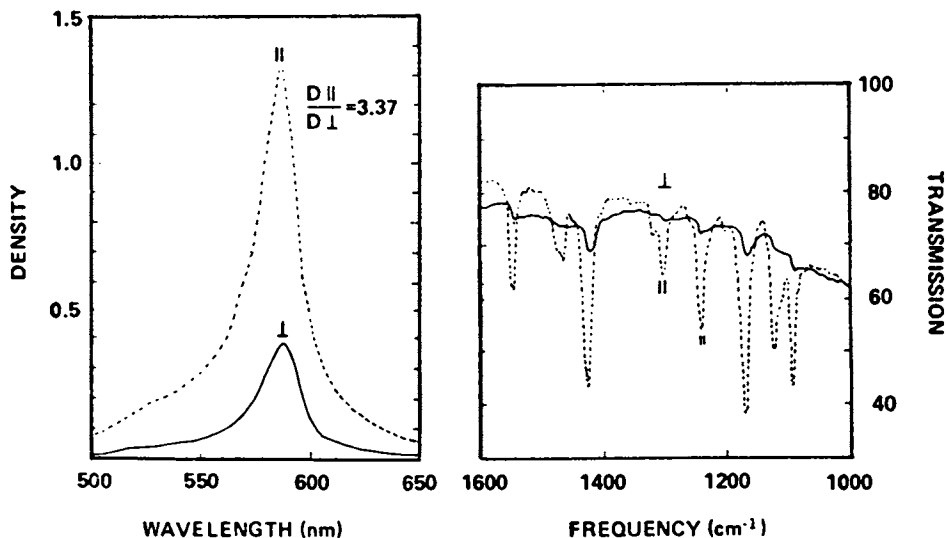


Figure 16. Results of dyeing one side of a single crystal of AgBr with the dye benzimidazolocarboyanine shown in Figure 12. (Reproduced, with permission, from Ref. 25. Copyright 1970, Society of Photographic Scientists and Engineers.)

organic chromophores. It is clear that the simple set of three (111) and two indistinguishable (100) J-aggregate structures does not satisfy his observations of the polarization and spectral shifting on the nominal (110) face of AgCl. For example, the preferentially herringbone-forming dye, 3,3'-carboxyethyl-5,5'-dichlorothiacyanocyanine (29), was forced into a simple J-aggregate with high dichroic ratio on this surface, and the observed absorption peak at 638nm was not appropriate for the (100) face, at least not for a face of large size and high order. The aggregate absorption peak of this dye was broad, suggesting that the aggregates were small and thus less than maximally red-shifted.

The most recent contribution to this increasingly complicated field of polarized aggregate spectra is a pair of papers by Saunders and Lovell (42). The first paper deals exclusively with the old faithful example 1,1'-diethyl-2,2'-cyanine. The twisted, helical structure of individual molecules of this dye precludes it from taking up epitaxial graphitic packing on a host. Saunders and Lovell have noted that the sheet aggregate on a crystal surface must consist of d,l,d,l, etc. enantiomers - a contrast to the helical and optically active solution aggregate. These authors concluded that the polarization of this dye was being governed by the location of terrace steps on their Mitchell-grown crystals (43) with rather arbitrary facial orientations. Their conclusion is supported by the fact that very large aggregates of the dye give the same absorption maximum, 578nm, independent of the approach of the underlying face to (100) or (111). This constancy of absorption wavelength suggests an absence of epitaxial contact for this dye, and potentially sets it apart from the class of modern, state-of-the-art sensitizers.

In the second paper, Saunders and Lovell examine a series of more modern red- and green-sensitizing dyes, and present a wide variety of polarization results. Some dyes do align parallel to the [110] intercept, but others align perpendicular to it. Most puzzling, these authors examined the two dyes oriented by Gray *et al.* and produced the opposite sense of polarization to that found in the earlier study. How is this to be explained?

We might do well to begin with the assumption that all of the observations are, in themselves, correct. There is no fundamental reason why the two studies should agree, since the crystal faces received totally different chemical treatments. Saunders and Lovell took their crystals directly from the growth out of the melt in contact with mica, treated the faces with bromine water to remove Ag_2O and other impurities, but did not reorganize the face with solvents or complexants for Ag^+ , and used only dyes having inactive counterions such as Br^- , Cl^- , or Tosylate $^-$. By contrast, Gray *et al.* had to remove the damaged layer of surface polish by a brief dissolution in photographic hypo ($\text{S}_2\text{O}_3^{=}$). Their

surface is thoroughly reorganized, and is left with adsorbed thiosulfate ions, most of which must be displaced by the adsorbing dye. The symmetrical benzimidazolocarbocyanine dye was added as the iodide, so that extensive surface exchange of I^- for Br^- must have occurred. However, a similar sense of polarization occurred with a Br^- salt of a thiocarbocyanine. We might characterize the two kinds of crystal surfaces as "inorganic, as melted" and "etched and dirty". It is a matter of taste which of these is preferred for a particular investigation, but hereafter the choice should be carefully considered. The schemes of interpretation put forward by the two sets of authors are consistent with their regimens of treatment for the crystals. It seems possible that Gray *et al.* are examining (111) facets, while (100) facets occur in the more recent work.

There are two points on which the writer must register a personal disagreement with some of the conclusions of Saunders and Lovell. One is with the notion, already discussed, that a silver halide surface is inviolate in time, and consists only of flat planes and steps. All of the silver halides have a small but finite solubility in water, and this solubility opens the possibility that the individual Ag^+ and X^- ions can reorganize to accommodate organic dyes while preserving charge neutrality or near-neutrality for the overall surface, as envisioned by Mastropaolo *et al.* (7). Neglect of this possibility tends to trap one into the dogma that silver-sulfur ligand attachments cannot occur in specific cases. The added attractive force of this sort of attachment can be documented from many sources other than arguments from polarization spectra.

The second disagreement concerns the argument surrounding the double-banded absorption of their dye 6: 3,3'-diethyl-9-methyl-thiocarbocyanine⁺ Br^- . Saunders and Lovell obtained on an (014) face (approaching (001)) a double-banded absorption spectra with peaks at 513nm and 580nm and a polarization spectrum which changed angular direction by 60-70° in the center of the band as shown in Figure (17). Noting that the dichroism passed to a minimum value of 0.2 rather than zero in the center of the transition, the authors concluded that the "experimental findings do not agree with the prediction of the herringbone model...". Here we are on very slippery optical ground. The Beckman DU spectrometer used in their investigation has less polarization than a grating spectrometer, but more absolute polarization than is contributed by the weakly absorbing dye layer. The polarizer, rather than the sample is being rotated, and the admittedly strained and birefringent crystal is dyed on both sides. This particular piece of data seems to the writer to be a candidate for the first clear observation of the predicted perpendicular polarization of the two Davydov (exciton) bands of the herringbone structure. Many cases of herringbone aggregates have been seen, including some on hosts such as NaCl, which have very little affinity for monomeric dye or small aggregates.

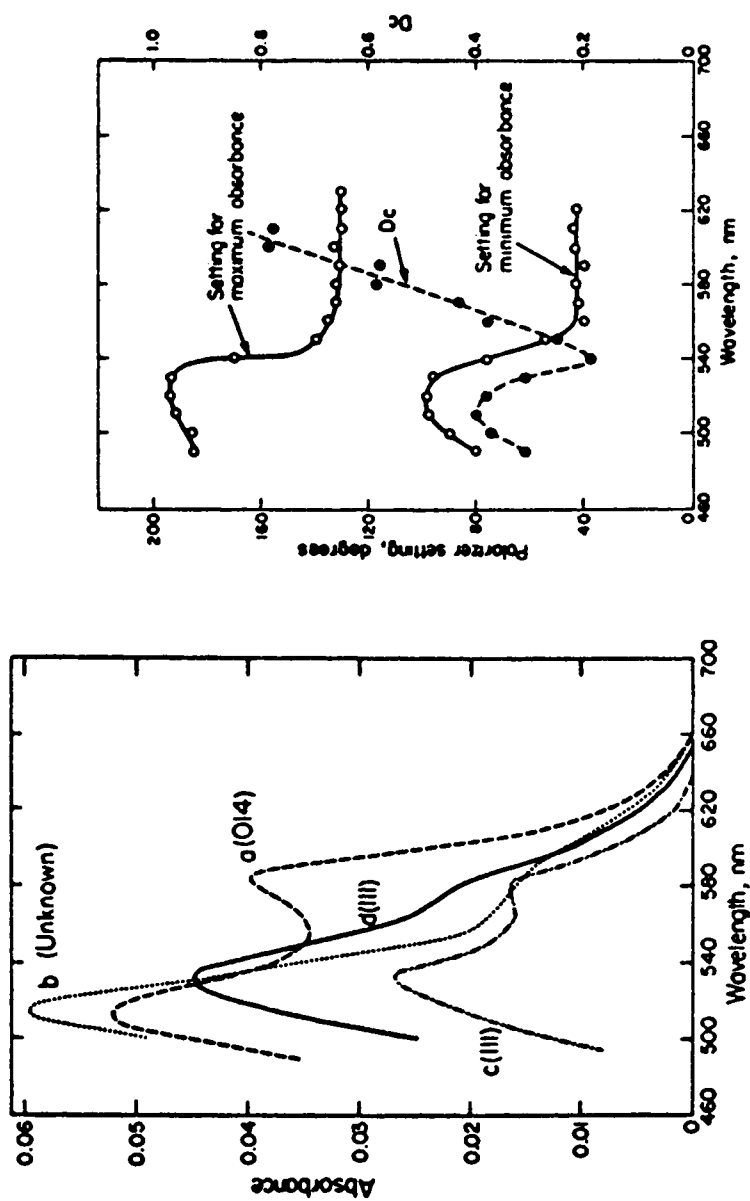


Figure 17. Absorption spectra on selected crystals of the dye, 3,3'-diethyl-9-methylthiacarbocyanine Br⁻, and comparison of dichroism of this dye on a (014) crystal with the absorption spectrum. (Reproduced, with permission, from Ref. 42b. Copyright 1958, Society of Photographic Scientists and Engineers.)

Quibbles aside, the investigation of Saunders and Lovell is a landmark in the field of polarized aggregate spectra, and the point of departure for any future work. Clearly, we need more independent, supportive evidence from other sources. As an example, Pandolfe and Reich in collaboration with Dr. Stephan Platzer attempted to obtain actual electron micrographic evidence for the existence and form of the terrace steps which all of the workers in this field have invoked. Their attempt was not successful, but it ought to be repeated with higher resolution and more sophisticated methods of measurement in future investigations of polarized aggregate spectra. It might also be worthwhile to seek for some independent confirmation of some of Pandolfe's hypothetical (100) and (110) structures of J-aggregated systems, all of which give polarization perpendicular to the [110] edge, and may be a factor in the most recent observations.

To close the discussion of optical studies with dyes, we'll examine a case in which the boundary between epitaxial and non-epitaxial attachment of dyes to a substrate is clearly exposed. This case arose during a 1975 investigation of the ordered attachment of surfactant (N,N' -dioctadecyl) dyes to gypsum with Frau G. Debuch and Prof. D. Möbius at the Max Planck Institute for Biophysical Chemistry at Göttingen (24). The goal of this investigation was to find a method for producing a completely ordered and polarizing dye monolayer in the process of lifting a compressed dye monolayer off the water surface of a Pockels-Blodgett-Langmuir balance (16). Freshly cleaved gypsum was chosen as the lifting material because the cleavage separates the crystal along a set of hydrogen-bonded water contacts, leaving a surface which has parallel lines of Ca^{++} and SO_4^- lines along the crystallographic "a" axis. While gypsum has a highly directing face, it completely lacks any structural coincidence with the graphitic packing of planar dye molecules. Further, one notices that the parallel C_{18} chains tend to impose their own packing order on a typical dye film (19), and thus diminish the possibility of any ordered contact with the surface. Figure (18a) shows three dyes which form reproducible monolayers on the water surface, but give no polarization and very little spectral shift on gypsum relative to films lifted onto glass or glass coated with layers of arachidic acid. When an elongated dye molecule is attached to a highly anisotropic substrate without polarization of absorption, non-epitaxial attachment is all but proved. Figure (18b) shows the very highly polarized spectrum of the last dye tried in this series. This dye has the exact same framework as one of the dyes which gave no polarization, but it also has a central ethyl group which "indexes" the lateral placement of nearest neighbor dye molecules in the monolayer. Further, this dye is probably unique in having a nonplanar structure enforced by the steric repulsion

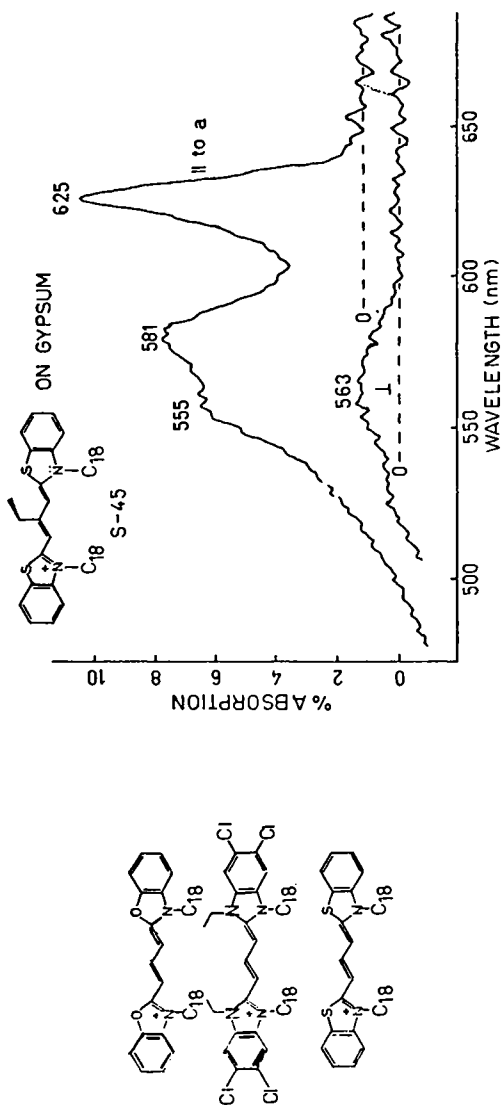


Figure 18. Unambiguous polarization spectrum and three cases of nonepitaxial attachment and unpolarized spectra, and three dyes.

The bands at 555 nm, 581 nm, and 625 nm always appear in the same intensity ratio. These bands are assigned to a single aggregate which has all molecular long axes oriented parallel to the gypsum *a* axis, with at least two molecules in the unit cell. The weak perpendicular band at 563 nm is assigned to a flat-on monomeric dye. To obtain these high polarization ratios, a gypsum cleavage section was dyed on both sides, then cleaved again and measured with dyed sides facing the polarizer and polarizer oriented to favor the internal polarization of the monochromator. (Reproduced from Ref. 24. Copyright 1977, American Chemical Society.)

between the central methylene hydrogens and the heterocyclic sulfur atoms, much like the crystal structure of Potenza and Mastropaolo. A hypothetical epitaxial structure has been proposed for this dye on gypsum, but we do not really understand why this dye orders so well on gypsum. The fact of epitaxial ordering is made especially clear when n-octadecane is added to stiffen the film. This produces no difference at all in the spectrum on gypsum, until the molar ratio of octadecane to dye exceeds 2:1. It would be hard to find a clearer proof of epitaxial attachment. In the end of these considerations of epitaxial attachment, one is left with a certain appreciation for the comic figure of a befuddled man standing in the rain with a large ring of keys and trying to open his front door. When the right key (molecule) is found for the particular door (substrate), the result is most gratifying.

We turn now to a brief consideration of the mysterious "latent image", that entity which is produced by the action of light on the individual grains of silver halide in a photographic film. There is no reasonable doubt that the various latent images consist of clusters of silver atoms (5,44), differing in size (N atoms) and in location. The work of producing a modern high speed commercial emulsion is largely dedicated to optimizing the location of the latent images, their stability, and the level of atomic cluster size at which catalysis of development occurs. One problem in trying to examine the various latent images is that most of the operations for studying them also effectively destroy them - as witness photographic development, which establishes the presence of a successful latent image by destroying (reducing) both the image and the grain of silver halide.

A second problem in examining latent images is that a fully optimized photographic film, as sold, contains so many additives at the level of ca. 10ppm. that it inhibits a rational investigation. Yet this is a field in which non-establishment scientists have been making meaningful contributions and are likely to make more. What one needs is a simple model system derived from the complete commercial negative: this may be either a completely non-photographic experimental system, or it may be a film which has been simplified by the omission of some of the normal proprietary additives such as sulfur, gold, tetraazaindene stabilizers, mercaptan restrainers, and deliberate overgrowth of extra silver halide (which converts a surface latent image into a sensitized internal image). The most sensitive operations of photography are done with surface images, or with the buried images which form on deliberately constructed internal surfaces (45). For some of the investigations to be discussed below, one must make at least a quasi-equilibrium contact with the latent images through the use of electrochemical reagents. Since this necessity is precluded by the internal images, the surface images are the investigator's target of choice.

To give some examples of non-photographic investigations, we note two areas in which the properties of isolated silver clusters have been determined. In the mass spectrometry of negative ions (Ag_N^-), Hortig and Mueller (46) and also Joyes (47) have established a systematic alternation in the magnitude of ion currents, favoring those negative ions which have an odd number of silver atoms. This should be no surprise to a chemist, since the odd anions carry an even number of electrons, whereas the even anions are simply free radicals. One can predict qualitatively that the ionization step from an odd-atom cluster to the anion will proceed easily and without the loss of an atom.

On a more sophisticated plane, Schumacher has initiated a series of investigations in which a tunable laser selectively imparts momentum and thus ejects those clusters in an undifferentiated molecular beam which are absorbing at the particular laser wavelength. The beam emerging from the optical interaction space is then sampled with a simple mass spectrometer, so that the ejected cluster sizes can be identified as to mass (M). Working with this apparatus, Schumacher and his colleagues at Bern have measured excited states and ionization thresholds (48) for discrete small clusters of Na_N , K_N , and Ag_N . Prof. Schumacher is a former director of research of the Ciba Photochemical Division, and has done his share of worrying about silver clusters. Still, his work stands as an investigation which in itself required no special insights or proprietary information from any photographic manufacturer.

Unfortunately, investigations of disconnected clusters are not going to inform us as to what happens on a face of $\text{AgBr}\cdot\text{I}$. The chemical fact is that the cluster of silver atoms is in intimate contact with several silver ions, and its properties must be modified by consideration of electron exchange among these neighbors. The art of quantum mechanical computations has now progressed to a level at which problems of this complexity can be attacked with a large digital computer. Baetzold has initiated this attack, calculating the properties of a variety of sizes and shapes of clusters on flat, terraced, or terrace-kink sites on a model AgBr surface (49). The reader is directed to Baetzold's most recent report in this volume, but we should note two major conclusions for the continuity of this discussion. Baetzold finds that the positive kink site, which has figured strongly in the discussion of latent image formation since the early works of Mitchell (50), is indeed the most stable site for formation of small silver clusters. The cycle of trapping an electron at this site (going from $+1/2e^-$ formal charge at the site to $-1/2$) and then reactivating the site for further electron capture by attracting a mobile interstitial Ag_i^+ ion is indeed the easiest way to form latent images.

Most important is the finding from these calculations that there is an alternation of properties from odd-sized to even-sized latent images. The latent images representing the collection of 2,4,6, etc. photoelectrons are stable with respect to the odd-electron images. This is to say that the positive ion images have special stabilities at Ag_3^+ , Ag_5^+ , and Ag_7^+ as indicated by large ionization energies and relatively small electron affinities. It is difficult to add an electron (small affinity) and difficult to remove an electron. The consequences of these stabilities for photographic development with ordinary developers have not been widely appreciated. This may well be one of the areas where a last state-of-the-art improvement of a fundamental nature can be made in photographic technology.

The best available description of latent image formation is a solid state kinetic model (51) developed by Hamilton and Bayer and subjected to parallel testing on trial emulsions by Spencer, Atwell and Brady. This model has been, from the start, a model for surface latent images. The model makes no direct statement about the threshold for photographic development, but the consequences of any particular threshold are easily tested by assigning developability to any model grain which has one or more latent images at or above the threshold value. The first model dealt only with sulfur sensitization (formation of epitaxial surface Ag_2S over only part of the grain surface) and gave the best comparison with the experimental emulsions when the development threshold was set at $N=5$, producing the cationic image Ag_6^+ . Seen now from the perspective of Baetzold's calculations, this has a ring of truth, as one would expect a relatively easy initiation of reduction at a center bearing an odd number of electrons.

This original model was extended by Harbison and Hamilton to include gold sensitization, the great advance in photographic sensitivity which occurred ca. 1940. Harbison and Hamilton (44) concluded that the presence of gold at the level of 5ppm. allowed the incorporation of gold atoms into the latent image. This stabilized the small latent images considerably, and also seemed to lower the threshold for development. The actual level of sensitivity obtained with gold is a full factor of 10 higher than with sulfur alone, and would be appropriate for a threshold of $N=3$ or possibly $N=2$.

One of the most intriguing entities to be formed on a photographic negative is the "sub-developable latent image" or "latent sub-image" (LSI). This has some very real consequences. One can bring the LSI up to developability by treating a weakly exposed film with a dilute gold solution (gold latensification), or one can resort to optical latensification. This latter is a method of bathing a weakly exposed film with a uniform secondary exposure, necessarily delivered over a long time at very low intensity (1). The trick behind optical latensification is that grains

which do not originally bear a latent image are never nucleated to the level of the first LSI, presumably Ag_3^+ . Grains which do bear one or more LSI's are able to collect additional photoelectrons so that the LSI(s) grow to developable size.

The best point of attack for a determination of the surface electrochemical properties of latent images is at the level of latent sub-images. There can hardly be more than three sizes (2, 3, 4) without gold sensitization, and only one size ($N=2$) with gold. Indeed, the continued presence of optical latensification effects after the application of optimal gold sensitization established the development threshold at $N=3$, not 2, in the presence of gold atoms.

There has been a continuing effort to establish the electrochemical properties of surface latent images through the use of redox buffers as preliminary developers, Reinders (52), Hillson (53), and Berg and Frei (54) have all shown that fully developable latent images can be oxidized (destroyed) by solutions which are reducing with respect to bulk silver. This is in general accord with the relative instability of colloidal particles. It has the odd consequence that buffers as much as 100mv more reducing than the bulk silver potential may destroy the latent images on a film and then, on long standing, fog or reduce the entire film. The early work with buffers has also been troubled by the use of pH-dependent buffers, particularly the $\text{Fe}^{++}/\text{Fe}^{+++}$ -citrate system. Frei has shown that when this redox buffer system penetrates and swells a photographic gelatin coating, the potential measurement at an electrode located at the base of the gelatin layer records a serious excursion from the equilibrium value of the redox potential (55).

Dr. Stephan Platzer and the writer have attempted to produce definitive measurements on the redox properties of images at threshold or in the LSI domain (56). To avoid the complications of pH dependence, redox buffers were chosen which had at least a range of independence to pH excursions, and to avoid selectively rapid diffusion of the reducing or oxidizing components, buffers were selected having 1:1 Fe:Ligand in both the oxidized and reduced forms. This leads us to the iron-EDTA buffer (57), and to a more reducing system, iron-DTPA (diethylenetriaminepentaacetic acid). The price to be paid for increased reliability of the buffer is the natural limitation to a potential range of 120 millivolts, since redox buffering action is lost as the buffer ratio goes outside the limits of 1:10 and 10:1. Thus one requires a set of related buffers to span the potential range of interest. This set is not yet complete, but the partial results using the buffers on hand do reveal some of the critical redox levels in latent image growth and decay.

To gain access to the LSI domain, a new kind of measurement cycle was devised (56). The old cycle was:

**American Chemical
Society Library
1155 16th St., N.W.**

Expose, treat with buffer, develop.

This now becomes the control cycle for the new experimental cycle:

Expose, treat with buffer, optically latensify, develop.

Any major change which comes about as a result of the optical latensification must relate to the LSI which was stable (for a reasonable time) to the buffer, but did not grow to developable size through the action of the buffer. According to the classical theory of latent image stability, the Gibbs-Thompson equation applied to supposedly-round latent image particles (58), there should be no such residue of stable LSI's. Baetzold's calculations encouraged us to seek out the opposite result of stable LSIs.

This kind of investigation can hardly be done without access to research-grade emulsion coatings. This work was performed on a series of special emulsion coatings provided to the writer and Prof. Wolf Berg at the Photographisches Institut in Zurich by Prof. Eric Moisar of the Research Department of the Agfa-Gevaert AG, Leverkusen. The successful redox experiments were done on a lightly sulfur-sensitized monodisperse cubic emulsion of size $0.50\mu\text{m}$ on edge. The emulsion was thinly coated on a film base having a removable antihalo coating on the back side. The properties of single grain size and thin coating are a great help in the investigation, since it is desirable to obtain a maximal fraction of grains bearing LSI(s) but not ordinary developable images.

Figure (19) shows the D/Log E plots for a single buffer treatment at -105.4 mv relative to bulk Ag/AgBr in the same solution. This is a plot of the white light transmission density as a function of the exposure (here calculated in photons/grain from the known grain density, film absorption for 420nm radiation, and the known flux from the xenon flash lamp making the exposure). The exposure is plotted on the customary log scale. The blocks along the x-axis indicate that the buffer alone produced no perceptible gross reduction of the images on the film. The lower curve is the control sequence of Expose, redox, develop, while the upper curve is the result of the full experiment: Expose, redox, latensify, develop. Here it is clear that the buffer treatment leaves undisturbed some LSI(s) which require subsequent growth to enter the developable size range. A similar plot at -160mv shows that at that potential substantially no change results from the latensification, but as the limit of strongly reducing potentials is entered in the DTPA buffer from -170mv to -210mv , a new latensification effect appears. The potential dependence is best seen by plotting curves connecting points of equal exposure on a plot of D vs. Buffer potential. These are the isoexposure curves, shown in Figure (20). On this curve the x's mark the rather abrupt change of slope as the image attack increases from -160mv to -100mv and the + signs mark the mid-density of this transition range. Here it can also be seen that the highest density

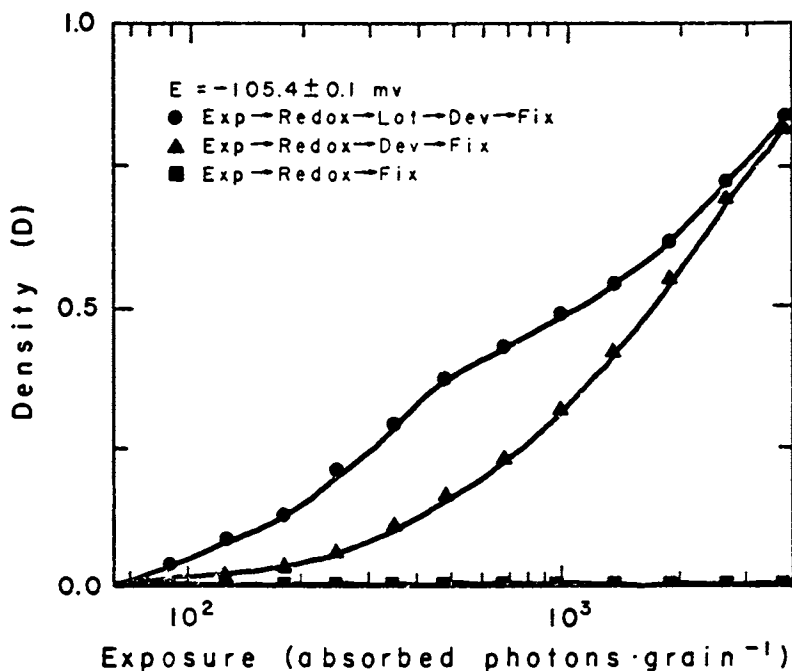


Figure 19. Three photographic characteristic curves for a monodispersed AgBr cubic emulsion (0.5 μ cube edges) bearing a low level of surface sulfur sensitization. In all cases the film was given a 10^{-3} s flash exposure through a photographic step tablet with a step interval of 0.15 density units. The film was then immersed for 15 min in a redox buffer of ferrous/ferric EDTA with a potential of -105.4 mv relative to bulk Ag/AgBr at the same Br⁻ concentration. It is concluded that the small silver clusters of the subdevelopable image are unexpectedly stable (56C).

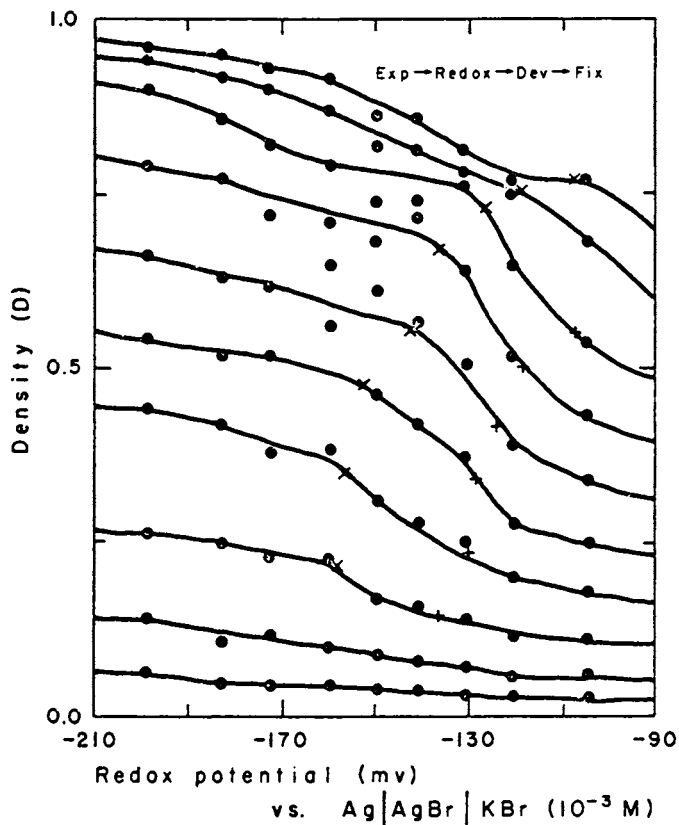


Figure 20. Results of a family of experiments with ferrous/ferric DTPA buffers. Each vertical line of dots corresponds to an experiment like the middle (triangles) plot of $D/\log E$ of Figure 19. There is a region of increasing latent image degradation from -160 mv to -100 mv and beyond. None of the films going into this data plot were treated by optical latensification (56C).

levels, having been produced by large local exposures, represent very large latent images which are relatively invulnerable to the oxidizing action of the buffer. No latensification has been applied to the films of Figure (20).

The density increase (ΔD) produced by latensification is shown in Figure (21). The location of the right hand density growth curve matches the decay curve of Figure (20), and in fact, the growth equals the earlier decay for the lower density curves. In other words, few of the small latent images which are carried down into the LSI range by bleaching at -160 to -100mv are actually destroyed. They persist as more stable LSI's, and can be fully restored by optical latensification. This is completely in accord with Baetzold's calculations and completely contrary to the Logic of the Gibbs-Thompson equation. While we have no first hand knowledge as to the size of the image(s) undergoing bleaching in the range from -160mv to -100mv , the hypothesis can be offered that the transition from $N=5$ to $N=4$ occurs in this potential range. The process follows a Nernst equation or pseudo-Nernst equation with a central potential of -130mv relative to bulk silver.

The return of optical latensification in the range from -170 to -210mv indicates that there is a less stable LSI which is being destroyed completely at potentials less negative than -170mv . This must be the species $N=3$, and possibly $N=2$. The characteristic point of maximum curvature occurs at about -195mv (x's in Figure 21), and it is not possible to fix a reliable mid-point because of the nearness of the other oxidation process. Since $N=3$ images are predicted to be less stable than $N=2$, we offer the hypothesis for future work that this transition goes at least from $N=3$ to $N=2$, and possibly on to complete destruction. We have neither a reliable third buffer selected at this moment, nor any experimental coatings to allow us to proceed farther.

These results have some far reaching implications for the current practices of photographic development. As implied, the LSI is unused in ordinary development. The consequence is a serious loss of film "speed" or sensitivity. Hamilton and Bayer (51) concluded that it took about 30 absorbed photons to bring half of their more heavily sulfur-sensitized grains to threshold at $N=5$. The remaining 25 photons were wasted in $e^- + h^+$ recombination and in the formation of single or multiple LSI's on single grains. It is a basic feature of the kinetics of nucleation that the relative losses decline as the threshold is reduced, and examination of the model for an imaginary threshold of $N=3$ predicts a gain of sensitivity of $2x\frac{5}{3}$ rather than $5/3$. In other words, it would take only 9 absorbed photons to render half of the grains developable at $N=3$. This, roughly, is what happens with gold sensitization.

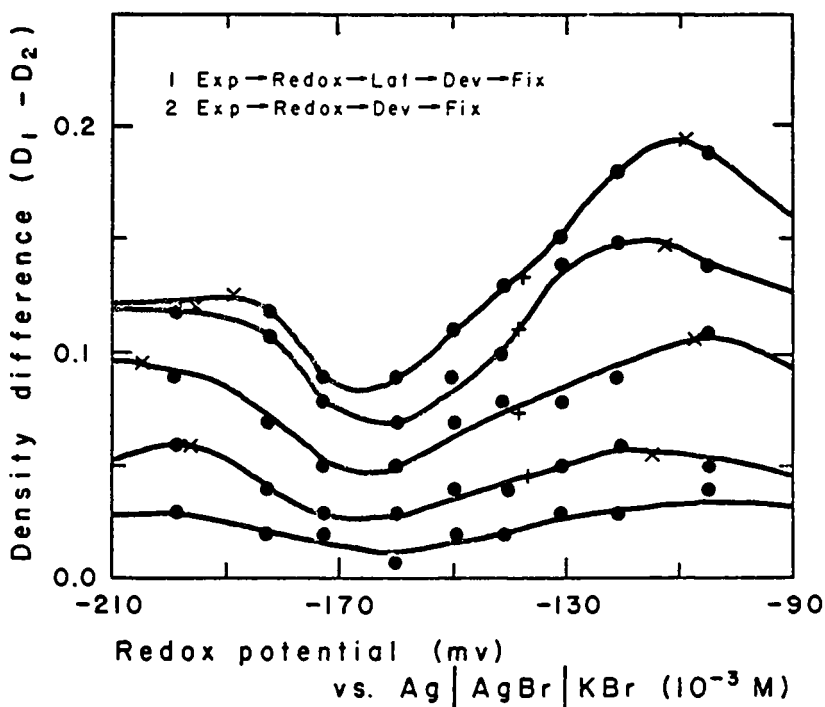


Figure 21. A family of experiments, of the silver density difference produced by treating film samples paralleling Figure 20 with optical latensification after latent image degradation by one of several buffer solutions.

This figure presents a partial analysis of the electrochemical properties of surface silver clusters of discrete sizes, and it established the preferential stability of the small clusters which contain an even number of electrons (as does Ag_5^+).

The unfinished business on silver clusters has to do with the properties of Ag_3^+ and AuAg_2^+ , the smallest possible LSI clusters. The consequences predicted from the Hamilton-Bayer model for threshold at $N=2$ collected photoelectrons are development at approximately 3.5 average absorbed photons per grain, and a total elimination of the loss of sensitivity (High Intensity Reciprocity Failure) suffered in the recording of very short duration exposures. Thus we are considering a potential speed gain of nearly 3 times. Why hasn't this been exploited sometime between 1940 and 1981? It has, of course, but only by those few individuals who practiced optical latensification. An increase of comparable magnitude has also been obtained by those astronomers who employ hydrogen sensitization to eliminate $e^- + h^+$ recombination and thus obtain developability at $N=3$ absorbed photons (59). There remains a need for a comparable increase in sensitivity for the great majority of photographic applications where optical latensification and hydrogen sensitization are equally impractical. At present, we do not know enough about the properties of these smallest clusters to devise a new method of photographic development.

The difficulty in developing the $N=2$ clusters is an indirect problem of selectivity. One can increase the reduction potential of a developer system indefinitely, but at some point the indiscriminate development (fog) of the entire film outruns any success in developing the $N=2$ species. The best modern developers appear to work close to this limit. We do get a tantalizing hint from the buffers, which operate at very mild reducing potentials. In particular, the most reducing DTPA buffer at -210mv might even be in the stability range of the $N=2$ and $N=3$ images, particularly if these contain an atom of gold. The final developer used in our investigation had a reduction potential of about -400mv ; however, as a $2e^-$ organic exchange system, it did not seem to muster this potential effectively to reduce the smallest clusters before the onset of fog generation by prolonged development. Question for future research: Will it be possible to find a $1e^-$ buffer system to be used as a pre-developer to grow the presently sub-developable $2e^-$ cluster AuAg_2^+ to the developable size AuAg_3^+ ? At that point the gross development process could be accomplished by a conventional developer. This would seem to be a worthy problem in surface electrochemistry.

Conclusions

In this paper we have attempted to explore useful tools and unfinished business in the surface science of silver halide photographic systems. The sensitizing dye/AgBr system has been explored as a compliant model system for persons who might wish to carry out fundamental investigations in modes of adsorption and surface phase transitions. Many of the experimental and conceptual tools developed within the photographic industry are

available to facilitate new investigations having little to do with the practice of photographic technology. Please be our guest.

There is one last speed gain to be sought in the silver halide photographic system. This is the lowering of the current development threshold from the surface cluster AuAg_3^+ to the next smaller cluster AuAg_2^+ , representing the successful collection of just two photoelectrons. This may be an attractive problem for chemists interested in the electrochemistry of surfaces and surface clusters. It is a good basic problem and a good applied problem.

Acknowledgements

One of the unexpected pleasures of writing this paper has been to see the emergence of a list of inquisitive friends and colleagues from half a lifetime of research, appearing in the text and bibliography. I greet and thank each of them across the years and the miles. My colleague, Dr. Allan P. Piechowski, has read the emerging manuscript and offered many helpful suggestions. His aid is gratefully acknowledged. Dr. Arthur H. Herz has also read the manuscript and offered critical improvements.

The writer wishes to thank the Society of Photographic Scientists and Engineers for permission to reproduce figures 2,4,5, 6,8,9,10,11,13,14,15,16, and 17 from "Photographic Science and Engineering"; the MacMillan Publishing Company for permission to reproduce figures 1,3, and 7 from "The Theory of the Photographic Process", 4th edition, J.H. James, editor; and the American Chemical Society for permission to reproduce figure 18.

The early work on dye adsorption at Rutgers in the period 1971-4 was supported under a grant from the Air Force Office of Scientific Research (grant AF 2026), and more recent work has been supported by a succession of grants from the Rutgers Research Council.

Literature Cited

- 1a. Bird, G.R.; Jones, R.C.; Ames, A.E. Applied Optics 1969, 8, 2389.
- 1b. Bird, G.R.; Cox, M.D. Photographic Science and Engineering, 1981, 25, 246.
2. Herz, A. Adsorption of Sensitizing Dyes to Silver Halides, Chapter 9 of "The Theory of the Photographic Process", 4th ed., James, T.H., editor, MacMillan Co., New York, 1977.
3. Sturmer, D.M.; Haseltine, D.W. Sensitizing and Densitizing Dyes, Chapter 8 of Ref. 2.
4. West, W.; Gilman, P.B. Spectral Sensitivity and the Mechanism of Spectral Sensitization, Chapter 10 of Ref. 2.

5. Hamilton, J.F.; Kellogg, L.M. Mechanism of the Formation of the Latent Image, Chapter 4 of Ref. 2.
6. Klein, E.; Metz, H.J.; Moisar, E. Photogr. Korresp. 1963, 99, 99.
7. Mastropaolo, D.; Potenza, J.; Bird, G.R. Photog. Sci. and Eng. 1974, 18, 450.
8. Smith, D.L. Ibid. 1974, 18, 309.
9. Bird, G.R.; Norland, K.S.; Rosenoff, A.E.; Michand, H.B. Ibid. 1968, 12, 196.
- 10a. Newmiller, R.J.; Pontius, R.B. Ibid. 1961, 5, 283.
- 10b. Unpublished work of Gray, W.E. and Brewer, W.R., private communication.
- 11a. Corbin, D.; Gingello, A.; MacIntyre, G.; Carroll, B.H. Photog. Sci. and Eng. 1980, 24, 45.
- 11b. Tani, T.; Saito, M. Ibid. 1979, 23, 323.
12. Bird, G.R. Ibid. 1974, 18, 562.
13. Möbius, D.; Kuhn, H. Ibid. 1974, 18, 629.
14. Gilman, P.B., Jr. Ibid. 1974, 18, 475.
- 15a. Structural Study of Sensitizing Dyes and Their Aggregate Formation on Solid Substrates, Pandolfe, W.D. Doctoral Thesis, Rutgers University, 1974.
- 15b. Unpublished joint investigation by Prof. W. Bottoms, Dept. of Electrical and Electronic Engineering, Princeton University and W.D. Pandolfe and G.R. Bird, Dept. of Chemistry, Rutgers University in the period 1973-4.
16. Kuhn, H.; Möbius, D. Angew. Chemie, Internat'l. Ed. 1971, 10, 620 (in English).
- 17a. Spence, J.; Carroll, B.H. J. Phys. Colloid Chem., 1948, 52, 1090.
- 17b. Borin, V.I. Uspeki Nauch. Fotogr. Akad. Nauk SSSR, Otdel Khim Nauk 1969, 7, 183. (Translation available from Assoc. Technical Services).
- 18a. Penner, T.L.; Gilman, P.B., Jr. Photog. Sci. and Eng. 1975, 19, 102.
- 18b. Bird, G.R.; Rosenoff, A.E. U.S. Patent, 1971, 3,622,316.
19. O'Brien, D.F. Photog. Sci. and Eng. 1974, 18, 16.
20. Herz, A.; Danner, R.; Janusonis, G. Absorption from Aqueous Solution, Advances in Chemistry Series No. 79, Am. Chem. Soc., Washington, D.C., 1968, p. 173.
21. Rosenoff, A.E.; Walworth, V.K.; Bird, G.R. Photog. Sci. and Eng. 1970, 14, 328.
22. Pandolfe, W.D.; Bird, G.R. Ibid. 1974, 18, 340.
23. Zuckerman, B.; Mingace, H. J. Chem. Phys. 1969, 50, 3432.
24. Bird, G.R.; Debuch, G.; Möbius, D. J. Phys. Chem. 1977, 81, 2657.
25. Gray, W.E.; Brewer, W.R.; Bird, G.R. Photog. Sci. and Eng. 1970, 14, 316.
26. West, W.; Carroll, B.H.; Whitcomb, D. J. Phys. Chem. 1952, 56, 1054.
- 27a. Yoshioka, H.; Nakatsu, K. Chem. Phys. Lett. 1971, 11, 255.
- 27b. Dammeier, B.; Hoppe, W. Acta Cryst. 1971, B27, 2364.

28. McRae, E.G.; Kasha, M. J. Chem. Phys. 1958, 28, 721.
29. Reich, C. Photog. Sci. and Eng. 1974, 18, 335.
30. Norland, K.; Ames, A.; Taylor, T. Ibid. 1970, 14, 295.
31. Reich, C.; Pandolfe, W.D.; Bird, G.R. Ibid. 1973, 17, 334.
32. Energy Studies of Cyanine Dyes Free and Bound to Substrates, C. Reich, Doctoral Thesis, Rutgers University, 1977.
33. Walworth, V.K.; Rosenoff, A.E.; Bird, G.R. Photog. Sci. and Eng. 1970, 14, 321.
34. West, W.; Geddes, A.L. J. Phys. Chem. 1964, 68, 837.
35. Simson, J.M. Photog. Sci. and Eng. 1974, 18, 302.
36. Smith, D.L. Ibid. 1972, 16, 329.
37. Bird, G.R. Ibid. 1971, 15, 134.
38. Potenza, J.; Mastropaolo, D. Acta Cryst. 1974, 30B, 2353.
- 39a. Sage, J.P. J. Phys. Chem. Solids 1965, 26, 1245.
- 39b. Zuckerman, B. Photog. Sci. and Eng. 1967, 11, 156.
- 40a. Photoconductivity of Silver Halide-Dye Systems. A.P. Piechowski, doctoral thesis, Rutgers University 1976.
- 40b. Gardner, W.L.; Herz, A.H. Photog. Sci. and Eng. 1978, 22, 13.
41. West, W.; Saunders, V.I. Wiss. Photog. (Proc. 1956 Cologne Conf., Verlag Dr. O. Helwich, Darmstadt, 1958).
- 42a. Saunders, V.I.; Lovell, S.P. Photog. Sci. and Eng. 1980, 24, 171.
- 42b. Saunders, V.I.; Lovell, S.P. Photog. Sci. and Eng. 1980, 24, 176.
43. Hedges, J.M.; Mitchell, J.W. Phil. Mag. 1953, 44, 223 and 357.
44. Harbison, J.M.; Hamilton, J.F. Photog. Sci. and Eng. 1975, 19, 322.
- 45a. Moisar, E.; Wagner, S. Ber. der Bunsenges. 1963, 67, 356.
- 45b. Junkers, G.; Klein, E.; Moisar, E. J. Photog. Sci. 1974, 22, 174.
- 45c. Sturmer, D.M.; Blackburn, L.N. Photog. Sci. and Eng. 1975, 19, 352.
46. Hortig, G.; Muller, M. Z. Phys. 1969, 221, 119.
47. Joyes, P. J. Phys. Chem. Solids, 1971, 32, 1269.
48. Herrmann, A.; Schumacher, E.; Woste, L. J. Chem. Phys. 1978, 68, 2327.
49. Baetzold, R. Photog. Sci. and Eng. 1973, 17, 78.
50. Mitchell, J.W. Photog. Sci. and Eng. 1978, 22, 249 and 1979, 23, 1.
- 51a. Hamilton, J.F.; Bayer, B.E. J. Opt. Soc. Am. 1965, 55, 528.
- 51b. Bayer, B.E.; Hamilton, J.F. Ibid. 1965, 55, 439.
- 51c. Spencer, H.E.; Atwell, R.E. Ibid. 1964, 54, 498.
- 51d. Spencer, H.E.; Brady, L.E.; Hamilton, J.F. Ibid. 1964, 54, 492.
52. Reinders, W. J. Phys. Chem. 1934, 38, 783.
53. Hillson, P.J. J. Photog. Sci. 1958, 6, 97.
54. Berg, W.F.; Frei, E.A. Photog. Sci. and Eng. 1969, 13, 81.
55. Frei, E.A. Photog. Korresp. 1969, 105, 5.

- 56a. Bird, G.R., lecture and manuscript presented at the Chibissoff Symposium, Moscow, U.S.S.R., May, 1977.
- 56b. Platzer, S.J.W.; Bird, G.R., Alternation of the Electrochemical Properties of Surface Sub-Latent and Latent Images, XIV Int'l. Cong. on Photog. Sci. (ICPS), Rochester, New York, August 1978, pp. 75-7 of Conf. Book (Avail. Soc. Photog. Sci. and Eng., Washington, D.C.).
- 56c. Electrochemical and Fading Properties of Surface Sublatent and Latent Images, S.J.W. Platzer, Doctoral Thesis, Rutgers Univ., 1978.
- 57a. Rzymkowski, J. Pharmazie, 1951, 6, 155; Sci. Ind. Photog. 1954, 25, 385.
- 57b. James, T.H. Photog. Sci. and Eng. 1960, 4, 271.
- 58a. Konstantinov, I.; Panov, A.; Malinowski, J. J. Photog. Sci. 1973, 21, 250.
- 58b. Ibid. 1975, 23, 1.
- 59a. Babcock, T.A.; Ferguson, P.M.; Lewis, W.C.; James, T.H. Photog. Sci. and Eng. 1975, 19, 49.
- 59b. Babcock, T.A.; James, T.H. Ibid. 1976, 24, 19.
60. Hill, T.L. An Introduction to Statistical Thermodynamics, Addison-Werley, Massachusetts, 1960.
61. Ross, S.; Olivier, J.P. On Physical Adsorption, Interscience Publishers, New York, 1946.
62. Vanassche, W. Photog. Sci. and Eng. 1974, 18, 288.

RECEIVED December 21, 1981

Properties of Silver Particles

R. C. BAETZOLD

Eastman Kodak Company, Research Laboratories, Rochester, NY 14650

Small silver particles form the amplification center in conventional photographic processes. Although these particles play an important role in technology, the understanding of their microscopic physical and chemical properties is in a rather rudimentary stage. This paper will focus on the properties of these particles as probed by molecular orbital calculations and photoemission spectroscopy.

Calculations have shed light on the mechanism of formation of silver particles by the action of light on silver halide. We find that surface defect sites present a particularly favorable trapping level for electrons. After this trapping step, silver ions diffuse to the electron, forming a deeper trap for additional electrons.

Ultraviolet photoemission spectroscopy (UPS) has been used to measure the energy levels of small silver particles in a model system. We find that small particles have properties quite different from those of the bulk and that their electron-donating ability increases with size. The UPS difference spectrum of halogen chemisorbed to silver particles changes up to a size of ~40 silver atoms, indicating the size range over which chemical properties are size dependent.

I will illustrate the application of two techniques to the study of problems involving latent-image silver. These techniques are molecular orbital calculations and ultraviolet photoemission spectroscopy (UPS). The calculations are used to model the processes of formation of silver particles through photolysis. The spectroscopic measurements are used to determine properties of the silver particle as a function of its size.

Results

We begin by considering the photolysis of AgBr in Figure 1. Here bandgap excitation produces an electron and a hole. We consider that the hole is removed at a special site or impurity (T). The electron is trapped at another special site (S) in the crystal. At this time an interstitial silver ion (Ag_i^+) diffuses to the trapped electron, forming a silver atom. Now if the trapping level of the silver atom is sufficient, another electron will be trapped at the original site and the whole process will be repeated many times. This process follows the mechanism of Gurney-Mott (1).

Now let us consider the nature of the special sites. We have performed CNDO calculations (2,3) for silver cluster species adsorbed at various defects in the AgBr model to learn how the defect might influence the growth of silver particles. The AgBr models are shown in Figure 2. We consider 22-ion models having a planar array with a partial overlayer of ions as shown in Figure 2. The single kink can be positive or negative, depending upon ion placement, and should bear a partial charge as determined by the missing ions. The double kink is neutral.

Let us calculate the electron affinity (EA) and ionization potential (IP) of clusters of silver species adsorbed to virtual sites near the defect. These levels are shown for the positive kink in Figure 3 relative to their positions in the valence and conduction bands of the model. The EA has a sawtooth behavior but is larger than the AgBr EA for neutral clusters of all sizes up to 8 atoms. Thus, electron trapping will occur at clusters on the positive kink. Corresponding data for the negative and double kink are shown in Figure 4.

The Ag_2 and Ag_4 species on the negative kink cannot trap conduction-band electrons, based upon the energetics in Figure 4. In addition, Ag_4 cannot trap electrons at the double kink, as illustrated by this figure. These results show that the most favorable site for electron trapping is at the positive kink and that latent image would not grow at the negative or double kink. These results are in accord with expectations based purely upon coulombic considerations and thus seem very reasonable.

Let us consider the energetics of Ag_i^+ attraction at the clusters. We have calculated the binding energy of Ag^+ at a bare negative kink and various clusters to make this analysis. If the cluster has a net negative charge it is always energetically favorable for the Ag^+ to be attracted to the cluster as compared to binding at a negative kink. However, this is not the case if the cluster net charge is zero, as the data of Table I show. An interstitial silver ion is more favorably bound to the bare negative kink than the clusters on the positive kink, except for Ag_5 .

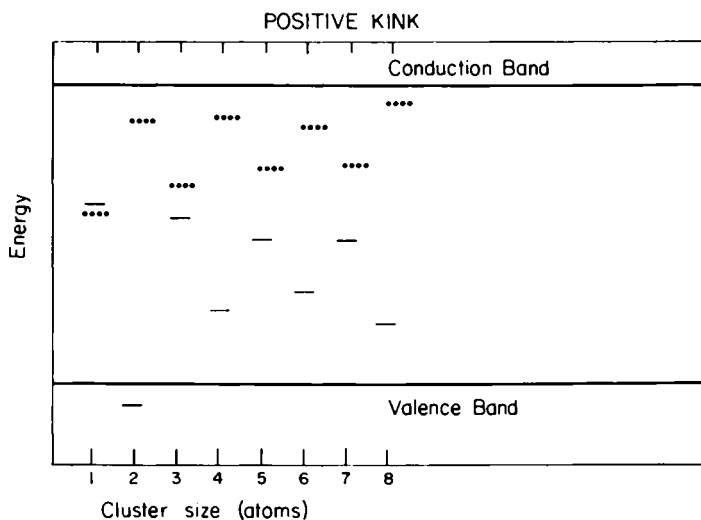


Figure 3. Electron affinity ($\cdot \cdot \cdot$) and ionization potential (—) for silver clusters on positive-kink model vs. the conduction- and valence-band edges.

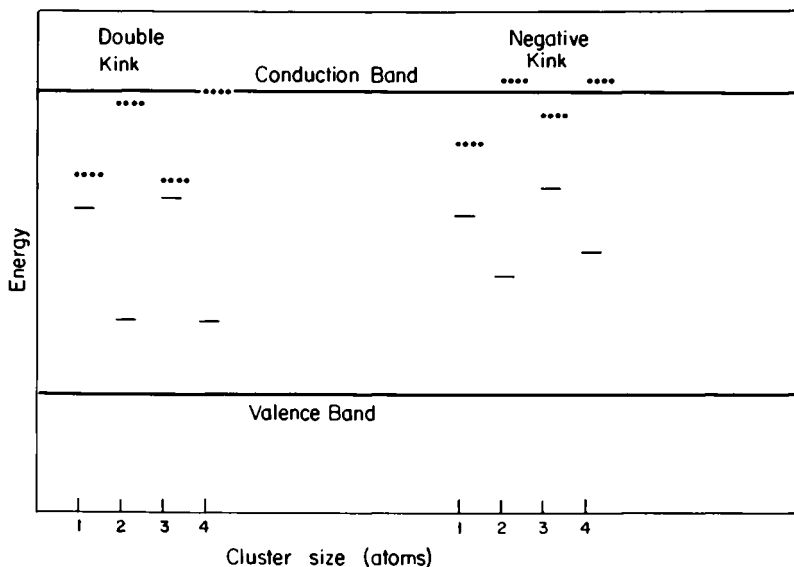


Figure 4. Electron affinity ($\cdot \cdot \cdot$) and ionization potential (—) for silver clusters on double- and negative-kink models vs. the conduction- and valence-band edges.

Table I
Binding Energy of Ag⁺ at Various Sites

Binding Energy of Ag⁺ (eV) at Negative Kink = 1.68 eV

<u>Number of Ag Atoms in Cluster</u>	<u>On Positive Kink</u>	<u>On Negative Kink</u>	<u>On Neutral Kink</u>
1	0.22	2.15	1.26
2	1.06	1.97	2.31
3	1.05	2.34	1.40
4	1.19	--	0.97
5	1.71	--	--
6	0.93	--	--

This is true for most of the species on the neutral kink, but not true on the negative kink. Adsorption of an Ag⁺ species at the negative kink would convert it to a positive kink, so this would provide a path for latent-image growth.

This work shows that a positively charged site provides an energetically favorable site for silver cluster growth on AgBr. Certainly the site need not be restricted to the positive kink site as we considered in this work. Any site with partial positive charge will suffice. The important point is that the site determines the path of growth and in particular its charge plays a dominant role.

Let us consider silver particles prepared on a model system for our experimental studies. The clusters were prepared inside the spectrometer by evaporation from thermally heated tungsten sources using high-purity wires. The substrate used was carbon prepared by prior evaporation onto mica with the technique and equipment described by Hamilton et al. (4). Upon introduction into the spectrometer, the carbon film was ion-etched with Xe, to remove traces of O₂ or S. These samples remained clean for a few days before use as substrates for the evaporated metal.

The metal coverage was monitored by Auger spectroscopy (AES) and with a quartz crystal oscillator. These data were calibrated by neutron activation analysis to ensure proper determination of the amount of material deposited. The change in frequency of the quartz oscillator was proportional to the film thickness.

Gaseous CHCl₃ was obtained from the vapor phase in equilibrium with liquid. Several freeze-pump-thaw cycles were used before vapor was admitted to the chamber. Vapor was admitted with all electron guns turned off and the ion pump isolated from the chamber. Exposure levels were monitored with an ionization gauge.

All photoemission spectra were recorded using He(I) emission. The photons were incident upon the sample at ~70° from the sample

normal, which was aligned with the analyzer axis. The double-pass CMA was operated at a resolution of 0.16 eV for photoemission. Typically 50-100 scans were signal-averaged over a time span of 30 min to reduce noise levels. These spectra were stored on tape for data manipulation.

Auger spectra were taken to ensure cleanness of the metal deposits. These were not recorded until after photoemission was completed. Using AES, we found that exposure of Cu single crystals to CHCl_3 or CH_3I produced a halogen layer with no detectable C fragments on the surface (5). Of course, it is possible that some level of C below AES detection limits could be deposited on the surface of the metal. For Ag single crystals the situation is more ambiguous because of the coincidence of a minor Ag peak with the C peak in the AES spectrum. We are sure that principally halogen is deposited on the Ag surface, but we cannot eliminate the possibility that small amounts of C are also deposited (6). Evidence for halogen deposition on the metal surface includes the observation that the Ag/C signal ratio measured by AES decreases ~10% after chemisorption.

The He(I) photoemission spectra of clean silver clusters evaporated onto carbon are shown in Figure 5. Here we observe coverage-dependent effects (7). The d threshold is particularly sensitive to cluster size. It is much sharper and shifted to lower binding energy for larger cluster size. From measurements at the half-maximum we estimate a shift of 1.0 eV from the lowest to the highest coverage in Figure 5. This region occurs at the top of the d band of silver and shows up only at higher coverages because the silver d band threshold has shifted 1.0 eV towards smaller binding energies. We conclude that 150 atoms are required to give a bulklike photoemission spectrum of silver, which provides one measure of the convergence of cluster properties to bulk. For this result, we used the nucleation data of Hamilton et al. (4) to associate a mean size with each coverage in Figure 5.

Exposure of clean silver clusters to CHCl_3 produces a layer of Cl on the cluster surface. We have measured the photoemission He(I) spectrum before and after chemisorption of CHCl_3 and show these difference spectra for several metal coverages in Figure 6. We note that there are two peaks in the halogen spectrum which change in intensity as the silver coverage changes. The low-binding-energy peak gains in intensity as the coverage increases, just as was observed for I_2 chemisorption (7). In addition there is a shift in halogen peak position with size. The low-binding-energy peak shifts from 4.4 eV at the lowest coverage to 3.9 eV at the highest silver coverage. The spectral shape becomes constant in the region 8×10^{14} to 1.0×10^{15} atoms/cm², which corresponds to hemispherical particles containing on the mean average 30-40 atoms. All of these spectra correspond to halogen saturation coverage (i.e., 1000 L exposure by CHCl_3), which is monitored by Auger spectroscopy. The Cl/Ag signal ratio measured by this technique has the value 0.65 below 1×10^{15} atoms/cm² of silver

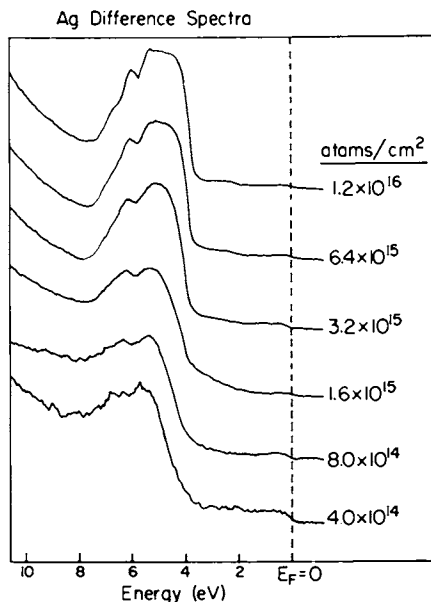


Figure 5. Difference spectra for Ag clusters evaporated on carbon as measured by He(I) photoemission for various silver coverages (Reproduced from Ref. 12.)

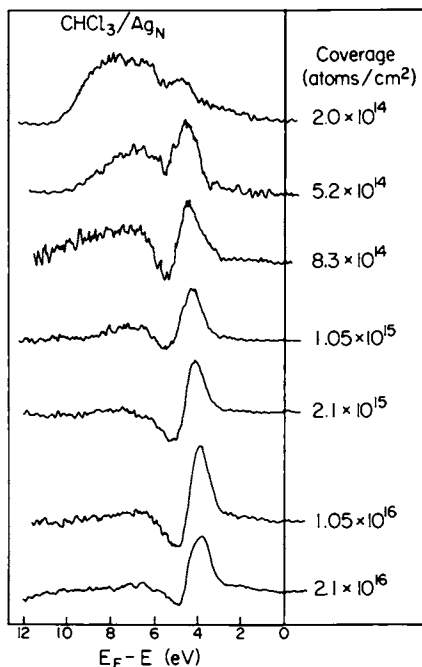


Figure 6. Difference spectra for Cl chemisorbed to Ag clusters of different coverage obtained through CHCl₃ exposure and He(I) photoemission. (Reproduced from Ref. 12.)

coverage and showed a small decrease with increasing silver coverage.

Experiments were also done with Cl_2 as the gaseous reactant in place of CHCl_3 . The same behavior was found in both cases. This result shows that if any C is deposited along with Cl during exposure of Ag to CHCl_3 , it has minor influence on the difference spectra.

We note that the work function increases upon CHCl_3 chemisorption for silver and copper clusters. The work-function change is monitored by the change in width of the photoelectron energy distribution curve (Table II). We find an increase in work

Table II

Position of d Edge (d), Position of the Cl Adsorbate Peak (p^d), and Change in Work Function ($\Delta\Phi^{\text{Cl}}$) for CHCl_3

Chemisorption on Ag Clusters

Coverage, <u>atoms/cm²</u>	d, <u>eV</u>	$\Delta\Phi^{\text{Cl}}$, <u>eV</u>	p^d , <u>eV</u>
2×10^{14}	5.8	0.0	4.4
5×10^{14}	5.6	0.1	4.4
1×10^{15}	5.5	0.2	4.2
2×10^{15}	5.3	0.3	4.0
5×10^{15}	5.2	0.9	3.9
1×10^{16}	5.1	0.9	3.9

function increase in work function for Cl chemisorption which becomes greater as the metal coverage increases. These data indicate that as the fraction of surface covered by metal increases, the electron-withdrawing properties of Cl become more apparent. We have also shown in Table II the position of the leading edge of the d band (at half-maximum) and the peak position of the low-binding-energy Cl-induced peak as a function of metal coverage. These data show a decrease in binding energy of both quantities but they do not seem to scale with the work-function change.

Discussion

Chemisorptive properties of small metal particles depend upon the size of the particle. We find that the orbital spectrum of halogen (Cl) is dependent upon the size of the silver particle to

which it is chemisorbed. A particle size of ~ 30 -40 atoms is required for this spectrum to reach a limiting shape. This result suggests that rather large clusters are required to model chemisorption involving the strong interactions present in the halogen-silver system.

The interactions between different halogen atoms and metal clusters may be understood on the basis of Figure 7, which shows the interaction of a halogen p orbital with a silver d orbital. As the levels are separated in energy, the mixing decreases and the situation corresponds more to that on small particles. Of course, in all cases there is an interaction between halogen p orbitals and s orbitals of the metal. This interaction is less apparent in our experiments because in the UPS technique s orbitals have a relatively small cross-section. Nevertheless, the positive region in the halogen difference curves on the low-binding-energy side of the d band is partly caused by this type of interaction.

The understanding of the basic mechanism of photolysis of silver halide is incomplete yet vital for the planning and interpretation of experiments. This fact is illustrated by the ramifications inherent in the contemporary discussions of the latent image in silver halide. There are the conventional Gurney-Mott mechanism (1) and the thermodynamic model (8,9). We have described the Gurney-Mott model. The thermodynamic view envisages nucleation of a supersaturated concentration of silver atoms in silver halide as induced by light. Obviously the effect of external variables is quite different in the two mechanisms.

Our calculations and experiments have shown that at the critical development size (10,11) the silver cluster is not metallic. Computationally the IP and EA values have not converged and are quite sensitive to location of the cluster on the ionic lattice. Experimentally we see photoemission properties of the cluster that deviate markedly from the bulk up to 150 atoms. For Cl chemisorption a cluster of ~ 40 atoms is necessary to give a "bulklike" adsorbate spectrum.

The interaction of a chlorine atom (hole) with a silver cluster depends markedly upon cluster size. This effect can be inferred from the general decrease in IP as cluster size increases (Figure 3) as manifested in the Cl difference spectra (Figure 6). The Cl difference spectra show a shift of 0.5 eV towards E_F (Table II) with increasing cluster size. Of course only the direction of shift is important in correlations with the IP change since the partially covalent bonding with Cl complicates the situation.

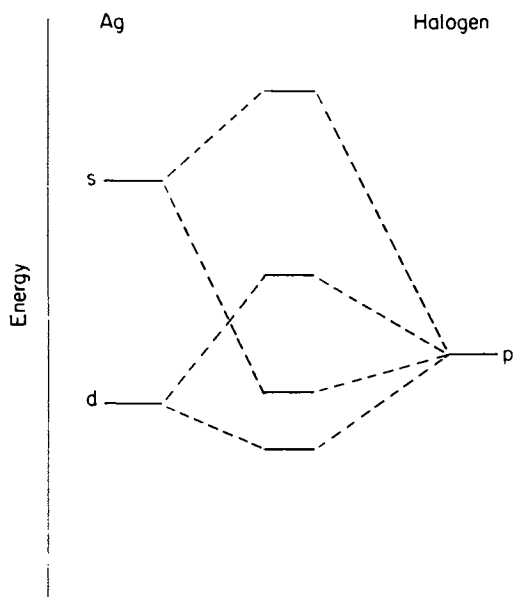


Figure 7. Orbital interaction scheme for Ag s and d orbitals with halogen p orbitals.

Literature Cited

1. Gurney, R. W.; Mott, N. F. Proc. R. Soc. London, Ser. A 1938, 164, 151.
2. Baetzold, R. C. Photogr. Sci. Eng. 1975, 19, 11.
3. Baetzold, R. C. J. Photogr. Sci. 1980, 28, 15.
4. Hamilton, J. F.; Logel, P. C. Thin Solid Films 1973, 16, 41; 1974, 23, 89.
5. Baetzold, R. C. Surf. Sci. 1980, 95, 286.
6. Gerenser, L. J.; Baetzold, R. C. Surf. Sci. 1980, 99, 259.
7. Baetzold, R. C.; Gerenser, L. J. Chem. Phys. Lett. 1980, 73, 67.
8. Moisar, E.; Granzer, F.; Dantrich, D.; Palm, E. J. Photogr. Sci. 1977, 25, 12.
9. Malinowski, J. Photogr. Sci. Eng. 1979, 23, 99.
10. Hamilton, J. F.; Logel, P. C. Photogr. Sci. Eng. 1974, 18, 507.
11. James, T. H., Ed., "The Theory of the Photographic Process," 4th ed.; Macmillan: New York, 1977.
12. Baetzold, R. C. J. Am. Chem. Soc., submitted.

RECEIVED April 7, 1982

Light-induced Electron Spin Resonance Signals of Dyes on the Surface of Silver Bromide Microcrystals: Photographic Effects

TADAAKI TANI

Fuji Photo Film Company, Research Laboratories, Ashigara,
Minami-ashigara, Kanagawa, Japan

Analysis of light-induced ESR signals of sensitizing dyes on the surface of AgBr microcrystals in photographic emulsions revealed that positive holes trapped by the dyes were responsible for the ESR signals and desensitization caused by the dyes. It was demonstrated from the ESR and sensitometric measurements that positive holes trapped by the dyes could react in several minutes with latent images on the surface of the microcrystals.

It was found that photographic sensitizing dyes exhibited light-induced ESR signal when adsorbed to the surface of large crystal of silver bromide (1,2) or silver bromide microcrystals (grains) in photographic emulsions (3, 4, 5, 6). Since the light-induced ESR signal was caused by the interaction between sensitizing dyes and silver halide under illumination, it is of great importance to analyze the ESR signals of various photographic sensitizing dyes adsorbed on the surface of silver halide grains in photographic emulsions in order to understand the mechanisms of photographic effects caused by the dyes.

Experimental

Photographic emulsions composed of octahedral silver bromide grains were used in these experiments. The average grain size was $0.7 \mu\text{m}$, or $0.2 \mu\text{m}$. Methanolic solutions of various dyes were added to the emulsions, which were then coated at about $40 \text{ mg silver bromide/dm}^2$ and at about $30 \text{ mg gelatin/dm}^2$ on cellulose triacetate film base. The coated films were subjected to both ESR and sensitometric measurements at room temperature.

The measurements of ESR spectra were made by use of Electron Spin Resonance Spectrometer Model JES-ME-3X made by Japan Electron Optics Laboratory Co. Ltd. with X band and magnetic field

0097-6156/82/0200-0071\$06.00/0
© 1982 American Chemical Society

modulation of 100 KHz. Several strips of the coated film were put into a quartz sample tube and subjected to measurements of ESR signals with a Xenon lamp (500 W) made by Ushio Electric Co. as a light source.

The sensitometric measurements were made as follows : The coated films were exposed for 10 sec to a tungsten lamp (color temperature : 2854 K) or for 10^{-3} sec to a Xenon flash lamp in an EG & G sensitometer through a filter and a continuous wedge. The exposed films were subjected to surface development at 20°C for 10 minutes. The surface developer used was MAA-1 described by James et al. (7).

Dyes Studied and Their Electronic Energy Levels

The molecular structures of the dyes studied in this paper are shown in Table 1. According to the earlier papers (3, 8, 9) the lowest vacant and the highest occupied electronic energy levels of dyes, ϵ_{lv} and ϵ_{ho} , respectively, were estimated on the basis of the following correlations.

$$\epsilon_{lv} = - E_{Red} + C$$

$$\epsilon_{ho} = - E_{Red} - E_{tr} + C$$

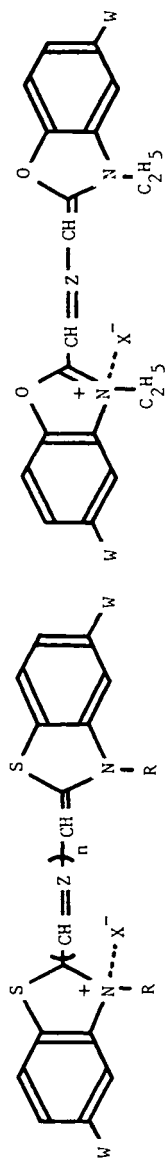
where E_{Red} and E_{tr} are polarographic half-wave reduction potential and transition energy of a dye respectively, and C is electrochemical constant. The estimated electronic energy levels of the dyes studied are shown in Figure 1, where horizontal lines marked by C.B. and V.B. are the estimated positions of the bottom of the conduction band and of the top of the valence band of silver bromide.

Analysis of Light-induced ESR Signals of Dyes

The coated emulsions gave no ESR signal in the dark regardless of the presence of any sensitizing dye. The coated emulsions without any dye added gave no ESR signal even when they were exposed to light. The emulsions to which particular sensitizing dyes were added gave ESR signals under illumination, and light absorption by the sensitizing dyes as well as by silver halides in emulsions resulted in the appearance of the ESR signals. The light-induced ESR signal of Dye 1 in emulsions is shown in Figure 2.

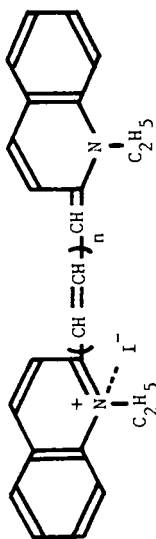
The appearance of the light-induced ESR signal of dyes were dependent neither upon molecular structures nor upon the height of the lowest vacant electronic energy level of the dyes, whereas it depended upon the height of the highest occupied level of the dyes. As shown in Fig. 1, the highest occupied levels of the dyes which gave the ESR signals were higher than those of the dyes which did not give any ESR signals, and by more than 0.3 eV higher than the top of the valence band of silver bromide.

Table 1. Dyes Studied in This Paper.

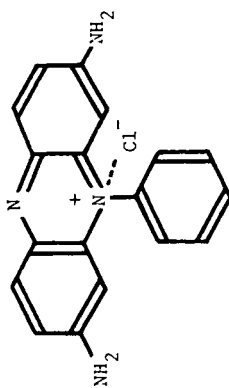


Dye	n	R	W	Z	X
1	1	C ₂ H ₅	H	CCH ₃	Br
2	1	C ₂ H ₅	Cl	CC ₂ H ₅	pts
3	1	C ₃ H ₆ SO ₃ ⁻	Cl	CC ₂ H ₅	-
4	0	C ₂ H ₅	H	CH	Br ⁻
5	1	C ₂ H ₅	H	CH	Br ⁻
6	2	C ₂ H ₅	H	CH	Br ⁻
7	3	C ₂ H ₅	H	CH	Br ⁻

Dye	Z	W	X
10	CH	H	I
11	CC ₂ H ₅	H	I
12	CC ₂ H ₅	Cl	I
13	CC ₂ H ₅	Ph	SCN



Dye	n
8	0
9	1



Dye 14

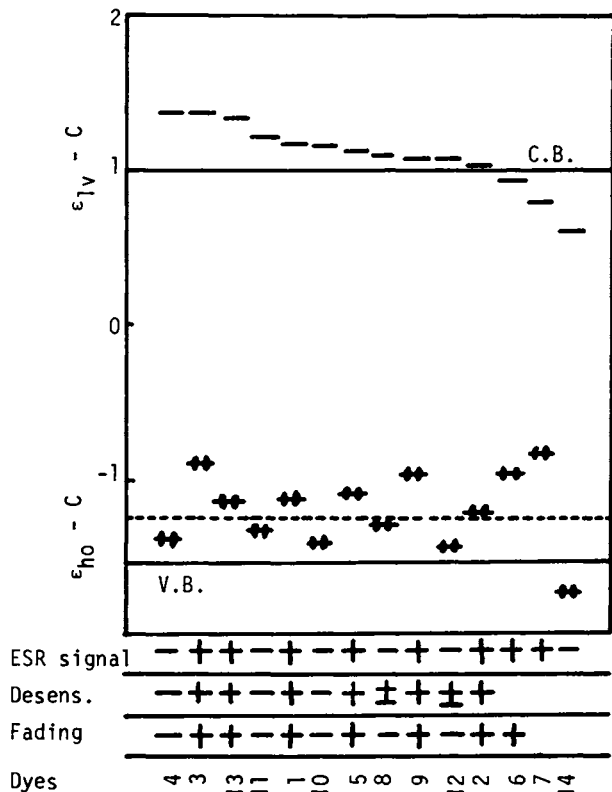


Figure 1. The lowest vacant electronic energy level (ϵ_{lv}) and the highest occupied one (ϵ_{ho}) of dyes as correlated with the appearance of the light-induced ESR signal, desensitization, and latent image fading by the corresponding dyes.

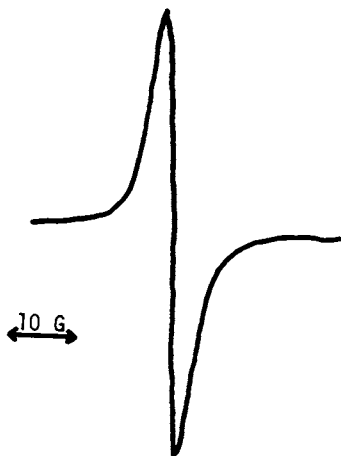
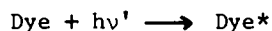
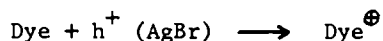
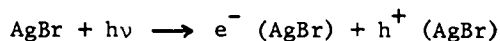


Figure 2. Light-induced ESR signal appeared at $g = 2.005$ of $0.7 \mu\text{m}$ AgBr emulsion to which 7×10^{-5} mol Dye / mol AgBr was added.

Figure 3 shows decay curves of the light-induced ESR signals of various dyes in emulsions. As shown in Figure 4, the decay time was in the order of several minutes, depending upon the kind of dyes, and increased with the increase of the height of the highest occupied level of dyes.

In general, the higher the highest occupied level of a dye is, the longer is the residence time of a positive hole trapped by the dye, and thus the higher is the concentration of dye positive holes on the grain surface under illumination. Therefore, the above-stated results indicated that the light-induced ESR signals were caused by the formation of dye positive holes Dye^{\oplus} through the following processes.



where $e^{-}(\text{AgBr})$ and $h^{+}(\text{AgBr})$ are an electron and a positive hole in AgBr grains.

It should be noted that the observed light-induced ESR signal of dyes was sharp and lacked any hyperfine structure. The signal, which was broad and Gaussian in shape at liquid nitrogen temperature, became sharper as the temperature of the ESR measurement was increased, and was Lorentzian in shape at room temperature.

Y. Sano (15) examined the dependence of the intensity of the ESR signal of Dye 3 upon microwave power, and observed the appearance of saturation phenomenon of the signal intensity at the microwave power which was much larger than that for the ESR measurement in this paper. The microwave power at which the saturation phenomenon appeared increased with the increase of the amount of the dye adsorbed on the emulsion grains. It is considered that the increase in the amount of the adsorbed dye resulted in the increase in the size of dye aggregates and thus in the acceleration of the interconversional interaction through each dye aggregate.

The above-stated results could indicate that some kind of interconversional interaction such as rapid spin exchange or intermolecular electron transfer was taking place through each dye aggregate during the ESR measurement.

Correlation between ESR Signals and Photographic Phenomena

Several strips of coated film were exposed to light in the sample tube of the ESR spectrometer and developed. Figure 5 shows

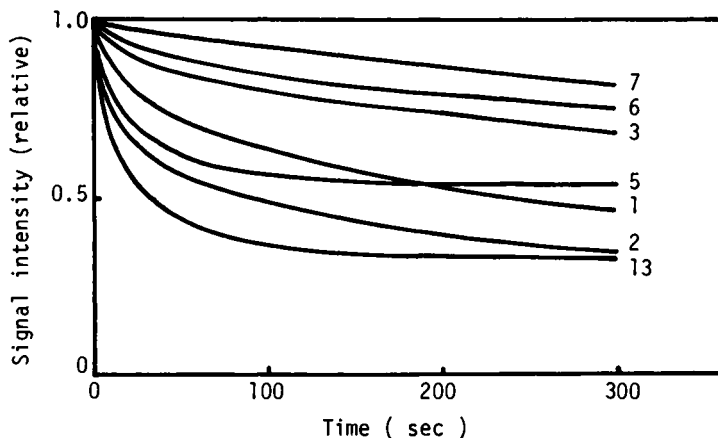


Figure 3. Decay curves of light-induced ESR signals of various dyes in $0.7 \mu\text{m}$ AgBr emulsion. The numbers in this figure denote the dyes listed in Table 1. The amount of the dye added to the emulsion was 7×10^{-5} mol/mol AgBr.

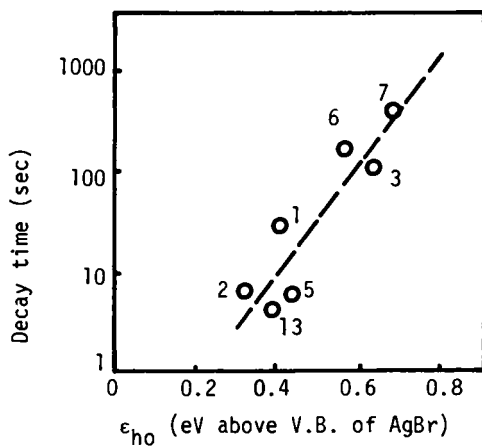


Figure 4. Decay time of light-induced ESR signal of dyes in $0.1 \mu\text{m}$ AgBr emulsion as a function of the height of the highest occupied electronic energy level ϵ_{ho} of the corresponding dyes with reference to the top of the valence band of AgBr.

The numbers refer to the dyes listed in Table 1. The amount of the dyes added to the emulsion was 7×10^{-5} mol/mol AgBr.

the relation between optical density of the developed strips and the amount of the exposure. As shown in this figure, the exposure amount used for the ESR measurement was not so overwhelmingly large as compared with the exposure amount required for latent image formation. Therefore, it was considered that the ESR measurement could be used for the analysis of photographic processes.

Figures 6 and 7 show the dependence of the intensity of the light-induced ESR signals of Dye 3 in emulsions upon reduction sensitization by use of stannous shloride and upon addition of Rh (III) to the emulsions. In accord with the view that small silver specks formed during reduction sensitization capture positive holes (10, 11), the above-stated reduction sensitization decreased the intensity of the ESR signal, which were related to dye positive holes. In accord with the view that Rh (III) captures photoelectrons in AgBr (12), thus accelerating the separation between photoelectrons and positive holes, the addition of Rh (III) to emulsions increased the intensity of the ESR signal.

Sensitizing dyes often brought about the decrease in blue (intrinsic) sensitivity of emulsions, which was called desensitization. As shown in Figure 8, both degree of desensitization and ESR signal intensity increased with the increase of the height of the highest occupied level. The above-stated result indicated that the ESR signal reflected the behavior of dye positive holes.

In accord with the fact that the ESR signal of dyes, which correlated well with degree of their desensitization, decayed in several minutes as shown in Figures 3 and 4, latent images also faded in several minutes in the presence of various dyes. Figure 9 shows the latent image fading in the emulsions containing Dye 3. As summarized in Figure 1, only the dyes which gave the light-induced ESR signal and strong desensitization caused the latent image fading.

The above-stated results indicate that the desensitization which was observed in this paper was mainly caused by the reaction of dye positive holes with latent images, being similar to that observed in core/shell emulsions (13,14). In addition, the present investigation indicated that, being correlated well with the behaviors of light-induced ESR signal of dyes in emulsions, the above-stated desensitization occurred in several minutes after exposure to light in the presence of the dyes whose highest occupied levels were higher than the top of the valence band of silver bromide by 0.3 eV or more.

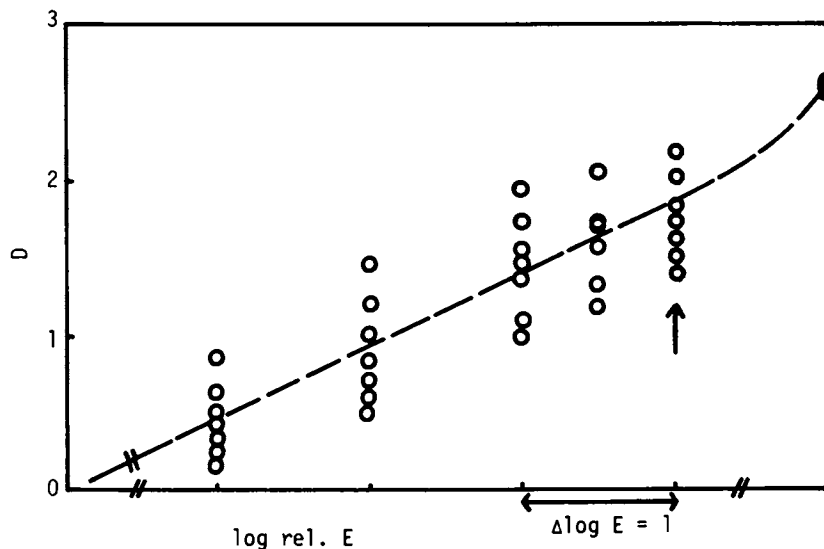


Figure 5. D -log E curves of strips of film coated with $0.2 \mu\text{m}$ AgBr emulsion containing 5.5×10^{-4} mol Dye 3/mol AgBr, which was exposed to light with exposure amount E in a sample tube in an ESR spectrometer and developed. The exposure amount for the ESR measurement is shown by the arrow.

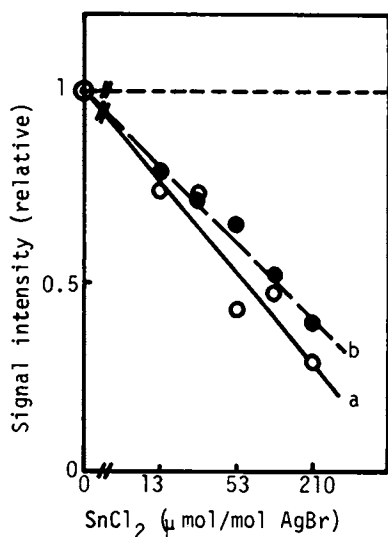


Figure 6. ESR signal intensity for Dye 3 in $0.2 \mu\text{m}$ AgBr emulsion under illumination to blue (a) and minus-blue light (b) as a function of the amount of SnCl_2 used for reduction sensitization of the emulsion. The amount of Dye 3 was 5.5×10^{-4} mol/mol AgBr.

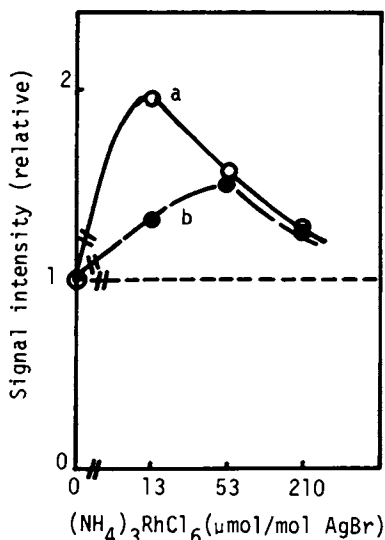


Figure 7. ESR signal intensity for Dye 3 in $0.2 \mu\text{m}$ AgBr emulsion under illumination to blue (a) and minus-blue light (b) as a function of $(\text{NH}_4)_3\text{RhCl}_6$ added to the emulsion. The amount of Dye 3 was 5.5×10^{-4} mol/mol AgBr.

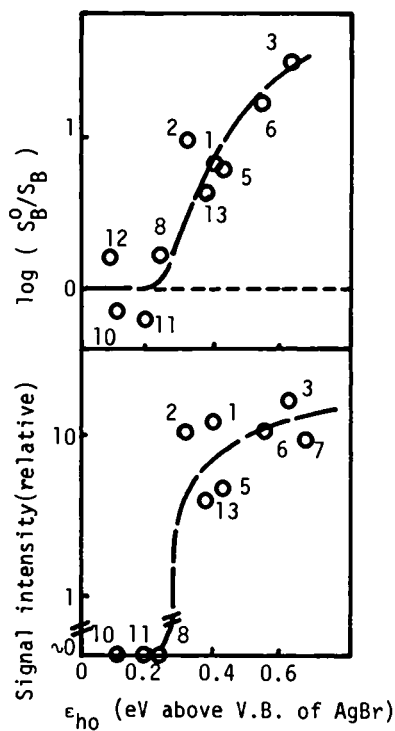


Figure 8. Intensity of light-induced ESR signal and degree of desensitization (S_B^0/S_B) by dyes in $0.7 \mu\text{m}$ AgBr emulsion as a function of the height of the highest occupied electronic energy level ϵ_{ho} of the corresponding dyes with reference to the top of the valence band of AgBr, where S_B^0 and S_B are blue (intrinsic) sensitivities of the emulsion without and with dyes. The numbers refer to the dyes listed in Table 1.

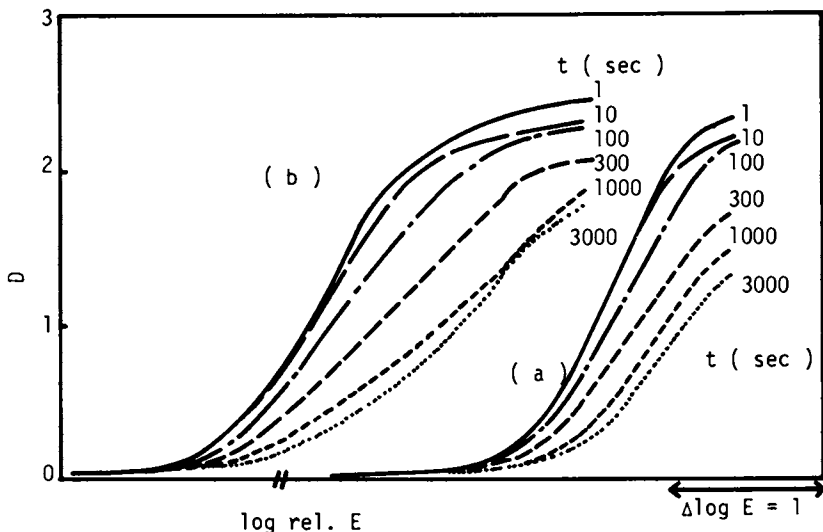


Figure 9. D -log E curves showing latent fading in $0.2 \mu\text{m}$ AgBr emulsion to which Dye 3 was added. Coated film was exposed for 10^{-3} s to blue (a) and minus-blue light (b), kept for t (s), and developed. The amount of Dye 3 was 5.5×10^{-4} mol/mol AgBr.

Acknowledgement

The present author should like to thank Mr. Yasuhisa Sano for his helpful cooperation and discussions.

Literature Cited

1. Needler, W. C.; Griffith, R. L.; West, W. Nature 1961, **191**, 902.
2. Kholmogorov, V. F.; Akimov, I. Dokl. Akad. Nauk SSSR 1962, **144**, 402.
3. Tani, T. Photogr. Sci. Eng. 1975, **19**, 356.
4. Kocherov, N. P. Photogr. Sci. Eng. 1978, **22**, 132.
5. Tani, T.; Sano, Y. J. Photogr. Sci. 1979, **27**, 231.
6. Tani, T.; Sano, Y.; Saito, M. Photogr. Sci. Eng. 1979, **23**, 240.
7. James, T. H.; Vanselow, W.; Quirk, R. F. Photogr. Sci. Tech. 1953, **19B**, 170.
8. Tani, T.; Honda, K.; Kikuchi, S. J. Electrochem. Soc. Japan 1969, **37**, 17.
9. Tani, T. Photogr. Sci. Eng. 1970, **14**, 72.
10. Spencer, H. E.; Brady, L. E.; Hamilton, J. F. J. Opt. Soc. Am. 1967, **57**, 1020.
11. Tani, T. Photogr. Sci. Eng. 1972, **16**, 35.
12. Eachus, R. S.; Graves, R. E.; J. Chem. Phys. 1973, **59**, 2160.
13. Evans, F. J.; Gilman, P. B. Photogr. Sci. Eng. 1975, **19**, 333.
14. Simson, J. M.; Gaugh, W. S. Photogr. Sci. Eng. 1975, **19**, 339.
15. Sano, Y., to be published elsewhere.

RECEIVED April 30, 1982

Silver Halide Precipitation and Colloid Formation

INGO H. LEUBNER

Eastman Kodak Company, Research Laboratories, Rochester, NY 14650

Formation of colloidal silver halide dispersions (photographic emulsions) is one of the principal steps in the preparation of conventional photographic materials. At the same time it presents scientific challenges, some of which are common to general colloid formation, such as control of crystal size, size distribution, and morphology. In precipitation, two processes are of special interest, i.e., formation of stable crystal nuclei (nucleation) and subsequent growth. This sequential process is specifically involved in the double-jet precipitation of silver bromide. For this case, a theoretical model of nucleation was derived which is based on a dynamic mass balance and a growth mechanism which includes bulk diffusion and the Gibbs-Thomson effect. In qualitative agreement with this theory, experiments showed that the number of stable nuclei increased with increasing reactant addition rate and decreased with increasing solubility and temperature. Subsequent growth of the crystals can be described by a simple mass-balance equation, as long as the growth rate is below a limiting maximum growth rate above which renucleation occurs. The growth rate was related to a growth model based on bulk diffusion and crystal number density. For AgBr, the morphology is dependent on the pAg of the crystal suspension.

In the formation of colloids, the control of particle size, size distribution, and particle morphology is a great scientific and technical challenge. Colloidal silver halide dispersions in gelatine (photographic "emulsions") can be considered as model systems for colloids which are formed by precipitation of sparingly soluble salts. The formation of silver halide emulsions has been studied in great detail¹⁻⁴ and it is likely that the results of these studies can be applied to other colloidal systems.

Three basic methods have generally been employed in the precipitation of silver halides: single-jet, double-jet, and continuous (Figure 1).^{1,5,6} In the single-jet method, the silver

0097-6156/82/0200-0081\$06.00/0

© 1982 American Chemical Society

solution (usually silver nitrate) is introduced into an agitated solution of excess halide and gelatin. In the double-jet method, silver nitrate and halide solutions are introduced simultaneously into a stirred gelatin solution. In the continuous process, silver nitrate, halide, and gelatin solutions are combined simultaneously and product is removed continuously to achieve steady-state conditions.

Of these methods, the double-jet method leads generally to a relative uniform ("monodisperse") crystal population with uniform morphology when material addition rates, temperature, and pAg are closely controlled (Figure 2).^{1,6} For such systems, nucleation and subsequent growth have been studied in detail. The present review will concentrate on some recent developments in these areas.

The course of precipitation of most sparingly soluble salts in double-jet precipitations can be illustrated by the schematic plot of the supersaturation ratio S vs. time (Figure 3). S is defined as the ratio of the bulk solute concentration C to the equilibrium solubility C_s . As soon as the reactants are introduced, S increases very rapidly and exceeds the critical value S_c for spontaneous nucleation at $t = t_1$. S will now increase at a lower rate owing to solid-phase nucleation and subsequent growth until a maximum is reached. Thereafter, S will decrease and drop below S_c at $t = t_2$; observable nucleation will then stop. The region between t_1 and t_2 is usually referred to as the "nucleation region." Between t_2 and t_3 is a "transient region" where S continues to decrease rapidly. In this region the number of nuclei may actually decrease owing to dissolution of some of the smaller crystals. At $t > t_3$ a quasi-steady state is obtained where further decrease is not appreciable and the total number of crystals remains practically constant. This quasi-steady state region is also characterized as the "growth region" of precipitation.

In kinetic studies of the formation of silver bromide, Meehan and Miller⁷ found that formation of colloidal material was complete within 6 msec or less. They further concluded that fast flocculation, in which every collision of particles results in an agglomeration, occurs during the mixing process and for a few seconds thereafter. Berry and Skillman⁸ and Berriman⁹ determined that the total number of silver halide crystals remained essentially unchanged after the first minute of double-jet precipitation.

The Nucleation Stage

For the nucleation in double-jet precipitation of silver halides, a dynamic model was derived which relates the final number of stable nuclei to various precipitation variables:²

$$Z = \frac{R R T}{8\pi\gamma DV_m C_s (\bar{r}/r^*-1)} \quad (1)$$

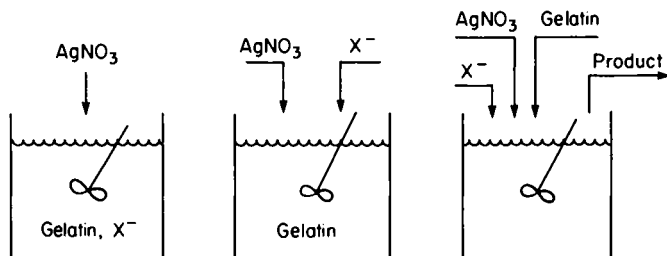


Figure 1. Schematic of basic AgX precipitation methods. Key: single-jet, left; double-jet, middle; and continuous, right. (Reproduced, with permission, from Ref. 6. Copyright 1981, Marcel Dekker, Inc.)

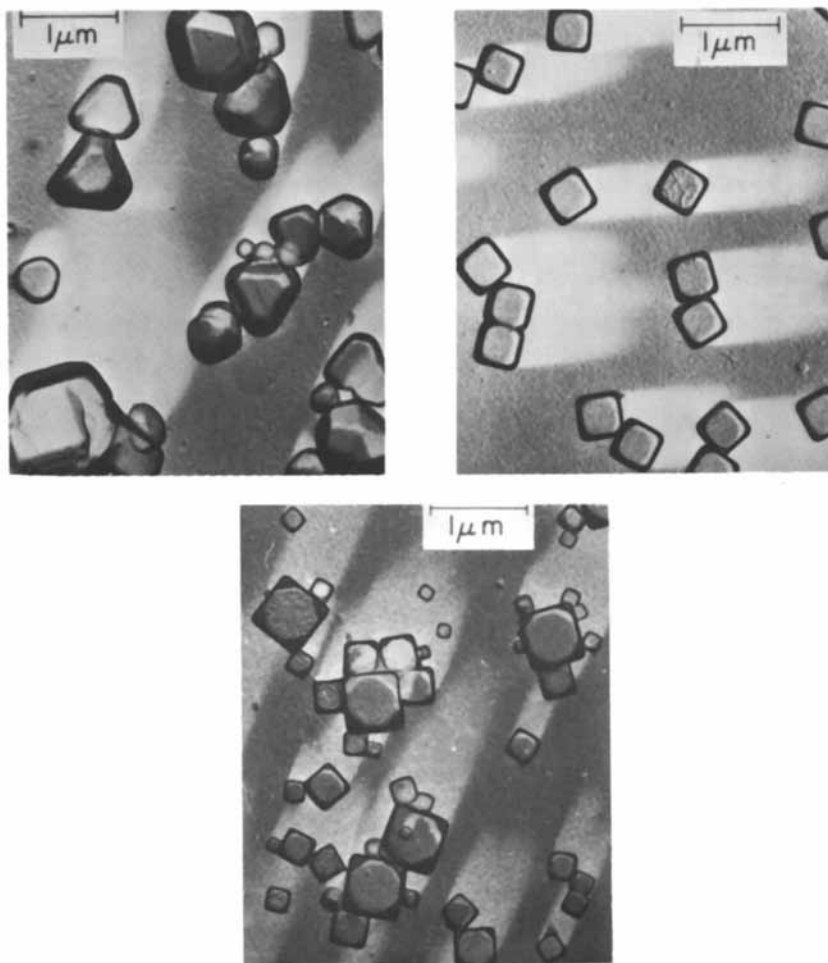


Figure 2. Electron micrographs of AgBr crystals produced by the basic precipitation methods. Key: single-jet, upper left; double-jet, upper right; and continuous, lower. (Reproduced, with permission, from Ref. 6. Copyright 1981, Marcel Dekker, Inc.)

where

$$\bar{r} = \frac{\int_0^{\infty} nrdr}{\int_0^{\infty} ndr} \quad (2)$$

Here, Z is the final number of stable nuclei, R represents the reactant addition rate, R is the gas constant, T is the absolute temperature, γ is the surface energy, D is the diffusion coefficient, V_m is the molar volume, and C_s is the solubility of the precipitate. \bar{r} represents a number average crystal radius and is greater than the critical radius r^* . The critical size r^* is defined as the size at which a crystal has an equal probability of dissolution by Ostwald ripening vs. growth to stable sizes. Equation (1) is based on a model where crystal growth is dominated by bulk diffusion and the Gibbs-Thomson effect (e.g., AgCl and AgBr systems). This equation differs from previous models^{10,11} by the factor $(\bar{r}/r^* - 1)$ which results from considerations of the dynamic mass balance and the influence of supersaturation. Its importance will become apparent during the discussion of experimental results. The validity of eq (1) was experimentally tested by double-jet precipitation of AgBr where reactant addition rate R , p_{Ag} and solubility, and temperature were closely controlled. In these experiments, initial reactor volume and gelatin concentration (2-8% range) did not significantly affect the number of stable nuclei.

Effect of Reactant Addition Rate - According to eq (1), the number of stable nuclei should increase with increasing addition rate. For the slope of the correlation of $\ln Z$ vs. $\ln R$, the following expression is obtained:

$$\frac{d \ln Z}{d \ln R} = 1 - \left(\frac{R}{\bar{r}/r^* - 1} \right) \times \left(\frac{d(\bar{r}/r^*)}{dR} \right) \quad (3)$$

The first term of the product on the right side of eq (3) is positive since $\bar{r}/r^* > 1.0$. It can be shown that the second term $(d(\bar{r}/r^*)/dR)$ is also positive. Therefore, a plot of $\ln Z$ vs. $\ln R$ (or $\log Z$ vs. $\log R$) should have a slope less than one. This is consistent with experimental results for AgBr shown in Figure 4. The slopes for the ascending part of the data by Klein and Moisar¹⁰ and Loginov and Denisova¹² are 0.8 and 0.5, respectively. Leubner, Jagannathan, and Wey² did not observe the bend-over observed by the other authors, and the slope of their correlation was 0.84. Different experimental techniques by these authors may account for the observed differences in the experimental results.

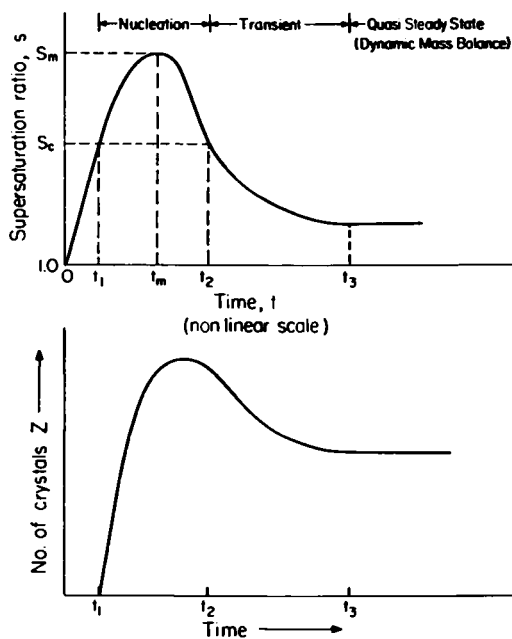


Figure 3. Supersaturation ratio, S , vs. precipitation time, t . (Reproduced, with permission, from Ref. 2. Copyright 1980, J. Photogr. Sci. Eng.)

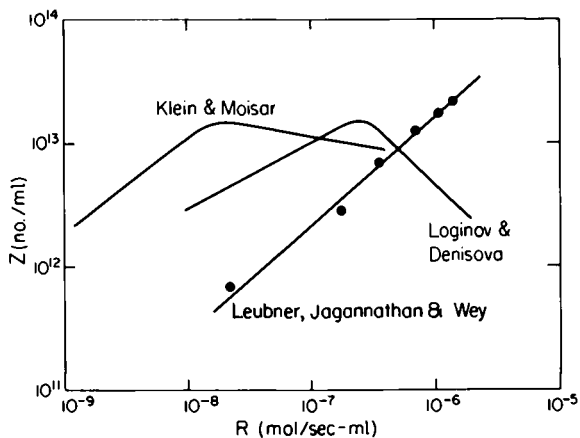


Figure 4. Number of stable AgBr crystals, Z , as a function of reactant addition rate, R . (Reproduced, with permission, from Ref. 2. Copyright 1980, J. Photogr. Sci. Eng.)

Effect of pAg and Solubility. Solubility and pAg are intricately^{2,6,13} related for a given temperature as shown in Figure 5. It was expected from eq (1) that the number of stable nuclei would be inversely related to the solubility. The correlation of log Z vs. pAg for AgBr is indeed inverse to that of the log solubility/ pAg correlation (Figure 6). From eq (1), the slope of the correlation of ln Z vs. ln C_s can be derived as:

$$\frac{d \ln Z}{d \ln C_s} = - \left[1 + \left(\frac{C_s}{\bar{r}/r^* - 1} \right) \times \left(\frac{d(\bar{r}/r^*)}{dC_s} \right) \right] \quad (4)$$

The first term of the product on the right side is positive since $\bar{r}/r^* > 1.0$. It can be shown that the second term is negative and that therefore the slope of a plot of ln Z vs. ln C_s (or log Z vs. log C_s) should be greater (more positive) than -1.² This is consistent with a plot of log Z vs. log C_s where slopes of -0.76 and -0.40 were obtained for cubic and octahedral crystals, respectively (Figure 7).

For the AgBr system, the crystal morphology is determined by the pAg and temperature of the crystal suspension.¹ As indicated in Fig. 6, at 70°C the octahedral morphology is stable at pAg's greater than about 8, whereas the cubic morphology is stable at lower pAg's. There is a continuous transition from cubic to octahedral morphology via cuboctahedral shapes. At pAg's higher than about 9.5, crystal morphologies based on twinned crystal structures are also obtained.¹

Effect of Temperature. The effect of temperature was studied for constant addition rate R and constant solubility C_s (1.6 x 10⁻⁶ mole/L). At each temperature, two pAg's were chosen which correspond to this solubility value (see Fig. 5). The higher and lower pAg's usually lead to octahedral and cubic crystal habits, respectively. From eq (1), the slope of the ln Z/ln T (or log Z/log T) correlation can be given as:

$$\frac{d \ln Z}{d \ln T} = 1 - \frac{d \ln D}{d \ln T} - \left(\frac{T}{\bar{r}/r^* - 1} \right) \times \left(\frac{d(\bar{r}/r^*)}{dT} \right) \quad (5)$$

It can be shown from the Stokes-Einstein equation¹⁴ that $d \ln D/d \ln T$ is equal to unity. It can be established² that $(d(\bar{r}/r^*)/dT) > 0$ and that therefore

$$\frac{d \ln Z}{d \ln T} < 0 \quad (6)$$

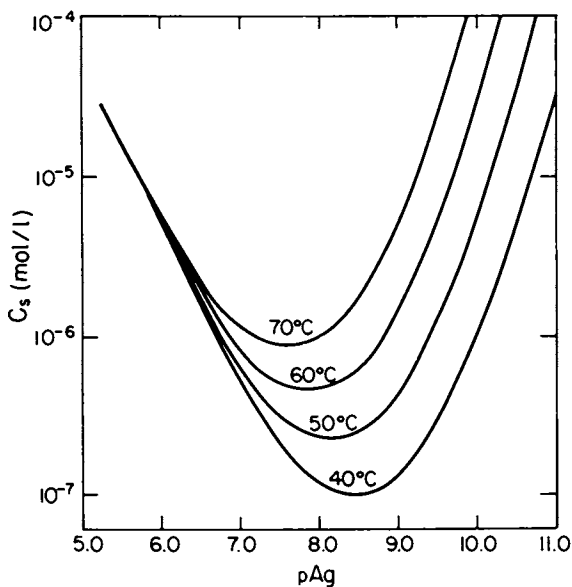


Figure 5. Solubility of AgBr crystals, C_s , as a function of pAg and temperature in a 4% gelatin solution. (Reproduced, with permission, from Ref. 2. Copyright 1980, J. Photogr. Sci. Eng.)

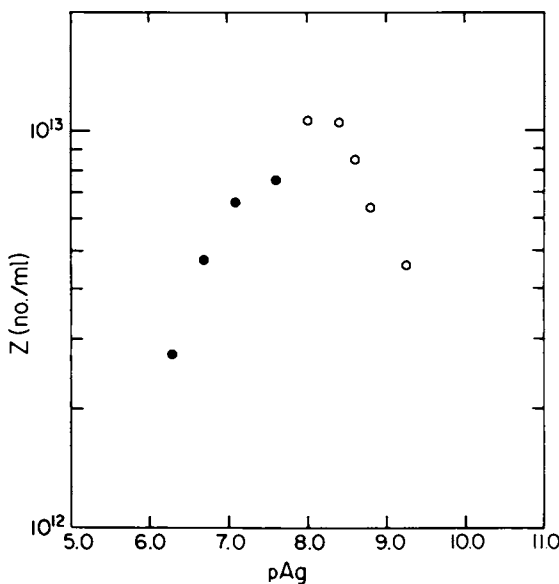


Figure 6. Number of stable AgBr crystals as a function of pAg . Conditions: temperature, 70°C; and R , 3.56×10^{-7} mol/s mL. Key: ●, cubes; and ○, octahedra. (Reproduced, with permission, from Ref. 2. Copyright 1980, J. Photogr. Sci. Eng.)

A plot of $\log Z$ vs. $\log T$ (Figure 8) indeed has a negative slope, which agrees with the theoretical prediction.

The experimental results obtained from balanced double-jet precipitations of AgBr crystals can thus be qualitatively explained reasonably well by the dynamic model of nucleation which includes both diffusion and the Gibbs-Thomson effect.

The Growth Stage

Once the number of stable nuclei has been established in the nucleation stage, their growth rate g , for constant addition rate can be given by a simple mass-balance

$$g = \frac{dr_o}{dt} = \frac{V_m R}{4\pi Z r_o^2} \quad (7)$$

if

$$g \leq g_c \text{ (critical growth rate)} \quad (8)$$

Here, V_m , R , and Z have the same meaning as in the previous discussion. t is time and r_o is the crystal diameter at time t . Here, spherical morphology^o is assumed for simplicity. The correlation is essentially the same for cubic and octahedral crystals except for different proportionality constants. g_c is the critical growth rate above which renucleation occurs. It is equal to the maximum growth rate that a system can sustain without going into renucleation. Its value is dependent on the temperature, pAg , average^{3,4,15,16} crystal size, and particle density of the silver halide system. For a dispersion of AgCl in gelatin, a pH effect was also observed.¹⁶

Another approach for determining the growth rate g is based on considerations of supersaturation, growth kinetics, and crystal number density. For diffusion-controlled growth systems, like AgBr, eq (9) was derived, which relates the growth rate³ to the supersaturation ratio, S , and crystal number density, ρ .

$$g = \frac{dr_o}{dt} = \eta g_\infty \quad (9)$$

where

$$g_\infty = \frac{DC (S - 1)}{\rho r_o} (1 + 1/\bar{\delta}) \quad (10)$$

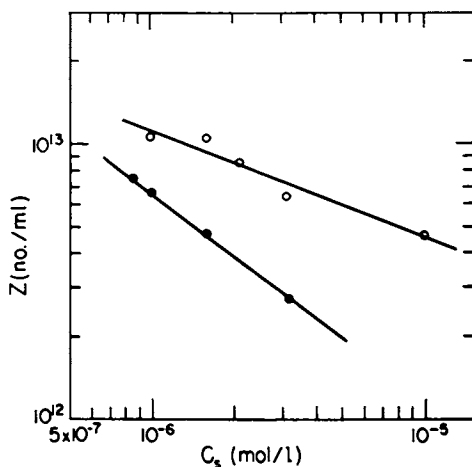


Figure 7. Number of stable AgBr crystals as a function of solubility. Conditions: temperature, 70°C ; and R , 3.56×10^{-7} mol/s mL. Key: ●, cubes; and ○, octahedra. (Reproduced, with permission, from Ref. 2. Copyright 1980, J. Photogr. Sci. Eng.)

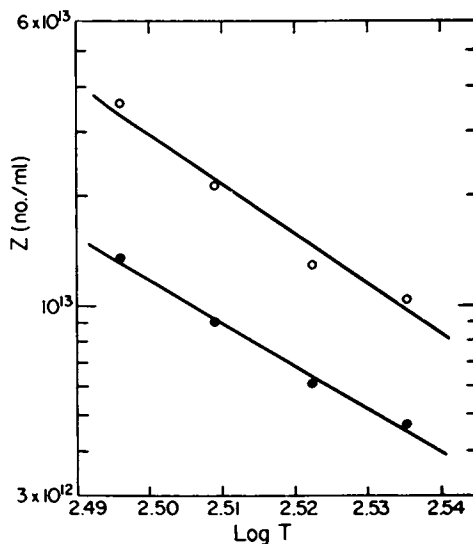


Figure 8. Number of stable AgBr crystals as a function of temperature. Conditions: C_s , 1.6×10^{-6} mol/L; and R , 3.56×10^{-7} mol/s mL. Key: ●, cubes; and ○, octahedra. (Reproduced, with permission, from Ref. 2. Copyright 1980, J. Photogr. Sci. Eng.)

$$\eta = \frac{3\bar{r}_1^2(\bar{r}_1^3 - 1)}{(\bar{r}_1 - \emptyset)(2\bar{r}_1^2\emptyset^2 - \bar{r}_1 - \emptyset)(1 + 1/\bar{\delta})} \quad (11)$$

$$\bar{r}_1 = r_1/r_0 \quad (12)$$

$$\bar{\delta} = \delta/r_0 \quad (13)$$

\emptyset is defined as follows:

$$\emptyset = 1 \text{ for } \bar{r}_1 \leq 1 + \bar{\delta} \quad (14)$$

$$\emptyset = \bar{r}_1(1 + \bar{\delta}) \text{ for } \bar{r}_1 > 1 + \bar{\delta} \quad (15)$$

Here, g is the growth rate for a crowded system, η is the crowding factor, and g_∞ is the growth rate for a noncrowded system. A crowded system is obtained when the particle suspension density is so high that the diffusion layers of adjacent particles overlap, i.e., $r_1 < r_0 + \delta$ as sketched in Figure 9. Here, r_0 is the particle radius, r_1 is the interparticle distance, and δ is the diffusion layer thickness. The other symbols in eqs (9-15) are the same as defined previously. The numerical evaluation of this growth model (eqs 9-15) is generally difficult for sparingly soluble precipitates since the determination of the supersaturation ratio S presents significant experimental difficulties. However, when g is equal to the critical growth rate g_c , the supersaturation becomes constant and equal to the critical supersaturation S_c (Fig. 1). Determination of the critical growth rate of a system thus allows verification of the proposed growth model and determination of S_c and δ .

The validity of this model was tested by the critical growth rate method on the AgBr system (Figure 10). $\bar{\delta}$ was arbitrarily chosen as 10 for all crystal sizes. The data correlate reasonably with a straight line; however, the line does not intercept the origin. Possibly, a more detailed knowledge of the value of the diffusion layer thickness δ will improve this correlation. The inclusion of the crowding factor η significantly improved the correlation vs. a previous model where this factor had not been included.

Summary

The formation of colloidal silver halide dispersions (photographic emulsions) was reviewed as a model system of colloids which are formed by precipitation of sparingly soluble salts. For such systems, models for crystal nucleation and growth were derived which were verified for the AgBr system. These models can probably be extended to the study of nucleation and growth of other highly insoluble colloidal systems.

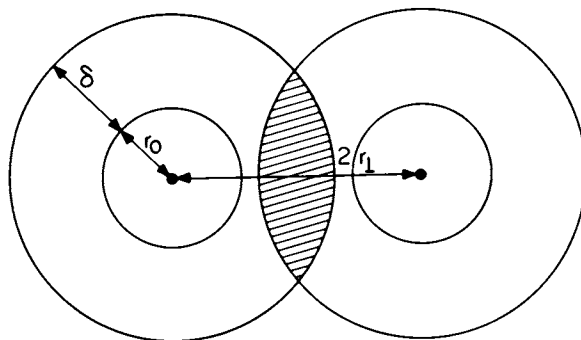


Figure 9. Schematic of a two-particle crowded system. Key: r_0 , particle radius; δ , diffusion layer thickness; and $2r_1$, interparticle distance.

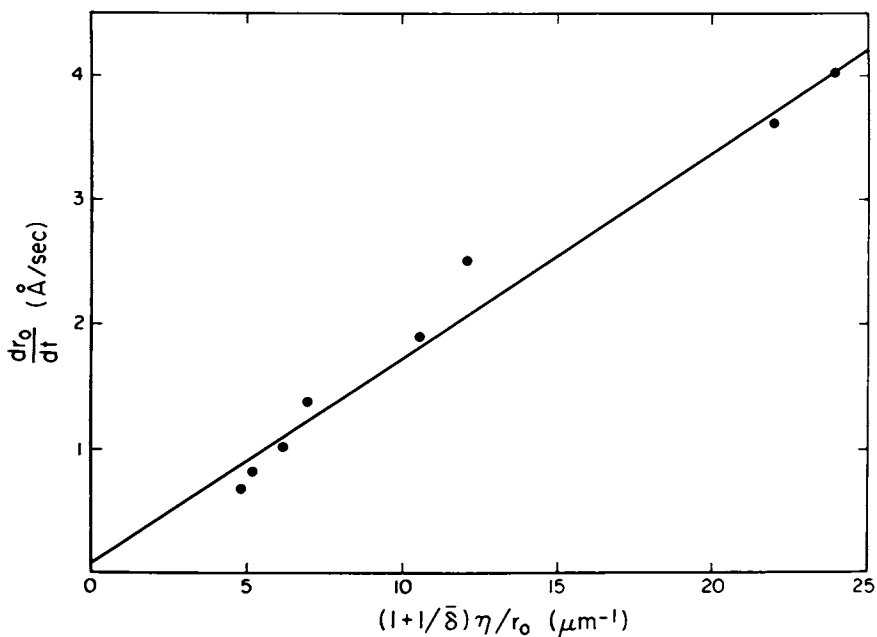


Figure 10. AgBr growth rates vs. $(1 + 1/\bar{\delta})\eta/r_0$. (Reproduced, with permission, from Ref. 3. Copyright 1981, North-Holland Publishing Company.)

Literature Cited

- (1) Berry, C. R. In "The Theory of the Photographic Process", 4th ed.; James, T. H., Ed.; Macmillan: New York, 1977.
- (2) Leubner, I. H.; Jagannathan, R.; Wey, J. S. Photogr. Sci. Eng. 1980, 24, 268.
- (3) Jagannathan, R.; Wey, J. S. J. Cryst. Growth 1981, 51, 601.
- (4) Wey, J. S.; Strong, R. W. Photogr. Sci. Eng. 1977, 21, 14; ibid. 1977, 21, 248.
- (5) Wey, J. S.; Terwilliger, J. P.; Gingello, A. D. AIChE Symposium Series 1980, 76, 34.
- (6) Wey, J. S. In "Preparation and Properties of Solid State Materials", Vol. 6, Wilcox, W. R., Ed.; Marcel Dekker: New York, 1981.
- (7) Meehan, E. J.; Miller, J. K. J. Phys. Chem. 1968, 72, 2168.
- (8) Berry, C. R.; Skillman, D. C. J. Phys. Chem. 1964, 68, 1138.
- (9) Berriman, R. W. J. Photogr. Sci. 1964, 12, 12.
- (10) Klein, E.; Moisar, E. Ber. Bunsenges. Phys. Chem. 1963, 67, 348.
- (11) Kharitonova, A. I.; Shapiro, B. I.; Bogomolov, K. S.; Zh. Nauchn. Prikl. Fotogr. Kinematogr. 1979, 24, 34.
- (12) Loginov, V. G.; Denisova, N. B. Ibid. 1975, 20, 231.
- (13) Harding, M. J. J. Photogr. Sci. 1979, 27, 1.
- (14) Perry, R. H.; Chilton, C. H. Chemical Engineers' Handbook, 5th ed., McGraw-Hill: New York, 1973; pp 3-235.
- (15) Strong, R. W.; Wey, J. S. Photogr. Sci. Eng. 1979, 23, 344.
- (16) Matsuzaka, S.; Yamamichi, E.; Koitabashi, T. presented at the SPSE 34th Annual Conference, New York, 1981.

RECEIVED April 30, 1982

Transfer of Photons, Electrons, and Information in Monolayer Organizates

DIETMAR MÖBIUS

Max Planck Institut für Biophysikalische Chemie (Karl-Friedrich-Bonhoeffer-Institut)
Abt. Molekularer Systemaufbau, D-3400 Göttingen, Federal Republic of Germany

The methods of assembling and manipulating monolayers have been used to arrange different molecules for cooperation in model systems. In such monolayer organizates the combination of photoinduced electron transfer or reversible photoisomerization with energy transfer results in signal amplification and signal transduction. The short range interlayer interactions are used for information transfer from one monolayer to another. A non-random pattern of chromophore orientations in a template monolayer is copied by contacting and separating a second monolayer.

The organization of molecules at interfaces and the formation of complex assemblies of molecules are the basic procedures for the construction of devices in molecular dimensions. The appropriate components must be adequately arranged in space and energy to achieve the intended function (1). A variety of different types of molecular assemblies have been studied like ion-polyelectrolyte associates (2), monolayers at interfaces (3), lipid monolayer (4) and bilayer (5) membranes, micelles (6,7), vesicles (8) and monolayer assemblies (9) particularly with regard to their suitability as systems for solar energy conversion.

The essential requirement for molecular organization is the amphiphilic structure of the molecules, i.e.

0097-6156/82/0200-0093\$06.00/0

© 1982 American Chemical Society

the molecules are composed of a hydrophilic group and a hydrophobic part. The long chain fatty acids like stearic acid are typical for this structure. In solution the formation of the molecular aggregates occurs spontaneously and size and composition of complex aggregates are determined by thermodynamics and by the kinetics of formation and disintegration. At the air-water interface, however, the organization of monolayers consisting of different molecular components can readily be controlled and modified by variation of the relevant parameters like the molar fractions of the components, the applied external surface pressure, the composition of the aqueous subphase, etc. The mobility of molecules in monolayers can be made so small that rotational or lateral diffusion is inhibited. Consequently, the position and orientation of molecules or of chromophoric parts are fixed and can be determined by spectroscopic measurements with linearly polarized light (9). This is essential for the stepwise assembly of different complex monolayers to monolayer organizations of planned structure and function.

The complex monolayers may be composed of an inert matrix and active components like dye molecules (10) or electron donors and electron acceptors (11). The matrix is then used to separate the chromophores laterally, to inhibit diffusion and to provide optimal conditions for monolayer transfer.

In monolayer organizations information can be carried by photons or electrons and may be stored in the position and orientation of molecules. The transfer of a signal from one monolayer to another and signal amplification can be achieved by the cooperation of different molecular components. This has been demonstrated in systems combining energy transfer with photochemical processes. The information in the orientation of dye chromophores may be copied by using dimer formation as a means to organize the chromophores of the copy monolayer on the template monolayer. Methods of monolayer manipulation have been developed for the separation of monolayers with molecular precision (12). A procedure along this lines clearly proved the feasibility of information transfer between monolayers although the transfer was not complete.

Construction of Monolayer Organizations

Monolayers at the air-water interface are usually formed by spreading a solution of the molecules in a volatile solvent on the water surface (3). The solvent evaporates and the remaining surface active molecules are packed by application of an appropriate external surface pressure. In the case of complex monolayers, e.g.

of a surface active cyanine dye and arachidic acid as matrix, a mixed monolayer may result, in which the dye molecules are homogeneously distributed or a separation occurs yielding a dye phase in an arachidic acid monolayer phase (13) or dye phase in a mixed monolayer of dye and fatty acid. The phase separation may be caused by the kinetics of monolayer formation during solvent evaporation, and then the addition of hexadecane as a very slowly evaporating solvent can lead to formation of homogeneous monolayers (transient modification of the environment), (14).

Dye molecules in mixed monolayers form dimers (9) and higher aggregates depending on the dye molar fraction in the monolayers, subphase composition and matrix composition. The inert matrix may consist normally of a fatty acid, typically arachidic acid for reasons of monolayer transfer since multilayer systems of fatty acid monolayers can easily be built up by the Langmuir-Blodgett method (15). It can be advantageous, however, to replace part of the fatty acid molecules by other amphiphilic molecules like long chain fatty acid methyl esters or long chain alcohols. Such a modification of the monolayer matrix influences the dye association and mobility. We will see the importance of mobility control in the procedure for information transfer from a template to a copy monolayer.

A monolayer kept under constant surface pressure is transferred from the water surface to a hydrophobic solid substrate, e.g. a glass plate coated with a fatty acid monolayer, by immersion of the plate into the water (15). The hydrophobic outer surface of the monolayer adheres to the hydrophobic surface of the plate, the hydrophilic groups of the attached monolayer are exposed to the water. The remaining monolayer on the water surface may be removed and be replaced by another monolayer. On withdrawal of the plate the hydrophilic groups of the monolayer at the water surface adhere to the hydrophilic surface of the deposited monolayer and the second monolayer is then transferred to the plate. The layered structure resulting from a transfer of several monolayers in this way has interfaces of hydrophilic groups and interfaces constituted by the methyl end groups of the amphiphilic molecules (see Figure 1a).

Many dye chromophores or reactive groups of electron donors and electron acceptors are hydrophilic and are therefore located at the hydrophilic interfaces of the mixed monolayers. According to the normal structure they are at the same interface or separated by at least two hydrocarbon chains yielding a distance of the order of 50 Å between the interfaces. This is an appropriate spacing between an excited energy donor layer

and an energy acceptor layer, since energy transfer is possible over distances of the order of 50 Å. For electron transfer from excited dyes to electron acceptors a separation of the order of 20 Å is desirable, corresponding to the thickness of one fatty acid spacer layer. A structure of such a type as shown schematically in Figure 1b requires the contact of hydrophilic groups of one monolayer with the hydrophobic surface of the preceding monolayer.

The deposition of a mixed cyanine dye arachidate monolayer on top of a hydrophobic surface of a monolayer assembly on a glass plate might be done by immersion of the plate through the clean water surface, subsequent formation of the mixed cyanine dye monolayer on the water and withdrawal of the glass plate across this monolayer. The amount of monolayer deposition depends strongly on the composition of the underlying hydrophilic interface. In Figure 2, top, the resulting structure after deposition of the mixed dye-arachidate monolayer (layer 6) is shown schematically. The composition of layer 4 was varied by changing the molar ratio of arachidic acid and methylarachidate. The transfer ratio of layer 6, i.e. the ratio of decrease of monolayer area on the water surface and of the coated geometrical area, is plotted against the molar fraction of ester in layer 4 (Figure 2). When layer 4 contains no methylarachidate the mixed dye-arachidate monolayer 6 is not deposited on top of the hydrophobic surface. After replacement of 1/20 to about 1/5 of the arachidate molecules in layer 4 by methylarachidate, the transfer of monolayer 6 is complete within the experimental error of 5%. Further increase of the ester molar fraction up to 0.6 causes incomplete irreproducible monolayer transfer. Complete transfer is again observed at ester molar fractions of 0.66 and 0.83.

A small change in the molecular structure at the interface between layers 4 and 5 causes a macroscopically observable change, since the presence or absence of the layer 6 can easily be detected by inspection of the fluorescence of the cyanine dye incorporated in layer 6 as indicator. The drastic change in adhesion of layer 6 in the system of Figure 2 encourages the search for a system with photochemical modification of the layer 4 which might cause imagewise change of adhesion for an appropriate "developing" monolayer.

Signal Amplification by Combination of Energy Transfer and Photoinduced Electron Transfer

A molecule in the electronically excited state can act as electron donor since it has an electron in the excited state orbital, and also as electron acceptor since

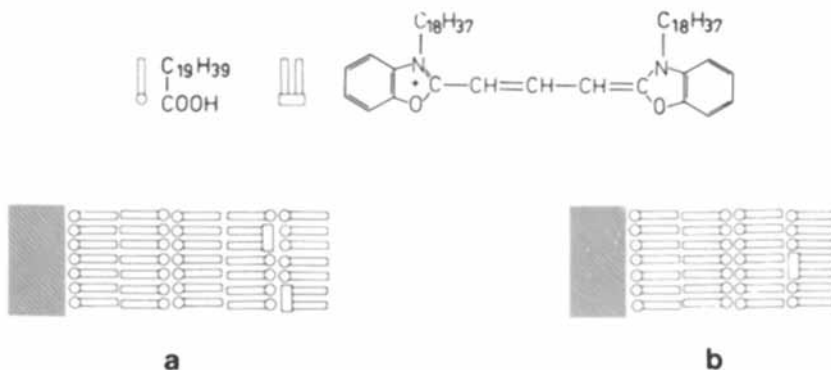


Figure 1. Amphiphilic molecules and schematic representation of arachidic acid and N,N'-dioctadecyloxycarbocyanine. Layer system assembled according to the usual technique with monolayer contacts at the hydrophilic interfaces and hydrophobic interfaces (left) and with the unusual contact of one hydrophilic interface with a hydrophobic interface (right). Key: ○, hydrophilic groups; and □, hydrocarbon chain.

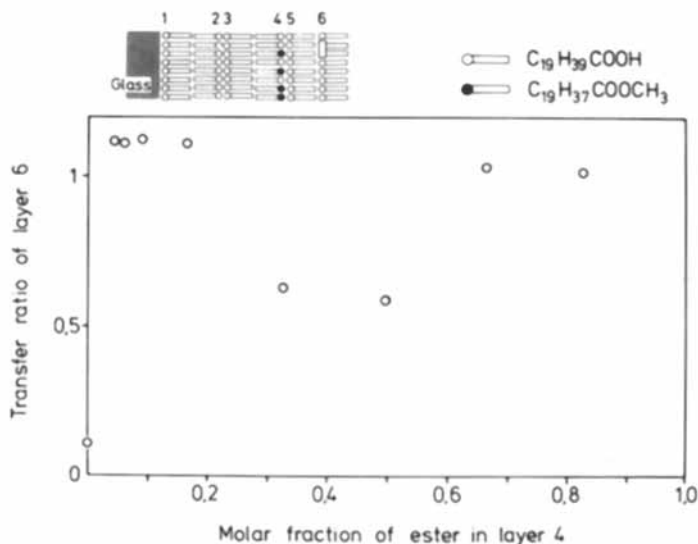


Figure 2. Control of monolayer adhesion to a hydrophobic surface by interface modification. Transfer ratio of monolayer 6 vs. the molar fraction of methyl arachidate (ester) in monolayer 4. Complete monolayer transfer in the ranges of 0.05 to 0.2 and 0.66 to 0.83 of the molar fraction of ester. No deposition of monolayer 6 when no ester in monolayer 4. Representation of the monolayer assembly on a glass plate after transfer of monolayer 6 with unusual contact (top).

it has a vacancy in the ground state orbital. Consequently, the fluorescence of an excited dye is quenched in the presence of an appropriate electron acceptor (photooxidation) or electron donor (photoreduction). In monolayer organizations with excited cyanine dyes and acceptor or donor molecules, respectively, at the same hydrophilic interface both processes have been observed (11). A situation of this type is shown schematically in Figure 3. The blue fluorescence of the N,N' -dioctadecyloxycyanine on excitation with UV radiation is quenched due to the presence of the electron acceptor N,N' -dioctadecyl-4,4'-bipyridinium (PQ). The matrix molecules in the mixed monolayers of the dye and the acceptor have been omitted in Figure 3 for clarity. The extent of fluorescence quenching depends on the acceptor molar fraction in the mixed acceptor monolayer and on the nature of the excited electron donor. The efficiency of the photoinduced electron transfer in systems as shown in Figure 3 with different cyanine dyes has been correlated with the energetic position of the excited state dye orbital (16).

The transferred electron returns in a dark process from the reduced acceptor molecule into the ground state orbital of the oxidized donor. If, however, the oxidized donor is regenerated by getting an electron from a different donor, the vacancy is delocalized from the original reaction site, and the dark recombination reaction of the electron primarily transferred to the acceptor molecule with the vacancy is inhibited. Consequently, the violent radical formed by a one-electron reduction of the electron acceptor PQ is accumulated on irradiation. This radical has been detected by measuring the optical absorption (17) or the EPR signal (18) of the radical. In Figure 3, the spectrum of the radical absorption built up under nitrogen atmosphere on irradiation of a monolayer system with 5 units of the schematic structure is shown. This spectrum agrees very well with the radical absorption spectrum measured in solution (19). Only the absorption bands in the long wavelength range of the visible spectrum are shown, but the main absorption band of the violent radical with maximum around 400 nm has also been observed in monolayer organizations with different cyanine dyes (20).

The radical formed by photoinduced electron transfer is stable in high vacuum but is oxidized to PQ in room air by oxygen. The maximal value of the radical absorption under irradiation of the layer system in air is therefore smaller than under inert atmosphere or in the vacuum and vanishes in the dark. Thus, the radical absorption can be "turned on" by irradiation of the monolayer system with UV radiation and "turned off"

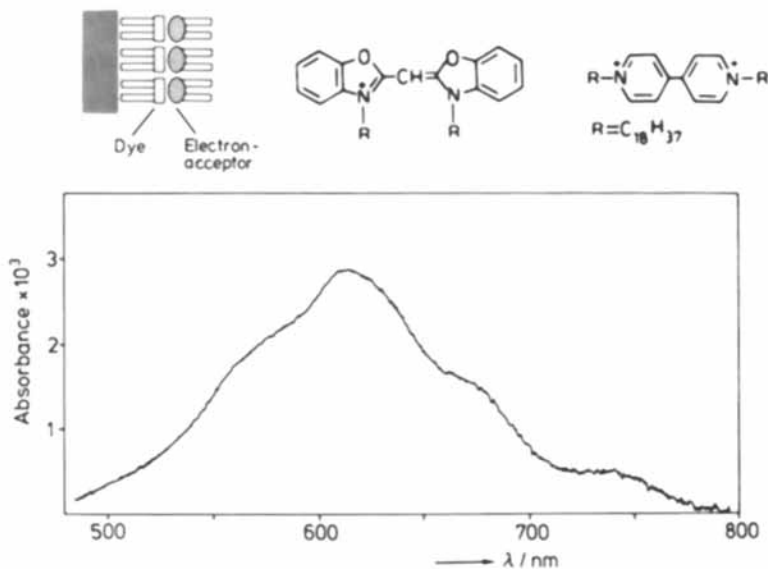


Figure 3. Monolayer assembly on a hydrophobic support for the investigation of photoinduced electron transfer. The N,N'-dioctadecyloxacyanine dye is excited with UV radiation and transfers an electron to the electron acceptor, N,N'-dioctadecyl-4,4'-bipyridinium, in the adjacent monolayer.

The matrix molecules of the mixed dye and acceptor monolayers have been omitted for clarity. Absorption spectrum of the viologen radical formed by the photoinduced electron transfer under nitrogen atmosphere, measured with an assembly of 5 dye-acceptor units with molar ratios of dye : arachidate = 1 : 20 and acceptor to arachidate = 1:10.

by turning off the radiation. This transient absorption can be used to quench the fluorescence of an energy donor with an emission in the spectral range of the radical absorption around 600 nm in the case of Figure 3. For this purpose, a monolayer of N,N'-dioctadecyl-indocarbocyanine in a matrix of arachidate and methylarachidate can be used with absorption maximum at 565 nm and fluorescence maximum at 590 nm. Since there is considerable overlap of this emission with the transient radical absorption, Förster energy transfer is expected. In order to exclude fluorescence quenching of this dye by electron transfer to the PQ monolayer in contact with the oxocyanine dye monolayer, the electron transfer system is separated from the red fluorescing monolayer by 54 Å. The geometry of the monolayer organization is shown in Figure 4, inset. In Figure 4, the intensity of the indocarbocyanine fluorescence, $I(590)$, excited at 545 nm, is plotted against time. When the UV radiation (366 nm) is turned on the photoinduced electron transfer causes the formation of the radical which acts as energy acceptor, and accordingly the fluorescence intensity $I(590)$ drops to about 0.9 of the unquenched value. When the 366 nm radiation is turned off the radical disappears and the indocarbocyanine fluorescence recovers to the unquenched intensity. This process can be done repeatedly (11).

The optical density of the transient absorption in the maximum at 610 nm is 0.0004 in room air, i.e. about 0.1 % of the incident light is absorbed. In the complex monolayer organization this small optical change is amplified to an intensity change of about 10 % or by a factor of 100. The amplification of the signal (transient absorption) would not be possible at larger separation of energy donor and photoreaction system or with a different donor that emits in a different spectral range. This signal amplification is a consequence of the cooperation of the different components appropriately selected and arranged in space.

Signal Transduction by Combination of Energy Transfer with a Bistable Photochromic System

Photochemical reactions which involve a change in chemical structure like photodimerization, photoisomerization or photodissociation reactions are very often sensitive to the flexibility of the environment. Some reactions occurring in homogeneous solution have also been investigated in organized systems like micelles, monolayer vesicles, monolayer organizations and in the organic solid state (21). Large differences in reactivity have been observed in these different environments. In particular, photoisomerization reactions like the

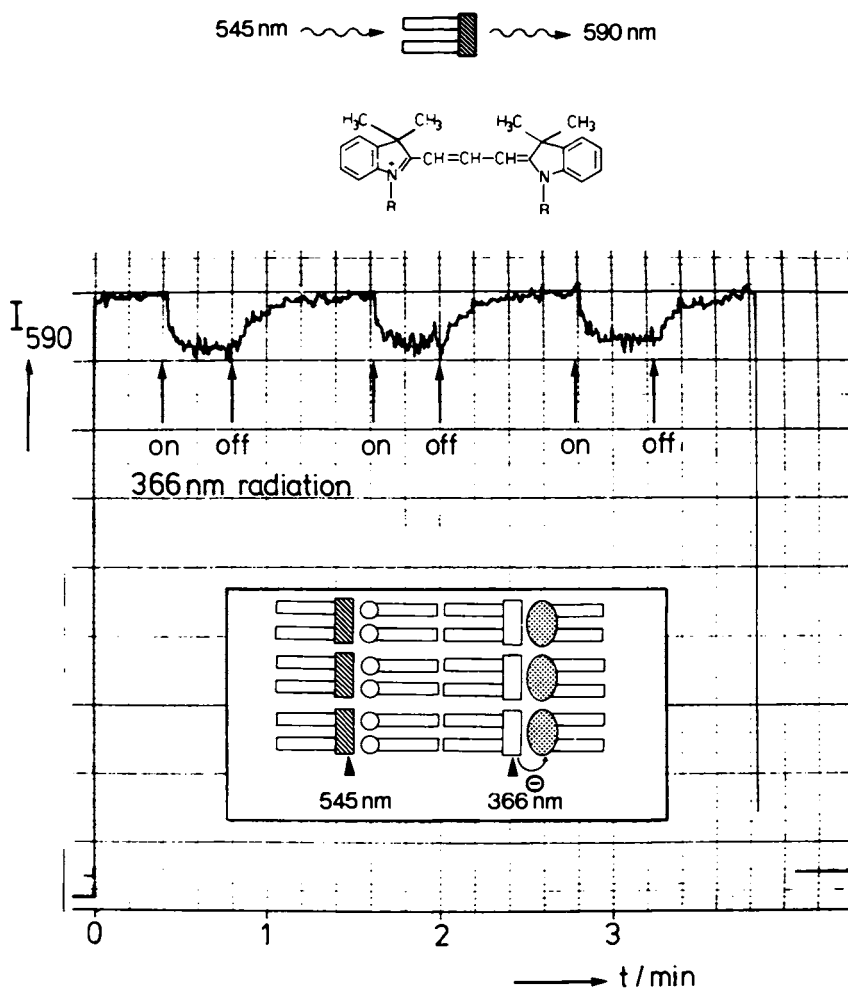


Figure 4. Combination of energy transfer and photoinitiated electron transfer for signal amplification. The transient radical absorption (see Figure 3) generated by excitation of the oxycyanine dye with UV radiation (366 nm) acts as energy acceptor and quenches partly the red emission at 590 nm of the monolayer of N,N'-dioctadecylindocarbocyanine excited simultaneously at 545 nm. The periodical irradiation of the complex system with the UV radiation causes a modulation of the indocarbocyanine fluorescence.

cis-trans photoisomerization of thioindigo derivatives which are entirely reversible in solution can be irreversible in monolayer organizations. This is reasonable, if one molecular form is more bulky or if the formation of one form requires considerable motion of a molecular fragment. Therefore, photoisomerizations which involve cleavage of a chemical bond and rotation of one part of the molecule e.g. as in the case of a photochromic system, reversibility of the reaction can be observed when the system is organized into an appropriate monolayer at the air-water interface (22). When built into a monolayer organization the mobility normally is so strongly reduced that reactions proceed only in one way without dark back reaction to the original form.

In the case of a surface active spiropyran-merocyanine system (see Figure 5) it has been possible to adjust the flexibility of the microenvironment so as to enable the photochromic system to reestablish the equilibrium in the dark after having reached a different equilibrium under irradiation (23). The spiropyran form of the system absorbs in the near UV with maximum at 360 nm. On irradiation with UV radiation the merocyanine is formed with absorption maximum at 580 nm. The merocyanine has an emission in the red part of the visible spectrum with maximum at 675 nm. The merocyanine, according to the absorption between 500 and 650 nm can act as energy acceptor for the excited N,N'-distearylthiacyanine dye (see Figure 5) incorporated in a mixed monolayer either at the same interface as the photochromic system or spaced away by fatty acid interlayers, distance of chromophoric planes about 54 Å. In the presence of the merocyanine under irradiation with 366 nm radiation the thiacyanine fluorescence is partly quenched. When the UV radiation is turned off the merocyanine disappears to a large extent due to isomerization to the spiropyran and consequently the thiacyanine fluorescence intensity increases to the unquenched value (23).

In the energy transfer system of Figure 5 the small absorption of the merocyanine can easily be transduced into an emission of either the energy donor (fluorescence quenching) or the sensitized emission of the merocyanine. The original signal can therefore be transduced into a smaller wavelength signal or into a longer wavelength signal. The molecular environment of the photochromic system can be controlled in order to obtain a bistable situation. Then, both the ring-opening of the spiropyran and the ring-closure of the merocyanine require activation by absorption of light. The merocyanine reacts back to the spiropyran on illumination with a pulse of green light (545 nm) as indicated in Figure 5. Now the entire system of thiacyanine

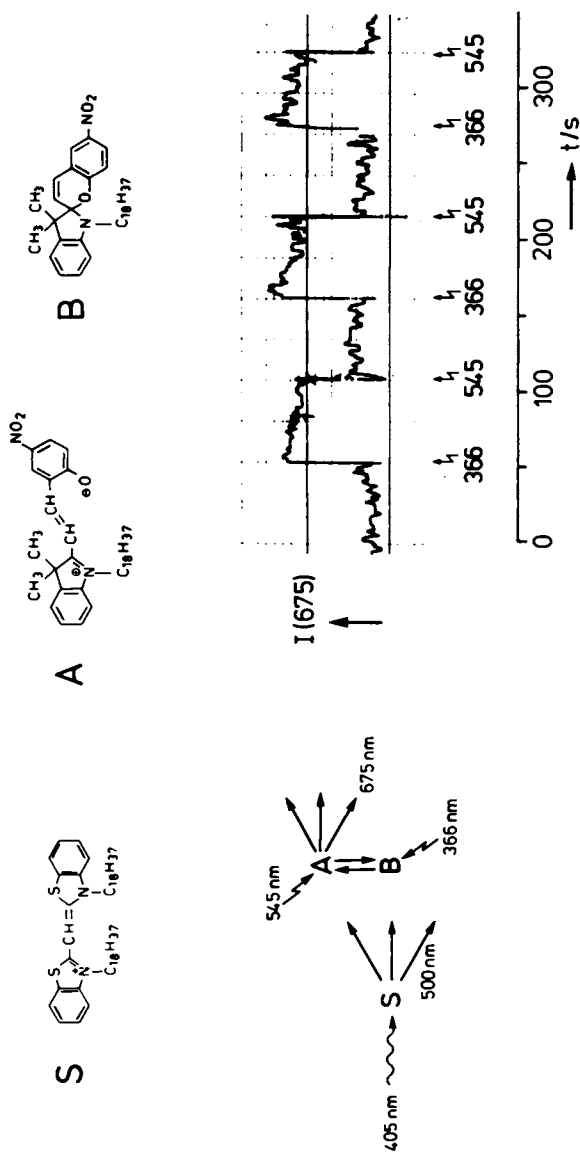


Figure 5. Combination of energy transfer and a reversible photoisomerization for signal transduction in a bistable system.

In a layer system with a monolayer of N,N'-dioctadecylrhodamine the cyanine is excited at 405 nm and transfers energy to the merocyanine which emits a sensitized fluorescence. The fraction of merocyanine is periodically varied by short pulses of UV radiation at 366 nm (increase of fluorescence at 675 nm) and green light, and 545 nm (decrease of fluorescence at 675 nm), respectively.

monolayer and spiropyran-merocyanine monolayer exhibits a bistable behavior: The thiocyanine emission drops rapidly to a constant value on irradiation with a pulse of UV radiation (formation of the merocyanine) and recovers only after irradiation with green light (bleaching of the merocyanine). Consequently, the sensitized emission of the merocyanine steps up when the merocyanine is formed and drops off on rapid bleaching of the merocyanine. This effect is shown in Figure 5, where the intensity $I(675)$ of the emission of the complex system at 675 nm is plotted against the time. The change in fluorescence intensity correlated with the presence of the merocyanine is clearly seen. This signal is the result of the cooperation of different components of the complex system arranged to function as a molecular bistable system.

Information Transfer by Monolayer Manipulation

In biological systems the genetic information is stored in a linear system of molecular dimension, the DNA or RNA molecules. A complex apparatus has evolved for duplicating the information and translating it into structures of biomolecules and organisms. It is challenging to attempt the organization and manipulation of molecularly organized two-dimensional systems in order to create an analog of the natural linear arrays.

A principle of molecular organization for duplication similar to the base-pairing in biological systems could be the formation of spectroscopic dimers of molecules like cyanine dyes. The information can be laid down in the distribution and orientation of chromophores in an appropriate matrix. In monolayer organizes with cyanine dyes in arachidate matrix the formation of interlayer dimers has been observed and analyzed (24). A procedure for copying a given two-dimensional pattern of chromophores goes through the following steps: (1) A mixed monolayer of a cyanine dye in a matrix (copy monolayer) is brought with its hydrophilic groups in contact with the hydrophilic groups of the original monolayer. The chromophores of the copy monolayer diffuse laterally and form spectroscopic dimers with the chromophores in the original monolayer, thereby forming the mirror image pattern of the template. (2) The copy monolayer is rigidified in order to inhibit diffusion after the reorganization is finished. (3) The copy monolayer is separated from the original monolayer.

The mobility of cyanine dye molecules incorporated in a matrix of long chain fatty acid and methyl-ester of a long chain fatty acid can be controlled in

different ways. The rigidity of the matrix monolayer depends on the ratio of acid to ester, on the chain length of the matrix molecules and on the interaction with the subphase. An aqueous solution of 2×10^{-4} M cadmium chloride at pH = 6.2 is widely used for formation and transfer of long chain fatty acid monolayers at room temperature. The divalent ions have a strong rigidifying effect on these monolayers and facilitate assembling multilayer systems. This effect and its consequence on interlayer dimer formation of the oxacarbocyanine dye chromophores anchored in the monolayer matrix by two octadecyl substituents (see Figure 1) has recently been demonstrated (25). For a monolayer of the dye in a matrix of methylstearate and behenic acid, molar ratios dye : ester : acid = 1 : 20 : 5, the absorption spectrum shows the monomeric absorption band with maximum at 495 nm. When another monolayer of same composition is deposited with contact at the hydrophilic groups the absorption band of the dimer with maximum at 450 nm dominates. Transfer of the second monolayer from cadmium chloride solution instead of bidistilled water yields a system whose absorption spectrum shows only a small amount of dimer formation, and the monomer band dominates.

Obviously, there are possibilities to overcome the difficulties encountered with steps 1 and 2 of the copying procedure outlined above. The most difficult step certainly is the separation of the copy from the original without molecular rearrangement. Techniques for manipulation of monolayers and monolayer organizates have been worked out and tested several years ago, involving the separation and the contacting at the hydrophobic interfaces with the aid of thin polymer films (12). The hydrophilic interface was not accessible in those experiments. In first attempts of information transfer a separation of cyanine dye containing monolayers at the hydrophilic interface was achieved, again with the aid of a polymer film. Separation of a dye monolayer from an anisotropic solid surface provided evidence for the persistence of the induced preferential chromophore orientation during separation and transfer of the dye monolayer to a different solid substrate (26).

Compared with the early attempts the sequence of manipulations has been considerably improved. Since the cyanine dye chromophores in the mixed monolayers normally are homogeneously distributed in the layer plane a non-random pattern of chromophore orientation was introduced as information. This can be done by deposition of the mixed monolayer on a freshly cleaved gypsum crystal surface. In the case of monolayers forming large

two-dimensional arrays of ordered dye aggregates the cooperative effect enhances the reorganization on the gypsum crystal surface to preferentially oriented chromophores (27). However, the formation of large aggregates has to be avoided, when information transfer in molecular dimensions is attempted.

The preferential orientation of single chromophores is obtained when a monolayer of *N,N'*-dioctadecyl-2,2'-cyanine (dye A, Figure 6) in a mixed monolayer with arachidic acid and methylarachidate, molar ratio dye A : acid : ester = 1 : 1 : 9, is slowly transferred to a freshly cleaved gypsum crystal at 18° C. The monolayer is subsequently removed from the crystal by immersion of the crystal into the water in a nearly horizontal orientation with the monolayer on top. The surface of the water is covered with a monolayer of behenic acid under a surface pressure of 30 dyn/cm. This monolayer prevents disintegration of the dye monolayer which floats off the crystal. The piece of mixed dye monolayer enclosed by the behenic acid monolayer is attached to a glass plate with hydrophobic surface by lowering the plate in a nearly horizontal orientation. This differs from the usual Langmuir-Blodgett type of transfer, where the plate is passing through the monolayer in a vertical orientation. The horizontal contacting method (28) avoids mechanical stress, and the preferential orientation of the chromophores in the mixed monolayer is not affected. The glass plate coated with the "original monolayer" is then completely immersed, the monolayer of behenic acid is removed from the water surface and the "copy monolayer" is spread on the water. The chromophores of this monolayer of *N,N'*-dioctadecyl-oxacyanine (dye B, see Figure 6) should reorganize according to the chromophore pattern of the mixed monolayer of dye A. The glass plate is withdrawn from the trough and the dye B monolayer is deposited on top of the dye A monolayer.

Figure 6, top, shows the absorption spectrum of the resulting monolayer organization measured with linearly polarized light. The electric vector is oscillating in the layer plane parallel (\parallel) to the direction that coincided originally with the \bar{a} -axis of the gypsum crystal and perpendicular (\perp) to that direction. The monolayer of dye A which has been reorganized on the gypsum crystal shows a strong anisotropy (absorption band between 400 nm and 600 nm). The monolayer of dye B exhibits the expected anisotropic absorption between 300 nm and 400 nm. However, the anisotropy is somewhat smaller than in the original monolayer. This indicates that under the conditions of the experiments the reorganization of the dye B monolayer to a mirror

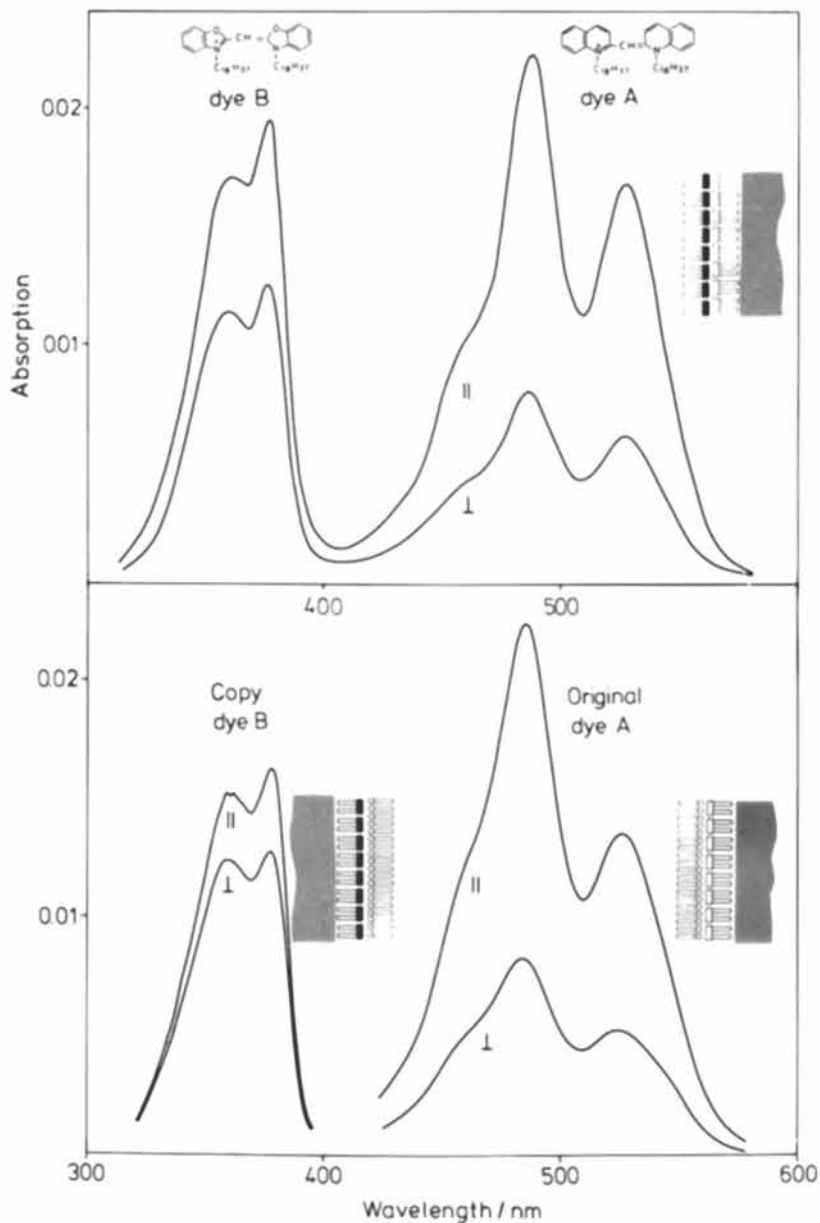


Figure 6. Information transfer in monolayer organizates. Absorption spectra before separation of the dye B copy monolayer from the original dye A monolayer (top), and of the two plates after separation of the monolayers (bottom). Composition of the mixed monolayers (molar ratios) is dye A:methylarachidate:arachidic acid = 1:9:1 and dye B:behenic acid = 1:10. (Reproduced, with permission, from Ref. 25. Copyright 1981, Pergamon Press, Ltd.)

image of the chromophore pattern of the dye A monolayer has not entirely been achieved.

The procedure of separation of the copy monolayer from the original is similar to that of separation of the dye A monolayer from the anisotropic gypsum crystal surface. The glass plate with the monolayer organization shown schematically in Figure 6, top, is brought in contact with an aqueous solution in a nearly horizontal orientation and slowly immersed. In order to reduce the interlayer interactions at the hydrophilic interface, now a solution of 0.1 M HCl and 0.1 M NaCl at 10° C is used as substrate, whose surface is covered with a monolayer of behenic acid. The dye B monolayer slowly floats off and is transferred to a hydrophobic glass plate by the horizontal contacting method. Both glass plates, one carrying the original dye A monolayer, one carrying the copy dye B monolayer are transferred to another monolayer trough containing an aqueous solution of 2×10^{-4} M cadmium chloride at pH = 6.2 and are covered with an arachidate monolayer for stabilization. The absorption spectra of the two plates are shown in Figure 6, bottom. Again the absorption was measured with linearly polarized light as in the case of Figure 6, top.

Obviously, the original monolayer (dye A) is unchanged after the separation procedure. The anisotropy is the same as in Figure 6, top, no loss of dye or of preferential orientation is observed. From the absorption spectra of the copy monolayer (dye B) it must be concluded, that information transfer from the original monolayer has been obtained and preserved through the entire procedure, although some loss of dye and of anisotropy has occurred. Through the described sequence of manipulations information can be transferred in molecular dimensions.

Conclusions

These examples of processes in complex monolayer organizations indicate the potential use of designed molecular machines as model systems in information processing. By using the restricted range of Förster energy transfer, submicroscopic pattern replication has been achieved with visible light(29). The molecular interactions according to the energetic and spatial coordination are the basis of different functions analogous to those used in macroscopic information handling. More and more elaborate systems have been assembled mainly for the purpose of studying the various parameters influencing a particular phenomenon (30-32). Further approach to the goal of creating a two-dimensional analog of the linear biological system for in-

formation storage and handling will lead to more and more sophisticated control of molecular dynamics and organization.

Literature Cited

- (1) Möbius, D., Acc. Chem. Res. 1981, 14, 63.
- (2) Sassoon, R. E., and Rabani, J., J. Phys. Chem. 1980, 84, 1319.
- (3) Gaines, G.L., Jr., "Insoluble Monolayers at Liquid-Gas Interfaces", Interscience, New York, 1966.
- (4) Okahata, Y., and Kunitake, T., J. Am. Chem. Soc. 1979, 101, 5231.
- (5) Tien, H., "Bilayer Lipid Membranes: Theory and Practice", Marcel Dekker, New York, 1974.
- (6) Turro, N.J., Grätzel, M. and Braun, A.M., Angew. Chem. Int. Ed., Engl. 1980, 19, 675.
- (7) Fromherz, P., Ber. Bunsenges. Phys. Chem. 1981, 85, 891.
- (8) Fendler, J., Acc. Chem. Res. 1980, 13, 7.
- (9) Kuhn, H., Möbius, D., and Bücher, H., in: "Physical Methods of Chemistry", A. Weissberger and B. Rossiter, Eds., Vol. I, Part 3B, Wiley, New York, 1972, p. 577.
- (10) Bücher, H., Drexhage, K.H., Fleck, M., Kuhn, H., Möbius, D., Schäfer, F.P., Sondermann, J., Sperling, W., Tillmann, P., and Wiegand, J., Mol. Cryst. 1967, 2, 199.
- (11) Möbius, D., Ber. Bunsenges. Phys. Chem. 1978, 82 848.
- (12) Inacker, O., Kuhn, H., Möbius, D., and Debusch, G., Z. Phys. Chem. (Frankfurt/Main) 1976, 101, 337.
- (13) Bücher, H., v. Elsner, O., Möbius, D., Tillmann, P. and Wiegand, J., Z. Phys. Chem. (Frankfurt/Main) 1969, 65, 152.
- (14) Möbius, D. in: "Topics in Surface Chemistry", E. Kay and P.S. Bagus, Eds., Plenum Press, New York, 1978, p. 75.
- (15) Blodgett, K.B., and Langmuir, I., Phys. Rev. 1937, 51, 964.
- (16) Seefeld, K.-P., Möbius, D. and Kuhn, H., Helv. Chim. Acta 1977, 60, 2608.
- (17) Möbius, D., and Ballard, G.S., unpublished.
- (18) Cunningham, J., Polymeropoulos, E.E., Möbius, D., and Baer, F., in: "Magnetic Resonance in Colloid and Interface Science", J.P. Faissard and H.A. Resing, Eds., Reidel Publ. Comp., Dordrecht, Holland, 1980, p. 603.
- (19) Kosower, E.M., and Cotter, J.L., J. Am. Chem. Soc. 1964, 86, 5524.

- (20) Penner, T.L., and Möbius, D., This volume, p.
- (21) Whitten, D.G., Angew. Chem. Int. Ed. Engl., 1979, 18, 440.
- (22) Möbius, D., Bücher, H., Kuhn, H. and Sonderrmann, J., Ber. Bunsenges. Phys. Chem. 1969, 73, 845.
- (23) Polymeropoulos, E.E., and Möbius, D., Ber. Bunsenges. Phys. Chem. 1979, 83, 1215.
- (24) Czikkely, V., Dreizler, G., Försterling, H.D., Kuhn, H., Sonderrmann, J., Tillmann, P. and Wie-gand, J., Z. Naturf. 1969, 24a, 1921.
- (25) Kuhn, H., Pure Appl. Chem. 1981, 53, 2105.
- (26) Möbius, D., and Debuch, G., Ber. Bunsenges. Phys. Chem., 1976, 80, 1180.
- (27) Bird, G.R., Debuch, G., and Möbius, D., J. Phys. Chem. 1977, 81, 2557.
- (28) Möbius, D., and Kuhn, H., Isr. J. Chem. 1979, 18, 375.
- (29) Fischer, U., Ch. , and Zingsheim, P., Appl. Phys. Lett. in press.
- (30) Fromherz, P. and Arden, W., J. Am. Chem. Soc. 1980, 102, 6211.
- (31) Steiger, R., Hediger, H., Junod, P., Kuhn, H. and Möbius, D., Photogr. Sci. Eng. 1980, 24, 185.
- (32) Polymeropoulos, E.E., Möbius, D., and Kuhn, H., Thin Solid Films 1980, 68, 173.

RECEIVED April 30, 1982

Supersensitization of Photoinduced Electron Transfer in Monolayer Assemblies

THOMAS L. PENNER¹ and DIETMAR MÖBIUS

Max Planck Institut für Biophysikalische Chemie, Abteilung Molekularer Systemaufbau, D-3400 Göttingen-Nikolausberg, Germany

Electron transfer from a photoexcited cyanine dye to an electron acceptor has been investigated in a monolayer assembly system via detection of the reduced acceptor. We report here the first observation in a monolayer system of the supersensitization or enhancement of the yield of such an electron transfer by the incorporation of a reducing agent (electron donor). For supersensitization to occur, the dye molecules must be organized into J aggregates, which implies that charge migration must be possible for the effect to occur.

Photoinduced redox processes involving organic compounds are of much current interest, ranging from the fundamental and theoretical (1-4) to practical applications where charge separation is sought (5, 6, 7). An organic molecule in an electronically excited state is generally both a better reducing agent and a better oxidizing agent than in its ground state so that thermodynamically unfavorable redox reactions can be light-driven (8). This process usually results in reactive ground-state products, often ionically charged. It is common for these products to recombine, resulting in no net change except for wasting photon energy. For many purposes maximization of the electron-transfer yield and minimization of recombination is desirable. Techniques to do so include physically separating the products (9) or removing one of them by further reaction either unimolecularly or in a bimolecular reaction with added substances (10, 11). Examples of the former include photoredox reactions in micellar suspensions (6, 12, 13) as well as the spectral sensitization of electron transfer at a semiconductor surface (14, 15, 16) (where an electric field, either externally applied or resulting from interfacial space-charge, can assist charge separation).

¹ Current address: Research Laboratories, Eastman Kodak Company, Rochester, NY 14650.

A number of recent systems incorporate both physical charge separation and added substances to enhance electron-transfer yields (17-20).

Such an enhancement by added compounds is called supersensitization, and the additive a supersensitizer. These terms were originally used in the photographic industry to describe the enhancement of the spectral sensitization of silver halide by adding to the sensitizing dyes compounds which did not themselves show spectral sensitization activity. The enhancement is now known to proceed via the same sort of mechanisms by which we understand supersensitization to occur in more well-defined photo-redox systems (21, 22). These mechanisms are outlined below. As an example of a photoinduced redox reaction, in electron transfer from an excited sensitizer C^* to an acceptor A [reaction (1)] additives that enhance the yield of this reaction are usually good reducing agents, i.e., electron donors (D). The most direct mechanism for this supersensitization is reaction (3) between donor and oxidized photosensitizer, inhibiting the recombination reaction (2).



If D can photoreduce C^* directly, an alternative mechanism of supersensitization is possible:



Photoinduced electron-transfer reactions have also been observed in monolayer assemblies (23, 24). Such systems can be made essentially free of molecular diffusion and thus most closely resemble the solid state. They can be fabricated with precise geometry and therefore provide well-defined structures often lacking in amorphous solids or adsorbed layers. However, until now no evidence for enhancement of the yield of reaction (1) by added supersensitizers had been obtained, although the concept had been discussed (25).

This work explored whether supersensitization of electron transfer could be demonstrated in a monolayer assembly. We also studied the properties of excited cyanine dyes, the class of compound used almost exclusively as photographic spectral sensitizers (26). Kuhn, Mübbs, and co-workers have demonstrated the detailed information that can be gained on energy and charge-transfer properties through the use of monolayer assemblies of such dyes (23, 27). We emphasized investigations of cyanine dye

as photosensitizer incorporated into the system in the so-called J-aggregate form described below (28). In silver halide photographic systems supersensitization is generally most pronounced when the cyanine spectral sensitizer is present as its J aggregate (26, 29). If this is also true in the monolayer assembly, it would be of interest to consider the monolayer system as a model for the photographic one.

Sensitizer-Acceptor System: Electron Transfer

To investigate supersensitization, we had to characterize the electron-transfer reaction in the two-component sensitizer-acceptor system. Figure 1 shows the structure of the cyanine dye used as sensitizer (C) and the absorption and emission spectra of a single monolayer of dye. The spectra exhibit the characteristics of J aggregates: a narrow absorption band and near-resonant emission with the absorption maximum red-shifted by 50 nm from the monomer band peak (not shown). To obtain a monolayer of the dye in aggregate form, we mixed it in a 1:1 molar ratio with methyl stearate. The electron acceptor (A) used was *N,N'*-dioctadecyl-4,4'-bipyridinium di-*p*-chlorobenzenesulfonate (viologen). The arrangement of the layers is shown in Figure 2. The viologen was coated in a layer diluted with arachidic (eicosanoic) acid in head-to-head contact with the cyanine dye in the adjacent layer. Details of the fabrication of the monolayer assemblies and the techniques of performing experiments on them are given elsewhere (27, 30). All experiments were done at room temperature, ca. 20°C.

Figure 3 shows the quenching action of the viologen on cyanine dye fluorescence, obtained by varying the ratio of arachidic acid to acceptor in the contact layer. This allows the average distance between viologen molecules to be calculated. When the data are plotted this way, the long-range nature of the quenching is clearly seen. When the dye was present in its aggregate form, 50% quenching occurred when viologen molecules were 60 Å apart. When the dye was incorporated in monomeric plus dimeric form, with no J aggregate present, as was confirmed from its absorption spectrum (not shown), the quenching influence of the viologen was relatively short-range, with 50% quenching at 15 Å separation. The quencher is colorless and cannot act via energy transfer. Evidence reported below demonstrates that it accepts electrons from the excited dye as would be expected from its redox potential (6). The long-range influence of the quencher presumably reflects excitonic energy migration within the dye aggregate. The fluorescence data can also be plotted as the reciprocal of residual fluorescence versus quencher concentration (Figure 4). The linear relationship demonstrates that the rate of the quenching by acceptor is directly proportional to the concentration of quencher, in competition with a constant rate of unimolecular deactivation of excited dye (fluorescence, radiationless deactivation, etc.). The slope of the quenching equation is

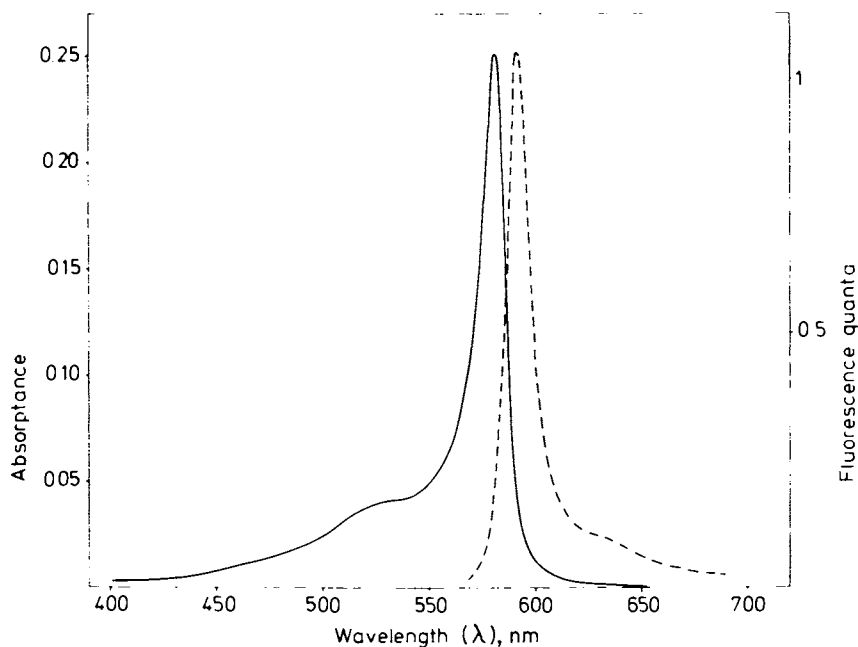


Figure 1. Absorption and normalized fluorescence (545-nm excitation) spectra of a single monolayer of cyanine dye in J-aggregated form.

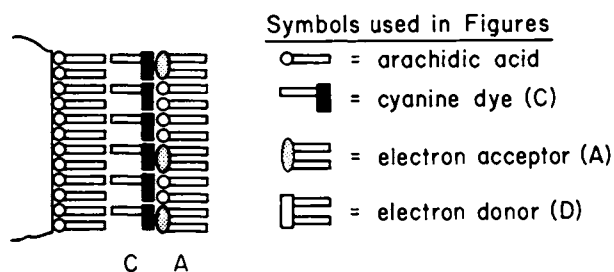


Figure 2. Arrangement of layers in monolayer assembly of cyanine sensitizer (C) and viologen electron acceptor (A) on glass coated with an arachidic acid spacer layer.

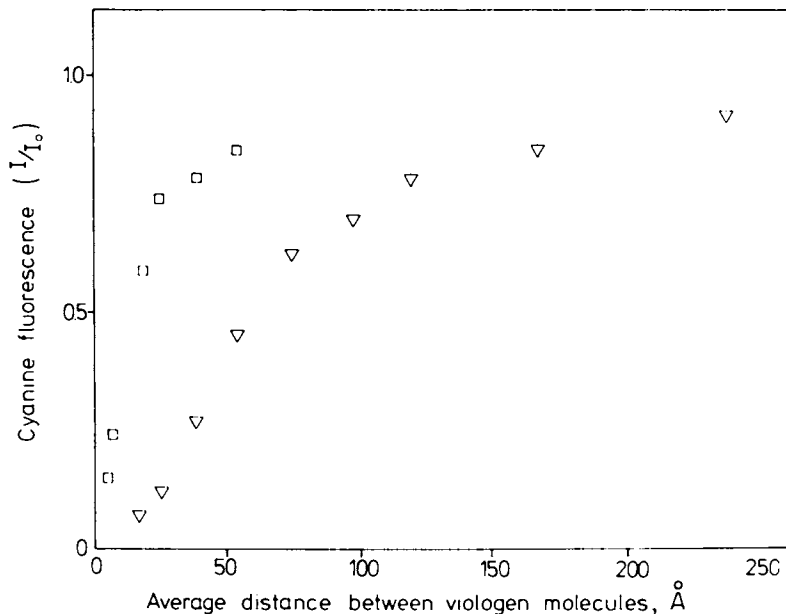


Figure 3. Dependence of cyanine J aggregate (∇) or monomer (\square) fluorescence on the spacing between viologen molecules in adjacent layer. Measurement was made on systems in which J-aggregate formation was respectively maximized or excluded.

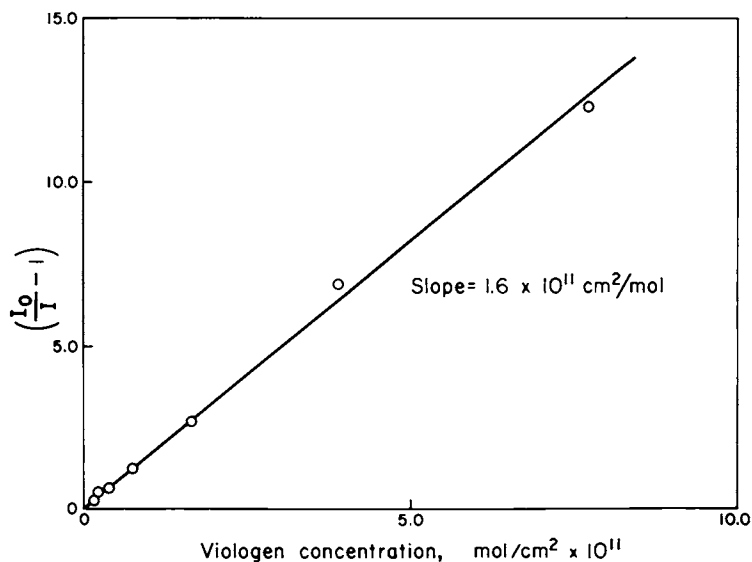


Figure 4. Reciprocal plot of residual cyanine J-aggregate fluorescence vs. two-dimensional viologen concentration in adjacent layer.

$1.6 \times 10^{11} \text{ cm}^2/\text{mol}$. If the excited-state lifetime for cyanine J aggregate is assumed to be 10^{-10} s , which is in fact a measured upper limit (31), an electron-transfer rate constant of $3 \times 10^{-3} \text{ cm}^2 \text{ molecule}^{-1} \text{ s}^{-1}$ is calculated. A recent rough estimate of a diffusion-controlled rate constant in a monolayer is $2.5 \times 10^6 \text{ cm}^2 \text{ molecule}^{-1} \text{ s}^{-1}$ (32). This calculation used a diffusion coefficient obtained for fluid bilayers, and the actual diffusion rate in a rigid monolayer is probably lower than that calculated. Clearly the large rate in the present case rules out appreciable involvement of molecular diffusion. The process is dominated by static quenching, and the high rate constant is the result of rapid migration of the excitons generated in the dye aggregate, allowing contact with the widely spaced quencher molecules, as M \ddot{u} bius and Kuhn concluded (33, 34). (Note that if this reaction occurred in solution with a diffusional rate constant of $10^{10} \text{ L mol}^{-1} \text{ s}^{-1}$, a concentration of 1 M would be required to achieve 50% quenching.)

Although the fluorescence quenching by viologen electron acceptor measures the extent of the primary electron transfer from excited dye [reaction (1)], it cannot be used to determine the supersensitizing influence of an added third component that may act by a mechanism such as reaction (3) that does not influence the quenching reaction. It is thus necessary to measure A directly. This is relatively easy in solution but, because of the low concentrations involved, rather difficult in monolayers. However, the electron-adduct radical is relatively stable and in fact has been detected optically in a monolayer assembly (33, 35). We have detected it in the present system by irradiation of the monolayer assembly under nitrogen at 545 nm, where the cyanine dye is the only absorbing species. The viologen single-electron adduct spectrum was detected in the 400 nm region. Comparison of the absorption spectrum with that in the literature (36) confirmed the species identity (Figure 5). Figure 6 illustrates the growth in yield of this radical with illumination time. Note that radical growth occurs in seconds or minutes, whereas the primary electron transfer must occur in less than a nanosecond, since with the ratio of viologen to arachidic acid used (5 mol % viologen), dye fluorescence quenching is >90% efficient. The radical growth that we detect in this steady-state experiment is clearly the result of a secondary process of radical stabilization. The radical is in fact not completely stable under our conditions, decaying slowly (over many minutes) when the light is turned off. This is consistent with the fact that an invariant incomplete conversion is reached on prolonged irradiation. This conversion is a constant fraction of initial viologen concentration if all other conditions are kept constant.

We have no direct information concerning the nature of the slow reaction leading to stabilization of the radical. Reasonable mechanisms for a slow process leading to stabilization, such as positive charge diffusion away from the electron-transfer center

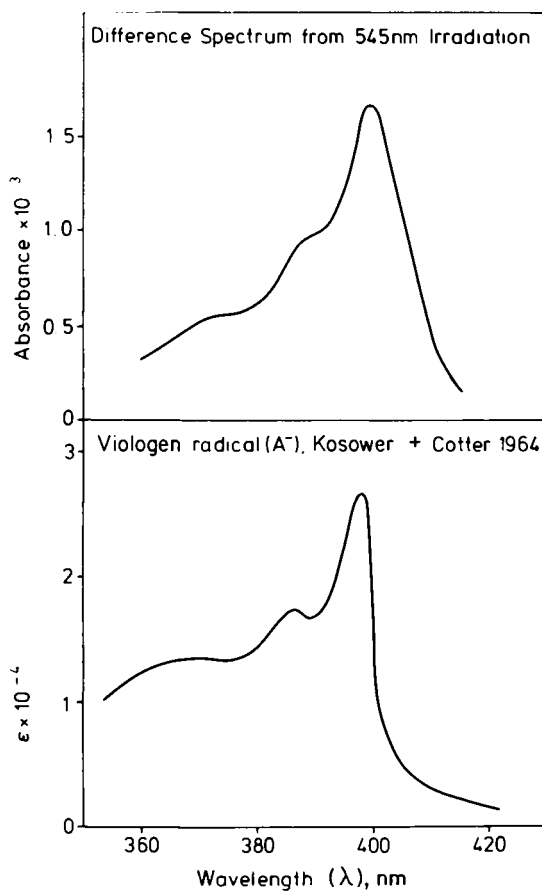


Figure 5. Observed photosensitized absorption in dye aggregate–viologen monolayer system compared with literature spectrum of the radical produced from one-electron reduction of dimethylviologen (36).

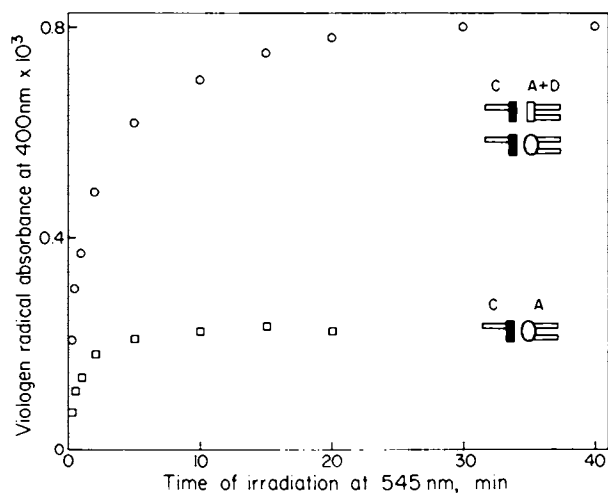


Figure 6. Time-dependent growth and steady-state yield of radical absorption at 400 nm on illumination at 545 nm of the two-component dye aggregate–viologen system (□) and the three-component donor–dye aggregate–viologen system (○). Donor and acceptor concentrations are each 5 mol % diluted with arachidic acid.

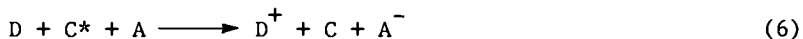
or reorientation of the acceptor-electron adduct, can be envisioned, but are only speculative.

Donor-Sensitizer-Acceptor System: Supersensitization

We now have an analytical means to measure the yield of the electron-transfer product radical that escapes recombination. We can therefore study factors that influence this yield. As mentioned, our present interest is in the possibility of enhancing this yield with added supersensitizers. The compounds we chose to study are colorless reducing agents. The reducing agent or donor was usually placed in the same layer as the electron acceptor in contact with the cyanine dye layer. Figure 6 shows the yield of radical obtained with such a three-component system, containing 5 mol % of *N,N'*-dioctadecyl-*p*-phenylenediamine as donor along with an equal amount of viologen acceptor, in comparison with that obtained in the absence of donor. This is our best-case result, showing a 3.5-fold enhancement in steady-state yield. In fact, the initial rate of radical growth shows a similar enhancement, demonstrating that the effect is kinetic in origin.

Figure 7 compares the enhancement obtained with four donors under the same conditions. Also shown is the effect of these donors on cyanine dye aggregate fluorescence in the absence of acceptor in the monolayer assembly. Several of the donors quench this fluorescence, presumably because they can photoreduce the excited dye [reaction (4)]. Qualitatively the extent of radical yield enhancement or supersensitization correlates with the extent of cyanine fluorescence quenching by the donors. This raises the possibility that reactions (4) and (5) are involved in the supersensitization. However, even the donor which causes virtually no fluorescence quenching still results in some supersensitization. Thus, some other mechanism such as reaction (3) is probably also involved.

Whatever the sequence of the events, the overall net effect of coupling either reactions (1) and (2) or (3) and (4) is a net electron transfer from donor to acceptor:



By diluting the amounts of donor and acceptor in the contact layer, we have demonstrated that supersensitization occurs down to levels where the average donor-acceptor separation is >40 Å. Molecular diffusion is not possible, and the arachidic acid spacer molecules are nonconductive within the layer. The electron transport from donor to acceptor site must occur through the dye aggregate. The distances involved require the participation of up to five dye molecules, assuming a linear electron movement.

Significantly, if the cyanine dye is incorporated into the system in monomeric-dimeric form, although radical formation can

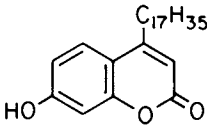
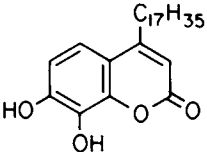
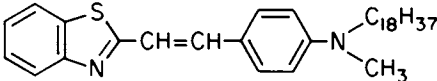
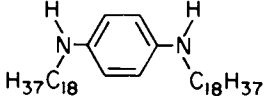
<u>Donor</u>	<u>Supersensitization</u>	<u>I/I₀</u>
	1.3	0.96
	1.9	0.90
	2.4	0.77
	3.5	0.24

Figure 7. Comparison of the ability of different donors to supersensitize the yield of radical and to quench the cyanine dye aggregate fluorescence.

be photosensitized (in much reduced yield), this yield cannot be enhanced by added donor. In such a case, where the individual or pairs of dye molecules are surrounded by arachidic acid, there is apparently no path for the electron transfer between donor and acceptor. The possibility that preassociation between donor and acceptor is responsible for our observations is unlikely in view of the following results: (a) The fluorescence quenching by acceptor and those donors which induce it is additive when the two are present together. (b) Donor incorporated into the dye layer enhances radical yield to the same extent as when incorporated into the acceptor layer. In this case, premixing of donor and acceptor does not occur.

Summary

We have constructed a monolayer assembly in which electron transfer occurs from excited cyanine dye J aggregates to a viologen electron acceptor. This process is manifested by efficient, rapid quenching of the dye fluorescence accompanied by slow, inefficient growth of relatively stable radicals, detected by absorption. If electron donors are added to either acceptor or dye layer, this radical yield can be enhanced. This enhancement or supersensitization can be as large as a factor of 3.5, depending on donor and conditions. The supersensitization is due to electron transfer from donor to either excited dye or the dye radical cation. The net effect is photocatalyzed electron transfer from donor to acceptor. Electron transport through the dye aggregate appears to be necessary for supersensitization.

Acknowledgments

The authors acknowledge valuable discussions with Professor H. Kuhn during this work. T. Penner particularly thanks Professor Kuhn for the research opportunity at the Max Planck Institut and acknowledges the continued financial support of Eastman Kodak Company through its academic assignment program.

Literature Cited

1. Gerischer, H.; Katz, J. J., Eds; "Light-Induced Charge Separation in Biology and Chemistry"; Dahlem Konferenzen: Berlin, 1979.
2. Schumacher, E. *Chimia* 1978, 32, 193.
3. Marcus, R. A. Ref. 1, p 15.
4. Weller, A. In "Fast Reactions and Primary Processes in Chemical Kinetics"; Claesson, S., Ed.; Interscience: New York, 1967; p 413.
5. Hautala, R. R.; King, R. B.; Kutal, C., Eds.; "Solar Energy: Chemical Conversion and Storage"; Humana Press: New Jersey, 1979.

6. Brugger, P.-A.; Infelta, P. P.; Braun, A. M.; Grätzel, M. J. Am. Chem. Soc. 1981, 103, 320.
7. Bolton, J. R. Science 1978, 202, 705.
8. Gerischer, H.; Willig, F. Top. Current Chem. 1976, 61, 31.
9. Calvin, M. Acc. Chem. Res. 1978, 11, 369.
10. Takuma, K.; Kajiwara, M.; Matuo, T. Chem. Lett. 1977, 1199.
11. Kalyanasundaram, K.; Kiwi, J.; Grätzel, M. Helv. Chim. Acta 1978, 61, 2720.
12. Katušin-Ražem, B.; Wong, M.; Thomas, J. K. J. Am. Chem. Soc. 1978, 100, 1679.
13. Schmehl, R. H.; Whitten, D. G. J. Am. Chem. Soc. 1980, 102, 1938.
14. Gerischer, H.; Selzle, H. Electrochim. Acta 1973, 18, 799.
15. Broich, B.; Heiland, G. Surf. Sci. 1980, 92, 247.
16. Carroll, B. H. Photogr. Sci. Eng. 1977, 21, 151.
17. Pileni, M.-P.; Braun, A. M.; Grätzel, M. Photochem. Photobiol. 1980, 31, 423.
18. Willner, I.; Otvos, J. W.; Calvin, M. J. Am. Chem. Soc. 1981, 103, 3203.
19. Arden, W.; Fromherz, P. J. Electrochem. Soc. 1980, 127, 370.
20. Memming, R. Photochem. Photobiol. 1972, 16, 325.
21. Gilman, P. B., Jr. Photogr. Sci. Eng. 1968, 12, 230.
22. Gilman, P. B., Jr. Photogr. Sci. Eng. 1974, 18, 418.
23. Seefeld, K.-P.; Möbius, D.; Kuhn, H. Helv. Chim. Acta 1977, 60, 2608.
24. Whitten, D. G.; Mercer-Smith, J. A.; Schmehl, R. H.; Worsham, P. R. In "Interfacial Processes: Energy Conversion and Synthesis"; Wrighton, M. S., Ed; American Chemical Society: Washington, D. C., 1980; p 47.
25. Kuhn, H. Chem. Phys. Lipids 1972, 8, 401.
26. West, W.; Gilman, P. B., Jr. In "The Theory of the Photographic Process"; 4th ed.; James, T. H., Ed.; Macmillan: New York, 1977; p 251.
27. Kuhn, H.; Möbius, D.; Bücher, H. In "Physical Methods of Chemistry"; Weissberger, A.; Rossiter, B. W., Eds.; Wiley: New York, 1972, 1 Pt. IIIB; p 577.
28. Herz, A. H. Adv. Coll. Interface Sci. 1977, 8, 237.
29. Rosenoff, A. E.; Norland, K. S.; Ames, A. E.; Walworth, V. K.; Bird, G. R. Photogr. Sci. Eng. 1968, 12, 185.
30. Möbius, D.; Penner, T. L. unpublished.
31. Muentzer, A. A. private communication.
32. Dodelet, J.-P.; Lawrence, M. F.; Ringuet, M.; Leblanc, R. M. Photochem. Photobiol. 1981, 33, 713.
33. Möbius, D. In "Topics in Surface Chemistry"; Kay, E.; Bagus, P. S., Eds.; Plenum Press: New York, 1978; p 75.
34. Möbius, D.; Kuhn, H. Isr. J. Chem. 1979, 18, 375.
35. Möbius, D.; Ballard, S. B. unpublished.
36. Kosower, E. M.; Cotter, J. L. J. Am. Chem. Soc. 1964, 86, 5524.

RECEIVED April 30, 1982

Monolayer Particle Arrays Formed by Vapor Deposition

DAVID ROBERTSON¹ and ARNOLD L. PUNDSACK

Xerox Research Centre of Canada, Mississauga, Ontario, Canada L5L1J9

The process by which vapor-deposited material forms two-dimensional arrays of spherical particles just beneath the substrate surface has been studied in detail. A model has been proposed in which the numbers and sizes of particles are determined by the coupled processes of particle growth (by capture of diffusing molecules) together with particle coalescence. Expressions have been derived for particle size and number density as functions of deposition parameters. Experimental evidence is presented in support of the model for the case of selenium physically vapor-deposited onto a heated thermoplastic substrate. Finally, the technological application of the deposit morphology as dry microfilm is reviewed.

In conventional physical vapor deposition, the material to be deposited is emitted in atomic or molecular form from a heated source and is allowed to impinge on a solid substrate. The process is carried out in a vacuum chamber in order to avoid contamination of the deposit and also to avoid the possibility that the emitted vapor may condense in the gas phase. The rate of evaporation from the source is controlled via the source temperature which is normally much higher than the substrate temperature. Atoms or molecules impinging on the substrate may be more or less elastically reflected back into the gas phase or, more commonly, they stick to the substrate where they are held by attractive forces. If the energy of attraction is very high relative to the thermal energy of the substrate, the deposited molecule is effectively bonded or chemisorbed to the substrate.

¹ Current address: St. Regis Technical Center, West Nyack, NY 10994.

For less strong binding, we have a state of physical adsorption in which the adsorbed species is mobile -- able to migrate parallel to the surface by means of thermally-activated hops. Adatoms (or adsorbed molecules as the case may be) may also receive enough thermal energy from the substrate to desorb and return to the vapor phase. The probability of desorption per unit time depends on the temperature and binding energy to the substrate through an Arrhenius-type rate expression

$$\alpha = \nu \exp(-\Delta G_{\text{des}}^*/kT) \quad (1)$$

where ν is a frequency the same order of magnitude as the substrate's Debye frequency, that is, typically 10^{12} to 10^{14} Hz, k is Boltzmann's constant and ΔG_{des}^* is the activation free energy for desorption which, for systems of interest to us, takes values the order of 0.1 to 0.3 eV.

While adatoms are migrating over the substrate and occasionally re-evaporating, they continue to impinge at a rate β . For high substrate temperatures, when desorption is frequent, or for low rates of impingement, it is possible that an equilibrium adpopulation n will be established so that the rate of impingement β is balanced by the rate of desorption αn . This equilibrium will be stable provided that the adpopulation β/α is sufficiently small so that encounters between migrating adatoms are infrequent compared to the rate of dissociation of the clusters which form when adatoms meet and bind with each other. Under those conditions of high temperature and low rate of impingement, no macroscopic deposit will be formed. On the other hand, if the adpopulation becomes large enough, cluster formation and growth is favored. Once a cluster grows in excess of a critical size (depending on temperature and deposition rate), the probability of capture of an adatom exceeds the probability of decay and the cluster then grows spontaneously. Eventually, growing clusters merge to form a continuous film.

It is clear that whether we deposit a film or not depends on the impingement rate and substrate temperature for a given combination of materials. We can, in fact, map out the conditions for film deposition, usually on a plot of \log (impingement rate) versus reciprocal temperature as shown in Figure 1. At high temperatures and low rates of impingement, there is no deposit aside from the equilibrium adpopulation while for low temperatures (when binding to the substrate is influential) and rapid deposition rates, we observe film formation.

This is a highly simplified picture of film deposition in the conventional sense. In the present work, we will relax the unstated assumption that the substrate is impermeable to

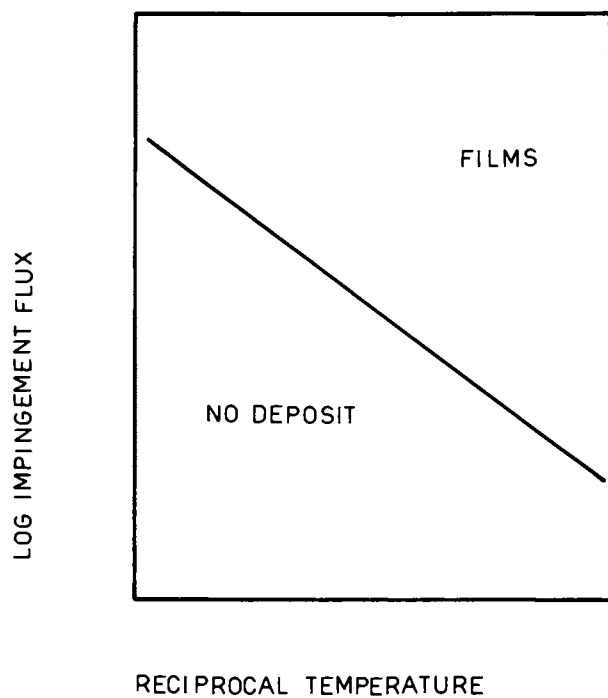


Figure 1. Schematic plot of impingement rate vs. reciprocal absolute temperature showing conditions for film growth in conventional physical vapor deposition.

the deposited material and observe contrasts and similarities to conventional vapor deposition. First, however, it is appropriate to present some background on the discovery of subsurface particulate deposits.

Normally, substrates are impermeable and deposits are held out on the surface. However, some years ago, workers (1) at Xerox observed, while depositing selenium onto flexible plastic substrates, that "good", continuous films were grown except under certain circumstances when the deposit took the form of particles. Examination of these deposits revealed that the particles were spherical, fairly uniform in size and, most remarkable, were organized into a monolayer array just beneath the surface of the substrate. Figure 2 shows a top view of a typical deposit as observed using the transmission electron microscope. There are usually the order of 10^9 particles per cm^2 of deposit. These measure 100 to 200 nm in diameter and reside at a depth of a few tens of nm. The sizes and numbers of particles depend on deposition conditions as will be shown in the next section.

Figure 3 illustrates the restricted range of conditions in which particulate deposits were observed for a particular thermoplastic substrate. As in Figure 1, we observe no deposit for sufficiently low rates of impingement and/or high substrate temperatures. Under those conditions, frequent desorption insures that supercritical aggregates do not form. The "activation energy" associated with the slope of that boundary corresponds to the desorption process. For rapid impingement and/or low temperatures, macroscopic deposits form but there is a transition between continuous films and subsurface particles. The slope of the line forming the particle/film boundary corresponds to the activation energy for the fluidity of the substrate as a function of temperature. This suggests that at low temperatures, the substrate behaves as a solid, impermeable to the deposited material which is held out on the surface in the form of a film. For high temperatures, the substrate behaves like a viscous fluid which is capable of wetting and engulfing particles by capillarity forces and into which material can diffuse. If the rate of impingement is very high, particles formed on the surface grow very rapidly and coalesce into a stable film before they are able to migrate below the surface.

With this semi-quantitative explanation as a starting point, we'll now proceed to develop a quantitative model of particle growth and coalescence in terms of deposition conditions which can be used in a process control strategy.

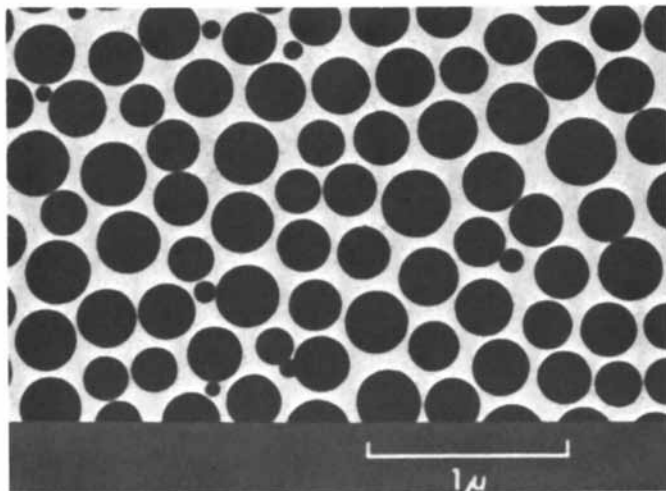


Figure 2. Plan view transmission electron micrograph of spherical selenium particles grown in a thermoplastic substrate. (Reproduced, with permission, from Ref. 2. Copyright 1981, American Institute of Physics.)

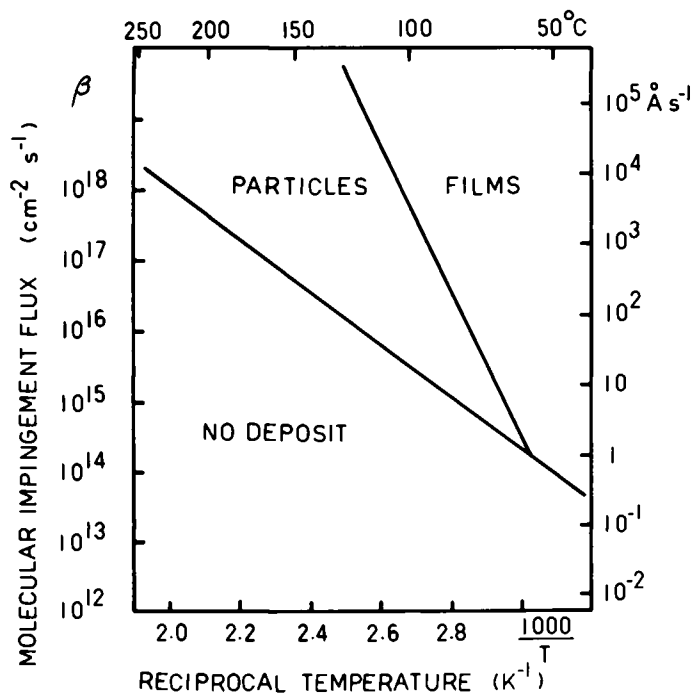


Figure 3. Plot of deposit morphology as a function of deposition rate and substrate temperature showing region of no deposit, continuous surface films, and subsurface particles for a given substrate material. (Reproduced, with permission, from Ref. 2. Copyright 1981, American Institute of Physics.)

Model of Subsurface Growth and Coalescence

Our contention is that the ultimate morphology of the film -- that is, the numbers and sizes of particles -- is governed primarily by the processes by which those subsurface particles grow and coalesce.

First, consider growth. In the absence of any near neighbors, a particle grows by capture of atoms or molecules which diffuse through the substrate following deposition on its surface. The situation is illustrated in Figure 4. We assume that Fick's Law of diffusion applies to transport of molecules through the substrate and that a quasi-steady state is achieved. This means that the concentration f of diffusing species satisfies Laplace's Equation with quasi-constant boundary conditions: $f=0$ at the (absorbing) surface of the particle and $f=f_s$ at the surface of the substrate. We are not particularly interested in the concentration field itself but only in the integral of the diffusion flux (proportional to the concentration gradient) over the particle surface. This is obviously proportional to the rate of addition of molecules to the particle and thence to the rate of increase of its radius. The integral we seek can be easily determined through the use of an electrostatic analogy as described previously (2). It turns out that

$$\iint \vec{J} \cdot d\vec{S} = 4\pi R D f_s \quad (2)$$

$$= \frac{d}{dt} \left(\frac{4}{3} \pi R^3 / \Omega \right) \quad (3)$$

where Ω is the increase in the particle's volume due to the addition of one diffusing species (atom or molecule). Simplifying,

$$\frac{dR}{dt} = \Omega D f_s / R \quad (4)$$

is the rate of growth due to capture of diffusing species.

The surface concentration f_s must satisfy a quasi-steady state mass balance in which the difference between the rates of impingement β and desorption $\alpha b f_s$ is equal to the rate at which the N growing particles per unit area capture diffusing species or

$$\beta - \alpha b f_s = 4\pi R D f_s N \quad (5)$$

whence

$$f_s = \beta / (\alpha b + 4\pi R D N) \quad (6)$$

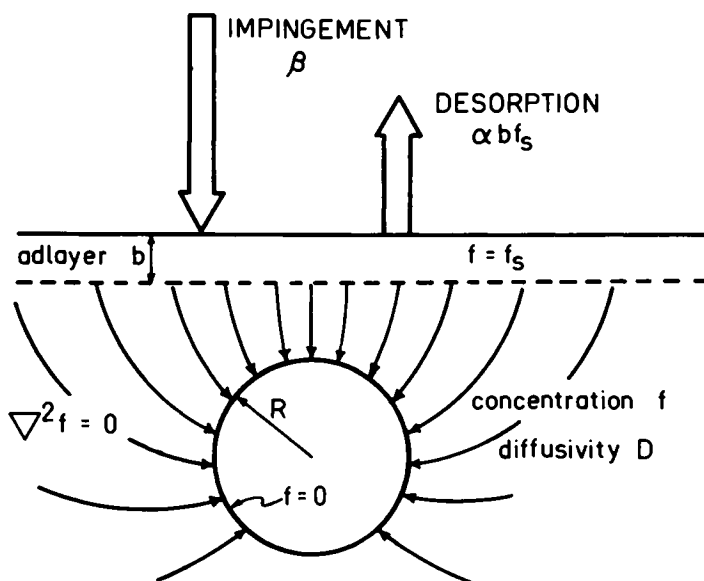


Figure 4. Mass transport configuration for an isolated spherical particle growing in the proximity of a surface where impingement/desorption is occurring.

Combining equations (4) and (6), we arrive at an expression for diffusion-controlled growth rate in terms of particle size and number density (competition between particles for molecules is implicit), deposition rate, desorption frequency and diffusivity in the substrate. The parameter b represents the thickness of the adlayer and is of molecular dimensions.

The growth process itself is not sufficient to explain deposit morphologies: coalescence must also be considered. In reality, the particles are not isolated; in a typical deposit (Figure 2), they are almost close-packed. This means that whether by motion of the particles or by their growth, they occasionally come into contact. When they do, coalescence occurs. That is, the pair of particles "fuses" into a single larger particle so as to reduce the total surface free energy. Consideration of various mechanisms for the coalescence process (3) leads to the conclusion that it takes much less than one second for particles of interest to us. Therefore, we will treat that process as if it were instantaneous.

Whereas growth alone leads to an increase in the size of particles but no change in their numbers, coalescence reduces their numbers and increases their average size. The processes are coupled, however, since the rate of coalescence or, more properly, the rate at which particles disappear as a result of coalescence is given by:

$$-dN/dt = 4 \pi \zeta R (dR/dt) N^2 \quad (7)$$

In deriving Equation (7), we have neglected the possibility that the particles may themselves be mobile and have calculated the rate at which randomly-distributed particles of radius R and number density N grow into contact, given that each particle's radius increases at a rate (dR/dt) before encounter. The factor ζ accounts for the fact that the particles are not randomly distributed in space but must be more or less ordered due to their close-packing. Experimentally, a value of 2 is found for ζ .

The numbers and sizes of particles are also coupled through a mass balance since the total amount of material deposited in some interval of time must equal the difference between the amount impinged and the amount re-evaporated in that same interval. Furthermore, we are safe in assuming that the total amount of material deposited is accounted for by the mass of the particles; that is, we neglect the small amount of material present as atoms or molecules in comparison with the amount incorporated in particles. Thus, for conditions such that re-evaporation is slow compared to impingement, we have

$$\frac{4}{3} \pi R^3 N = Vt \quad (8)$$

where $V = \beta\Omega$ is the rate of deposition expressed as the rate of thickening of a uniform film of equivalent volume. It is possible to derive the mass balance analogous to (8) for the general case when re-evaporation is significant but the special case above, called "complete condensation" is very common and technologically very important.

If we now combine our expressions (4) and (6) for the isolated particle growth rate, (7) for the coalescence rate and (8), the mass balance and integrate from some initial time t_0 when N_0 particles are present, we arrive at the analytical results:

$$N^{-1/3} - N_0^{-1/3} = \frac{\zeta}{2} \left(\frac{4}{3} \pi v^2 \right)^{1/3} (t^{2/3} - t_0^{2/3}) \quad (9)$$

and

$$R = \left(\frac{3V}{4\pi} \right)^{1/3} t^{1/3} \left[\frac{\zeta}{2} \left(\frac{4\pi v^2}{3} \right)^{1/3} (t^{2/3} - t_0^{2/3}) + N_0^{-1/3} \right] \quad (10)$$

Comparison with Experiment

In a vacuum chamber held at about 2×10^{-4} Torr, selenium was evaporated from a source at 250°C and allowed to impinge, through an adjustable slit, onto a travelling web of thermoplastic-coated polyester film maintained at 105°C. The time of exposure of the substrate to the vapor source is simply the slit width divided by the web speed. Deposits were made for a series of slit widths (i.e. exposure times) and the resulting samples were examined in the transmission electron microscope. From image analyser studies of the micrographs, average particle size and number density were determined. These data appear in Table I together with some quantities derived from the data. If the model is correct and Equations (9) and (10) apply, we would expect the quotients

$$Q' = [N^{-1/3} - N_0^{-1/3}] / [t^{2/3} - t_0^{2/3}] \quad (11)$$

$$= \frac{\zeta}{2} \left(\frac{4}{3} \pi v^2 \right)^{1/3} \quad (12)$$

and

$$Q'' = NR^3/t \quad (13)$$

$$= 3V/4\pi \quad (14)$$

to be constant. These have been calculated from the data and

appear in Table I. They appear to be reasonably constant with the possible exception of data for the longest exposure time. The model also predicts that the "coverage" or $\theta = \pi R^2 N$ should tend to a constant value of $3/2\zeta$. This is observed. All these data are consistent with values: $\zeta = 2$ and $V = 4.72 \times 10^{-6} \text{ cm s}^{-1}$ or $2.8 \text{ } \mu\text{m min}^{-1}$. The latter agrees with what is expected under the experimental conditions employed. Particle sizes and numbers are shown in Figure 5 plotted as experimental data and from Equations (9) and (10). Error bars are estimated from the statistics of measurements from the TEM frames. Agreement is very good.

Another prediction of the model is that the size and number of particles are uniquely determined by the total amount of material deposited, irrespective of conditions, provided complete condensation is operative. This can be readily appreciated by noting that, in Equations (9) and (10), time appears only in conjunction with rate so that Vt (the quantity deposited) is the effective independent variable. This prediction has been verified through experiments in which rate and temperature were varied for a given specimen. The deposit morphology depended only on how much material was deposited and was insensitive to the way in which it was done.

These, and other, observations confirm the validity of the model at least under conditions of complete condensation.

Table I. Experimental data for number density of subsurface particles and their average radius at different deposition times. Q' , Q'' and θ are defined in text.

<u>t(s)</u>	<u>N(cm⁻²)</u>	<u>R(cm)</u>	<u>Q'</u>	<u>Q''</u>	<u>θ</u>
1.50	3.05×10^9	0.080×10^{-4}	-----	1.041×10^{-6}	0.613
1.67	2.69	0.085	3.033×10^{-4}	0.989	0.610
1.88	2.13	0.095	4.118	0.921	0.604
2.14	1.78	0.110	3.871	1.107	0.677
2.50	1.43	0.125	3.725	1.117	0.802
3.00	1.02	0.160	3.950	1.393	0.820
3.75	0.64	0.195	4.268	1.265	0.765
5.00	0.29	0.305	5.089	1.646	0.848

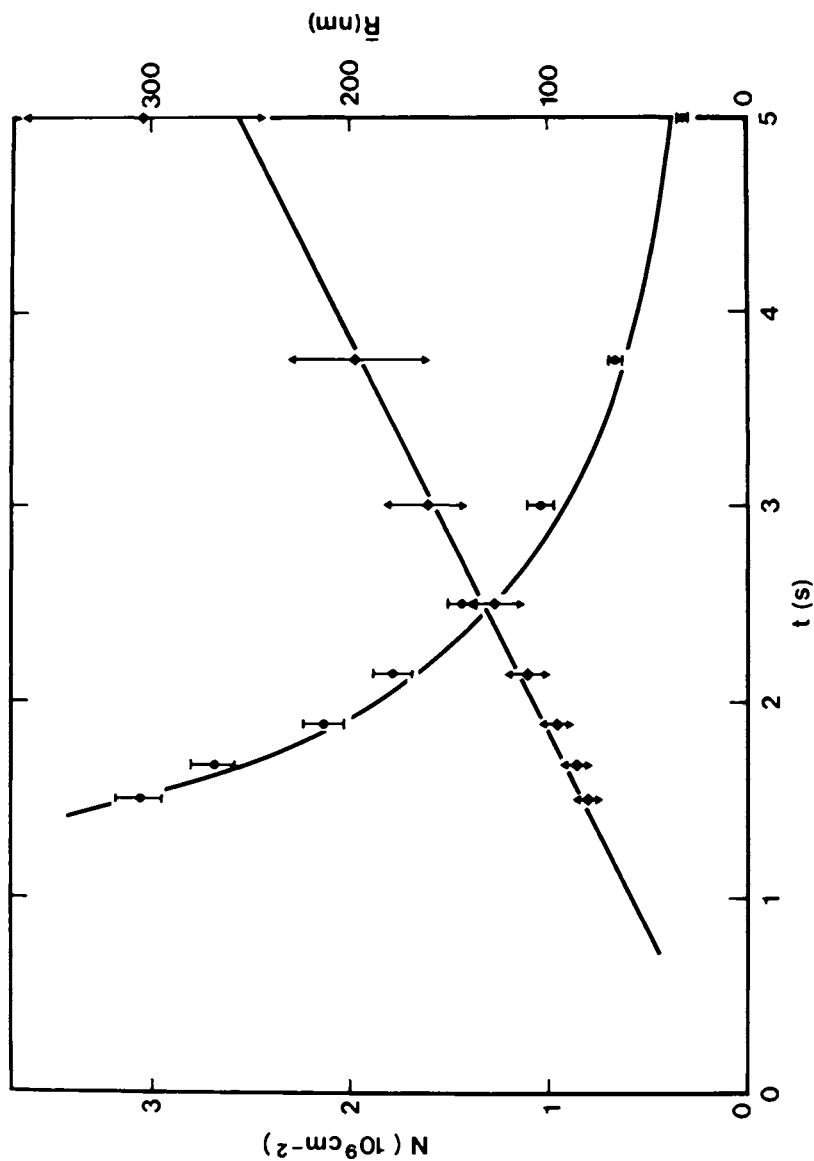


Figure 5. Mean particle number density, N , and radius, \bar{R} , plotted for various deposition times, t . Solid lines are plots of Equations 9 and 10. (Reproduced, with permission, from Ref. 2. Copyright 1981, American Institute of Physics.)

Imaging Technology based on Monolayer Particle Array

The geometry of the deposit has led to the development of a novel imaging system. As described by Goffe (1) and Pundsack (4), images are formed due to electrophoretic migration of light-struck particles. The materials package is sketched in Figure 6. The film consists of an aluminized polyester base overcoated with a 1.5 μm layer of thermoplastic. A monolayer of selenium particles is formed just beneath the upper surface of the thermoplastic layer by vapor deposition as described above.

Images are formed by: first, sensitizing the film with a positive or negative corona charge; second, imagewise exposure and finally, development in which the thermoplastic layer is softened either by heat or exposure to a swelling solvent, allowing light-struck particles (which had acquired a charge in the exposure step) to migrate to the opposite surface of the layer under the influence of electrophoretic forces. Contrast is achieved by removing un-migrated particles by flushing them away with solvent, for example.

The film's mid-exposure sensitivity is about 1 erg cm^{-2} at 400 nm. The image shows a maximum optical density of about 2 and a background density of 0.2. Gamma lies in the range 1 to 3 and resolution is better than 250 lines per mm. Pundsack (4) showed that the film's imaging characteristics depend on the particle size distribution: optical density is found to be proportional to the total volume of selenium migrated per unit area and that is equal to the cumulative volume of all particles which have received more than some minimum exposure. But since the minimum exposure varies inversely as the square of the particle size, it follows that a plot of cumulative volume of oversize particles versus the inverse square of particle size has the same form as the plot of optical density versus exposure. This relationship between imaging properties and deposit morphology, together with the ability of the model to predict particle sizes and numbers as functions of deposition time and conditions, makes it possible to prepare films with predetermined functional characteristics.

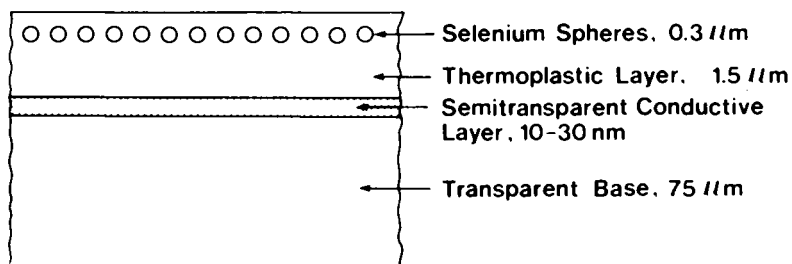


Figure 6. Cross-sectional view of particle migration film structure. (Reproduced, with permission, from Ref. 2. Copyright 1981, American Institute of Physics.)

Literature Cited

1. Goffe, W. L. Photogr. Sci. Eng. 1971, 15, 304.
2. Robertson, D.; Pundsack, A. L. J. Appl. Phys. 1981, 52, 455.
3. Stowell, M. L. Thin Films 1968, 1, 55.
4. Pundsack, A. L. Photogr. Sci. Eng. 1974, 18, 642.

RECEIVED April 30, 1982

Interfaces in Electrophotography

JOHN W. WEIGL

Xerox Corporation, Joseph C. Wilson Center for Technology, Webster, NY 14580

Practically all interesting effects in electrophotography occur at contact zones between different materials. Examples will illustrate a variety of interfaces and their functions.

For instance, the photoconductive dielectric used in xerography must be provided with surface and base contacts which block the injection of charge under high electric field conditions. Contiguous layers of photosensitive and charge transporting materials may be used to separate two essential functions required of xerographic photoreceptors--the photo-generation of mobile charge carriers, and the amplification of contrast potential. The "toner" powder used to develop the latent charge pattern must itself be charged prior to use, by a process which requires close control of its interaction with several other materials in the development system. Nonaqueous colloids, used as "liquid developers" for xerography or as imaging fluid for photoelectrophoresis depend on their surfaces for electrostatic and entropic stabilization. The adhesion of toner particles to photoreceptors, their removal in the transfer and cleaning step, and the processes by which they may be permanently affixed to the surface of the paper all involve the formation and breaking of interfacial bonds. Finally, the effect of electrostatic fields upon surface energy has been utilized for a selective wetting

0097-6156/82/0200-0139\$12.05/0

© 1982 American Chemical Society

development process, as well as for display devices and photoplastic microfilms in which the surface of the polymer layer deforms in response to local electrostatic field patterns.

Electrophotography is largely a surface process, and most interesting steps involve interfaces between materials. In this brief survey we shall attempt to provide a rough outline of these, and to describe some of the main issues. No attempt can be made to be detailed or comprehensive.

In the forty-odd years since Chester Carlson's initial inventions, electrophotography has evolved pretty much in the direction envisioned by him (1). For conventional xerography, the image is formed by the deposition of a black thermoplastic powder on the surface of a photoconductive dielectric surface bearing an electrostatic charge pattern. The powder is transferred to plain paper and fused to it to form the final image. This is the process used in the ubiquitous xerographic office copier (2).

Significant variants exist: electrostatic charge patterns may be transferred instead of powders, charged colloids dispersed in dielectric liquids may be used as developers, images may be formed directly on photoconductive coated paper; or even by the deposition of electrically photosensitive particles (3). We shall return to some of these alternatives later--after describing the roles of interfaces in conventional dry transfer xerography.

Xerography from the Viewpoint of the Photoreceptor

The key process steps may be illustrated by a schematic cross-section of a typical xerographic copier (Figure 1). The photoconductor drum is rotated past a series of process stations, where it is, in turn, charged, exposed to a projected image pattern, developed by an oppositely charged "toner" powder, then pressed lightly against an electrically biased sheet of paper to transfer the image. Any remaining charge on the photoreceptor may be neutralized by an erasing lamp or an AC charging device, after which the last residue of the powder is brushed off and the photoreceptor is ready for

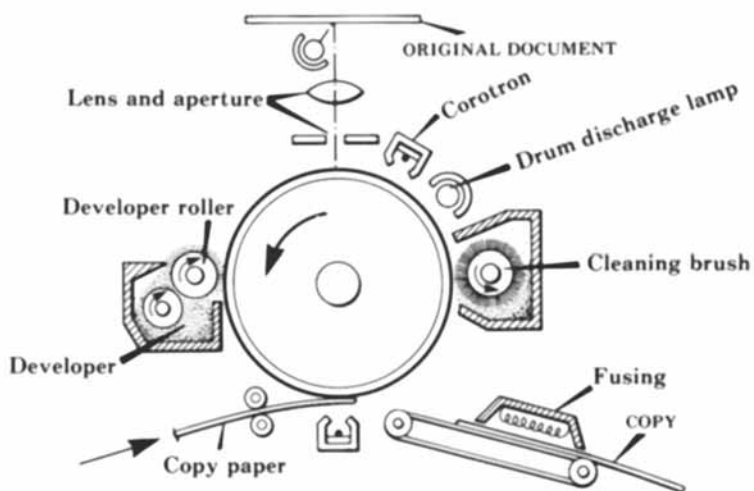


Figure 1. Schematic of typical xerographic copier. Process elements are clustered about the photoconductor-coated drum.

another cycle. In a modern copier, the whole series of steps may take only five seconds. The powder pattern on the paper is melted into the fibers to form a permanent image.

Some of the interfaces meeting the photoreceptor are obvious: its surface encounters ionized gas which serves to deposit or remove corona charge, the developer mass, the transfer sheet, and cleaning devices. Other interfaces with essential functions are found in the internal structure of the photoreceptor itself. Let us now look at these in some detail.

Charging of the Photoreceptor

The xerographic process places extraordinary demands upon the re-usable photoconductive dielectric which is the active element of the photoreceptor (4, 5). It must be capable of retaining the applied surface charge without significant dark potential loss between the charging and developing steps. To produce adequate image contrast, internal fields of the order of 20 to 50 V/ μ m are required. If inert dielectrics could be used, this would present no particular problem: one could rely on a high density of deep traps throughout the bulk of the dielectric to retain charge in the face of the driving field.

Not so in the xerographic photoreceptor. Recall that majority carriers generated near the surface in the exposure step must be free to migrate from the top to the bottom of the dielectric layer to enable imagewise photodischarge in the fraction of a second, available between exposure and development. While the time scale of the process does not require high mobility, deep traps for the majority carrier must be excluded from the bulk; otherwise, residual potential and background will build up as the photoreceptor cycles.

Therefore, the photoconductor must not only be free of thermal carriers but it must be protected against the dark injection of external charge, as well. Injection from the base electrode may be avoided by a thin blocking dielectric--typically 50 A.U. of a dense oxide or polymer--thin enough to allow any accumulated residual charge to leak off between cycles.

The injection barrier at the top surface is more difficult to understand. Although attempts have been made to deposit surface charge by induction or surface

contact, these have been generally much less successful than the unipolar ion stream from a corona device. Indeed, Carlson's invention of corona charging was one of his most valuable innovations (6)(Figure 2). Evidently the corona ions can be made to deposit on the surface in such a way as to form a blocking layer. The mechanism for this may well differ from photoconductor to photoconductor. In the case of zinc oxide-binder layers there is extensive evidence that negative corona charge consists of stably adsorbed oxygen anions (Figure 3), which can be discharged upon illumination (5, 7-11). For selenium it has been found that corona ions inject charge into the photoconductor, forming trapped charge sites just below the surface (12, 13).

Multi-Layer Photoconductors

The xerographic photoreceptor converts the projected image into a charge pattern residing at the surface of the dielectric. To be developable this electrostatic image must present contrast potentials of the order of 400-600V. Single layer photoconductors therefore serve two functions: photogeneration of a mobile charge carrier close to the surface of illuminated areas, followed by their field-assisted separation (14) and transport across sufficient dielectric thickness to develop the desired contrast potential (15-18). If a single material is used it must combine high photosensitivity with excellent transport properties and exceptionally high dielectric strength (19).

Can one separate these functions? Yes! It is possible to use a layer of one material as photo-sensor and another as voltage amplifier. For example (Figure 4), a sub-micron film of amorphous selenium suffices to absorb visible light and to generate mobile holes. If such a layer is coated over a 15 μ m layer of an aromatic polymer which has little photosensitivity but excellent dielectric and transport properties, one derives an excellent photoreceptor (20-22). The composite has essentially the full photosensitivity of selenium--spectacularly greater than that of the polymer alone. But it also has much better dielectric properties and a high degree of mechanical flexibility. It can be fabricated into belts which run around small rollers and offer considerable advantage to the system designer. Similar results have been reported for inverted

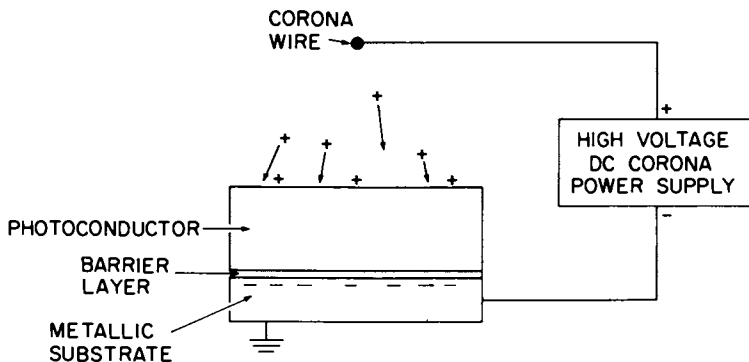


Figure 2. Photoreceptor and corona charging process.

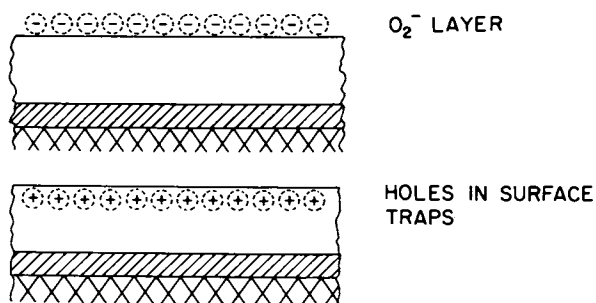


Figure 3. Schematic representation of the charge deposited on two photoconductor materials: ZnO-binder dispersion (top) and amorphous selenium (bottom).

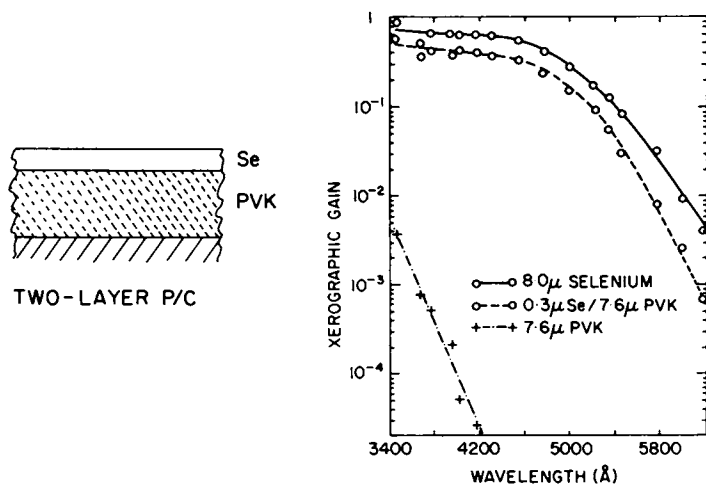


Figure 4. Double layer photoreceptor—schematic structure, with selenium generator overlying a poly(N-vinyl carbazole) (PVK) transport layer (left). Performance of such a composite ($\circ - - \circ$), compared to selenium ($\circ - \circ$) and to PVK without generator layer ($+ - - +$) (right). (Reproduced, with permission, from Ref. 20. Copyright 1968, Pergamon Press, Ltd.)

structures (Figure 5), for a variety of organic pigment generators, and for transport layers in which monomeric hole- or electron-transport molecules are used in crystalline form or in polymer solution (23-26).

Materials flexibility has thus been achieved--albeit at the cost of introducing an internal interface within the photoreceptor structure--an interface which must be carefully controlled in the coating process to prevent undesirable intermixing of layers, delamination, and the formation of barriers impeding charge carrier injection.

Pigment-Binder Composites

A very different type of interface dominates the behavior of an important class of xerographic photoconductors consisting of photoconductive pigment dispersions in dielectric binders. Familiar examples include zinc oxide (7-10, 27), and other inorganic pigments (28-31), as well as organic microcrystals dispersed in dielectric binders (32-36). In these systems, charge must travel through a loosely connected chain of pigment particles; the concentration required for effective contact depends on particle shape, and varies from about 25 volume percent for isotropic chunks of zinc oxide and cadmium sulfide (7, 9) to a mere 5 volume percent for needle shaped crystals of phthalocyanine (32) or filaments of a thiapyrylium-polycarbonate complex (36) (Figure 6).

The binder serves, not only to provide mechanical integrity and moisture proofing; it also adds interfaces which strongly affect electrical performance. The matrix material is carefully (and rather empirically!) selected to enable reliable charging, efficient photodischarge (minimal trapping), and stable repetitive cycling. A quasi-crystalline complex of thiapyrylium salt with polycarbonate, dispersed in a "doped" outer resin phase, appears to be a particularly elegant solution (34-36). Photoinduced discharge curves of most pigment-binder composites tend to be S-shaped rather than capacitive, as are those for selenium and other homogeneous photoconductors. This has been tentatively attributed to trapping at inter-particle contacts, followed by a field-induced trap emptying, which restores the interface to its initial state (28, 32, 36).

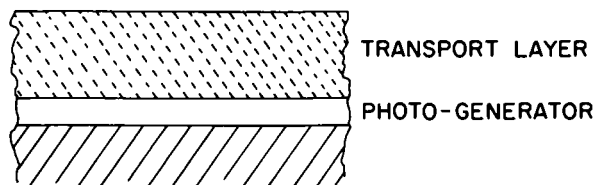


Figure 5. Double layer photoreceptor—inverted structure. The photo-generator is protected against environmental damage by the active dielectric transport layer.

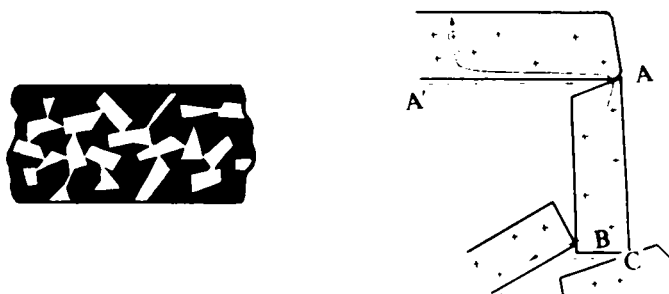


Figure 6. Cross-section (left) and schematic diagram illustrating charge transport through a chain of photoconductive pigment particles (A, B, C) dispersed in dielectric binder (right). Contact impedance and trapping at interfaces are critical to performance. (Reproduced, with permission, from Ref. 28. Copyright 1972, Walter de Gruyter & Co.)

Zinc oxide also illustrates one further interaction. Since this photoconductor intrinsically only responds to ultraviolet radiation, it is commonly sensitized to visible light by the adsorption of a monolayer of one or more dyes (Figure 7). This adds yet another essential interface to an already complex system (37-40).

Xerographic Process Steps

Black "toner", which is generally used to develop the electrostatic latent image, is a dispersion of $\sim 10\%$ carbon pigment in a thermoplastic. The powder is usually produced by shear milling and high-impact fracture. Carbon, as well as plastic, is exposed at the surface, and both materials may therefore be expected to influence the electrical properties of the composite (41-44). Toner serves to transform the electrostatic latent image on the photoreceptor into invisible image; therefore, particle size and charge/mass ratio must be closely controlled: typical values are $12\ \mu\text{m}$ and $20\ \mu\text{c/g}$, respectively; the latter corresponds to a density of some 300,000 electronic unit charges per particle.

Figure 8 shows the xerographic process from the viewpoint of the toner. The material is fed into the development chamber, charged (usually by triboelectricity), and applied to the photoconductor surface. Powder which adheres to charged areas of the latent image is then transferred and fused to a sheet of paper or film; the residue is cleaned off. Let us now consider these steps in greater detail.

Development

We shall illustrate the materials interfaces involved in development for a specific system in common use: the "two-component magnetic brush" (45-47) (Figure 9a). In such a device, 1-2 weight percent of toner is intimately mixed with relatively massive "carrier" beads having magnetic cores and (usually) thin dielectric coatings. A cylindrical shell or sleeve rotates above the developer reservoir. Bar magnets mounted within the shell attract the mixture of toner and magnetic beads and form them into a loose "brush-like" structure, whose "bristles" are really chains of carrier particles, loosely linked by the magnetic field lines (Figure 9b).

American Chemical
Society Library
1155 16th St., N.W.

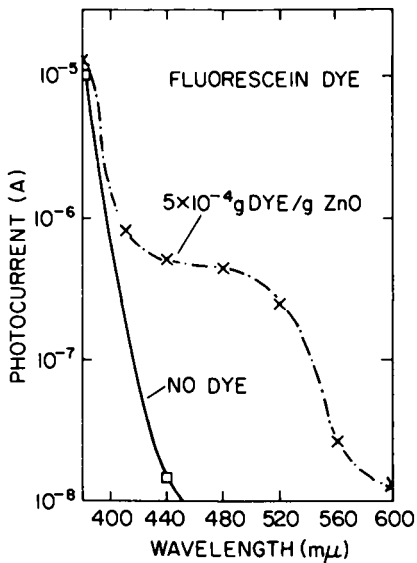


Figure 7. Photoresponse of zinc oxide-binder layer with ($- \cdot - \times -$) 5×10^{-4} g fluorescein dye and without ($—$) sensitizing dye. (Reproduced, with permission, from Ref. 40. Copyright 1970, American Institute of Physics.)

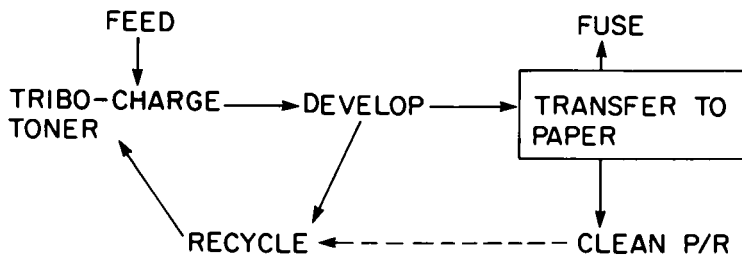


Figure 8. Toner interactions in xerography.

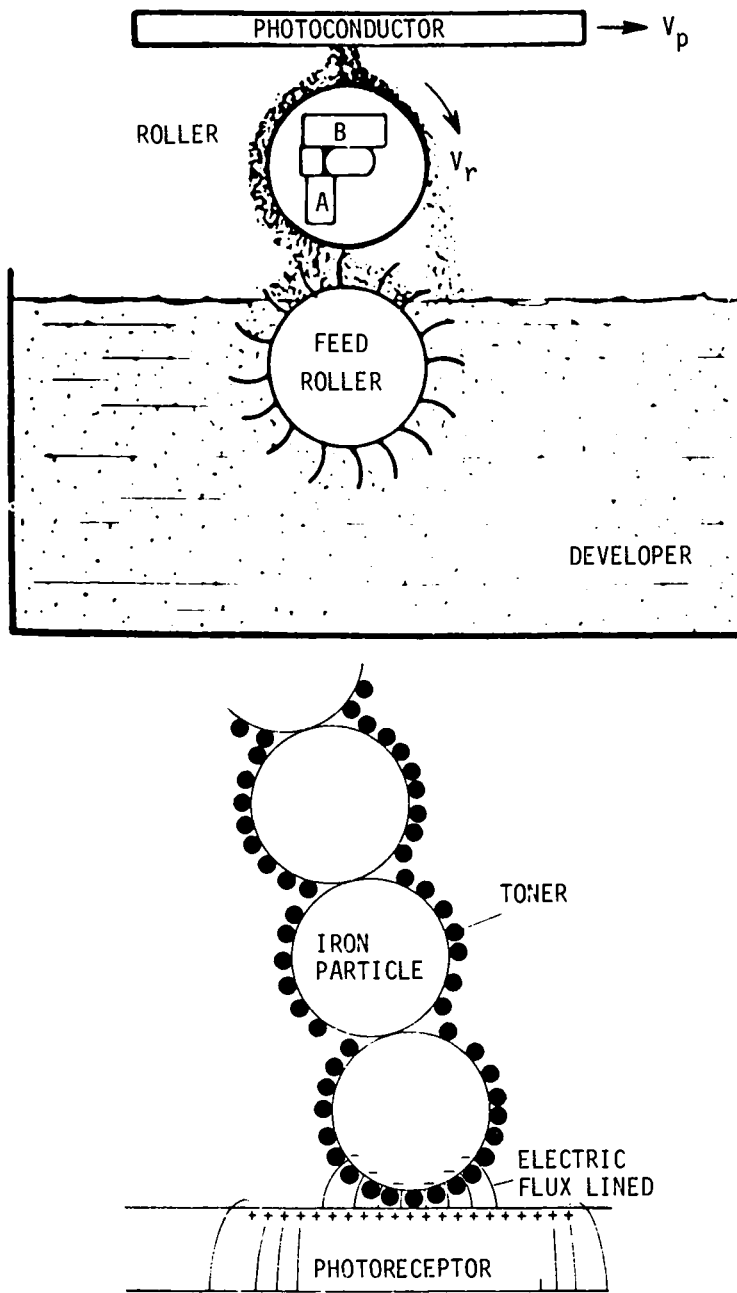


Figure 9. Magnetic brush (top) and magnetic brush "bristle" consisting of chain of large carrier beads covered with toner powder (bottom). Key: A, pickup magnet; and B, magnet. (Reproduced, with permission, from Ref. 50. Copyright 1974, Society of Photographic Scientists and Engineers.)

As the roll rotates, it agitates the developer mass by continuous tumbling, collapse, and re-formation of these bead chains. Toner and carrier undergo repeated bouncing contacts and separations, providing ample opportunities for charge exchange (55). As the tip of the brush sweeps across the photoconductor surface, a combination of mechanical impulses and the electric field from the latent image detaches toner from the carrier and attracts it to the charge pattern on the photoconductor surface (48, 49). The roll is usually electrically biased to augment the detachment threshold provided by the carrier charge, and to compensate for residual charge in exposed areas of photoconductor. Even after initial deposition, toner particles are likely to be scavenged by the brush and redeposited elsewhere on the latent image.

It is beyond our scope to review the detailed models for magnetic brush development which have been published (47, 50-53). Clearly, the process is dynamic, and must be optimized to the specific materials, configuration, and development speed to be used. Sufficient current must flow from the development electrode through the developer mass to charge the toner layer closest to the latent image and to compensate for a significant fraction of the charge on the photoconductor. A current of about 1 ma would be required to neutralize a fully charged latent image passing through a 30 cm wide development nip at 20 cm/second. As Hays (54) has shown, the electrical interfaces involved in the charge transport through the developer bed are quite complex. Conduction through the magnetic "bristles" is limited by the dielectric coating on the beads as well as by the thickness of intervening toner. Charge transport by the forward motion of charged toner particles through the developer mass is impeded by particle crowding, which in turn depends upon field strength, and geometrical factors such as bead shape (50-52).

Schmidlin (56) has pointed out that the commonly observed broad range of van der Waals forces between toner and carrier particles causes xerographic development to require much higher electric fields for toner release than those required to establish a sharp threshold. In fact, he argues that if the adhesive forces between these surfaces could be made sufficiently small and uniform ("noise-free"), it should be possible to reduce electrostatic charge density required for a given

developed contrast by a factor of 50-100. If this could be achieved in practice, it would offer an opportunity to cut optical exposure by nearly two orders of magnitude!

A second adverse effect of van der Waals adhesion is a tendency of carrier and photoconductor surfaces to become coated with a thin film of toner residue--a film which progressively impairs the efficiency of toner charging and photoreceptor performance. Salaneck et al. (57) have reported that material transfer amounting to as little as 1 atom/ 10^5 surface sites is measurable as a shift in "triboelectric" charging behavior!

Charge Exchange Between Carrier and Toner

We now consider the interface between carrier and toner, as these components interact in a dynamic development system. As we have noted, toner is commonly fabricated by "jet impacting" a brittle pigmented thermoplastic to form irregularly shaped particles of about $12\mu\text{m}$ cross-section--particles whose surface comprises resin and carbon black (2, 43, 58). The carrier cores are magnetic (ferrite or steel), typically about $250\mu\text{m}$ in size and therefore relatively massive. They are generally coated with a dielectric oxide or resin, which participates in the tribo-electrification process (2, 47, 59).

The action of xerographic developer is highly leveraged: a mere 30 fc of charge causes development by a $12\mu\text{m}$ sized toner particle (59). While this is the basis of image amplification which gives xerography "projection speed" (equivalent to ASA 2-10) (2, 3, 60) it is also inevitably a source of image noise (56, 61). Saturation charge on dielectrics is reached at surface densities of 1-10 nc/cm², corresponding to only one charge per 10^3 - 10^4 surface atoms. Thus a reversal of the polarity on less than one tenth of a percent of the surface sites on a toner particle suffices to double (or nullify) the charge per particle!

Developer materials are chosen so as to assure that frictional electrification produces toner of the desired polarity (which is generally opposite that of the charged photoreceptor surface). Because "real" development systems are complex, and must operate under highly variable conditions, "practical" materials choices must be made on an empirical basis. Nonetheless, physical models have served as useful guides. Investigations of

"clean" model surfaces suggest that charge exchange between metals and insulators is driven primarily by differences between accessible electronic energy levels. In metals these are readily defined, e.g., in terms of contact potentials; and, indeed, charge transfer to a common dielectric from a series of metals having different contact potentials gives fairly predictable results (62), provided that effects like surface oxidation are taken into account (63). Even charge exchange between pairs of dielectrics may be predicted--at least in a semiquantitative way--by reference to their work functions, relative to a common metal (62, 64) (Figure 10).

Successful attempts have been made to correlate "tribo" charging to chemical structure in model materials (Figure 11). Cressman, Gibson and their co-workers (65, 66, 67, 154) have found persuasive correlation between the Hammett "sigma" function (a measure of substituent electronegativity) of three series of ring-substituted aromatics with the ability of these materials to accept electric charge from common metal contact electrodes. In polymers of xerographic interest, Duke and Fabish (68) have used spectroscopic techniques to identify donor and acceptor states, capable of forming localized molecular ions upon charge transfer. Surprisingly, such states are sufficiently sharply defined to control charge exchange, as though they were communal energy levels--even though they are much too localized to admit charge transport.

While it thus seems plausible that charge exchange in "dry" model systems is driven by differences in electronic contact potential, most "real world" surfaces are covered by moisture films which enable the exchange of any soluble ions which may be present. For example, according to the classic experiments of Knoblauch (144) and Rudge (145, 146, 147), acidic surfaces generally tend to charge inert materials positively, while basic surfaces are a source of negative charge. Harper (149) suggests that this may well be due to the selective transfer of mobile protons and OH^- ions, respectively. More work needs to be done on this interesting subject, which may have important implications for the use of charge control agents in xerographic developer materials (150, 151). Model experiments, using ion exchange resins and zeolites, might be most instructive!

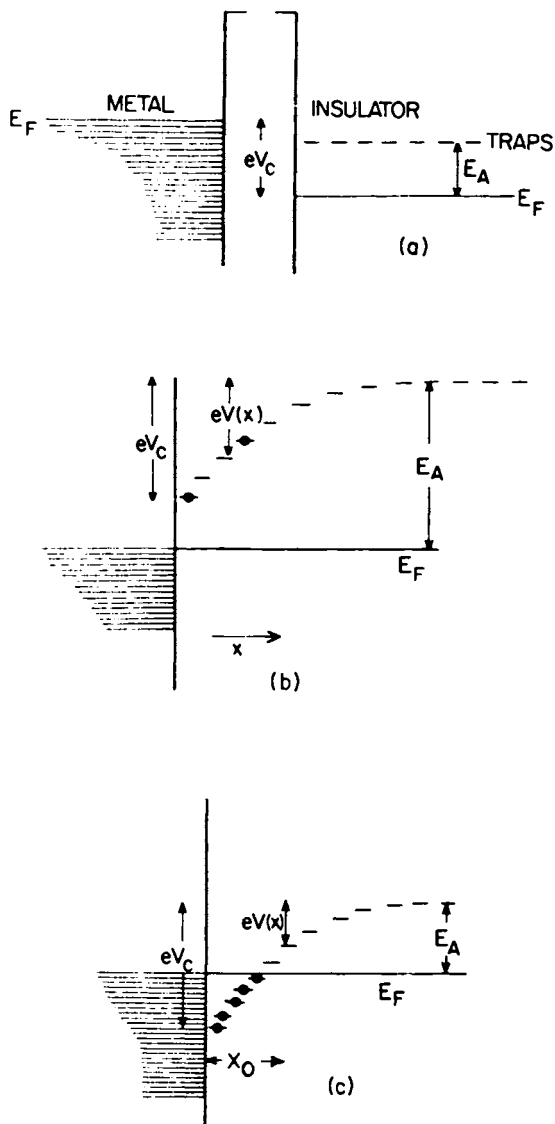


Figure 10. Energy levels at metal/dielectric interface: separated surfaces (a), blocking junction (b), and interface allowing efficient injection of electrons into insulator (c). (Reproduced, with permission, from Ref. 62. Copyright 1980, Taylor & Francis, Ltd.)

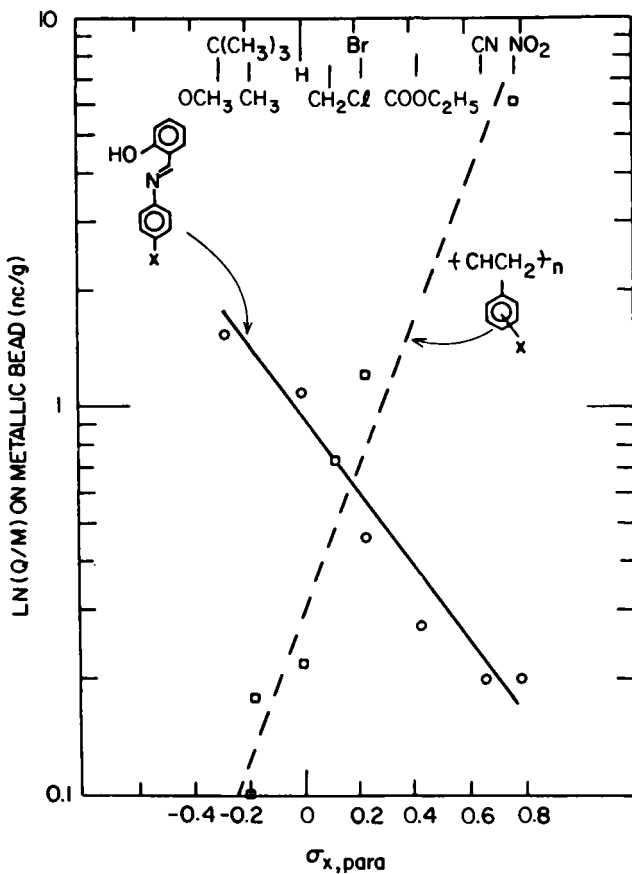


Figure 11. Correlation of triboelectric charging with electronegativity, as measured by Hammett sigma function. (Reproduced from Ref. 66. Copyright 1975, American Chemical Society.)

Observations that contact charge exchange can be quite rapid relative to the dielectric relaxation times (63, 69, 152), and the demonstration that "clean" polymers have well defined sets of surface states (44, 58, 70), suggest that these latter may be more important than bulk states for charging of dielectrics (62). On the other hand, Williams (71, 72) has shown that one can make bulk states accessible on a ten millisecond time scale by "doping" dielectrics to induce a bulk conductivity of the order of 10^{-11} sie/cm, and this approach has found useful applications (73).

Practical developer systems are, of course, much more complex and operate (at best!) under steady state conditions controlled by mechanical agitation, geometry, ambient conditions, and materials aging. Thermodynamic equilibrium is neither reached nor recognizable. Surface states are readily altered by abrasion, filming, and oxidation (63). In toners, the network of carbon pigment, which is distributed on and through the polymer matrix (43, 44, 155), must surely allow internal sites to participate in both the transfer and storage of toner charge. Finally, as we have already noted, the process requires that there be negligible charge transfer between all components of the developer and the latent image-bearing photoconductor.

Image Transfer

After development, the toner pattern is transferred to a sheet of paper placed face-to-face with the photoconductor. To overcome the electrostatic and van der Waals forces holding the charged powder to the photoconductor surface, an electric field is applied through the paper, e.g. by means of a corona spray or a biased, conformable semiconductive roller (Figure 12). The paper must present an electrically blocking interface to the toner.

Paper properties are critical at this stage (74). Wrinkles and asperities, in excess of the toner pile height (about 20-30 μ m) must be avoided. Paper conductivity must be kept within bounds: excessive moisture, absorbed in the fibers under high humidity conditions, can not only collapse the transfer field, but also generate ions whose own transfer across the gap competes with that of the charged powder. On the other hand, the paper must not remain so highly charged that it clings

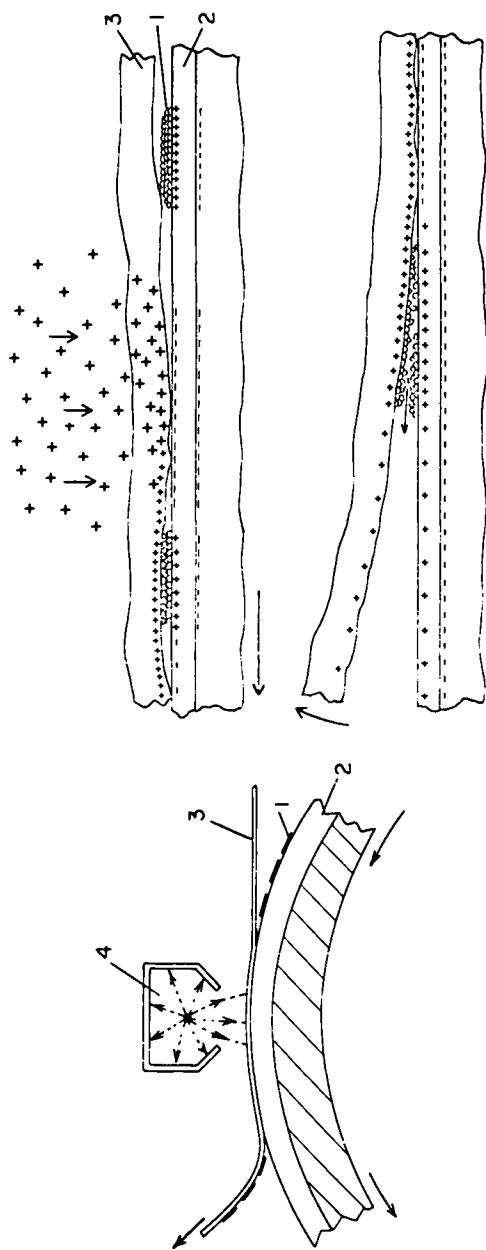


Figure 12. Corona-assisted electrostatic toner image transfer from photoconductor to paper: overall configuration (left), and detailed cross section through contact zone (right). (Reproduced, with permission, from Ref. 75. Copyright Butterworth & Co.)

to the photoreceptor, or to transport belts and rollers which are used to remove the final copy from the processor. Residual charge may be reduced by neutralizing the back of the paper by means of an AC plasma (75). Stripping may be assisted by mechanical means: intermittent air jets or guiding fingers may be applied to the lead edge of the paper, narrow tracking belts can be used to lift the edges of the sheet. Plastic-based photoconductor belts can be made sufficiently flexible to be tracked around a small diameter stripping roll; here the stiffness of the sheet itself ensures reliable separation (76) (Figure 13).

As charged toner is removed from the drum in the exit nip, the potential between the photoconductor and powder surfaces rises past the threshold for the initiation of Paschen discharge across the air gap. Reverse charge transfer, and lateral fields between toner and substrate at this point can degrade both the density and the resolution of the transferred image (62, 77). Toner transfer, as well as cleaning, may be facilitated by including sub-micron flow aids and lubricants (78-81). Although no detailed model for their mode of action appears to have been published, we speculate that the powder layer can be split, so as to leave a monolayer of colorless silica on the photoreceptor while the toner is lifted off to the paper (Figure 14). The forces adhering the innermost particle layer to the photoconductor have been extensively discussed by Krupp (77, 82). It would be interesting to extend Schmidlin's model for adhesion controlled xerographic development (4, 56) to the transfer process.

Cleaning

Transfer is never quite complete; toner residues, as well as paper fibers and stray beads, must be removed from the photoconductor before the latter can be recycled. Krupp et al. have classified the forces which adhere powders to surfaces in general (77) and to xerographic photoreceptors in particular (83) in order of their decreasing range of action:

- 1) Electrostatic forces (acting on a scale of many micrometers),
- 2) van der Waals forces (4-8 A.U.), and
- 3) Sintering or interdiffusion (less than 4 A.U.).

Typical forces are of the order of 50 millidynes/particle (84).

Amongst these, the electrostatic forces are the only ones which can be deliberately reduced prior to xerographic cleaning: it is common practice to eliminate residual charge on the photoreceptor by uniform illumination, and to neutralize toner charge by atmospheric ions supplied by an AC corotron. Neither of these "erasure" steps is fully effective. For example, Nebenzahl et al. (84), who used Krupp's centrifuge technique to quantify adhesion forces, found an electric field dependence for adhesion which was, surprisingly, an order of magnitude smaller than that predicted from a simple dipole model. The authors noted that, to be effective, the blanket exposure and AC corona current used for neutralization must be kept within well-defined operating limits--i.e., a range in which the residual toner retains as little of its original charge as possible, without acquiring undesirable charge of reversed polarity (Figure 15). A complete model would therefore have to include local charge exchange between toner and photoconductor under the corotron--an effect whose quantification will be extraordinarily difficult, because the very act of removing toner in the course of the measurement would be expected to alter the charge distribution across the interface.

Mechanical force and surface chemical finesse must be used to overcome van der Waals forces, which may account for as much as 75% of the total adhesion (83, 84) (Figure 16). A rapidly rotating fiber brush is often used to produce a local cloud of toner, which is then drawn away through a vacuum filter. The bristle tips may be "flicked" against a bar or edge to free them of dust. Teflon fiber brushes (85), stearate wax dispensers (86), and fluorocarbon powder (87) have been effectively used to deposit thin low-energy films on the photoconductor surface to facilitate release.

Scraper blades are sometimes substituted as inexpensive alternatives, particularly in simple copiers (Figure 17). Here dry lubricants (like silica aerogel, stearate, etc.) become indispensable, to avoid blade sticking, deformation, and streaking (78-81, 88-93). Toner may be recycled into the developer station, but care must be taken to allow its charge to be equilibrated with the fresh supply before it returns to the development zone. Other cleaning systems, which have been

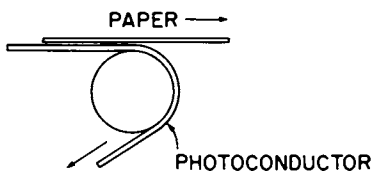


Figure 13. Self-stripping of paper from sharply curved belt photoconductor.

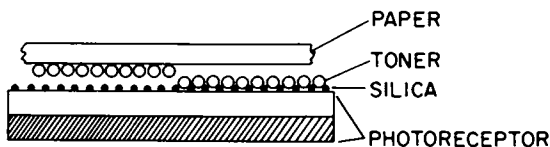


Figure 14. Illustration of hypothesis for role of silica in facilitating image transfer by a layer of fine silica aerogel which prevents intimate contact between toner and photoconductor surface.

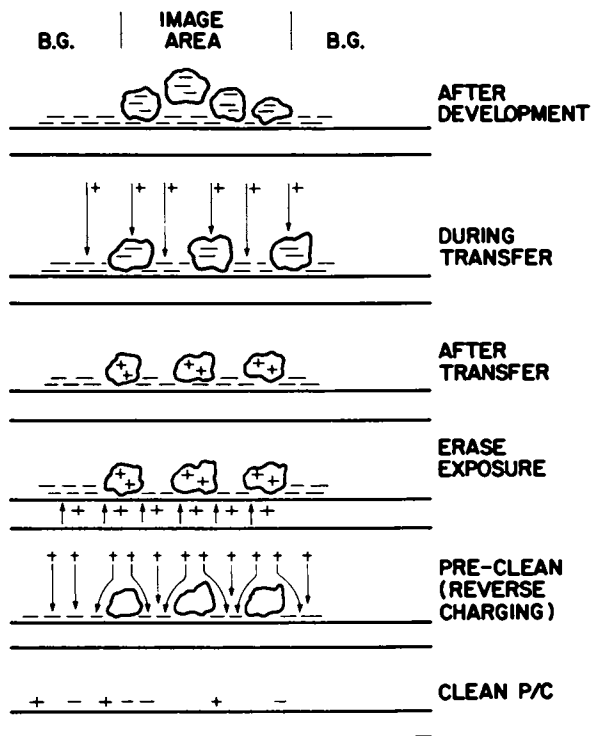


Figure 15. Neutralization of toner and photoconductor charge prior to cleaning. (Reproduced, with permission, from Ref. 84. Copyright 1980, Society of Photographic Scientists and Engineers.)

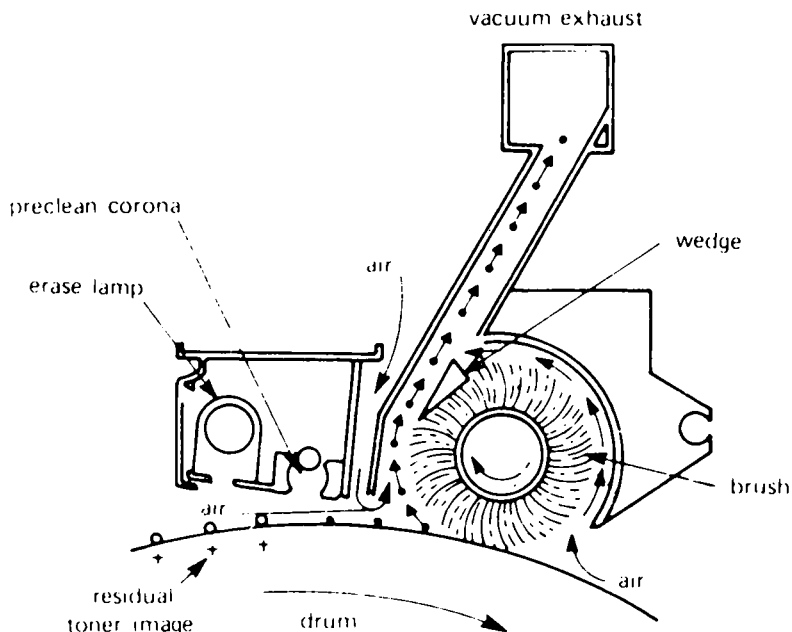


Figure 16. Typical apparatus for erasure of electrostatic image and vacuum-brush cleaning. (Reproduced, with permission, from Ref. 84. Copyright 1980, Society of Photographic Scientists and Engineers.)

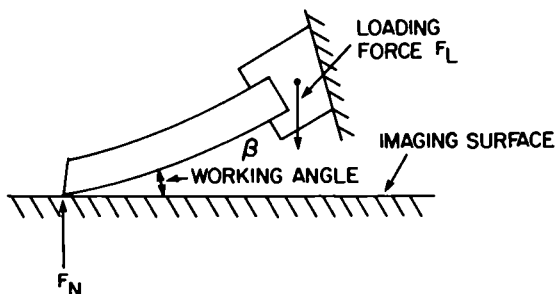


Figure 17. Schematic of typical blade cleaning device. Since the blade must scrape residual toner off the surface without leaving dust trails or scratches, lubrication is generally considered essential. (Reproduced, with permission, from Ref. 92. Copyright 1976, Institute of Electrical and Electronics Engineers.)

described, include wax impregnated webs (94) and untuned ("starved") magnetic brushes (95-97).

The closest-range forces discussed by Krupp--sintering and interdiffusion--are best avoided, rather than corrected. They manifest themselves in the cleaning process as a gradual filming or "scumming" of the photoconductor. The interactions here involve rheology of toner deformation, the energy of wetting for the photoreceptor, and the ability of the materials involved to interdiffuse. Sintering forces are proportional to the area of intimate contact between toner and photoconductor; therefore they, like the longer-range van der Waals forces, may be minimized by the interposition of thin release layers of sub-micron silica and fluorocarbon wax particles.

Image Fixing

At the end of the process, the loose toner image is melted to fix it to the paper. We shall illustrate the interfaces involved for hot roll fusing, a process of choice for modern high volume duplicators. Radiant heaters, flash lamps, and cold pressure roll systems have all been incorporated in low volume copiers, whose intermittent mode favors instant start-up and low standby power. In continuous use, on the other hand, hot roll fusers have an approximately threefold advantage over their competitors in terms of power economy (98). The toner comes into contact with more toner, with paper, and with the fusing roll. The first important interaction is one which must be avoided, and which therefore sets a temperature threshold for the materials and process: it is a premature sintering ("blocking") of toner powder at ambient temperature in storage and under impact forces in the development chamber. O'Reilly and Erhardt (86) have shown that the temperature at which "blocking" begins is approximately equal to T_g , the glass transition temperature of the toner plastic. This consideration sets the minimum safe T_g to $\sim 60^\circ\text{C}$. A particulate flow-aid, such as silica aerogel, is frequently added to maintain the separation of toner particles and minimize ambient coalescence (88).

Figure 18 shows a typical roll fusing configuration (100). A $100\ \mu\text{m}$ thick sheet of bond paper, bearing an approximately $30\ \mu\text{m}$ thick toner pattern enters the zone between a pair of rolls, one of which is compressible, the other rigid. The hot roll briefly presses the toner into

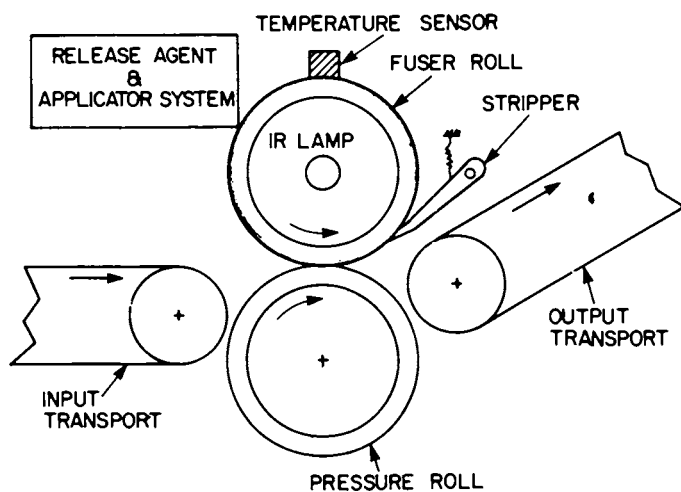


Figure 18. Fusing apparatus based on internally heated release roll. (Reproduced, with permission, from Ref. 100. Copyright 1978, Society of Photographic Scientists and Engineers.)

the paper, transfers sufficient heat to cause the thermoplastic to flow, and forces the latter into the fibers. The roll then releases the toner surface and recycles to accept the next image portion.

There must be no direct contact between the melted toner and the hot metal core of the roll. Therefore, the latter is generally protected by a thin sleeve of fluoropolymer (101) or silicone rubber (102, 103), having a critical surface energy (20-28 dy/cm) well below that of the toner melt (35-38 dy/cm) (99). Usually a very thin film of silicone oil is applied as parting fluid, to maintain a weak boundary layer at the interface, and to assure that the effective work of adhesion of toner to roll is always less than the cohesive strength of the toner melt (100, 104). Additional functions of the oil film include covering or washing off any high energy spots on the release coating (such as reinforcing pigment exposed by abrasion, surface oxidation products, or rosin contaminants left by the paper). The fact that silicone rubber sleeves are slightly swelled by hot silicone oil allows such elastomers to meter out an ultra thin oil film, right under the toner to be released, while avoiding deposition of excessive oil on the copies (2, 102, 103). Wilson (98) and Jachimiak (105) have devised a "dry" silicone roll covering which requires no external oil applicator. From their descriptions, it appears that a carefully controlled slow thermal degradation of their elastomer furnishes the surface of the roll with just sufficient low-molecular weight silicone fragments to serve as release layer.

The electrical power required for hot roll fusing is not trivial: Wilson (98) estimates it to be of the order of 300 jou/letter sized copy (about 0.5 jou/cm²). While this is only one-third the requirement of a typical radiant fuser, it is power which must be supplied continuously, because the roll must be kept hot once the machine is turned on. Therefore the release coatings are filled with thermally conductive pigments and kept as thin as possible without undue sacrifice of releasability, conformability, coating life, and stability of paper tracking. A 1-mm thick oxide-pigmented silicone sleeve, for example, has been reported to require the interior temperature of the metal roll to be maintained about 50°C above the toner fusing temperature (98). The ultimate in heat transfer efficiency has been achieved by an ingenious system described by Seanor (100), who

reacted thio-functional silicone oil with a copper roll surface to form a stable, impenetrable release layer only one polymer molecule thick!

Let us now briefly consider the toner-paper interface. The critical surface tension of cellulose has been estimated to be 42-45 dy/cm (106, 107)--high enough to allow reliable wetting and spreading of melted toner resins (typically 35-38 dy/cm) (99). As Lee has shown (104) it is the rate of capillary penetration of the toner melt, rather than the energy of wetting, which sets a limit on the rate of formation of a permanent adhesive bond. At typical machine speeds, the effective residence time of toned paper in the heated zone is of the order of 20-50 ms (98); within this time, the polymer must flow into the network of cellulose fibers and surface sizing which comprises the paper surface. (Lee reports typical asperities of about 20 μ m on commercial xerographic bond paper.) The role of sintering during the fusing process has been discussed by Strella (160), and a comprehensive model for contact and non-contact fusing has recently been presented by Prime (156). The fusing temperature is chosen to yield a viscosity (about 5×10^5 ps) which allows the polymer to coalesce, penetrate, and wet the fibers on this time scale. For typical toner resins, the fusing point is about 70-100°C above T_g . If the toner is overheated and becomes too fluid, there is danger that its cohesive strength will be insufficient to ensure complete release, and that it will offset to the roll (104).

Finally, Wilson (90) has pointed out a subtle but significant mechanical interface between the paper and the two rolls through which it must pass. As Figure 19 shows, paper tends to wrap itself around a hard fuser roll backed by a soft back-up roll, whereas it strips more reliably from a compliant fuser sleeve opposed by a hard backing roll.

In summary, the interfacial relationships required to form an efficient roll fusing system are highly complex. The toner must interact weakly with the hot roll and strongly with the paper. Sintering and flow must be avoided right up to the moment of fusing, and then forced to occur in milliseconds. Heat transfer must be optimized, and mechanical drives kept stable and reliable under difficult conditions.

Electrophoretic Liquid Development

Let us now turn to a liquid immersion development (LID) process of special interest to an audience of colloid chemists. About 25 years ago Metcalfe et al. in Australia (108) and Mayer in the U.S. (109) independently discovered that colloidal dispersions of charged pigment particles in insulating hydrocarbons like decane could be used to develop xerographic images. "Liquid development" of this type requires only very simple equipment (Figure 20), and has therefore found good use in simple copiers and in electrographic printers.

The imaging behavior of such colloids has been discussed by several authors (108-114) and will be covered in some detail by other speakers in this symposium. The sensitometry of the process depends critically upon latent image charge density, the charge/mass ratio for the particles, and the ratio of migration rate to process speed. In dispersions having exceptionally low charge/particle mass ratios, adequate image density may be reached without complete neutralization of the latent image (114).

The prime advantages of LID are its great simplicity, and the high image resolution enabled by the close approach of small particles to the latent image. Metcalfe (108) and others (115, 116) have described development of 500 lp/mm images on ultra-thin photoconductors. The main drawbacks are carryout of hydrocarbon liquid and vapor, and considerable difficulty in image transfer and photoreceptor cleaning, inherent in the small size and strong adhesion of the particles.

While many developer compositions have been published in the patent literature, surprisingly few attempts have been made to relate these to basic principles. In contrast to dry developers, in LID the charge on the particles is dominated by ions. A typical developer comprises a carbon pigment coated with a monolayer or less of a "charge control" agent, which usually consists of a long-chain aliphatic salt capable of partial ionic dissociation in the hydrocarbon medium. Metal soaps are commonly used for positively charged colloids (108, 114, 117): the long-chain fatty acid anion is sufficiently soluble to allow slight dissociation, leaving the cation adsorbed, to provide net positive charge on the carbon particle. Novotny estimates that ionization of only about 1/10,000 part of

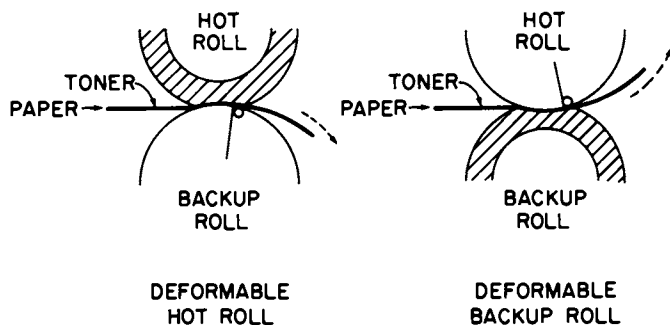


Figure 19. Paper stripping from fuser is more reliable if the heated roll is deformable and the backup roll hard, than vice versa. (Reproduced, with permission, from Ref. 98. Copyright, 1979, Society of Photographic Scientists and Engineers.)

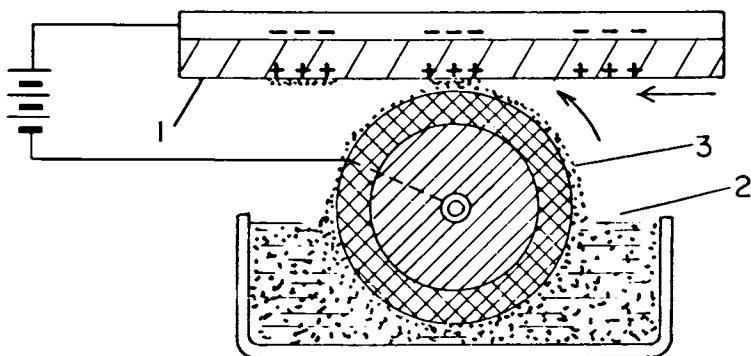


Figure 20. Electrophoretic liquid development apparatus. Key: 1, photoconductive insulator; 2, liquid toner suspension; 3, toner suspension enroute to development zone; and 4, developed image. (Reproduced, with permission, from Ref. 2.)

a monolayer of adsorbed soap suffices to charge the colloid to the requisite degree: a net of only 35-150 positive ions suffices to render a $0.5\mu\text{m}$ particle useful for the development of a latent image (113, 114).

The counter ions in solution form a diffuse double layer. Effective zeta potentials of 35-250 mv and mobilities from 0.3 to $0.8 \times 10^{-5} \text{ cm}^2/\text{Vsec}$ have been reported for typical compositions. In fields of about 10^5 V/cm , at spacings of about 1 mm, this suffices for development times of 50 milliseconds or less. The conductivity of the hydrocarbon dispersant is kept below about 10^{-11} sie/cm to minimize electrophoretic deposition of colorless ions, whose migration competes against that of the charged toner. Although the ultimate particle size of the pigment is generally of the order of $0.03\mu\text{m}$ or less, aggregates of $0.3\text{-}3\mu\text{m}$ form in the developer, and electrostatic repulsion must be augmented by polymeric shells to stabilize the colloid. Entropic stabilization is especially useful for materials used in electrode-addressed electrophoretic displays, where the particles must remain reliably dispersed, charged, and mobile over many thousands of display cycles and years of service (118, 119).

Neutral polymers are generally adsorbed for this purpose (118, 119); these may also serve to adhere the final pigment image to the plain or coated paper on which the final image is formed.

In summary, the following interfaces are important in electrophoretic liquid development:

- 1) the contacts between the colloidal dispersion and the photoconductor on the one side, and the counter electrode on the other side of the sub-millimeter gap across which development takes place: no charge should pass across either interface, at least not before the toner particle pattern has been deposited;
- 2) the adsorbate-covered carbon surface: sufficient dissociation is required to provide the requisite charge/mass ratio for charge control;
- 3) interactions between charged particles, modified by stabilizing protective colloids: such interactions should be minimized;
- 4) the receiving sheet and the liquid film which has coated it: excess hydrocarbon must be stripped off to prevent its carryout into the environment;

- 5) the photoconductor and the pigment image: electrostatic image forces and van der Waals forces must be overcome in those systems in which the image is to be transferred to paper (56).

Photo-electrophoresis

In conventional xerography with liquid or dry development, light is used to modulate the field, E , above the large area photoconductor, and the resultant field patterns are developed by pigment particles, each having a (constant) charge, Q . The force driving image development is $\Delta F = Q\Delta E$. Is it possible to devise imaging processes in which the field is kept constant and the charge per particle is changed by image illumination? Certainly! The development force now becomes $\Delta F = EAQ$. Processes of this type have been called "photo-active pigment electrography" or "PAPE" (56, 120, 121). Although both dry and liquid versions are known, only the latter have been characterized in detail.

Figure 21 shows a typical imaging configuration. A PAPE imaging ink consists of "electrically photosensitive" microcrystals, dispersed in a high resistivity fluid. The particles serve both as individual photosensors and as the colorant for the image to be formed. Charge control agents, or corona devices, are used to make the particles unipolar prior to imaging. A film of this ink is coated on the transparent base electrode and introduced into a narrow imaging zone. Here a counter electrode approaches to a gap of about $50 \mu\text{m}$ to apply an electric field of the order of 10^6 V/cm . One of these electrodes must be free to exchange charge with the pigment (the "injecting" electrode), the other must be coated with a thin dielectric to block destructive breakdown currents and prevent pigment oscillation (121, 123). The image to be recorded is projected into the high-field region, and the particles migrate to one electrode or the other, depending on whether they have been exposed or kept dark. As the electrodes separate a few milliseconds later, they carry complementary positive and negative image patterns, which may later be transferred or fixed. Particles kept in the dark have become attached to the transparent base electrode, while illuminated pigment particles have reversed their initial charge and migrated to the counter electrode. A typical set of materials might be: tin oxide coated glass as transparent injecting electrode,

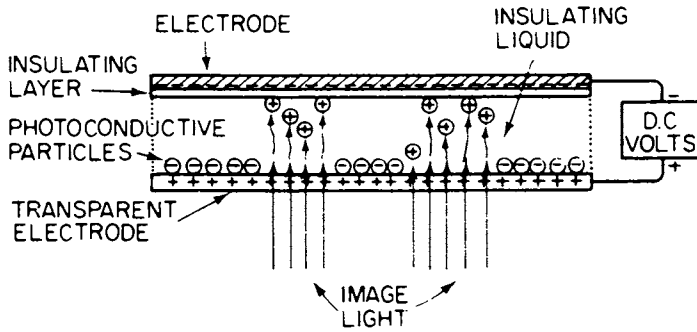


Figure 21. Photo-electrophoretic imaging configuration (2). The light pattern to be reproduced must be projected into the imaging nip through a transparent electrode.

rear-metallized 50 micron polyester film as blocking electrode, and a 10% dispersion of negatively charged phthalocyanine microcrystals in decane as ink (121).

Let us list the interfaces which govern the behavior of such a system. The first one is that which exists between the pigment and its medium: polymeric dispersants and charge control agents are used to stabilize the suspension, and to assure that particles which are not illuminated will follow the field to the positive transparent electrode. Exposure in the strong electric field applied in the imaging zone generates hole-electron pairs within the phthalocyanine. The electrons are injected into the fluid, captured by impurities, and carried off towards the tin oxide electrode in the form of ions.

The second interface is therefore the electrical boundary between the pigment and the medium. Hartmann and his coworkers have studied this interface in model systems, in which the steps of charge carrier generation, separation, and transport within the particles can be separated from the charge injection step which follows (120-125). Figure 22 shows the energy levels of phthalocyanine in relation to those of soluble charge trapping agents, which may be added to the liquid to facilitate injection. Weak electron acceptors enable efficient electron transfer, soluble electron donors, hole injection (Figure 23). Redox potentials provide a quantitative guide (123-125). The charge acceptors must, of course, be freely mobile in the hydrocarbon vehicle. Cressman (126) has documented an interesting counter-example: a firmly adsorbed monolayer of the electron donor (hole trap), nigrosine, suppresses 99.9% of hole injection from selenium into dodecane!

The ions quickly shuttle their charge to the nearby imaging electrode; the imaged particles move somewhat more slowly across the gap and attach themselves to the counter electrode. The whole process is complete in 2-5 milliseconds (127). Typical mobilities in decane have been estimated to be about 2×10^{-4} cm²/Vsec for soluble anions (120); and $1-5 \times 10^{-5}$ cm²/Vsec for pigment particles (119). Under extremely high applied field conditions, and in highly resistive liquids, Vincett (127) has demonstrated that substantially the entire current across a model cell can be carried by PAPE pigment particles, at a rate limited by their own space charge.

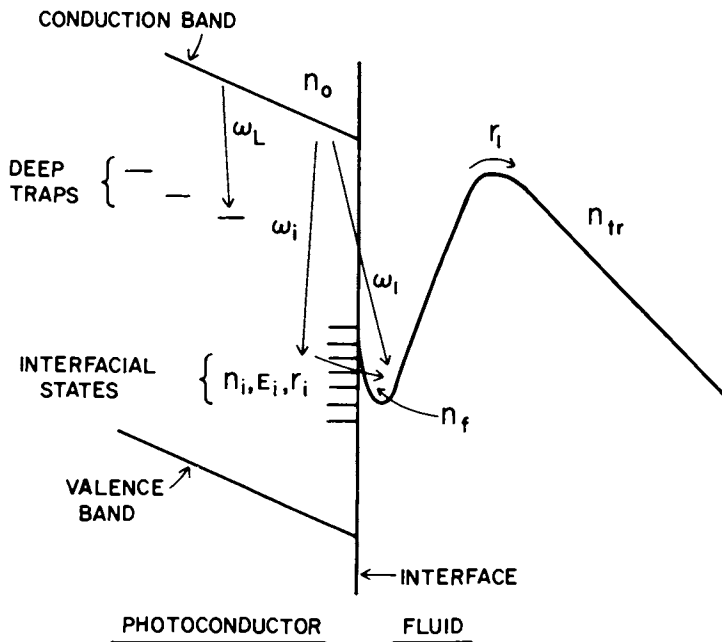


Figure 22. Energy level relationships at a phthalocyanine/decane interface.
 Key: n , carrier densities in solid phase, and ion densities in liquid; ω , charge capture rates; and r_i , rate of diffusion of ions across the potential barrier. (Reproduced, with permission, from Ref. 122. Copyright 1977, American Institute of Physics.)

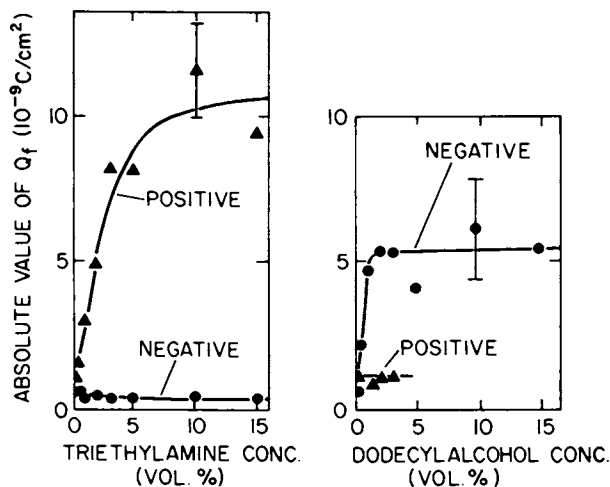


Figure 23. Effect of electron donors (left) and acceptors (right) on efficiency of charge injection from phthalocyanine into decane. (Reproduced, with permission, from Ref. 122. Copyright 1977, American Institute of Physics.)

A threshold field of over 2×10^5 V/cm is required to initiate imaging. The primary quantum yield is modest: for phthalocyanine at 3.6×10^5 V/cm, only one electron is injected per 500 photons absorbed by a micron-sized particle (120). However, the overall process exhibits gain because it is leveraged by the relatively large mass of pigment which is deposited for each unit charge. Assuming an initial charge of about 400 electrons/particle (127), 2×10^5 photons are required to deposit the $\sim 10^9$ phthalocyanine molecules contained in a $1 \mu\text{m}$ crystallite (128). This corresponds to an overall gain of about 5000 molecules/photon. Observed exposures required for PAPE (about 10^{13} quanta/cm²) (121) are therefore comparable to those for conventional xerography. Murray (157) has recently published a comprehensive model for this process.

Tulagin (129) has described an ingenious positive-working "instant" full color reproduction process based upon photo-electrophoresis (Figure 24). The ink contains pigments of three primary colors. Each particle selectively absorbs radiation to which it alone is sensitive (i.e. red, green, or blue) and deposits its own cyan, magenta, or yellow colorant, respectively, on the transparent electrode. Excellent color reproduction has been demonstrated under laboratory conditions. A significant problem with this process is that three additional interfaces have been introduced. Light absorption, by, say, a cyan particle, can lead to charge exchange with its magenta neighbor, causing deposition of the wrong colorant. Interactions of this degree of complexity cannot be described by any published model; however, they have been addressed with considerable success by careful materials control (130, 131).

Conclusion

We could go on:

- o There is a process called TESI in which the transfer of an electrostatic image replaces toner transfer. What matters here is the motion of ions in the narrow air gap between the photoconductor and a dielectric coated paper (2, 132).
- o The effect of an electric field pattern on the surface energy of a photoconductor has been exploited for "selective wetting" development

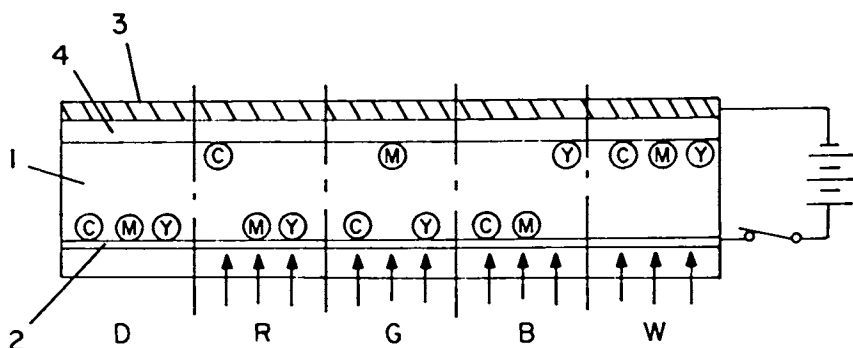


Figure 24. Polychrome photoelectrophoresis.

A mixture of electrically photosensitive pigment particles of three primary subtractive colors (cyan, magenta, yellow) in decane (1) is illuminated by a color image, projected through a transparent imaging electrode (2). Particles respond selectively to radiation which they absorb (red, blue, green), exchange charge with (2) and move to a counter-electrode (3) which has a dielectric coating (4). (In white regions everything moves, in dark regions, nothing.) A positive full-color image which remains on (2), may be transferred to paper. Key: C, cyan; M, magenta; Y, yellow; R, red; B, blue; and G, green. (Reproduced, with permission, from Ref. 2.)

(133-135). (Here the problem is what to do about conductive contaminants left on the surface by the water-based ink.)

- o In photo-plastic processes like "frost," the electrostatic component of the surface tension is modulated image-wise so as to cause a softened thermoplastic film to become wrinkled on a microscopic scale (136, 137).
- o Clever manipulation of charge at the interface between photoconductive pigments and a plastic or waxy matrix has been used to produce micro-images by particle migration (138, 139) and by the splitting of a layer between donor and receiving sheets (140, 157).

There are also many undesirable interactions in electrophotography--for example:

- o Silicone oil has a remarkable facility to distill out of the fuser cavity onto belts, optics, and electrical components--wherever it is least welcome.
- o Corotron wires become coated with unwanted oxides, nitrates, and toner residues.
- o Paper curls and wrinkles as its moisture content is changed by ambient humidity and the fusing process. Sheets become charged and stick to surfaces where they are not wanted. To the engineer, paper is a source of fibers, clay, rosin, and other forms of aggravation (74, 141, 142).

This completes our necessarily cursory overview. Other speakers at this symposium will address several of these topics in detail--including the ancient and fascinating problem of charge exchange between dielectrics (143). By way of conclusion, we outline some problems in surface chemistry and physics whose understanding will advance the field of electrophotography.

- 1) The energy levels and molecular ion states in dielectric media which are responsible for charge acceptance and charge transfer require better definition to provide an understanding of several processes important to electrophotography:
 - o Charge injection and transport in multi-component photoreceptors
 - o tribo-electrification of xerographic developers, and

- o the exchange of charge between the photo-receptor surface and every process element which interacts with it.
- 2) There is need to distinguish more generally between those processes in which charge transport across interfaces is driven by electron exchange and those in which ions and charge-bearing particles are transferred.
- 3) Much needs to be learned about the micro-structure, microscopic rheology, and electronic properties of particle-polymer composites, such as are met in aggregate photoconductors and xerographic developer materials.

Interfaces between materials in electrophotography pose many fascinating problems in surface physics and chemistry. Their solution is likely to bring significant rewards in scientific insight, as well as in improvements in the art of electrophotography.

Acknowledgements

The author acknowledges instructive discussions with many colleagues, especially S.B. Bolte, P.F. Erhardt, T.J. Fabish, E.J. Felty, R.W. Gundlach, M.L. Hair, G.C. Hartmann, E.M. Pell and M.E. Scharfe; the assistance of N. MacDonald and G. Sherman in the preparation of the manuscript; and constructive criticism by a referee (J.M.) who prefers to remain anonymous.

LITERATURE CITED

1. C.F. Carlson, "History of Electrostatic Recording," Chapter 1 of "Xerography and Related Processes", ed. J.H. Dessauer and H.E. Clark, Focal Press, London and N.Y., 1964.
2. R.M. Schaffert, "Electrophotography", 2nd ed., John Wiley & Sons, N.Y., 1975.
3. J.W. Weigl, Angew. Chem. (International Ed.) 16, (6), 374 (1977).
4. M.E. Scharfe and F.W. Schmidlin, Adv. in Electronics and Electron Physics 38, 83 (1975).
5. H. Kiess, RCA Rev. 36, 667 (1975).
6. C.F. Carlson, U.S. Patent 2,588,699 (1952).
7. W. Maenhout-van der Vorst and F. Craenest, Phys. Stat. Solidi 5, 357 (1964).
8. K. Hauffe and R. Stechemesser, Phot. Sci. Eng. 11, 145 (1967).
9. F. Schelfout and W. Maenhout-van der Vorst, Appl. Optics, Supplement 3, Electrophotography (op. cit.) 96 (1969).
10. W. Ruppel, H.J. Gerritsen, A. Rose, Helv. Phys. Acta. 30, 495, 504 (1957).
11. D.B. Medved, J. Chem. Phys. Solids 20, 255 (1961).
12. Dennis W. Vance, J. Appl. Phys. 42, 5430 (1971).
13. P.K. Watson, Inst. Phys. Conf. Series, No. 48, "Electrostatics" (1979), p. 2.
14. D.M. Pai and R.C. Enck, Phys. Rev. B 11, 5163 (1975).
15. W.D. Hope and M. Levy, Chapter 4 of "Xerography and Related Processes" (op. cit.).
16. M.D. Tabak and P.J. Warter, Phys. Rev. 173, 899 (1968).
17. P.J. Warter, Appl. Optics, Supplement 3, Electrophotography, 65 (1969).
18. J.C. Knights, E.A. Davies, J. Phys. Chem. Sol. 35, 543 (1974).
19. J.S. Berkes, "Electrophotography: Second International Conf." (Soc. Phot. Scient. & Eng., 1974), p. 137.
20. P.J. Regensburger, Photochem. Photobiol. 8, 429 (1968).
21. J. Mort, Phys. Rev. B5, 3329 (1972).
22. J. Mort and P. Nielsen, Phys. Rev. B5, 3336 (1972).
23. P.J. Melz, R.B. Champ, L.S. Chang, C. Chiou, G.S. Keller, L.C. Liclican, R.R. Neiman, M.D. Shattuck, W.J. Weiche, Phot. Sci. and Eng. 21, 73 (1977).

24. J.W. Weigl, Photochem. Photobiol. 16, 291 (1972).
25. P.M. Borsenberger and W. Mey, J. Non-Cryst. Sol. 28, 305 (1978).
26. R.L. Emerald and J. Mort, J. Appl. Phys. 45, 175 (1974).
27. J.A. Amick, RCA Rev. 20, 753, 770 (1962).
28. V. Gaidelis, E. Montrimas, A. Pazera, J. Viscacas, "Current Problems in Electrophotography" (ed. W.F. Berg and K. Hauffe) W. de Gruyter, Berlin/N.Y., 1972), p. 115.
29. C. Wood, Chapter 5 of "Xerography and Related Processes" (op. cit.).
30. M. Abkowitz and R.C. Enck, J. Appl. Phys. 50, 3423 (1979).
31. R.N. Jones and R.L. Lane, Bull. Amer. Ceramic Soc. 46, 462 (1967).
32. J.W. Weigl, J. Mammino, G.L. Whittaker, R.W. Radler, J.F. Byrne, "Current Problems in Electrophotography" (op. cit.), p. 287.
33. C.F. Hackett, J. Chem. Phys. 55, 3178 (1971).
34. W.J. Dulmage, W.A. Light, S.J. Marino, C.D. Salzberg, D.L. Smith and W.J. Staudenmayer, J. Appl. Phys. 49, 5543 (1978).
35. P.M. Borsenberger, A. Chowdry, D.C. Hoesterey and W. Mey, *ibid.* 5555
36. P.M. Borsenberger, A. Chowdry, W. Dulmage, D. Hoesterey, W. Light, S. Marino, W. Mey, C. Salzberg, D. Smith and W. Staudenmayer, "Third International Conference on Electrophotography", (Soc. Photo. Sci. Eng., Washington, D.C., November 15-18, 1977).
37. E.C. Giaimo, RCA Rev. 23, 96 (1962)
38. E. Inoue and T. Yamaguchi, Bull. Chem. Soc. Jap. 36, 1573 (1963)
39. K. Hauffe, TAPPI 57, 136 (1974).
40. R.B. Comizzoli, J. Appl. Phys. 41, 4148 (1970).
41. M. Insalaco, U.S. Patents 2,892,794 and 3,079,342.
42. R.B. Nelson, U.S. Patent 3,639,245.
43. A. Orzechowski, Microscope 27, 5 (1979).
44. C.B. Duke and T.J. Fabish, J. Appl. Phys. 49, 315 (1978).
45. C.J. Young, U.S. Patent 2,786,439
46. E.C. Giaimo, U.S. Patents 2,786,440 and -1.
47. T.L. Thourson, IEEE Trans. Electron Devices ED-19, 495 (1972).
48. D.A. Hays, Phot. Sci. Eng. 22, 232 (1978).

49. D.K. Donald and P.K. Watson, Phot. Sci. Eng. 14, 36 (1970).
50. L.B. Schein, "Electrophotography: Second International Conference" (op. cit.), p. 65 (1974).
51. L.B. Schein, Phot. Sci. Eng. 19, 3 (1975).
52. L.B. Schein, Phot. Sci. Eng. 19, 255 (1975).
53. L.B. Paxton, Phot. Sci. Eng. 22, 159 (1978).
54. D.A. Hays, J. Appl. Phys. 48, 4430 (1977).
55. S.K. Ahuja, J. Phys. D-9, 1305 (1976); J. Appl. Phys. 47, 4706 (1976).
56. F.W. Schmidlin, "Electrophotography," Chapter 11 of "Photoconductivity and Related Phenomena", ed. by J. Mort and D.M. Pai (Elsevier Publishing Co., Amsterdam/Oxford/N.Y., 1976).
57. W.R. Salaneck, A. Paton, D.T. Clark, IEEE Trans. Indust. Applic. IA-5, 443 (1978).
58. L.H. Lee, Phot. Sci. Eng. 22, 228 (1978).
59. C.R. Raschke, "Electrophotography: Second International Conference" (op. cit.) 104.
60. J.H. Dessauer, "Xerography - A New Method of Image Recording," Chapter in "Photographic Science Symposium, Zurich (1961)" (ed. W.E. Berg, Focal Press, London/N.Y., 1963).
61. R.N. Goren and J.F. Szczepanik, Phot. Sci. Eng. 22, 235 (1978).
62. J. Lowell and A.C. Rose-Innes, "Contact Electrification," Adv. in Physics 29, 947 (1980).
63. D.A. Hays and P.K. Watson, "Electrophotography: Second International Conference", (op. cit.) p. 108.
64. D.K. Davies, J. Phys. D-2, 1533 (1969).
65. P.J. Cressman, G.C. Hartmann, J.E. Kuder, F.D. Saeva, D. Wychick, J. Chem. Phys. 61, 2740 (1974).
66. H.W. Gibson, J. Am. Chem. Soc. 97, 3832 (1975).
67. H.W. Gibson, F.C. Bailey, Chem. Phys. Lett. 51, 352 (1977).
68. C.B. Duke and T.J. Fabish, J. Appl. Phys. 49, 315 (1978).
69. D.K. Davies, "Static Electrification", Inst. Phys. Soc. Conf. Ser. No. 4, 29 (1967).
70. T.J. Fabish, M.M. Saltsburg and M.L. Hair, J. Appl. Phys. 47, 930, 940 (1976).
71. M.W. Williams, J. Macromol. Sci. - Rev. Macromol. Chem. C14, 251 (1976).
72. M.W. Williams, IEEE Trans. Indust. Appl. IA-12, 213 (1976).

73. R. Hagenbach, U.S. Patent 3,533,835.
74. C.J. Green, Jr., TAPPI 64, 79 (1981).
75. P.G. Andrus and F.W. Hudson, "Principles of Image Transfer and Fixation," Chapter 14 in "Xerography and Related Processes" (op. cit.).
76. W.S. Jewett, Ind. Appl. Soc. IAS '77 Annual, 557 (1977).
77. H. Krupp, "Particle Adhesion: Theory and Experiment," Adv. Coll. & Interface Sci. 1, 113 (1967).
78. F. Palermi and A. Chatterji, U.S. Patent 3,655,374.
79. A. Chatterji, M. Custazzo, D. Kiriazides, J.J. Russell and J.P. Serio, U.S. Patent 3,819,367.
80. D.J. Fisher, U.S. Patent 3,900,588.
81. D. Jugle and C. Levine, U.S. Patent 3,983,045.
82. H. Krupp, "Static Electrification", Inst. Phys. Conf. Ser. No. 11, 1 (1971).
83. W. Kottler, H. Krupp, H. Rabenhorst, Zs. Angew. Physik 24, 219 (1968).
84. L. Nebenzahl, J. Borgiolo, V. de Palma, K. Gong, C. Mastrangelo, F. Pourroy, Phot. Sci. Eng. 24, 293 (1980).
85. W.A. Franta, Canadian Patent 639,611; R.L. Dueltgen, C.A. Queener, U.S. Patent 3,682,689.
86. R.J. Joseph, U.S. Patents 3,489,560 and 3,501,294.
87. W. Crooks, U.S. Patent 3,977,871.
88. D. Barby, "Silicas," Chapter 8 of "The Characterization of Powders" (ed. G.D. Parfitt and R.S.W. Sing, (Acad. Press, London/N.Y./San Francisco, 1976).
89. S. Royka and R.L. Emerald, U.S. Patent 3,552,850.
90. D. Gerbasi, U.S. Patents 3,590,412 and 3,660,863.
91. H.R. Till, U.S. Patent 3,724,020.
92. H.R. Till and N.R. Lindblad, IEEE Indust. Appl. Soc., 1976, IAS Annual, p. 1094.
93. G.L. Harpavat, IEEE Trans. Indust. Appl. IA-15, 681 (1979).
94. W. Graff and R.W. Gundlach, U.S. Patent 3,186,838.
95. F.Y. Yang, U.S. Patent 3,580,673
96. C.A. Queener, U.S. Patent 3,647,293
97. L.M. Cooper, U.S. Patent 3,637,306.
98. C.C. Wilson, J. Appl. Phot. Eng. 5, 148 (1979).
99. J. O'Reilly and P.F. Erhardt, "Electrophotography: Second International Conference" (op. cit.) p. 95.
100. D.A. Seanor, Phot. Sci. Eng. 22, 240, 243 (1978).

101. F.W. Hudson, U.S. Patent 3,256,002.
102. R. Moser, U.S. Patent 3,498,596.
103. Anon., U.K. Patent 1,458,694.
104. L.H. Lee, "Thermal Fixing of Electrophotographic Images" in "Adhesion Science and Technology" (ed. L.H. Lee), B-831 (Plenum Press, 1975).
105. P.D. Jachimiak, IEEE-Indust. Appl. Soc. IAS Annual IIB, 295 (1977).
106. J.J. Scholz, B.R. Ray, J.R. Anderson, J. Phys. Chem. 62, 1227 (1958).
107. P. Luner and M. Sandell, J. Poly. Sci. C28, 115 (1969).
108. K.A. Metcalfe and R.J. Wright, J. Sci. Inst. 32, 74 (1955); ibid. 33, 194 (1956).
109. C.J. Claus and E.E. Mayer, "Liquid Development", Chapter 12 of "Xerography and Related Processes" (op. cit.).
110. J.A. Dahlquist and I. Brodie, J. Appl. Phys. 40, 3020 (1969).
111. R.B. Lewis and H.M. Stark, "Current Problems in Electrophotography" (op. cit.), p. 322.
112. R. Koehler, D. Giglberger and F. Bestenreiner, Phot. Sci. Eng. 22, 218 (1976).
113. P.M. Cassiers, K. Verhille, J. van Engeland, Appl. Optics, Supplement 3 (op. cit.) 83 (1969).
114. J. Halfdarnarson and T.K. Hauffe, Phot. Sci. Eng. 23, 27 (1979).
115. F.J. Madden, Optical Storage Materials and Methods, SPIE 123, 86 (1977).
116. M.R. Kuehnle, Appl. Phot. Eng. 4, 155 (1978).
117. J. Novotny, Coll. and Surf. 2, 373 (1981).
118. M.D. Croucher and M.L. Hair, Ind. Eng. Chem. (Prod. Res. Dev.) 20, 324 (1981).
119. M.D. Croucher, J. Harbour, M. Hopper, M.L. Hair, Phot. Sci. Eng. 25, 80 (1981).
120. G.C. Hartmann and F.W. Schmidlin, J. Appl. Phys. 46, 266 (1975).
121. G.C. Hartmann, L.M. Marks, and C.C. Yang, J. Appl. Phys. 47, 5409 (1976).
122. G.C. Hartmann and J. Noolandi, J. Chem. Phys. 66, 3498 (1977).
123. J.C. Chang, R.O. Loutfy, G.C. Hartmann, J. Josefowicz, Phot. Sci. Eng. 23, 357 (1979).
124. J.C. Chang, R.O. Loutfy, G.C. Hartmann, C.C. Yang, J. Josefowicz, Phot. Sci. Eng. 23, 357 (1979).

125. C.C. Yang and J. Noolandi, Can. J. Chem. 55, 2107 (1977).
126. P.J. Cressman, Phot. Sci. Eng. 18, 284 (1974).
127. P.S. Vincett, J. Coll. Interf. Sci. 76, 83, 95 (1980).
128. R.P. Linstead and J.M. Robertson, J. Chem. Soc. (1936), 1736.
129. V. Tulagin, J. Opt. Soc. Amer. 59, 328 (1969).
130. B. Grushkin, E. Forest, L. Carreira, U.S. Patent 4,032,339.
131. J. Schneider, E. Forest, Personal Communications.
132. R.L. Jepsen and G.F. Day, "Electrophotography: Second International Conference" (op. cit.), p. 28.
133. W. Gesierich, E. Weyde, H. Haydn, U.S. Patent 3,285,741.
134. W. Gesierich, International Cong. Scient. Photog. (Paris, 1965).
135. P.M. Cassiers, R.S. Noë, J.L. van Engeland, U.S. Patent 3,486,922.
136. C.J. Claus and R.W. Gundlach, "Imaging by Plastic Deformation," "Xerography and Related Processes", (op. cit.) Chapter 13.
137. J.E. Gaynor, IEEE Trans. Electron Devices ED-19, 512 (1972).
138. W.L. Goffe, Phot. Sci. Eng. 15, 304 (1971).
139. A.L. Pundsack, Y.C. Cheng, G.C. Hartmann, L.M. Marks, Appl. Optics 17, 2650 (1978).
140. R.H. Luebbe, M.S. Maltz, G.J. Reinis, W.G. van Dorn, "Electrophotography: Second International Conference" (op. cit.), p. 48.
141. I. Seldin, TAPPI 54, 397 (1971).
142. I. Hansson and N. Jonassen, J. Electrostatics 4, 335 (1978).
143. I. Bernard Cohen (ed.), "Benjamin Franklin's Experiments" (Harvard University Press, Cambridge, MA, 1941).
144. O. Knoblauch, Zs. Phys. Chem. 39, 225 (1902).
145. W.A.D. Rudge, Phil. Mag. 23, 85 (1912).
146. W.A.D. Rudge, *ibid.* 25, 481 (1913).
147. W.A.D. Rudge, Proc. Roy. Soc. A90, 256 (1914).
148. D.A. Seanor, International Symposium on Physicochemical Aspects of Polymer Surfaces: Tribology and Triboelectrification, ACS Division Colloid Surf. Chem., August 1981, Paper #85.
149. W.B. Harper, "Contact and Frictional Electrification" (Oxford, Oxford Univ. Press, 1967).

150. T.J. Fabish and M.L. Hair, J. Coll. Interf. Sci. 62, 16 (1977).
151. D. MacArthur Burness, T.K. Dykstra, T.A. Jadwin and H.G. Ling, U.S. Patent 4,079,014.
152. H. Bauser, W. Klopffer and H. Rabenhorst, "Advances in Static Electricity" (Brussels, Auxilia) 1, 2 (1977).
153. C.B. Duke, International Symposium on Physiochemical Aspects of Polymer Surfaces: Tribology and Triboelectrification, ACS Division Colloid Surf. Chem., August 1981, Paper #83.
154. H.W. Gibson, F.C. Bailey, J.L. Mincer and W.H.H. Gunther, J. Poly. Sci. (Poly. Chem. Ed.) 17, 2961 (1979).
155. P.C. Julien, Abstract Bulletin, Fourth International Conference on Electrophotography, Soc. Phot. Scient. & Engrs., Nov. 1981, p. 63.
156. R.B. Prime, *ibid.*, p. 68.
157. H. Murray, *ibid.*, p. 89.
158. S.B. Bolte, R.J. Gruber, R.F. Koehler and E.W. Connors, U.S. Patent 4,304,830.
159. C.H. Lu, U.S. Patent 4,161,454.
160. S. Strella, J. Appl. Phys. 41, 4242 (1970).

RECEIVED March 19, 1982

Contact Charging of Polymeric and Composite Powders

G. T. BREWINGTON

Xerox Corporation, Webster Research Center, Webster, NY 14580

Contact electrification of insulative materials, predominantly in film form, has been studied in many laboratories. In this paper, electric field dependent charging of polymeric and polymer-carbon black powders in contact with a metallic electrode has been studied. Results show the charging behavior to be strongly dependent on the composition of the powder surface. Carbon black loading, type of carbon black and degree of dispersion are methods used to alter the powder surface. The field dependent contribution to the charge exchange dominates over the zero field values.

Contact charging, contact electrification or triboelectrification, the exchange of charge between materials brought into contact and subsequently separated, has been investigated for centuries, and is well covered in the review literature (1-5). Presently, metal-metal contact charging is well understood in terms of charge flow driven by the difference in Fermi levels descriptive of the two surfaces (1,2). Metal-insulator contact charging is not totally characterized, however, because of incomplete knowledge of the insulator energy levels. Metal-insulator charging is the focus of the review by Lowell and Rose-Innes (2). Gallo and Ahuja (6) have reviewed microscopic models of charging, indicating the mobile species and driving force in each model. Much of what is published on contact charging is based on macroscopic observations which do not elucidate the microscopic mechanisms that would attribute charging to electron flow or ion flow.

0097-6156/82/0200-0183\$06.00/0

© 1982 American Chemical Society

Many commonly encountered materials have been placed in a triboelectric series such as shown by Davies (5) or Seanor (3) based on the relative charging behavior. Any given material is placed in the tribo series so that it charges negatively in contact with those materials higher in the series, and positively in contact with those materials lower in the series. Inconsistencies in results from different laboratories can usually be traced to sample preparation and handling techniques which alter the sample surface.

Polymeric materials are usually studied in the form of films in various experimental setups (3,5,8-13). These setups include rubbing or sliding contact of the film with another surface (3,5,8-12), simple touching contact (13), and rolling contact with 100-300 μ beads on a sloped piece of film (3).

For processes such as electrostatic spraying or xerography, the charging of small particles less than 25 μ in diameter is of interest. Contact charging of powders of varied composition has been studied in inclined plane setups (14), by electric field induction of charge flow in conductive powders from a conductive contact (15), or by contact with another insulator, such as the inner surface of a transport tube (1,15) or the carrier beads used in two component xerography (4,15,16). Charging insulative composite powders with biased conductive electrodes has been described in the patent literature (17,18). The dependence of charge exchange on the applied electrode potential was not discussed in these reports.

Nordhage and Backstrom (12) found the charging of polyethylene film in rubbing contact against aluminum, platinum or gold electrodes to have a linear dependence on the applied potential. Hays (19) investigated the effects of surface oxidation and applied electric field on mercury-polyethylene contact charging and discussed the results in terms of a model based on polymer surface states.

The purpose of these experiments is to study the effects of particle composition, preparation techniques and applied electrode potential on charge exchange with a metallic electrode in a specific contact configuration. The contact area has not been quantitatively defined in this configuration, but is presumed to be independent of powder composition and flow properties, and remain constant in all these measurements. Equilibrium charge exchange is not attained with these techniques. The electric field experienced by the particles is not easily calculated

because of the complex nature of surfaces (1) and the dynamics of the charging zone.

Experimental

The schematic diagram shown in Figure 1 represents a 4 mil stainless steel charging electrode with a ground edge, and a 10 μ thick donor surface of polycarbonate doped with a charge relaxable material. A bead of the sample powder was first applied to the donor surface, then metered and charged by movement of the electrode at 0.3 inch/sec. The electrode is spaced from the donor surface by the particles passing under the edge. Charge of the powder was measured using a Keithley 610 BR electrometer to monitor the loss of charge from the donor surface-powder system during an air jet blowoff. The donor surface was cleaned with a soft cloth for subsequent measurements. All measurements were performed in a controlled environment at 70°F and 11% relative humidity.

Powder samples of 10 μ average diameter were prepared by air jet micronization of polymeric or composite chunks. Composite materials were prepared by melt mixing of polymer and carbon black. Carbon black was added to the surface by milling the polymer powder and carbon black with glass beads for an hour, and subsequently heating the particles to tack the carbon black to the particle surface. Static resistivity measurements were performed on packed powders in a procedure similar to ASTM D257.

Results and Discussion

Charge levels given by the charge to mass ratio in microcoulombs per gram are plotted as a function of applied electrode voltage in Figure 2 for a pure polymeric powder of a styrene copolymer, and for composites of Regal 330 carbon black with the same styrene copolymer. The reproducibility of these measurements is about $\pm 0.5 \mu\text{C/g}$. There is no substantial charging of the pure polymer particles except at -400V. Addition of 0.1% Regal 330 carbon black by weight to the surface of the polymer particles has only a small effect on the charging. At this carbon black loading less than 5% of the particle surface is estimated to be carbon black, using a rough calculation of the residual carbon black aggregate size as 500 Å, a carbon black density of 2.0 g/ml and a polymer density of 1.1 g/ml.

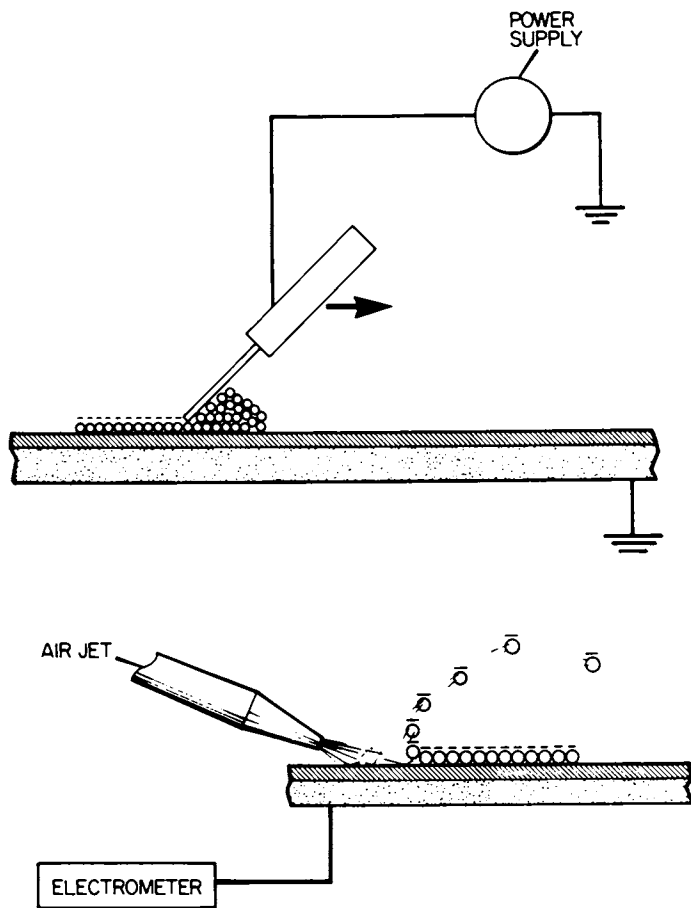


Figure 1. Schematic of charging configuration.

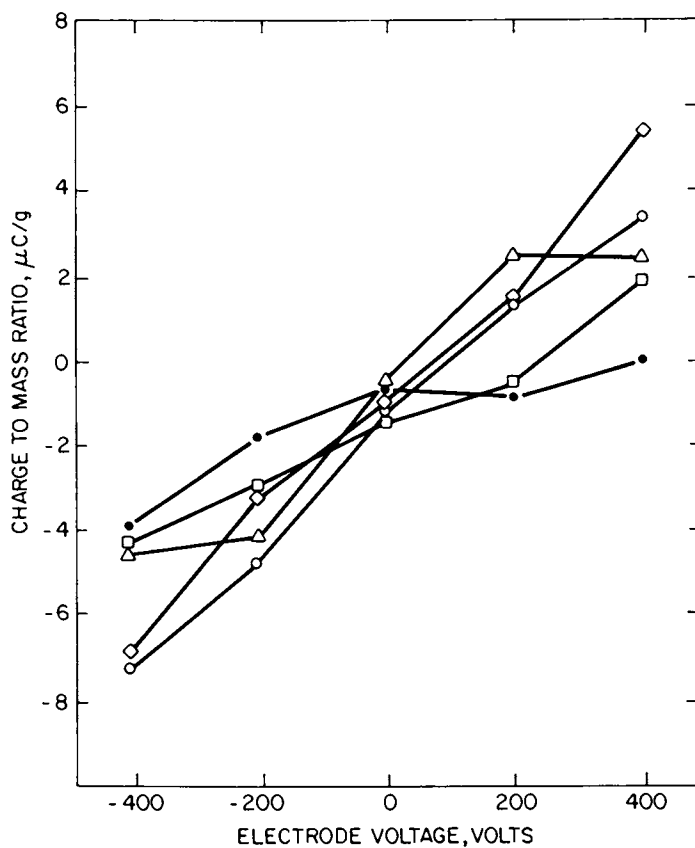


Figure 2. Charge levels of various polymeric and composite powders as a function of applied electrode potential. Key: ●, styrene copolymer; □, 0.1% Regal 330; ○, 0.5% Regal 330; ◇, 10% Regal 330, bulk; and △, 5% Regal 330.

Addition of 0.5% Regal 330 by weight to the polymer particles results in a surface that is approximately 10% carbon black. SEM pictures of the particle surface at 8kx and 17kx are shown in Figure 3. The small nodules are probably carbon black aggregates. This composite material shows a significant increase in charge levels over the pure polymer, and charging that is proportional to the applied electrode voltage. Another composite material with 10% Regal 330 mixed in the bulk, equivalent to a 6% particle surface coverage of carbon black shows very similar behavior to the preceding material (Figure 2).

The last sample in Figure 2 has 5% Regal 330 on the surface of the styrene copolymer particles, giving almost complete surface coverage, as shown in the SEM pictures in Figure 4. Between -200V and +200V this composite material charges similarly to the sample with approximately 10% surface coverage of carbon black. At +400V, however, there is no additional increase in charge level. A possible explanation is back flow of charge upon separation of the particle from the electrode. In metal-metal contacts backflow of charge during separation of the surfaces results in very little net charge exchange (1,4). Packed powder resistivity measurements of the material with 5% Regal 330 on the particle surface showed non-ohmic behavior with a resistivity of $8.6 \times 10^{13} \Omega\text{-cm}$ between 100 and 200V/mm, which dropped to $4.7 \times 10^{11} \Omega\text{-cm}$ between 200 and 400V/mm. Whether the region of decreased resistivity is simply fortuitous or whether it corresponds with decreased charging under the metal electrode is not totally clear because the electric field the powder sample sees is difficult to calculate. A dynamic resistivity measurement would generally show the sample to have a resistivity several orders of magnitude lower than the static measurement used here, and would also be more representative of the dynamics of the charging zone. However, the curve shape of the voltage/spacing versus current/area plot is similar for either static or dynamic measurements, with the drop off in resistivity occurring at the same field.

This data demonstrates that the amount of carbon black at the particle surface is an important factor in charging. Pure polymer shows only slight charging, an intermediate amount of small carbon black patches results in reasonable charging, with charge level proportional to applied voltage, and a high loading of surface carbon black results in a nonlinear charging behavior.

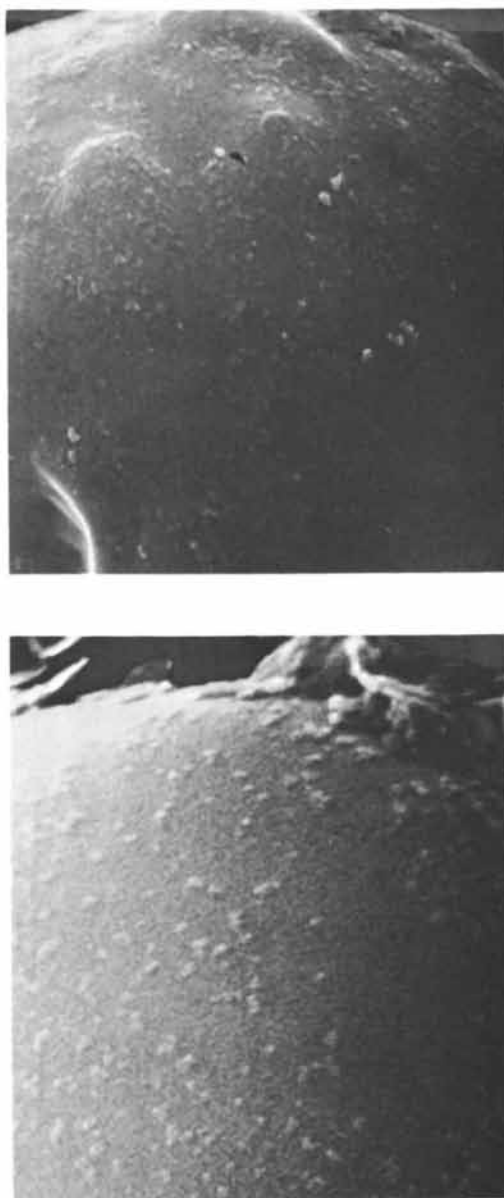


Figure 3. SEM picture at 8k \times (top) and 17k \times (bottom) of styrene copolymer particles with 0.5 wt % Regal 330 carbon black on the surface. The nodules are probably carbon black aggregates.

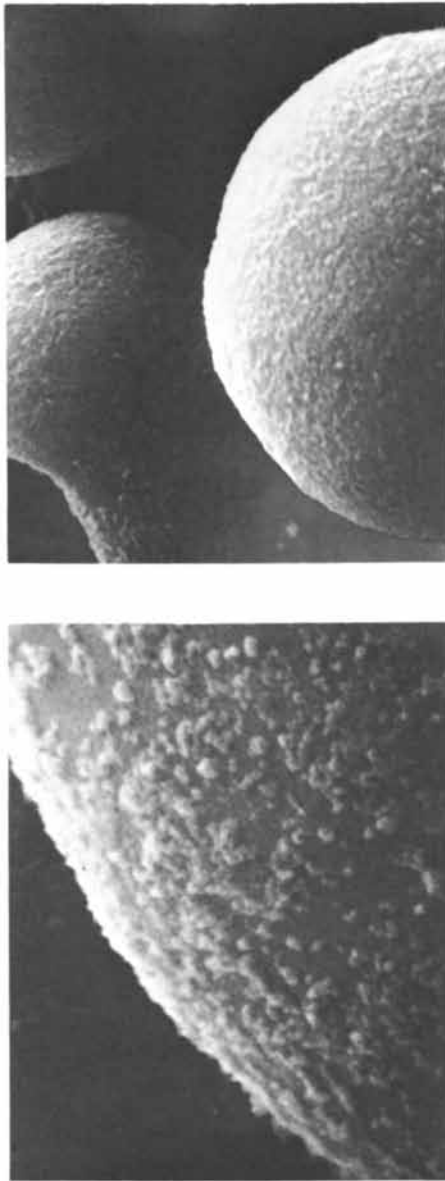


Figure 4. SEM picture at 6k \times (top) and 17k \times (bottom) of styrene copolymer particles with 5 wt % Regal 330 carbon black on the surface.

A typical charge level of 5 microcoulombs per gram corresponds to an average surface charge density of $2.5 \times 10^{-6} \text{C/m}^2$, using a typical value for surface area of a micronized particle given by B.E.T. nitrogen adsorption measurements (7). Larger charge densities would be calculated if charge were localized on the particle surface. This result is similar to charge densities observed for sliding or rolling contact of polymers such as polyethylene, polytetrafluoroethylene, nylon and polycarbonate against metal surfaces (8-12).

Usually, mixing polymer and carbon black does not result in a uniform material on the scale of 0.5-1.0% of the micronized particle diameter. For specific processing conditions and a constant weight percent of carbon black the resultant dispersion of carbon black aggregates in polymer can vary significantly. A well dispersed composite sample which has been spread into a thin transparent film using solvent vapors (20) is shown in Figure 5 in a transmission picture at a magnification of 500x. The uniform dark gray appearance shows finely divided carbon black, with only a few individual chunks discernable.

A transparent film prepared from a poorly dispersed composite by the same method is shown in Figure 6. Chunks of carbon black, about 2 μ m diameter are readily visible. During micronization, fracture could conceivably occur in the middle of a large carbon black chunk, leaving the uncoated surface exposed. In the well dispersed material, fracture through the smaller carbon black aggregates seems less likely, thus the surface of this sample powder probably has less exposed carbon black.

The effect of dispersion level on contact charging is shown in Figure 7. The pure styrene copolymer particles show very little charging. The well dispersed sample of 10% by weight DeGussa Sp.4 carbon black in styrene copolymer charges negatively more readily than the polymer particles. The poorly dispersed sample of 10% by weight Raven 8000 in styrene copolymer charges strongly in both directions with the charge to mass ratio proportional to the applied voltage. Poorly dispersed, exposed carbon black on the particle surface facilitates charging from the conductive electrode.

The changes in contact charging observed with different carbon blacks at the surface of styrene copolymer particles is shown in Figure 8. These samples all have 5% of a carbon black tacked onto the

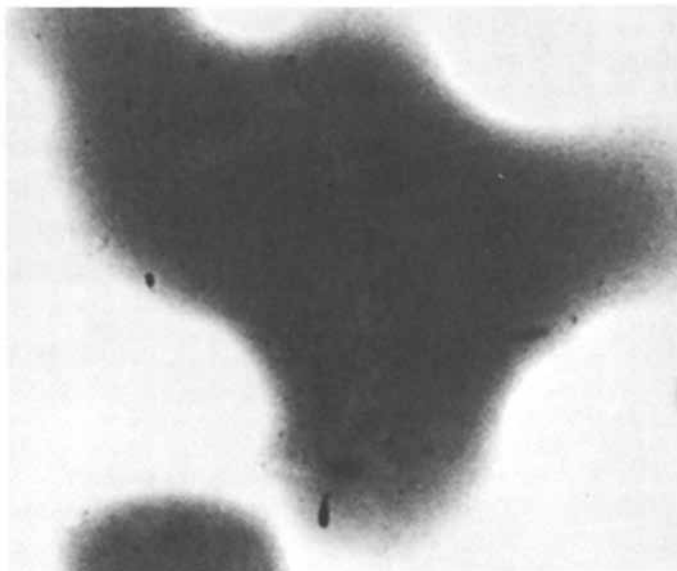


*Figure 5. Transmission picture at 500 \times of a 10% DeGussa Sp. 4; 90% styrene-*n*-butyl methacrylate blend demonstrating a good dispersion.*

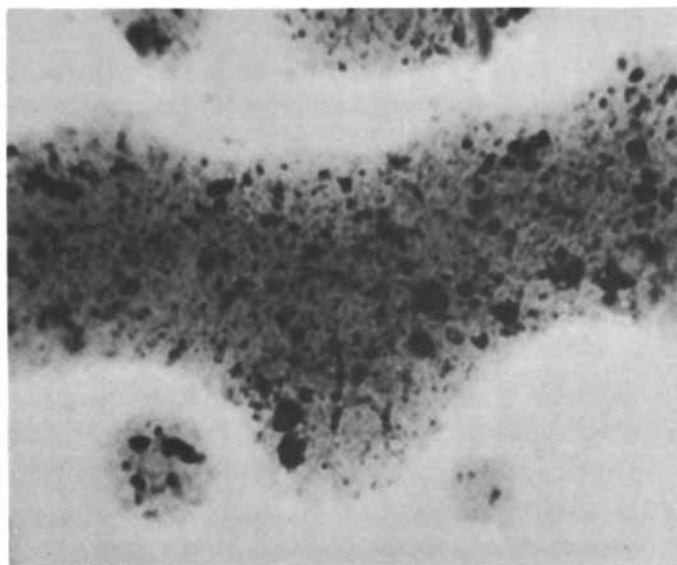


*Figure 6. Transmission picture at 500 \times of a 10% Raven 8000; 90% styrene-*n*-butyl methacrylate blend demonstrating a poor dispersion.*

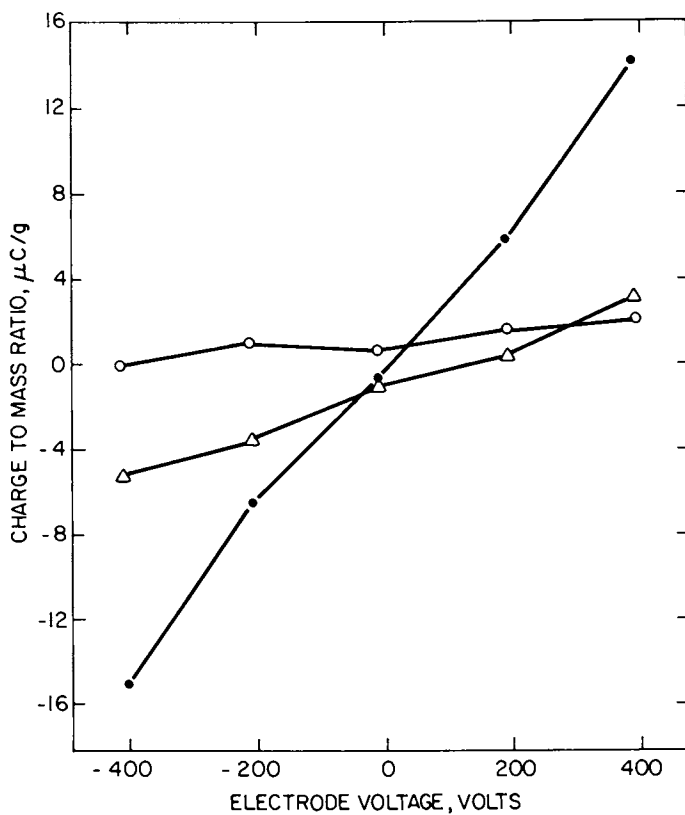


Figure 7. Charge levels of polymer-carbon black blends of varying dispersion levels as a function of applied electrode potential. Key: \circ , styrene copolymer; \bullet , poor dispersion; and \triangle , good dispersion.

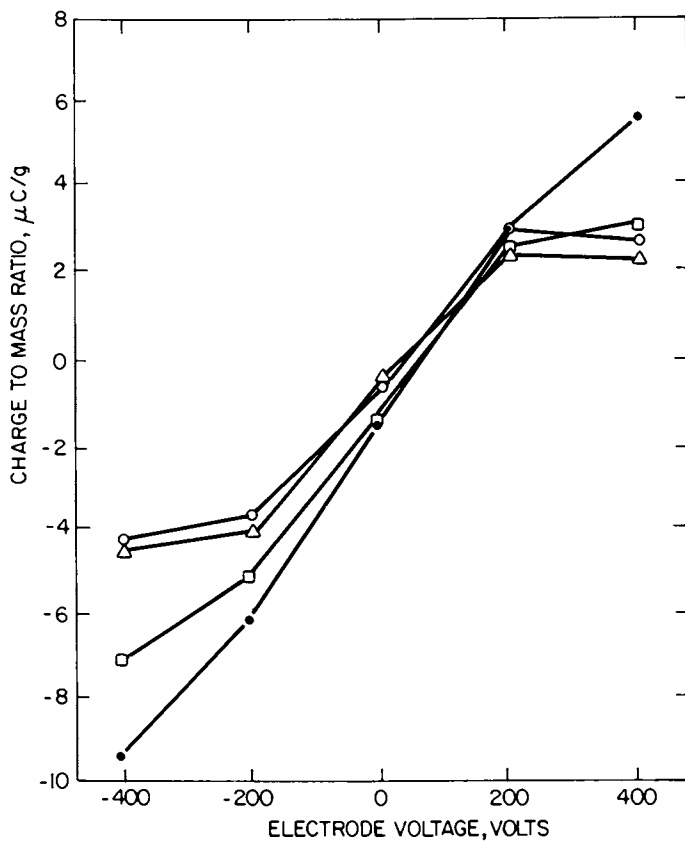


Figure 8. Charge levels of particles with 5 wt % carbon black on the surface of styrene copolymer particles as a function of applied electrode potential. Key: ○, Vulcan XC72R; △, Regal 330; ●, Black Pearls L; and □, Raven 5750.

surface, enough carbon black to almost completely cover the particle surface (Figure 4). Data for the sample with Regal 330 is reproduced from Figure 2. The sample with Vulcan XC72R shows the same behavior with a leveling off of charge level at 400V. In packed powder static resistivity measurements, these particles also showed non-ohmic behavior with a resistivity drop from $2.7 \times 10^{15} \Omega\text{-cm}$ at 50 to 200V/mm down to $4.4 \times 10^{12} \Omega\text{-cm}$ at 200 to 400V/mm.

The sample with Black Pearls L carbon black shows charging proportional to the applied voltage. The higher resistivity of this sample, $2.1 \times 10^{16} \Omega\text{-cm}$, was sufficiently insulative to prevent charge back flow or leakage.

The sample with Raven 5750 carbon black shows a decrease in charge at $\pm 400\text{V}$ from linear behavior although not as large a drop as with the Regal 330 or Vulcan samples. The Raven 5750 sample has a constant resistivity of $2.3 \times 10^{14} \Omega\text{-cm}$, somewhat lower than the resistivity for a true insulator. The charge leakage phenomenon may be present for this sample.

There is no apparent difference in behavior between the unoxidized blacks, Regal 330 and Vulcan XC72R, and the oxidized blacks, Raven 5750 and Black Pearls L. The two groups differ in estimated work function (4) by about half a volt, a very small difference compared to the applied potential on the charging electrode.

Summary

Contact charging of polymeric and polymer-carbon black powders against a metallic electrode shows a strong dependence on the electrode potential and the particle surface. For the samples studied, only slight charging occurred with no applied potential on the electrode. Sufficiently insulative particles show charging proportional to the applied potential. Carbon black at the particle surface facilitates charging from the electrode. This has been investigated by changing carbon black loading on the surface, comparing carbon black in the bulk with that added on the surface, and examining different carbon black dispersion levels. Samples with different carbon blacks on the particle surface show changes in contact charging that may be correlated with the particle resistivity. Samples of lower resistivity show charging that deviates from a linear dependence on the electrode potential, with no increase in

charging at higher potentials, possibly due to charge leakage.

Acknowledgements

I would like to thank my colleagues at Xerox for helpful discussions and sample preparation support, and Sue Kremer for the dispersion photomicrographs and SEM pictures.

Literature Cited

1. Harper, W. R. "Contact and Frictional Electrification"; Oxford University Press: Oxford, 1967.
2. Lowell, J.; Rose-Innes A. C. Advances in Physics 1980, 29, 947.
3. Seanor, D. A. in "Electrical Properties of Polymers"; eds. K. Frisch and A. V. Patsis, Technomic Press: New York, 1972.
4. Julien, P. C. in "Carbon Black - Polymer Composites"; ed. E. Sichel, Marcel Dekker, Inc.: New York, in press.
5. Davies, D. K. in "Methods of Exp. Physics: Polymers III"; ed. R. A. Fava, Academic Press: New York, 1980.
6. Gallo, C. F.; Ahuja, S. K. IEEE Trans. on Industry Applications 1977, IA-13, 348.
7. Raschke, C. R. "Proc. Second International Conference on Electrophotography"; 1974, 104.
8. Wahlin, A.; Backstrom, G. J. Appl. Phys. 1974, 45, 2058.
9. Davies, D. K. J. Phys. D 1969, 2, 1533.
10. Davies, D. K. in Static Electrification, "Institute of Physics Conference Series" 1967, 4, 29.
11. Haenen, H. T. M. J. Electrostat. 1976, 2, 151.
12. Nordhage, F.; Backstrom, G. in Static Electrification, "Institute of Physics Conference Series" 1975, 27, 84.
13. Fabish, T. J.; Saltsburg, H. M.; Hair, M. L. J. Appl. Phys. 1976, 47, 930.
14. Cassiers, P. M.; Van Engeland, J. Photogr. Sci. Eng. 1965, 9, 273.
15. Dessauer, J. H.; Clark, H. E., eds.; "Xerography and Related Processes", Focal Press: New York, 1965.
16. Williams, M. W. J. Macromol. Sci. - Rev. Macromol. Chem. 1976, C14, 251.
17. U. S. Patent 4,121,931 in 1978 to Minnesota Mining and Manufacturing Company.
18. Japanese Patent 54-51846 in 1979 to Ricoh Co., Ltd.
19. Hays, D. A. Deut. Ges. Chem. Apparatew. Monogr. 1974, 72, 95.
20. Orzechowski, A. Microscope 1979, 27, 5.

RECEIVED April 30, 1982

Particle Interactions in Binary Mixtures of Carbon Black and White Solid Acids

T. J. FABISH

Ashland Chemical Company, Columbus, OH 43216

The interaction of carbon black with selected solids is studied in non-aqueous particulate systems. Lewis and/or Bronsted surface acid sites on solid white acid particles are manifested in non-aqueous titrations employing a series of visible indicators to define the strengths of the various surface acid groups present. Carbon surface acid groups are subsequently detected by inference through their effect on the intrinsic acidity of the white reference solid. Non-aqueous electrophoretic mobility measurements define the signs of the charge exchanged in the interaction, and contact potential difference measurements on the carbon blacks serve to correlate colloid behavior with particle electronic structure. A key factor in the interpretation is the recognition of broad distributions in those properties that are dependent upon particle charge. Contact-induced alterations in the acidity of the white solids are indicated to be accompanied by charge transfer. The results from the various experiments can be correlated under the viewpoint that Lewis acid sites dominate the interaction between the oxidized carbon black and the silica-alumina white acid. The Lewis sites associated with the carbon black surface oxide structure seem to be essential for interaction with the white solids since a graphitized black lacking significant oxide structure is totally benign in the binary mixture experiments in spite of its having a work function equal to that of the oxidized black. The variability of the interaction

strengths found for the different binary combinations precludes derivation of a unique intrinsic acid group distribution for the carbon black from the behavior of the white reference solids.

The surface chemical structure of carbon black is an important factor in determining many physical properties of the carbon black in its dry solid state, in aqueous and non-aqueous suspensions, and in carbon black-polymer composites, as a catalyst, as a colorant and charge control agent in dry and liquid inks, and as conductance control and reinforcing agents in polymers and elastomers. The chemical activity of carbon black derives from acidic and basic surface molecular groups attached largely at the energetic edge sites of the fundamental two dimensional arrangement of highly conjugated polyacene-like (sp^2 hybridized carbon bonds) repeat units that comprise the crystallite basal plane(1, 2). While surface groups of a basic character are known to exist on carbon black, attention has been focused almost solely on the surface acid groups since these exert a controlling influence on the gas-solid, liquid-solid, and solid-solid interactions of carbon black. It is the roles of the surface acid groups and the basal plane electronic structure in solid-carbon black interactions that are the subject of this work.

Extensive studies of the surface chemical structure of carbon black have identified aromatic carboxyl groups (strong acids), phenols and hydroquinone derivatives (weak acids), and quinones and normal lactones (neutral groups)(1), although a more suitable structure for the strong acids may be cyclic esters (of a fluorescein type lactone structure)(3, 4, 5), while the weak acidic responses may be manifestations of hydroxyl groups occupying various edge positions relative to the cyclic ester groups(4, 5). Models of the carbon black surface chemistry are presently too imprecise to offer much in the way of predictive capabilities. It may be said however, that the strength of the surface acid group depends upon the amount and type of oxygen contained in the oxide structure. In this sense, carbon blacks experiencing a variety of post-preparative oxidative procedures tend to form a homologous series of materials so that the higher the total oxygen content of the black, the more acidic is the black(6). The prospect of a more-or-less con-

tinuous variation in selected carbon black properties with the degree of oxidation of the black offers a potential means of identifying the systematics of solid-carbon black interactions.

Microscopic interactions of the carbon black with other materials will occur through the electronic system of the polyacene crystallite and the surface chemical groups. Three different experimental techniques are utilized herein to observe the macroscopic effects of the equilibration processes: (1) Surface group titration of surface acid groups in mixtures of carbon blacks and white reference solids. (2) Non-aqueous electrophoretic mobility (EM) measurements of the quiescent carbon blacks and of carbon blacks that have been contacted to the white reference solids. (3) Contact potential difference (CPD) measurements on the carbon blacks. Surface group titration can, in principle, give information about the distribution in number density and strengths of the carbon surface acid groups (but nothing about their functionality). The EM measurements can provide information about the charge state of the carbon black following contact-interaction with the white reference solids. The relative CPD values for carbon blacks are sensitive to surface structure variations and are relevant to the characterization of electronic charge injection processes, especially in a series of homologous materials.

The titration of the carbon black surface acid groups as performed in the present experiments utilizes visible indicators to define the titration end point. The inclusion of a white reference solid with the carbon black is thus essential to the observation of the indicator color. While the use of mixtures of light and dark particles has previously been suggested (7, 10) and used (11, 12) for the study of the surface acidity of dark catalysts, the implications of an interaction occurring between the two kinds of particles that might significantly alter the surface acid group distribution from its intrinsic pattern were not explicitly pursued. In fact, the solid-carbon black interactions can be the dominant feature of the experiment, and represents in the present work the primary means for gaining insight into the material parameters that govern the contact-induced surface chemical modifications. Because the perceived activity of the carbon black is dependent upon the chemical and physical structures of the white reference solid, some consideration must be given the choice of white solids.

Two white solids differing widely in intrinsic surface acidity are utilized as reference materials: α alumina which possesses a very low intrinsic acidity, and a silica-alumina of a composition ratio near that which gives maximum catalytic activity for this family of materials.

Some of the surface aluminum atoms of alumina lack full coordination to neighboring aluminum atoms thereby providing cationic sites whose degree of exposure is dependent upon the degree of hydroxylation. At heat treatment temperatures of 550C such as employed in the present work, highly strained oxygen linkages begin to be created upon dehydroxylation of the more tenacious sites. Complete dehydroxylation must ultimately lead to the formation of oxide ion and adjacent charged vacancy sites which further exposes the tetrahedral aluminum cationic sites(13, 14). The dehydroxylated alumina surface is thus expected to contain Lewis base and acid sites of varying strengths(13, 15). Hydroxylation produces a more regular lower energy surface and may convert some Lewis sites to weak Bronsted sites(7, 13, 15). The different forms of alumina will be distinguished by their spectrum of acid and base sites. Exactly which sites are energetically and structurally allowed will depend upon the specific mixture of low index crystallographic planes that comprise the alumina surface. The particularly low acidity of α alumina results from relatively more complete coordination of the surface aluminum atoms(14).

A silica-alumina is formed upon isomorphous substitution of a trivalent aluminum atom for a tetravalent surface silicon atom in the silica lattice. The commensurate incomplete coordination of the aluminum atom generates charged structural sites that, in the absence of surface hydroxyl groups, behave as Lewis acid and base sites(7). The presence of a proton as a counterion or a hydroxyl group as occurs upon hydrolysis can produce strong Bronsted acid sites(7, 15, 16). Removal of the hydroxyl groups may convert Bronsted sites to Lewis sites reversibly(9, 15). Similar complexities as alluded to previously with the alumina surface arise in a detailed discussion of the nature of the active sites on silica-alumina so that several kinds of sites are usually invoked in interpretations of experimental measurements of surface acidity and catalytic activity(14, 15).

The surfaces of the carbon blacks and white solids are clearly too complex to allow meaningful predictions about the nature of the interactions that

can be expected between the materials. The previous discussion does suggest that the materials will exhibit a broad range of effective Pk_a values in an interaction with another medium. Amongst the materials utilized herein, the graphitized carbon black and the α alumina will certainly be much more restricted in the range of their effective Pk_a than will the highly oxidized black and the silica-alumina. The set of binary combinations possible with these four materials can thus be expected to show a large variability in their interaction strengths which will aid identification of systematics present in the solid-carbon black interaction.

Surface Group Titration

Experimental. Characterizations of a heterogeneous surface by means of surface group titration utilizing visible and ultraviolet chemical indicators to define the titration end point have frequently been employed with white solid catalysts (7-12), (17-20). Aspects of the surface acid group distribution have often correlated with the catalytic activity of the solid (7-9), (21-25). An adaptation of the technique appears to be suitable for studying the interactions between the surface acid groups in mixtures of carbon black and white reference solids.

The surface group titration experiment may be described in two steps. The first involves adsorbing visible or ultra-violet chemical indicators onto the surface of the solid particles of interest in an inert solvent. The acid indicators exhibit a definite color in their normal basic state in the benign solvent and a different distinct color when adsorbed onto an acidic surface site. Hence, simple observation of the presence or absence of the distinctive color change of the indicator on the surface of the solid particle is sufficient to signal the presence of surface acid groups having "strengths" defined by the known "strength" of the indicator (measured in Pk_a units in aqueous solution). All types of surface groups possessing strengths greater than that of the indicator will effect the color change. The second step in the experiment is to measure the magnitude of surface group concentration effecting the indicator color change by measuring the amount of a suitable strong base that is required to regain the original basic color of the indicator adsorbed on the surface. The result of the experiment is the magnitude and distribution of strengths of the solid surface acid groups.

Because the surface acid groups typically are strongly affected by the presence of water, the materials must be thoroughly dehydrated prior to use and the titrations performed in a non-aqueous medium.

Advantages and disadvantages of the titration technique are discussed in detail elsewhere(26). It suffices here to state that the surface acid group distributions on the white reference solids are sufficiently well defined by the experiment to provide a gauge by which to measure the interaction of carbon black with the white solids in binary mixtures.

The present study includes two carbon blacks differing greatly in their surface oxide structure: Black Pearls L (BPL), an oxidized Cabot Corp. black containing approximately 4 percent by weight acidic oxygen groups of the functionality previously described, and Cabot Graphon, which is Cabot Spheron 6 heat treated to above 2500C. The high heat treatment temperature removes almost all chemisorbed oxygen and hydrogen from the carbon platelets and promotes crystallite growth with commensurate graphite-like organization but over a much shorter range than found in graphite. We may thus anticipate an influence from electronic states associated with localized surface oxide groups in the case of BPL, while the behavior of Graphon should be dominated by the π electron structure of the "pure" carbon platelet. The carbon blacks were heated in vacuum at 100-120C for three hours prior to each experiment to reduce the influence of adsorbed water on the measured surface properties.

The white solids used as reference surfaces by which to gauge the color changes of the indicators included a Davison 86/13 $\text{SiO}_2/\text{Al}_2\text{O}_3$ high surface area (475 m^2/g) catalyst designated MS13/110, and a Linde3A α Al_2O_3 of low surface area (21 m^2/g). These materials were activated prior to each experiment by heating them in air to 550C for three hours.

The indicators were obtained from Kodak Laboratory Chemicals, Aldrich Chemical Company, and J.T. Baker and were used without further purification. The indicators employed in the majority of the titrations were bromocresol green and bromothymol blue each of which exhibits two acid-base transitions at $\text{pK}_a = -3.7, +4.6, \text{ and } -1.5, +6.8$, respectively(20, 22, 26). The medium for the titration and electrophoretic mobility experiments was benzene (Burdick and Jackson Laboratories) having a water content of less than 0.03 percent. The base used as titrant was n-butylamine, Baker analyzed reagent grade.

The procedure for the titration experiment consisted of activating the white solid, dehydrating the black, mixing the two powders to the desired mass ratio in 10 ml serum vials, adding benzene to immerse the powder, adding about 0.3 ml of nominal ten percent indicator solution (in benzene) and capping with a rubber stopper (to exclude contamination by water vapor) through which the 1N n-butylamine titrant could be injected from a microsyringe. Once prepared, the sample was shaken for one-half hour to promote intimate contact between the materials and then stored in a desiccator until titrated at room temperature. The titration was performed by injecting titrant through the serum bottle cap dropwise and mixing until equilibrium was achieved whereupon visual inspection through a 7X magnifier revealed the presence or absence of a color change on individual white solid particles.

Overall, it is estimated that below monolayer coverage acidity values from different series of samples may be compared with a precision of 25 percent (26). The uncertainty existing in the acidity measurements with respect to the question of how well they represent the true nature of the surface cannot be described by a percentage figure due to incomplete understanding of these surfaces.

Results. The smoothed surface acid group distributions up to monolayer coverages of one acid group per 20Å^2 are given for MS13/110 and $\alpha\text{Al}_2\text{O}_3$ in Figure 1. Both mass and total surface area normalization are shown.

On an area basis $\alpha\text{Al}_2\text{O}_3$ exhibits significant intrinsic surface group densities at high $\text{P}k_a$, but differs greatly from MS13/110 in possessing no surface acid groups of strength greater than about $\text{P}k_a = 3$. In this sense MS13/110 is a "strong" solid acid and $\alpha\text{Al}_2\text{O}_3$ a "weak" solid acid. The heterogeneous nature of the surfaces of the white reference solids is clearly reflected in the titration results.

An example of the behavior of the MS13/110 titer at different loadings of BPL carbon black and at $\text{P}k_a = 4.6$ is given in Figure 2. The dashed line in Figure 2 represents the result anticipated if contact of the two solids resulted in no disturbance of the white solid acid groups of any sort, i.e. constant white solid acidity. A large deviation in the mixing curve from the zero interaction case is apparent. The white solid, in effect, loses considerable acidity in contact with BPL.

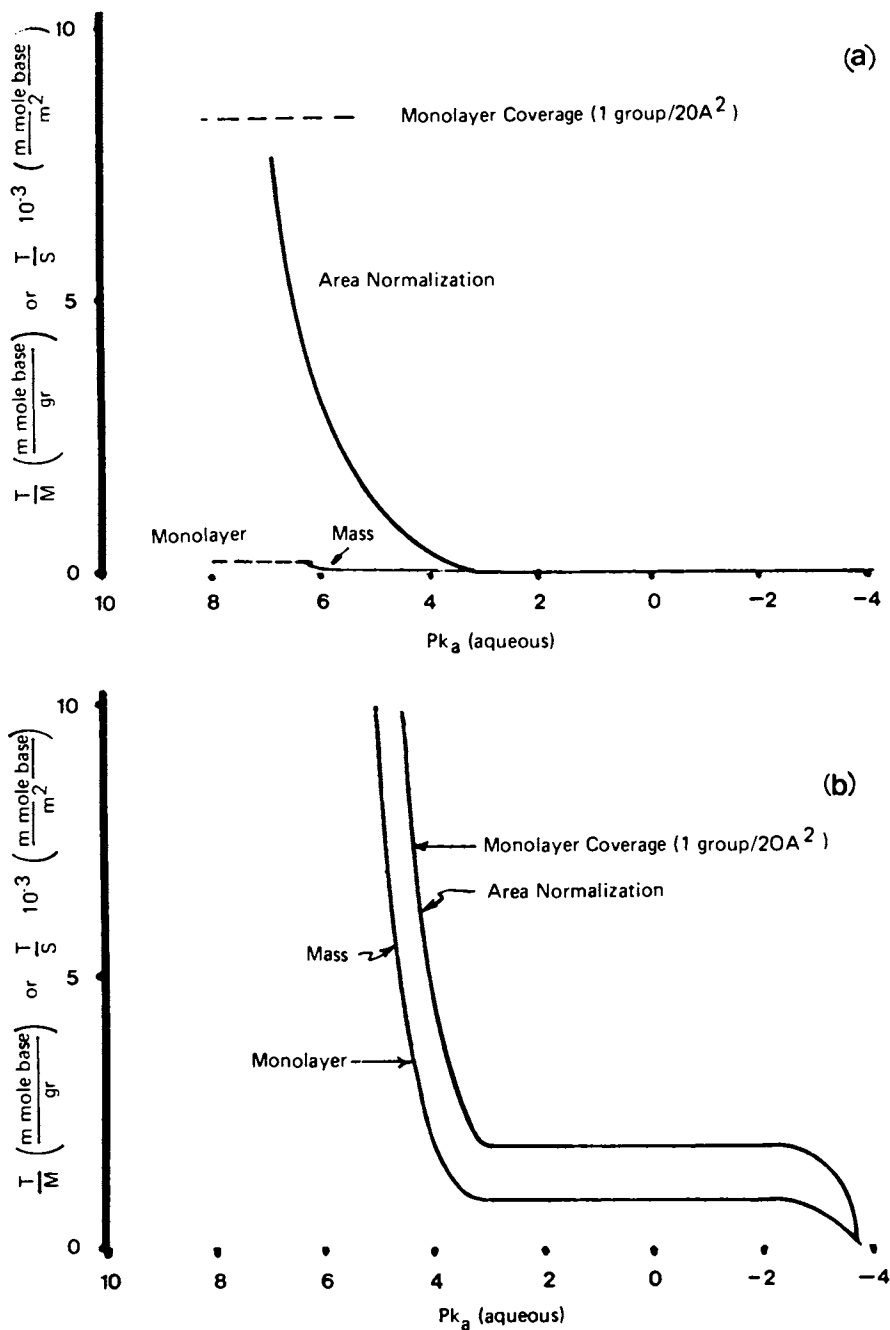


Figure 1. Smoothed intrinsic acid group distribution normalized to total sample mass and total B.E.T. sample surface area for α alumina (a), and 86/13 silica-alumina (b). Monolayer coverage is defined as one (arbitrary) acid group per 20\AA^2 of sample surface area.

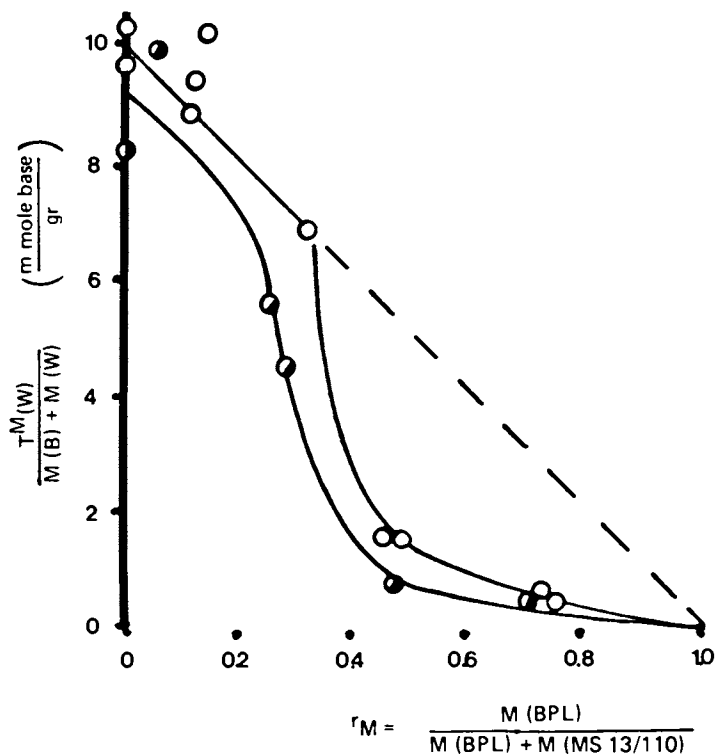


Figure 2. Dependence of the acidity of 86/13 silica-alumina at a pK_a of 4.6 (aqueous) on the fraction of Black Pearls L carbon black in binary mixtures using mass normalization. Key: ---, zero interaction; and ●, mixtures with BPL and refluxed in toluene for 48 hours.

Also shown in Figure 2 are data for BPL samples that were extracted by refluxing in toluene for 48 hours. Little effect of the extraction is discernible at $Pk_a = 4.6$, and none at $Pk_a = -3.7$ (not shown(26)).

Quite the opposite response is obtained when BPL is contacted to the weak solid acid, αAl_2O_3 (Figure 3). No intrinsic acidity was detected for αAl_2O_3 stronger than about $Pk_a = 3$ (Figure 1a), and none was found at Pk_a of -1.5 and -3.7 when in contact with BPL. However, the acidity of αAl_2O_3 at Pk_a of 4.8 and 6.8 increases considerably above the intrinsic values in the presence of BPL (Figure 3). The contact of BPL to αAl_2O_3 is seen to result in an increase in the acidity of the white solid only at acid strengths where intrinsic acidity exists on the white solid, as was the case with BPL on MS13/110.

The alterations of white solid acidities as a result of contact with BPL are summarized graphically in Figure 4. The fractional loss or gain over the intrinsic white solid acidity is greatest for the weakest surface acid groups and monotonically decreases with decreasing Pk_a . The maximum loss in MS13/110 acidity remains large however ($\sim 40\%$ at $r_M = 0.5$) for the strongest detectable acid groups.

Similar data (not shown(26)) for the graphitized black, Graphon, exhibits little evidence for significant interaction with either white reference solid.

The contact interaction of the two white reference solids is interesting to study because the transition of the visible indicator can, in principle, be observed on both components of the mixture. In the case of αAl_2O_3 -MS13/110 mixtures, it proved possible to observe the color changes of both materials only at certain mass ratios, and then only with considerable imprecision (for αAl_2O_3) because of the large differences in intrinsic acidity of these solids. The mixing curve for MS 13/110 contacted with αAl_2O_3 is given in Figure 5. The effect of αAl_2O_3 on the acidity of MS13/110 is quite similar to that of BPL on MS13/110 at the same Pk_a ; a large net loss of MS13/110 intrinsic acidity with a sharp onset occurring at low surface area coverages.

The best independent estimates of the αAl_2O_3 titers obtained in this experiment at $Pk_a = -1.5$ are included in Figure 5. The acidity of αAl_2O_3 rises as that of MS13/110 falls. In the region of the available αAl_2O_3 data and within the uncertainty in the measurement, the total acidity may be said to be conserved in the contact interaction. The extent of the data and its accuracy are insufficient to provide an acceptable test of this statement, however.

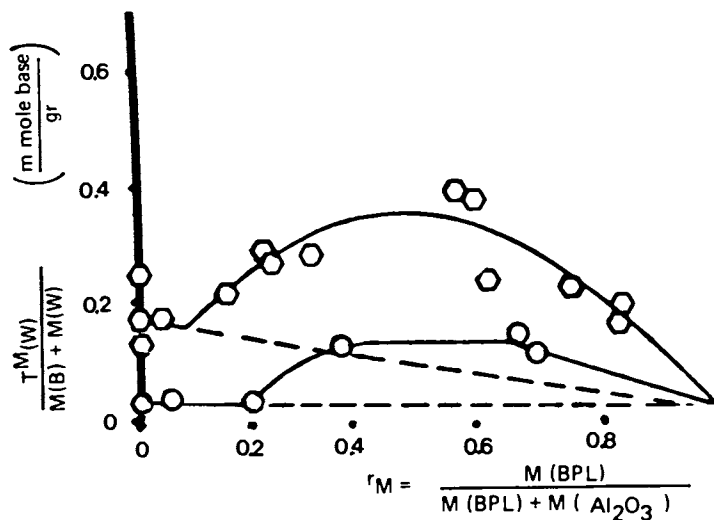


Figure 3. Dependence of the acidity of α alumina at a pK_a of 6.8 (○) and at a pK_a of 4.6 (○) on the fraction of Black Pearls L in binary mixtures using total sample mass normalization.

The characteristic acid colors of the indicators were not achieved at a pK_a of -1.5 or -3.7 demonstrating zero surface acidity at these strengths for all $r_M \geq 0$. Zero interaction between the mixture components is represented by the dashed line.

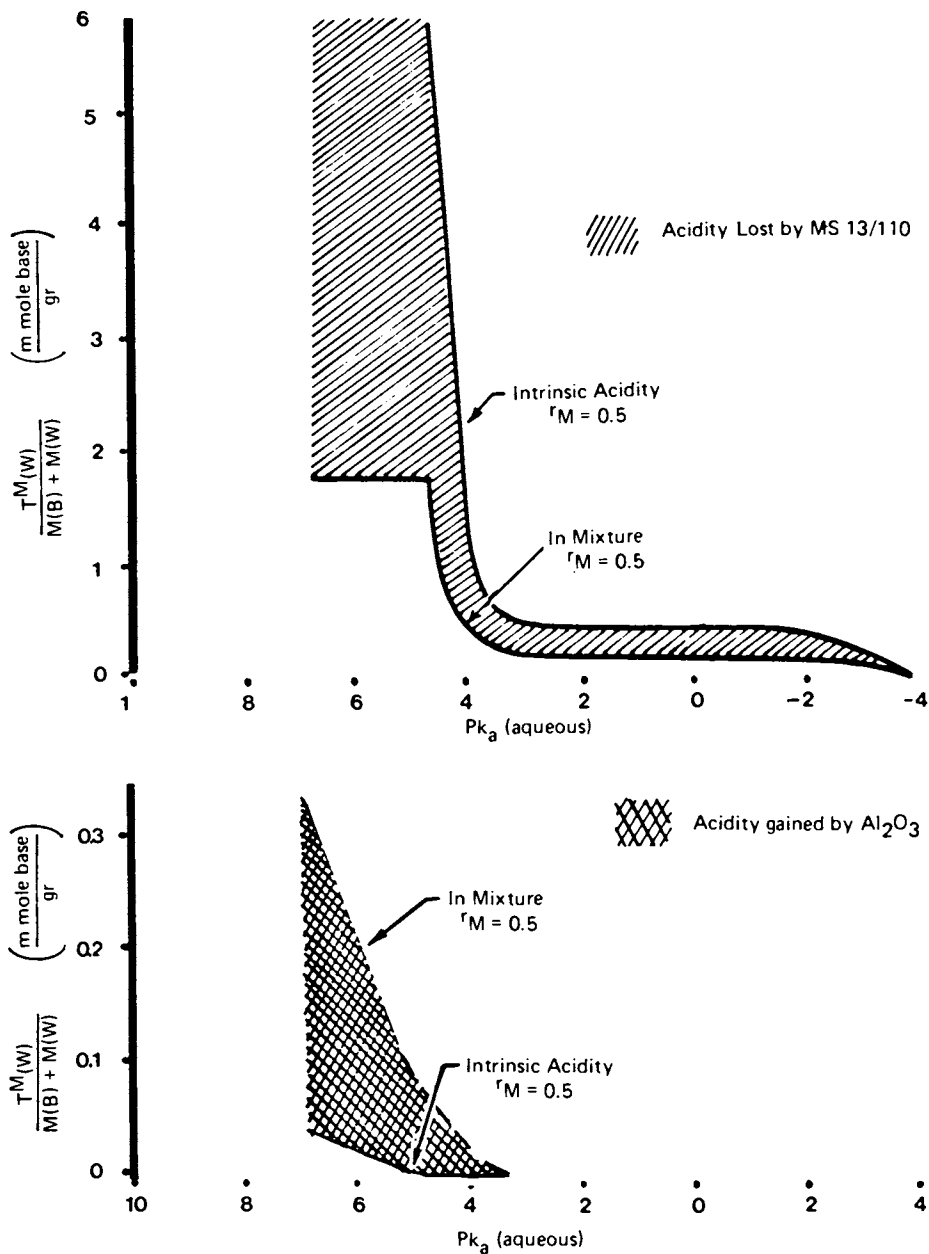


Figure 4. Titration results for Black Pearls L contacting 86/13 silica-alumina (top) and α alumina (bottom) at a mixture ratio of $r_M = 0.5$ (equal parts by weight of carbon black and white solid). The silica-alumina loses acidity across the spectrum of intrinsic acid strengths (see Figure 1b), while α alumina gains acidity across its spectrum of intrinsic acid strengths (see Figure 1a) in the contact with BPL.

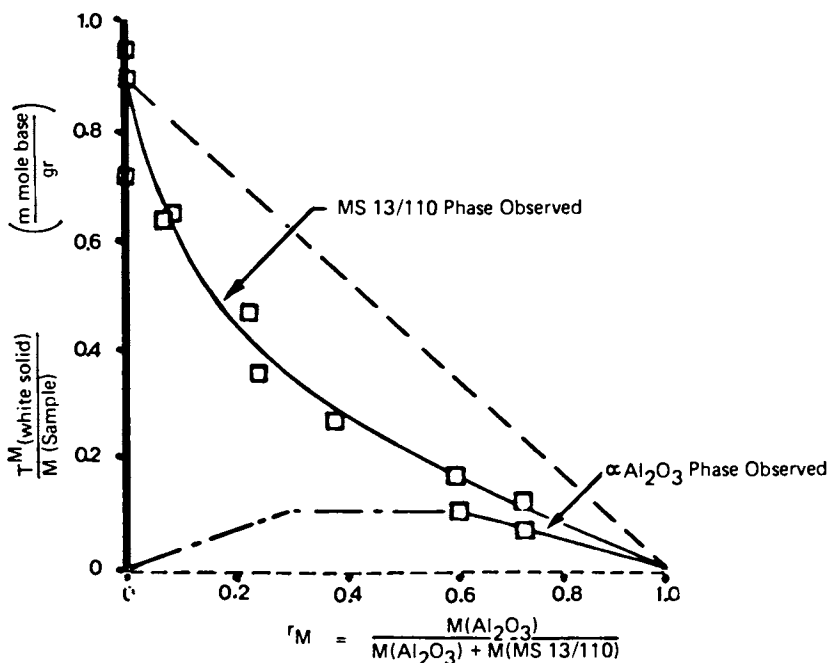


Figure 5. Independently measured white solid acidities in binary mixtures of 86/13 silica-alumina and α alumina at a pK_a of -1.5 (aqueous) using mass normalization.

The intrinsic acidity of alumina is zero at a pK_a of -1.5 (see Figure 1a). Within the region of mixture ratios where observation of both mixture components was possible and within the uncertainty of these measurements, the acidity lost by the silica-alumina is equal to that gained by the α alumina. Key: ---, zero interaction between the mixture components; —, observed MS 13/110 phase; and - · - ·, observed α alumina phase.

The effect of the MS13/110 contact on the α Al₂O₃ acidity is more clearly shown in Figure 6 for Pk_a of 6.8 and -1.5. The finite acidity appearing at Pk_a = -1.5 shows that this interaction causes acid groups to appear on α Al₂O₃ at strengths where no intrinsic acidity exists (Figure 1a). (Although quantitatively unmeasurable at the sensitivity employed in the present titrations, the absence of the clearly distinguishable yellow base color of the bromothymol blue indicator on α Al₂O₃ prior to the start of titration demonstrated the presence of acid groups at Pk_a = -1.5 for all $r_M > 0$). For the sake of comparison, the increase in α Al₂O₃ acidity at Pk_a = 6.8 is an order of magnitude greater as a result of contact with MS13/110 than with BPL (Figure 4b), and MS13/110 produces acidity on α Al₂O₃ at Pk_a = -1.5 where BPL does not.

The extent of the interactions witnessed in the visible indicator titration of mixtures suggests a ranking for the four materials included in this study in order of increasing intrinsic solid acidity: α Al₂O₃ \leq Graphon $<$ BPL $<$ MS13/110. In addition, the ability of a material to alter the intrinsic acidity of another in a contact (interaction strength) lies in the order Graphon \ll BPL $<$ α Al₂O₃ $<$ MS13/110. We have yet to inquire about the relevance of solid acidity measured in this way to the physical and chemical properties of the materials and to the nature of the contact interaction. It would be revealing to discover if a net charge exchange is associated with the interaction, if the charge is electronic or protonic in nature, and to gain some insight into the energetics governing the interaction.

Electrophoretic Mobility

Experimental. Samples for electrophoretic mobility (EM) measurements were prepared as previously described for the titration experiments except that violent mixing with destruction of carbon agglomerates was desirable here and was promoted with a 5-10 minute treatment of the capped serum bottles in an ultrasonic bath. The indicator was, of course, deleted in the EM sample preparation procedure. Following mixing, a few drops of the mixture was transferred to a 25 ml flask of benzene and given another ultrasonic treatment. This procedure produced a fairly stable colloid suspension of the carbon black which was used to fill the glass-Teflon commercially available EM cell manufactured by Zeta-Meter, Inc.

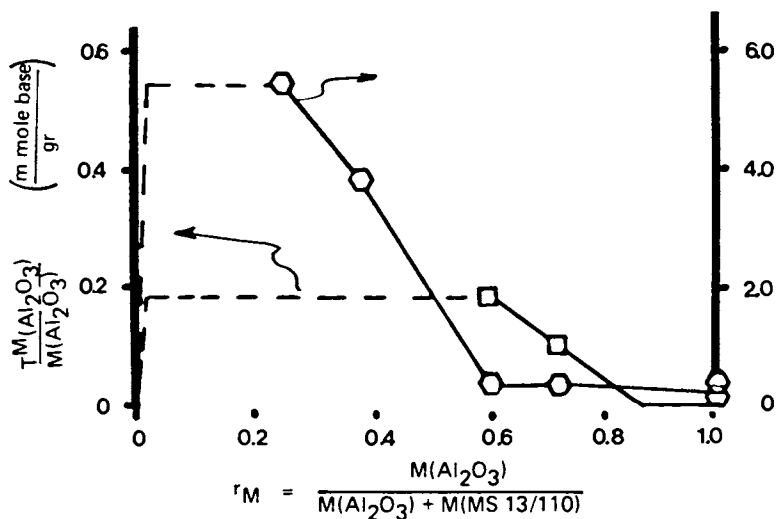


Figure 6. Contact-induced alteration of the acidity of α alumina by 86/13 silica-alumina at a pK_a of 6.8 (\circ) and -1.5 (\square).

The acidity of α alumina in the binary mixture must go to zero at zero mixture ratio. The extended dashed line for a pK_a of -1.5 is employed to indicate that the acidity was indeed greater than zero for all $r_M > 0$ at this pK_a (as demonstrated by the indicator color). The intrinsic acidity values of α alumina are achieved at $r_M = 1.0$.

Only colloid suspensions from mixtures of α Al_2O_3 and carbon black with MS13/110 were employed because the relatively large ($\sim 60\mu\text{m}$) and tough MS13/110 particles maintained their structural integrity and sank to the bottom of the EM cell thus assuring that the carbon black or α Al_2O_3 moiety actually comprised the colloid measured.

Experimental details of the measurement are described elsewhere(26). It is noted here that many of the difficulties described by van der Minne(27, 28) in connection with non-aqueous EM measurements of carbon particles were avoided or minimized in concentrating on the low field motion of colloids obtained from the quiescent materials (i.e. materials not experiencing a contact interaction with the silica-alumina) and from the binary mixtures. A single EM measurement as utilized herein consists of measuring the transit times of 5 to 30 particles traveling distances of 40 to 160 μm , averaging the velocity values and dividing by the applied electric field strength. Such measurement groups were accumulated for a given colloid sample at several values of applied field and under field reversal to verify scaling of particle velocity with field strength.

Results. The results of individual EM measurements on groups of colloidal particles of varying size and at different applied fields and field polarities are presented in Figure 7 in the format of a histogram located at the parent mixture mass ratio. The bars appearing in Figure 7 include the total range of 3 to 10 measured EM values for each of one to three colloid samples prepared from each parent mixture.

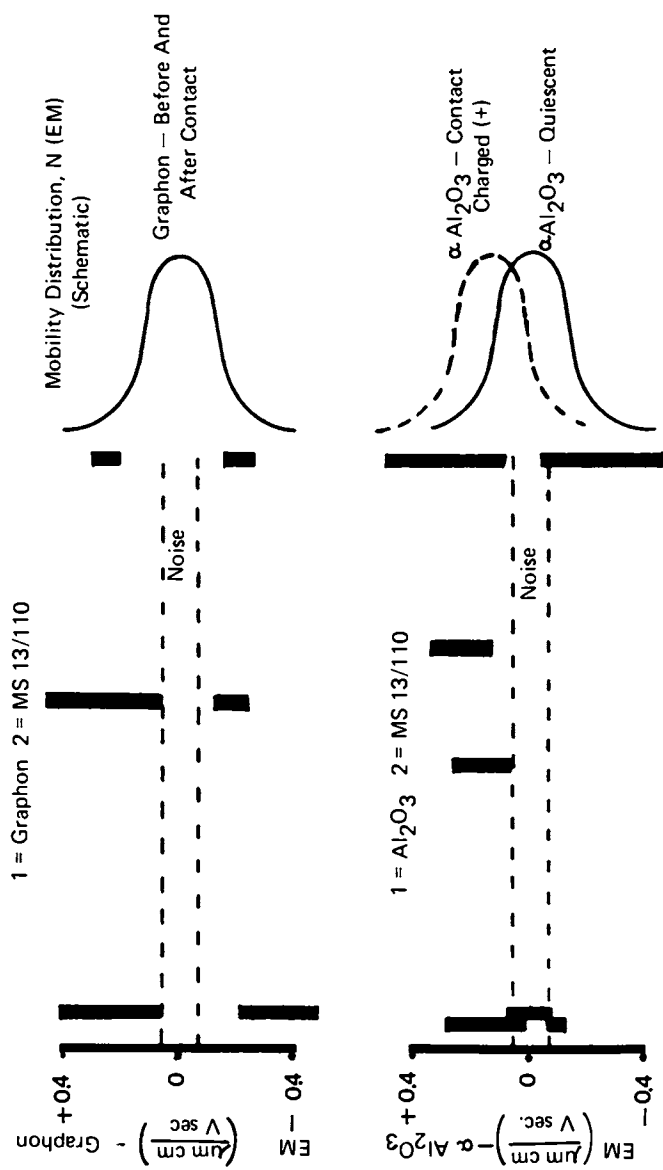
It became apparent during the course of the measurements that the mixtures did not lend themselves to characterization by a single well-defined average EM value. While each sample in the field of focus of the EM cell behaved well with regard to particle statistics, and applied field strength and polarity scaling, these characteristics of the observed sample could change with mixing of the cell and with the addition of a fresh colloid sample obtained from the same parent mixture. Some samples contained both positive and negative-going particles that scaled reasonably well with the applied field strength. An average EM value could be evaluated for each such sample, both with and against the applied field if called for, as previously described. The interpretation suggested was to consider each of these individual EM values as a valid sample of a distribution of EM values inherent to the particular mixture.

Precedents for EM distributions of similar width to those depicted in Figure 7 have been generated for other material systems by a measurement technique that is capable of directly resolving the distribution: laser-doppler spectroscopy(29). While the present measurement technique provides no information about the frequency function for the distribution, a physical basis does exist for the creation of such a distribution within a powder comprised of nominally identical particles as well as within the two component mixtures.

An EM value greater than the experimental noise can arise as a result of adsorption of ions from the solution onto the colloid surface, or from excess charge generated within the mixture of dissimilar materials by a contact charge exchange process. The EM measurements were performed in pure benzene to minimize the presence of extrinsic ionic charge that could mask the properties of the mixture(27). Alternatively, solvation of ions from the carbon black could occur, but the insensitivity of the titration results to prolonged extraction of the carbon black in toluene suggests that at least the ionic groups that determine the solid acidity are stable against solvation. It is reasonable, therefore, to inquire into the characteristics of charge generation processes arising from basic thermodynamic constraints on the electronic structures of the materials. Such a process would have to account for the observation of broad EM distributions for the colloids obtained both from the binary mixtures and from the quiescent material.

The exchange of charge, electronic or protonic, during a contact event is a fundamental microscopic process for equilibrating the electrochemical potentials of two dissimilar materials such as those comprising the mixtures used in these experiments(30, 31). Moreover, contact charge exchange is a likely occurrence even among the nominally identical particles of each component of the mixture because of compositional variations and differing particle charge capacities resulting from finite particle size distributions. The only question is one of the magnitude of the various interparticle charge exchanges. We shall examine the EM data under the hypothesis of contact charge exchange-generated distributions in the spirit of gaining an estimate of the quantities of charge involved.

The EM results for the quiescent colloids of Graphon, α Al₂O₃, and BPL appear at $r_M = 1.0$ in Figure



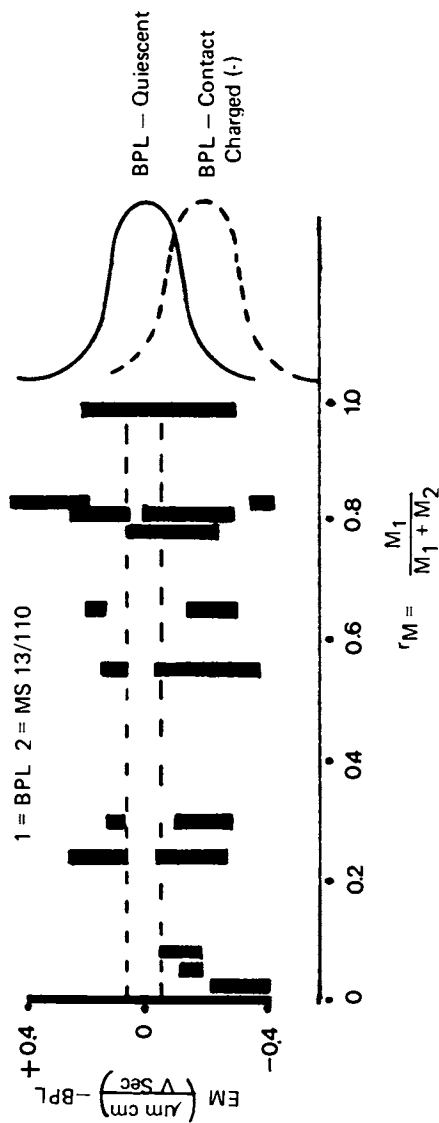


Figure 7. Histograms encompassing the measured electrophoretic mobility values for colloids of Graphon, α -alumina, and Black Pearls L in their quiescent state ($r_M = 1.0$) and after contact with 86/13 silica-alumina ($r_M < 1.0$).

Gaussian distributions (right) are schematic representations of these data suggested by an interpretation of each measurement as a sample of a distribution having its origin in a variation of particle charge. Distribution frequency factors are wholly unknown. Shifts in the distributions, indicated to occur by the measurements results at $r_M \approx 0$ compared to those for $r_M > 0$ and $r_M = 1$, suggest the α -alumina is charged positive as a result of contact with the silica-alumina. Black Pearls L is charged negative, and Graphon is benign with respect to contact with silica-alumina. The "noise" band shown corresponds to a basic uncertainty met in experimentally defining zero mobility.

7. A schematic Gaussian representation of the EM distribution that encompasses the quiescent measurements is given on the right in Figure 7 to aid in visualizing the indicated trends with varying r_M . The EM distributions for the three quiescent colloids all contain both positive and negative charged particles but appear to be symmetric about $EM = 0$. This continues to be the case for Graphon at all r_M , but only positive α Al_2O_3 colloids were observed for α Al_2O_3 contacted by MS13/110, while only negative BPL colloids were observed for BPL-MS 13/110 mixtures at low BPL loadings where observation of contact-charged colloid is most likely. The dashed hypothetical distributions schematically depict the contact-charged colloids.

The contact-induced shift in particle mobility is about $0.2 \frac{\mu m \cdot cm}{V \cdot sec}$ (Figure 7), on the average. Equating the coulomb force to Stokes' drag gives the particle charge density that would produce this change in mobility(26). Viewing a calibrated lined microscope slide under the conditions of the EM measurement verified that the colloids included in these measurements were largely in the range of 1-10 μm . For 1 μm diameter particles, the particle charge density is: $\sigma = 4 \times 10^{-6}$ coul/ m^2 . The net particle charge is 13×10^{-18} coul, or about 80 electronic charges. Colloids 10 μm in diameter would acquire about 800 electronic charges on the average in altering their mobility by $0.2 \frac{\mu m \cdot cm}{V \cdot sec}$. A maximum charge exchange, represented by a transition of a particle from the positive tail of the quiescent distribution to the negative tail of the contact-charged distribution, would involve an exchange of about 3200 electronic charges on a 10 μm particle.

The EM results may thus be summarized in two relationships wherein the lower material charges negatively in a contact with the higher material; BPL < MS 13/110, and MS 13/110 < α Al_2O_3 . The average charge imparted to 1 μm particles is 80 electronic charges. In addition, Graphon is essentially benign in a contact with MS 13/110.

Contact Potential Difference

Experimental. The carbon blacks were used as received and hand pressed into 3/4-inch diameter recessed stainless steel holders until firm, close-packed films, about 0.050-inch thick, were formed. The samples were outgassed at room temperature for several hours (10^{-5} Torr) and their contact potentials

measured relative to a gold reference surface utilizing the Kelvin-Zisman reciprocating capacitor technique(32). The precision of the CPD measurement in our configuration is ± 50 mV.

The outgassing at room temperature will remove only the most loosely bound water from the carbon surface. The blacks were then heated to 100-110C for prolonged periods of time beyond the point where the contact potential difference (CPD) ceased to change in time. The CPD was followed during cooling back to room temperature. The CPD samples prepared in this manner should be in approximately the same state with respect to water content and other loosely bound volatiles as the carbon black samples used in the titration and EM experiments.

The CPD measurement is a relative measurement of the difference in electrostatic potential existing between two opposing surfaces that are in thermodynamic equilibrium. In the event the electronic structures of the bulk materials continue unchanged to their surfaces, the measured CPD will equal the negative of the difference in work functions between the two materials. In the more general case, a space charge layer and/or a surface dipole layer is present which alters the electrostatic vacuum potential outside the surface relative to the inner potential. Interpretation of the CPD measurements then requires more detailed knowledge of the electronic structure of the near surface region. Subject to these qualifications, the CPD value can be converted to an absolute work function value for the surface in question if the work function of the reference surface is known.

Results. The CPD's of Graphon and BPL relative to a gold reference following outgassing as previously described are -0.34 ± 0.06 V and -0.39 ± 0.06 V, respectively. That is, Graphon and BPL have work functions, ϕ , that are equal and about 0.4 eV greater than that of the gold reference surface.

For metals or semiconductors without dominating surface features such as thick oxides or high densities of intrinsic surface states, the magnitude of the ϕ of one material relative to that of another will define the direction of electronic charge transfer occurring in a contact of the two materials(30). The work function of insulating powders such as the MS13/110 and α Al_2O_3 used in the present experiments is not a well defined material property. But the carbon blacks behave as semi-metals, and previous contact charging(33, 34) and transient charge

injection(35) experiments on carbon loaded polymer films have demonstrated the relevance of ϕ to the description of charge injection processes in carbon blacks. A relationship between ϕ of the blacks and the charge transfer observed in the present EM experiments as well as to the acidity ranking of the materials found in the titration experiments was, therefore, anticipated.

However, Graphon proved to be almost totally benign in the titration and EM experiments, while BPL was very active in both experiments though the equality of the ϕ values for Graphon and BPL would indicate similar behavior for the two blacks if the physical and chemical processes involved were governed solely by an electronic structure that was well characterized by ϕ . Clearly, details of the electronic structures of the carbon black are important to understanding their interactions with other materials.

Discussion

The titration experiments, the EM measurements, and the ϕ measurements provide complementary information about the properties of the carbon black as manifested in their interactions with the white reference solids. It is appropriate to ask what these results taken together say about the surface properties of carbon black.

We note first that the results from the titration experiments show that such measurements performed on mixtures of white and dark solids cannot be used to obtain a unique intrinsic acid group distribution for the dark solid as has been proposed in the literature(7-12). Even though conservation of total acidity of the mixture components is suggested in one case (Figure 5), the interaction strengths and the direction of the acidity transfer depend upon the particular materials employed in an as yet undetermined way. Clearly, an intrinsic acidity for BPL deduced from its interaction with MS13/110 would be quite different from that deduced from its interaction with α Al₂O₃ (Figure 4), and an intrinsic acidity for α Al₂O₃ calculated as equivalent to the loss of acidity from MS13/110 in that mixture (Figures 5, 6) would bear no relation to the actual intrinsic acid group distribution (Figure 1a).

Correlation of the results of the present three experiments requires knowledge of the nature of the carbon black and white acid surfaces with respect to their Bronsted or Lewis character. Few analytical

techniques can distinguish between Bronsted and Lewis sites (7-9), (13-16), (18, 36). Either kind of site will be similarly manifested in the titration experiments, and the EM measurement cannot distinguish a proton from an electron in the charge exchange.

The white solids were utilized in their dehydrated state in the present work. The fully dehydroxylated surface acid sites of alumina and the silica-alumina are reported to be Lewis in character (7-9), (13-15). However, the degree of hydration is important to determining the nature of the acid site. Alumina apparently retains some chemisorbed water at heat treatment temperatures below 1000C (13, 37), and these hydrated sites could impart (weak) Bronsted character to the interactions of alumina with the other materials (14, 38). Similarly, the silica-alumina retains both Bronsted and Lewis acid sites at heat treatment temperatures at least as high as 500C (7, 39, 40). It may be assumed that dehydration of the oxidized carbon black, BPL, at 110C in vacuum will not be totally effective in dehydroxylating the surface acid groups. It is probable, therefore, that both Lewis and Bronsted sites were present on all our materials except Graphon (40) in the present experiments.

Given the presence of such a wide variety of surface groups, several kinds of interaction mechanisms are possible. One we shall consider might involve the direct contact transfer of electrically neutral acid groups in response to a thermodynamic drive. A second would be the exchange of a proton if Bronsted character predominates, or thirdly, an electron transfer between Lewis groups.

To decide the most likely mechanism we have the observations that the materials gained acidity in contact with the higher member of the series in the order, α Al₂O₃ < BPL < MS13/110, while the lower materials gained negative charge from contact with the higher material for, BPL < MS 13/110, and MS13/110 < α Al₂O₃; Graphon was nearly benign in the contact interactions even though its work function was nearly equivalent to that of BPL.

The observation that charge transfer accompanies acidity transfer immediately rules out the possibility of an interaction mechanism involving only electrically neutral surface groups.

Electronic charge transfer via Lewis sites occurs in the direction from lower to higher electrochemical potential, while positive charge transfer flows in the opposite direction. We may thus consider that the order given above based upon the sign of the contact

charge exchange defines the direction of decreasing electrochemical potential.

It is impossible to unambiguously identify the nature of the charge carrier involved in the contact charge exchange solely on the basis of the electrochemical potential series. However, the idea of localized Lewis sites governing the interaction for BPL in the binary mixtures reconciles the present non-aqueous medium results with previous interpretations of solid state experiments that emphasize the role of Lewis sites in defining the thermodynamic drive governing charge injection at carbon-polymer interfaces(33-35) through their control of the carbon surface dipole layer characteristics(32). Presumably in the BPL - MS13/110 binary mixture, weak acid groups occurring at high Pk_a on MS13/110 act as a Lewis base (i.e., electron donor) towards stronger Lewis acid sites on BPL.

In contrast, the loss of acidity of MS13/110 to α Al₂O₃ in their mixtures (Figure 5) is accompanied by a positive charge transfer from MS13/110 to α Al₂O₃. Here, the idea of proton transfer dominating the α Al₂O₃ interaction with MS13/110 not only satisfies the particle charge requirement but also provides a basis for the increase in acidity of α Al₂O₃ observed to occur in regions of acid strengths where no intrinsic acidity existed (Figure 6) since the extra protons on α Al₂O₃ can be expected to be more labile than those associated with the localized intrinsic Bronsted sites. The increased strength of the α Al₂O₃ interaction with MS13/110 compared to BPL with MS13/110 as discussed previously in the text also suggests that Bronsted sites are generally dominant over Lewis sites on MS13/110, in agreement with previous findings(7, 18).

The inactivity of Graphon in the contacts with the white solids despite the near equivalence of its work function with that of BPL demonstrates an absence of coupling of the delocalized π electron system of Graphon with the localized Bronsted and Lewis sites of the white solids. It is to be noted that electron transfer between the π electron systems of different carbon blacks occurs quite readily. The oxide structures of carbon blacks are seen to play a fundamental role in this viewpoint at the microscopic level akin, for example, to the critical importance of the molecular structures of the adsorbates in chemisorption from the gas phase onto metals(41, 42) and metal oxides(43).

It is worth noting that the model for the carbon black surface deduced from these observations possesses a limited predictive capability for other materials systems than those studied herein. The current viewpoint that polymer interactions may be discussed in terms of Lewis acidity and basicity associated with particular molecular groups comprising the polymer(44-46) coincides with the present description of the origin of carbon black activity. Specifically BPL, which contains localized Lewis acid sites, can be expected to interact readily with polymer sites that are capable of acting as a Lewis base towards the carbon sites. On the other hand Graphon, which lacks these localized Lewis acid sites, is predicted to interact weakly with the same polymer sites. Contact charge injection experiments(33) provide a particularly sensitive probe of the carbon-polymer interaction and may supply the best means to test such model predictions.

Acknowledgments

The author gratefully acknowledges the support of W.R. Wright, the support and guidance of Dr. W.A. Brown, the aid of Dr. P. Buscemi and Messrs. D.E. Schleifer, J.E. Henry, and L.R. Brostrom, and the assistance of M. Garges and J. Salyer. He also recognizes Cabot Corporation for kindly supplying selected samples of their carbon blacks.

Literature Cited

1. Rivin, D., Rubber Chem. Technol., 1971, 44(2), 307.
2. Boehm, H.P., Advan. Catal., 1966, 16, 179.
3. Garten, V.A., and Weiss, D.E., Proc. of the Third Carbon Conf., Pergamon Press, New York, 1957, 295.
4. Barton, S.S. and Harrison, B.H., Carbon, 1975, 13, 283.
5. Barton, S.S., Gillespie, D.J., and Harrison, B.H., Carbon, 1978, 16, 363.
6. Smith, W.R., "Carbon Black" in Encyclopedia of Chem. Technol., 2nd Edition, Interscience, New York, 1964, 4.
7. Tanabe, K., "Solid Acids and Bases", Academic Press, New York, 1970, Chapt. 2, 4.
8. Forni, L., Catal. Rev., 1973, 8(1), 65.
9. Atkinson, D., and Curthoys, G., Chem. Soc. Revs., 1979, 8(4), 475.
10. Johnson, O., J. Phys. Chem., 1955, 59, 827.

11. Tanabe, K., and Watanabe, Y., J. Res. Inst. for Catal., Hokkaido, 1963, 11, 65.
12. Voltz, S.E., Hirschler, A.E., and Smith, A., J. Phys. Chem., 1960, 64, 1594.
13. Peri, J.B., J. Phys. Chem., 1965 69(1), 211, and 69(1), 220.
14. Knozinger, H., and Ratnasamy, P., Catal. Rev.-Sci. Eng., 1978, 17(1), 31.
15. Parry, E.P., J. Catal., 1963, 2, 371.
16. Mapes, J.E., and Eishchens, R.P., J. Phys. Chem., 1954, 58, 1059.
17. Benesi, H., J. Phys. Chem., 1957, 61, 970.
18. Holm, V.C.F., Bailey, G.C., and Clark, A., J. Phys. Chem., 1959, 63, 129.
19. Bertolacini, R.J., Analyt. Chem., 1963, 35, 599.
20. Atkinson, D., and Cuthoys, G., J. Phys. Chem., 1980, 84, 1358.
21. Hirschler, A.E., J. Catal., 1963, 2, 428.
22. Drushel, H.V., and Sommers, A.L., Analyt. Chem., 1966, 38(12), 1723.
23. Beaumont, R., and Barthomeuf, D., J. Catal., 1972, 26, 218.
24. Beaumont, R., and Barthomeuf, D., J. Catal., 1972, 27, 45.
25. Barthomeuf, D., and Beaumont, R., J. Catal., 1973, 30, 288.
26. Supplementary material is available upon request from the author.
27. van der Minne, J.L., and Hermanie, P.H., J., J. Colloid Sci., 1952, 7, 600.
28. van der Minne, J.L., and Hermanie, P.H. J., J. Colloid Sci., 1953, 8, 38.
29. Uzgiris, E.E., Adv. Colloid Interface Sci., 1981, 14, 75.
30. Harper, W.R., "Contact and Frictional Electrification", Claredon Press, Oxford, 1967.
31. Fabish, T.J., and Duke, C.B., J. Appl. Phys., 1977, 48(10), 4256.
32. Fabish, T.J., and Hair, M.L., J. Colloid Interface Sci., 1977, 62(1), 16.
33. Duke, C.B., and Fabish, T.J., J. Appl. Phys., 1978, 49(1), 315.
34. Brasefield, C.J., J. Franklin Institute, 1960, 270(4) 283.
35. Chü, J.Y.C., 1977, Private Communication.
36. Liang, S.H.C., and Gay, I.D., J. Catal., 1980, 66, 294.
37. Roy, P., and Fuerstenau, D.W., J. Colloid Interface Sci., 1968, 26, 102.
38. Wade, W.H., and Hackerman, N., J. Phys. Chem., 1960, 64, 1196.

39. Hair, M.L., and Hertl, W., J. Phys. Chem., 1969, 73, 4269.
40. Zettlemoyer, A.C., and McCafferty, E., Croatica Chemica Acta., 1973, 45, 173.
41. Gustafsson, T., Plummer, E.W. Eastman, D.E., and Freeouf, J.L. Solid State Comm., 1975, 17, 391.
42. Applebaum, J.A., and Hamann, D.R., Phys. Rev. Lett., 1975, 34(13), 806.
43. Rubloff, G.W. Luth, H., and Grobman, W.D., Chem. Phys. Lett., 1976, 39(3), 493.
44. Fowkes, F.W. in "Polymer Science and Technology", Vol. 12A Lee, L-H, edt., Plenum Press, New York, 1980, 43.
45. Fowkes, F.W. in Abstracts of 182nd ACS National Meeting, New York, N.Y., Aug. 23-28, 1981, Division of Colloid and Surface Chem., Paper 090 and Paper 099.
46. Duke, C.B., Salaneck, W.R., Fabish, T.J., Ritsko, J.J., Thomas, H.R., and Paton, A., Phys. Rev. B, 1978, 18(10), 18.

RECEIVED March 28, 1982

Fourier Transform IR Spectroscopic Characterization of the Functional Groups on Carbon Black

W. M. PREST, JR. and R. A. MOSHER

Xerox Corporation, Webster, NY 14580

The chemical and physical properties of carbon black are strongly influenced by the presence of surface oxides which are formed during the manufacturing process. This paper demonstrates that the nature and relative concentrations of these species can be determined using the high signal to noise and energy throughput capabilities of Fourier transform infrared spectroscopy. Spectra associated with the functional groups have been derived from transmission measurements of dilute dispersions of carbon black in KBr using computer assisted techniques. The resultant spectra consist of characteristic bands at 1725, 1595 and 1245 cm^{-1} whose intensities are strong functions of the manufacturing conditions. The concentration and thickness dependence of the absorbance follows Beer's Law indicating that this method can be used to quantitatively characterize the concentrations of each species. The technique is used to compare the characteristics of commercially available carbon blacks and to determine the changes that occur as the result of selective heating and titration experiments.

Reprographic technologies rely on the high optical density of carbon black to pigment the wet and dry inks called toners. The carbon, present in the form of finely divided particles, is manufactured by a variety of methods from the partial combustion of fossil fuels [1]. Each process produces characteristic changes in the properties of the black as the result of the chemistry which occurs during the oxidative step and the impurities introduced through the feed stock or condensation procedure. The resultant carbon blacks are often further chemically modified to improve such properties as their ability to be dispersed in a given resin and/or the subsequent rheology of the composite. In addition to influencing the optical and rheological properties of a toner, the surface chemistry of the

0097-6156/82/0200-0225\$07.00/0
© 1982 American Chemical Society

carbon black has an important effect on the electrical properties. Fabish and Hair [2] have shown that chemical modifications which change the apparent acidity and oxygen content of a black produce corresponding changes in the contact potential (work function). Recently, Julien [3] has illustrated how the triboelectric charging characteristics of a toner are related to the contact potential. These examples of the importance of the surface characteristics of carbon black have motivated a variety of attempts to characterize the functional groups on the surface. However, while there is abundant evidence for the presence of different types of functional groups from such measurements as the chemical reactivity, the acidity and the volatile components of the black [1], there is insufficient data to unambiguously identify the species responsible for the desired properties. This paper extends previous investigations of the infrared spectra of carbonaceous compounds [4-18] to the characterization of the functional species which are present on commercial carbon blacks. It is shown that the high signal to noise and energy throughput capabilities of Fourier transform infrared spectroscopy (FTIR) enable the quantitative measurement of the spectra of the surface species. This technique is applied to the characterization of the distinguishing features of commercial carbon blacks and to the analysis of the products of selective heating and neutralization experiments.

BACKGROUND

Numerous analytical procedures have been developed to characterize the chemical species that are present on the surfaces of carbonaceous materials [1]. One simple measure is the volatile content, which is defined as the weight lost as the result of heating to 900°C in an inert atmosphere. Carbon blacks used in reprography typically have volatile contents ranging from five to sixteen percent. These thermally evolved gases consist primarily of carbon monoxide and carbon dioxide in such proportions that oxygen constitutes approximately 60% of the volatile products [19-20]. The nature of the oxygen containing groups have been explored by different chemical analysis methods. Selective neutralization experiments using bases of increasing strength have been used to argue for the presence of carboxylic acids, lactones, phenols, and quinones. The most extensively used technique, developed by Boehm [21] and Schubert et al. [22], determines the carboxyl, lactone, phenol and quinone concentrations from the respective back titrations with NaHCO_3 , Na_2CO_3 , NaOH and NaOC_2H_5 . However, as pointed out by Mattson [9] and Rivin [20], this technique sets arbitrary limits on the acidity ranges for each group, which in fact may be substantially perturbed by the strong electronic interactions between groups through the conducting substrate. Thus, for example, there is the question of whether the NaHCO_3 neutralization measures all or only the most acidic of the carboxylic acids.

Infrared spectroscopy has been used to probe the surface functionality of a variety of carbonaceous materials since the early 1940s [4-18]. These attempts to define and characterize the surface groups have been restricted by the relatively low concentrations of the functional species. More significantly, the characteristic absorptions are often masked by the high optical absorption edge of the carbon substrate. This requires that the instrument be able to resolve small signals superimposed on a large background absorbance.

The assignment of the observed bands is particularly complicated because the functional groups are present in such a wide variety of electronic and chemical environments that the absorption bands are much broader than those of the isolated compounds. Furthermore, these carbon surfaces are so reactive and absorbent that extreme care must be exercised to avoid the artifacts that result from contamination. In spite of these difficulties, several infrared studies have succeeded in measuring the spectral characteristics of different carbonaceous compounds and have associated the features with the vibrational modes of an often conflicting variety of functional groups. A schematic representation of the oxygen related functionalities and band assignments which have been proposed for a variety of carbon based compounds is presented in Figure 1. In addition to the carboxylic acids (1725 cm^{-1}), quinones (1675 cm^{-1}), phenols ($1200, 3600\text{ cm}^{-1}$) and lactones ($1775, 1250\text{ cm}^{-1}$) mentioned above these species include aldehydes (1700 cm^{-1}), aryl ethers (1260 cm^{-1}), cyclic anhydrides ($1775, 1740$ & 1260 cm^{-1}) and the skeletal modes of carbon (1600 cm^{-1}) [17]. Attempts to resolve these ambiguities by measuring the spectra of chemically or thermally modified carbons have often been indecisive because of the extremely small resolvable signals and the associated experimental difficulties in defining absolute changes in band intensity. Earlier work by O'Reilly and Mosher [18] demonstrated that FTIR spectroscopy could be used to quantitatively measure the vibrational spectra of carbon black. They showed that at low carbon black concentrations Beer's Law was followed and that, in principle, the concentration of functional groups could be obtained. This paper describes the extension of this FTIR technique to the quantitative measurement of the vibrational spectra of different types of carbon black and its application to the analysis of the characteristic features of these blacks.

EXPERIMENTAL MATERIALS AND TECHNIQUES

The carbon blacks used in this study were obtained from the Cabot Corporation, Billerica, Massachusetts through the courtesy of Dr. John Riehl. They were chosen to be representative of a variety of surface characteristics ranging from the graphitized Sterling MT and the devolatilized Regal 330R to the highly oxidized Carbolac 2. Also included is a sample of HTT 5.3, a black prepared by Cabot Corporation from the selective oxidation of CSX 99. The nitrogen surface areas and

volatile contents of these blacks and the concentrations of functional groups defined by the Bohem scheme (from back titrations) are listed in Table I.

Each black was initially dried at 105°C for one hour to remove moisture and adsorbed components. Care was taken to insure that the oven was clean and free of contaminants such as silicone grease, oils and other samples. All subsequent sample manipulations were conducted in a nitrogen purged dry box. A master dispersion, consisting of 10 mg of black and 1 gram of potassium bromide (KBr, Spectra grade, Harshaw Chemical Company), was placed in a cleaned and dried 2cc stainless steel canister containing a 0.64 cm steel shot and milled for 5 minutes on a Crescent Dental Mfg. Co. Wig-L-Bug. The master dispersion was further diluted with KBr to produce a sample with a nominal composition of 0.47 mg of carbon black per gram of KBr and milled for another 5 minutes. A Perkin-Elmer KBr vacuum die was used to produce sample disks ~ 12mm in diameter and 1 mm thick. Spectra were obtained with a Digilab Model FTS 15B Fourier transform infrared spectrometer equipped with a HgCdTe detector. Typically, 512 scans were run in both the reference and sample beams at a resolution of 4 wavenumbers. Critical band positions were subsequently defined from spectra obtained at a resolution of one wavenumber. Spectra of freshly prepared KBr reference disks were interspersed throughout the measurement cycles. In spite of the above drying precautions, moisture related bands at 3390 and 1640 cm^{-1} were always present in the milled KBr dispersions and, as has been previously noted [11], are enhanced by the grinding process. The spectra of these "false" KBr-H₂O species was obtained by subtracting the spectra of reference disks which had been milled for different periods of time. The spectra of "computer dried" carbon black was obtained by subtracting a multiple of this moisture spectra using the elimination of the 3390 cm^{-1} band as the criteria for complete removal. Following this correction, the spectra of a KBr disk of the same thickness as the sample was subtracted from the experimental data. Complementary experiments in which the carbon blacks were milled in Cesium Iodide, dusted or solvent deposited on silver chloride plates, or milled in Nugol demonstrated that the measured spectral features are characteristic of the particular type of carbon black and are not the result of chemical reactions with the KBr matrix. As demonstrated below, these techniques permit absorbances to be defined to better than ± 0.005 .

RESULTS and DISCUSSION

Carbon Black Spectra

Typical absorbance spectra of Monarch 1300 carbon black are presented in Figure 2. The spectra consist of small signals in the vicinity of 900-1800 cm^{-1} and 3200-3600 cm^{-1} superimposed upon a broad background which is almost a linear function of the wavelength. This intense dispersion has been attributed to the intrinsic absorption edge of the particular carbon

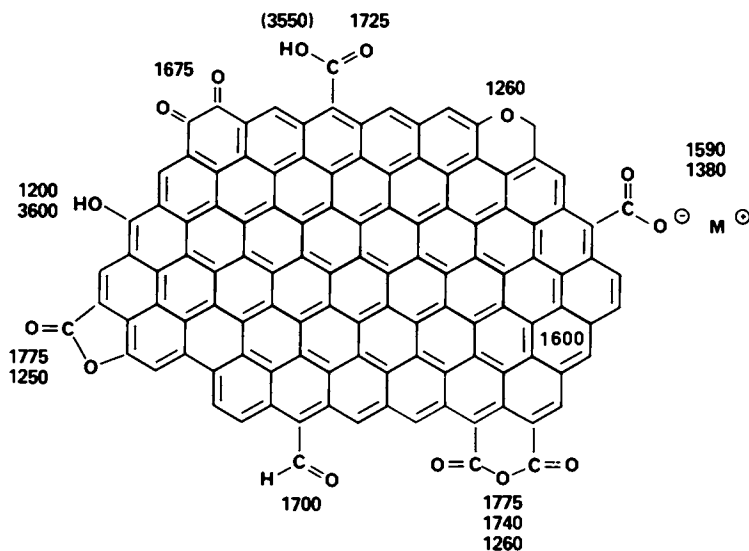


Figure 1. Schematic of oxygen containing species which have been proposed to exist on carbon surfaces and the associated IR band assignments.

TABLE I

Carbon Black	N ₂ area m ² /g	Volatiles wt %	O ₂ [#]	Functional groups in $\mu\text{eq/g}^*$		
				Carboxyl ¹	Lactone ²	Phenol ³
Carbolac [®] 2	935	15.6	12.9	569	333	408
Monarch [®] 1300	530	10.8	13.9	504	259	288
HTT 5.3	618	5.8	5.3	265	219	303
CSX-99	520	2.5		94	0	312
Regal [®] 330R	91	1.1	2.4	60		
Sterling [®] MT	70	0.6	0.0	30		

* Determined from the Boehm Scheme

1- Carboxyl = NaHCO₃ - ionized acids

2- Lactone = Na₂CO₃ - NaHCO₃

3- Phenol = NaOH - Na₂CO₃

Oxygen content by difference from elemental analysis of H & C (includes some sulfur and ash)

® Carbolac, Monarch, Sterling and Regal are Registered Trademarks of Cabot Corporation, Inc.

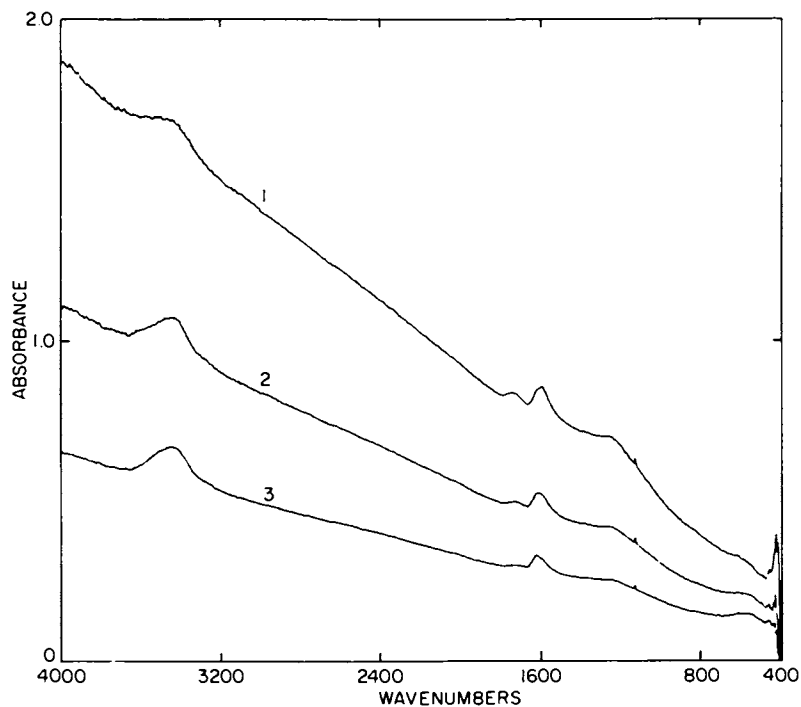


Figure 2. The absorbance of Monarch 1300 dispersed in KBr as a function of concentration. Key: 1, 7.05×10^{-4} g CB/g KBr; 2, 4.70×10^{-4} g CB/g KBr; and 3, 2.35×10^{-4} g CB/g KBr.

and/or to interparticle scattering. However, scattering can be expected to be minimal for several reasons. First, the size of the scattering elements, which are composed of ~ 50 nm elemental carbon black particles fused into ~ 500 nm aggregates, are significantly smaller than the infrared wavelengths of interest (ie. 2.5-20 μm). Secondly, the inhomogeneous Rayleigh scattering from such small particles would be proportional to the fourth power of the frequency instead of the observed linear dependence [23]. Finally, there is no evidence for multiple scattering events since the absorbance of this dispersion, as characterized by its magnitude at 2800 cm^{-1} , is a linear function of both the concentration of the black and the thickness of the pellet as shown in Figure 3. In other words, the magnitude of this apparent background follows Beer's law and, as shown below, directly scales with the absorbances of the functional groups on a particular black. These results indicate that this background dispersion is the intrinsic absorbance of the particular carbon black analogous to the band edge of conducting materials [14,15,18]. As will be shown below, the presence of surface species has a profound effect on the shape of this absorption edge.

The data manipulation capabilities of the FTIR spectrometer can be used to quantitatively resolve the structural features which are superimposed upon the intrinsic absorption. The spectral features which exceed a baseline drawn between 1880 and 880 cm^{-1} in five independent preparation and measurement experiments are shown in Figure 4. The superposition of these five spectra illustrate both the reproducibility and the quantitative nature of this technique. The "resolved" spectra consist of three broad absorptions centered around 1725 , 1595 and 1245 cm^{-1} and two superimposed sharp bands at 1135 and 1340 cm^{-1} . These latter peaks are characteristic of the particular type of carbon black and are presumably caused by impurities introduced in the manufacturing process. They may reflect the presence of residual sulfur compounds present in the form of sulfones or sulfonic esters in which the symmetric and antisymmetric stretching modes of the SO_2 vibrational modes occur in the range of 1140 - 1160 cm^{-1} and 1300 - 1350 cm^{-1} [24]. Note the absence of discernable bands above $\sim 1730\text{ cm}^{-1}$. This implies that these carbon blacks do not contain the lactone and cyclic anhydride functionalities observed on other carbon surfaces (see Figure 1) [17].

The dominant bands in the resolved spectra obey Beer's law in that the magnitude of the absorbance (defined in terms of the peak heights relative to a linear baseline drawn between 880 and 1880 cm^{-1}) is linear in both concentration and thickness (Figures 5 A&B). Furthermore, when these spectra are divided by the magnitude of the intrinsic absorption at 2800 cm^{-1} , the resultant absorbances are independent of sample thickness and concentration as shown in Figure 6. This supports the previous conclusion that both the broad background absorption and the superimposed spectra are directly related to the chemical structure of the black. The data also demonstrate that the spectral features of carbon black can be routinely measured to within ± 0.005 absorbance units. This capability for the quantitative measurement of the effects of various modification procedures

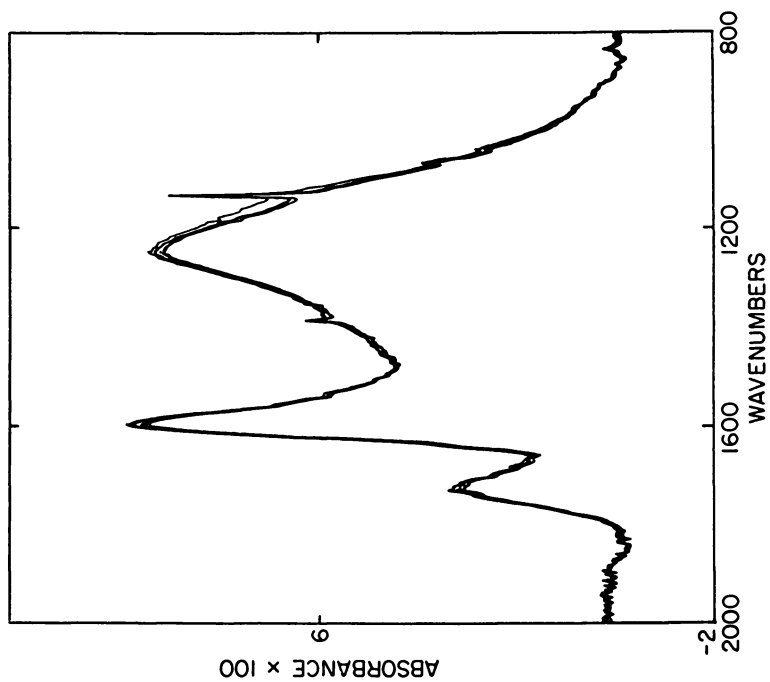


Figure 4. Resolved spectra of five separate preparations of Monarch 1300 obtained by subtracting the linear extrapolation of the background absorbance between 1880 and 880 cm^{-1} .

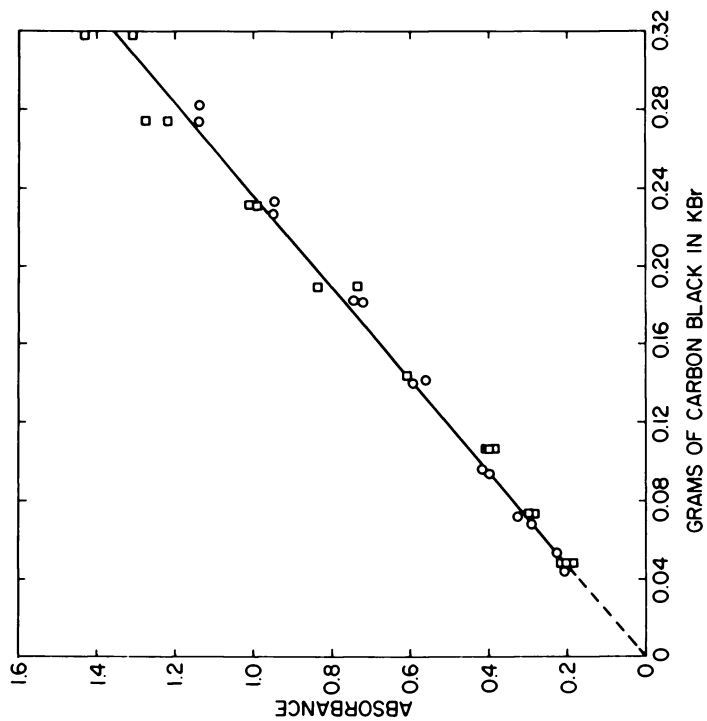


Figure 3. Absorbance at 2800 cm^{-1} of Monarch 1300 dispersed in KBr as a function of concentration (□) and thickness (○).

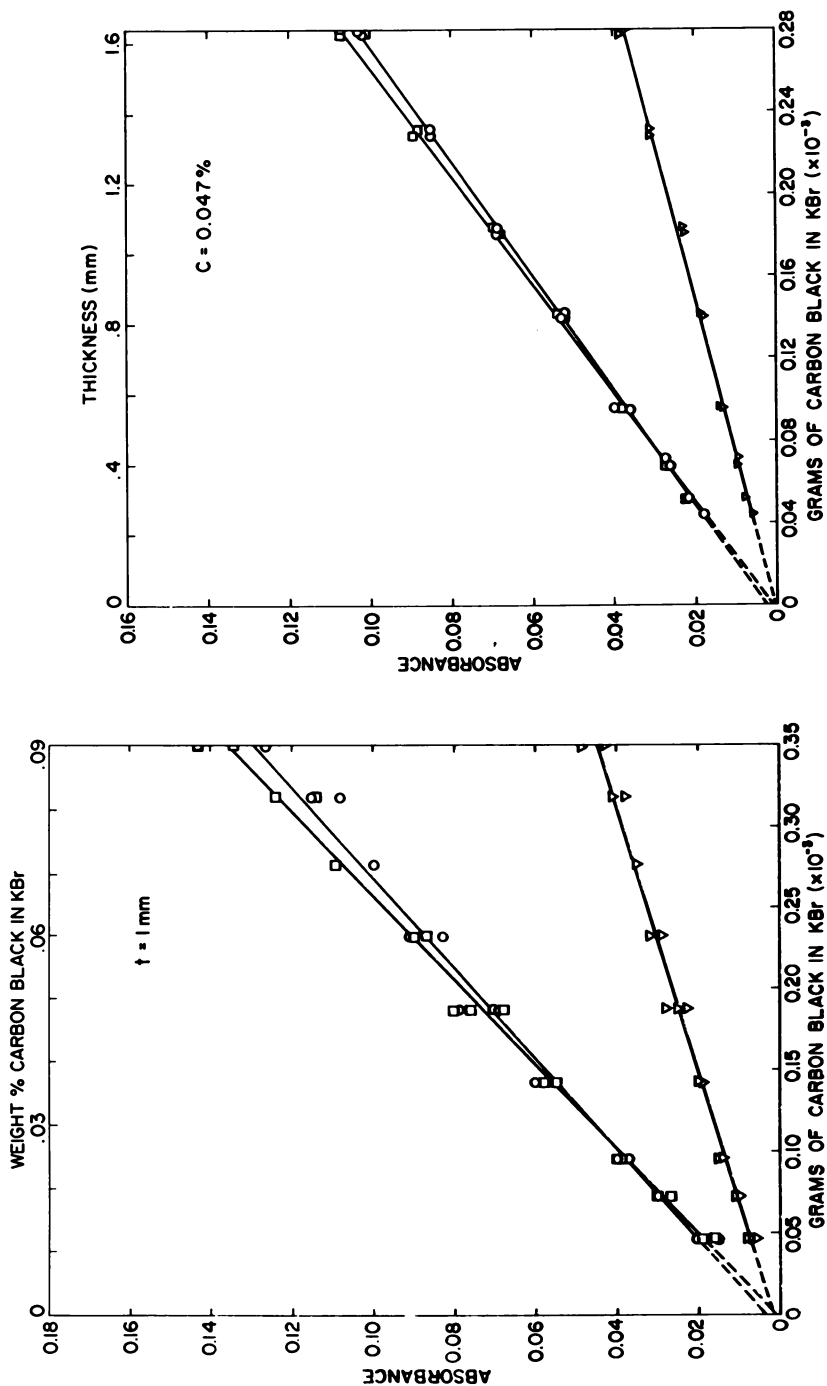


Figure 5. Absorbance at 1245 (□), 1595 (○), and 1725 cm⁻¹ (∇) of resolved spectra of Monarch 1300 as a function of concentration (left) and thickness (right).

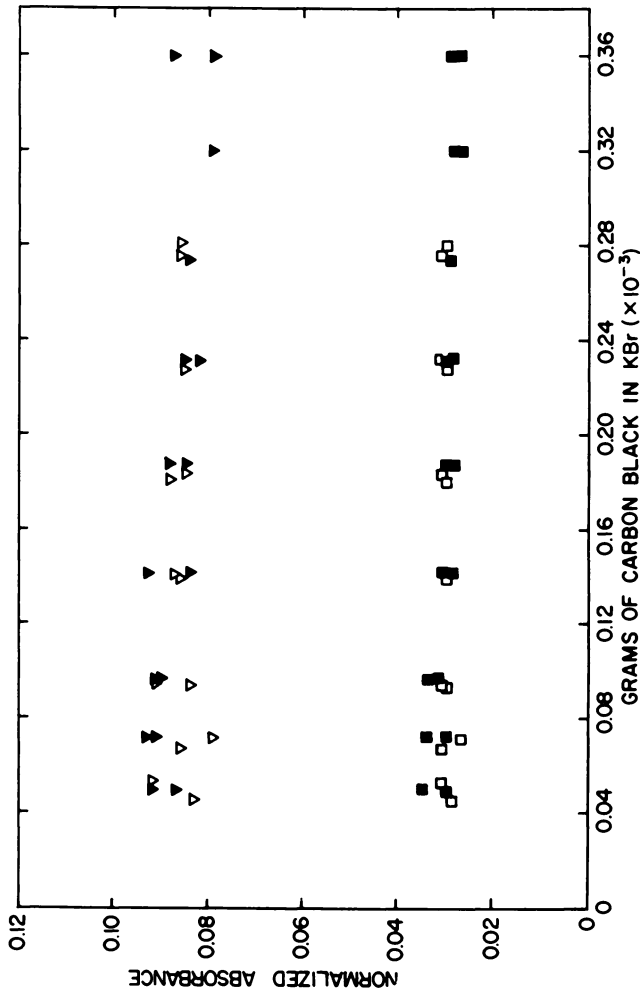


Figure 6. Absorbance of the resolved spectra at 1725 and 1595 cm^{-1} normalized by the absorbance at 2800 cm^{-1} as a function of the total amount of Monarch 1300 carbon black dispersed in KBr discs of varying concentration and thickness. Key: \square , thickness (1725 cm^{-1}); \blacksquare , concentration (1725 cm^{-1}); ∇ , thickness (1595 cm^{-1}); and \blacktriangledown , concentration (1595 cm^{-1}).

on the absolute magnitudes of the absorbances of different bands permits tests of proposed band assignments.

Heat Treated Blacks

Information about the origin of the spectral features can be obtained from selective heating studies [5,11,13,15,17]. Figure 7 shows the weight change and rate of weight loss [dW/dt] of dried Monarch 1300 as it is heated at 40K/min. in argon (thermogravimetric analysis - TGA). Note that by 900°C the sample has lost 10.8% of its weight. This corresponds to the "volatile content" of this material (Table I), a number which is often used to define the total oxygen content of the black. However, since there is a continuing loss of weight at and above this temperature, the data indicate that the black contains substantially more volatile components than are assessed in the traditional analysis.

Figure 7 indicates that there are at least two mechanisms of desorption: a relatively rapid process which appears to be completed by 400°C superimposed upon an approximately constant loss process. Analysis of the gases evolved during the heating of similar carbon blacks have shown that carbon dioxide is the primary product of this initial process [19,20]. This has been associated with the removal of labile carboxylic acid functionalities [11]. The infrared spectra of selectively heated Monarch® 1300 carbon blacks are shown in Figure 8. Each sample was held at the indicated temperature for one hour. Care was taken to maintain the sample in an inert atmosphere throughout the heating, milling and measurement steps. The 1725 cm⁻¹ band disappears by 400°C in parallel with the TGA loss mechanism which has been associated with the production of CO₂. This further supports the assignment of this band to carboxylic acid. A surprising feature of the spectra shown in Figure 8 is that the loss of the 1725 cm⁻¹ carboxylic acid absorption reveals the presence of a sharp band at 1700 cm⁻¹. While this band may be attributed to the presence of aldehydes, its thermal stability and narrow band width in this carbon black are surprising.

Of particular interest is the persistence of the 1595 and 1245 cm⁻¹ bands in carbon blacks which have been heated to 1700°C. The presence of these bands in these thermally "devolatilized" blacks suggests that they are characteristic of the basic carbon substrate rather than a surface group. The ~1600 cm⁻¹ band, which has been observed in a variety of carbonaceous compounds, has been associated with the aromatic skeletal modes of carbon. Furthermore, it has been proposed that the relative intensity of this band is enhanced by the presence of surface species [4,17]. In the context of the theory of the optical properties of dielectric media containing small dispersed conducting islands, these groups can be expected to change in dielectric constant of the surface of the conducting carbon particles thus modifying the boundary conditions between the black and the matrix [25]. This would have the effect of shifting the absorption band edge to higher frequencies as has been observed in dispersions of oxidized metal particles.

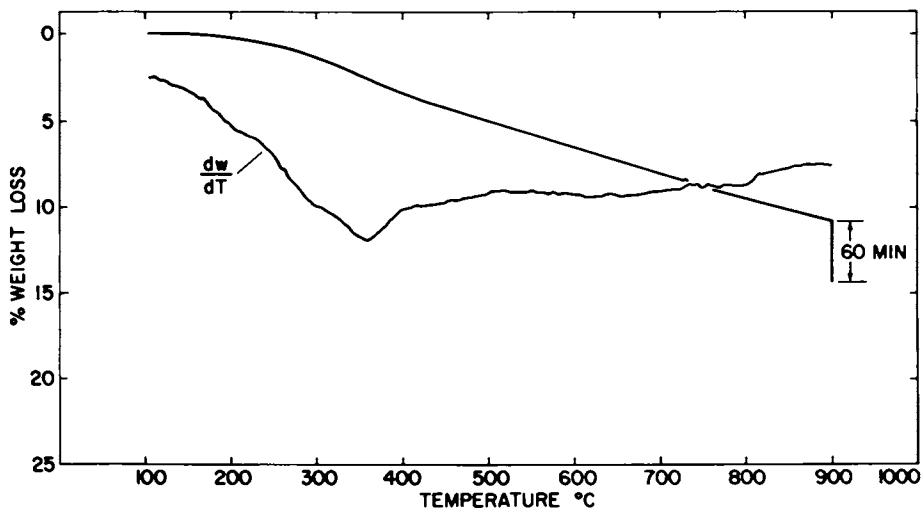


Figure 7. Thermogravimetric analysis of Monarch 1300. Percent weight loss and rate of loss (dW/dT) as a function of temperature when heated in argon at 40 K/min.

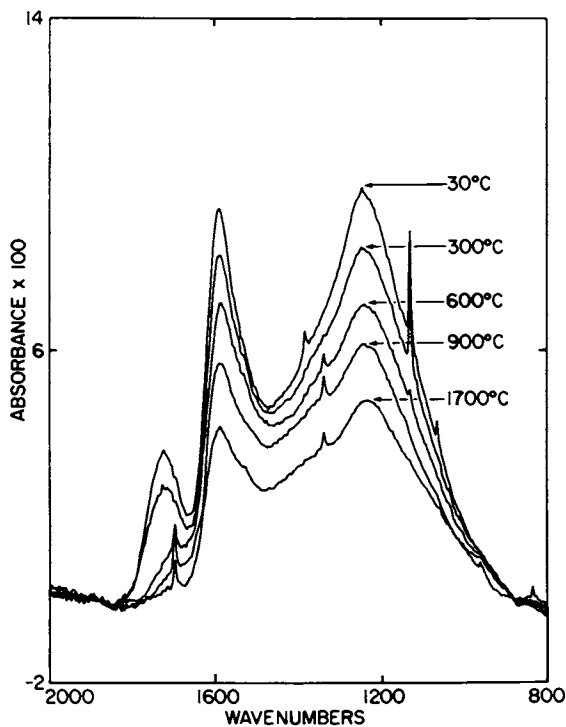


Figure 8. Resolved spectra of Monarch 1300 carbon blacks which were held at the indicated temperature for one hour in a dry nitrogen atmosphere and milled in KBr in an inert atmosphere (N_2).

This mechanism provides an explanation for the apparent decrease in the magnitude of the 1595 cm^{-1} absorption which occurs as the volatile species are removed at elevated temperatures (Figure 8). It should be noted that other vibrational processes can contribute to the intensity of 1595 cm^{-1} region in addition to the ring modes of the carbon, as illustrated by the selective neutralization experiments described below.

In contrast to the 1595 cm^{-1} band, the assignment of the extremely broad ($>130\text{ cm}^{-1}$ half width at half height) [18] absorption centered at 1245 cm^{-1} is uncertain. The thermal stability of this absorption implies that it reflects a characteristic feature of the bulk rather than the surface. The intensity of this band is completely synchronized with that of the 1595 cm^{-1} ring mode throughout the heating studies (Figure 8). Furthermore, while the relative magnitudes of the 1595 and 1245 cm^{-1} bands differ from black to black, the ratio of these bands in a given black is independent of subsequent thermal treatments. The 1245 cm^{-1} band thus appears to be related to the bulk absorption of the carbon black substrate because the presence of surface species equally enhances the absorptions at 1245 and 1595 cm^{-1} . These results are consistent with proposals for aryl ethers [17], although the extreme breadth of this band suggests the possibility of other underlying absorption processes.

The heat-treated materials are very reactive and are readily reoxidized in the presence of air. For example, the carboxylic acid band at 1725 cm^{-1} reappears when the sample heated to 600°C is milled in air instead of nitrogen (Figure 9). As expected from the above discussions, the presence of these new surface species also enhances the absorptions at 1595 and 1245 cm^{-1} . Interestingly, the air and nitrogen milling conditions have different effects on the magnitudes of the 1135 and 1340 cm^{-1} impurity bands of this carbon black.

In summary, in the context of the previous infrared work, the results of the selective heating experiments show that the spectra of carbon blacks are composed of bands associated with: carboxylic acid, the skeletal modes of aromatic carbon and, perhaps, thermally stable aldehydes and aryl ethers.

Selective Neutralization

Selective neutralization experiments provide another method for evaluating the relationship between the absorption spectra and the identity of the surface species [6,16]. Samples of Monarch 1300 carbon black which had been back titrated with different strength bases as per the Boehm scheme (see Table I) were filtered, washed with neutral water and then reacidified with dilute HCl. Spectra were obtained on samples dried after each of these steps. In these samples, the reacidification process completely reversed the changes in the spectra which had been produced by the selective neutralizations. Figure 10 compares the result of the NaHCO_3 titration with that of the reacidified black. This weak base, which is used to measure the carboxylic acid content of the black, reduces the 1725 cm^{-1} band and increases the intensity of the 1595 cm^{-1} band. Furthermore, there

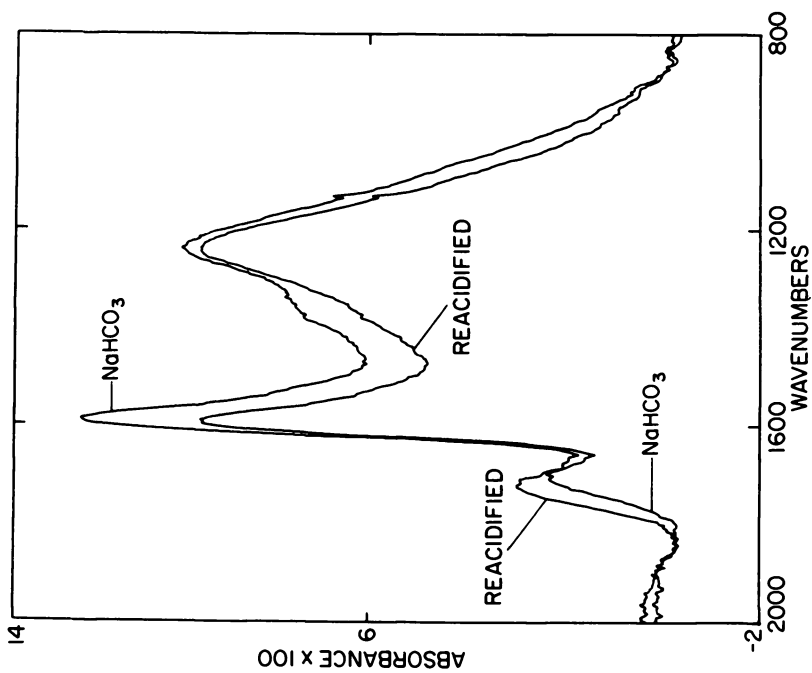


Figure 10. Resolved spectra of Monarch 1300 carbon black neutralized with NaHCO_3 and reacidified.

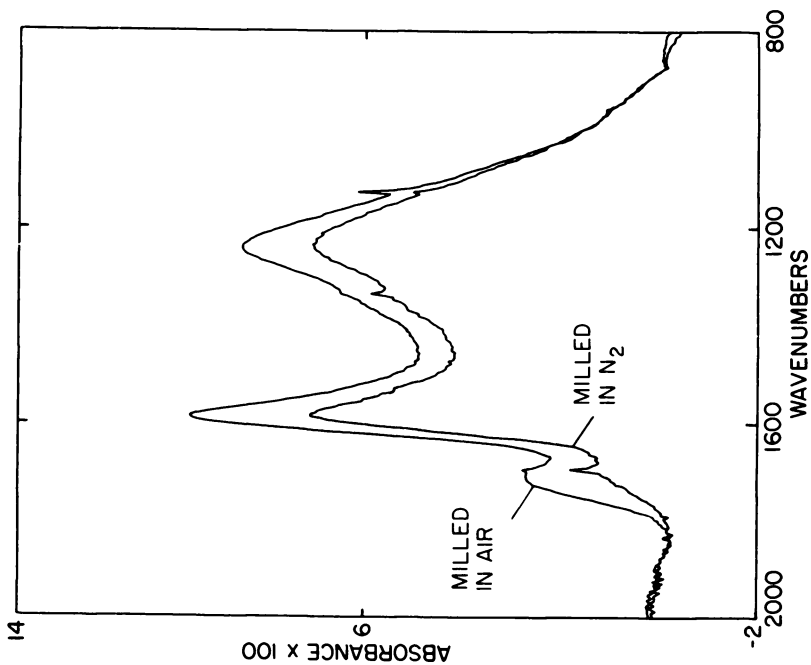


Figure 9. Resolved spectra of Monarch 1300 carbon black which has been heated in nitrogen at 600°C for one hour and milled in KBr in a nitrogen or air atmosphere.

is a corresponding appearance of a broad band between 1340 and 1380 cm^{-1} . These results are consistent with the formation of sodium salts of the carboxyl groups to produce the asymmetric (1590 cm^{-1}) and symmetric (1380 cm^{-1}) stretch of the carboxylate anion [6, 16]. Note that the 1725 cm^{-1} carboxyl group is not completely neutralized by this weak base. This reinforces the proposals that the titration schemes do not quantitatively determine the concentrations of each species because the acidity of each group is strongly modified by the local chemical and physical environments of the conducting substrate [20].

Figure 11 compares the spectra of the Na_2CO_3 titrated and the subsequently reacidified Monarch 1300 carbon black. This stronger base continues the neutralization of the 1725 cm^{-1} carboxyl band and, in so doing, reveals the presence of the sharp band at 1700 cm^{-1} seen in the heating experiments. In addition to the increase in the 1595 and 1380 cm^{-1} bands associated with the formation of the carboxylate ion, a small dispersion at 1675 cm^{-1} appears. It is significant to note that these titrations do not change the intensity of the broad absorption centered around 1245 cm^{-1} and that the changes of carboxylic acid (1725 cm^{-1}) to the carboxylate ion (1590 & 1380 cm^{-1}) are reversible. In the Boehm scheme the Na_2CO_3 titration provides a measure of the lactone functionality. However, the absence of discernable bands above $\sim 1740 \text{ cm}^{-1}$ in any of the blacks is not consistent with the presence of the lactone (or cyclic anhydride) functionalities observed on other carbonaceous materials. Instead, the Na_2CO_3 titration appears to be measuring the less acidic carboxylic acid groups and forming (or perhaps enhancing the presence of) a band at 1675 cm^{-1} . The appearance of this new band is particularly interesting in light of the model proposed by Garten, Weiss and Willis [6]. They suggested that the acidity of a black might be derived from lactones (1760 cm^{-1}) which, when in conjunction with a phenol, could be hydrolyzed to form quinones (expected but not observed at 1680 cm^{-1}) and aldehydes or ketones ($\sim 1720 \text{ cm}^{-1}$). However, the 1675 cm^{-1} bands shown in Figures 11 & 12 cannot be used to support the reaction schemes that yield the quinone functionality because these bands are removed by washing with neutral water or dilute HCl. An alternative suggestion is that the band at 1675 cm^{-1} is caused by the sulfur impurities in the carbon black such as the C=S frequency of the thioketones (1670 cm^{-1}) or the carbonyl stretch of thioesters (1680 cm^{-1}) [24].

The spectra of the titrated Monarch 1300 carbon blacks are compared as a function of the strength of the base in Figure 12. This shows that the NaOH titration enhances the effects described above with a further development of the structure of the 1300-1400 cm^{-1} region and the further increase in the 1675 cm^{-1} absorption. No other changes in the spectra are observed. In the Boehm scheme [21], the NaOH titration measures the phenolic content of the black. The phenolic functionality would be expected to give rise to bands at $\sim 1160 - 1200 \text{ cm}^{-1}$ (the OH bending mode)

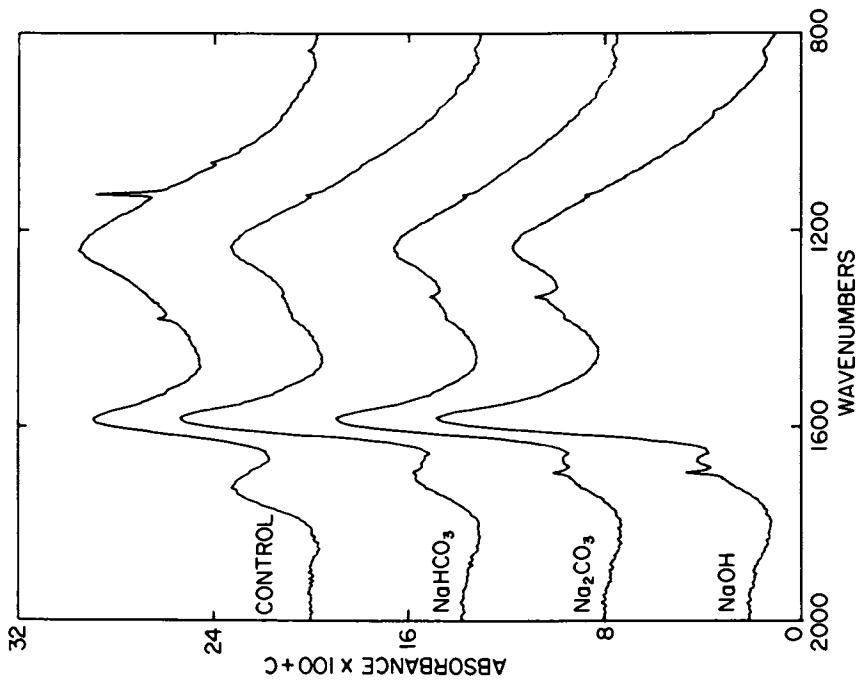


Figure 12. Resolved spectra of Monarch 1300 carbon black neutralized with different strength bases.

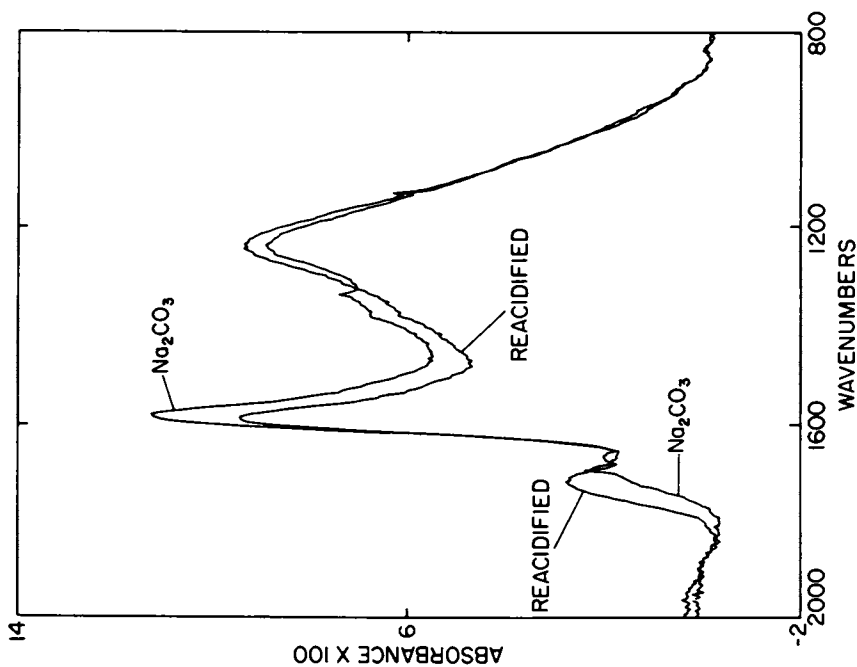


Figure 11. Resolved spectra of Monarch 1300 carbon black neutralized with Na_2CO_3 and reacidified.

and at 3600 cm^{-1} (the OH stretch). Not only is the expected phenolic OH deformation mode ($1160 - 1200\text{ cm}^{-1}$) not observed in the original black but there are no discernable changes in this region of the spectra as the result of the titration. The phenolic OH stretch should be observable at $\sim 3600\text{ cm}^{-1}$ as part of the broad band from $\sim 3200 - 3600\text{ cm}^{-1}$ (Figure 2). This region also contains the hydroxyl stretching contributions from absorbed water and the false KBr- H_2O bands mentioned above [11]. However, as shown in Figure 13, the subtraction of the water based spectra derived from the bands that develop in milled KBr is sufficient to account for all the intensity observed above 3000 cm^{-1} . It therefore appears unlikely that a significant number of hydroxyl groups are the result of the phenolic functionality.

In summary, the titration experiments show that the 1235 cm^{-1} band is unaffected by any of the neutralization processes while progressively stronger bases increase the intensity of the 1595 cm^{-1} region by converting the carboxylic acid functionality (1725 cm^{-1}) to the carboxylate ion (1590 & 1380 cm^{-1}). In addition, these (and other related) experiments indicate the presence of a very stable compound in these carbon blacks which is characterized by an absorption at 1700 cm^{-1} (aldehyde?). There is no evidence from the vibrational spectra for the phenolic and lactone functionalities seen on other carbonaceous compounds.

Spectra of Different Blacks

The characteristics discussed above are not unique to Monarch 1300 but are in fact typical of a number of commercial carbon blacks. This is illustrated in Figure 14 by the spectra of carbon blacks which have the different surface characteristics listed in Table I. Each of these samples was prepared by dispersing the same (0.047 weight %) concentration of carbon black in KBr. The presence of the surface species, as indicated by the magnitude of the features in the vicinity of 1600 cm^{-1} , is seen to have a pronounced effect on the intrinsic carbon absorption (band edge). The greater the number of surface species, the lower the background absorption. This is equivalent to the effects noted in the heating experiments, in which the loss of the surface groups had the effect of shifting this absorption edge to longer wavelengths, presumably because of the change in the boundary conditions between the particles and the KBr dispersion medium [25].

The resolved spectra of these carbon blacks are shown in Figure 15. The bands at 1725 , 1595 and 1245 cm^{-1} observed in Monarch 1300 are also present in the different carbon blacks, but in varying proportions. Note that the bands at 1595 and 1245 cm^{-1} are even present in the completely unoxidized Sterling MT black. This reinforces the proposal that these bands are associated with the bulk carbon black structure and are only enhanced by the presence of surface species. As mentioned above, the sharp bands at 1135 and 1340 cm^{-1} appear in some of the carbon blacks but not in others as might be expected from sulfur impurities introduced from different feed stocks.

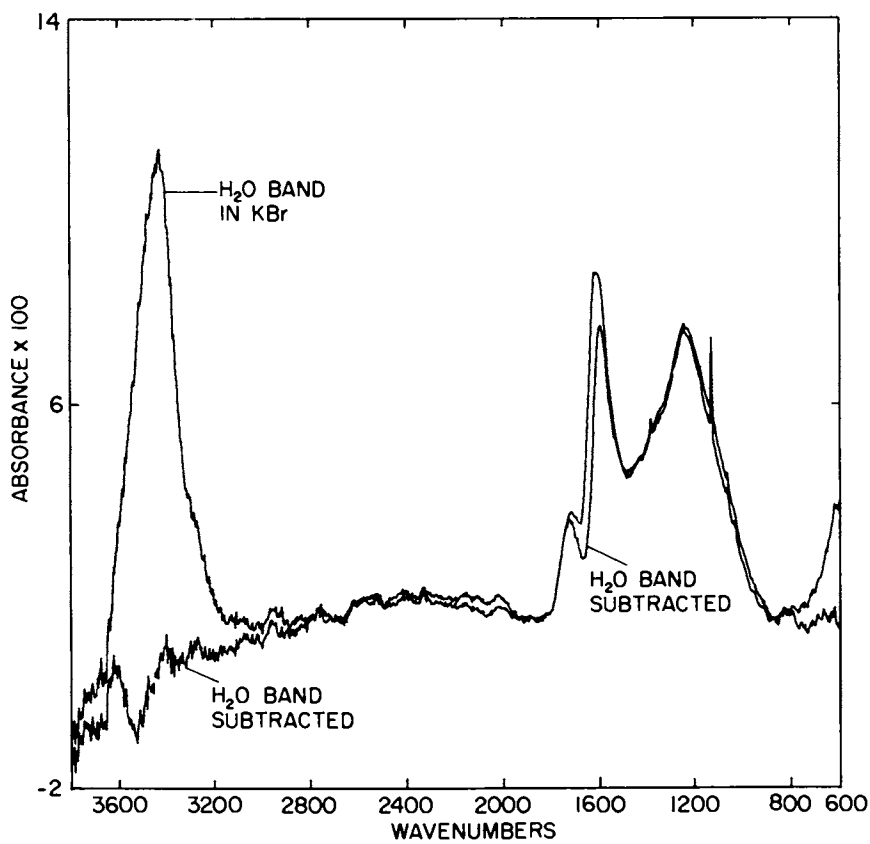


Figure 13. Resolved spectra of the initial and computer dried Monarch 1300 carbon black.

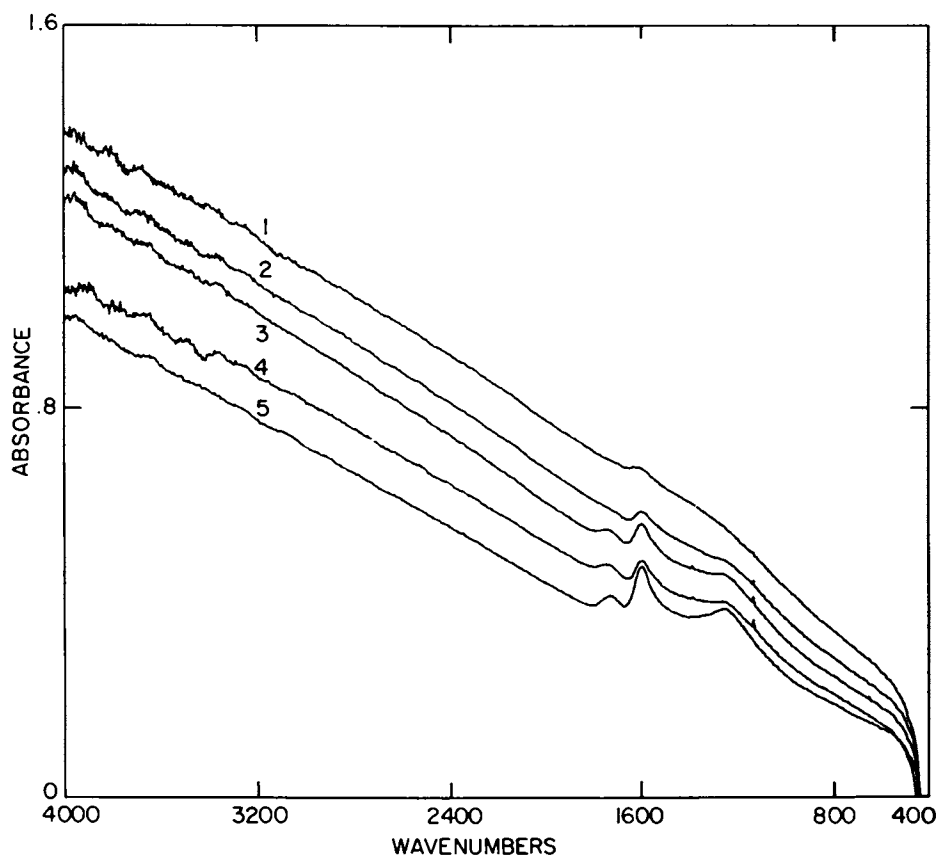


Figure 14. Absorbance spectra of 0.047 wt % KBr dispersions of carbon blacks with different oxygen contents. Key: 1, Regal 330 R; 2, CSX 99; 3, BP 1300; 4, Monarch 1300; and 5, Carbolac 2.

Interesting speculations can be derived from comparisons between these spectra and the analytical data presented in Table I. Note that magnitude of the 1725 cm^{-1} band increases with the volatile content of the black but is not strictly a linear function of the total oxygen content nor the weak base (ie. NaHCO_3) measure of the carboxyl concentration. For example, while the magnitude of the 1725 cm^{-1} band in Carbolac 2 is ~40% greater than the corresponding band in Monarch 1300, the NaHCO_3 defined carboxyl concentrations differ by only ~10%. Similarly, the magnitude of this same band in HTT 5.3 is within 70% of the Monarch 1300 standard, while the oxygen and carboxyl concentrations differ by fifty percent. These results reinforce the hypothesis that the carboxyl groups reside in a variety of environments which change their effective acidity [9, 20]. Thus, in the special case of conducting carbon substrates, the neutralization experiments measure the distribution of acidities of the surface groups rather than the quantitative populations of the different chemical species. In other words, the results of the Na_2CO_3 and possibly even the NaOH neutralization may be reflecting the presence of weakly acidic carboxyl groups in place of or in addition to the proposed lactone, phenolic and quinone functionalities.

The data in Figure 15 and Table I also imply that the magnitudes of the bulk carbon bands below 1700 cm^{-1} are enhanced as the result of the presence of the oxygen in the less acidic environments and/or functionalities. The correlation between the size of the bands in Carbolac 2 and the nominal lactone and phenolic concentrations is apparent. Note also that the spectra of the HTT 5.3, is essentially identical to that of Monarch - 1300 below 1700 cm^{-1} , even though its oxygen and carboxyl content are substantially smaller. Similarly, it can be argued that the magnitude of the vibrational bands in CSX 99 is derived from the concentration of the weakly acidic groups measured by the NaOH titration. Again, the least acidic groups, be they of the same or different chemical species, have the effect of enhancing the bulk carbon based absorptions (ie. 1245 & 1595 cm^{-1}) more than the stronger acids.

CONCLUSIONS

This paper has demonstrated that quantitative measurements of the vibrational spectra of carbon blacks can be made using the high signal to noise and data processing capabilities of Fourier transform infrared spectroscopy. This capability was used to analyze the results of selective heating and titration experiments in the context of the previous band assignments for the spectra of carbonaceous materials and to compare the properties of a variety of commercial carbon blacks. The results indicate that the spectra of carbon black is dominated by the structural modes the bulk carbon enhanced by the presence of carboxyl groups which are present in a variety of acidic environments. No evidence has been observed for the phenolic, lactone or cyclic anhydride functionalities observed on other carbon based materials or implied by selective neutralization experiments.

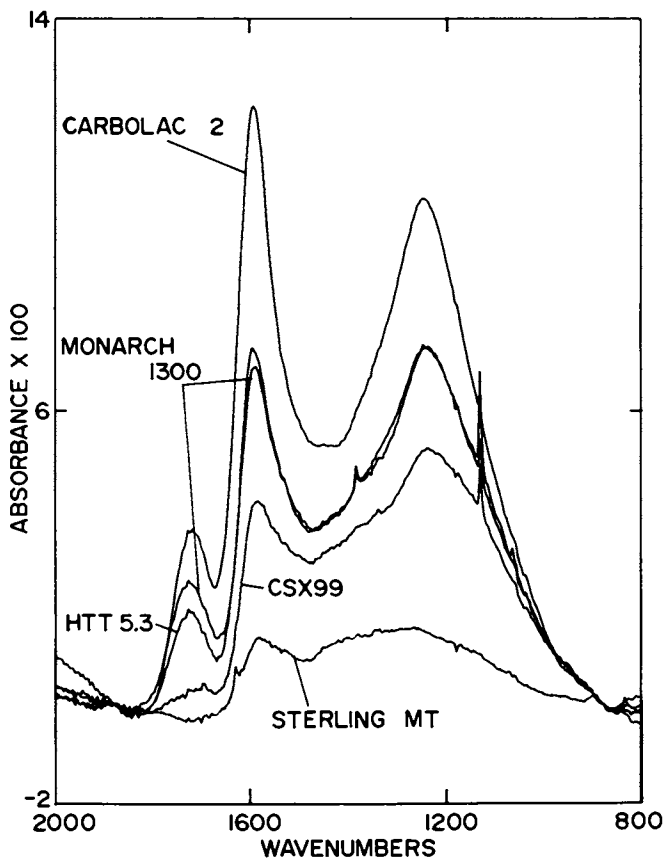


Figure 15. Resolved spectra of carbon blacks with different surface characteristics as listed in Table I superimposed on a linear baseline between 1880 and 880 cm^{-1} .

ACKNOWLEDGEMENTS

We would like to acknowledge the essential experimental assistance of: Dr. John Lin and Mr. Les Dudek for performing the TGA analysis; Dr. Haig Donoian for the Boehm scheme analysis; Dr. Santokh S. Badesha for drying and reacidifying these titrated samples; Mr. F. J. Roberts Jr. for his constructive comments; and Dr. Thomas W. Smith for his technical guidance and advice on the chemistry of carbon black surfaces. In addition we are grateful to Dr. John Riehl of Cabot Corporation and Dr. Paul Julian for helping us acquire the samples and to Dr. James M. O'Reilly for the initial conception and direction of the project.

LITERATURE CITED

- 1- See for example Donnet, J.; Voet, A. "*Carbon Black*"; Marcel Dekker, New York, 1976 and references therein.
- 2- Fabish, T. J.; Hair, M. L. *J. Colloid Interfac. Sci.* 1977, **62**, 16-23
- 3- Julien, P. "*Carbon-Polymer Composites*", Enid Sichel, Ed., Marcel Dekker, N.Y., 1981; in press.
- 4- Brown, J. K. *J. Chem. Soc. (London)* 1955, **1**, 744-751
- 5- Brown, J. K. *J. Chem. Soc. (London)* 1955, **1**, 752-757
- 6- Garten, V. A.; Weiss, D. E.; Willis, J. B. *Australian J. Chem.* 1957, **10**, 295-308
- 7- Smith, R. Nelson *Quart. Revs. (London)* 1959, **13**, 287-305
- 8- Smith, R. Nelson; Young, D. A.; Smith R. A. *Trans. Faraday Soc.* 1966, **62**, 2280-2286
- 9- Mattson, J. S.; Mark Jr., H. B. *J. Colloid Interfac. Sci.* 1969, **31**, 131-144
- 10- Friedel, R. A.; Hofer, L. J. E. *J. Phys. Chem.* 1970, **74**, 2921-2922
- 11- Friedel, R. A.; Retcofsky, H. L. "*Spectrometry of Fuels*", Plenum Press, New York 1970, Chapter 5.
- 12- Studebaker, M. L.; Rinehart Sr., R. W. *Rubber Chem. Technol.* 1972, **45**, 106-1165
- 13- Papirer, E.; Guyon, E.; Perol, N. *Carbon* 1978, **16**, 133-140
- 14- Zawadzki, J. *Carbon* 1978, **16**, 491-497
- 15- Zawadzki, J. *Carbon* 1980, **18**, 281-285
- 16- Zawadzki, J. *Carbon* 1981, **19**, 19-25
- 17- Keifer, J. R.; Novicky, M.; Akhter, M. S.; Chughtai, A. R.; Smith, D. M. *1981 International Conference on FTIR, Proc. SPIE* 1981, **289**, 184-188.
- 18- O'Reilly, J. M.; Mosher, R. A. submitted to *Carbon*
- 19- Puri, B. R.; Bansal, R. C. *R.G.C.* 1964, **41**, 445-451
- 20- Rivin, D. *Rubber Chem. Tech.* 1971, **44**, 307-343
- 21- Boehm, H. P. *Advances in Catalysis* 1966, **16**, 179

- 22- Schubert, B.; Ford, F. P.; Lyon, F. *Encyclopedia of Industrial Chemical Analysis* 1969, **8**, 179
- 23- Debye, P.; Bueche, A. M. *J. Appl. Phys.* 1949, **20**, 518-525
- 24- Avram. M.; Mateescu, G. D. 1972. *Infrared Spectroscopy Applications in Organic Chemistry*, Translated by L. Birladeanu, Wiley-Interscience, New York, Chapter 4.
- 25- See for example: Granqvist, C. G.; Hunderi, O., *Phys. Rev. B.* 1976. **16**, 3513-3534 and reference therein.

RECEIVED April 30, 1982

**American Chemical
Society Library
1155 16th St., N.W.**

Charge Transport Experiments in Monocomponent Toners

W. IMAINO, K. LOEFFLER, and R. BALANSON

IBM Research Laboratory, San Jose, CA 95193

Charge transport through insulating, agitated monocomponent toners, first observed by Nelson, has been investigated in greater detail. Employing a standard monocomponent developer, the dc and transient currents through the agitated toners have been measured. It is apparent that current flows due to some kinetic mechanism; specifically, the experiments indicate that charge is injected onto the toner surface and current results due to the toner translational motion.

In the monocomponent development process^{1,2} for copying onto plain paper³, a magnetic and highly insulating toner is employed to render visible the latent electrostatic image on the photoconductor. As shown by Nelson³, the toner brush is inductively charged and subsequently attracted and deposited onto the high charge areas of the photoconductor. He notes that the inductive charging is made possible, in these usually highly insulating materials, by a kinetically enhanced conductivity, i.e., the conductivity of the toner powder increases dramatically with greater agitation. This kinetically enhanced conductivity is the subject of the present investigation.

The topic of electrical or thermal conduction through particulate media has been the subject of numerous theoretical and experimental investigations, encompassing a wide variety of applications. For example, the electrical conductivity of two phase dispersions with results of experiments on fluidized beds of spheres has been studied by Connelly and Turner.⁴ Charge transport of individual particles in electrostatic precipitators has been studied by McDonald et al.⁵ while Vincett⁶ investigated the high field electrophoresis of insulating particles in insulating liquids. These authors as well as others in related studies, demonstrate that electrical conduction in a system of insulating particles may take place as a result of mass transport (electrophoresis, electrostatic precipitators) or by interparticle contact (fluidized beds). For charge transport through a magnetically agitated,

0097-6156/82/0200-0249\$06.00/0

© 1982 American Chemical Society

insulating powder one can envision current flow due to charge injection across interfaces and charge migration by both interparticle contact and mass transport.

In Section II a description of the monocomponent developer is provided, in Section III the static (bulk) resistivity of the toners is discussed, the results of the kinetic conductivity experiments are displayed in Section IV, and we close with a few concluding remarks.

Monocomponent Development

Figure 1 displays a highly schematized illustration of a monocomponent developer station; the multi-poled cylindrical magnet sheathed in a non-magnetic (stainless steel) shell serve as a convenient reservoir of toner, forming a so-called magnetic brush, which can be rotated and swept across the latent charge image rendering it visible, due to the deposition of toner in the high charge areas. For adequate toner deposition, the magnets and shell must be rotated rapidly, so as to increase the kinetically enhanced conductivity which permits the induced charging. Figure 2 shows a more detailed schematic view of the nip region indicating the charging of the toner brush which may be represented by a simplified equivalent circuit shown in Fig. 3. Here, C_{pc} is the capacitance of the layered photoconductor, C_{pt} is the capacitance between the photoconductor and toner, and R_t is the effective resistance of the agitated toner. In a straightforward procedure, one finds

$$q_{pc}/C_{pc} + q_t/C_{pt} + iR_t = 0$$

and

$$-q_{pc} + q_t = -q_o \quad (1)$$

where q_{pc} and q_t are the charges on C_{pc} and C_{pt} , respectively, and q_o is the initial charge on the photoconductor. Combining these two equations, the charge accumulated on the toner brush must satisfy the following relation:

$$\frac{dq_t}{dt} + \frac{q_t}{C_\xi} + \frac{q_o}{C_{pc}} = 0$$

where

$$C_\xi = \frac{C_{pc} \cdot C_{pt}}{C_{pc} + C_{pt}} \quad (2)$$

The solution to Eq. (2) is

$$q_t = \frac{-C_\xi q_o}{C_{pc}} \cdot (1 - e^{-t/R_t C_\xi}) \quad (3)$$

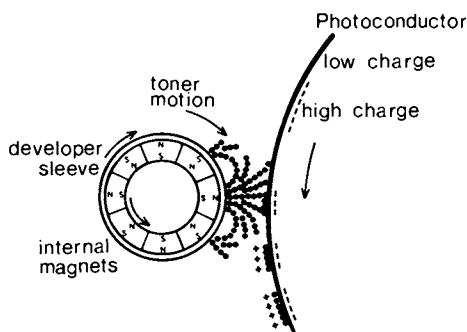


Figure 1. Schematic of a monocomponent developer consisting of an array of rotating magnets within a concentric, independently rotatable, nonmagnetic (stainless-steel) shell. The magnets retain the toner while the motion of the shell and the magnets agitate and brush the toner onto the photoconductor, depositing it on the high charge areas. The toner particles have been exaggerated for clarity.

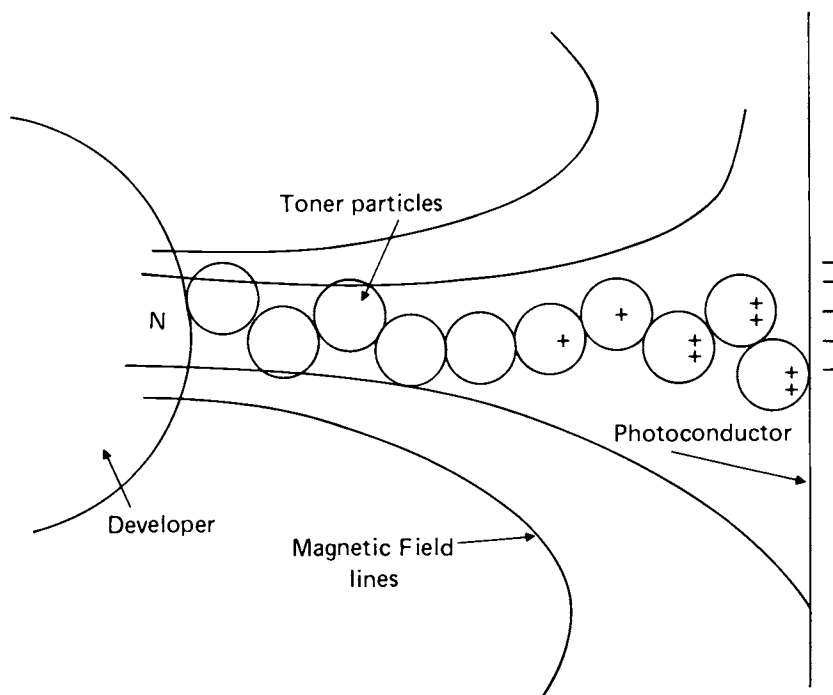


Figure 2. Schematic of the nip region indicating the charging of the toners and the magnetic field lines when a pole is in the nip.

Thus charge accumulates on the brush with a time constant of $R_t C_\xi$, exhibiting the role of the effective toner resistivity in controlling the transient toner brush charging. At first blush this simple analysis appears to preclude the use of highly resistive toners in monocomponent development, however this judgement ignores the kinetic induced conductivity; in the next section, the static bulk resistivity of two commercially available Hitachi toners are displayed. These toners are representative of a conductive and of a resistive type of toner used in monocomponent copiers.

Static Resistivity

To facilitate the measurement of the bulk conductivity, the toner powders were compressed into thin cylindrical disks under a hydrostatic pressure of 100,000 psi. Under these pressures the toner flowed readily and formed a uniform pellet in which the toner particle surfaces were in more intimate contact than in a loose powder. Gold electrodes were evaporated onto the flat faces and the current as a function of the applied electric field measured. This measurement method of the conductivity has certain inherent disadvantages, however, this measurement was intended to be used simply to contrast the kinetic conductivity values reported in Section IV, not to extract absolute values of the material parameters. Nonetheless, several samples of various thicknesses were prepared and measured for each type of toner and the results were found to be quite reproducible.

Figure 4 shows the current density as a function of the applied electric field for the two Hitachi toners. These toners may be considered as solid state colloidal suspensions of iron oxide and carbon black particles in a polymer resin. Note the scale of the axes; in these toners, and most toners measured, the experimental data was of the form

$$i = a \exp(-b\sqrt{E}) \quad (4)$$

where i = current, E , the applied electric field and a and b are constants. This behavior is reminiscent of the Poole-Frenkel effect where current flows because of a field-enhanced thermal ionization of donors, i.e.,

$$i = CE^\alpha \exp\left(\frac{-\phi_i + e\beta E^{1/2}}{kT}\right) \quad (5)$$

where c is a constant, α is an exponent on the order of 1 or 2, ϕ_i is the ground state of the donor, e is the electronic charge, T , the temperature, and k Boltzmanns constant, $\beta = (e/\pi k')$ where k' is the permittivity of the media. Although the Poole-Frenkel effect correctly explains the E -field dependence of the data, it is questionable whether hydrogenic donors exist in the toner colloidal system; in fact, a fit of the slope of the curves in Fig. 4 yields unrealistic values for the relative permittivity. It is more likely that the donors are strongly bound by non-Coulombic forces where the assumption of an effective k is unreasonable. We attribute the difference in resistivity of the two toners to a difference in carbon particle loading where the carbon

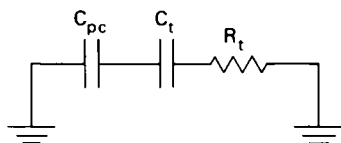


Figure 3. Equivalent circuit of the monocomponent developer. Key: R_t , equivalent resistance of the agitated toner; C_t , capacitance between the photoconductor and toner; and C_{pc} , capacitance of the layered photoconductor.

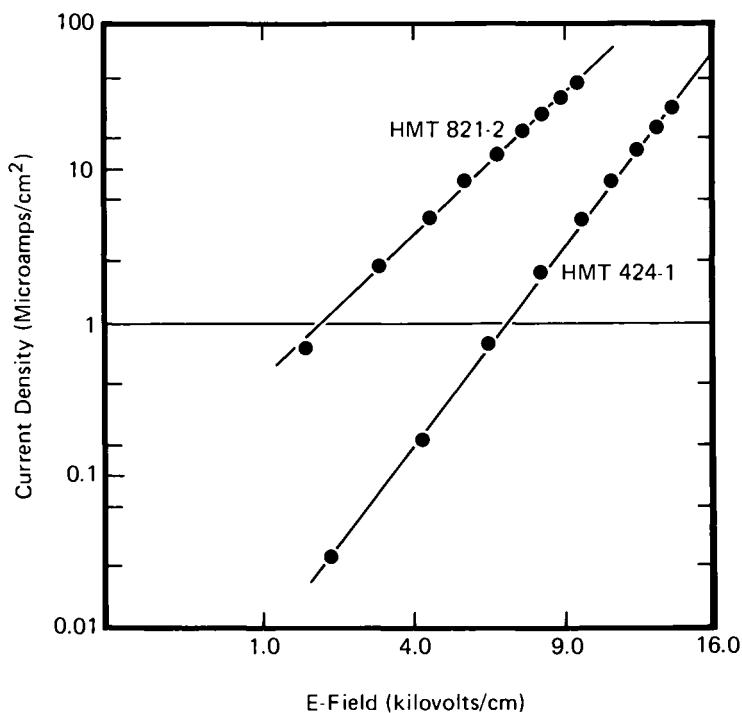


Figure 4. Bulk resistivity of two commercially available Hitachi toners, HMT-821-2 and HMT424-1. It is apparent that HMT424-1 is much more resistive, especially at lower E fields.

particles provide an easy pathway for carriers. A more detailed study and treatment of this is underway.

The dependence of the apparent resistivity of the toner materials with inorganic loading (i.e., iron oxide and carbon content) is perhaps most appropriately explained in terms of percolation theory,⁷ where conduction arises due to electron tunneling between islands of free-carriers. The dramatic increase in conductivity at a certain critical volume concentration predicted by the theory has been observed experimentally for metal colloids in ionic crystals⁸ and fine metal powders in insulating polymers.⁹ In fact, Kolosova and Boitsov⁹ showed that for non-agglomerated 0.1μ diameter metal powders dispersed within a polymer, the critical volume concentration was 10%.

Kinetic Resistivity

Figure 5 shows a schematic diagram of the apparatus used to measure the so-called kinetic resistivity or conductivity. It resembles quite closely, the magnetic developer illustrated in Fig. 1 so as to replicate the magnetic agitation of the toner in an actual measurement. The photoconductor drum has simply been replaced by a gold-coated optical flat. A voltage is applied to the developer roll, using a Fluke high voltage power supply¹⁰ and the voltage drop across the load resistor measured with an oscilloscope. In certain instances the load resistor was replaced with a Keithly piccoammeter¹¹ and the voltage could also be applied to the gold-coated flat and the current measured from the developer to ground. It was found that reversing the polarity of the applied voltage had the same effect as applying the same polarity voltage to the developer or to the gold plate if there were no leakage currents through the insulating stand-offs or the rubber drive belts. In fact, this procedure was used to check for extraneous current leaks. In the following experiments, the magnet core was held stationary with the radial magnetic field lines in the nip, while the shell was rotated. Rotating the magnetic core caused intermittent contact of the toner layer with the gold plate and this further complication was not added in these preliminary experiments. The nip width was set at 10 mils and contact length was 10 cm.

Figure 6 and 7 display the measured currents as a function of the applied voltage with various shell rotational speeds for the Hitachi toners HMT424-1 and HMT821-2, respectively. Note that the scales of the current and voltage axes are linear in contrast to the bulk resistivity measurements, i.e., the agitated toner powder is more nearly ohmic, within the experimental error, however HMT821-2 shows some nonlinear behavior of current versus voltage. This was attributed to the contribution of the bulk conductivity to the currents measured in Fig. 7. In the experimental arrangement shown in Fig. 5, there are two parallel paths for charge transport; charge may be transported through the bulk as mentioned in Section III or by a particle to particle or a particle to metal contact mechanism where charge is separated across the interfaces due to the applied electric field. One can envision two

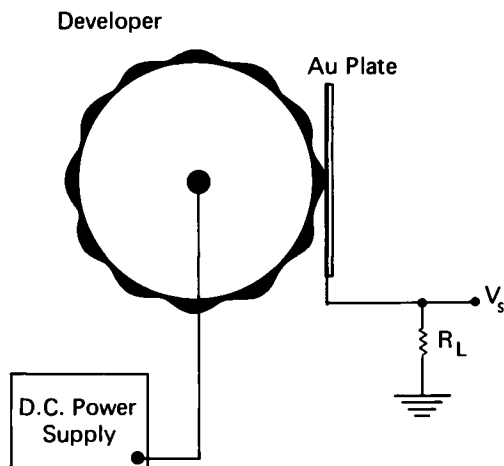


Figure 5. Schematic of the apparatus used to measure kinetic charge transport of toners. The magnetic poles are not shown but their presence is indicated by the undulations in the toner layer. All experiments were performed with a stationary magnet core and a pole in the nip.

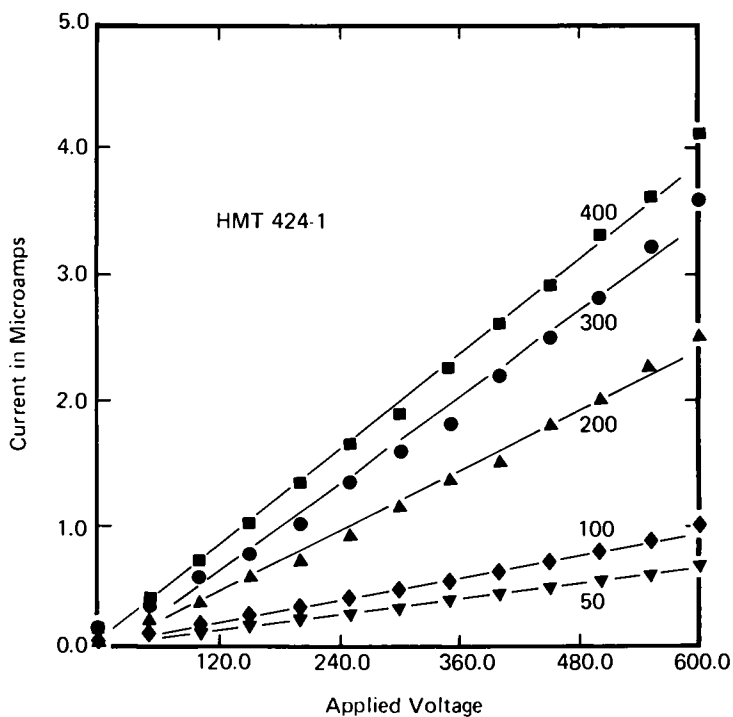


Figure 6. Measured current vs. applied voltage for HMT424-1 for several values of developer shell rotational speed (RPM), obtained using the apparatus in Fig. 5.

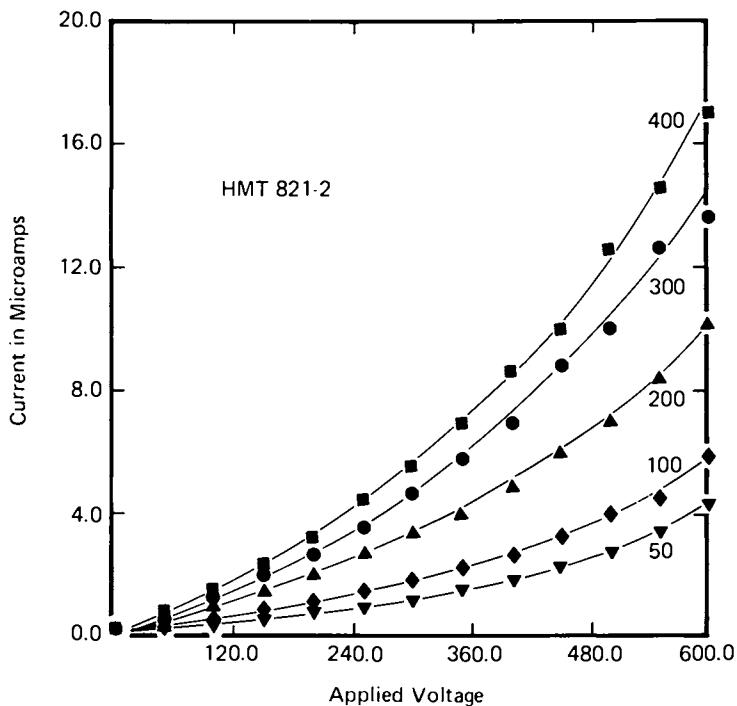


Figure 7. Measured current vs. applied voltage for HMT821-2 for several values of developer shell rotational speed (RPM), obtained using the apparatus in Fig. 5.

kinetic mechanisms for charge transport in an insulating powder. If charge separation occurs only at the particle-metal interface, we term this convective transport in analogy with heat flow. (In this instance one may regard this as magnetically driven convective transport.) We term charge transport by particle-particle charge separation as contactive charge transport. Thus in highly insulating materials, most of the charge transported will be through one of the kinetic mechanisms while in less insulating materials charge may be transported both through the bulk and by a kinetic mechanism, i.e., convective or contactive. Moreover the linear dependence of the current versus voltage measured in the kinetic case is very different from the characteristic current-voltage dependence for bulk resistivity (Fig. 4) and hence suggests that current is not principally transported in the bulk for HMT424-1. On the other hand, HMT821-2 exhibits a finite bulk conductivity so that current may be transported through the bulk and by a kinetic mechanism. Thus current versus voltage curves in Fig. 8 are somewhat nonlinear due to a contribution from the bulk resistivity. The linearity of the current-voltage curves for constant rotational speed of the shell, is related to the linearity of charge injection across interfaces with applied voltage.

Figures 8 and 9 display the current as a function of the developer shell rotation speed for various applied voltages; the current is nearly linear with rotational speed. This exemplifies the kinetic nature of this type of charge transport, where the rotational motion of the shell serves to transport toner into and out of the high field area. We believe that charge is injected into the toner adjacent to the gold plate and stainless steel shell, while current results due to the mass transport of toner out of the nip area. In contact electrification experiments, it is typically found that many repeated contacts are necessary to saturate the charge separated between two surfaces, due to the roughness of the surfaces. In a similar manner, the toner particle acquires charge through repeated contacts. Let there be N sites for charge exchange on each particle, and let S be the number of sites that have contacted the metal, then

$$\frac{dq}{dX} = \frac{ds}{dX} \cdot \Delta q \cdot p(1 - S'/N) \quad (6)$$

where X is the distance the particle has contacted the metal, Δq is the charge transferred per site, p is the probability of transfer, and $S' = sp$ is the number of filled sites. So

$$q = \int dq = \Delta q \cdot p \int_0^s (1 - S'/N) ds \quad (7)$$

$$= \Delta qp \left(s - \frac{s^2 p}{2N} \right) \Big|_0^s \quad (8)$$

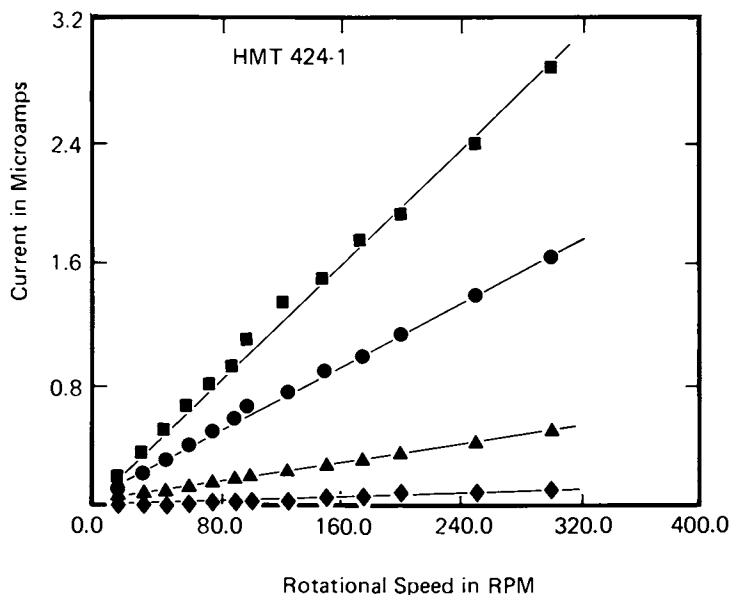


Figure 8. Current as a function of the developer shell rotation speed (RPM) for HMT424-1, for various applied voltages. Key: ■, 500 V; ●, 300 V; ▲, 100 V; and ♦, 0 V.

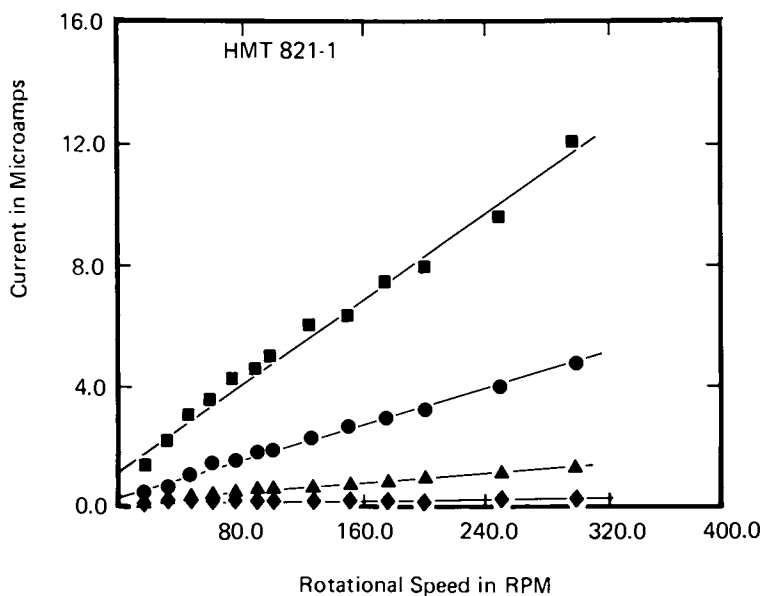


Figure 9. Current as a function of the developer shell rotation speed (RPM) for HMT821-2, for various applied voltages. Key is the same as in Figure 8.

Using the relation

$$s = \int_0^X \frac{ds}{dX} dx = aX \quad (9)$$

where $a = \frac{ds}{dx}$, Eq. (8) may be written

$$q = \Delta q \cdot pa \left(X - \frac{a^2 x^2 p}{2N} \right) \quad x < N/a \quad (10)$$

and

$$q = \Delta q pa \left(\frac{N}{a} - \frac{Np}{2} \right) \quad x \geq N/a \quad (11)$$

Assuming that

$$\Delta q = CV \quad (12)$$

where C is the effective capacitance of the contact site, the current due to a collection of charge particles will be given by

$$i = \rho \mu = \rho r \omega \quad (13)$$

where ρ is charge density, μ is the velocity, r is the radius of the developer, and ω is the shell rotational velocity. Thus in this simple model, the current is linearly proportional to both the rotational velocity of the developer and the applied voltage.

Figure 10 displays the apparatus used to measure transient currents through the agitated toner powder. A Burleigh ramp generator¹² with a Hewlett-Packard signal generator¹³ was used to impress a square pulse voltage on the developer while the current amplified by a fast pre-amp¹⁴ was sampled by a PAR boxcar integrator.¹⁵ The average signal was then output to an X-Y recorder. The response of the toner-developer system can be better understood by analyzing its equivalent circuit shown in Fig. 11. In the figure, V is the applied voltage, C is the developer shell to gold plate capacitance, R_T the toner equivalent resistance, R_L the apparent resistance of the current-voltage pre-amp, and V_s the output signal voltage. One can show that the response of that circuit to a step voltage applied at $t=0$ is

$$V_s = V_A \left[1 - \frac{C'}{C_T} (1 - e^{-t/R_L C'}) \right] \quad (14)$$

where

$$C' = \frac{C_T R_T}{(R_L + R_T)}$$

Figure 12 displays the relevant waveforms; the top trace represents the input square wave voltage, the middle trace the output V_s or the capacitive current if $R_T \rightarrow \infty$, and the bottom trace, a schematic representation of the actual output voltage. Note that if $R_T \rightarrow \infty$, the output voltage is due solely to the

capacitive current and the signal due to the leading edge of the voltage pulse would be

$$V_s = V_A e^{-t/R_L C_T} \quad (15)$$

If $R_T < \infty$, then the output voltage would be proportional to the sum of the resistive current, which would replicate the input voltage in shape, and the capacitive current, shown in the second trace in the figure. However, what is actually observed is shown schematically in the bottom trace of the figure, where there is an apparent time dependence of the effective resistivity of the toner. Figure 13 displays the actual signal voltages in the region close to the initial capacitive spike showing the apparent risetime of the effective resistivity of the toner, for various shell rotational speeds. The large initial capacitive spike prevented an accurate measure of the resistive risetime for higher shell rotational speeds. Figure 14 is a plot of the inverse of the time for the signal to rise to its steady state, $1/t$, versus the shell rotational speed, demonstrating the linear relationship between shell and toner rotational velocity.

In our experimental arrangement, both metal contacts are injecting, therefore the risetimes shown in Fig. 13 are not an indication of the time for charge to transit the nip. Rather, this risetime is related to the time the toner spends in the high field region near the pole of the magnet. In this region the toner particles are acquiring charge but current does not flow until there is a separation between the charge on the toner and its image charge in the gold. Thus current only flows when the toner exits the nip area; the first particles that exit the nip have very little charge since x is small as shown in Eq. (10), while the particles that traverse the full width of the nip will have a greater charge and hence represent a larger current. From this simple analysis, the risetime of the current is simply the time it takes for a particle to traverse the nip width. Thus, the data presented here suggests that current flows by a convective (mass transport) mechanism, where charge is injected at the gold plate.

Concluding Remarks

The effectiveness of kinetic motion in allowing charge transport in an otherwise insulating powder has been demonstrated. Specifically, we have investigated magnetically agitated toners (as in a monocomponent developer) where the kinetic motion or agitation is unique in having a large amount of rotational motion. Conceptually current flow in such powders may be due to charge migration from particle to particle or charge migration due to the translational motion of the individual particles. Our experiments indicate that charge is injected at the metal contacts and current results due to the mass motion of the toner. The rotational motion of the toner permits more effective toner translational motion. Studies of the magnetic forces involved and their specific role in the agitation of toner are underway and a more

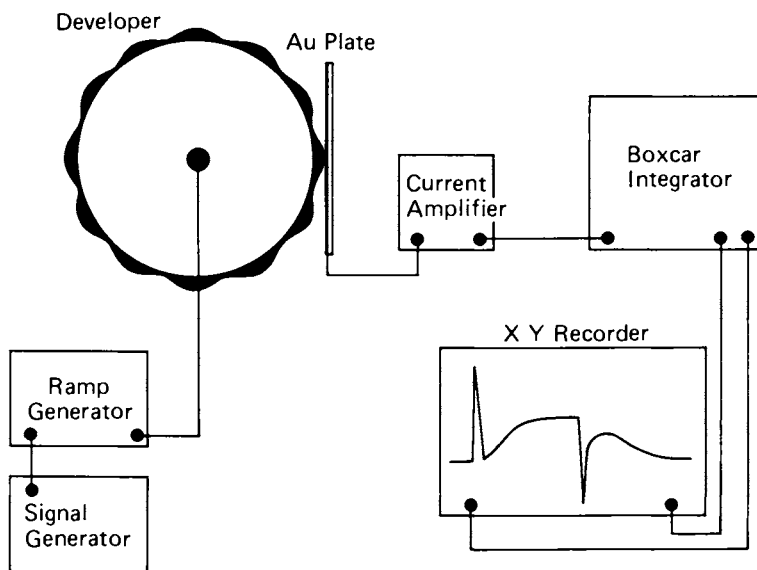


Figure 10. Apparatus used to measure the transient current through the agitated toner powder. A square pulse provided by a Hewlett-Packard signal generator (13) was amplified by a Burleigh ramp generator (12) and impressed onto the developer. The transient current was amplified using a fast pre-amp (14) and the signals were sampled by a PAR boxcar integrator (15). The averaged signals were output to an X-Y recorder.

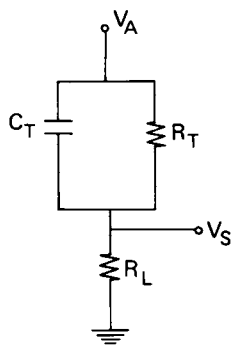


Figure 11. Equivalent circuit of the toner-developer-gold plate shown in Fig. 10. Key: V_A , applied voltage; C_T , developer-gold plate capacitance; R_L , effective resistance represented by the current-voltage pre-amp; and V_S , output signal.

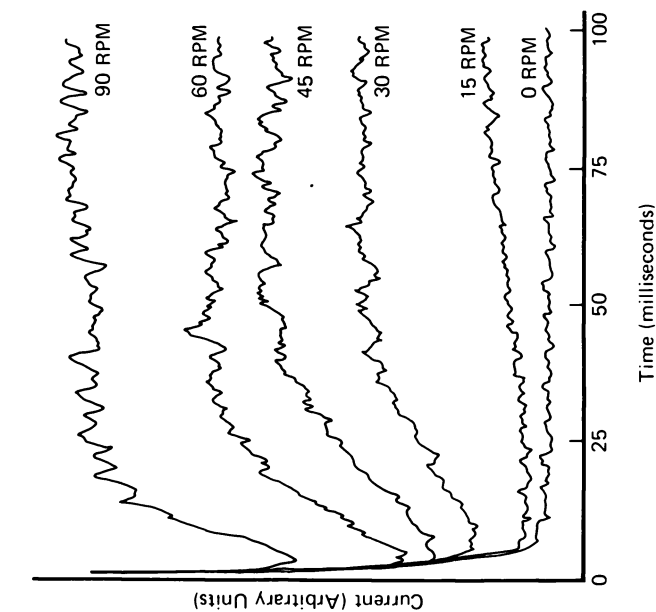


Figure 13. The actual measured transient currents in the region near the capacitive spike due to the leading edge of the input voltage. The individual traces were taken with different shell rotational velocities and have been shifted vertically for clarity.

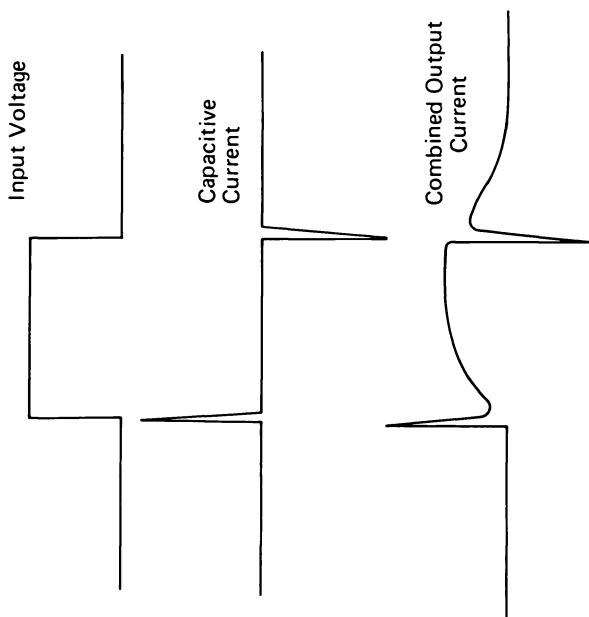


Figure 12. Schematic of the transient currents measured using the apparatus shown in Fig. 10 for a square pulse input voltage.

The second trace shows the output voltage if the toner effective resistance is very large. For a normal resistance, R_1 , the output current would be a superposition of the waveforms shown in the first and second traces. However, for agitated toner the typical measured signal is shown in the lowest curve.

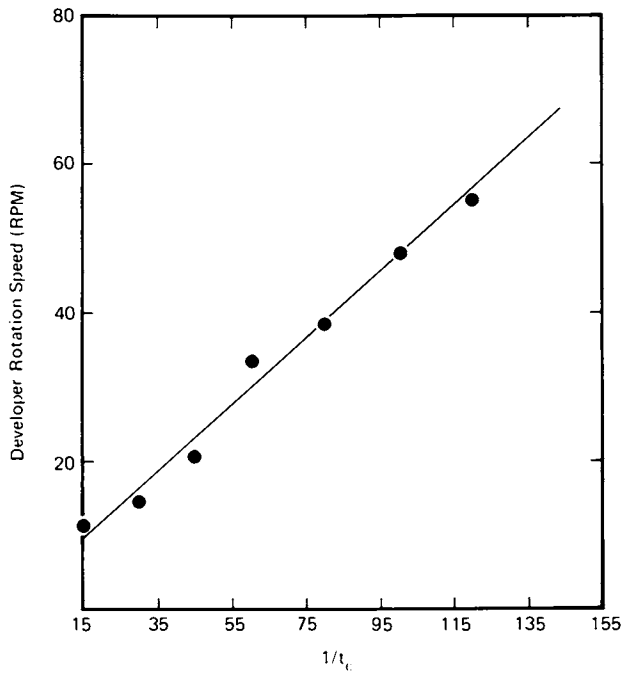


Figure 14. A plot of the shell rotational velocity (RPM) vs. $1/t_s$, where t_s is the time for the current to reach a steady state value, as determined from Fig. 13.

complete description of these and other charge transport experiments in monocomponent toners will be published later.

Literature Cited

1. Wilson, J. C. U.S. Patent 2,846,333 (1958).
2. Kotz, A. R. U.S. Patent 3,909,258 (1975).
3. Nelson, K. S. U. S. Patent 4,121,931 (1978).
4. Connelly, T. M.; Turner, J. C. R. Chem. Eng. Sci. 1979, 34, 319.
5. McDonarld, J. R.; Anderson, M. H.; Mosley, R. B.; Sparks, L. E. J. Appl. Phys. 1980, 51, 3632.
6. Vincett, P. S. J. Coll. and Int. Sci. 1980, 76, 83.
7. Kirkpatrick, S. Rev. Mod. Phys. 1973, 45, 574.
8. Hughes, A. E.; Jain, S. C. Adv. Phys. 1979, 28, 717.
9. Kolosova, N. N.; Boitsov, K. A. Sov. Phys. Solid State 1979, 21, 1332.
10. Model 410B, John Fluke Mfg. Co., P.O. Box 43210T, Mountlake Terrace, Washington 98043.
11. Model 416, Keithley Instruments Inc., 28775-T, Aurora Road, Cleveland, Ohio 44139.
12. Model DAS1, Burleigh Inst. Inc., 100 Despatch Dr., East Rochester, New York, 1445.
13. Hewlett-Packard Co., 1501 Page Mill Road, Palo Alto, California 94304.
14. Model 101A, United Detector Technology, 3939 Landmark St., Culver City, California 90230.
15. Princeton Applied Research, P.O. Box 2565, Princeton, New Jersey, 08540.

RECEIVED February 3, 1982

Measuring Toner Particle Size Distributions Using Spatial Frequency Analysis

O. L. NELSON, T. W. KING, and M. R. V. SAHYUN

3M Center, Central Research Laboratories, St. Paul, MN 55144

Experimental data relating the spatial frequency dependence of image quality parameters obtained from electrophotographic toner deposits with the toner particle size distributions are presented. Models are constructed which suggest that these optical measurements can be used to determine the effective particle size distribution parameters, mean diameter and sigma. Assumptions include multilayer particle deposit, the log-normal distribution of the diameters of the spherical, opaque particles, and no sorting of size classes during particle deposition. The optical measurement include edge trace analysis to derive the contrast transfer function, and density fluctuation measurements to derive the Wiener spectrum. Algorithms to perform these derivations are outlined.

The basis of this report is a continuing program to evaluate and understand the information and noise content of electrographic images created by toning electrostatic charge patterns with charged particles. Four parameters or functions, borrowed from photography, to characterize these toner deposits are resolving power, contrast transfer function, granularity and the Wiener spectrum. These are all statistically determined functions, measured using statistical averaging. This analysis of data and comparison to model predictions also is statistically based, using regression analysis. The correlation coefficients are then used to judge the applicability of the models.

As this work developed it became a working premise that the toner particle size distribution was a major factor determining the image quality characteristics (1,2). The particle size distribution in the following analysis is presumed to be of lognormal form,

0097-6156/82/0200-0265\$06.00/0

© 1982 American Chemical Society

$$\phi(\ln d) = \frac{1}{\sqrt{2\pi} \ln \sigma_g} \exp\left[-\frac{\ln^2(d/\bar{d})}{2 \ln^2 \sigma_g}\right] \quad (1)$$

where d is particle diameter, \bar{d} is the (geometric) mean diameter and σ_g is the geometric standard deviation. The parameter \bar{d} may represent a mass (weight) or a number mean, depending on whether $\phi(\ln d)$ is expressed in terms of mass of material or number of particles in a particular size class. These will be designated \bar{d}_m or \bar{d}_n , and are related: $\ln \bar{d}_n = \ln \bar{d}_m - 3 \ln^2 \sigma_g$.

The toners used for this study were size-classified segments of a single-component conductive magnetic toner (3). The particle size distribution (PSD) parameters of the samples used, all fractions of one parent population, were measured using an adaptation of the method of King, Shor and Pitt (4). These are listed on Table I. The parent toner has a bimodal distribution and a resulting apparent larger σ_g value. Figure 1 shows representative distributions. The toner deposits were prepared by loading the respective magnetic toner sample onto a magnetic applicator roll (5) and using it to develop a charge pattern on the receptor (6). The resulting deposits were not fused or fixed. For the granularity and noise spectrum measurements, the receptor was polyester film (ca. 25 μm thick) which was uniformly charged with a corona device to a potential sufficient to develop to optical density near unity. For the edge trace measurements, samples of an electrofax type paper (7) was light exposed in contact with a metal edge. This exposure method yielded an optical transfer function of unity to greater than 20 cycles/mm on a hard photographic paper. The exposed electrofax type paper was then developed with the toner sample. The edge traces showed no apparent "edge-effect" development.

Preliminary Considerations

It is assumed that the toner deposits are built up as partially-ordered layers of opaque toner particles and that the optical systems used for measuring the resulting transmission optical density of these deposits can resolve the particle size dimensions. A consequence of the assumptions is an a priori relation between limiting resolution or resolving power of the image and mean particle size, of the form $\nu_R \propto 1/\bar{d}$. Experimentally the resolving power is usually based on an observer's ability to visually discern the image of a pattern of equal sized bars and spaces, known as a bar target. From information-content arguments based on a series expansion of a bar-pattern (1), the proportionality constant can be assigned:

$$\nu_R = \frac{1}{\beta \cdot 3\bar{d}_m} \quad (2)$$

where \bar{d}_m is the geometric (weight) mean particle diameter and β relates to the observer's ability to distinguish bar from space;

TABLE I. PARAMETERS FOR TONER SAMPLES

Sample	$\bar{d}_m, \mu\text{m}$	σ_g
Parent	21.4	1.96 *
1	22.0	1.43
2	15.0	1.50
5	13.2	1.34
6	9.5	1.60
9	7.0	1.44
12	10.5	1.59
15	17.4	1.31
18	13.6	1.38

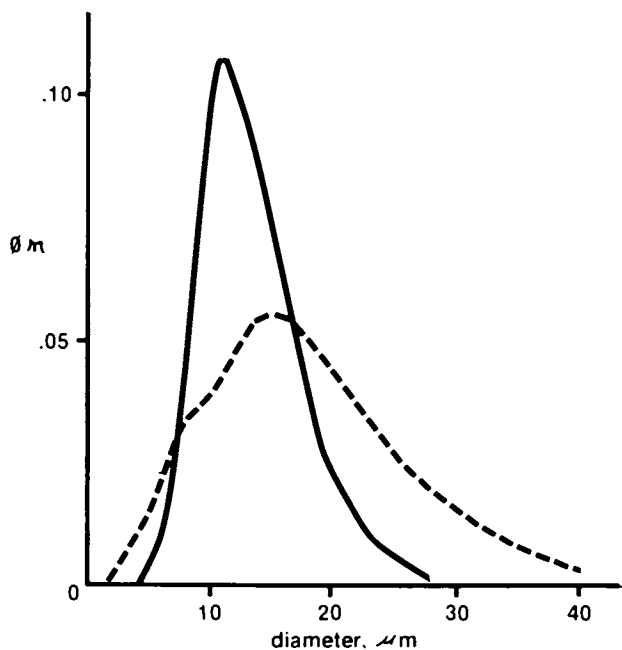


Figure 1. Representative toner particle size distributions used in this study. Key: —, fraction #5; and ---, parent.

β is given a value of ca. 1.5 from experimental observations. Analysis of data from these studies as well as data from the literature shows good correlation between this relation and experimental values of ν_R .

Another consequence of the layered deposit assumption is that granularity (a measure of the variance of the transmission optical density measured with a circular aperture) is proportional to an effective particle size corresponding to the geometric effect of statistically adding another particle to an already existing layer. The form of the resulting relationship is (1,2)

$$\sigma_D \sqrt{2a} = g = 1.88 d_{\text{eff}} \cdot D = 1.88 \left(\frac{d_{\text{eff}}}{d_m} \right)_D \cdot d_m \cdot D \quad (3)$$

where g is the Selwyn granularity coefficient, σ_D is the rms variation of optical density D , a is the measuring aperture area, and d_{eff} is the effective particle diameter; d_{eff} is a function of density.

The two image quality parameters introduced above are single values which are determined from single observations. The aperture used to measure these values is fixed and no explicit information is contained about different dimensions. The corresponding functions which do contain information over a range of dimensions are the contrast transfer function, CTF, and the Wiener spectrum, or noise content of the deposit as a function of spatial frequency (8). These functions also have been found to contain information which correlates to the particle size distribution, as will now be discussed.

Contrast Transfer Function

The square wave contrast transfer function, CTF, is a measure of the contrast with which the toner deposit can reproduce a bar pattern exposure as a function of the bar pattern dimensions. Those dimensions are represented as the number of bars and spaces per mm, or cycles per mm, ν . As bar spacing decreases to the dimensions of the toner particles the particles will no longer be able to distinguish bar from space, and will simply "fill in" causing an apparent uniformly random deposition. This is illustrated schematically in Figure 2. Since the toner contains a range of particle sizes, the CTF should decrease at a spatial frequency ν and at a rate reflecting the particle size distribution. This assumes that other image-degrading factors such as optical spread and charge pattern spread are not dominating. For the spatial frequencies of interest here (0 to 20 cycles/mm) that seems justified (2).

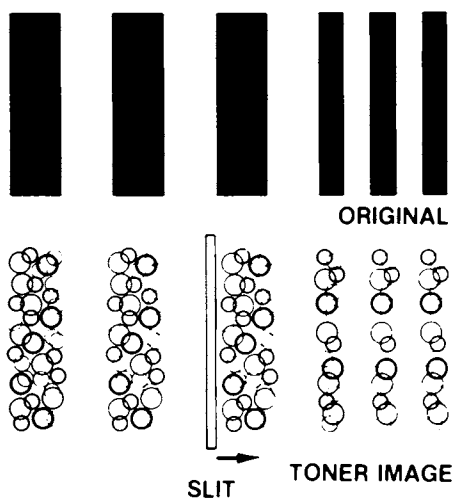


Figure 2. Schematic of original bar pattern, toner image of bar pattern, and scanning slit aperture used to measure edge transition.

The experimental square wave CTF was calculated from toned images of a sharp edged metal mask, contact exposed on Electrofax type paper. The calculation was made using an algorithm described by Scott (9). The edge image was scanned with a micro-densitometer in the reflection mode using a slit aperture $3.5\mu\text{m}$ wide and $280\mu\text{m}$ long, taking 200 points at $5\mu\text{m}$ intervals. The resulting data were smoothed using a 9-point digital filter (10) which limited the useful spatial frequencies to values less than 22 cycles/mm. The algorithm synthesized a bar pattern response by normalizing the edge trace, inverting and then combining these with offset traces to simulate a bar of width corresponding to the offset distance. The CTF is then calculated as

$$\text{CTF}(\nu) = \frac{D_{\max}(\nu) - D_{\min}(\nu)}{D_{\max}(\nu) + D_{\min}(\nu)} \quad (4)$$

This procedure is illustrated in Figure 3. Use of the algorithm requires location of the "true edge." Two definitions, the location of the half-value point or the location of steepest edge slope, were used and yielded indistinguishable results. The CTF values were finally corrected for high frequency fluctuations which yielded a non-zero baseline. Figure 4 shows the computed experimental results for the toner fraction 1.

From the toner geometric and sampling theory considerations which lead to equation (2), only those particles of diameter $d \geq 1/3\nu$ contribute to the CTF at frequency ν (1). The fraction which satisfies the inequality is

$$\phi(1/3\nu) = \int_{-\infty}^{\ln(1/3\nu)} \phi_m(\ln d) d(\ln d) \quad (5)$$

The remaining larger particles should not be able to reveal the modulation and thus should contribute to the background. Relating this to observed optical density, $D_{\max} \propto \phi(\infty)$, while $D_{\min} \propto \phi(\infty) - \phi(1/3\nu)$. Therefore the model CTF should be:

$$\text{CTF}_M(\nu) = \frac{\phi(1/3\nu)}{(2 - \phi(1/3\nu))} \quad (6)$$

Figure 4 shows the resulting model-calculated CTF, CTF_M , for the toner fraction 1 along with the CTF computed from experimental data for the same toner. The limiting resolution ν_R from equation (2) is indicated and agrees quite well ($\pm 15\%$) with the value from observations of a developed USAF resolution target (2).

Figure 5 shows experimental and simulated CTFs from two additional toner samples, the parent and fraction 18. The agreements are reasonable, and show an increased squareness of the CTF for fraction 18 corresponding to a lower PSD σ_g value of 1.38 versus 1.96 for the parent. This effect can be related to the information content of the image (2). This analysis of CTF then,

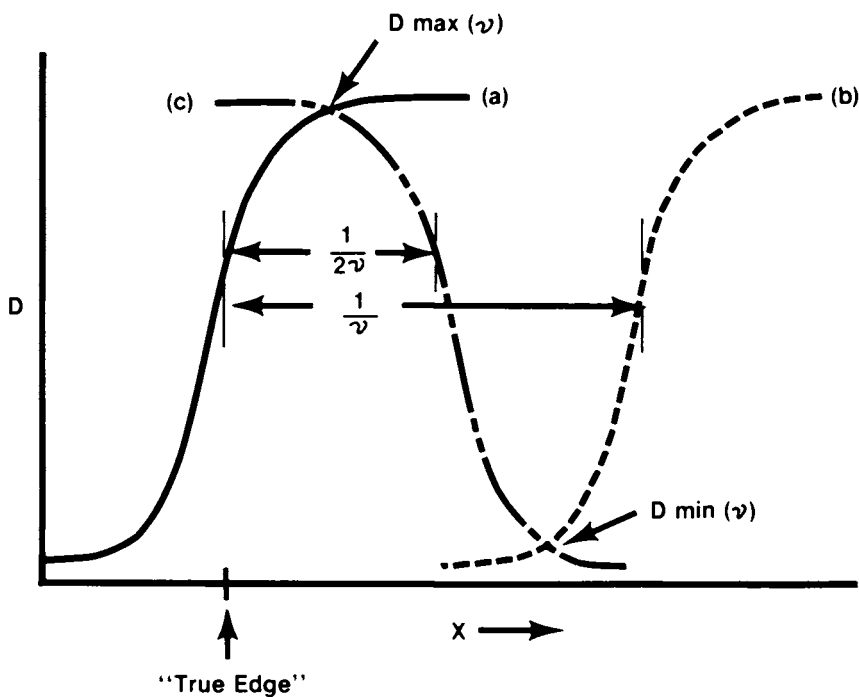


Figure 3. Simulation of a periodic image of spatial frequency from the microdensitometer trace of the image of a shape edge (a), translated by $1/\nu$ (b), and reversed about the true edge and translated $1/2\nu$ (c).

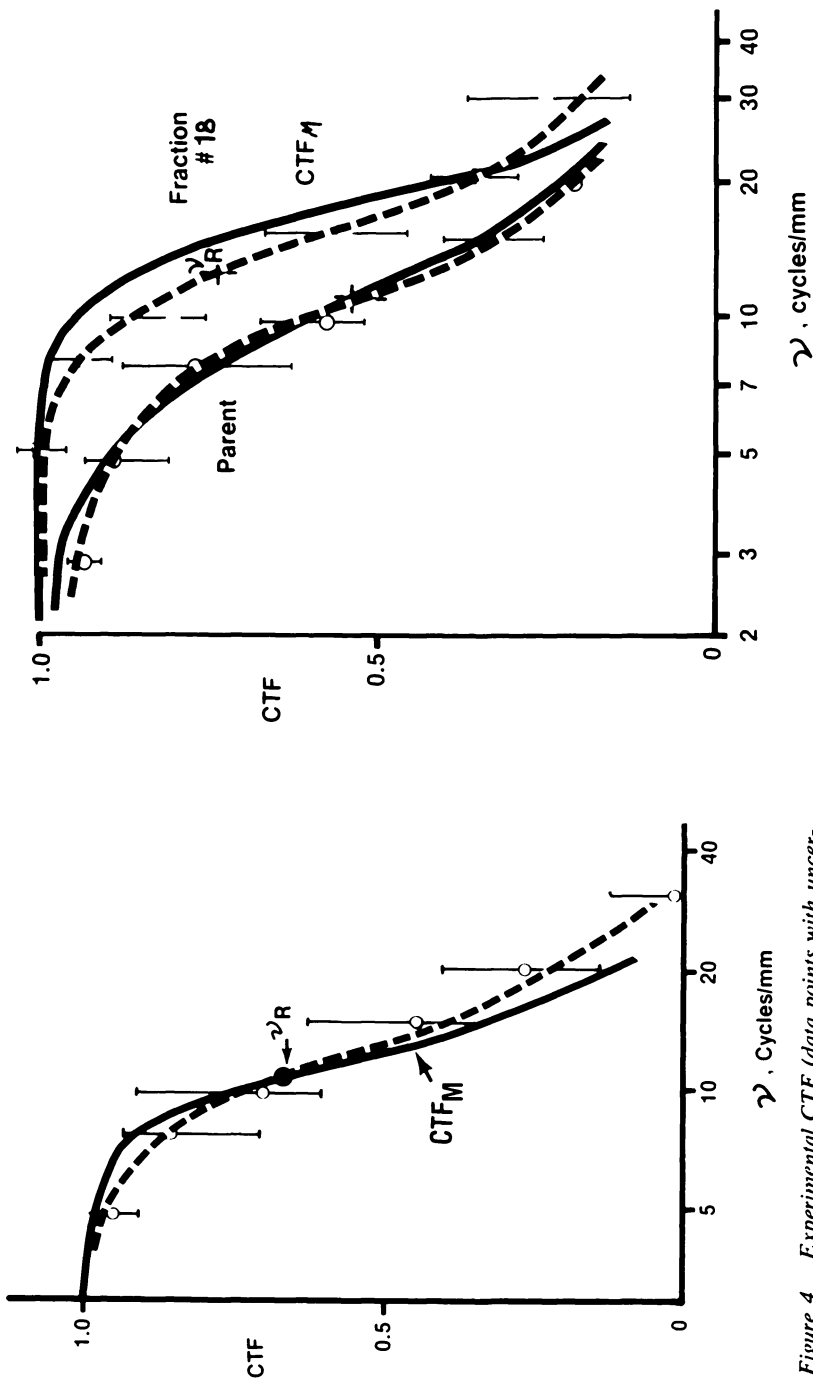


Figure 4. Experimental CTF (data points with uncertainties indicated) and simulated CTF_m (solid) for image made using toner fraction #1. (Reproduced, with permission, from Ref. 2. Copyright 1980, Society of Photographic Scientists and Engineers.)

Figure 5. Experimental and simulated CTF's for images made using indicated toners.

as derived for an edge of the toner deposit, shows experimental verification of the strong relationships between the toner deposition CTF and the particle size distribution parameters.

Noise

The statistical fluctuation or noise level of a toner image is also by these postulates dependent on the particle size distribution. The function which relates the statistical fluctuations to spatial frequency is the Wiener spectrum, which is the Fourier transform of the optical density autocorrelation function. In terms of toner images, it is a measure of the dimensional extent over which the presence or absence of a particular toner particle will contribute to density. The density fluctuations can be measured as a function of position, normally with a slit aperture. This is schematically represented in Figure 6 where the left-hand sketch is related to large particles and the right-hand one to small particles. The density data can be used to calculate noise power or Wiener spectrum (8). Formally, the Wiener spectrum is:

$$W(\nu) = \lim_{X \rightarrow \infty} \frac{L}{X |T(\nu)|^2} \left| \int_{-X/2}^{X/2} (D(x) - \bar{D}) \exp(-2\pi i \nu x) dx \right|^2 \quad (7)$$

where $W(\nu)$ is the noise power value at frequency ν , L is the length of the scanning slit, $T(\nu)$ is the transfer function of the measuring system, $D(x)$ is the density at x , \bar{D} is the mean density and X is the distance scanned.

Samples were made for this study by uniformly charging polyester film and then developing with the various toners. The raw data were collected using a scanning microdensitometer with a slit aperture $3.5\mu\text{m}$ and $280\mu\text{m}$ long. Density values were recorded every $2.8\mu\text{m}$, to collect 4096 values. These data were read by a computer program (2) which fitted blocks of values (typically 512) to a smooth function $A+Bx$, then calculated the fluctuations. Spuriously large values were clipped to remove "pinhole" effects. A Fast Fourier transform algorithm then computed the transform values which were squared and averaged over blocks and over appropriate ranges of frequency to provide approximately 25 values with an expected standard error of 12% (8).

The dimension of $W(\nu)$ is (distance)², e.g. μm^2 . For comparison with particle parameters, the square root of the Wiener spectrum values were used. This gives a function of linear distance dimension and is analogous to use of an RMS value such as granularity. Figure 7 shows examples of these experimental Wiener spectra, plotted as the square root of $W(\nu)$ vs. $\log(\nu)$, for parent fractions 18 and parent toner. Note that the bimodal parent toner yields a spectrum with an inflection point, another supportive observation for the correlation of image parameters and toner PSD.

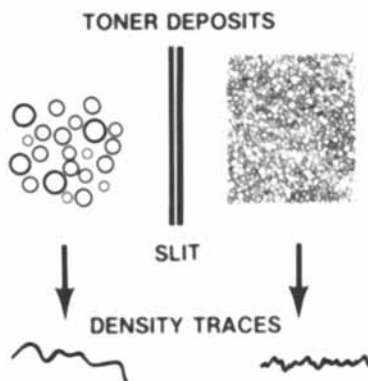


Figure 6. Schematic of toner deposits and optical density traces, obtained using a slit aperture, of large particles (left), and small particles (right).

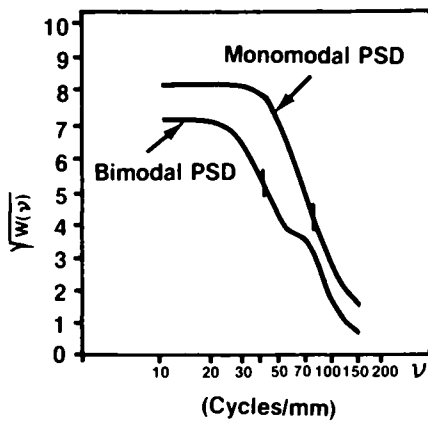


Figure 7. Typical experimental Wiener spectra for indicated toner samples. (Reproduced, with permission, from Ref. 2. Copyright 1980, Society of Photographic Scientists and Engineers.)

A theoretical model to relate the Wiener spectrum to the toner deposit parameters is difficult to construct because the mathematical difficulties of dealing with projections of transforms of probability distributions quickly "hide" any simple relationships. Models have been constructed however for a crowded monolayer photographic emulsion (11), and for multilayers of emulsion (12). Although the analysis was done for one-dimensional geometry, extension to two dimensions was outlined. A different approach will be used here, which relies on the linearity property of the Fourier transform, and assumes that the location of the toner particles is independent of neighbors.

For a first approximation to a model for the Wiener spectrum constructed from the toner particle distribution data, consider a fraction of a deposit consisting of \bar{n}_i toner particles of circular projection area and diameter d_i . The expected circular aperture Wiener spectrum for a deposit of these particles is (10,2),

$$\hat{w}_i(\nu) = \bar{n}_i \left(\frac{d_i}{2\nu} J_1(\pi\nu d) \right)^2 \quad (8)$$

when toner particle presence or absence is the dominant fluctuation. J_1 is the first order Bessel function. An estimate of the Wiener spectrum resulting from a particle distribution $\phi_n(\ln d_i)$ can then be assembled by adding the contribution from each size class in accordance with the distribution. In integral form this would be

$$\hat{w}(\nu) = \bar{n} \int_{-\infty}^{\infty} \phi_n(\ln d) \left[\frac{d}{2\nu} J_1(\pi\nu d) \right]^2 d(\ln d) \quad (9)$$

where \bar{n} is the average number of particles per unit area, d is particle diameter and ϕ_n is the particle distribution according to number. The integration of this equation was done numerically by computer for each toner fraction for $\bar{n} = 1.2/\bar{d}_n$. According to the layered deposit, this should correspond to 1.5 to 2 layers and optical densities of ca. 1 (2), but more importantly should allow relative comparisons of the model spectra for different toners. An example of a computer model Wiener spectrum is shown in Figure 8, again plotted as the square root of $\hat{w}(\nu)$ versus $\log \nu$.

Two estimates of how well the particle size distribution shows through the computed Wiener spectrum were made. First, the extrapolated value of $\sqrt{\hat{w}(0)}$ was determined. This should be proportional to the granularity of the deposit (2,6), and according to the relation of equation (3), should in turn correlate with \bar{d}_m . Figure 9 shows this comparison, yielding a correlation coefficient of 0.985. Secondly, the spatial frequency ν_H at which $\sqrt{\hat{w}(\nu)}$ falls to $\frac{1}{2}$ the extrapolated maximum $\sqrt{\hat{w}(0)}$ should be correlated with the average particle size of those contributing to the spectrum.

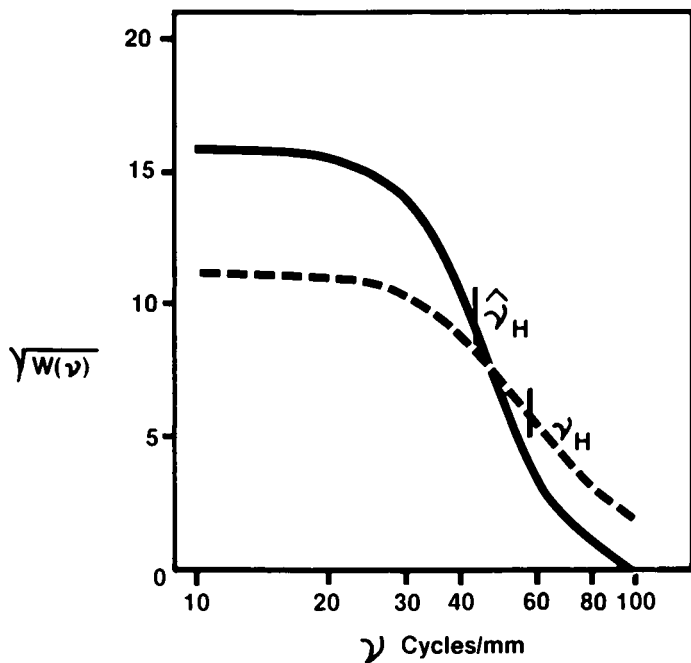


Figure 8. Wiener spectrum for toner Sample #1. Key: —, calculated from Equation 9; and ---, experimental.

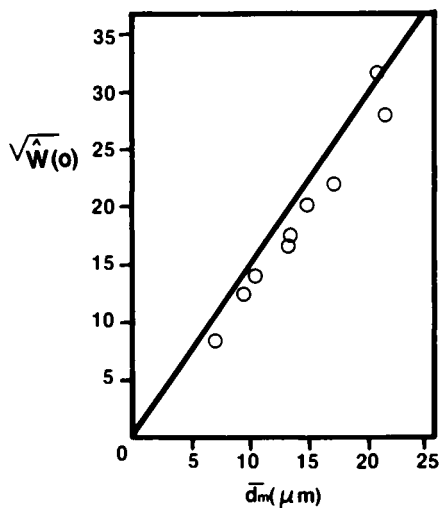


Figure 9. Predicted values of granularity as represented by $\sqrt{\hat{w}(o)}$ plotted versus the \bar{d}_m of the toner PSD used in Equation 9. (Reproduced, with permission, from Ref. 2. Copyright 1980, Society of Photographic Scientists and Engineers.)

Specifically $d_H = 1/v_H$ should be proportional to \bar{d}_m . Further, if the particle distribution dominates the noise spectrum, the slope of $\sqrt{w(v)}$ at $\frac{1}{2}$ amplitude should correlate with the particle distribution spread as represented by σ_g . The slope, designated as $\ln \hat{\sigma}_H$, of the form

$$\ln \hat{\sigma}_H = \left(\frac{-2.3}{\sqrt{2\pi}} \frac{d(\log v)}{d\left(\frac{\sqrt{w(v)}}{\sqrt{w(0)}}\right)} \right) v_H \quad (10)$$

was calculated for the several computed spectra and the resulting $\hat{\sigma}_H$ was compared with the σ_g for the respective toner. Figure 10 shows the correlation, yielding a correlation coefficient of 0.954. Also shown is the correlation of d_H versus \bar{d}_m , yielding a coefficient of 0.997.

These tests and manipulations with the model-computed Wiener spectra suggest that the particle size distribution parameters may be extractable from the experimental spectra. Similar calculations were thus made from the experimental spectra. Figure 11 shows the values of $d_H = 1/v_H$, computed from $\sqrt{w(v)}/w(0)$, plotted against \bar{d}_m for the respective toners. The dependence is linear with a correlation coefficient of 0.847. Also, values of the slope of $\sqrt{w(v)}/w(0)$ at v_H versus $\log v$ (analogous to equation (10)) were computed from the experimental data to calculate $\sigma_H(\text{exp})$ and compared with the geometric standard deviation σ_g of the respective toner fraction. The results, also seen in Figure 11, show again near linearity but with more scatter, giving a correlation coefficient of 0.598.

It is interesting to compare these correlation coefficients between noise spectrum analysis and the modified disc centrifuge method (4) used for a reference, with the correlation between disc centrifuge and the Coulter counter method. The correlation coefficients obtained in that comparison are 0.96 for \bar{d} , and 0.57 for σ_g . Thus the noise spectrum analysis method correlates as well with the disc centrifuge method as does Coulter counter data.

Conclusions

The correlation analyses of toner particle size and size distribution parameters and image quality characteristics of toner deposits as measured by the spectral dependence of contrast transfer function and noise show high coefficients of correlation. Specifically the Wiener spectrum data appear to yield the weight geometric mean and standard deviation of the toner population in this study. Therefore the Wiener spectrum may be another analytical tool in characterizing particle populations. It must be pointed out that the analysis reported here is mainly empirical. Further work is needed to refine the models and to examine the limits of applicability of these tests. Factors such as particle clumping, non-uniform depositions and optical limitations are specific areas for examination.

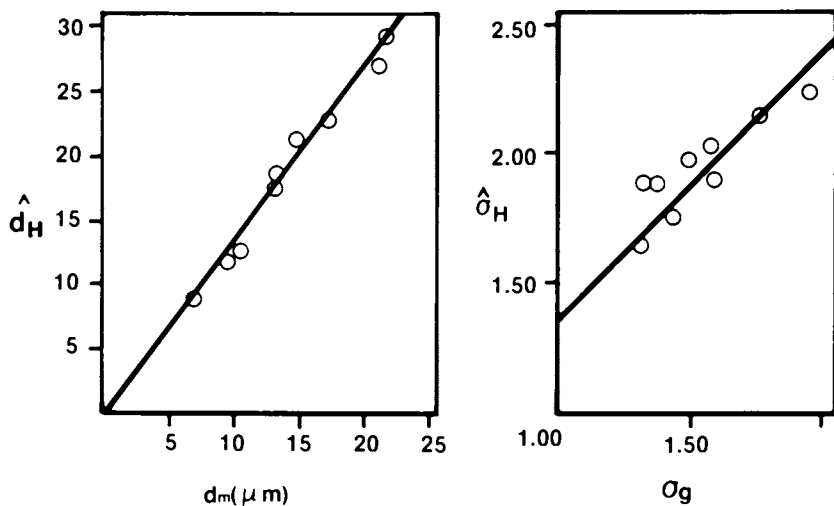


Figure 10. Two correlations of derived parameters from computed Wiener spectra vs. the corresponding toner PSD parameters.

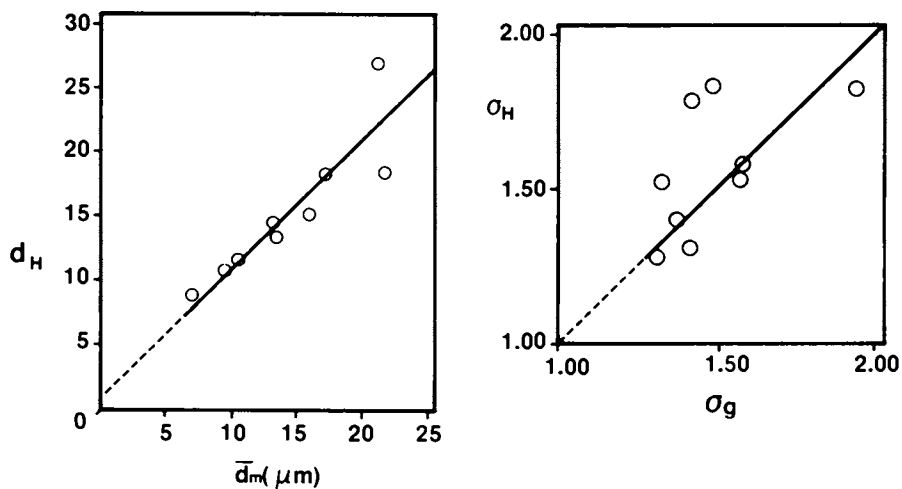


Figure 11. Two correlations of derived parameters from experimental Wiener spectra vs. the corresponding toner PSD parameters.

Literature Cited

1. Sahyun, M.R.V. J. Phot. Sci. 1978, 26, 177.
2. King, T.W.; Nelson, O.L.; Sahyun, M.R.V. Photogr. Sci. Eng. 1980, 24, 93.
3. Nelson, R.B. U.S. Patent 3,639,242, 1972.
4. King, T.W.; Shor, S.M.; Pitt, D.A. Photogr. Sci. Eng. 1981, 25, 70.
5. Kotz, A.R. U.S. Patent 3,909,258, 1975.
6. Takahashi, Y.; Sakata, T.; Kakei, T.; Sano, K. Electrophotography 1978, 16, 27.
7. Young, C.J.; Greiz, H.G. RCA Rev. 1954, 15, 471.
8. Dainty, J.C.; Shaw, R. "Image Science"; Academic Press: London, 1974.
9. Scott, F.; Scott, R.M.; Shack, R.V. Photogr. Sci. Eng. 1963, 7, 345.
10. Binckley, D.; Dessy, R. J. Chem. Educ. 1979, 56, 148.
11. Castro, P.E.; Kemperman, J.H.B.; Trabka, E.A.; J. Opt. Soc. Am. 1973, 63, 820.
12. Lawton, W.H.; Trabka, E.A.; Wilder, D.R. J. Opt. Soc. Am. 1972, 62, 659.
13. Baudry, P.; Despereoz, R.; Prectescille, J. Phot. Sci. 1968 16, 132.

RECEIVED March 22, 1982

Physics of Nonaqueous Colloids

V. J. NOVOTNY¹

Xerox Research Centre of Canada, Mississauga, Ontario, Canada L5L1J9

Nonaqueous colloids differ considerably from aqueous dispersions because of their low electrical conductivity. This low conductivity leads to non-uniform, time varying electric fields in classical electrophoretic geometries and thus creates difficulties in determining colloidal properties. Characterization methods, especially optical and electrical techniques, are reviewed and evaluated in terms of their utility in the study of nonaqueous colloids. Problems in the measurements of particle mobility, charge, particle-substrate forces, ionic concentrations and mobilities mainly due to space charge effects and electrohydrodynamics are also discussed. Based on colloid characterization, two classes of nonaqueous suspensions are distinguished. Colloids with intermediate conductivities correspond to physically adsorbed charge control agent (cca) which is in dynamic equilibrium with cca in solution. Low conductivity colloids have cca precipitated or chemically attached to the particle surfaces. The latter systems contain a few excess ions in solution and thus represent very non-classical colloids. Despite low dissociation of cca in nonaqueous media, high particle mobilities and charges are attainable. Aforementioned colloidal properties are related to liquid development of latent images and important characteristics of liquid ink are outlined. Also, effect of space charge and turbulence are assessed in liquid development of electrostatic images.

¹ Current address: Exxon Enterprises, Sunnyvale, CA 94086.

This paper is intended to review characterization methods of nonaqueous colloids, their physical properties and technological applications.

The description of a colloid should include particle size, mobility, charge and their distributions, charge/mass ratio, electrical conductivity of the media, concentration and mobility of ionic species, the extent of a double layer, particle-particle and particle-substrate interaction forces and complete interfacial analysis. The application of classical characterization methods to nonaqueous colloids is limited and, for this reason, the techniques best suited to these systems will be reviewed. Characteristic results obtained with nonaqueous dispersions will be summarized. Physical aspects, such as space charge effects and electrohydrodynamics, will receive special attention while the relationships between chemical and physical properties will not be addressed. An application of nonaqueous colloids, the electrophoretic development of latent images, will also be discussed.

Characterization Methods

The key parameters characterizing the colloid are particle mobilities and sizes. The most popular technique for mobility measurement is microelectrophoresis(1,2) in which the colloidal particles are allowed to move in a uniform electric field and their velocities are observed with an optical microscope. Measurements are limited to colloidal particles observable microscopically, which is above $\sim 0.1 \mu\text{m}$ with dark field illumination. When this technique is combined with light scattering detection-quasielastic(3,4) or crossbeam interference(5), particle velocities can be measured easily and the minimum detectable size is significantly reduced to $\sim 20\text{\AA}$. Application of these methods to aqueous colloids is straightforward because the suspending media generally have high electrical conductivity ($\sigma \geq 10^{-2} \Omega^{-1} \text{m}^{-1}$) and the electric field between distant electrodes is uniform. The same is true for high conductivity nonaqueous colloids.

In relatively nonconducting media ($\sigma \leq 10^{-4} \Omega^{-1} \text{m}^{-1}$), the electric fields are nonuniform and time varying in the standard microelectrophoretic geometries. The movement of particles is not rectilinear between electrodes, is not uniform, and the velocity is dependent on the position in the electric field(6,7) Mobility evaluation may not be possible even when the velocities are measured because the electric field in the measurement region may not be known. In addition, charged or uncharged particles with dielectric constant different from the suspending liquid move along the electric field gradients (dielectrophoresis or dielectric polarization(6,7)). Wide electrode separation requires higher applied voltages which may lead to turbulence in the colloid. Moreover, microelectrophoresis is

usually performed at low fields ($< 10^4$ V/m) while many technological applications require intermediate ($10^4 - 10^6$ V/m) or high ($> 10^6$ V/m) fields. The above deleterious effects and limitations can be precluded or at least considerably corrected for when planar electrode geometries are used. The set up demands parallel and closely spaced electrodes with linear dimensions which significantly exceed the electrode spacing. Mobility measurements were successfully performed with microscopic detection in planar geometries(8,9,10) for larger particles (> 5 μm dia.) at intermediate fields. However, it is difficult to apply microelectrophoretic methods in planar geometry to high fields and small particles and, therefore, alternative methods for mobility measurements were developed.

Optical transient techniques(11,12) are based on the detection of time dependent changes in the intensity of the light scattered from particles during their translational motion. The colloid is placed into the planar cell with one or two transparent electrodes. Monochromatic light is brought onto the cell and scattered or transmitted light is detected. The experiments can be performed in two basic modes - sweepout and transit. In the sweepout mode, the scatterers are initially uniformly distributed in the optical cell and are swept towards the electrode with the application of an electric field. In the transit experiment the charged particles are initially at one electrode in the non-dispersed state and then are driven with the field toward the opposite electrode. The removal time of particles from the electrode may be comparable with the transit time and for this reason the sweepout measurements will be emphasized here. When the suspending liquid contains contrasting medium which absorbs the monitoring light, the concentration of scatterers at and near the detection electrode can be measured with the backscattering geometry. Without an absorbing medium, optical transients rely on small multiple light scattering differences between the dispersed and non-dispersed states. This second method is an integral technique in which all particles contribute to the optical signal while the first method is differential as only scatterers at and near the observation electrode are detected. During sweepout the detected optical signal will increase for colloid containing scattering particles until all particle motion has ceased, at which point the signal will become time independent. The time dependence of the optical signal can be accounted for with simple models(11,12) and particle mobility determined.

Another optical technique useful for mobility measurements in planar electrode geometry is crossbeam velocimetry (5) in which the particles are allowed to drift through optical fringes created by two intersecting beams. The light scattered from the moving particles is then modulated in relation to the distance between fringes and the particle velocity. In a similar technique, light scattered by particles is passed through a grating

on a rotating disk(13). The resulting light intensity modulations have frequencies which are proportional to the particle velocities. Quasielastic light scattering velocimetry(3,4) has limited application with the planar geometry because a focused beam must pass through narrowly spaced electrodes, and the scattering wave vector cannot be perpendicular to the velocity vector.

Most colloids are polydisperse in terms of their particle size and charge and thus a single sample exhibits a distribution of mobilities. In principle the above mentioned techniques, in particular optical transients, quasielastic velocimetry in the frequency regime, crossbeam and rotating grating velocimetries, can measure the mobility distribution of a polydisperse colloid.

Electrical transients (12) can also be used to evaluate particle mobilities in special circumstances. Charged particles, their counterions and other excess ions present in the suspending fluid contribute to the electrical current. When the concentration of excess ions is very low compared to the concentration of counterions, it is sometimes possible to determine the current contributed by particles versus that contributed by ions. Ionic concentrations define the extent of double layers in colloids. Transient and AC conductivities can be related most directly to the ionic concentrations and mobilities. But, again, the measurements in low conductivity fluids have to be performed in planar cells with narrow electrode spacings in order to ensure well defined electric fields.

Colloidal particle size and shape can be evaluated directly by optical microscopy and by electron transmission or scanning microscopy. During preparation of samples for microscopy, agglomeration of particles often occurs, and thus it is important to complement microscopy with in-situ measurements. This can be done by a wide variety of optical techniques which include angular (14), low angle (15); and quasielastic light scattering(16,17). When colloidal particles settle gravitationally, a number of other optical methods can be used including optical transients, crossbeam and rotating grating techniques. Most of these methods can give particle distribution for spherical scatterers or average size and shape for relatively monodisperse scatterers. Polydisperse, nonspherical scatterers can be treated only approximately. The advantage of optical methods is that they can be used to follow the size stability of the colloid directly.

In most cases colloidal charges cannot be measured directly, but may be calculated knowing the particle size and mobility. Charge/mass, however, which is of technological interest, can be experimentally determined in the electrical plateout(18,19).

Initially charged particles and ions are uniformly distributed in the cell which contains a collection sheet covering one electrode. The particles and ions are swept out to the electrodes with the application of the electric field and the resulting current is recorded. In the plateout, particles remain at the electrode even after the applied field is removed due to adhesive (including van der Waals) and image forces. Integrated current gives a total collected charge, and the mass of plated-out particles on the collection sheet is determined gravimetrically. When the concentration of excess ions is relatively low and the colloid contains mainly the charged particles and their counterions, accurate measurements of charge/mass can be made.

Particle-wall and particle-particle interactions in the colloid can be evaluated by several techniques. For charged particles, the distribution of electric fields which are required to remove them from the wall can be readily obtained by optical methods(11,12). The removal fields together with particle charge, then yield the particle-wall forces which include electrostatic, van der Waals and steric forces. The most direct way of following particle-particle forces is to study the volume changes of the colloid caused by applied pressure (20) in an arrangement where liquid is allowed to escape freely.

The colloidal properties are controlled to a great extent by the species present at the solid-liquid interface. The vibrational spectra of the adsorbed or chemically attached species can be followed by infrared(21,22) or Raman(23) spectroscopy, usually on the centrifugate. Fluorescence of the high surface area substrates often prevents the use of Raman spectroscopy. The elemental composition of the surface can be obtained with ESCA (Electron Spectroscopy for Chemical Analysis or X-ray Photoemission), Auger (24) or X-ray fluorescence. In addition, the information on the chemical bonds can be recovered from the energy shifts in ESCA studies.

For colloids with a physically adsorbed surfactant or cca, the adsorption isotherm is important. The adsorbant concentration on the particle surface can be measured by infrared spectroscopy using diffuse reflectance and by ESCA. Absolute concentrations are difficult to determine with ESCA on "rough" surfaces, and a calibration point is required with other techniques. The change of the concentration of adsorbant in solution after adsorption on the colloid surfaces can be detected by elemental analysis of supernatant with plasma emission or atomic absorption if adsorbant contains specific element(s). When colloids are sterically stabilized, the effectiveness of the stabilization can be evaluated with solvent-nonsolvent techniques and with temperature studies (25,26).

Space Charge and Electrohydrodynamics

It is convenient to divide nonaqueous colloids into two categories - low and intermediate conductivity, which are schematically represented in Figure 1. Low conductivity (LC) colloids have very low concentrations of excess ions while intermediate conductivity (IC) colloids may have comparable concentrations of counterions and excess ions. Both LC and IC colloids are unlike aqueous systems in which the concentration of excess ions exceeds the concentration of counterions significantly.

The differentiation between LC and IC colloids can be made experimentally according to background conductivity which is measured immediately after all charged particles and their counterions are swept out from the dispersion and, therefore, do not contribute to the conductivity. Background conductivity, σ_b , is controlled by the concentration of ionic species generated by dissociation of neutral molecules in the bulk solution. The measurements should be performed under conditions in which charge injection from electrodes does not play an important role. Conductivities reflect the concentration, n_j , charges, q_j , and mobilities, μ_j , of all mobile species ($j = 1, N$) in the colloid and in a one dimensional case are given by:

$$\sigma(t) = \sum_{j=1}^N q_j \mu_j n_j(t) \quad (1)$$

When the electric field E in the colloid is uniform, the conductivities can be simply determined from the measured current densities I , as $\sigma = I/E$. The transition from LC into the IC regime can be somewhat arbitrarily set at $\sigma_b = 10^{-10} \Omega^{-1} m^{-1}$. LC colloids can be prepared by chemical attachment to the particles of charge control agent (cca) or other ionizable species or by irreversible physical adsorption of cca onto particle surfaces. Typical physically adsorbed colloids will have some cca remaining in solution at dynamic equilibrium and, as a result, will fall generally into the category of IC colloids.

Two effects which may be encountered during nonaqueous electrophoresis are space charge conditions and electrohydrodynamics (EHD). When an electric field is applied across a uniformly dispersed colloid the macroscopic charge density is zero and the field is uniform at the time of application. As the separation of opposite polarity charges occurs, a net internal

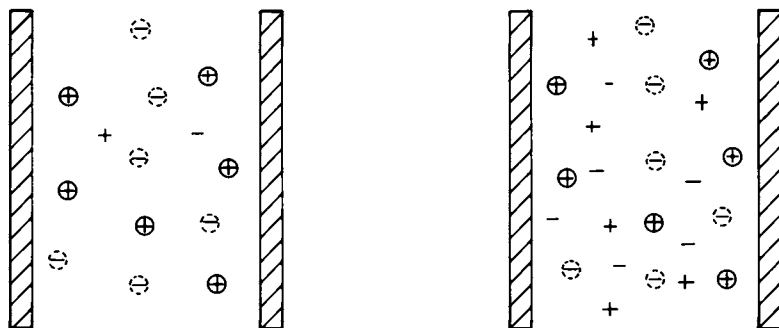


Figure 1. Schematic of low (left) and intermediate (right) conductivity nonaqueous colloids. Key: \oplus , positively charged particles; \ominus , counterions; +, positive excess ions; and -, negative excess ions.

charge distribution is created, which may lead to nonuniform, time varying electric fields in the colloid. This situation is referred to as "space charge limited" and is schematically represented in Figure 2. When ionic dissociation in the media or charge injection from the contacts is minimal, the condition can be characterized by a space charge parameter, s , defined as:

$$s = (Q/A) / \epsilon \epsilon_0 E \quad (2)$$

where ϵ and ϵ_0 are the permittivities of the media and a vacuum respectively. (Q/A) is the charge per unit area collected during plateout of charged particles and their counterions. Space charge effects are negligible when $s \ll 1$. For LC colloids, space charge effects can be avoided only at very low colloid concentrations and high electric fields. Due to ionic dissociation in the IC colloid, however, the uniform charge distribution is less perturbed and space charge conditions are less prevalent. In space charge conditions the transient conductivity can be evaluated at the moment an electric field is applied, $t = 0$, before bulk space charge develops, and AC conductivity can be measured at high frequencies ($f \geq \mu E/r$ where r is the particle radius).

The second important phenomenon which can be significant during electrophoresis is EHD(27), shown in Figure 3. This occurs when ions moving in the fluid drag along the fluid molecules and set up fluid motion, usually in the form of vortices. As a result of EHD, the apparent mobilities of ions and charged particles can be substantially higher than in the stationary fluid. In the colloid, EHD can be recognized easily because particles largely follow the fluid flow. The motion of charged particles is not colinear and many particles may move in different directions than expected from the polarity of their charge and direction of the field. When the charged particles are allowed to plate-out onto the electrode in the non-EHD regime, the deposit is uniform. During EHD, the plateout deposit is nonuniform and usually has features and dimensions corresponding to the size of the vortices. Charged particles tend to collect on the electrodes in relatively stationary areas where there is minimum fluid flow. At low voltages EHD is not present; at intermediate voltages (typically tens of volts) EHD is laminar with vortices of the size of the cell thickness while at higher voltages EHD is turbulent and vortices may be considerably smaller. The onset of turbulence is affected by many factors including the conduction mechanism, space charge effects, charge injection, type of transient, conductivities geometry and properties of the media. For unipolar conduction the threshold voltage V_C from laminar into the turbulent regime is roughly $V_C = 30 \eta / (\rho \epsilon \epsilon_0)^{1/2}$ or about 10^2 Volts for typical values of viscosity, η , and density, ρ .

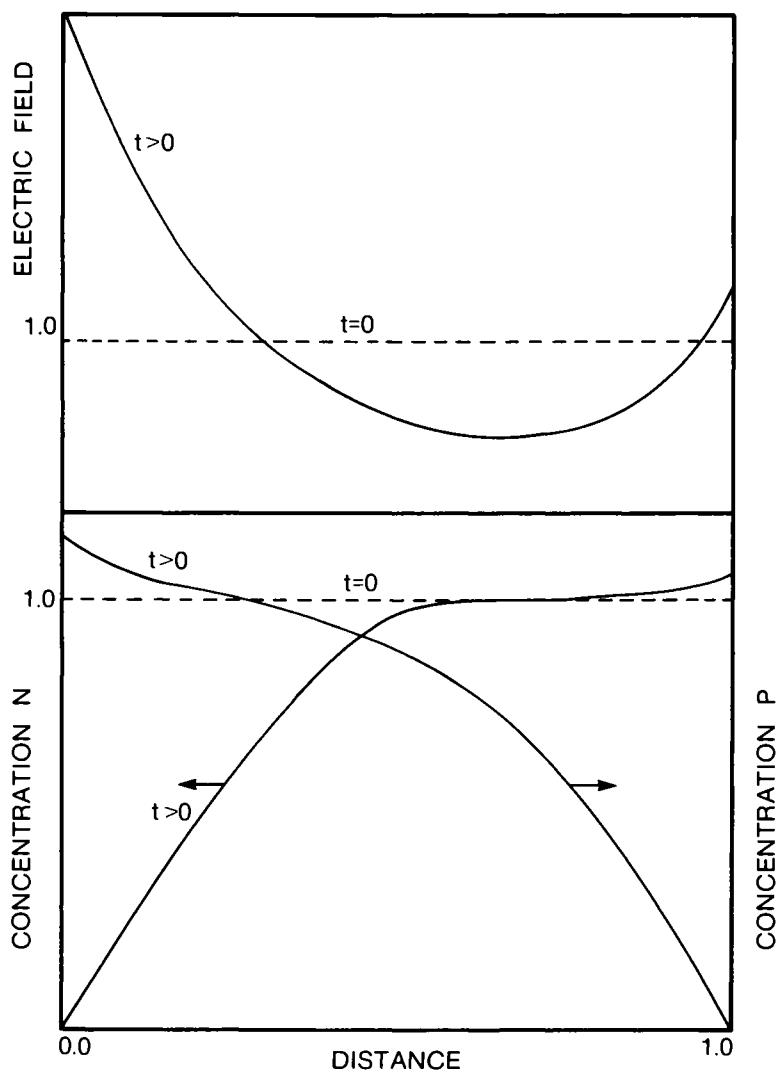


Figure 2. Representation of space charge limited conditions in one dimension showing the profile of concentrations of positive (P) and negative (N) species and electric field variations at time of the field application ($t = 0$) and at some later time ($t > 0$).

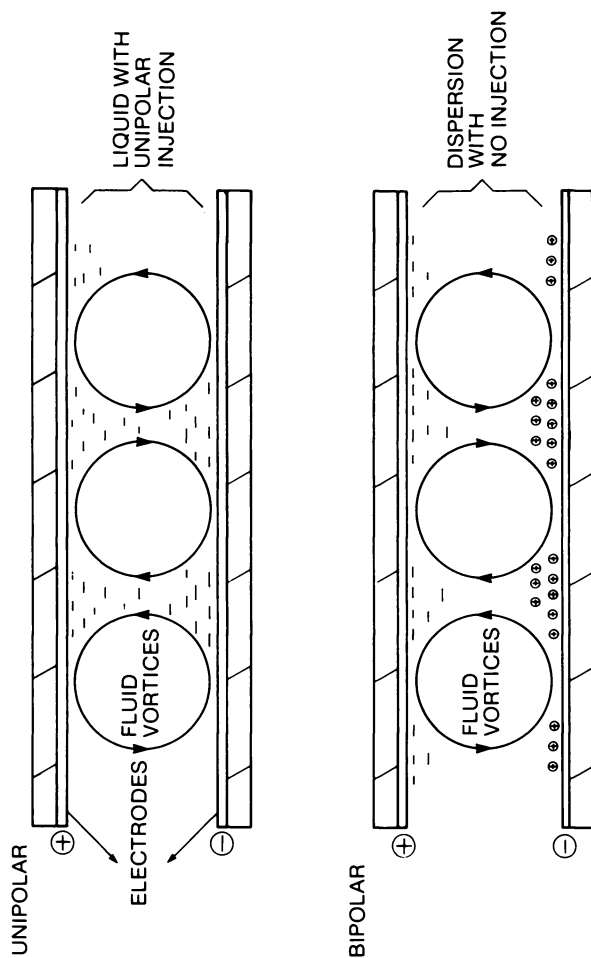


Figure 3. Schematic of electrohydrodynamic conditions in unipolar and bipolar conduction.

It is preferable to perform electrophoretic measurements without space charge and EHD effects, which is often difficult because high voltages (hundreds of volts) are required to avoid space charge conditions while lower operating voltages (tens of volts) are needed to prevent EHD. It should be emphasized that it takes time to establish EHD. It is anticipated that times longer than ionic transit times in the cell are needed to set up EHD motion. Space charge conditions can be described with numerical modelling and are more easily treated analytically than problems associated with turbulence. In some technological applications which are affected by space charge and turbulence, the apparent particle mobilities are relevant.

The relationship between particle charge, q , and mobility, μ , depends on the extent of the electrical double layer which is given by

$$\lambda = \kappa^{-1} = \left(\frac{\epsilon \epsilon_0 kT}{e^2 \sum_i n_i z_i^2} \right)^{1/2} \quad (3)$$

where n_i is the concentration of ions and z_i their valency, e is the electronic charge, k is the Boltzmann's constant and T is the absolute temperature. The ionic concentrations and mobilities can be determined from the analysis of electrical transients. When the double layers are extended ($\lambda \gg r$) relaxation and retardation effects (28) can be neglected. A particle with charge q moves with a uniform velocity v which is determined by the equality between the electric force qE and the Stokes friction force fv (where f is a friction coefficient equal to $6\pi\eta r$ for a spherical particle of radius, r , suspended in the media with viscosity, η). Thus, for a spherical particle in the LC colloid

$$q = 6\pi\eta r \mu \quad (4)$$

The corresponding relationship between the zeta potential, ζ , and mobility is

$$\mu = 2\epsilon\epsilon_0\zeta / 3\eta \quad (5)$$

Results

The typical results will be illustrated by one LC and one IC colloid. An example of an LC system (29) with background conductivities below $10^{-11} \Omega^{-1} m^{-1}$ will be carbon black dispersed in aliphatic hydrocarbon with polymeric materials and charged with a metal salt of stearic acid. Electron microscopy revealed that the particles are agglomerates in the

range of 0.1 - 0.8 μm , each composed of carbon black pigment as small as 0.03 μm . Due to the possibility of agglomeration in the preparation of microscopy samples, the particle size was determined by quasielastic light scattering. The auto-correlation function $C(\tau)$ is shown in Figure 4 together with an exponential fit giving the average diameter of $0.3 \pm 0.06 \mu\text{m}$. The method of cumulants (30) yielded a similar result. Nonsphericity of particles was neglected. Care was taken in these measurements not to induce thermophoresis. It demonstrates itself as excess motion of particles above their normal Brownian motion caused by the absorption of light by particles and the subsequent heating of particles and their surrounding fluid.

Electrical plateout gave a charge/mass ratio of $0.88 \pm 0.05 \text{ C kg}^{-1}$ and showed that the particles were unipolar and positively charged. Particle mobilities were determined by optical sweepout transients. For this colloid, a Maxwell, one parameter distribution provided a better fit of transients than Gauss, Gamma or Log-Normal distributions but no physical significance is assigned to it. The result in Figure 5 was obtained at an electric field of $0.8\text{V}/\mu\text{m}$, a cell thickness of 125 μm and a particle concentration of 15 ppm by volume. The corresponding space charge factor was $s = 0.15$. The average particle mobility obtained from the analysis was $0.305 \times 10^{-8} \text{ m}^2 \text{ V}^{-1} \text{ s}^{-1}$. Although the investigation was limited at low voltages by space charge effects and by electrical discharge across the cell at higher voltages, the mobility was studied as a function of field strength and was found to be independent of field. Most experiments at higher particle concentrations, lower applied voltages, and thicker cells than given above were in space charge limited conditions. The distribution of plated-out particles on the electrode was uniform in thin ($\sim 100 \mu\text{m}$) cells, indicating that turbulence was not important in these experiments.

The particle size was also calculated from (4) and charge/mass and was found to be $0.19 \pm 0.05 \mu\text{m}$. Differences between this estimate and the quasielastic light scattering value were probably due to nonsphericity of the particles. Using this size and applying (4) and (5) to this LC colloid gives $q = 56 \times 10^{-19} \text{ C} = 35$ positive unit charges and $\zeta = 250 \text{ mV}$. Ionic characteristics are evaluated from the electrical sweepout transient in Figure 6. The current density can be accounted for according to (1) by contributions from particles with the above mobilities and charges and with a counterion mobility $\mu_i = 0.4 \times 10^{-8} \text{ m}^2 \text{ V}^{-1} \text{ s}^{-1}$ and concentration $n_i = 1.3 \times 10^{17} \text{ m}^{-3}$. The double layer of LC colloid contains ions of mostly one polarity and the Debye length from (3) is indeed extensive $\lambda \approx 5 \mu\text{m}$.

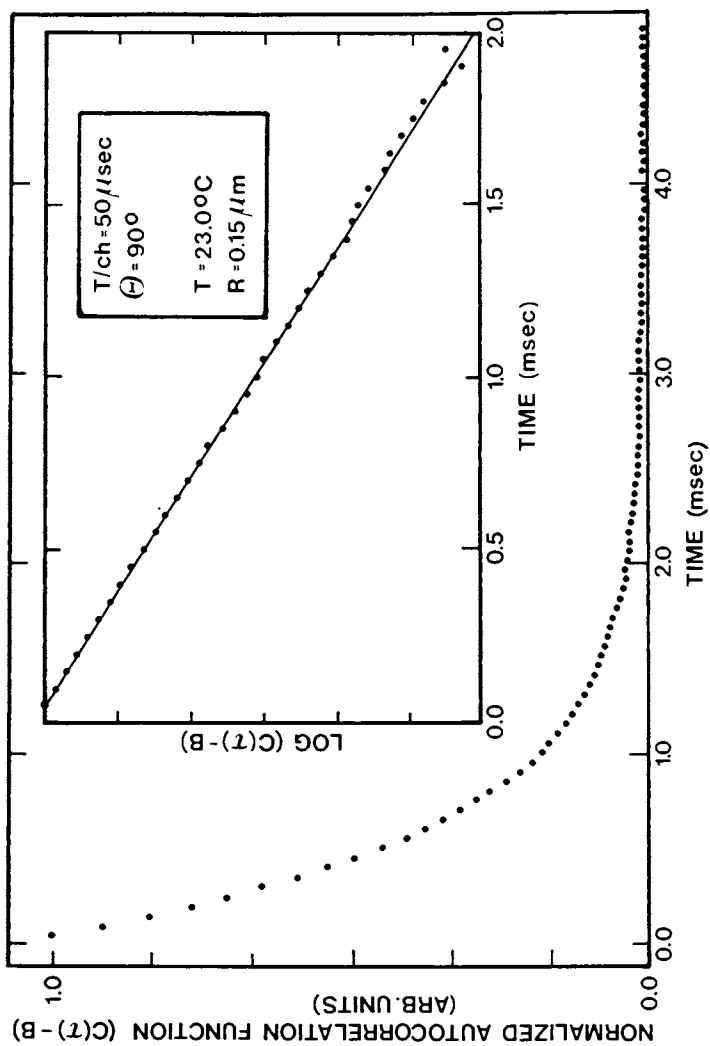


Figure 4. Autocorrelation function $C(\tau)$ after subtraction of background B and $\log(C(\tau)-B)$ with a solid line indicating the fit to the data.

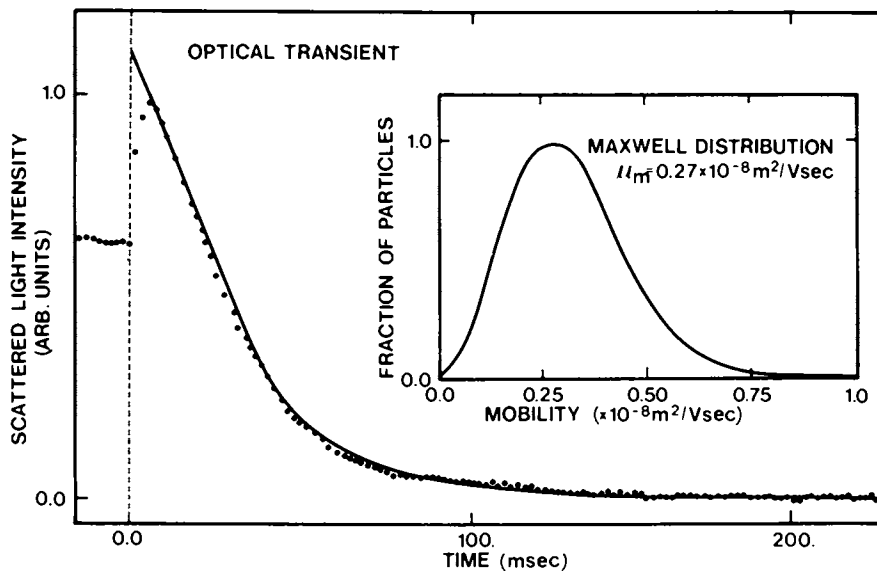


Figure 5. Optical transient from LC colloid and the mobility distribution used to provide a fit (solid line) to the experimental data. (Reproduced, with permission, from Ref. 29.)

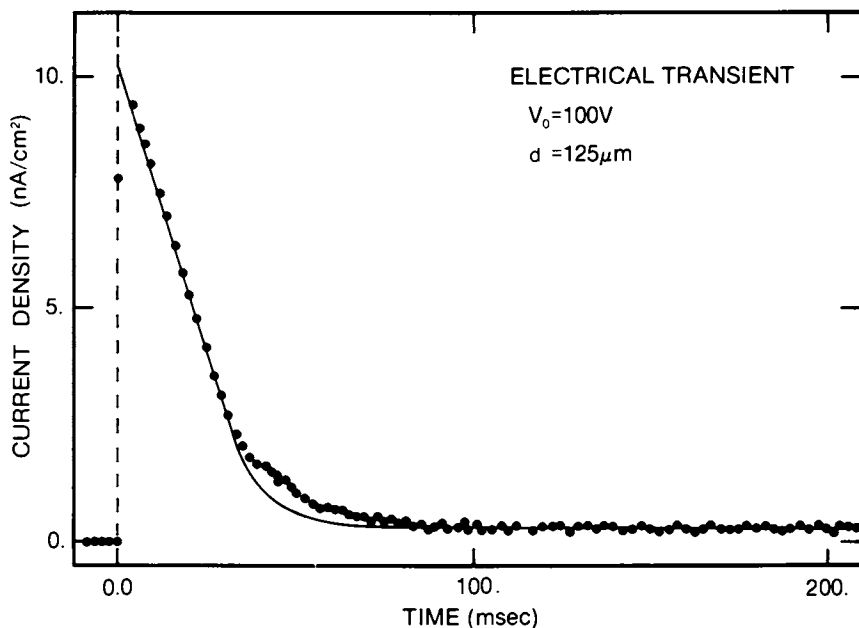


Figure 6. Electrical transient from LC colloid corresponding to the optical transient in Figure 5. Solid line is based on calculations using an estimate of ionic mobility and the particle mobilities determined by optical transients. (Reproduced, with permission, from Ref. 29.)

It appears that many of the results from similar LC systems reported in the literature (31,32,33) were unknowingly obtained under space charge limited conditions.

For a discussion of IC colloid properties a dispersion of inorganic oxide in aromatic hydrocarbon is selected. It is stabilized and charged with a cca, metal sulfonate, which is physically adsorbed on the oxide surfaces and is in equilibrium with some cca in solution. The concentration of cca in solution controls the background conductivities which are around $5 \times 10^{-10} \Omega^{-1} \text{m}^{-1}$. The adsorption isotherm of cca was determined by four techniques as shown in Figure 7. The "parking" area of the cca molecule as determined from a monolayer coverage is $\sim 70 \text{\AA}^2$. The average particle size plotted in Figure 8 as a function of cca concentration decreases initially with increasing cca concentration and stabilizes at high concentrations. Interestingly, the particle size dependence parallels the adsorption isotherm very well; i.e., the particle size becomes independent of the cca concentration at approximately a monolayer coverage implying that cca acts as steric and/or electrostatic stabilizer. The changes of particle mobility with cca concentration are shown in Figure 9 for this system together with another typical nonaqueous system. The concentration at which mobility reaches a maximum or saturates generally coincides with a monolayer coverage of cca. Surprising results are obtained when the mobility at a given cca concentration is examined as a function of the electric field. The mobility increases with increasing field at least within the range of 0.1 to 4.0V/ μm . Similar results were found in very different IC dispersions.

The summary of colloidal properties at a monolayer coverage of cca is as follows: At high fields, (3V/ μm), where equations (4) and (5) are applicable, the charge is $4.3 \times 10^{-17} \text{ C}$. The mobility does not vary with particle size. Electrical transients are dominated by cca in solution except at high particle concentrations and, therefore, cannot be used to estimate mobilities and sizes of particles. The concentration of ions is $2 \times 10^{18} \text{ pairs/m}^3$, and the mobility of the positive and negative ions is about 0.9 and $0.7 \times 10^{-8} \text{ m}^2 \text{ V}^{-1} \text{ s}^{-1}$ respectively, and the Debye length is $\lambda = 1.3 \mu\text{m}$. The average electric field necessary for the removal of a charged particle from the electrode is 0.6V/ μm , and the corresponding total particle-wall interaction force (34) is $0.7 \times 10^{-10} \text{ N}$. In IC colloids, space charge conditions cannot be simply determined from an expression (2) and numerical modelling is required. Modelling indicates that the presence of ionic dissociation in the bulk solution relaxes the space charge effects but that they do become important at fields below 0.1V/ μm even at low particle concentrations. The onset of turbulence is directly observable above

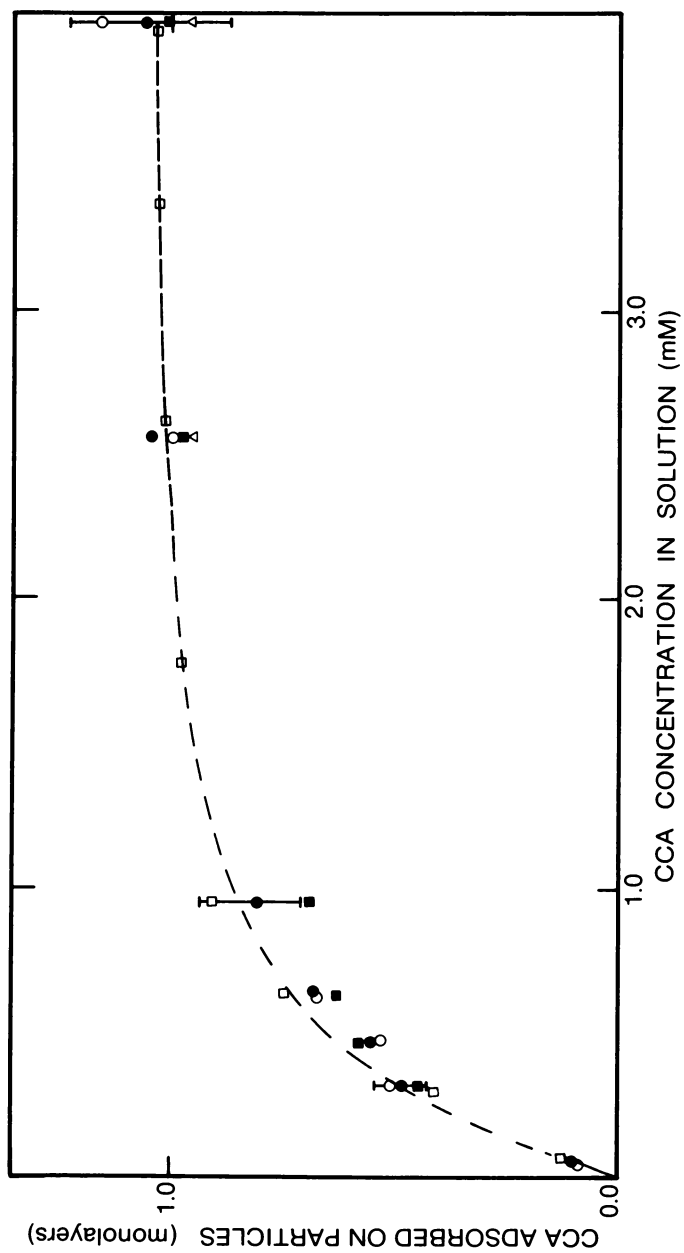


Figure 7. Typical adsorption isotherm of charge control agent on oxide particles in nonaqueous media. Key: ● and ○, atomic absorption; ■, electrical conductivity; △, IR absorption; and □, ESCA.

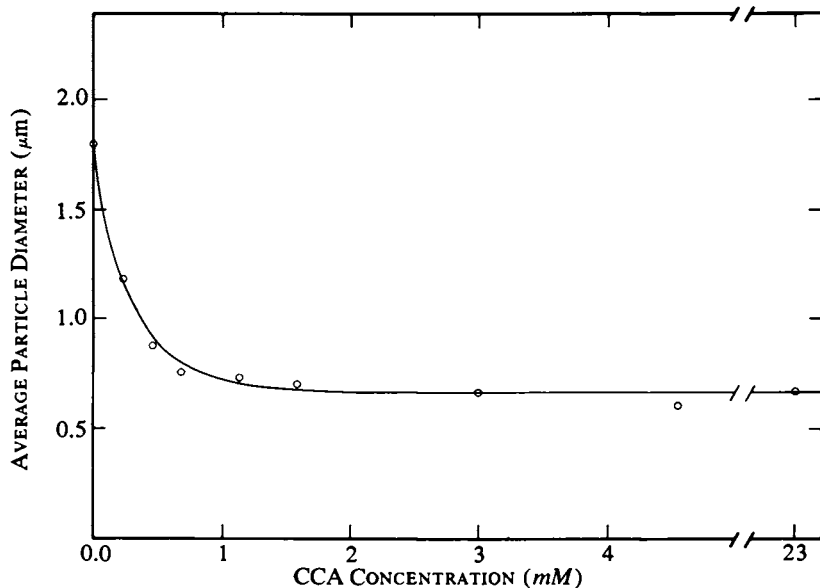


Figure 8. Dependence of average particle size on the concentration of charge control agent in nonaqueous media.

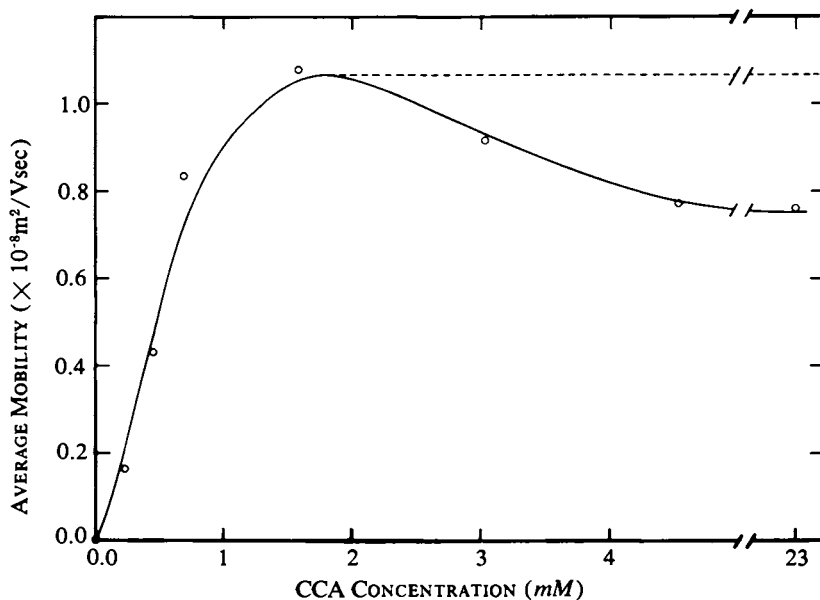


Figure 9. Two typical dependencies of mobility on the concentration of charge control agent in nonaqueous media.

50V in dispersions with high particle concentrations (above 1% by volume). Detectability is more difficult at low particle concentrations (<1000ppm) but the particle mobilities do not undergo sudden changes of magnitude or slope in the investigated range of voltages. Also, ionic mobilities determined from the electrical sweepout transients are independent of field. Field induced ionization of cca was not observed in solutions and, thus, it is unlikely to be responsible for the field-dependent mobility of particles. Increases of particle mobility and charge with field can be related to the removal of counterions from the double layer within the slippage plane(10,11,12). This interpretation would suggest that at very high fields the mobility should saturate when all counterions have been removed from the volume within the slippage plane. Presumably these conditions have not been reached in this experiment. Electrical breakdowns prevented the measurements at high voltages above ~ 500V (Figure 10).

Results reported here are characteristic for IC colloids(35-38). Similar adsorption isotherms were obtained for metal octoates on carbon black and metal sulfonates on phthalocyanines. Mobilities often exhibited maxima as a function of cca concentration. In other cases particle mobilities decreasing with, or independent of, cca concentration were reported, possibly due to the fact that the behavior at the lowest cca concentrations was not investigated. At low concentrations, below a monolayer of cca coverage, the mobility should increase as the concentration of cca molecules on the particle surface increases until the monolayer is reached. At concentrations above a monolayer, increased ionic concentrations in solution may lead to higher concentrations of counterions within a slippage plane of the double layer and to decreased charge and mobility. The magnitude and sometimes even the polarity of particle charge is dependent upon the concentration of water or other polar impurities in nonaqueous media (35,36). In several systems, intermediate water concentrations (~ 100 ppm) lead to a maximum particle charge. Water increases dissociation of ionizable species in nonaqueous media and, thus, the mechanism for optimum charging with various water concentrations may be similar to the one outlined for cca dependence.

For both LC and IC colloids, it was demonstrated that highly charged colloids are possible even in nonaqueous media. When the fraction of ionized molecules on the particle surface is compared with the total number of adsorbed molecules on the surface, it is found that approximately 1 out of 10^4 adsorbed molecules is ionized. The low dielectric constant of these media compared with water is primarily responsible for a low dissociation rate of the ionizable molecules. The fact that the dissociation in the solution is also low ensures that high concentrations of ions are not available to effectively screen the particle charge and high charges or zeta potentials are attainable.

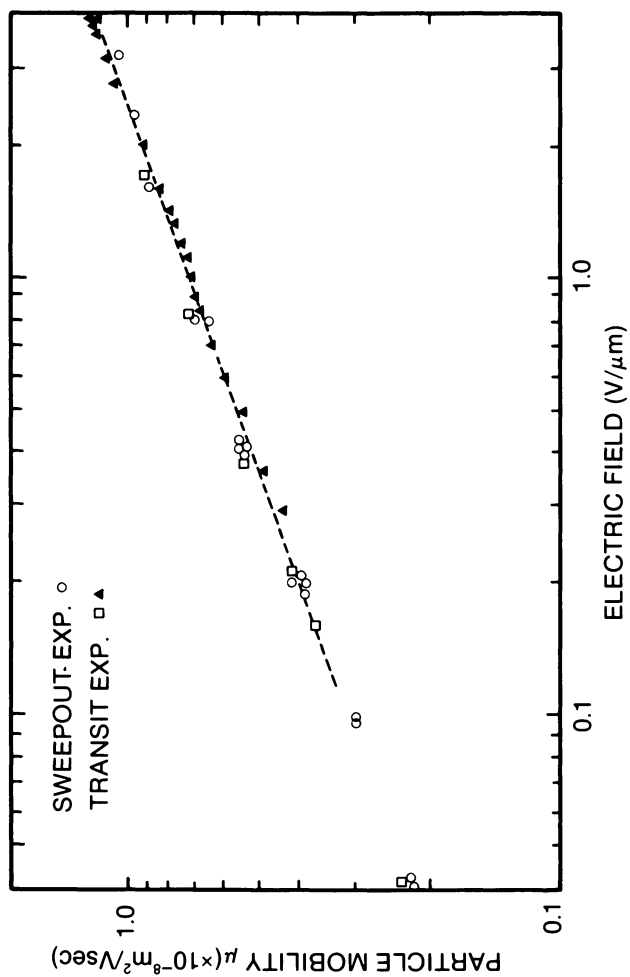


Figure 10. Dependence of particle mobility on the applied electric field. (Reproduced, with permission, from Ref. 12.)

With high particle charges and low ionic concentrations, electrostatic repulsion (39,40) alone should be capable of stabilizing the colloid. This typically occurs when surface potentials are around 100mV. Steric stabilization (41,42) in nonaqueous media is important to achieve stability in weakly charged systems. Direct experimental measurements of particle-particle forces or potentials in nonaqueous media are not yet available.

Applications

Nonaqueous dispersions have been used in a number of interesting technological applications, such as the electrophoretic development of latent images, electrophoretic displays, the deposition of special coatings and particle contaminant removal from nonaqueous media. Only liquid development of latent electrostatic images will be discussed here. These images can be formed by a number of processes. These include the standard light or x-ray exposure of a charged photoconductor and electrographic processes. In electrography, breakdown due to the application of a high voltage between a stylus and a conductor covered with a dielectric deposits a charge on the dielectric.

Liquid developers first demonstrated by Metcalfe(43) have to satisfy a number of requirements. The concentration of excess ions has to be very low, otherwise ions of the same polarity as particles will be effectively competing with particles for the development of the electrostatic image. This implies that liquid developers should be LC colloids. For fast development of images with high latent charge density, the colloid should have high charge/mass and mobility. For development of low charge densities (e.g., x-ray generated) where slow development is acceptable, the colloids should have low charge/mass and mobility. In order to achieve high spatial resolution, the particle size should be submicron. The colloid should adhere well to the substrate in both the liquid and dry states and should be self-fixing. Stability of size and charge is also very important.

The typical configuration for liquid development is shown in Figure 11. A liquid developer is contained between a charged dielectric plate and a development electrode. Normal electrostatic attraction between charged particles and the image is aided with development fields driving particles towards the image. If the space charge effects are ignored and the main parameters given in the result section are known, a simple model (44) can predict the discharge or development of the image. The model consists of the expression for the electric field in the dispersion and the discharge of the surface by a current of charged particles. The surface voltage $V(t)$ is

$$V(t) = V_b + (V_0 - V_b) e^{-t/\tau} \quad (6)$$

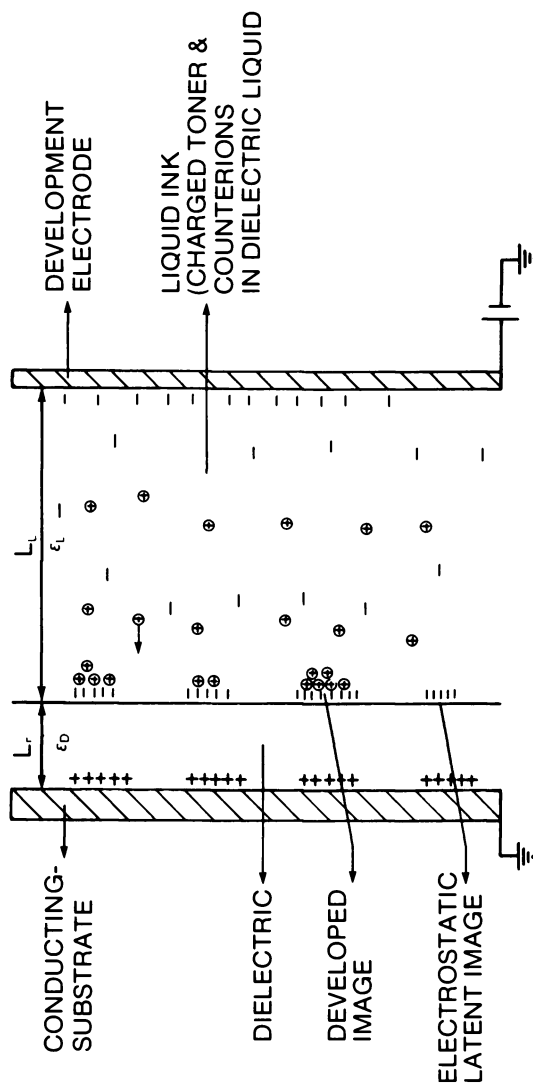


Figure 11. Typical configuration of liquid development of latent electrostatic images.

where V_0 and V_b are initial and bias voltages. The time constant

$$\tau = \frac{\epsilon_0}{nq\mu} \left(\frac{L_L \epsilon_D}{L_D} + \epsilon_L \right) \quad (7)$$

is dependent upon dielectric constants of the substrate, ϵ_D and the dispersion, ϵ_L , thickness of the dielectric, L_D , distance between charged surface and development electrode, L_L , and inversely proportional to the number density, n , charge, q , and mobility, μ of the ink particles.

The space charge factor s from (2) exceeds 0.3 at normal development densities 0.1-1.0 g/m² and wide range of charge/mass, 0.01-5C/kg, even at high development fields provided by $(V_0 - V_b) \approx 200V$ across a gap of $L_L = 1mm$. Charged particles will migrate in a nonuniform field and concentration gradients will be set up, causing back diffusion. The electrically driven motion will dominate when the field $E \gg D/\mu L$, where D is the diffusion coefficient. For typical values of r and μ the inequality is satisfied by several orders of magnitude even when the field is severely reduced due to space charge. This shows that diffusion can be neglected while space charge effects have to be included in a meaningful model. A mathematical model (45), consisting of equations of motion for charged particles and counterions, Poisson's equation and Gauss' law, has been developed. The model can predict the development of the image as shown in Figure 12. The main parameters in the model are particle charge and the ratio of particle to ionic mobilities. The graph compares the zero space charge prediction with a complete model. The realistic model predicts more complete development for shorter development times than the simplified model. For longer development times, the same occurs at low development voltages but the reverse is true at high voltages. A complete study of optimum development conditions can be performed with the realistic model which considers the effects of input voltage, initial charge densities, development time, electrode spacings and dispersion parameters. It should also be noted that turbulence is often present in liquid development and that this may affect or control development characteristics.

The development of electrostatic images can be achieved with either liquid or dry processes. Liquid developer usually provides higher resolution due to its smaller particle size. Images with low electrostatic densities can be developed with liquid inks which can have charge/mass much lower than dry powders. Liquid toners are often self-fixing and allow a simpler development system. Color printing with successive imaging and developments is also feasible. Disadvantages of liquid development compared with dry development include solvent carry-over, higher optical background and lower imaged optical densities. Application tradeoffs usually determine the desirable method of image development.

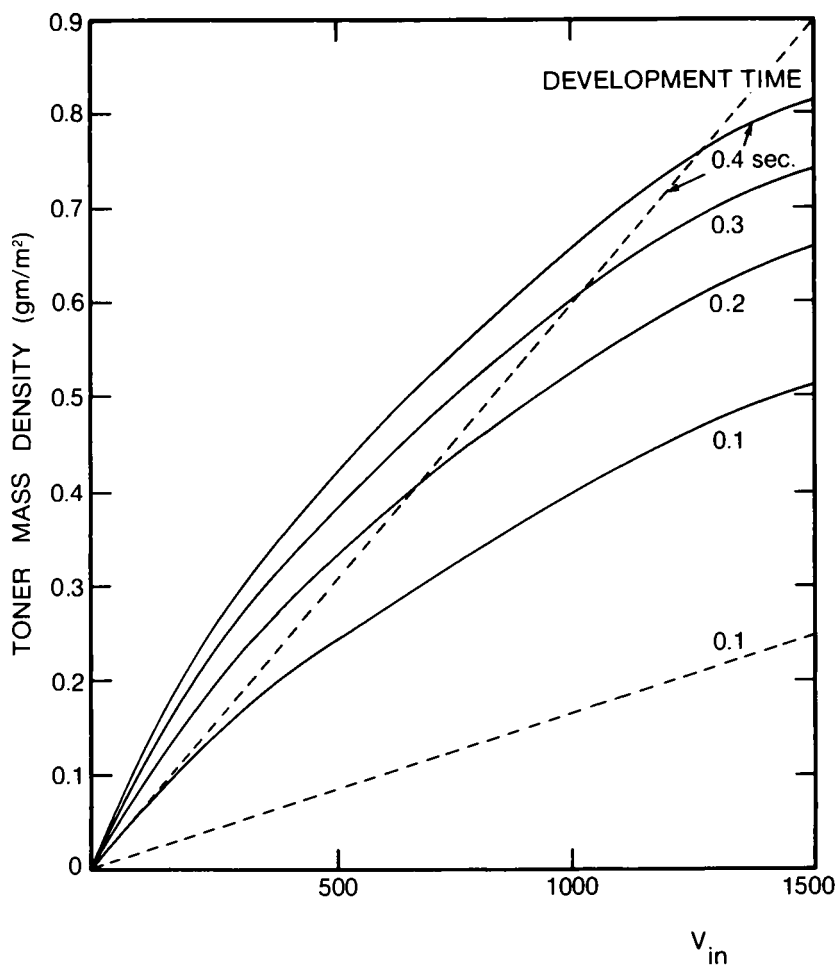


Figure 12. Development of electrostatic images as a function of the applied initial voltage with development time as a parameter. Key: —, space charge included; and ---, space charge not included. (Reproduced, with permission, from Ref. 45.)

Acknowledgments

Thanks are due to Dr. J. Becker and Dr. D. Zwemer for helpful discussions.

Literature Cited

1. Bier, M., Ed.; "Theory, Methods and Applications"; Academic Press: New York, 1967.
2. Shaw, D. J.; "Electrophoresis"; Academic Press: New York, 1969.
3. Ware, B. R.; Flygare, W. H. Chem. Phys. Lett. 1971, 12, 81.
4. Uzgiris, E. E. Rev. Sci. Instrum. 1974, 45, 74.
5. Watrasiewicz, B. W.; Rudd, M. J. "Laser Doppler Measurements"; Butterworths: London, 1975.
6. Pohl, H. A.; "Dielectrophoresis"; Cambridge Univ. Press: Cambridge, 1978.
7. Van der Minne, J. L.; Hermanie, P. H. J. Colloid Sci. 1952, 7, 690.
8. Kuo, S.; Osterle, F. J. Colloid Interface Sci. 1967, 25, 421.
9. Harris, L. B. Rev. Sci. Instrum. 1969, 40, 905.
10. Stotz, S. J. Colloid Interface Sci. 1978, 65, 118.
11. Novotny, V. J. Appl. Phys. 1979, 50, 324.
12. Novotny, J. J. Appl. Phys. 1979, 50, 2787.
13. Goetz, P. J. "Automated Electrokinetic Analyzer"; Pen Kem Inc.
14. Kerker, M.; "The Scattering of Light"; Academic Press: New York, 1969.
15. Kaye, W.; Havlik, A. J. Appl. Optics. 1973, 12, 541.
16. Berne, B. J.; Pecora, R. "Dynamic Light Scattering"; Wiley, New York, 1976.

17. Cummins, H. Z; Pike, E. R., Ed.; "Photon Correlation and Light Beating Spectroscopy"; Plenum Press: New York, 1974.
18. Dahlquist, J. A.; Brodie, I. J. Appl. Phys. 1969, 40, 3020.
19. Novotny, V.; Hair, M. L.. J. Colloid Interface Sci. 1979, 70, 273.
20. Homola, A.; Robertson, A. A. J. Colloid Interface Sci. 1976, 54, 286.
21. Hair, M. L.; "Infrared Spectroscopy in Surface Chemistry"; M. Decker: New York, 1967.
22. Little, L. H.; "Infrared Spectroscopy of Adsorbed Species"; Academic Press: New York 1966.
23. Chang, R. K.; Furtak, T. E., Ed.; "Surface Enhanced Raman Scattering"; Plenum Press: New York, 1981.
24. Kane, P. F.; Larrabee, G. B., Ed.; "Characterization of Solid Surfaces Plenum Press, New York 1974.
25. Napper, D. H. J. Colloid Interface Sci. 1977, 58, 390.
26. Vincent, B. Adv. Colloid Interface Sci. 1974, 4, 193.
27. Felici, N. J. J. Electrostatics. 1978, 4, 119.
28. Wiersema, P. H.; Loeb, A. L.; Overbeek, J. Th. G. J. Colloid Interface Sci. 1966, 22, 78.
29. Novotny, V. Colloids and Surfaces. 1981, 2, 373.
30. Koppel, D. E. J. Chem. Phys. 1972, 57, 4814.
31. Van Engeland, J.; Verlinden, W.; Marien, J.; Palmans, W. Internat. Congress for Reprography and Information, 1975, 117.
32. Halfdanarson, J; Hauffe, K. Photogr. Sci. Eng. 1979, 23, 26.
33. Kohler, R.; Giglberger, D.; Bestenreiner, E. Photogr. Sci. Eng. 1978, 22, 218.

34. Hartmann, G. C.; Marks, L. M.; Yang, C. C. J. Appl. Phys. 1976, 47, 5409.
35. McGown, D. N. L.; Parfitt, G. D.; Willis, E. J. Colloid Sci. 1965, 20, 650.
36. Cooper, W. D.; Wright, P. J. Chem. Soc. Faraday Trans. I. 1974, 70, 858.
37. Vijayendran, B. J. ACS Symposium Series No. 9, Colloidal Dispersions and Micellar Behavior 1975, 211
38. Parreira, H C.; J. Colloid Interface Sci. 1973, 43, 382.
39. Verwey, E. J. W.; Overbeek, J. Th. G.; "Theory of the Stability of Lyophobic Colloids"; Elsevier: Amsterdam, 1948.
40. Hamaker, H. C. Physica 1937, 4, 1058.
41. Ottewill, R. H. Kolloid Z. Polymers 1968, 227, 108.
42. Flory, P. J. "Principles of Polymer Chemistry"; Cornell U. Press: Ithaca, 1971.
43. Metcalfe, K. A. J. Sci. Instrum. 1955, 32, 79, 1956, 33, 194.
44. Schaeffert, R. M. "Electrophotography"; Focal Press: London, 1965.
45. Roselman, I. C.; Tait, W. SPSE Conference, Washington, 1977.

RECEIVED April 7, 1982

Mechanism of Electric Charging of Particles in Nonaqueous Liquids

F. M. FOWKES, H. JINNAI¹, and M. A. MOSTAFA²

Lehigh University, Bethlehem, PA 18015

F. W. ANDERSON³ and R. J. MOORE

Shell Development Company, Houston, TX 77001

In liquids of low dielectric constant, dispersants tend not to form ionic species in solution, but can form ions in adsorbed films on particle surfaces where acid-base interactions and proton transfer occurs between the particle surface and the dispersant. Particle potentials develop when adsorbed dispersant ions desorb into the organic medium where they become the counter-ions. Zeta-potentials well over a hundred millivolts result from the stronger acid-base interactions. Debye lengths in concentrated dispersions are typically 5 to 20 nm, and the DLVO energy barriers often exceed 25 kT with stability ratios of 10^3 or more.

The electrostatic charges on suspended particles or droplets in water which tend to stabilize them against flocculation or allow them to be electrodeposited are generated either by dissociation of ionic groups on the surface of particles or by preferential adsorption of ions from solution onto the particle surface. Both of these mechanisms are rather well understood. However when the suspending liquid is an organic liquid of low dielectric constant, such as a hydrocarbon, the nature of the charging mechanism and of the charge-carrying species dissolved in the organic liquid is so little known that there is wide-spread skepticism concerning the importance of electrostatics in organic media. Fortunately, those participating in this symposium are not among the skeptics because they are familiar with electrodeposition of toner particles from suspensions in hydrocarbons, but there is a need to know more about how these electrostatic charges develop.

For over thirty years it has been known that particles of inorganic pigments dispersed in hydrocarbons develop appreciable electric potentials. The early studies of van der Minne and

¹ Current address: Maruzen Oil Company, Japan.

² Current address: American Hoechst Corporation, Leomister, MA 01459.

³ Current address: IBM, Hopewell Junction, NY 12533.

Hermanie (1) (2) showed how electrophoretic measurements could be made on suspensions of carbon black in benzene, and demonstrated that dispersants stabilize dispersions only when appreciable zeta-potentials resulted. Stable suspensions resulted with positive zeta-potentials obtained with a calcium alkylsalicylate or with negative zeta-potentials obtained with a tetraalkyl ammonium picrate, but low zeta-potentials and unstable suspensions resulted when the two dispersants were both present. This mutual antagonism of the positive-charging and negative-charging dispersants is very strong evidence that these dispersants function by the electrostatic mechanism. Although the nature of the oil-soluble ions was not demonstrated in these studies, the importance of electrostatic charging in hydrocarbon solutions was established.

Electrostatic Charge Generation by Lubricating Oil Dispersants (3). Following a year with van der Minne (in Amsterdam) the author, together with coworkers F. W. Anderson and R. J. Moore, studied the charging of carbon black suspensions in mineral oil as a function of dispersant structure. Two kinds of dispersants were studied; oil-soluble micelle-forming metal alkyl aryl sulfonates, and oil-soluble copolymers of long-chain methacrylates or alphaolefins with acidic or basic co-monomers.

Materials. The micellar dispersants, some of which are referred to as heavy-duty dispersants, included dinonylnaphthalene sulfonates, tri-hexyl benzene sulfonates, and petroleum sulfonates. All of these form micelles at very low concentrations, on the order of one ppm or less. It was found, by using the Hammett acidity indicators (4), that the so-called "neutral sulfonates" are acidic, the acid strength increasing to rather high values in the order Na^+ , Ba^{++} , Ca^{++} , Mg^{++} , Zn^{++} , Cr^{++} , Al^{+++} (5). Basic micelles were obtained with basic sulfonates such as $\text{Ca}(\text{OH})\text{RSO}_3$ which give the deep blue violet color of pH 10 or more with Brom Phenol Magenta E (EK 6810). These micelles have twenty or more sulfonate anions per micelle with a central core of anions and cations, nearly as concentrated as a molten salt (6). It is the central cores of these "inverse" micelles which are the strongly acidic or basic regions in dispersant solutions.

The polymeric dispersants included random copolymers of long chain alpha olefins or long chain methacrylates with acidic or basic co-monomers such as vinyl acetate, vinyl alcohol, vinyl pyridine, vinyl pyrrolidone, hydroxyethyl methacrylate, etc. The alpha-olefin vinyl acetate copolymers had molecular weights in the 1-25,000 range and the methacrylates were in the 100,000 + range. All were oil soluble and reduced the oil-water interfacial tension appreciably.

Electrodeposition Tests. White oil solutions of the above dispersants were tested for charging of carbon black particles generated from the soot of a toluene flame. A hundred volts

potential was imposed between two electrodes about two centimeters apart, and after sixteen hours the percentage of deposited carbon on each electrode was estimated. Most experiments were done with electron microscope grids for electrodes and the percentage deposited was estimated from transmission electron micrographs. Because of inhomogenities in the surface chemistry of the carbon particles not all particles are equally charged so that there is always a distribution of particle potentials. If the centrum of potential distribution lies at high negative potentials a very small percentage of deposited carbon appears on the cathode, while if the centrum of potential distribution is at neutrality equal percentages of deposited carbon particles appear on the anode and cathode.

The results of electrodeposition tests are shown in Table I, in which the acidic or basic characteristics of dispersants are related to the location of the centrum of particle potentials. It can be seen that acidic dispersants provided positive potentials and that basic dispersants provided negative potentials. This is also true for the work of van der Minne and Hermanie; the calcium alkyl salicylate is weakly acidic because of the calcium ions and the quaternary ammonium picrate is weakly basic because of the basicity of the picrate anions.

It should be noted that in certain respects the relation of sign of charge to the acidity or basicity of dispersants is the opposite of what is observed in aqueous systems in which a surface active acid dissociates to give an adsorbable anion that can provide negative particle potentials, and a surface active base can become protonated to give an adsorbable cation that can provide positive particles potentials.

The explanation for the negative potential with basic dispersants and positive potential with acidic dispersants in liquids of low dielectric constant is that the charge separation occurs initially on the particle surface where hydrogen ions are transferred from acidic to basic sites in a region which may well have a higher dielectric constant than the liquid medium. Thus the hydrogens of the acidic sites on carbon black transfer to the basic nitrogens of pyridine groups in adsorbed pyridine-containing polymeric dispersants. The second step required for particle charging is desorption of the proton-carrying polymer off into the solution, leaving a negative charge on the particle. This mechanism is illustrated in Figure 1.

Detailed proof of this mechanism was achieved by using carbon-14 tagged copolymers of long chain methacrylates with vinyl pyridine. Carbon black dispersions stabilized with the tagged polymer were electrodeposited and then anode and cathode were assayed for carbon-14 in a scintillation counter. The carbon was deposited on the anode, but the clean cathode had the higher C-14 count, showing that the cations in the oil phase were indeed the dispersant polymer. The adsorption-desorption process which allowed dispersants to desorb from particles and to

Table I

Results of Electrodeposition Measurements

Additive	% of Deposited Particles on Positive Electrode	Stability Days	Disper- sancy
Pyridine-containing polyalkylmethacrylate	100	> 50	Good
Acryloid 917 (contains pyrrolidone)	100	> 50	"
OLOA 1200 (contains amines)	100	> 50	"
LOA 565	99.9	> 50	"
Basic Calcium Petroleum Sulfonate No. 1	99.9	> 50	"
Basic Calcium Petroleum Sulfonate No. 2	99.9	> 50	"
Cetyl alcohol	95		None
Tween 18	90		"
Dodecylamine	80	3	"
Acetic acid	50	2	"
Acryloid 618 (Polyalkyl methacrylate)	15	1	"
Polylaurylmethacrylate	20	2	"
Oleic acid	15	2	"
Ca dinonylnaphthalene sulfonate	1	1	"
Ditolylphosphoric acid	1	0	"
Dilauryl phosphoric acid	1	1	"
Paratone 460 (contains carboxylic acid)	0.1	> 50	Good

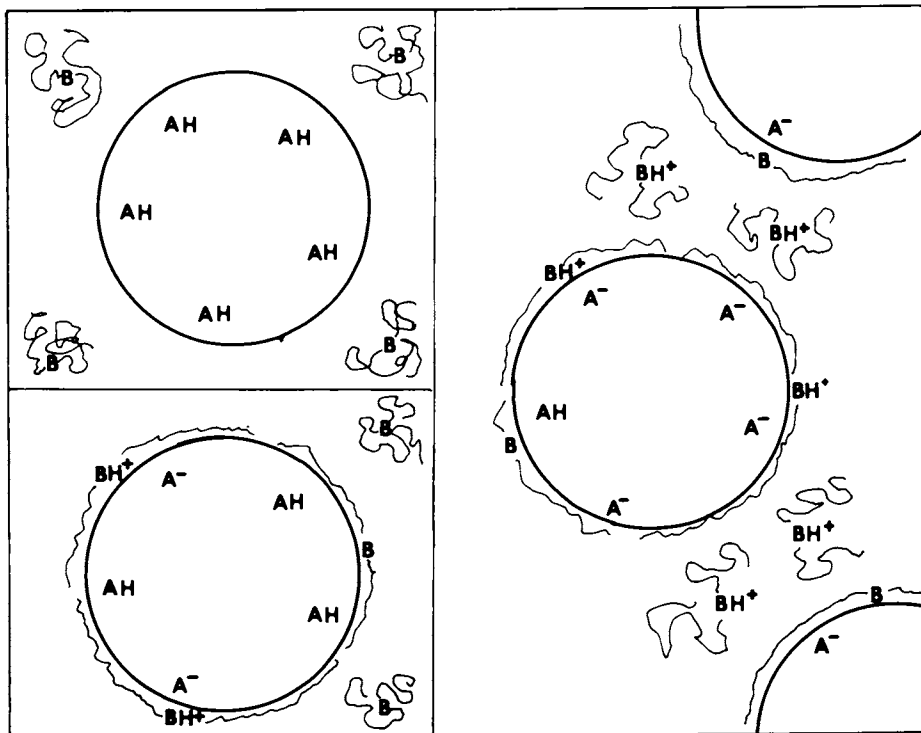


Figure 1. Mechanism of electrostatic charging of suspended acidic particles (with acidic sites AH) by basic dispersants (with basic sites B) in solvents of low dielectric constant (28).

carry protons into the oil, where they become counter-ions, was also studied with the C-14 tagged dispersant and with an identical, but untagged dispersant. First the tagged dispersant was adsorbed onto carbon black and after processing by sedimentation in a centrifuge, decantation and replacement with oil to remove all of the dispersant that would desorb, the carbon black was re-dispersed in oil with untagged dispersant. The tagged dispersant was found in the oil phase within a few minutes, showing that although rinsing with solvent did not displace an adsorbed polymer, adsorption of fresh (untagged) polymer could displace the firmly adsorbed tagged polymer.

Several simple but illuminating studies were made with the electrodeposition cell. After a few hours of applied potential carbon black built up on the anode, but a clear space built up around the cathode which was free of carbon black particles. Switching the leads between the two electrodes caused the clear region (a space-charge region) to move very rapidly to the new cathode; this clear region kept its shape during this movement. Some of the liquid from the space-charge region was pipetted out and bottled. When carbon particles were added to the oil in these bottles they immediately moved to the outer wall, indicating they had adsorbed polymer ions, became positively charged and were repelled to the outer walls. Even after a week much of the original space charge remained in this oil, showing that charge neutralization is slow indeed in such a poor conductor.

In another electrodeposition experiment the conductivity was measured, C-14 dispersant transfer was determined, and a particle count was made by TEM on the anode. From these measurements it was found that there was one electronic charge transported for each dispersant molecule on the cathode, and one electronic charge for each 10^{-11} cm² of carbon surface.

In a later experiment by members of the same research group, Tamarabuchi and Smith (7) confirmed the C-14 deposition on the cathode from dispersions made with the same C-14 tagged-dispersant but with a variety of acidic solids, and in addition demonstrated that the charge resulted from proton transfer on the acidic surfaces. This proof was done by first equilibrating the acidic particles with tritiated water vapor, making a dispersion in oil with the C-14 tagged basic polymeric dispersant, electrodepositing carbon on the anode, and then finding much of the tritium and C-14 on the clean cathode.

DLVO Theory and the Stability of Electrostatically Stabilized Dispersions in Oil. Critics of electrostatic stabilization in non-aqueous liquids point out that: 1) the low dielectric constant leads to much weaker repulsion between charged particles than in water and 2) the low ionic concentration in solution leads to enormous Debye lengths, resulting in weaker forces of repulsion than found in aqueous systems. (8) These charges are best answered by the full application of DLVO theory. The energy of

electrostatic repulsion between charged spheres of radius a with surface potential ψ_0 and separated by distance H in a liquid of dielectric constant ϵ having Debye length $1/\kappa$ is given by the Deryagin equation (9):

$$U_{121}^e = 2\pi\epsilon_r\epsilon_0 a\psi_0^2 \ln(1 + e^{-\kappa H}) \quad (1)$$

where ϵ_0 is the permittivity of free space. It is seen that if a ψ_0 of 20 mV is sufficient in water where ϵ_r is 80, a ψ_0 of 127 mV is needed for stability in oil when ϵ_r is 2, if everything else is the same. However we do find zeta-potentials of 100-200 mV in oil, so the low dielectric constant argument is not valid.

The argument of low Debye length is also not valid. In lubricating oils with micellar dispersants such as basic calcium petroleum sulfonates the conductivity rises to $10^{-8} \text{ ohm}^{-1} \text{ cm}^{-1}$ from $10^{-11} \text{ ohm}^{-1} \text{ cm}^{-1}$ on adding carbon black. The number of charge-carrying micelles can be determined by assuming one proton per micelle has been added or removed to provide the charge carrying species, as demonstrated by Briant (10). The number of ions per unit volume n is determined from the conductivity σ and the frictional coefficient f (equal to the diffusion coefficient D divided by kT):

$$n = 10^{-7} \sigma f / e^2 = 10^{-7} \sigma kT / De^2 \quad (2)$$

For the micellar dispersant giving a dispersion a conductivity of $10^{-8} \text{ ohm}^{-1} \text{ cm}^{-1}$ the frictional coefficient is found to be $10^{-6} \text{ dynes cm}^{-1} \text{ sec}$ (11), which corresponds to $n = 4 \times 10^{16}$ ionic micelles per cubic centimeter or 65 micromoles per liter. The Debye length $1/\kappa$ is calculated to be 59 \AA , using

$$1/\kappa = \left(\frac{\epsilon_r \epsilon_0 kT}{2nz e^2} \right)^{1/2} \quad (3)$$

This short Debye length results because the dielectric constant ϵ_r is only about 2.5% of the value for water.

The magnitude of the electrostatic contribution to stabilization of the dispersion against flocculation can be determined from the electrostatic energy barrier shown in Figure 2, a plot vs. interparticle distance H of the electrostatic repulsion U_{121}^e plus the dispersion force attraction term, U_{121}^d (in units of kT at 20°C).

$$U_{121}^d = \frac{-aA_{121}f}{12H} \quad (4)$$

in which A_{121} , the Hamaker constant, is determined from (12)

$$A_{121} = 1.5 \times 10^{-14} \text{ cm}^2 (\sqrt{\gamma_d^-} - \sqrt{\gamma_d^+})^2 \quad (5)$$

and in which H is the separation distance and f the correction factor for retarded dispersion force interactions (13).

In Figure 2 three curves are shown, for particle radii of 500, 1000, and 1500 Å, and the stability ratio W calculated for each by the Fuchs equation (14)

$$W = \frac{1}{2a} \int_0^{\infty} \exp[(U_{121}^e + U_{121}^d)/kT] dH \quad (6)$$

where W is the average number of collisions between particles per collision energetic enough to burst through the energy barrier and cause sticking of the particles. It is seen that as the particle size is increased, the electrostatic stability increases rapidly. When the radius is 1500 Å, only one in 140,000,000 collisions is energetic enough for flocculation when ψ_0 is 150 mV and $1/\kappa$ is 59 Å.

The flocculation rate for this system can be calculated from the stability ratio and the Smolukowski time (15) for rapid flocculation (T):

$$T = 3\eta/4kTv_0 \quad (7)$$

in which η is the viscosity and v_0 is the number of particles per unit volume before flocculation:

$$v_0 = 3\phi/4\pi a^3 \quad (8)$$

where ϕ is the volume fraction of the internal phase. If $\phi=0.1$, and $\eta=0.3$ poise, and $a=1.5 \times 10^{-5}$ cm (1500 Å), $v_0=2.5 \times 10^{13}$, $T=1.2$ seconds, and $WT=1.68 \times 10^8$ seconds, or 5.3 years. This is very stable indeed.

Similar results are found with polymeric electrostatic dispersants. A basic oil-soluble alkyl methacrylate polymer with vinyl pyridine basic sites and a molecular weight of 500,000 gave an oil of 0.3 poise a conductivity of $10^{-13} \text{ohm}^{-1} \text{cm}^{-1}$, but on adding acidic carbon black or sludge the conductivity rose to $10^{-10} \text{ohm}^{-1} \text{cm}^{-1}$. The frictional coefficient measured by diffusion was 7.7×10^{-6} dynes/cm/sec, and the calculated n (for one electronic charge per molecule) was $3 \times 10^{15}/\text{cm}^3$, or 5×10^{-6} moles/liter; the Debye length was 217 Å, the same as in an aqueous 1-1 electrolyte of 2×10^{-4} molar at room temperature. This dispersant gave carbon black a zeta-potential of -160 mV, which is used as an approximation of ψ_0 in the energy barrier calculation of Figure 3. Wiersema (16) has shown that ψ_0 values are higher than measured zeta-potentials (ζ) and has devised methods of estimating ψ_0 from ζ ; our measured ζ of -160 mV suggests ψ_0 is actually about -250 mV. Figure 3 illustrates the electrostatic energy barrier for this system, using $\psi_0=150$ mV, $\epsilon_r=2$, $1/\kappa=217$ Å, $A_{121}=2.8 \times 10^{-13}$ ergs, for radii (a) of 375 Å, 750 Å, and 1500 Å. These energy barriers extend to greater distances than in Figure 2 because ionic concentrations are lower; the barriers extend to about 1000 Å in this case.

The result of such extended electrostatic energy barriers in

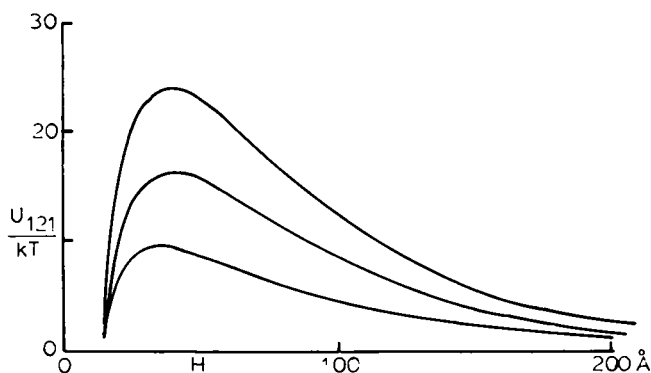


Figure 2. Electrostatic energy barrier between two carbon particles in oil with micellar dispersant. Conditions: ψ_0 , -150 mV; $1/\kappa$, 59 Å; ϵ_r , 2; λ_1 , 900 Å; T , 300° K; and A_{121} , 2.8×10^{13} ergs for all curves. For top curve $a = 1500$ Å, $W = 1.4 \times 10^8$; for middle curve $a = 1000$ Å, $W = 9 \times 10^4$; and for bottom curve $a = 500$ Å, $W = 200$.

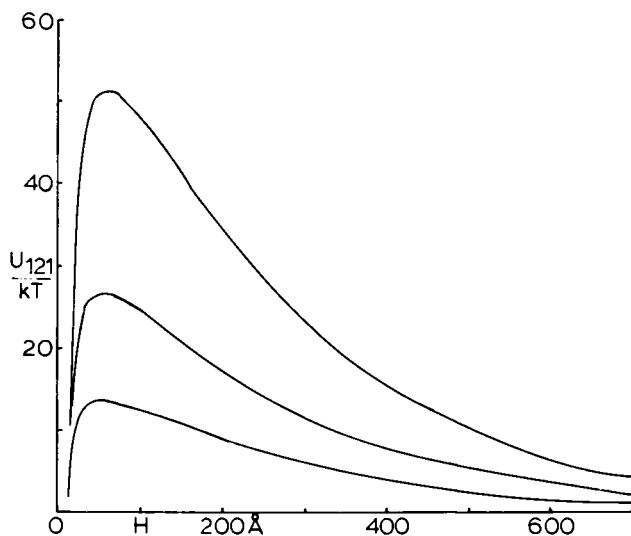


Figure 3. Electrostatic energy barrier between two carbon particles in oil with polymeric dispersant. Conditions: ψ_0 , -160 mV; $1/\kappa$, 217 Å; ϵ_r , 2; λ_1 , 900 Å; T , 300° K; and A_{121} , 2.8×10^{13} ergs for all curves. For top curve $a = 1500$ Å, $W = 1.6 \times 10^{20}$; for middle curve $a = 750$ Å, $W = 1.75 \times 10^9$; and for bottom curve $a = 375$ Å, $W = 4 \times 10^4$.

concentrated dispersions in oil is that the particles assemble into geometric lattice structures with uniform interparticle distances quite similar to those observed with the iridescent aqueous latex dispersions of low ionic strength (17). An illustration of this point is shown in a recent paper by deHek and Vrij (18) who unknowingly used a popular amine-containing negative charge control agent for liquid toners and electrophoretic display devices (19), and found that in dispersions of silica in hydrocarbons the particles formed a lattice-like structure with interparticle distances of about 500 Å, nearly ten times the molecular dimensions of the dispersant molecules; we have found that this dispersant gives carbon particles zeta-potentials of -140 mV in dodecane (20), and we expect similar or larger zeta-potentials with silica because of its pronounced surface acidity.

The role of basic polymeric dispersants in electrostatic stabilization of automotive lubricating oil sludges can be illustrated with calculations based on Figure 3. Sludges develop from very small particles which grow as contaminants, mostly from partially burned gases, are continually added. Particles as small as 375 Å in radius flocculate quickly, for the stability ratio W is only 4×10^4 , and the half-time for flocculation (WT) for $\phi=0.1$ is only 13 mins. However if these particles grow to a radius of 750 Å, W is 1.7×10^9 and WT is 8.2 years. Furthermore, if a becomes 1500 Å, W is 1.6×10^{20} , and WT is 6×10^{12} years. From a graph of $\log WT$ vs. $\log a$ it is found that a half-life of one day occurs when a is 500 Å, and a half-life of one week occurs when a is 560 Å. In such a lubricating oil the typical radius of stabilized particles is about 500 Å, in excellent agreement with these DLVO calculations.

Steric stabilizing mechanisms are also quite important, and most currently used crankcase oil dispersants make use of both mechanisms. In general the steric mechanism favors stabilizing the smaller particles best and the electrostatic mechanism favors stabilizing the larger particles best, as explained by Koelmans and Overbeek some decades ago (21). In some oils one can actually see a double-peaked distribution of particle sizes, the smaller ones presumably stabilized by the steric mechanism and the larger by the electrostatic mechanism.

Zeta-Potentials of Inorganic Pigments in Polymer Solutions of Low Dielectric Constant (22). Electrostatic stabilization of dispersions of solid particles in organic liquids is important in many everyday products. In addition to liquid toners or dispersions of sludge in lubricating oils we should also consider suspensions of pigments (largely inorganic) in polymer solutions, such as paints, inks, and the dispersions used in processing pigmented films such as magnetic tape. Those latter systems all involve dispersions of pigments in polymer solutions which are used to coat a surface. After solvent removal the pigment should remain uniformly distributed and tightly bound into the polymer

matrix. It is already known that acid-base interactions between polymer and pigment promote enhanced pigment-to-polymer adhesion and reinforcement of mechanical properties, and that strong acid-base interaction of the solvent with either the pigment or the polymer competes against and minimizes such enhanced adhesion and reinforcement (23, 24). However, the role of acid-base interactions between pigment and polymer in solutions is also very important in providing the uniform fine dispersions required for these products. These interactions can provide high zeta-potentials (over 100 mV) and the dispersion stability needed for the cast films to be uniformly pigmented and for the minimizing of particles clumping, a major failure mechanism of cast films.

Materials. The polymers included an acidic polymer, a post-chlorinated polyvinylchloride, CPVC (Geon 603x560 from B. F. Goodrich), and two basic polymers, a polymethylmethacrylate, PMMA (Lucite 4F from duPont), and a polycarbonate, PC (Lexan 145 from General Electric). The pigments included two of a basic nature, calcium carbonate (a 6 m²/g pigment from Chas. Pfizer) and calcium oxide (a 4 m²/g reagent from Fisher Scientific) and two of an acidic nature, acid-washed kaolin (a 120 m²/g sample from American Standard), and bentonite (~100 m²/g sample from Fisher Scientific). Three basic solvents used in this work were dioxane ($\epsilon_r=2.2$), tetrahydrofuran "THF" ($\epsilon_r=7.9$), and methyl ethyl ketone "MEK" ($\epsilon_r=18.5$). Three acidic solvents were dichloromethane ($\epsilon_r=9.1$), acetic anhydride ($\epsilon_r=20$), and nitrobenzene ($\epsilon_r=35$). All solvents were Fisher Analytical Grade.

Instrumentation. A Rank Bros. micro-electrophoresis unit was used in those studies, with a specially made quartz cell having a 6 cm. path length of rectangular inside cross-section (1 mm thick, 10 mm deep) in which the Komagata equation (25) predicts zero mobility of the liquid phase in planes located at 0.612 of the distance b from the center plane of the cell to the wall. In electrophoresis experiments 300 to 1200 volts were applied to the cell and mobilities measured in planes a distance h from the center plane. The results were graphed as observed velocity versus $(h/b)^2$ as proposed by van Gils (26), and if the straight lines characteristic of perfect parabolic flow resulted, the electrophoretic mobilities (v_e) observed at $h/b=0.612$ were considered acceptable for calculation of zeta-potential. Zeta-potentials were calculated by the Huckel equation (27):

$$\zeta = 3\eta_0 v_e / 2\epsilon_r \epsilon_0 \quad (9)$$

in which η_0 is the viscosity of the solvent medium, for in these measurements the pigment concentrations were very low and therefore the concentration of counterions was so low that the Debye length is expected to be much greater than the particle radius, thereby indicating that the Huckel equation is appropriate.

Experimental Results. The aims of this study were to use pigments, polymers, and solvents of known acidity or basicity (24) and determine zeta-potentials in organic media of low and high dielectric constant. It was expected that acidic polymers would give positive zeta-potentials to basic pigments dispersed in low dielectric solvents, and this did indeed occur, as is illustrated in Figure 4 for the (acidic) chlorinated polyvinylchloride with the basic pigments CaO and CaCO₃ when dispersed in dioxane ($\epsilon_r=2.2$). The high zeta-potentials (+137 mV with 1% polymer) of the basic particles might have developed by electron-donation from the basic particles to the electron accepting sites of the acidic polymer, but it is also possible that the CPVC donated hydrogen ions to the basic oxygens of CaO or CaCO₃.

It was also expected that the basic oxygens in the polycarbonate would provide negative charges to the acidic pigments (acid-washed kaolin and bentonite) when dispersed in the low dielectric solvent dichloromethane ($\epsilon_r=9.1$), and this was indeed observed, as is illustrated in Figure 5. However the zeta-potentials for these two clays in polymer-free dichloromethane (+105 mV with kaolin and -70 mV with bentonite) seem surprising and unexplainable. Dichloromethane's dielectric constant of 9.1 is appreciably greater than the 5.0 observed for chloroform, and this strongly suggests that dichloromethane has both acidic and basic sites and is therefore capable of forming acid-base molecular complexes which give rise to higher dielectric constants as is observed with water or acetone. Therefore it is expected that dichloromethane can be a weak electron donor as well as a weak electron acceptor; this might help explain why clay dispersions in this liquid can be charged positively or negatively.

The measured zeta-potentials are summarized in Tables II-IV. Table II lists the observed zeta-potentials for dispersions in polycarbonate solutions, where it is seen that increased concentration of this basic polymer generally makes the particles more negative; however in nitrobenzene ($\epsilon_r=35$) the polycarbonate has little influence on zeta-potentials. Table III lists the observed zeta-potentials for dispersions in solutions of chlorinated polyvinylchloride, where it is seen that the low dielectric constant basic liquids (dioxane and THF) the acidic polymer CPVC makes the particles more positive, but in methylethylketone with its higher dielectric constant (18.5), the CPVC has little effect on zeta-potential. Table IV lists the observed zeta-potentials for dispersions in solutions of polymethylmethacrylate, all in acidic liquids of high dielectric constant ($\epsilon_r=20$). The kaolin become more positively charged with increasing concentration of this basic polymer, which suggests that in these dispersions the basic PMMA became ionized by proton transfer in the high dielectric acidic solvent, and then the positively charged polymer ion adsorbed onto the clay particles to make them more positive. Thus we find that the charging mechanism observed in aqueous suspensions also applies in organic liquids of high dielectric

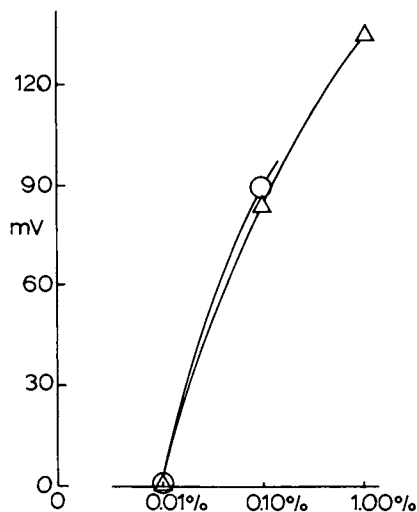


Figure 4. Zeta-potentials for the basic particles CaO (\circ) and CaCO_3 (\triangle) in dioxane ($\epsilon_r = 2.2$) in the presence of various concentrations of the acidic chlorinated polyvinyl chloride.

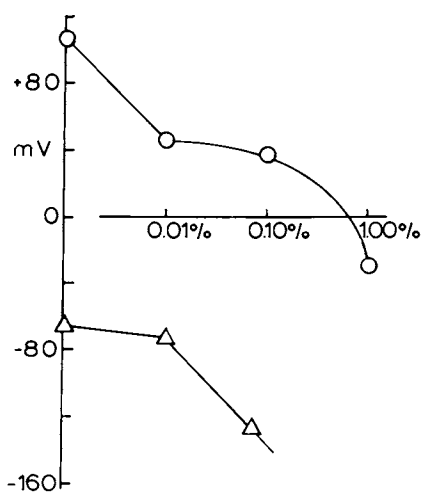


Figure 5. Zeta-potentials for acidic particles acid-washed kaolin (\circ) and bentonite (\triangle) in dichloromethane ($\epsilon_r = 9.1$) in the presence of various concentrations of the basic polycarbonate.

Table II

Effect of Change of PC conc. in Acidic and Basis Solvents
on Zeta Potential with Acidic and Basic Particles:

Particle	Solvent	Dielectric Constant,	Zeta Potential at xg PC/dl			
			$x=0.00$	0.01	0.10	1.00
CaO	THF	7.88	69	+65.8	+48.5	+43
Bentonite	THF	7.88	-10	-12	-79	
CaO	CH ₂ Cl ₂	9.08	-20	-23.2	-6.2	+7.9
CaCO ₃	CH ₂ Cl ₂	9.08	+116	+113	+99	+39
Acid Washed						
Kaolin	CH ₂ Cl ₂	9.08	+107	+46	+39	-35
Bentonite	CH ₂ Cl ₂	9.08	-71	-74	-127	
CaCO ₃	Nitrobenzene	35	-14	-22	-33	-34
Acid Washed Kaolin	"	35	-59.1	-73.7	-79.8	-64.8

Table III

Effect of Change of Cl-PVC conc. in Acidic and Basic Solvents
on Zeta Potential with Acidic and Basic Particles

Particle	Solvent	Dielectric Constant	Zeta Potential (mV) vs. % CPVC			
			0.00	0.01	0.10	1.00
CaO	Dioxane	2.2		0	+90	
CaCO ₃	Dioxane	2.2		0	+84	+137
CaCO ₃	THF	7.88	-42	-45.9	-45	-35.5
CaO	THF	7.88	+67	+65	+52	+4
Bentonite	THF	7.88	-61	-64.8	-18.7	+6.8
CaCO ₃	MEK	18.45	-4.5	-28.5	-20.1	-13.4
Acid Washed Kaolin	MEK	18.45	-48.6	-49.6	-51.8	-53

Table IV

Effect of Change of PMMA conc. in Acidic and Basic Solvents
on Zeta Potential with Acidic and Basic Particles

Particles	Solvent	Zeta Potential at xg PMMA/100 ml Solvent			
		x 0.00	0.01	0.10	1.00
CaCO Washed Kaolin	Acetic Anhydride (AA)	-59	-48	-45	-49
Acid Washed Kaolin	Acetic Anhydride 15% Acetic	-59.2	-60.2	-51.2	-13.7
Acid Washed Kaolin	85% Acetic Anhydride 15% Acetic Acid	+33.4	-22.6	+37.6	+48.4

constant when the polymer (or dispersant or charge control agent) and solvent have appreciable acid-base interaction.

These measurements have demonstrated the principal that pigments dispersed in organic polymer solutions can develop very large zeta-potentials, and the preceding section has shown how this situation leads to very stable dispersions. Not many investigators of paints, inks, or solution master-batched rubber dispersions have taken the trouble to check zeta-potentials, but one exception is well worth mentioning, a study by Franklin (27) of zeta-potentials in paints. Electrodeposition onto an electrode supported on a balance arm allowed determination of weight gain, from which zeta-potentials could be determined. In this study it was found that titanium dioxide particles with an alumina coating (basic) developed appreciably positive zeta-potentials with paint vehicles having larger acid numbers, in line with the mechanism described in this paper for low dielectric constant organic liquids.

There are many everyday applications of these principles, especially in coatings. Wherever there is a need for stable highly loaded dispersions in organic media the principle of acid-base interaction may be invoked to generate high zeta-potentials. To obtain suitable systems one must be concerned with the acidity or basicity of the particle surface, of the polymer, and of the solvent. It also appears important for the attainment of high zeta-potentials to shun solvents of high dielectric constant. Surface modification of particle surfaces is often the simplest route to enhanced acid-base interaction between particles and solutes and empirical testing of particle surface modification has sometimes lead to the enhanced acid-base interaction and high zeta-potentials which can now be attained more directly.

Conclusions

1. In organic liquids of low dielectric constant high zeta-potentials are obtained through proton-transfer or electron-transfer between particle surfaces and dissolved dispersants.
2. In the above systems acidic dispersants give positive zeta-potentials to basic particles and basic dispersants give negative zeta-potentials to acidic particles.
3. The magnitude of the zeta-potentials increases with stronger acid-base interaction and decreases with increase in dielectric constant of the medium.
4. Dispersants for low dielectric constant solvents are usually polymers or "inverse" micelles, and these usually carry one electron charge each when acting as counterions
5. Ionic concentrations in concentrated dispersion are in the micromolar range, giving rise to Debye lengths of 5-50 nm.
6. Electrostatic barriers range from 20 to 50 kT, giving stability ratios of 10^8 or higher, and predicting several year dispersion half-lives for concentrated dispersions.

7. In pigmented coating solutions high zeta-potentials and outstanding dispersions can be obtained by maximizing the acid-base interaction between particle surfaces and the matrix polymer.

8. In organic solvents of high dielectric constant ($\epsilon_r=20$) basic polymers accept protons from acidic solvents and adsorb as polymeric cations to confer positive charges on acidic solids.

Literature Cited

1. van der Minnie, P.H.J. Hermanie, J. Colloid Sci. 1952, 7, 600.
2. van der Minne, J. L.; Hermanie, P. H. J. J. Colloid Sci. 1953, 8, 38.
3. Fowkes, F. M.; Anderson, F. W.; Moore, R. J. Shell Development Co. Publication #1421, Abstract #66, Div. of Colloid and Surface Chemistry 150th American Chemical Society Meeting: Atlantic City, NJ, September, 1965.
4. Hammett, L. P.; Deyrup, A. J. J. Am. Chem. Soc. 1932, 54, 2721.
5. Fowkes, F. M.; Becher, D. Z.; Marmo, M.; Silebi, C.; Chao, C. C. Micellization, Solubilization, and Microemulsions ed. Mittal, K. L. (Plenum Press, NY, 1977), II, 665-673.
6. Fowkes, F. M.; Solvent Properties of Surfactant Solutions, ed. Shinoda (Dekker, NY, 1967), 65-112.
7. Tamaribuchi, K.; Smith, M. L. J. Colloid Interface Sci 1966, 22, 404.
8. Osmond, D. W. J.; Waite, F. A. Dispersion Polymerization in Organic Media, ed. Barrett, K. E. J. (Wiley, 1975), 19-22.
9. Deryagin, B. V.; Landau, L. D. Acta Physicochim URSS, 1941, 14, 633.
10. Briant, J.; Bernelin, B. Rev. Inst. Franc. Petrole Am. Combust. Liquides, 1961, 14, 1767.
11. Fowkes, F. W.; J. Phys. Chem. 1962, 66, 1843.
12. Fowkes, F. W.; Ind. Eng. Chem. 1964, 12, 40.
13. Clayfield, E. J.; Lumb, E. C.; Mackey, P.H. J. Colloid Interface Sci. 1971, 37, 382.
14. Fuchs, N.A.; Z. Physik, 1934, 89, 736.
15. Overbeek, J. Th. G. Colloid Science I. ed. Krupt, H. R. (Elsevier, 1952), 282.
16. Wiersema, P.H.; Loeb, A. L., Overbeek, J. Th. G. J. Colloid Interface Sci. 1966, 22, 78,
17. Attributed to I.M. Krieger by Osmond and Waite (see reference no. 8).
18. deHek, H.; Vrig, A. J. Colloid Interface Sci 1981, 79, 289.
19. Dalisa, A. L.; private communication.
20. Fowkes, F. M.; Matsunaga, T.; Pugh R. J., to be published.
21. Koelmans H.; Overbeek, J. Th. G. Disc. Faraday Soc. 1954, 18, 52-63.

22. Mostafa, M. A.; Ph.D. Thesis, Department of Chemistry, Lehigh University 1977.
23. Marmo, M. J.; Mostafa, M. A.; Jinnai, H.; Fowkes, F. M.; Manson, J. A. I&EC Prod R&D 1976, 15, 206.
24. Fowkes, F. M.; Mostafa, M.A.; I&EC Prod. R&D 1978, 17, 3.
25. Komagata, Researches Electrotech. Lab. Tokyo, 1933, No. 348.
26. Van Gils, G. E.; Kruyt, H. R., Kolloid Beih. 1937, 45, 60.
27. Franklin, M. J. B. J. Oil Col. Chem Assoc. 1968, 51, 499.
28. Disc. Faraday Soc. 1966, 42, 246.

RECEIVED February 17, 1982

Surface Chemistry and the Lithographic Process

ROBERT W. BASSEMIR

Sun Chemical Corporation, Carlstadt, NJ 07072

An overview of the lithographic process is presented with particular emphasis on the role that surface and colloid chemistry plays. Recent research has shown the importance of these chemistries in fountain solution, ink and plate interactions and the effect of these interactions on the dynamic behavior of the lithographic ink on press. Data on the rheological behavior of preformed fountain solution/ink emulsions is presented along with an evaluation of prints made with the inks on an actual press run. The importance of pre-testing the emulsification behavior of printing inks in predicting their printability is demonstrated. A laboratory procedure designed to measure the rate of emulsification of fountain solution into ink rather than merely the amount emulsified is shown to be predictive of press performance.

The related technology of waterless lithographic plates is described showing the importance of surface energy, plate chemistry and ink rheology on performance.

Lithographic printing which was invented by Alois Senefelder over 180 years ago, has probably been the most widely studied of all the printing processes. Despite this, many questions remain and a total understanding of the lithographic process still eludes us. This is due largely to the complex interactions which occur on press between the ink and the dampening solution.

In investigating these interactions it is evident that the chemistry of both the ink and dampening solution are directly involved as independent variables and that the rheology of the ink which results at the instant of printing has a strong effect on the runnability of the ink and the faithful reproduction of the plate and clarity of image produced.

0097-6156/82/0200-0327\$06.00/0

© 1982 American Chemical Society

In order for a lithographic ink to move smoothly and uniformly through the press to the substrate, it is essential that the ink be able to absorb a reasonable quantity of the fountain solution being used as emulsified droplets. Many authors have observed this fact (Banks, (1), Surland (15, 16), MacPhee (18)) and have tried to predict how the physical chemistry of the inks and fountain solutions could be used to predetermine its performance on a press.

Some workers have interpreted the emulsification of fountain solution in an ink from the point of view of surface energetics and colloidal behavior. Surface measurements in the form of contact angles, spreading coefficients, interfacial tensions and surface tensions have been widely used to explain the interactive behavior of inks and fountain solutions.

The role of interfacial tension between ink and water in the litho process has been studied by many workers. Hansen (6) observed that the emulsification tendencies of the ink depend to a great extent on the tension of the various components of the ink, because the presence of even a small quantity of one component with a low interfacial tension will influence the tension of the entire system. This is one of the reasons that certain pigments, notably reds, are more prone to cause scumming problems than other pigments even when dispersed in an identical vehicle. The interfacial tension of these pigments against water is shown to be very much lower than might be anticipated primarily because of impurities that are not completely removed during the manufacturing process.

Rosted (12) states that the amount of fountain solution emulsified in the ink is related to the plastic viscosity and tack and that interfacial tension between ink and fountain solution determines the amount of water adhering to the ink surface. The latter observation was confirmed by Karttunen (8), and he also observes that high interfacial tension is accompanied by low bonding efficiency of the water to the ink thus resulting in thin surface water films on press ink rollers.

Banks (1) in a paper on litho fountain solutions, observed that most abnormal litho behavior such as scumming is accompanied by the spread of an oily film over the fountain solution. He also claims that if the fountain solution is adjusted to a surface tension in the range of 36-30 dynes/cm, the spreading of this sensitizing film from the ink will be inhibited. He feels that the prevention of spreading is not dependent on the particular composition of the fountain solution but only on its surface tension.

Hansen (6) has observed that the interfacial tension of an offset ink with fountain solution should be neither too high, which would prevent sufficient emulsification, nor too low which would cause scumming. He states that the normal range for a good ink should be between 15-25 dynes/cm.

Padday (11) presented a theoretical explanation of the litho process in which he used the concept of cohesive and adhesive forces acting in and across surfaces to explain the action of the inking of image areas on a litho plate. His explanation rests entirely on the rupture of layers at the weakest point.

Kartunnen (9) discusses the polar balance and the surface roughness of the various layers in the litho process and concludes that the emulsification of water in the ink depends not only on the surface chemistry of these fluids but also on the thickness and surface structure of the ink and water films when they enter the various nips in the press.

Several workers have also commented on the possibility of using dynamic surface tension measurements on the fountain solution as being more realistic in view of the fast printing speeds used. This might also make measurements of dampening solutions containing surface active agents correlate better with actual press performance due to the rate of diffusion of materials to the surfaces of these fluids.

Fred Shubert (13) of our laboratory has made some studies using commercial photopolymer plates and experimental inks which were also studied for their emulsification and rheological behavior and are reported on later in this paper.

The image and non-image areas of a freshly exposed and developed Kodak LN plate were used to determine contact angles of water and methylene iodide in a controlled atmosphere. The Rame'-Hart contact angle instrument was used in these experiments at relative humidities of 100% and 0%. An S.E.M. photo of the virgin image area is shown in Figure 1, revealing the rough texture of the surface.

Contact angle measurements and S.E.M. photographs were also made on the image and non-image areas of the same plate after running it on the press for 1000 impressions with ink #C-4. A portion of the image area was measured with the ink still adhering to the image (see Figure 2). Another portion of the plate was washed free of ink with solvent (naphtha) and measurements taken on both image and non-image areas (see Figure 3). Some wear of the image is seen.

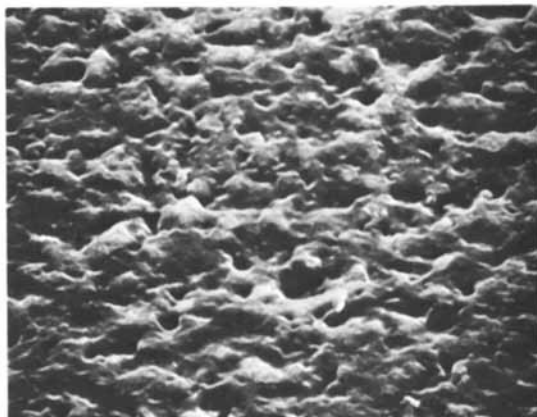


Figure 1. New plate image area (1200 \times).



Figure 2. Ink film on image area (1200 \times).

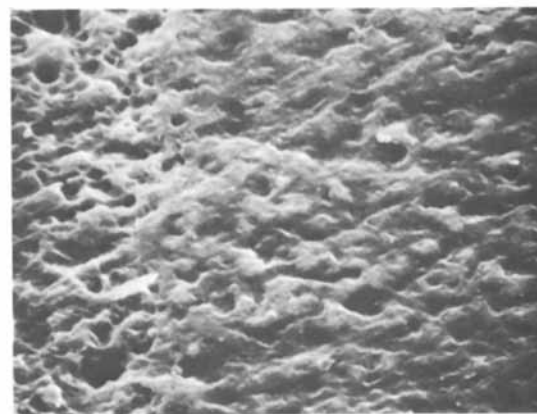


Figure 3. Used plate after cleaning (1200 \times , image area on right side of photo).

The contact angle measurements were used in a computer program to obtain values of the surface energy of the plate and this value resolved into dispersion and polar components. This program was written using the equations proposed by Wu (19). Table #1 lists these values on the new plate before running on press.

Table I, Surface Energies of Virgin Plate
Dynes/cm @25°C

		<u>S</u>	<u>S^{disp}</u>	<u>S^{polar}</u>
Image Area	0% Rel.Hum.	44.9	34.7	10.2
	100% Rel.Hum.	44.2	31.3	12.9
Non-Image Area	0% Rel.Hum.	76.5	34.7	41.8
	100% Rel.Hum.	72.8	22.2	50.6

In both areas of the plate, it is evident that adsorption of water vapor from the saturated atmosphere causes an increase in the calculated polar component. The increase in the non-image area polar component is greater, as might be expected from the chemical nature of the two areas.

After running on the press, the plate was removed without cleaning of the image, and measurements of contact angle made on the inked surface. The surface energies of the virgin ink were also determined by measurement of a series of dilutions in Bromonaphthalene and the contact angles on polyethylene pellets. The results are shown in Table #II.

Table II, Surface Energies of Ink Surfaces
Dynes/cm @25°C

		<u>S</u>	<u>S^{disp}</u>	<u>S^{polar}</u>
Inked Image Area of Plate Run on Press	100% R.H.	41.2	29.8	11.4
	Virgin Ink, C-4, 100% R.H.	33.5	27.7	5.8

The ink on the image area of the plate has increased in the polar component. This is likely due to the emulsification of fountain solution in the ink as well as surface fountain water both of which may leave a hydrophilic residue upon evaporation.

The used plate was then washed free of ink with naphtha and contact angles measured in both image and non-image areas. The results are given in Table III.

Table III, Surface Energies of Plate Areas
Dynes/cm @25°C

	<u>S</u>	<u>S^{disp}</u>	<u>spolar</u>
Image Area @100% R.H.			
Virgin Plate	44.2	31.3	12.9
Used Plate	48.8	28.3	20.5
Non-Image Area @100% R.H.			
Virgin Plate	72.8	22.2	50.6
Used Plate	72.6	18.2	54.4

The data indicate that the most significant change on running is an increase in the polar component of the image area. It is possible that some absorption of ink emulsion in the interstices of the photopolymer image area may have occurred during running. The cleaning process with hydrocarbon solvent may have selectively removed the more hydrophobic constituents of the ink. The non-image area shows the expected increase in polar component due to adsorption of fountain solution ingredients.

Work is continuing in an attempt to relate surface energetics to the precision of inking the plate and printability of the inks.

Ink Emulsification Tests

Many laboratory tests to find the emulsification behavior of inks have been proposed during the past several decades, an early one being Bowles and Reich (3), but only one, Surland (15, 16) suggested that measurement of the rate was more important than the amount emulsified. Since the ink/water interaction on the press is a dynamic one, this approach seems more rational than single point determinations of the percent emulsified, which are widely used in industry.

The essential features of his method are a mixer with specially designed blades and bowl, good control of speed and temperature and gravimetric determination of the percent water emulsified each minute for ten consecutive minutes. The data obtained is plotted as shown in Figure #4. This chart shows a series of rate

P	Water Balance Range	Damp. Sol'n. Effect	Image Area: <u>Print</u>	Ink Lay On Print	Rel. Print Density
A	zero		∞		
B	narrow	flotation	> 1		< 1
C	wide		$= 1$		$= 1$
D	narrow	tint	< 1		< 1
E	zero		$= 0$		$= 0$
F	narrow	tint	< 1		< 1

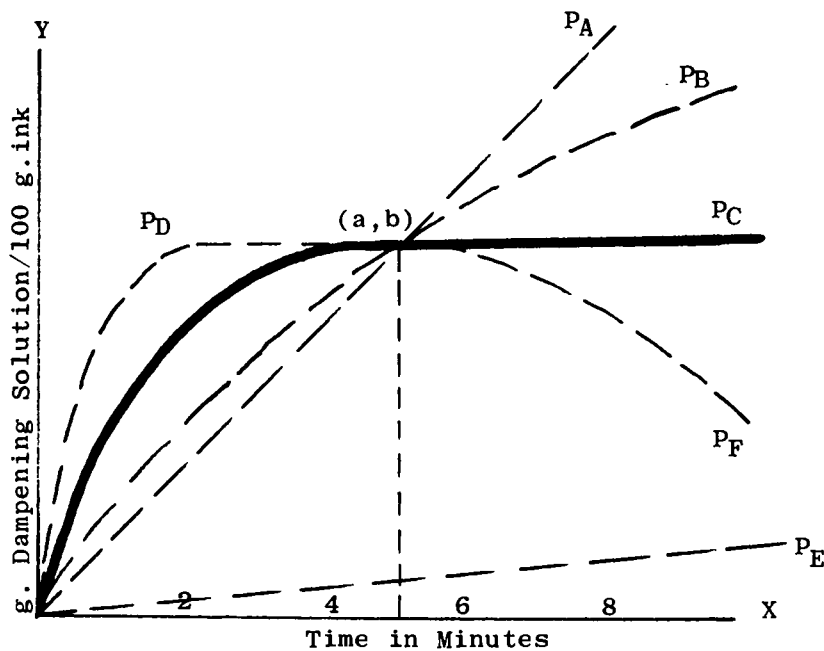


Figure 4. Emulsification rate curves and effects on printability.

curves that have been observed in measurements of over 1000 inks. Also shown are the press performance features associated with each type of rate curve. An interesting feature of Figure IV is the fact that all of the differing rate curves can be drawn through a common point at five minutes, the typical single point time used in other tests. Since the performance of these five inks is obviously greatly different, this illustrates very well the futility of single point test methods.

Emulsion Rheology

While it is evident that the rheology of lithographic inks has a profound effect on printability and press performance, most of the literature records only the rheology of the dry ink.

However, the ink as actually printed on a lithographic press is an emulsion which may contain as little as 20% or as much as 50% of fountain solution as a finely dispersed internal phase. It is the rheology of this ink emulsion which determines the configuration of the printed areas and the faithfulness of the reproduction of the plate image.

Recent work by the author, Bassemir (2), attempts to correlate the rheology of emulsified inks with their press performance under commercial printing conditions.

In this investigation, a set of six experimental heatset lithographic inks were subjected to a variety of rheological measurements both as a dry ink, as well as after being emulsified with a commercial fountain solution. Determinations of apparent viscosity at 2500 secs^{-1} and yield stress at 2.5 secs^{-1} were made @25°C from 5 point shear rate/stress curves, and inkometer tacks at 1200 RPM/90°F were also measured.

The six inks, which consisted of one pair of each of three different types of ink chemistry, were then lithographed on coated enamel paper, using a 25" Miehle press. The press was equipped with Dahlgren dampening and printed samples were examined microscopically and rated for printability and dot resolution after 5000 impressions had been taken. Printability refers to the total press performance of the ink as well as the fidelity of the printed images. Dot resolution was evaluated microscopically using the GATF Star Target and dot gain guides on an empirical scale of 0 to 10.

The emulsification rate curves were also determined using the technique described by Surland (16).

The rheological data and printability results for the six inks are shown in Table IV and the emulsification curves in Figure 5. To facilitate comparisons, viscosity, yield and shortness ratio (yield stress divided by viscosity) are also shown in bar chart form, Figures 6 through 8.

An examination of the emulsification rate curves indicates that most of the inks had an acceptable curve shape with the exception of ink C-1, which shows a "B" type shape (no equilibrium reached). All six inks were commercially acceptable in dot resolution although there were noticeable differences from the best to the poorest (Figure 9). Figure 10 shows photomicrographs of star targets printed with the inks rated at the two extremes, A1 and C4. A dot resolution rating of 7.0 is considered of normal commercial quality while the rating of 9.5 for ink C-4 is quite exceptional.

The data shows that the second member of each of the three pairs is better in dot resolution and printability than the first member. For example, ink A-3 with a rating of 8 was improved over ink A-1 with a rating of 7. The dry inks were of roughly equal tack and shortness ratio but the A-3 emulsion was much shorter than the A-1 emulsion. This factor plus the higher viscosity of A-3 is the probable reason for the improvement in dot resolution. In series "B", a similar trend was observed with emulsified ink B-5 being shorter than B-1 and also of better dot resolution.

Ink C-1, however, shows some anomalous behavior in that the shortness ratio of the emulsified ink is higher than C-4 whereas ink C-4 gave somewhat better dot resolution. A possible explanation of this is the anomalous emulsification rate curve of C-1 previously mentioned, which indicates no attainment of equilibrium up to the 10 minute limit. The dot resolution results obtained with C-4, on the other hand, are consistent with the ideal emulsification curve shape which it exhibited.

It is interesting to note that in all cases the inkometer readings of the emulsions either remained the same or increased slightly. Although many literature references to tackometer readings of emulsified inks indicate a decrease in apparent reading, these tests were done by adding water to the rollers of the tackometer after the dry ink had been distributed on them. Using this technique, it is likely that excessive water will remain on the outside of the oily phase thus aggravating the possibility of roller slippage to which tackometers of this type are very prone, Mewis (17).

The following conclusions were drawn from these data:

TABLE IV
EXPERIMENTAL BLUE H/S INKS

Ink#	App. Viscosity Pois@2500sec ⁻¹		Yield Stress Dynes/cm ² /@2.5sec ⁻¹		Shortness Ratio		Inko Reading 1200RPM/90°F/1 min.		Dot Resolution
	Dry	Emulsion	Dry	Emulsion	Dry	Emulsion	Dry	Emulsion	
A-1	55	45	210	600	3.8	13.3	13	13.5	7
A-3	75	55	300	1800	4.0	32.7	13	13.0	8
B-1	110	63	1000	5000	9.1	79.0	13	14.5	7.5
B-5	130	73	1700	7200	13.1	99.0	14	14.0	8.5
C-1	150	80	1400	12000	9.3	150.0	14.5	15.2	8.5
C-4	155	115	2400	7600	15.5	66.0	13.5	13.5	9.5

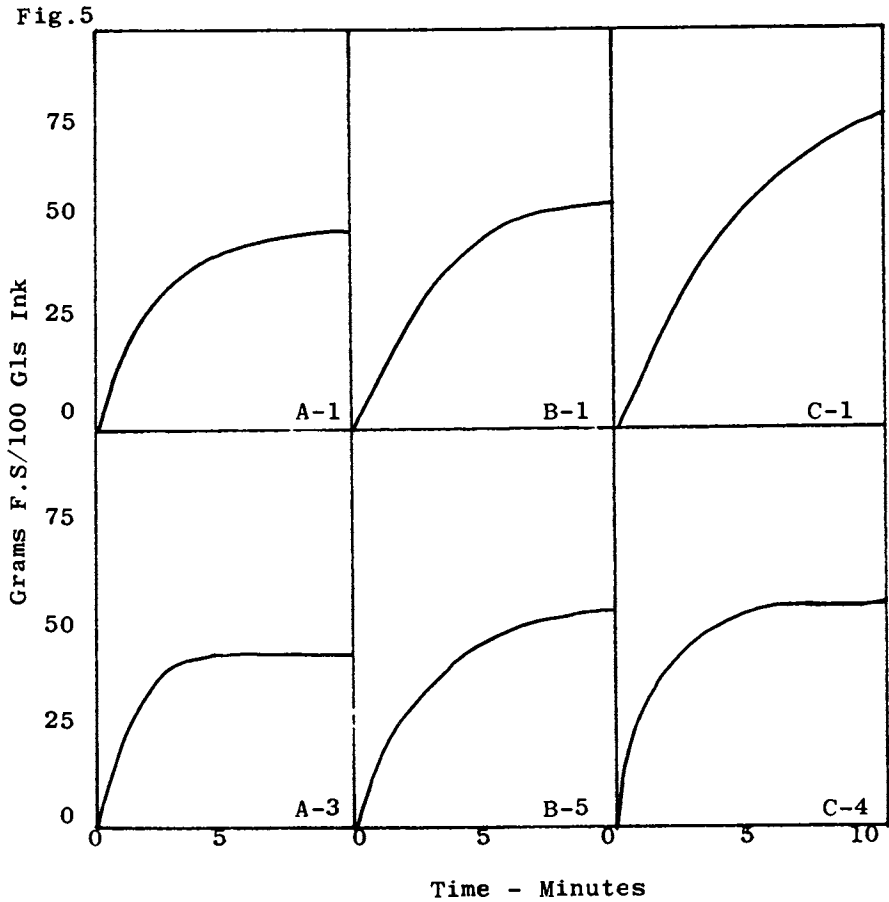


Figure 5. Emulsification curves of six experimental inks (25°C, 2 oz/gal Rosos, and 25% IPOH.)

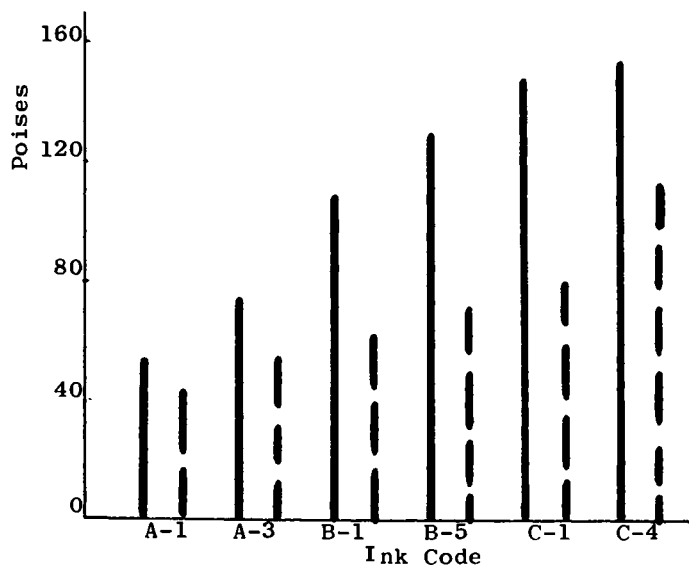


Figure 6. Comparison of apparent viscosities of dry inks and emulsified inks. Conditions: T , 25°C ; and apparent viscosity at 2500 s^{-1} . Key: —, dry ink; and ---, emulsion.

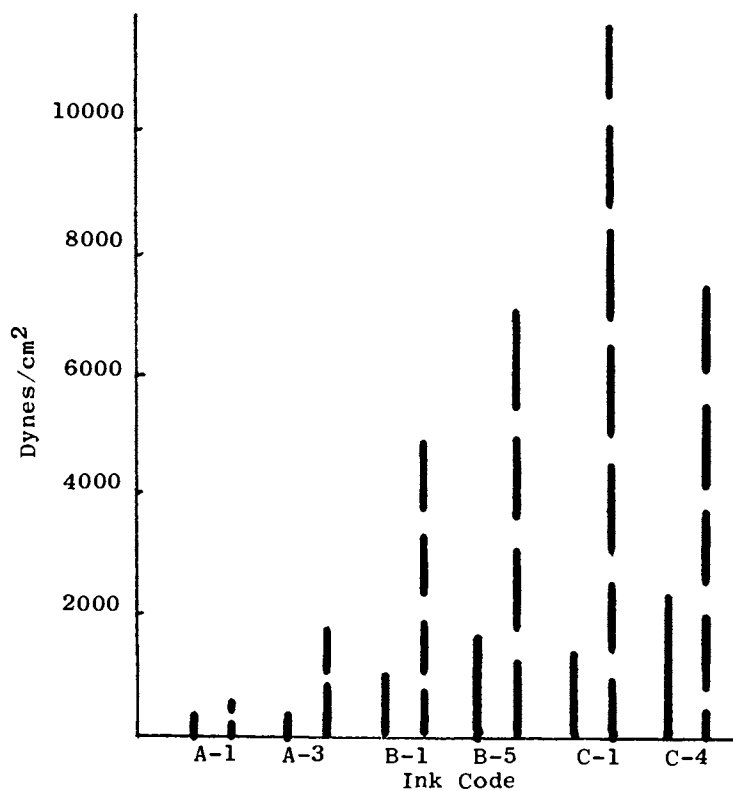


Figure 7. Comparison of yield stress (at 2.5 s^{-1}) of dry inks and emulsified inks (25°C). Key: —, dry ink; and ---, emulsion.

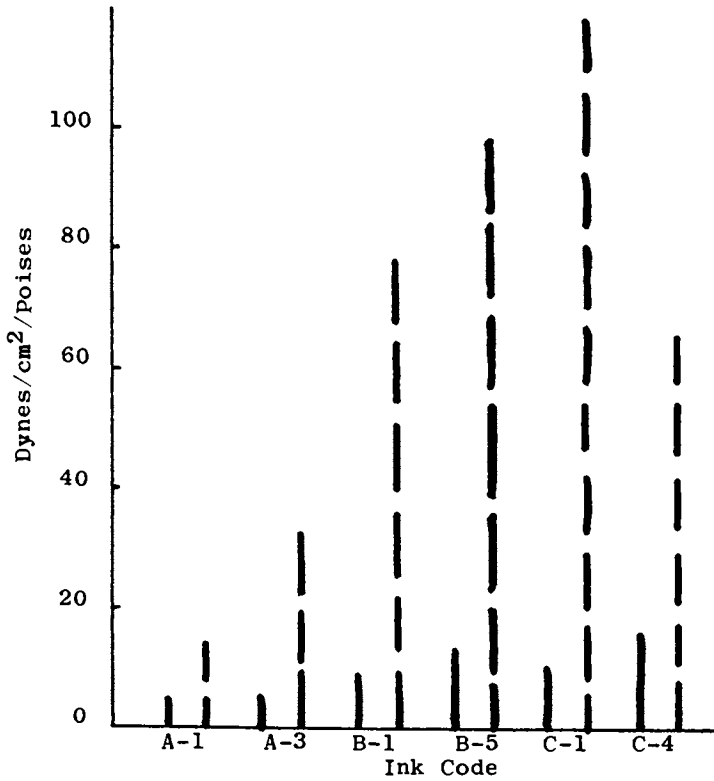


Figure 8. Comparison of shortness ratio (-25°C) of dry inks and emulsified inks.
Key: —, dry ink; and ---, emulsion.

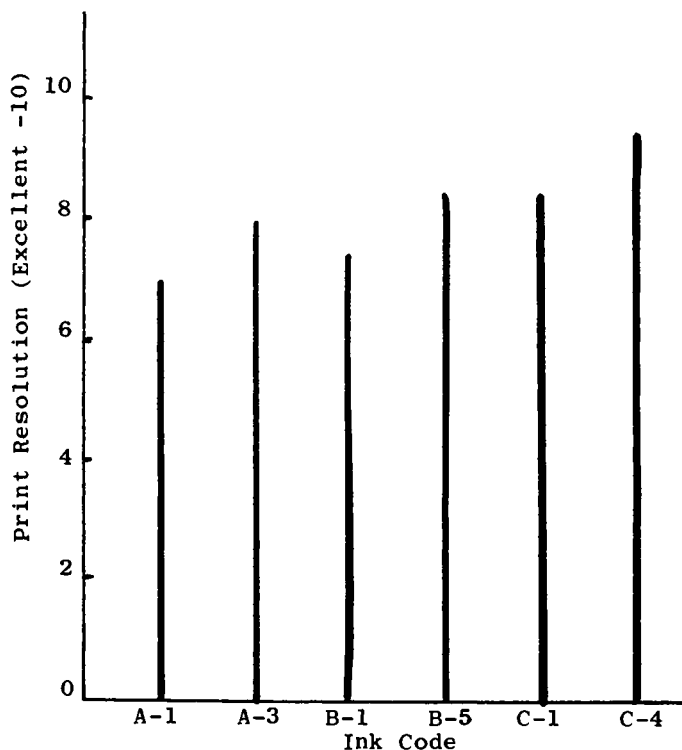


Figure 9. Comparison of dot sharpness of six experimental inks.

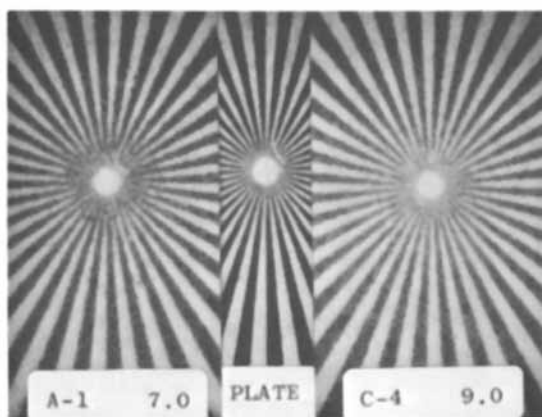


Figure 10. GATF Printed Star Targets and Dot Resolution Ratings for Inks A-1 and C-4 (original plate image in center) $36\times$.

1. Moderate to high shortness ratios of emulsified inks tend to improve half-tone dot resolution in lithographic printing.
2. Higher ink viscosities may also produce better dot resolution even though commercially acceptable results can be had over a wide range of apparent viscosity.
3. The rheology of ink emulsions is clearly of prime importance in the printability and dot resolution of an ink and is significantly influenced by both ink and fountain solution chemistries.
4. The shape of the emulsification rate curves is related to press performance of a lithographic ink.

Waterless Lithography

In view of the complex interactions which occur in lithography due to the presence of the fountain solution, it is not surprising that considerable research effort has been exerted to eliminate dampening systems from planographic press operations.

In this paper, the term waterless lithography is used to refer to a planographic printing system which uses no dampening or fountain solution whatever. This is in distinction to a process where the dampening solution is pre-emulsified into the ink and broken down on the press. The latter process might be referred to as self-dampening lithographic ink.

Over a decade ago, the 3M Company patented a special planographic plate, Curtin (4), which was produced under the tradename "Driographic Plate". This plate had a non-printing area which was surfaced with a silicone containing rubbery polymer having relatively low surface energy. Thus, it was able to repel the adhesion of inks which were properly formulated for the process and without any dampening. The printing area of this plate was composed of uncoated aluminum. The positive working plate was exposed photographically and developed in a special developing machine.

One major problem with the Driographic plate which caused its eventual withdrawal from the marketplace was high temperature "toning", a term analogous to scumming in conventional lithography, that is unwanted ink reception in the non-printing areas. While it was possible to make inks which would print successfully at

cooler ambient temperatures, when press temperatures reached 120-140°F toning eventually resulted. Water cooling of the plate cylinders was the only effective solution but this proved difficult and expensive to retrofit on many existing presses.

During the past several years, there has been a renewed interest in this field. A number of papers on the theory of waterless lithography and the production of duplicator masters were published by Xerox Corporation researchers, Packansky (10), Gaudioso (5).

The Toray Corporation of Japan has begun to market a planographic waterless plate which has apparently met with some success, particularly in Japan. This plate also utilizes a non-printing area of low surface energy which is surfaced with a polymer containing silicone moieties, but its image areas are surfaced with a photopolymer layer, Shimokawa (14).

While the Toray plate has apparently overcome some of the problems of the Driographic plate, toning of ink in the non-printing areas at high temperatures still remains a concern. There are several contributing factors to this problem which bear examination.

All inks decrease in tack as temperature rises, and the cohesive force of the ink is an important factor in removing residual ink from the non-printing area. Attempts to stabilize the tack or at least minimize its rate of change with temperature by use of viscosity index improvers have only been partially successful.

Low surface energy additives such as silicone oils have also been used to reduce toning, presumably by acting as a release layer between the ink and plate, since surface energetics alone would not predict its usefulness.

Gaudioso (5) proposed a theory of ink release from this type of plate, suggesting that ink solvent diffusion from the ink into the plate non-printing area is essential to the formation of a weak fluid boundary layer. This allows more complete removal of residual ink from these areas.

Clearly, the long term commercial viability of the current plates depends on the development of an ink of acceptable tack which will perform at normal press temperatures without toning. If this cannot be done with ink formulation alone, changes in the surface energy of the plate non-printing area may be required.

Conclusion

The importance of surface and colloid chemistry in the lithographic process has been pointed out. In particular the influence of surface energy on water/ink interaction and emulsification is illustrated. Work on the changes in surface energy of lithographic plates during the printing process was described. The strong influence of the emulsified phase on ink rheology and subsequently on dot resolution was shown by data obtained with a series of experimental inks.

A laboratory test for the important property of emulsification rate was described, including its relation to actual press performance.

A survey of waterless lithographic technology and of the present state of the art indicates a renewed interest in this area, even though some problem areas still exist. The long term future of this technology remains uncertain unless an ink that resists toning at moderately high temperatures can be developed.

Acknowledgments

The author wishes to thank Fred Shubert of Sun Chemical Corporation for determining the surface energy values and for helpful discussions of the results.

Literature Cited

1. Banks, W.; Smith, A; Charlesworth, D., Printing Technology 1968, 117-27.
2. Bassemir, R.W., Am.Ink Maker 1981, 59 , No. 2, 33.
3. Bowles, R.; Reich, W., British Ink Maker 1959, p38-40.
4. Curtin, J., U.S. Patent 3,511,178, 1970.
5. Gaudioso, S.; Becker, J.; Sypula, D., Technical Assn. Graphic Arts Proceedings 1975, 177-94.
6. Hansen, W., J. Oil Col. Chem. Asso. 1976, 59 , 127-40.
7. Kaelble, D.; Dynes, P.; Pav, D., "Adhesion Science & Technology", Vol 9B 1975, Plenum Press.
8. Karttunen, S.; Lindquist, V., Graphic Arts In Finland, 1978 2, 4-12.
9. Karttunen, S.; Manninen, M., "Advances in Printing Science & Tech.", Pentech Press, London, 1979.
10. Packansky, T.; Becker, J., A.C.S. Symposium on Polymers for Lithography 1975.
11. Padday, J., Printing Technology 1969, 13 No 1, 23-32.

12. Rosted, C.; Stenfeldt Madsen, E., Printing Technology 1966, 10 No. 1, 18-23.
13. Shubert, Fred, Sun Chemical Corp--private discussion.
14. Shimokawa, Y., Graphic Arts Japan 1979, 21, 96-7.
15. Surland, A., "Lithographic Dampening Conf", 1967, Chicago.
16. Surland, A., Tech. Assn. Graphic Arts Proceedings, 1980, 222-248.
17. Mewis, J., "Tack & Nip Flow of Printing Inks", 54th Colloid and Surface Science Symposium, June/1980.
18. MacPhee, J., Tech. Assn. Graphic Arts Proceedings, 1979.
19. Wu, S., J. Polymer Science C, 34, 19, 1971.

RECEIVED April 1, 1982

Surface Chemistry Control in Lithography

THOMAS A. FADNER

Rockwell Graphics Systems, Cicero, IL 60650

Results of recent research into ink/water interactions in lithographic printing are briefly reviewed and compared with predictions from surface chemistry principles. Contrary to popular belief, both image and nonimage areas of the printing plate act as water reservoirs during printing. And, ink is carried in both the image and nonimage areas. Viscous and dynamic mechanical forces account for most of the image/non-image differentiation. A model is proposed that explains the advantageous effects of isopropanol and its substitutes as additives to the aqueous dampening solution.

The lithographic printing process has been modelled mechanically, phenomenologically and by materials flow, often without reconciling the descriptions with principles of surface chemistry (1-6). Although the process may at times appear complicated, the simple concept of using oil-like inks and dilute water solutions to differentiate printing and non-printing areas of an essentially planar printing plate, should require only simple explanations and yet remain consistent with surface science principles.

Wetting of Ink by Water

To account for one aspect of image differentiation by a lithographic printing plate, reference has been made to surface chemistry principles such as Statement 1.

Statement 1. High energy liquids will not spontaneously wet nor spread onto immiscible low energy materials.

Accordingly, high surface energy, aqueous fountain solutions do not spread onto low surface energy, inked images on the printing plate. This appears to support the practical fact that water, sprayed, rolled, or otherwise conveyed as fountain solution onto the printing plate in appropriate amounts, does not ordinarily get in the way of the inked image with which we are printing.

0097-6156/82/0200-0347\$06.00/0

© 1982 American Chemical Society

American Chemical

Society Library

In Colloids and Surfaces in Lithographic Technology; Hair, M., et al.; ACS Symposium Series; American Chemical Society: Washington, DC, 1982.

Wetting of Water by Ink

The chemical converse of Statement 1, applied to wetting of aqueous fountain solution by the ink, introduces an often-overlooked dilemma in attempting to explain lithography.

Statement 2. Low energy liquids will spontaneously wet and spread onto immiscible high energy materials. Lithographic inks are low energy materials but generally are not found, en masse, in the high energy, aqueous-fountain-solution-covered, nonimage areas of the printing plate during printing. If they were, differentiation of image and nonimage areas would not have taken place. This implies either that lithography is wrong or that surface chemistry is wrong. Seldom do treatises on lithography adequately resolve this apparent dilemma.

In lithography we bypass the implied conditions of Statement 2 by introducing a force/time dependent factor; the ink is formulated to have high viscous resistance to flow. We can reconcile theory with lithographic fact by modifying Statement 2 to read:

Statement 3. Low energy, high viscosity liquids will spontaneously but not rapidly wet and spread onto immiscible high energy materials.

Viscous Flow in Lithography

These two statements are consistent with popular views of lithography, namely: the principle of Statement 1 is supposed to keep water out of the inked image areas; Statement 3 ostensibly explains keeping ink out of the aqueous, nonimage areas.

As already noted, however, in lithography we are not operating at equilibrium; we are not waiting for spontaneous wetting action; we are forcing the wetting action. The pressure and shearing forces at roller nips are purposely far in excess of the ink's viscous resistance to flow, to assure that the ink will move a small but finite distance at the ink-to-ink roller couples, within 10^{-2} to 10^{-3} second dwell times.

A low energy, high viscosity ink that is sufficiently forced to flow will of course be spread, in the surface chemical sense, onto the high energy, aqueous nonimage areas of the printing plate. Yet under normal printing conditions, it appears not to have done so. The image and nonimage areas remain differentiated. Further input is required to resolve this dilemma.

Ink and Water Mixing

Analyses have repeatedly shown that 15% or more water is found in lithographic inks during or after normal printing. And, inkmakers routinely formulate to allow water into the ink during printing operations (2, 3, 7, 8). Reportedly, most of the water throughput to the substrate being printed is by way of the ink, not by way of the aqueous, non-printing areas of the printing plate (1). Also, minute ink particles are often, if not always, found in the non-printing areas of plates or

blankets during normal printing operations. These observations imply that water and ink are not completely differentiated by the lithographic process. Apparently, surface chemistry principles that require exclusive ink/water differentiation are not controlling this process.

Isopropanol in Lithography

The first in a series of continuous-dampener patents by Dahlgren disclosed a direct-to-plate device (9). A practical way to bypass printing press manufacturers, who at the time were disinterested in this continuous-dampening innovation, was to retrofit the device onto existing presses in the field. Existing press configurations required using inked form-rollers. Dahlgren found that using inked form-rollers to convey aqueous fountain solutions to the printing plate, required generous amounts, 10 to 50%, of a water-soluble, ink-compatible, fountain-solution additive, as described in his subsequent patent (10). Isopropanol was cheap, relatively safe, available, and did not adversely affect image differentiation. Isopropanol has since become a widely-used industry standard.

The prevalent explanation for isopropanol's role in this kind of dampening system is that its surface tension, about 29 dynes/cm, sufficiently lowers the aqueous fountain solution surface tension to allow wetting of the inked form-roller by that solution, as illustrated in Figure 1. That is, the fountain solution wets and spreads onto, and is carried by the ink film on the form-roller to the printing plate, as a relatively thin, uniform film.

However, the most important fact about isopropanol, in understanding lithography, is not the advent and success of continuous dampening that ensued. Rather, it is the fact that pressmen found distinct and very important advantages in the use of isopropanol; advantages generally lumped together and termed "better ink/water balance control". These are seen over and over as the following qualitative observations:

1. Faster acceptable copy. This means faster attainment of steady state conditions; the point in the operation where ink and water feed rates no longer need critical adjustment to obtain desired quality, illustrated schematically in Figure 2.
2. Less variation. Quality variations are less extreme and less frequent, as depicted in Figure 2. Response to water or ink feed rates changes is faster.
3. Wider ink/water latitude. Pressmen find less variation in print quality due to form differences, and ink or press setting differences.
4. Less work. With isopropanol, less attention is required. The ink/water balance is more automatic.

An acceptable model of the lithographic process must ade-

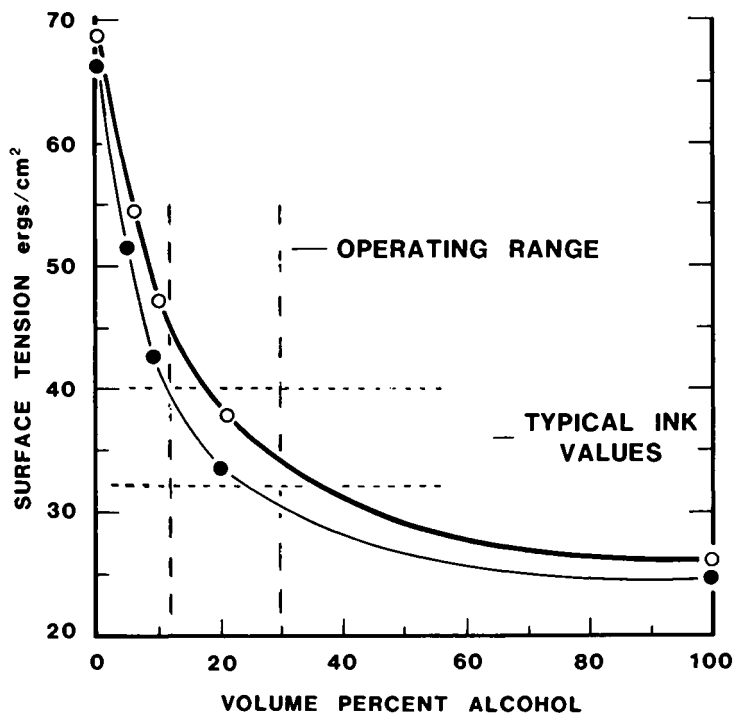


Figure 1. Surface tensions of propanol solutions. Key: ○, n-propanol; and ●, iso-propanol.

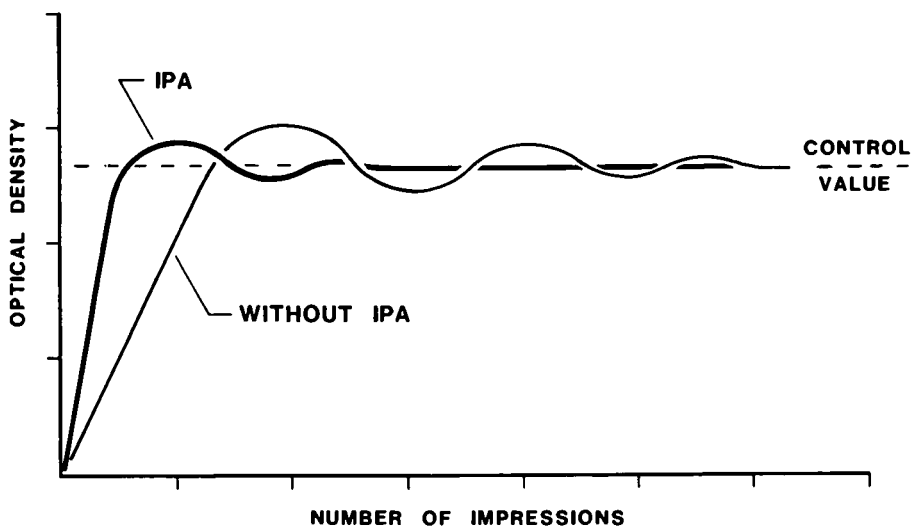


Figure 2. *Effects of isopropanol.*

quately explain these observations. It must also explain an additional dilemma. Based on surface science principles, we can accept that a low surface tension, aqueous solution in contact with a low energy, inked, form-roller surface will rapidly wet and spread as a thin film onto the ink, when forced at the nip. But, then, we must also admit that this same solution will readily wet and spread over any inked surface, including image areas of the printing plate. Overall wetting of the printing plate by the aqueous fountain solution appears as a necessary corollary to the use of isopropanol. How, then, do we explain that, during printing, this aqueous fountain solution film does not prevent ink-to-ink transfer? Why does isopropanol not thwart lithography?

Role of Isopropanol in Lithography

In a previous paper (5), we have shown that with this additive, an 84% isopropanol concentration exists in both phases at the vapor/liquid-solution interface. This high surface concentration is maintained at the press by automatic, recirculating control systems. Under these conditions, the highly volatile isopropanol has a continual, preferential surface-energy-lowering effect. It is a surface active material because of a colligative mechanism, rather than because of more familiar, slow-to-form, interfacial structure mechanisms (11). This bulk-reinforced, surface activity is important in understanding lithographic printing.

Since dampening form-rollers cannot differentiate between image and nonimage areas of a printing plate, the low-energy, isopropanol-containing, aqueous fountain solution spreads rapidly at the nip over all areas of the plate, independent of image and nonimage details. At the nip exit, this mechanical spreading force is released; there are no other significant forces acting at the interface; film splitting occurs within the aqueous phase; and a thin film of aqueous fountain remains in the image as well as the inked, nonimage areas. It follows that the uppermost surfaces of the inked, image areas on the printing plate, like the aqueous, nonimage areas, will be primarily isopropanol, not ink!

Lithography Simplified with Isopropanol

Within a few resolutions of the press, when isopropanol is used, an isopropanol-rich layer of fountain solution forms and is continuously maintained at all ink/air and fountain solution/air interfaces. Consequently, form-roller to printing plate contact at the nip entrances involves two layers of aqueous isopropanol first coming into contact, not ink films and/or fountain solution films! Since the incoming surfaces are virtually identical and the press is also forcing intimate contact, instantaneous wetting and spreading into an extensive, thin film is assured, independent of whether the area on the printing plate within the nip is an image or a nonimage area or any multiple combination that might exist because of the format

being printed. As already noted, these thin, isopropanol-rich, aqueous layers readily wet either fountain solution or ink, consequently, under nip pressure, they are easily forced to diffuse back and forth into or across the rapidly changing interface, to or from whichever portion of the printing plate or type of form-roller happens to be at the nip. That is, under these low-surface-energy, mechanically-forced wetting conditions, a rapid, diffusional displacement may occur in the film-thickness direction. Transport of thin layers in this direction will be much faster than lateral or circumferential bulk flow away from the nip would be. Since areal differentiation by the fountain solution is not involved, diffusional mixing will be largely independent of the printing plate format, independent of dimensions or location of halftones or line solids.

The rapid, diffusional displacement of fountain solution into or out of the ink, allows extremely rapid, intimate, ink-to-ink contact necessary for replenishing the ink in the image areas that was used in the printing process. It also allows rapid recovery when ink or water feed rates are changed. There is a place for spurious water to go.

Lithography is not thwarted by this omni-present, overall thin, aqueous, alcoholic film of fountain solution because it automatically gets out of the way of ink transfer as required, by instantly disappearing into whichever layer, ink or fountain solution, is relatively moisture-starved.

This view fits with the well-known fact that inks formulated to not accept water are inoperative in high-speed lithography. With nowhere to go, fountain solution that is continually forced into intimate contact with the whole printing plate will, sooner or later, interfere with normal ink transfer and differentiation. Modern, rotary, lithographic printing requires a fountain solution sink to counterbalance the mechanically-induced ink/water mixing. That sink is the ink itself! And, there is an interesting corollary from this printing-with-isopropanol model; the printing plate does not need to differentiate acceptance of fountain solution based on its image/nonimage content!

Lithography without Isopropanol

Without fountain solution additives, control of image differentiation has been found nearly impossible. Water feed rates must be significantly increased to keep nonimage areas free of ink. This may result at times in too much ink transfer and at other times, too little. To avoid these extremes, typical lithographic fountain solutions contain small amounts of natural or synthetic weakly acidic or neutral, water-dispersible gums. During operation, these gums concentrate in nonimage areas of the printing plate, acting as thin-film, water-absorptive reservoirs. Phosphoric or similarly weak acids are added to help control gum solubility. Also, not pertinent to this discussion, are fungicides, buffer and colorants. With these minimal ad-

ditives, lithographic printing becomes tolerable, but requires considerable attention to obtain and maintain consistent quality.

Long before the advent of isopropanol, inkmakers found that the inks serve as a reservoir or sink for fountain solution. This infers that some fountain solution may be forced into the ink at the nips, even without isopropanol present, as discussed by Bassemir (3). Schaeffer (5) has pointed out, particularly when using high energy fountain solutions, that most of the mixing may take place at nip exits where cavitation occurs during splitting of the ink film; an excellent condition for trapping or emulsifying spurious or free fountain solution into the ink. Whichever mechanism applies, under these high-energy-fountain-solution conditions, we are expecting the press system to work against surface chemical principles of wetting and spreading, rather than in concert with them. Consequently, the necessary mixing of water into ink will be slow, requiring many press revolutions to achieve a natural ink/water steady-state condition, or requiring higher energy input to reach this steady state condition in reasonable time, perhaps both. This is equivalent to the converse of the first isopropanol advantage statement; without isopropanol, approach to steady-state operation is slower.

Despite early recognition by inkmakers that lithographic inks must accept some water, temporarily excess fountain solution exists at the ink form-roller/plate image area couples, more often than not, and must be squeezed out of the way. As indicated, the ink cannot rapidly absorb this high-energy fountain solution because the system does not satisfy molecular wetting prerequisites. The excess fountain solution will have to flow laterally or circumferentially out of the way. If this bulk flow is not completed during each revolution of the press, it can lead to printing variances, such as snowflaking or washed-out images.

Most modern, commercial fountain solutions also contain 1% or less of a low-to-moderate surface energy, non-foaming surfactant or a soluble ink/water coupling agent, such as hydroxyethers or polyoxyethylene glycols. These additives cannot counteract the ever-present, format-dependent, excess fountain solution conditions during printing as effectively as a bulk reinforced, surface active compound like isopropanol. Using these will involve poor-to-incomplete wetting of the ink by the fountain solution; a wetting effectiveness that is dependent upon a fountain solution additive with poor ability to continuously maintain low surface tension under dynamic, high-speed, printing conditions. Consequently, printing is highly dependent upon the additive's concentration and chemical nature. The extent of aqueous phase film-splitting versus interfacial film-splitting at the nip exits, and therefore the completeness of retaining a thin, uniform fountain solution on the printing

plate after the nips, will therefore also be dependent on additive chemistry, and highly dependent upon the printing plate format. As a consequence of this limited-wetting condition, and of the 10-50 millisecond time restraints due to press design, and depending on the plate format, retractive formation of beads or disjointed, relatively-thick islands of fountain solution occurs to varying degrees in the inked areas of the printing plate. Thus, we encounter intermittent, sporadic, or retarded diffusional transport of fountain solution across interfaces into the ink, instead of smooth, instantaneous diffusion. We encounter bulk lateral flow of thicker fountain solution films, films of solution that could not radially diffuse into the ink rapidly enough. We encounter a behavior that will be more strongly dependent upon fountain solution feed rates and printing plate format, press design and roller interference settings. The practical results are converse to the second and third isopropanol advantages previously listed.

When we foster ink/water contact with additives like isopropanol, we overcome chemical barriers to water-in-ink mixing. The mixing process may become as rapid as the printing process; it becomes less dependent on details of ink and fountain solution chemistry, press settings and printing format. The process is easier to operate. We have introduced a measure of chemical automation.

It is apparent, then, that retraction of fountain solution from ink image areas, the formation of beads on ink areas, does not need to occur for image differentiation. The bulk retraction mechanism appears only as an artifact in a broader concept of lithographic printing, its relative importance during printing being dependent upon chemical and image format factors. It is not an essential mechanism in lithography.

Similar conclusions can be drawn regarding the film-splitting mechanism for water uptake by the ink at ink-to-ink nip exits. It may occur, but it is an artifact not a requirement in lithographic printing.

Lithography with Isopropanol Substitutes

There is one way, other than evaporation, to ensure high surface concentration of a soluble fountain solution additive. If we select a low-surface-energy compound having partial or limited water solubility, we will expect its saturated aqueous solution to readily separate into two phases, one rich in the additive, the other rich in water. Using the additive at or near its solubility limit will assure that some of the additive in concentrated form will always be available at the fountain solution interfaces.

With these criteria, and the desire to uncover a low-vapor-pressure, low-use-rate additive, a number of candidates were evaluated (11-14). One clearly repetitive characteristic of partially-water-soluble compounds is that their qualitative

water-transport capability as thin films on inked rollers was invariably greatest when the compound was used at or just below its water solubility limit; the condition where a separate liquid phase is likely to be present. Predictions based on these laboratory evaluations led to successful pressroom trials and then to marketing of a fountain solution additive product to rival isopropanol, 2-ethyl-1,3-hexanediol (15).

The compound is used at 1/2% to 1% of the fountain solution; 10 to 60-fold less than isopropanol. It is not as forgiving of mechanical press variables as isopropanol, a not surprising result, in view of the low concentrations that are used. It has had general success in meeting most of the isopropanol advantages in the field, most of the time. This success is strong support for the bulk-reinforced surface activity lithographic model and the limited solubility concepts presented here.

Driography is Lithography

Valid as the present model may be, the practical fact is that water in lithography is now an historical, albeit very useful, artifact. A number of printers are operating without water, using for instance, polymeric silicones as the non-printing, non-image areas of so-called driographic plates. In the inking form-roller/plate nips, the low surface energy, viscous ink will be forced into intimate, wetting, contact with the low surface energy, nonimage areas, as always in lithography. Rapid, cohesive relaxation of this forceably spread ink at the nip exits, precludes retention of an ink layer on the silicone surfaces by comparatively weak, interfacial forces, even if the forceably spread condition is thermodynamically favorable. The system is further biased against an ink layer adhering in nonimage areas, by the absence of adhesional penetration of the ink into the smoother, lower-surface-energy silicone. The energetically-receptive, diffusional-receptive image areas on the printing plate assure ink transfer and image differentiation. Image area surface energy is relatively unimportant since fountain solution is not present, tending to displace the ink.

In the nonimage areas of a lithographic printing plate, a thin, molecularly smooth, incompressible water layer, with isopropanol at its surface, is chemically and physically analogous to a thin, molecularly uniform, incompressible, polymeric silicone film. Thus, driography is entirely analogous to lithography. Water was available long before polymeric silicones; a fact that has confounded attempts to analyze the system. When we adequately help water to not interfere with the process, that is, when we foster rapid, on-press mixing of water into the ink with an instantaneously responsive, surface-tension-lowering additive like isopropanol or 2-ethyl-1,3-hexanediol, we optimize image differentiation by the printing plate.

Summary

Lithographic presses force water to mix with the ink at the printing plate, generally working against well-known principles

of molecular wetting. The printing press is easiest to control when this mixing can occur at press speeds. Overall wetting of the printing plate by fountain solution, both image and nonimage areas, allows formation of a uniform, thin film of fountain solution on the plate; it allows rapid, diffusional transport of fountain solution into and out of ink or fountain solution areas at the printing plate couples. Water in ink mixing at pressure nips becomes nearly instantaneous.

Improved control of and/or improved latitude in ink/water balance at the printing plate by this mechanism is accomplished best with isopropanol because of its bulk-reinforced surface activity. Limited-solubility additives, such as 2-ethyl-1, 3-hexanediol, function similarly but are slightly less effective. Commercial fountain concentrates using soluble, low-surface-tension additives provide some of this improved control but remain more dependent on printing format, ink and additive variables. Commercial concentrates having high surface tension provide none of this enhanced control and with no fountain solution additives the system is virtually inoperable.

Literature Cited

1. Kartunen, S. and Lindquist, U. 15th IARGAI Conference, Lillhammer, Norway, (1979).
2. MacPhee, J., TAGA Proc, 237 (1979).
3. Bassemir, R.W., Amer. Ink Maker, February 1981, 33ff.
4. Anon, Dampening Basics, Heidelberger Druckmaschine AG, (March 1980).
5. Fadner, T.A., Schaeffer, W.D. and Smith, D.E. 1978 Annual Research Department Report, Graphic Arts Technical Foundation, Pittsburgh, PA., 103-111 (1979).
6. Schlapfer, K., 13th IARIGAI Conference, Wildhaus, Switzerland (1975).
7. Albrecht, J. and Wirz, B., 9th IARIGAI Conference, Rome, 99-114 (1967).
8. Lehtonen, T., 13th IARIGAI Conference, Wildhaus, Switzerland, 269-298 (1975).
9. Dahlgren, H.P., U.S. 3,168,037, February 2, 1965.
10. Dahlgren, H.P., U.S. 3,259,062, July 5, 1966; U.S. 3,343,484, September 26, 1967.
11. Fadner, T.A., White, M.G. and Hayden, R.H., 1975 Annual Research Department Report, Graphic Arts Technical Foundation, Pittsburgh, PA., 103-124 (1976).
12. Smith, D.E. *ibid*, 35-44.
13. Smith, D.E. 1977 Annual Research Department Report, Graphic Arts Technical Foundation, Pittsburgh, PA., 135-144 (1978).
14. Fadner, T.A., *ibid*, 119-126.
15. Fadner, T.A., U.S. 4,178,467, July 14, 1981.

RECEIVED February 3, 1982

Electrostatically Assisted Ink Transfer in Gravure Printing

HARVEY F. GEORGE

Gravure Research Institute, Port Washington, NY 11050

Electrostatically assisted ink transfer has been widely accepted by gravure printers since its development by Gravure Research Institute in the mid sixties. There are more than 3,000 press units equipped with electrostatic assist world wide. The primary purpose of electrostatic assist is to eliminate skipping or missing of dots in an otherwise traditional gravure ink transfer process characterized by normal or moderately reduced impression pressures, the use of presses of traditional design and the use of fluid inks of traditional formulations. This paper describes the electrophysical basis of electrostatic assist and discusses a number of related aspects of the process including the effects of ink and paper properties, electrophoretic density shifts, ink whiskering, conductive impression roll coverings, etc.

This paper gives an outline of one of the most successful applications of electrostatic techniques in an existing production process, namely, the electrostatic assist process for ink transfer in gravure printing.

The electrostatic assist process was developed to overcome a specific print defect which had plagued printers and paper makers for years, namely, skipped dots. In this it has been very successful as can be seen from the side by side photographs in Figures 1 and 2. These show portions of a mail order catalog printed at high speed on a production press with and without the electrostatic assist turned on — all other printing conditions being identical. From the beginning of its development in 1961, the aim was to use electrostatic assist as an aid to enhance print quality in an otherwise conventional ink transfer process with minimum modifications on existing presses and using conventional printing inks, containing flammable vapors.

The term "electrostatic technique" tends to be usually associated in many minds with Leyden jars, high voltages and corona wires. There were indeed attempts in the late 1930's and 1940's to transfer paste type inks — mainly letterpress — across a gap by means of high voltages, air ionization and ion bombardment. The objective was to eliminate pressure and to permit the use of light weight presses. None of these schemes have found commercial applications.

The process that we will describe here does not fall into this category. The voltages which produce the desired skip suppression are usually below 1,000 V and the currents are limited to below 3 ma even for very large, fast press units.

The rotogravure process is one of the three major printing processes, the others

0097-6156/82/0200-0359\$06.00/0
© 1982 American Chemical Society

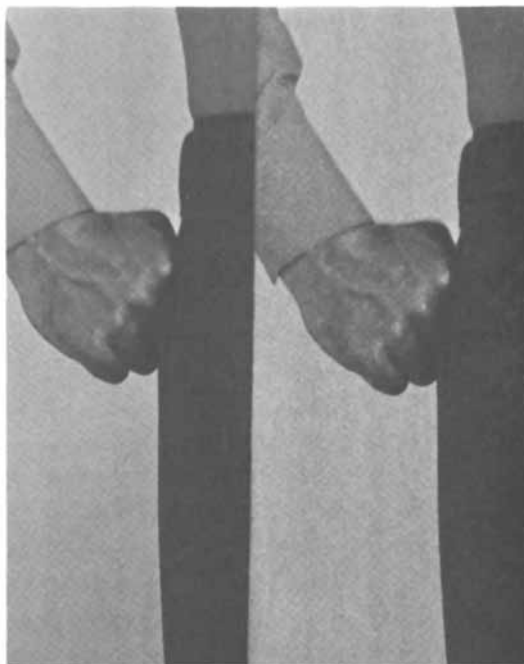


Figure 1. Comparison of a section of a catalog page with electrostatic assist on (left), and electrostatic assist off (right).

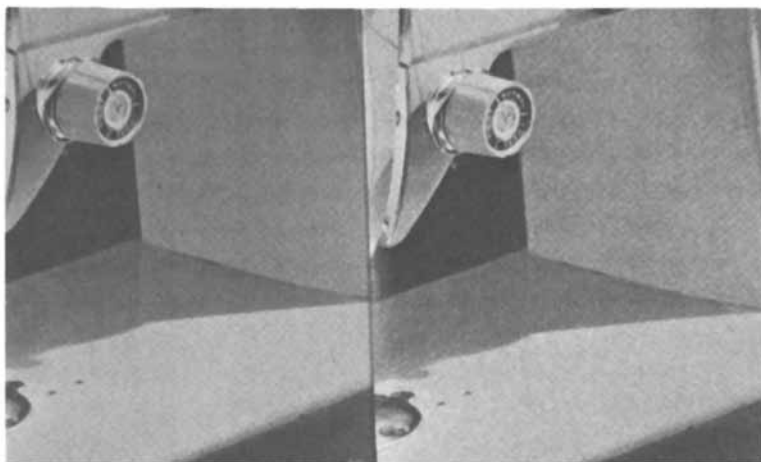


Figure 2. Comparison of a section of a catalog page with electrostatic assist on (left), and electrostatic assist off (right).

being letterpress and offset lithography. In the publication field, rotogravure is used to print such high color fidelity, high circulation products as the National Geographic Magazine, The Reader's Digest, Seventeen, Better Homes and Gardens and many other magazines. Almost all Sunday Newspaper Supplements and the catalogs of the large mail order houses, such as Sears and Penney's are generally gravure printed. Some of the newer publication gravure presses print on paper webs up to 100 inches wide at press speeds in the 2,000 feet per minute range.

In packaging, gravure is used to print a range of products from cereal and detergent boxes to cigarette packs and gum wrappers on substrates ranging from 30 point (mil) cardboard to unsupported polyethylene film. Specialty gravure is employed in the production of vinyl floor coverings, high pressure laminates such as Formica, cigarette tips and postage stamps.

The image carrier in gravure is a hard, polished layer of copper electroplated on the surface of a massive steel cylinder as shown in Figure 3. The image consists of small cells of varying sizes and depths that are either etched through a diffusion resist or engraved by means of a diamond stylus at a rate of 4,000 cells per second as shown in Figure 4. The cell density is generally in the 22,500 to 40,000 cells per square inch range corresponding to 150 to 200 lines per inch screen rulings. Cell depths range from about 7 micron for highlights to a maximum of half the thickness of a sheet of newsprint for deep shadows. After an engraving has been approved, it is usually protected against mechanical wear by a few micron thick layer of bright chrome.

As the cylinder rotates in the press, the lower part of the cylinder is flooded with ink having a viscosity in the low centipoise range. The press ready ink may contain 7% pigment, 18% binder, such as modified rosins, nitrocellulose or a synthetic resin and 75% solvent. The solvents are usually blends of such materials as aliphatic hydrocarbons in the heptane range, toluene, acetates and alcohol. Water based systems are used in a number of applications.

As a spot on the cylinder approaches the printing nip, the ink outside the cells is removed by means of a flexible steel doctor blade. Figure 5. In the printing nip, the paper web is pressed against the gravure cylinder by means of a rubber covered impression roll. On wide presses, a heavy back up cylinder is used to avoid minimize roll bending and the consequent uneven impression pressure. Typically 40% to 70% of the ink or ink solids are transferred to the web, the rest returns to the ink fountain. After each press station the ink is dried by passing the web through a high speed air dryer before the next color is layed down. The fact that only a portion of the ink is transferred is really of no concern. Shadow densities approaching the mass tone of the ink are readily obtained. The ink that remains on the cylinder returns to the fountain. With reasonable control over the ink viscosity, the transfer percentage and the spreading of the ink on the paper remains constant which explains the remarkable color consistency of gravure.

A situation that is of greatest concern is when isolated cells in light mid tones and highlights fail to print. Although the individual dots in a smooth print are below the power of resolution of the human eye, missing dots, or skipped cells, or snowflakes or whatever they might be called, distract greatly from the visual appearance of the print. Researchers in the 1950's and 60's had clearly established that the skipping was the result of mechanical imperfections in the paper surface such as protruding fibers and fiber bundles, suction holes or lack of fines and wire patterns on the wire side of the paper, which were too hard to be flattened out by impression pressures ranging in the 70 to 200 pounds per linear inch of web width for

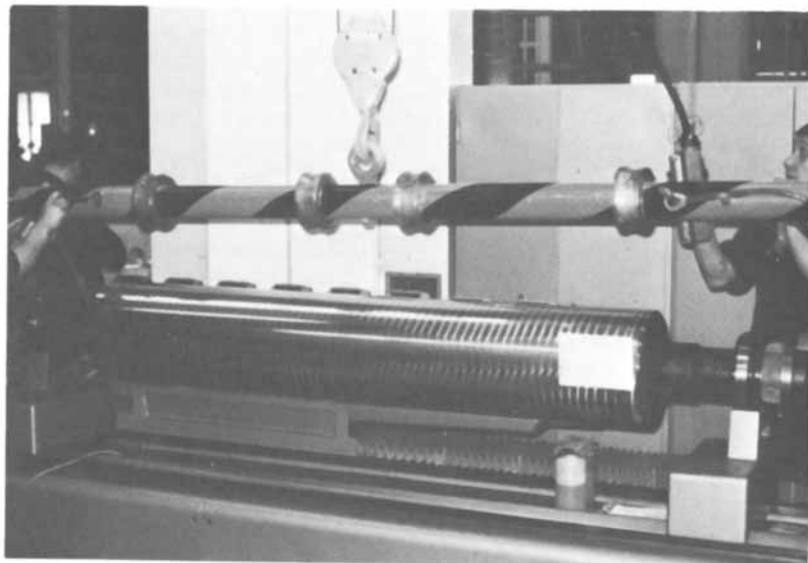


Figure 3. Polished gravure cylinder before engraving.

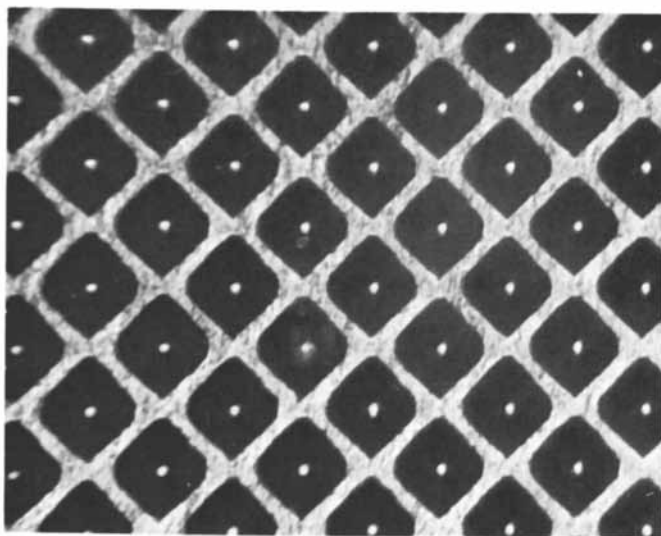


Figure 4. Diamond stylus engraved shadow area.

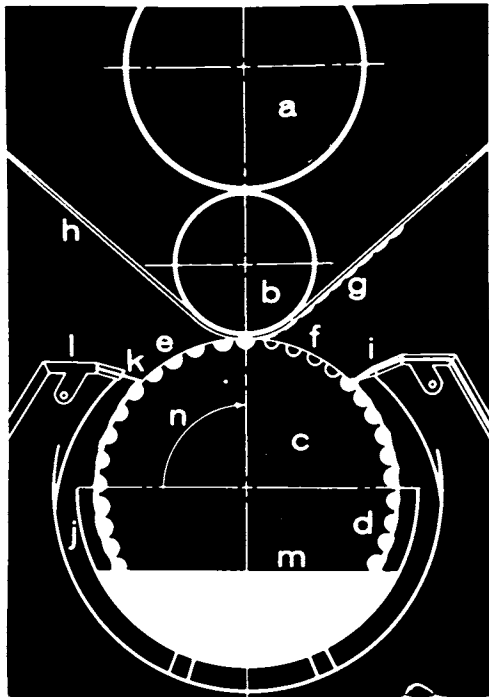


Figure 5. Schematic view of gravure printing unit.

paper or board. Coated papers are generally smoother than uncoated papers, but the surface hardness is also much higher and the visual effect of a skip is much more pronounced.

Attempts to overcome the problem by higher and higher impression pressures resulted in wear on press components and reduced productivity. Ink manipulations result in poor shadow ink lay and slower drying.

To understand the skipping problem, the ink transfer process must be understood. As a cell emerges from under the doctor blade, it is only partially filled because some ink adheres to the doctor blade. During the travel from the doctor to the impression, some solvent may evaporate, reducing the ink volume further. In the meantime, surface tension will form the surface of the ink into a fairly symmetrical concave meniscus. All this has been shown by high speed micro-photography. In the impression, ink transfer is initiated by a few points on the paper contacting and being wetted by fluid ink near the edges of the cell. The characteristic doughnut shaped print out of gravure highlights is evidence of that. Figure 6. After this initial contact, the ink transfer proceeds by means of capillary or surface forces. If an imperfection in the paper prevents the initial contact, and the gap may be only a few micron wide, the cell will skip.

The central idea behind the ESA process is as follows: Instead of using excessive pressures to try to make the paper surface contact wet ink near the cell edges, relatively weak electrostatic forces are used to deform the meniscus of the highly fluid ink in the cells in such a way as to improve the likelihood of contact between wet ink and paper. For this purpose, the gravure cylinder remains grounded. An electric charge of either polarity is applied to the impression roll. With conductive rubber rolls, this charge tends to concentrate in the printing nip, where the proximity of the grounded gravure cylinder greatly increases the capacity (or ability to hold a charge at a given voltage). The field lines emanating from this charge penetrate the (dielectric) printing substrate and terminate on charges which are induced on the surface of the cylinder and the ink. The field tends to concentrate near the cell edges and this concentration of upward pull deforms the meniscus of the ink in the cell in a manner that will assure contact between ink and paper. Figure 7.

Tests conducted under GRI sponsorship at Battelle Memorial Institute in 1962 and 1963 on a small laboratory test press using corona charging had demonstrated that charging did indeed affect gravure ink transfer. Similar effects were obtained by GRI by contact charging a layer of metallic paint on the impression roll of a production publication press. To arrive at a practical, effective and safe system, a scheme involving contact charging of a slightly conductive impression roll was adopted.

A major theoretical study was then undertaken at GRI to establish the major process parameters, such as the required voltage and rubber conductivity. The fact that surface tension is the major force opposing the formation of a bulge in the ink surface near the cell edge was established from a plausible model of the ink surface deformation. Figure 8. Viscosity plays a minor part opposing ink bulging and the effects of inertial forces are negligible. The relative degree of field concentration near the cell edges was estimated by conventional field plotting, i.e., such facts as the rule that the field near a conducting surface is perpendicular to that surface. Figure 9. The field strength needed to form a bulge in the ink was then calculated from the force and pressure balance on an element of the ink surface. Without electric field and a concave surface the hoop stresses resulting from surface tension are balanced by the negative internal pressure prevailing throughout the ink volume.

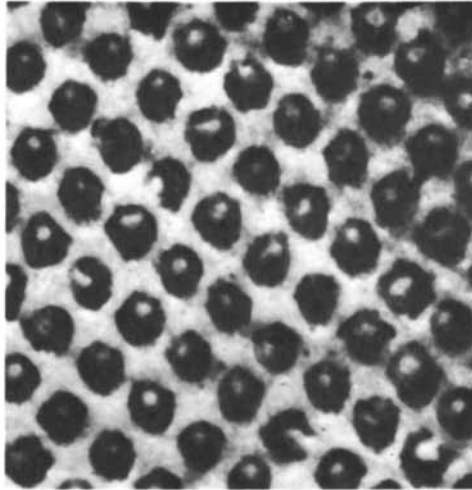


Figure 6. *Photomicrograph of a gravure printed midtone.*

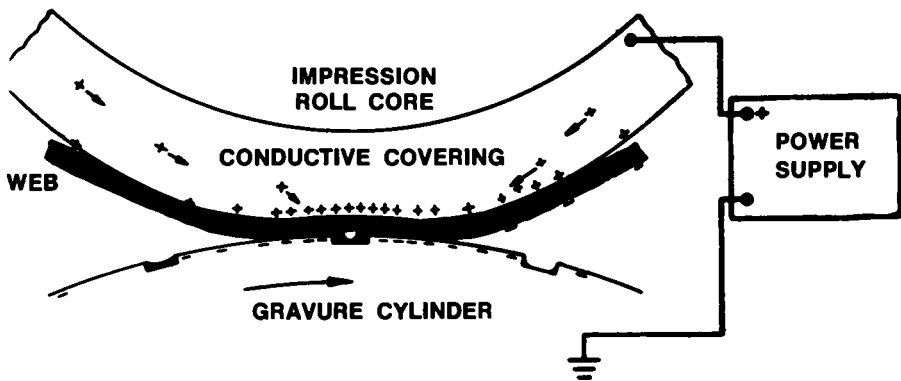


Figure 7. *Charge distribution and ink deformation in a gravure printing nip with electrostatic assist.*

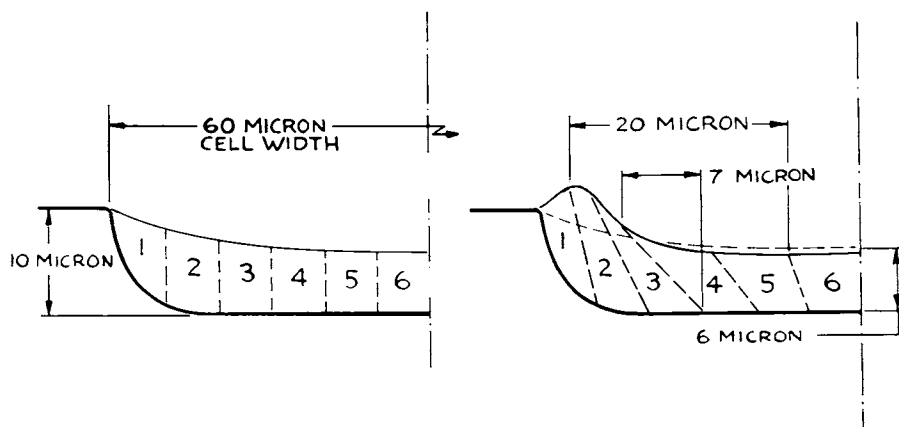


Figure 8. Scale model of ink meniscus used to estimate inertial and viscous forces without charging (left), and with charging (right).

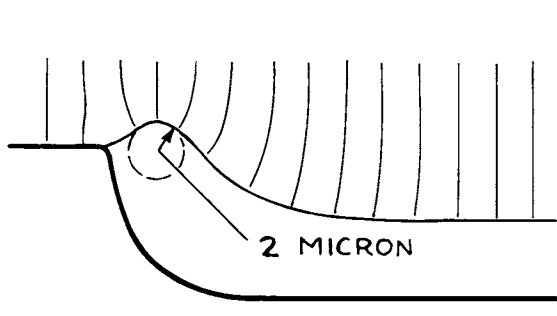


Figure 9. Scale model of ink meniscus and field lines at advanced bulging used to estimate radius of curvature and relative field strength.

To locally flatten the ink surface, the electrostatic pull must equal that internal negative pressure. To cause local bulging up, the electrostatic pull must balance the downward hoop stresses from surface tension as well as the negative internal pressure. The field strength in the air or vapor space on top the cell needed for effectiveness was thus calculated to be about 30 million volt per meter. Taking the dielectric constant of typical printing papers into account, this amounts to about 200 volt per .001 inch of paper thickness. In practice, the voltage in the nip needed for effectiveness has been found to be in the 100 to 200 volt per .001 inch range. The objection has been raised that at field strength above two (2) million volt per meter air breakdown would effectively short out the field. The figure of two (2) million volt per meter is however only valid for large air spaces. For small gaps, the breakdown strength of air is much higher. Figure 10.

The resistivity of the rubber covering of the impression roll had to be such that the assist retained its effectiveness without permitting any local discharge fast enough and powerful enough to ignite flammable vapors. There is little danger in the nip itself where air is effectively excluded, or near the nip because the gravure cylinder represents a large and effective heat sink. As far as energy thresholds for ignition in larger spaces are concerned, NFPA Bulletin No. 77 indicates that saturated hydrocarbon gasses and vapors require about .25 millijoules of stored energy for ignition in optimum mixtures with air. A rubber resistivity in the 10^7 Ohm cm. range suitable for effective use of electrostatic assist will limit any local discharge below that limit. The charging unit also contains a thyatron crowbar circuit which will discharge the whole system within microseconds if the total current exceeds a level that can be adjusted in a range up to 3 milliamperes. With over 3,000 electrostatic assist units in daily production in this country alone, the safety record has been excellent.

To retain effectiveness at reasonable power supply voltages, the covering resistivity should not be too high, otherwise the voltage drop between the charging unit and the printing nip proper becomes too high to obtain effective results. Current flow from the power supply to the printing nip consists of two components. We have leakage through the web and at the ends of the impression where the roll may touch the cylinder directly. On fast running presses, these conduction currents represent only a small part of the total current. Here the convection currents predominate. Charges are carried away by the web in inked and non inked areas. It is not that all charges that accumulate in the nip area are carried away. It has been found that the web outside the nip can carry a charge of the same polarity or of opposite polarity to that applied at the impression roll. The polarity depends on the relative ease of ink transfer between the impression roll and the top side of the web or the cylinder and the bottom side of the web. In printing areas, where the induced charges are transferred together with the ink, the net charge is always of a polarity opposite to that applied to the impression roll.

A third effect, also related to convection will reduce the voltage in the nip below the value that can be calculated from the power supply voltage minus the product of the roll resistance and the power supply current. As a point on the impression roll approaches the nip, its capacitance to ground will increase drastically. Unless current can flow through the rubber into the nip, the voltage will drop in proportion. As explained before, the charge transfer in the nip is far from complete. As the point moves out of the nip, charges are carried out of the nip area by the rubber. For effectiveness and to prevent any Van de Graaff effects, the rubber must be conductive enough to let these charges flow back into the nip. Figure 11.

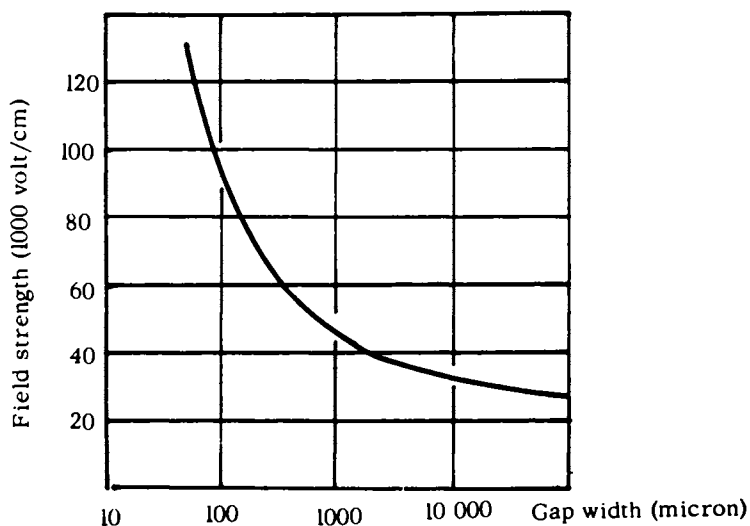


Figure 10. Breakdown field for sparking between parallel plates as a function of gap width.

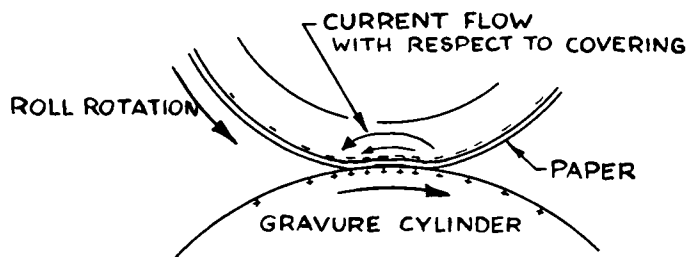


Figure 11. Current flow with respect to rotating impression roll covering needed to overcome voltage drop due to high nip capacitance.

A rubber resistivity of 10^7 Ohm cm. and at layer thickness of about $\frac{1}{4}$ inch is suitable to overcome this charge transport, even at very high press speeds.

In the early stages of the development, the electrical properties of impression roll coverings were rather erratic. In this country, conductivity was imparted by means of conductive, structured carbon black fillers. It turned out that the exact steps in manufacture, such as milling temperature were as important as formulations. The conductivity of compounds made with Buna N was very strain sensitive. In Europe, conductivity was imparted by Anti-static additives. The electrical properties were more predictable, but resistance to wear left much to be desired. The manufacture of suitable roll coverings has been a real challenge to roll manufacturers, and suitable coverings have been available in the last five years on a very consistent basis. New Material which contain conductive polymers (Hercules Inc.) require some warm up before the desired conductivity level is reached, but have very uniform predictable electrical properties and stand up well to the wear and tear of press operations.

Now to side effects. When printing the more conductive inks, those with water base or polar organic solvents, such as alcohol and acetates, there are none. With the more resistive inks using toluene or aliphatic hydrocarbon solvents and certain pigments there were some polarity dependent density shifts, with a positive applied charge tending to repel the pigment. Figures 12 and 13. As this is due to particle drift in a field in the ink, it is more pronounced at slow press speeds and higher leakage current through the paper. These density shifts have generally not been found to be a major detriment to the use of the electrostatic assist process.

Another side effect, again restricted to inks with non polar solvents is whiskering, that is, the spreading of ink from the edges of a shadow patch over non printed areas. Originally, the effect was thought to originate at the printing nip exit, because filamentation had been photographed in the ink split zone. This may indeed have been the case with non conductive or old impression rolls which lost their conductivity temporarily due to compression in the nip. Low air and paper moisture, slow drying ink, overetched shadow patches on the engraving and high press speeds all contributed to the problem. The basic reason for the whiskering is the difference in charge pick up in inked and non inked areas. Anything that helps to increase the charge transfer to the web in non inked areas will help. A major study a few years ago has shown that with the newer impression rolls, the whiskering occurs after the web has separated from the impression roll flank. The fact that the effect occurs at this rather accessible location permits effective remedial action, such as the strategic placement of static eliminators or shielding with grounded conductors, which will change the direction of the electric fields from a direction parallel to the web to a direction more perpendicular to the web.

The strong point of the gravure process has always been the consistently high quality and good productivity of its press operations on a given paper stock. The development of the electrostatic assist process has overcome one of the major print defects of gravure and thereby greatly strengthened its competitive position. Since its introduction a number of leading publications have gone over to gravure, as have a number of large jobs in the packaging field.

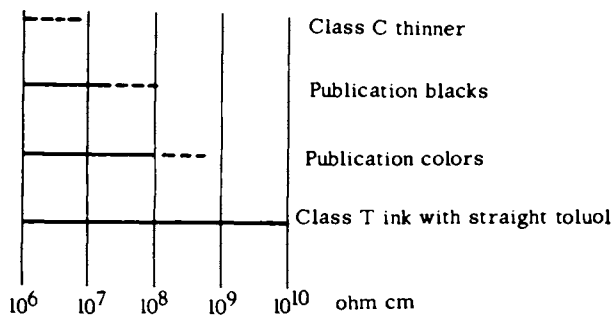


Figure 12. Approximate volume resistivities of different ink types.

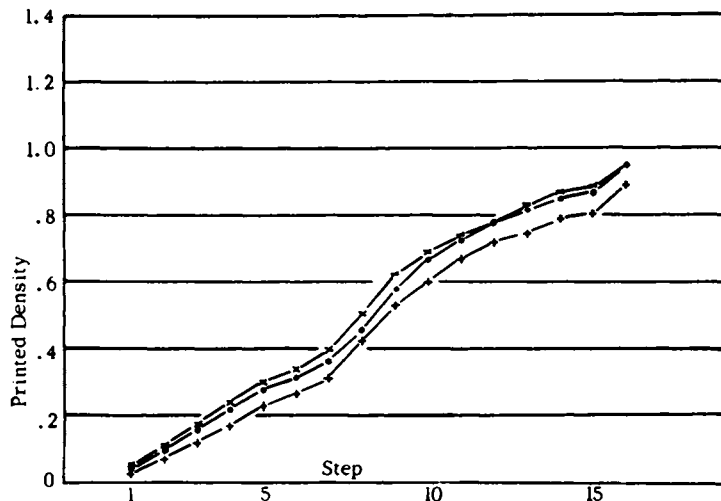


Figure 13. Printed density of magazine yellow on coated magazine paper at no charge ($\cdot - \cdot$), $+650\text{ V}$ ($+ - +$), and -550 V ($\times - \times$).

Acknowledgement: The valuable assistance of Robert H. Oppenheimer, Chief Engineer at Gravure Research Institute, in the preparation of this paper is gratefully acknowledged.

RECEIVED June 18, 1982

Image Generation by Peel Development: Adhesion Control Through the Use of Photolabile Blocking Groups and Surfactants

J. E. TREND and G. L. EIAN¹

3M Company, Central Research Laboratories, 3M Center, St. Paul, MN 55144

A peel-apart imaging system with high resolution (>100 cycles/mm) has been developed using the ability to photochemically control the specific adhesion of solution coated resins for thin (500-1000Å), yet opaque, vapor deposited metal films. The system is ultraviolet sensitive, contact speed, and is comprised of four layers: 1) cover film, 2) photosensitive coating, 3) metal film, 4) transparent support. Small amounts of surfactants masked with photolabile protecting groups present in layer 2 provide the required photo-control of the adhesion of the photosensitive layer for the metal surface. When the construction is imaged through a mask, the adhesion of the photosensitive layer for the metal surface becomes vanishingly low in the irradiated areas resulting from the photoliberation and subsequent resin-metal interfacial orientation of the surfactants. In the unirradiated areas the resin-metal adhesion remains high. By peeling the layers 1 and 2 from layer 4 the metal film is selectively delaminated from the support to form complementary images, a reversal image on the support and a duplicate of the original on layers 1 and 2. Details of the photo- and surface chemistries are presented. Factors governing performance are discussed.

In the panoply of photoactivated imaging materials and processes, peel-developed systems constitute an intriguing but sparsely populated niche. Common to these systems is the need to photochemically differentiate adhesive forces within a collection of layers. In the past this has been accomplished through photopolymerization (1), apparent photocrosslinking (2,3,4), or photo-

¹ Current address: 3M Company, Occupational Health and Safety Products Laboratory, 3M Center, St. Paul, Minnesota 55144.

0097-6156/82/0200-0371\$06.00/0

© 1982 American Chemical Society

generation of gas (5,6). The changes in adhesion which accrue reflect photo-induced effects on the viscoelastic properties of the layers (polymerization, crosslinking) or macroscopic shear forces accompanying interfacial bubble formation. The peel-developed system presented here relies on the photoliberation of agents which interfere with the chemical components of adhesion at polymer-metal (oxide) interfaces. A proper presentation of the chemical details of the imaging process requires a discussion of the mechanics of the peel-developed system.

Mechanics of the Peel-Developed Construction

Figure 1 depicts the four-layer composite for the peel-developed imaging system comprising 1) a transparent, adherent cover film; 2) a photosensitive polymeric coating; 3) a thin, yet opaque, vapor deposited metal layer which constitutes the image [also used in previously described systems (2,3,4)]; 4) a transparent base film, usually polyethylene terephthalate. In the absence of irradiation, peeling the cover film (1) versus the base film (4) causes separation to occur cleanly at the metal-base film interface (2/3). The adhesion of the cover film for the photosensitive layer is sufficient to prevent separation of the 1/2 interface so that layers 1 and 2 act as one. When exposed through a mask and developed by peeling, the composite yields a metallic reversal (negative) image of the mask on the base film (4) and the complement (duplicate or positive) image on combined layers 1 and 2 (Figure 1).

Since the photochemical dissipation of the adhesion between the polymeric coating and the metal layer is the key to the imaging process, attention must be turned to the characteristics of the polymeric coating and the metal layer. Useful polymeric coatings may be composed of resins drawn from Table 1 or similar resins. The coatings are cast from ketone, ketone-aromatic hydrocarbon, or chlorocarbon solutions (10-20 percent solids) using conventional coating techniques to give dried coating thicknesses ranging from 5-50 μ . These resins bear polar, adhesion-promoting groups like carboxylic acids, esters, and alcohols: the carboxylic acid groups in particular promote adhesion to the native metal oxide surface of the metallized base film through acid-base interactions (7). Usable metal layers include copper, gold, nickel, silver, tin, zinc, preferably aluminum or aluminum topped with silicon oxides. These are vapor deposited onto unprimed, unsubbed polyethylene terephthalate film base (50-175 μ) to a thickness of 500-1500 Å . For aluminum, 1000 Å gives an optical density of ca. 4.

The Mechanism for Dissipation of Adhesion

Photoliberation of surfactants (anionic--in the acid form

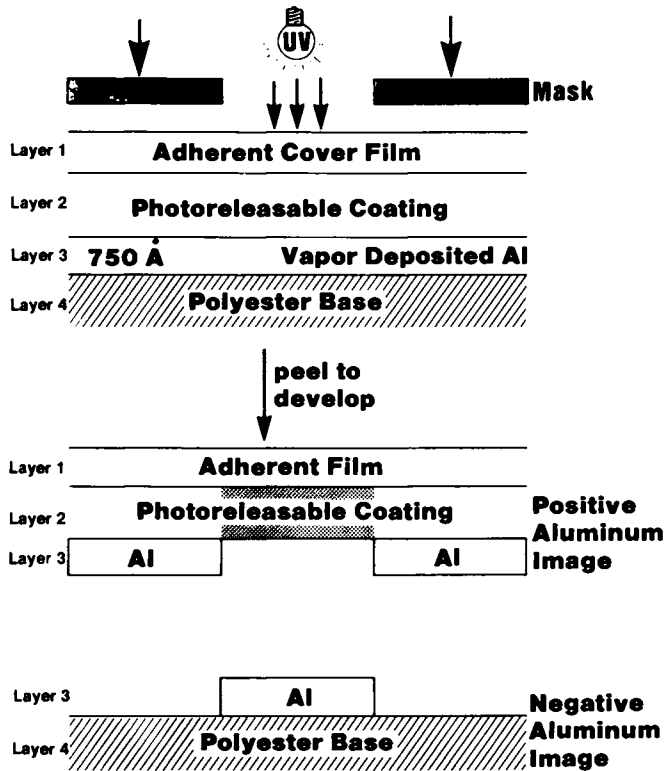


Figure 1. Schematic of the peel apart construction and complementary images formed by peel development.

Table I

Suitable Coating Resins

<u>Trade Names</u>	<u>Manufacturer</u>	<u>Generic Type</u>	<u>Tg°C</u>
Carboset 525	B.F. Goodrich	carboxy functionalized acrylic	23-36°
Elvacite 2044	DuPont	high molecular weight <u>n</u> -butyl methacrylate	24-37°
Estane 5715	B.F. Goodrich	urethane	not measured
Vinac ASB516	Air Products	vinyl acetate	39-48°
Vitel PE-200	Goodyear	linear saturated polyester	67°
Vitel PE-222	Goodyear	linear saturated polyester	47°
VAGH	Union Carbide	vinyl chloride- vinyl acetate- maleic acid	75-82°
VMCH	Union Carbide	vinyl chloride-vinyl acetate-maleic	74-81°
VYHH	Union Carbide	vinyl chloride-vinyl acetate	72-79°

or, less often, cationic--in the free base form) within the polymeric coating provides the mechanism for diminishing the coating-metal adhesion: the liberated surfactant is free to accumulate and orient at the resin-metal interface and competes with the resin for acid-base interactions at the metal (oxide) surface. The photoliberation of surfactants is made possible through the implementation of photolabile protecting groups. Until cleaved by photolysis, the photolabile protecting groups, covalently bonded through the polar functionality of the surfactant, largely suppress the surfactant properties. Photolabile protecting groups have been recently reviewed (8,9). Because of their easy auxochromic modification, synthesis, incorporation, and photoefficient removal (8,9), the family of 2-nitrobenzyl protecting groups have surfaced as the most useful.

Relatively small amounts of the 2-nitrobenzyl-protected surfactant (1-7 percent of the total solids in the coating) are needed to effect the required change in adhesion of the polymeric coating for the metal surface on photolysis. A specific example best illustrates the phenomenon.

Example. Sufficient 4,5-dimethoxy-2-nitrobenzyl-hexadecanesulfonate (λ_{max} , chloroform, 345 nm, $\log \epsilon 3.5$) is dissolved in a 15 percent solution of Vitel PE-222 resin in methylethylketone to give 3 percent relative weight of solids of the additive in the resin. The solution is knife coated at a 50μ orifice onto the metal surface of polyethylene terephthalate film base vapor coated with 750\AA of aluminum. The sample is allowed to air dry to a tackfree surface and then hot-roll laminated with a cover film of 3M 707 type Laminating Film. Half of the sample is covered with an opaque sheet; the other half is exposed to a 2KW mercury lamp at a distance of 70 cm through glass (radiant energy at 360 nm 5.7×10^{-2} watts/cm²) for 45 seconds. On peeling the cover film away from the base film, the aluminum layer delaminates from the base film in the unexposed areas, yet remains tightly adhered to the base film in exposed areas. When exposed through a negative 1951 United States Air Force Resolving Power Test Target, the sample yields a positive aluminum image of the target on the base film having a resolution of at least 100 cycles/mm.

Surfactants tested in this manner are listed in Table II along with pertinent physical data. The efficiency of a given surfactant, in terms of exposure time required to obtain photo-diminished adhesion in the above example, depends on two factors: the pK_A of the surfactant and the log (critical micelle concentration), log (CMC).

pK_A Dependence. For an aluminum image layer, the efficiency of photodissipation of adhesion decreases with decreasing acidity (larger pK_A) of the liberated surfactant. With the photolabile stearate derivative, 6-10 times the exposure (or a corresponding increase in stearate concentration) is required to effect the same result as the hexadecanesulfonate; the N-(4,5-dimethoxy-

Table II

Surfactant Data

<u>Active Surfactants</u>	<u>Approximate pK_A</u>	<u>Log (CMC)</u>
$C_{16}H_{33}SO_3H$ hexadecanesulfonic acid	-1-0	-3.5
$C_7F_{15}CO_2H$ perfluorooctanoic acid	0-0.5	-2
$C_{17}H_{35}C(=O)N(CH_3)CH_2CO_2H$ stearoylsarcosine	3	-3
$C_{17}H_{35}CO_2H$ stearic acid	5	-3
$C_{15}H_{31}CO_2H$ hexadecanoic acid	5	-2.5
$CH_{18}H_{37}N(CH_3)$ N-methyloctadecylamine (conjugate acid)	11	-3.5
<u>Inactive Surfactants</u>		
$CH_3C_6H_4SO_3H$ 4-toluensesulfonic acid	0-0.5	>-1.5
$C_5F_{11}CO_2H$ perfluorohexanoic acid	0-0.5	-1
$C_{12}H_{25}CO_2H$ tetradecanoic acid	5	-1.5

2-nitrobenzyl) derivate of N-methyloctadecylamine is inactive under these conditions. If the aluminum surface is first over coated with a vapor deposited layer of silicon oxides (using silicon monoxide) the N-methyloctadecylamine derivate is the most efficient with the acyl sarcosinate derivate inactive and the hexadecanesulfonate showing some imaging efficiency. These results can be crudely modeled by a comparison of the isoelectric point of solid surfaces (IEPS, pH units) and the pK_A of the liberated surfactant. A large difference between the IEPS of the metal surface and the pK_A provides a measure of the ionic interaction between surfactant and surface. The extent of the interaction is described by the Δ s defined below (7):

$$\begin{aligned}\Delta_{\text{acid surfactant}} &= \text{IEPS} - \text{pK}_A \\ \Delta_{\text{basic surfactant}} &= \text{pK}_A - \text{IEPS}\end{aligned}$$

A large and positive Δ indicates a strong interaction and would imply an efficient photodissipation of adhesion for the surface-surfactant pair. Figure 2 shows that this expectation is born out for nickel (IEPS = 10), aluminum (9), tin (4), and silicate (2) with the surfactants tested.

Log (CMC) Dependence. A minimum level of surfactant activity is required of the surfactant to diminish adhesion on photoliberation. In the series of straight-chain carboxylic acids, photolabile derivatives of members with fewer than 16 carbons show essentially no photodissipation of adhesion. Derivates of perfluorohexanoic acid and 4-toluene-sulfonic acid are inactive also. Although strictly a measure of surfactant behavior in aqueous media, the log (CMC) seems to provide a good indication of performance in this application. Photolabile derivate of surfactants having a log (CMC) significantly more positive than -2 show no activity even under prolonged irradiation (10-20 times normal) and at elevated concentration (10-15 percent of the total coating weight).

Spectroscopic Evidence for Interfacial Surfactant Activity

Evidence presented thus far for the putative role played by the photoliberated surfactants has been somewhat circumstantial. Conventional infrared and ultraviolet spectroscopy establish that the photolabile protecting group is photolyzed and the surfactant released under photolysis; acid-base indicators, when added to the photosensitive coating, confirm the release of acid for the anionic surfactant derivatives. The surface sensitive spectroscopic techniques of ESCA (Electron Spectroscopy for Chemical Analysis) and RAIR (Reflection-Absorption Infrared) spectroscopy establish the involvement of the surfactant more unequivocally.

ESCA Analysis. Samples prepared in a manner similar to that described in the Example (Carboset 525 was substituted and the

	Ni	Al	Sn	SiO _x
RSO ₃ H	Δ11 ★★	Δ10 ★★★	Δ5 ■-★	Δ3 ■-★
R-CO ₂ H		Δ9 ★★		
R-SARC		Δ7 ★★		Δ-1 ■
R-CO ₂ H	Δ5 ★	Δ5 ★		
$\begin{array}{c} \text{CH}_3 \\ \\ \text{R}-\text{NH} \end{array}$	Δ1 ■	Δ2 ■-★	Δ7 ★	Δ9 ★★★

Figure 2. Correlation between surfactant-surface acid-base interactions and photoresponse of the peel developed imaging system.

Δ represents the difference between the isoelectric point of the surface oxide of the metal (IEPS) and the acidity of the photoliberated surfactant (pK_a). Key to photoresponse (min): ★★★, 0.5-1.5; ★★, 3-5; ★, 6-10; and ■, no photoresponse after 15 min exposure.

cover film omitted) were examined by ESCA in the irradiated areas at the aluminum surface and coating surfaces (top of layer 3, top and bottom of layer 2 in Figure 1) for the presence of photolytic fragments of 4,5-dimethoxy-2-nitrobenzylhexadecanesulfonate. The C,N,S atom ratios show that 1) only the hexadecanesulfonic is present on the aluminum surface, 2) there is an accumulation of the hexadecanesulfonic portion at the expense of the 2-nitrobenzyl portion at both top and bottom of irradiated layer versus unirradiated layer 2 (top surface only). The data are shown in Table III.

Table III

ECSA DATA

<u>Surface</u>	<u>C/N Atom Ratio</u>	<u>C/S</u>	<u>S/N</u>
Al (layer 3-top)	-	34	-
Irradiated Coating (layer 2-bottom)	139	38	3.7
Irradiated Coating (layer 2-top)	390	68	5.7
Unirradiated Coating (layer 2-top)	230	130	1.7

RAIR Results. RAIR spectroscopy provides information about the orientation of thin layers of molecules at interfaces through selection rules governing infrared absorption (10). Preliminary results indicate that on photoliberation, the sulfonate group of the hexadecanesulfonic fragment undergoes a reorientation at the coating-aluminum interface suggesting that an interaction develops between the singly bonded sulfonate oxygen (R-SO₂-O-H) and the aluminum oxide surface.

Factors Governing Imaging Performance

The image quality of the system depends on the frangibility of the metal layer and the ability of the photosensitive coating to impart the necessary peel forces on the metal layer so that the metal layer separates smoothly from the base film in the unexposed areas. Ductile metals such as copper and gold do not provide the edge acuity afforded by the comparatively more brittle aluminum. Not all resin coatings are capable of causing the metal layer to delaminate from the base film. Resins which are either too brittle (such as epoxy resins, methylmethacrylates) or too viscoelastic (2-ethylhexylacrylate pressure sensitive adhesives, ethylene-polyvinylchloride polymer)

fail to concentrate peel forces at the proper film interface. Usable resins are selected empirically.

Physical properties of the resin also govern the apparent photosensitivity of the system. Resins which have their T_g near room temperature exhibit higher apparent photosensitivity than resins with their T_g well above room temperature. Gentle heating (40-90°C, 30-90 sec) or the presence of plasticizers or residual solvents increase the photosensitivity of otherwise identical examples.

The maximum resolution obtainable depends on the mode of fringing of the metal layer. If an image is produced in which most of the background is removed to leave islands of metal on the base (dots) resolution as high as 144 cycles/mm has been obtained; however, if small islands of metal are removed from a largely continuous background (screen) much lower resolution is possible, (60 cycles/mm). Resins with low percent elongation under tensile stress produce superior edge acuity as do resins with T_g s above room temperature.

This peel-developed system presents an unusual and, at the time of its somewhat serendipitous discovery, unexpected implementation of surface and interfacial phenomena to create a convenient method of graphic reproduction. At the same time, development of the system (which continues) has added to the understanding and control of surface active species and their influence on the complicated phenomenon of adhesion.

Acknowledgments

Dr. H.E. Mismash (for ESCA data) and Dr. M.K. Debe (for RAIR data and analysis) of the 3M Central Research Laboratories are thanked for their contributions.

Literature Cited

1. Berkower, I.J.; Beutel, J.; Walker P. Phot. Sci. Eng. 1968, 12, 283-7.
2. Moriya, T.; Yamagata, T. U.S. 4,205, 989.
3. Inoue, E; Honma, S; Nakayama, T. Nippon Shashin Gakkaishi 1978, 41, 245-9; Chem. Abstr. 1979, 90, 31871x.
4. Honma, S; Inoue, E. Nippon Shashin Gakkaiski 1978, 41, 250-3; Chem. Abstr. 1979, 90, 31872y.
5. Nakayama, T.; Shimazu, K. Photo. Sci. Eng. 1978, 22, 138-141.
6. Honma, S.; Inoue, E. Nippon Shashin Gakkasihi 1980, 43, 74; abstract only.
7. Bolger, J.C. Soc. Plast. Eng. Tech. Pap. 1972, 18 (Pt. 1), 402-7.

8. Amit, B.; Zehavi, U.; Patchornik, A. Isr. J. Chem. 1974, 12, 103-113.
9. Pillai, V.N.R. Synthesis 1980, 1-26.
10. Tompkins, H.G. in "Methods of Surface Analysis"; Czanderna, A.W. Ed.; Elsevier Scientific: New York, 1975; p. 447-72.

RECEIVED April 30, 1982

Ink-Paper Interactions in Printing: A Review

M. B. LYNE and J. S. ASPLER

Pulp and Paper Research Institute of Canada, Pointe Claire, Quebec, Canada

Physical and surface chemical models for the application of ink and fountain solution to paper under printing conditions are reviewed. Initial transfer of ink to paper is primarily by hydraulic impression, and subsequently by wetting, adhesion, and film splitting. The effects of cavitation and filamentation on the uniformity of ink transfer and the influence of ink rheology on transfer and linting and picking are reviewed. Wetting delays for water and fountain solution are discussed and the mechanism by which sizing and self-sizing of paper increases the wetting delay is described. The implications of fountain solution wetting delays for multicolour offset printing are described.

Post-printing nip capillary sorption of ink and ink vehicles is discussed using Lucas-Washburn theory and the influence of the rate of capillary sorption on ink hold-out, show through and set off are discussed. Finally, the long-term migration of oil vehicles over fibre surfaces by spreading with the attendant loss of paper opacity is described.

0097-6156/82/0200-0385\$09.95/0

© 1982 American Chemical Society

The commercial printing industry embraces a wide variety of processes for putting ink on paper. This review will be concerned with letterpress and offset lithography in their conventional forms.

Ink formulations, printing forms, and printing pressures differ considerably in these processes, but the ink is invariably transferred from the printing medium to paper in a printing nip. At full commercial printing speeds paper passes through this printing nip in approximately one millisecond. As depicted in Figure 1 for the letterpress case there are several factors involved in the transfer of ink to paper and subsequent migration of ink and ink vehicles in the paper structure. As shown in Figure 2 an asymmetric pressure pulse is created during the passage of the paper through the nip which both compresses the porous network structure of the paper and hydraulically impresses the ink into the compressed pores in the surface of the paper. Penetration rates of between 250 and 525 $\mu\text{m/s}$ for the simulated letterpress printing of newsprint have been reported. This may be compared to 0.1 $\mu\text{m/s}$ for penetration 10 seconds after printing¹.

Inks are thixotropic and pseudo-plastic so the hydraulic impression of the ink also depends on the shear history of the ink in the inking system of the printing press and on the shear conditions in the printing nip. Paper is a viscoelastic material and thus the shape and duration of the pressure pulse affect its compression in the nip. On the outgoing side of the nip sub-atmospheric pressures are created which cause cavitation and the onset of filamentation in the ink film. The transfer process is complete with the fracture of the lengthening ink filaments. Since the sub-atmospheric pressure pulse is much smaller than the positive pressure pulse ink which has been forced into the capillary structure in the paper on the ingoing side of the nip is not withdrawn significantly on the outgoing side.

Hydraulic impression of ink into the surface capillaries of paper does not require that the ink wet the surface of the capillaries, but uniform ink film splitting does require the ink to wet and adhere to the surface of the paper during the millisecond of contact in the printing nip. In fact the uniformity of the printed image depends on the ink contacting and wetting the surface of the paper in the nip, on the rheological properties of the ink during lateral spreading and film splitting processes, and on local variations in the amount and depth of ink impressed into the surface capillaries in the paper.

A slight redistribution of the ink can occur after the paper leaves the printing nip due to aspiration as the network struc-

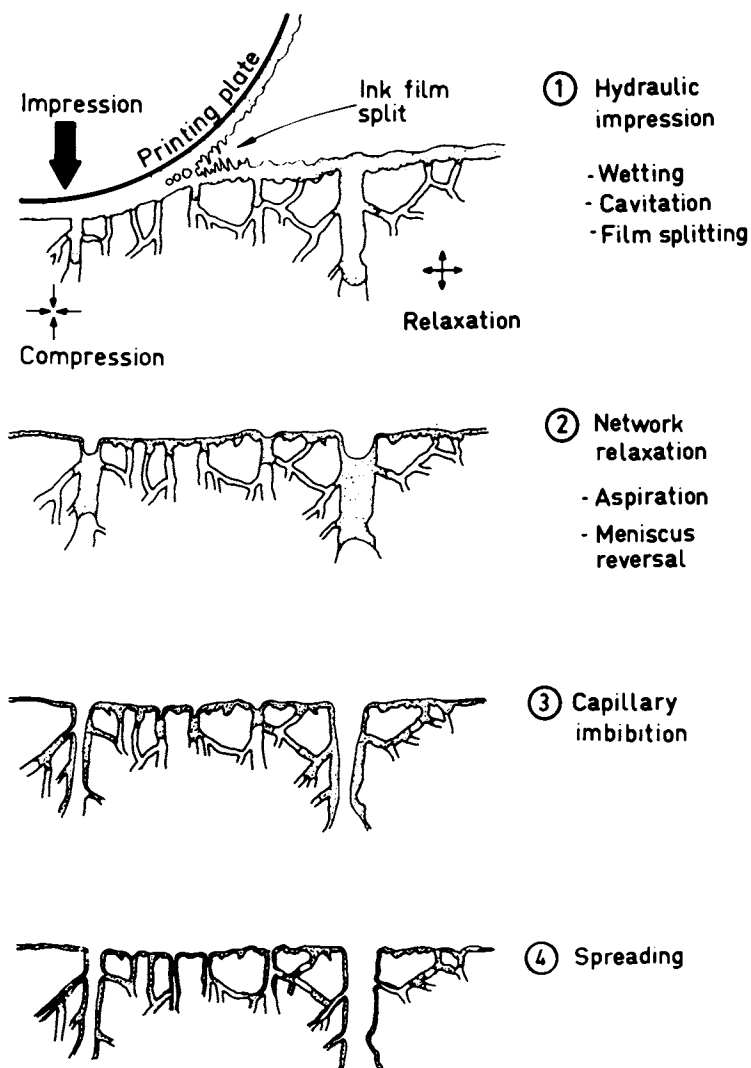


Figure 1. A simplified model of ink impression and absorption.

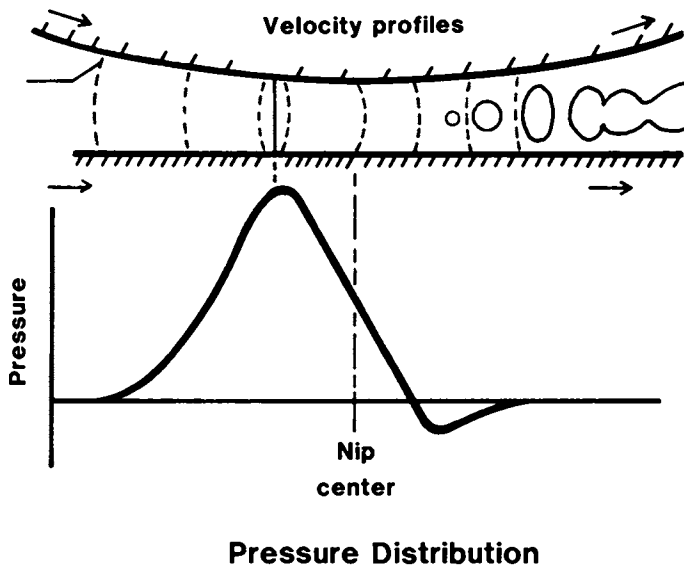


Figure 2. Pressure distribution and velocity profiles in the splitting of a film of Newtonian fluid.

ture of the paper relaxes. Initial capillary imbibition may also cause ink to be drawn into the paper, but the oil vehicle is soon drawn into progressively finer capillaries setting the ink by increasing the pigment concentration². When oil vehicles move into pores which would otherwise scatter light the opacity of the paper decreases. In this way, it has been demonstrated that the vehicle continues to fill pores larger than the wavelength of light for 5 to 15 minutes after printing. Using radioactive tracers it has also been shown that the oil continues to migrate for two to three weeks after printing, finally penetrating to approximately three quarters of the thickness of the newsprint paper studied³. Since the surface energy of the oil vehicle is usually lower than that of the paper, it can be presumed that this long-term migration is due to spreading. Thus, paper printed with non-drying inks must have a high surface area in order to separate the oil phase from the pigment without the oil penetrating to the other side of the paper (which would cause show through of the image due to opacity loss in the paper). On the other hand, if the capillary structure of the surface of the paper is too fine the rate of capillary imbibition of the oil vehicle will be too slow causing set off of the fresh ink onto the printing press and onto inappropriate paper surfaces.

Printing with inks which dry by solvent evaporation or by polymerization can be done on very smooth papers since rapid vehicle absorption is not required to set the ink. In fact, uniform ink holdout is generally a prime requisite for printing with drying inks. Coating paper with mineral pigments in a suitable binder is a common way in which to provide a smooth and less porous surface for printing. The mean pore size in the surface of coated paper is about one order of magnitude smaller than that of the uncoated paper⁴. Ink penetration during impression is thereby decreased. Thus, inks which set by solvent evaporation (heat set) or by polymerization must be used on coated papers in order to avoid set off and smearing.

Offset lithography involves a further complication of the model depicted in Figure 1. The image is offset from the printing plate to a corded rubber blanket which then transfers the image to paper in the printing nip. More importantly, fountain solution, commonly consisting of gum arabic in aqueous solution, is applied to the nonimage areas of the plate and finds its way onto the paper surface along with the ink. Fountain solution is also emulsified in the ink which changes its rheological and wetting properties^{5, 6}. The paper must then absorb both an aqueous solution and an oil-based ink with a delay that does not exceed the time for the paper to pass from one colour printing unit to another.

In this review, ink-paper interactions during and after the printing nip will be examined starting with the least complicated

process, letterpress, and then dealing with specific interactions peculiar to the offset process.

LETTERPRESS PRINTING

Perhaps the simplest form of printing is the transfer of an oil-carbon black ink from an unscreened printing plate to porous paper. Walker and Fetsko² were among the first to mathematically model this process. They considered ink transfer to be influenced by three factors: contact between the ink film on the plate and the surface of the paper in the printing nip, immobilization of the ink in the surface pores of the paper, and splitting of the remaining portion of the ink film as the plate leaves the paper at the exit of the nip. Figure 3 shows a typical ink transfer curve for newsprint when the amount of ink on the printing plate is varied over a broad range.

The initial dip in the transfer curve is due to increasing contact between ink and paper as the ink film thickness is increased and progressively shallower pores in the surface of the paper are bottomed. As the amount of ink on the plate approaches commercial levels (about 5 g/m²) a maximum in the fraction of ink transferred from plate to paper is reached. The fractional ink transfer exceeds 50 percent at this point due to the ink immobilized in surface capillaries. This is shown graphically in Figure 4 where the fraction *f* of the remaining or 'free' ink film which splits and stays with the paper is calculated. The free ink film split is invariably much less than 50 percent at normal printing speeds. Thus as the amount of ink on the printing plate reaches a level where the surface pores begin to be satisfied the free ink film split predominates and the fraction of ink transferred declines.

These concepts are modelled in the Walker-Fetsko ink transfer equation:

$$y = A [bB + f(x - bB)] \quad (1)$$

where: $A = 1 - e^{-kx}$ (fraction of contact)
 $B = 1 - e^{-x/b}$ (fraction of immobilized)
y = amount of ink transferred to paper
x = amount of ink on printing plate
k = rate at which contact is achieved with increasing ink on plate
b = maximum amount of ink that can be immobilized in the paper
f = fraction of free ink film that splits and stays with the paper.

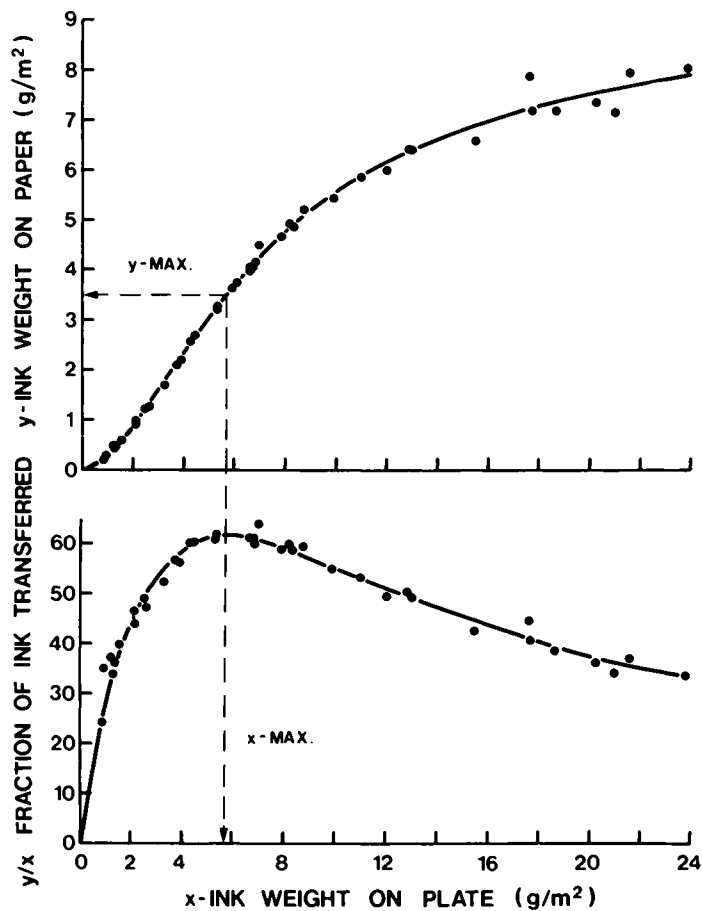


Figure 3. Typical ink transfer (top) and fractional ink transfer (bottom) curves for newsprint printed at 4.6 m/s and 15.4 kN/m in a GFL rotary press (8).

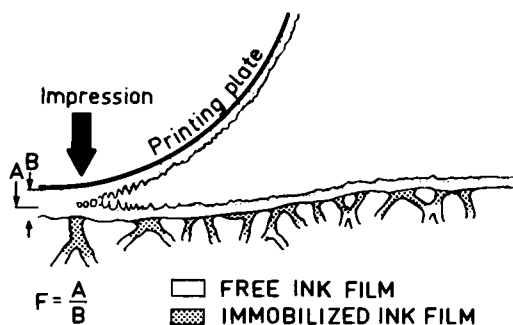


Figure 4. Splitting of free ink film in printing nip. (F = fraction of free ink film split that stays with paper.)

The equation is fitted to the fractional ink transfer curve in order to maintain residual error homogeneous over the whole range of ink weights on the printing plate². The estimates obtained for the parameters k , b , and f reflect fundamental printing characteristics of the paper. For example, as shown in Figure 5 the k parameter is a measure of the smoothness of the paper under printing conditions.

By differentiating the Walker-Fetsko equation with respect to each of the parameters and multiplying the derivative by one standard deviation about the mean value of these parameters for 29 different printings of newsprint Mangin et al⁸ showed the influence paper characteristics can have on ink transfer. As shown in Figure 6 the main influence of the smoothness parameter k is at lower ink weights. The influence of the porosity related parameter b peaks and then declines as the split parameter f begins to predominate. At commercial ink weights of about 5 g/m² the smoothness and porosity parameters are equally important while the split parameter (related to the affinity of the paper to ink and ink rheology) cannot be neglected.

Contact

In 1947, Chapman⁹ developed a instrument to measure the optical contact between a flat glass prism and the surface of paper. The idea of measuring the smoothness of paper under pressure simulating the compression of paper in a printing nip has been explored by several authors since¹⁰⁻¹³. Perhaps the most striking result of this work is the low fraction of contact that is achieved. Under printing compression optical contact with smooth newsprint is about 20 percent and seldom above 50 percent for coated papers.

Clearly, the deformation of the fluid ink in the printing nip must raise the total contact considerably. One way of calculating the effective contact between ink and paper is to measure the fraction of the paper surface covered with ink when printing with a solid printing form. Using a black ink it is possible to calculate the fractional coverage from the reflectances of the printed and unprinted paper:

$$R_p = CR_I + (1 - C) R_\infty \quad (2)$$

where: R_p = reflectance from printed paper
 R_∞ = reflectance from unprinted paper
 R_I = reflectance of ink
 C = fractional ink coverage

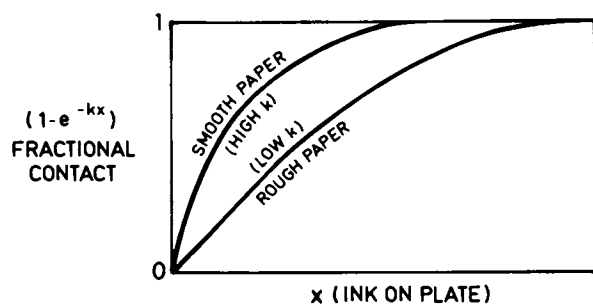


Figure 5. Effect of paper smoothness on contact fraction.

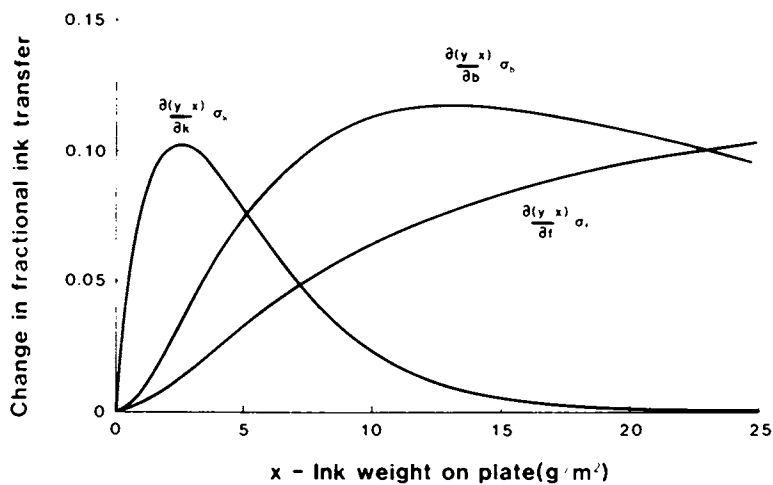


Figure 6. Change in fractional ink transfer with a shift in parameters k , b , and f in the Walker-Fetsko equation equal to one standard deviation about their mean fitted values for 29 printings of newsprint (8).

Assuming the reflectance of the ink is approximately equal to zero (i.e. neglecting translucence of the pigment and gloss):

$$R_I \doteq 0$$

$$\text{then} \quad C = 1 - \frac{R_p}{R_\infty} \quad (3)$$

This is the basis of the Larocque letterpress quality test¹⁴ wherein 2 g/m² of ink is used on the printing plate. At this ink level the fractional coverage varies from 0.3 to 0.6 for rough and smooth newsprint, respectively.

Even at 0.5 fractional coverage the resulting print appears visually to be a relatively uniform gray at reading distance. For just-noticeable differences in contrast the resolution of the human eye at this distance is about 100 μm . Much of the noncontact area in a solid print is finer than this resolution limit and is thus integrated to gray by the eye. It should also be mentioned that the area covered by ink is overestimated by equation (3) and by the eye due to a reduction in the reflectance from the unprinted portions of the printed solid caused by the shadow effect of adjacent inked area (i.e. the light scattered back from the unprinted areas is less than that from an unprinted sheet of the same paper). This optical spreading phenomenon is commonly known as the Yule-Neilsen effect¹⁵.

Lateral spreading of ink in the printing nip is also a factor in solid coverage and in halftone dot reproduction. In fact, Oittinen¹⁶ has calculated the relative effects of physical spreading and optical spreading on the modulation transfer function for halftone printing and found the former to be generally more significant.

The equation used to calculate lateral spread of ink during impression was that of Dienes and Klemm¹⁷ for flow between parallel plates:

$$\Delta d = \sqrt{d^2 + 8/3 \frac{Px^2 t}{\eta}} - d \quad (4)$$

where: d = dot diameter
 P = printing pressure
 x = ink film thickness
 t = dwell time under pressure
 η = viscosity

Immobilization

From the foregoing, it is clear that the contact between ink and paper depends on the dynamic compressibility of the paper.

The void volume and the distribution of pore sizes also change with compression of the paper affecting the hydraulic impression of ink during impression.

Colley and Peel¹⁸ proposed the following master creep equation to describe the compression of paper:

$$\frac{\Delta L}{L_0} = A (1 - \tanh \mu) \quad (5)$$

$$\mu = \alpha \log P_{\max} + \beta \log t + \gamma M + \alpha\theta + \epsilon$$

where $\frac{\Delta L}{L_0}$ = compression

A , α , β , γ , σ and ϵ are empirically derived parameters.

P_{\max} = maximum pressure

t = dwell time at P_{\max}

M = moisture content of paper

θ = temperature of paper

The equivalence for creep compression of altering pressure, dwell time, moisture, or temperature is explicitly expressed in the argument μ .

Hsu¹⁹ made a modification of the Kozeny equation using a simpler compression model to describe the hydraulic impression of ink into paper under printing compression. Knowing the void fraction and effective capillary radius for newsprint from mercury intrusion measurements, the void fraction and effective capillary radius under print compression can be calculated using Equation (5) with the empirical parameters derived by Colley and Peel. The void fraction and effective capillary radius under printing compression can also be measured via a specially constructed mercury intrusion apparatus.⁴ In either case, these values can be used to calculate the volume per unit area of ink impressed into paper during its passage through the printing nip assuming Poiseuille flow into a structure having a void fraction made up of cylindrical capillaries which are tortuous but not interconnected:

$$\frac{V}{A} = \frac{\epsilon r}{2\tau} \sqrt{\frac{Pt}{\eta}} \quad (6)$$

- where: $\frac{V}{A}$ = mean depth of penetration of ink into paper
- ϵ = void fraction of paper under printing compression
- r = effective capillary radius of paper under printing compression
- t = time under pressure
- η = viscosity of ink
- P = printing pressure
- τ = tortuosity (actual length of capillary/projected length of capillary).

According to equation (5) and using the parameters reported by Colley and Peel, the void fraction of newsprint under letterpress printing pressures of 2.5 MPa for 1 ms (approximate figures based on effective height and width of the nip pressure pulse) will be reduced from 0.6 for the uncompressed state to 0.48 (assuming equilibrium with a standard temperature and humidity atmosphere of 23°C and 50% RH). If the effective pore radius for newsprint was 2 μm before compression, it will be 1.75 μm under compression.

Taking a viscosity of 2 Pa.s and a surface tension of 30 mN/m for the ink and a tortuosity factor of 5 for newsprint, equation (6) predicts a hydraulic impression of 3 μm for the above printing conditions. This agrees reasonably well with the amount of ink transferred to newsprint in commercial letterpress printing. Since, as shown in Figure 1, the dynamic contact angle is greater than 90 degrees during impression, capillary imbibition may be neglected as a contributor to ink transfer.

Under the same printing conditions and taking the effective pore radius, void fraction, and tortuosity of a coated paper to be about 0.2 μm , 0.3 and 5, respectively, the calculated hydraulic impression becomes 0.2 μm . Thus, for coated papers the total amount of ink impressed is a small fraction of the amount of ink transferred to the paper during printing. In other words, the immobilization of ink is predominant in the transfer of ink to newsprint, while the free ink film split is predominant in the case of coated papers.

A practical implication of these calculations is shown in Figure 7. The optical density (blackness) of a solid print is plotted as a function of the amount of ink on three types of paper and a non-porous plastic film (mylar). The less porous the

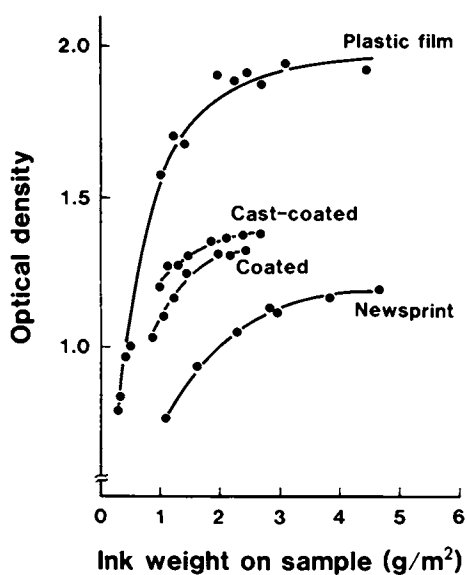


Figure 7. Optical density (blackness) as a function of the amount of ink on paper or mylar film (48).

paper, the less ink is impressed into the paper. Ink holdout results in a greater optical density at a given weight of ink on the paper.

Ink rheology affects the ink immobilization, lateral spreading, and ink film splitting components of ink transfer. More pseudoplastic inks have lower viscosities during impression, and as predicted by equations (4) and (6) this results in greater lateral coverage and higher immobilization. Ink elasticity (ratio of storage modulus to dynamic viscosity) has also been shown to improve coverage and transfer²³. Finally ink shortness (ratio of apparent yield stress to plastic viscosity) has been found to affect transfer²⁴ ²⁵ and lateral coverage (halftone dot sharpness)²⁴. Presumably, the filaments of shorter inks fracture closer to the nip center leading to a more uniform transfer.

Free Ink Film Split

The mechanism of ink immobilization is an important factor in determining the amount that will be free to split at the exit of the printing nip. As shown in Figure 2, the positive pressure generated in the nip is much greater than the negative pressure pulse which follows it. Hydraulic impression into interfibre capillaries in paper against the viscous resistance of the ink is not significantly reversed during ink film splitting. Thus, the impressed ink can be considered immobilized with respect to the ink film split. Note that the ink does not need to wet the surface of the pores for this form of immobilization. However, optical contact measurements show that there is a significant portion of the surface of any paper when compressed that lies parallel to the surface of the printing plate. Here wetting and adhesion of the ink to the paper must occur for the ink to be transferred since ink cannot be immobilized in these regions by hydraulic impression. It is also apparent that the smoother the surface of the paper the more important wetting and adhesion becomes for good transfer.

DeGrâce and Mangin²¹ have treated the case of ink transfer to nonporous model substrates such as mylar. The surface of mylar contains pits of about 1 μm depth. Very little void volume exists for ink immobilization, thus allowing ink film splitting to be examined in isolation. The transfer of two ink vehicle oils of differing viscosities and corresponding inks to mylar is shown in Figure 8 as a function of ink weight on the printing plate and printing speed in a rotary letterpress unit using a 100 percent tone plate. The fraction of ink transferred to the mylar decreases with ink weight on the plate and as the printing speed or viscosity is increased and can be as low as 0.25 at commercial printing speeds.

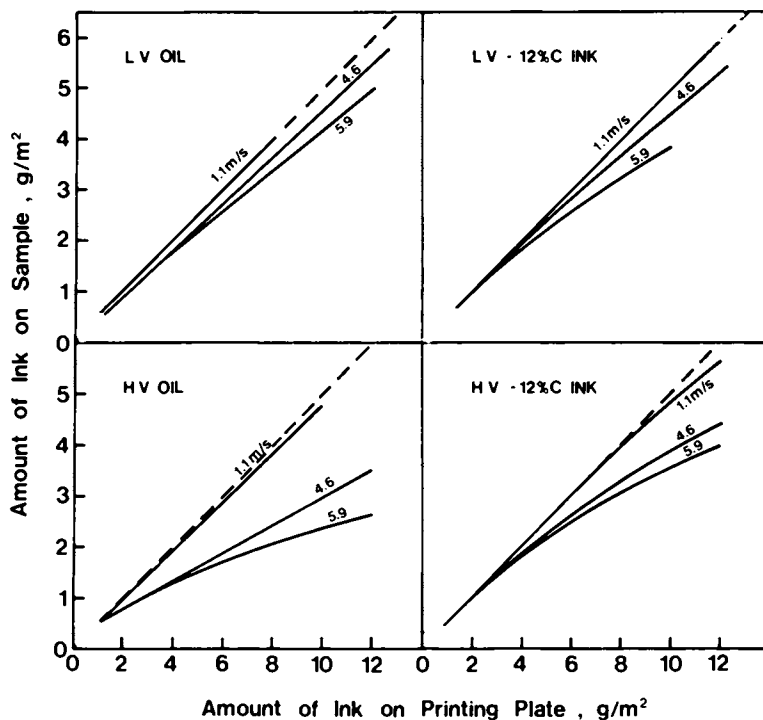


Figure 8. Transfer of letterpress inks and oil vehicles to smooth mylar as a function of weight of ink or oil on the printing plate and of printing speed.

Key: LV oil, low viscosity oil; HV oil, high viscosity oil; LV-12% C ink, LV oil with 12% by weight of carbon black pigment; and HV-12% C ink, HV oil with 12% by weight of carbon black pigment (21).

The chemistries of commercial oil vehicles vary with respect to the ratio of aromatic, paraffinic and cycloparaffinic carbon (generally about 20, 40, and 40 percent, respectively), degree of oxidation, and amount and character of impurities. The surface energies of the high and low viscosity ink vehicles shown in Figure 8 were 31.3, and 26.0 mN/m, respectively (as measured by the Du Noüy ring method).

The viscosities of the oils and the oils mixed with 12 percent carbon black pigment are shown in Figure 9 as a function of the rate of shear in a cone-plate viscometer²². In this range of shear rates the oils are Newtonian fluids while the corresponding inks are markedly pseudoplastic. As the pigment in the inks is broken down to progressively finer agglomerates at increasing rates of shear the viscosities of the inks approach those of their respective oil vehicles. Thus, at the high rates of shear encountered in the printing nip the viscosities of the oils and the corresponding inks can be expected to be similar.

On a fundamental level, wetting and adhesion should be improved by decreasing viscosity and/or surface tension. Thus, the lower viscosity, lower surface tension oil and corresponding ink should wet and adhere to the mylar better than the higher viscosity oil and ink. Zisman⁴⁷ has also pointed out that air bubbles trapped between a liquid and asperities in the surface of impervious materials like mylar can seriously inhibit adhesion and cause a Griffith fracture when the adhesive bond is stressed. Thus, at the outgoing side of the printing nip, nonuniform adhesive failure between the ink and the mylar could result in less ink transfer. This effect could be expected to become more pronounced with greater printing speed, and higher viscosity and higher surface tension of the oil or ink. However, DeGrâce and Mangin²¹ observed that the ink totally covered the surface of the mylar even at the higher press speeds (5.9 m/s), and thus concluded that wetting and adhesion occurred uniformly over the surface of the mylar.

Filamentation of the ink film occurs as the result of cavitation in response to sub-atmospheric pressures that occur beyond the centre of the printing nip (see Figures 1 and 2). DeGrâce and Mangin²¹ have pointed to asymmetric cavitation favouring the substrate surface as the cause of ink filaments forming closer to the paper surface than the surface of the printing plate. They argue that the surfaces of paper and mylar provide more nucleation sites for cavitation than exist in the bulk of the oil or ink. Air entrained in the printing nip could also provide sites for cavitation near the surface of the substrate. Ink filaments thus form closer to the substrate than the plate - an effect which becomes more pronounced with thicker ink films. Filament flow tends to equalize the asymmetric position of the filament. Increasing the printing speed reduces the time for filament flow

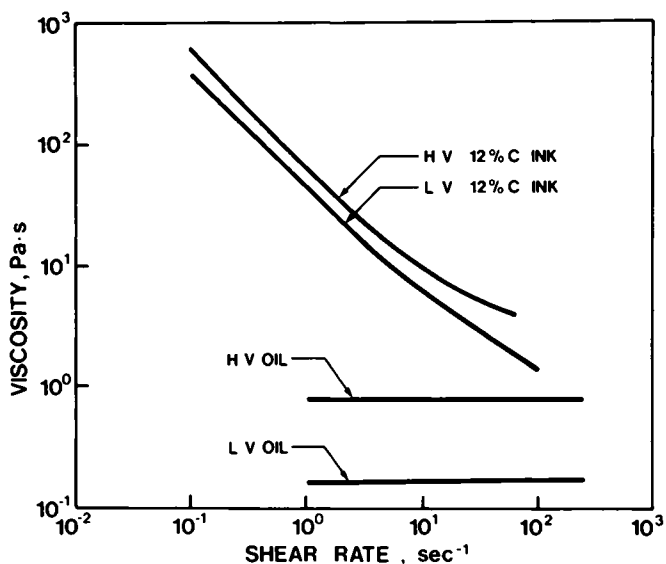


Figure 9. Viscosity of letterpress ink and oils (described in Figure 8) measured as a junction of shear rate in a Rheometrics Mechanical Spectrometer with cone and plate fixtures and a cone angle of $2^{\circ} 20'$ (22).

before rupture and thus, increasing printing speed or viscosity will result in filament splitting closer to the mylar or paper surface and decreased ink transfer.

Cavitation, filamentation, viscoelasticity and tack will be discussed further in connection with lithographic printing.

Post-Transfer Phenomena

Paper relaxes viscoelastically following the post-nip decompression. This recovery of void volume results in aspiration of ink into expanding capillaries in the paper. This may be the last effective movement of the whole ink - thereafter the vehicle migrates increasing the pigment concentration and leaving the pigment distributed exponentially through the thickness of the paper².

Three mechanisms can be considered for the migration of an ink vehicle such as oil: capillary imbibition, spreading, and bulk diffusion. It takes about 100 ms for a fresh print to travel from one nip of the printing press to the next in a commercial multicolor printing press. In this time the oil vehicle is sufficiently drained from the ink that set off does not occur in the second colour unit. The driving force for capillary imbibition is surface tension:

$$P = \frac{2\gamma \cos \theta}{r} \quad (7)$$

where: P = capillary pressure
 γ = surface tension of vehicle
 r = effective capillary radius
 θ = contact angle between vehicle and capillary walls.

Assuming that the advancing contact angle for oil on the capillary walls is approximately zero equation (7) may be combined with equation (6) to yield:

$$\frac{V}{A} = \frac{\epsilon}{\tau} \sqrt{\frac{r\gamma t}{2\eta}} \quad (8)$$

If the oil vehicle has a surface tension of 30 mN/m and a viscosity of 0.5 Pa.s and if the paper is uncompressed newsprint the void fraction, tortuosity and mean effective capillary radius will be approximately 0.6, 5 and 2 μm, respectively. Equation (8) then predicts that in 100 ms capillary imbibition could withdraw 9 μm of vehicle from the surface.

This is more than adequate to set news inks at commercial levels of ink application. Capillary imbibition is thus the predominant ink setting mechanism since spreading and bulk diffusion are much slower processes. However, two complications arise in this simplistic model. Implicit in the model is the assumption that the capillaries are connected to an inexhaustible supply of liquid. This is not the case, and it would be more reasonable to assume that as the larger capillaries drain the oil from the surface of the paper differential capillary pressures in the interconnected network drain the vehicle into progressively smaller capillaries emptying the larger ones (see Figure 1). These differential pressures can be expressed as:

$$\Delta P = 2 \gamma \cos \theta \left(\frac{1}{r'} - \frac{1}{r} \right) \quad (9)$$

where r' is the radius of the smaller capillary.

Secondly, the concept of capillary imbibition being responsible for the setting of an ink by draining the vehicle away from the pigment can be disputed. Larsson and Sunnerberg²⁶ used radioactive tracers to monitor pigment concentration in news inks after the printing nip. The average pigment concentration rose from 14.4 percent to 25.5 percent in one hour and reached equilibrium after 24 hours. The average pigment concentration did not rise appreciably in the first second after printing suggesting that whole ink may be imbibed initially after printing. The setting effect may occur at the surface of paper where pigment is left behind as the whole ink is imbibed. This kind of chromatographic effect is more reasonable than drainage by capillary imbibition because at some point during the concentration of the pigment capillaries will be created in the concentrated ink that are finer than those in the paper. Thus, according to equation (9) the vehicle will thenceforth be retained by the pigment.

The dendritic structure portrayed in Figure 1 is not valid for the structure of paper coatings. The more regular packing of clay platelets, or calcium carbonate particles probably leads to a structure consisting of larger voids joined by smaller interstices. Equation (9) predicts that ink cannot penetrate by capillary imbibition beyond the first interstitial void, thus effectively reducing the void volume and rate of penetration. For this reason inks which set by solvent evaporation and/or polymerization are generally used on coated papers instead of penetrating inks.

According to equation (8) the rate of penetration of ink vehicle into newsprints observed by Lyne and Madsen¹ 10 to 100 seconds after printing of 0.1 $\mu\text{m/s}$ corresponds to capillaries having a mean effective radius of about 0.2 μm . This agrees well

with the observation that the opacity of paper continues to decrease for a few minutes after printing³ since pores of 0.2 μm radius and larger would scatter light until filled by the ink vehicle. Bulk diffusion of oil vehicle into the cell walls of fibres is a very slow mechanism. The half time for diffusion of an oil of about C_{30} through a single fibre wall of a glassy polymer such as cellulose at room temperature would be in the order of weeks. This leaves spreading of the low surface energy oil vehicle (circa 30 mN/m) over the surface of the fibres as a reasonable long-term mechanism for oil migration in paper. The surface of mechanically prepared wood fibres is primarily lignin while bleached chemically pulped fibre has a cellulosic surface. Surface energies for various forms of lignin and cellulose are listed in Table I along with their London components. The surface energy of paper coatings varies principally with the binder used, natural binders being more polar than latexes.

Table I. Surface Free Energies of Paper and Related Substrates

	γ	γ^L	Reference
	mN/m		
Crystalline cellulose		48	(27)
Thermomechanical pulp fibres		37	(27)
Holocellulose		48	(28,29)
Fatty-acid surface		24	(47)
Mylar poly(ethylene terephthalate)		40	(45)
Coated Paper	30-45	30	(44)
Regenerated (low crystallinity) cellulose	68.7	38-42	(28)
Lignin	52.5	36-43	(30)
Water	72	22	

Using values from Table I it is possible to calculate Young's spreading coefficient:

$$S = \gamma_2 - \gamma_1 - \gamma_{12} \quad (10)$$

$$= W_A - W_C \quad (11)$$

$$W_A = 2(\gamma_1^L \gamma_2^L)^{\frac{1}{2}} + 2(\gamma_1^P \gamma_2^P)^{\frac{1}{2}} \quad (12)$$

$$W_C = 2\gamma_2 \quad (13)$$

where: W_A = work of adhesion
 W_C = work of cohesion

Neglecting the polar components for the case of oil on lignin S is + 10 and for oil on cellulose is + 16. These values are sufficiently large that conditions for spreading are highly favourable. However, if all the oil transferred to paper spread to a monolayer it would more than cover the total surface area of newsprint (circa $1 \text{ m}^2/\text{g}$). Thus, oil must also be retained in the finer capillaries in the paper and in the ink pigment.

Finally, three important factors in print quality - print density, show through, and set off are graphed in Figure 10 as a function of the amount of ink on the printed paper. The printer generally controls the amount of ink on the printing plate in order to arrive at a predetermined print density, or contrast in the printed image. Papers of differing smoothness, porosity, and affinity to ink will exhibit considerable variation in the relationships among these three properties. Ideally, a paper should give a print density of 1.0 at as low an ink level as possible in order to avoid show through and set off problems.

OFFSET LITHOGRAPHY

With respect to the ink-paper interactions two major factors separate offset lithography from letterpress: fountain solution is transferred to paper in nonimage areas and to paper in image areas by emulsification in the ink, and, since the rubber blanket used in offset creates close contact with the paper surface, thinner and more highly pigmented ink films can be applied to paper, aiding ink holdout. Thus, paper for the offset process must wet rapidly with polar fountain solution as well as oil-based inks, and must withstand ink film splitting forces without linting, picking, or delaminating. Excessive absorption of fountain solution may result in rupture of interfibre hydrogen bonds liberating fibres and debris, and it may soften coating binders leading to picking. If the pH of the paper is too low, acid solubilization by the sorption of fountain solution will cause interference with ink drying. The hygro-stability of the paper and its tensile strength when moistened with fountain solution can also pose press runnability problems. Nonabsorption of fountain solution transferred to the paper in the nonimage area of one colour unit can cause refusal of the ink to transfer to the paper in the next colour printing unit. This is illustrated in Figure 11 for varying times between the application of a water film to paper and overprinting with oil-based ink.

Dynamic Wetting of Paper by Fountain Solution

Bristow³² has described a device for measuring the sorption of various liquids into paper. As shown in Figure 12 a paper strip is mounted on a rotating wheel, and is drawn past a minia-

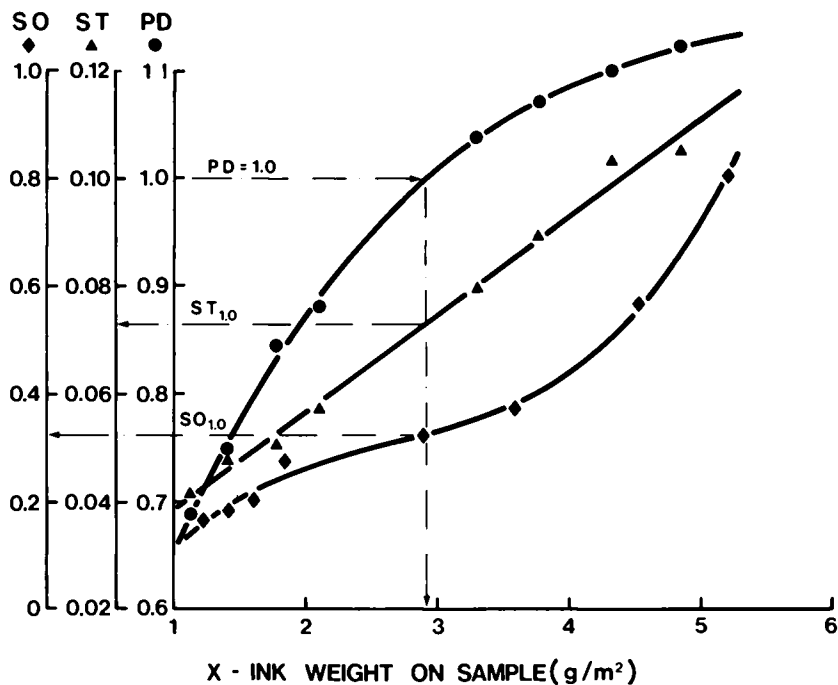


Figure 10. Print density (●), show through (▲) and set off (◆) as a function of the amount of ink on the printed sample (48).

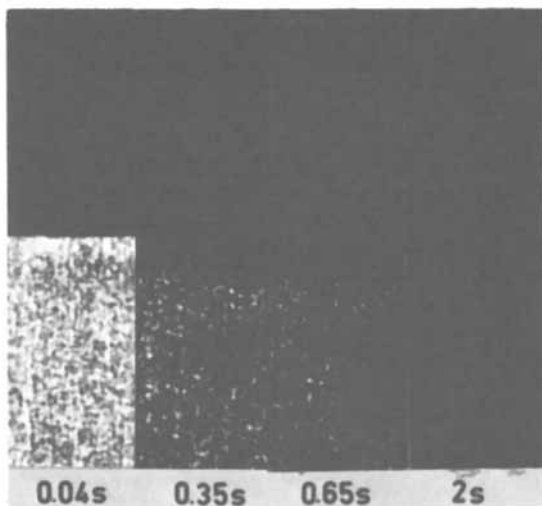


Figure 11. The effect of altering time between the application of water to the surface of a coated board and overprinting with a lithographic ink. (Reproduced, with permission, from Ref. 31. Copyright, Marcel Dekker, Inc.)

ture distributor (or open headbox) which is deadweighted so that it rests on the paper strip with a pressure of 0.1 MPa. The distributor is filled with a known amount of liquid which has a time available for sorption determined by the peripheral speed of the wheel V and the width of the slice opening ($L = 1$ mm) in the distributor. Since this speed may be varied, the relationship between the amount of liquid transferred per unit area of paper and the time available for sorption may be established as in Figure 13.

The amount of liquid which transfers to the paper can be described by:

$$A = K_r + K_a t^{\frac{1}{2}} \quad (14)$$

where K_r is the volumetric surface roughness, or the amount of liquid which would theoretically run into the surface topography of paper at zero time, and K_a is an absorption coefficient. K_r is also the mean depth to which the fluid may penetrate before capillary forces are initiated. As shown in Figure 13, there is a wetting delay before water begins to be sorbed into interfibre capillaries. The wetting delay for mineral oil is too short to be resolved by the Bristow instrument.

The wetting and spreading of high viscosity fluids on paper is affected by surface roughness⁴⁹. Hoyland et al.⁵⁰ found that the wetting delay for water was unaffected by the surface roughness of bleached kraft paper, but that increasing the viscosity of water with starch brought about a roughness effect on the wetting delay.

A porous, pure cotton cellulose paper such as Whatman chromatographic paper does not show a wetting delay to water. However, as shown in Figure 14 sizing the Whatman paper in a 2 percent isopropanol solution of Dupont Quilon-C causes a wetting delay of about 80 ms and a severe reduction in the rate of absorption, K_a , despite the fact that the mean pore size measured by mercury intrusion does not change as the result of the sizing. Quilon-C creates a fatty acid barrier to wetting in much the same way as naturally occurring fatty acids in wood create barriers to wetting of the kraft liner shown in Figure 13 and newsprint as shown in Figure 15.

The resulting wetting delay is exacerbated by aging or heating^{33 34}. As shown in Figure 15 the newsprint manufactured from fresh pulp has a wetting delay of 80 ms (generally the wetting delay for fresh newsprint lies between 40 and 80 ms) while newsprint made from flash dried bale pulp aged for one year exhibits a wetting delay of about 0.5 seconds. This progressive spreading of the resin and fatty acids with aging is therefore referred to as self-sizing.

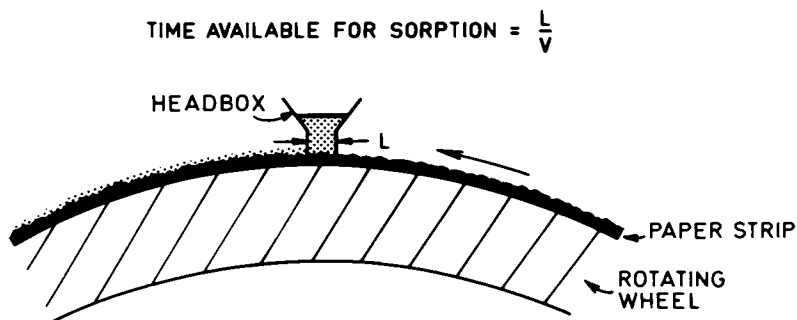


Figure 12. Principle of Bristow's instrument for dynamic wetting and absorption studies. (Reproduced, with permission, from Ref. 31. Copyright, Marcel Dekker, Inc.)

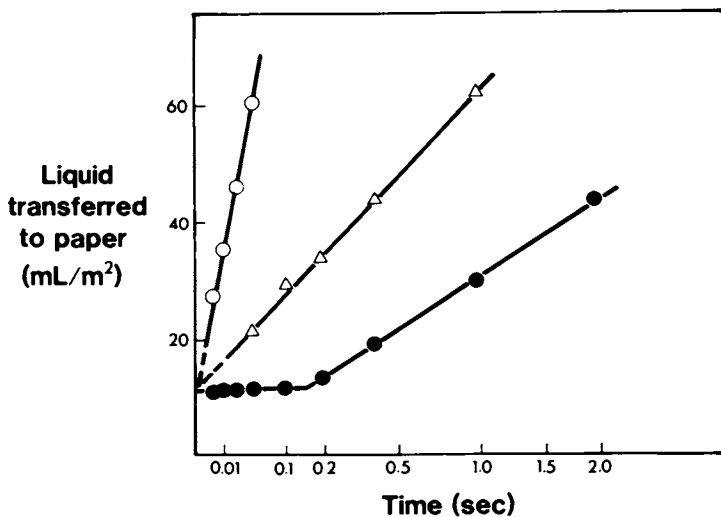


Figure 13. Amount of liquid transferred to paper (kraft liner), on a square-root time axis (32). Key: ○, oil-A; △, oil-B; and ●, water.

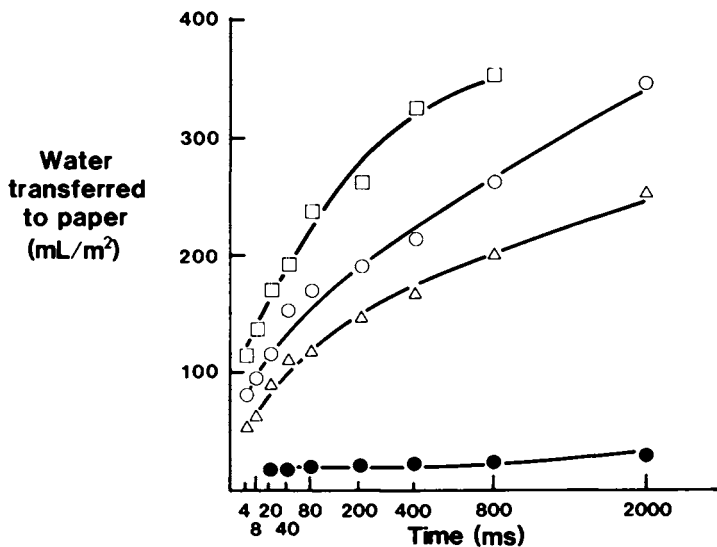


Figure 14. Dynamic absorption of water by chromatographic papers (46). Key: \square , Whatman #4 (coarse); \triangle , Whatman #5 (fine); \circ , Whatman #1 (medium); and \bullet , Whatman #1 (sized).

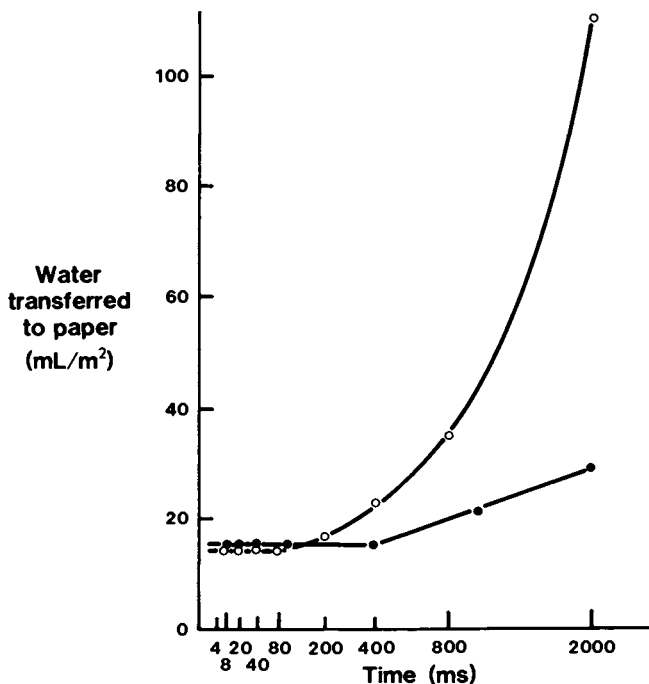


Figure 15. Wettability of newsprint made from fresh pulp (\circ) and from a flash dried bale pulp aged for one year (\bullet) (33).

Lyne³³, Suranyi et al.³⁴, and Takeyama and Gray³⁵ have shown that solvent extraction of fatty acids has little effect on wetting time. On the other hand Suranyi et al.³⁴ showed that corona discharge could reduce the wetting delay and Takeyama and Gray³⁵ found that a sodium methoxide extraction was necessary to reduce the wetting delay of paper heated in the presence of stearic acid. Thus, it appears that with heating or aging the fatty acids in wood may become chemically bound to fibre surfaces in paper.

The question remains as to whether uncontaminated cellulose has a wetting delay to water. Hoyland³⁶ has reported a wetting delay of 21 ms for water penetration into compacted pad of fully bleached kraft fibre using a conductance probe technique. Using the Bristow apparatus on a pure, clean, regenerated cellulose film (cellophane) and on Whatman chromatographic paper which had been repulped, beaten to low freeness and then calendered heavily to avoid rapid interfibre sorption the authors⁴⁶ have demonstrated a wetting delay of about 8 ms on both surfaces. The authors have postulated that the wetting delay is the time required before liquid-like water is absorbed onto fibre surfaces - a process which is impeded by sizing or self sizing⁴⁶. After liquid-like water begins to be absorbed on fibre surfaces, bulk water can advance on the walls of interfibre capillaries initiating rapid capillary sorption.

The rate of sorption through the porous, unsized Whatman papers is so rapid that saturation effects can be seen as a downward curvature of the sorption curves shown in Figure 14. On the other hand, the sorption curve for fresh newsprint shown in Figure 15 is curved upward. Capillary sorption is slow enough in the finer pores of newsprint that sorption of water into fibre walls and the resulting swelling of the fibres can significantly increase the size of interfibre capillaries during sorption. This increase in the interfibre capillary size can be seen as an increase in the rate of sorption with time (or upward curvature) for the conventional newsprint in Figure 15.

Can these results for water sorption be related to the application of fountain solution to paper during lithographic printing? In Figure 16 the addition of a surfactant is seen to have little effect on the dynamic surface tension of water at a surface age of 3 ms. Thus, on the time scale of the wetting of newsprint, fountain solutions which consist principally of an aqueous solution of gum arabic may behave similarly to the case of water alone. Conversely, as shown in Figure 17 fountain solutions containing isopropanol exhibit lower dynamic surface tensions and should wet paper more readily than water alone.

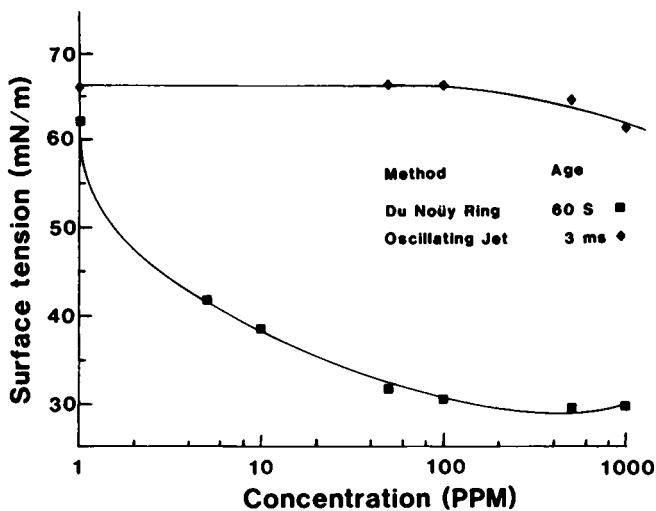


Figure 16. Effect of surfactant concentration on the static and dynamic surface tension of water (37).

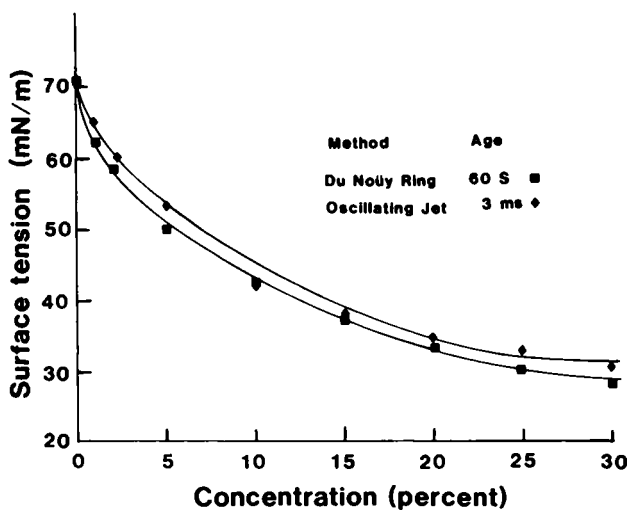


Figure 17. Effect of isopropanol concentration on the static and dynamic surface tension of water (37).

The Effect of pH on Ink Drying

The extractive pH of paper depends on manufacturing processes (e.g. the pulping method used, bleaching, papermachine additives such as alum, sizing agents, and coating). Inks used in sheet-fed offset lithography set and dry by the oxidation initiated polymerization of linseed oil or synthetic polymer components. Metal salts are used in order to accelerate the rate of polymerization and thereby avoid set off and smearing of the fresh ink. As shown in Figure 18 the action of these catalysts is interfered with if the extractive pH of the paper is below about 5.5. To some degree the pH of the fountain solution can be varied to compensate for too low an extractive pH in the paper.

Tack Forces and Ink Film Splitting

Offset lithographic printing involves an extra ink film split between the printing plate and the offset blanket. For this reason and because the offset blanket conforms to the paper surface the ink film transferred to paper can be thinner than in letterpress printing. The pigment content of offset ink has to be greater than for letterpress in order to compensate for the thinner ink film. Thicker ink films are also not possible because halftone dot definition would be lost due to ink spread on the flat lithographic plate. Offset inks also contain more polymer resins (e.g. polyindene) than letterpress inks in order to improve ink transfer and reduce waterlogging. A major disadvantage of the higher pigment and polymer content of offset inks is that much higher tack forces are generated during ink film splitting than in the letterpress case. These tack forces are responsible for linting of weakly bonded fibres from the surface of newsprint and picking of fibres and coating from the surface of fine papers.

Two important factors in the generation of tack forces in a printing nip are cavitation and ink rheology.

Cavitation

At low speed, film splitting may be described by a simple hydrodynamic model. However, above a critical speed, the film will split by the formation and rupture of the ink filaments.

The sub-atmospheric pressure developed in the ink film shown in Figure 2 has never been directly measured or precisely located with respect to the nip centre. Nor is it even certain whether the minimum occurs just before cavitation, or at the point of filament rupture.

Cavitation will commence when the cohesion of the ink is overcome locally, so that points of nucleation are helpful. Miller and Myers³⁸ found by high speed photography of films splitting in a low pressure chamber that while the film splitting pattern was unchanged down to 0.1 atm. pressure, the work of separation increased due to the loss of the contribution of air expansion within the film. In general, suspensions will cavitate more readily than their vehicle fluids, and large pigment particles will initiate cavitation sooner, thus causing tack forces to be smaller. On the other hand, smaller particles which cause cavitation later will lead to finer filaments, thereby improving print quality by improving the uniformity of ink transfer.

The cavities thus formed will expand. This would suggest that the increase in total surface energy due to the creation of new surface would be a contributor to the tack force. However, in an analysis of cavity expansion within a polyisobutene oil, Hoffman and Myers³⁹ found that surface tension contributed only 7 percent and the viscosity contributed 93 percent to the work of separation of the oil film.

The final stage in the film split is the formation and subsequent breakage and recoil of the ink filaments. Viscosity, elastic response of the ink, and surface tension forces contribute to the force required to fracture the filaments.

Ink Rheology and Tack Force

Letterpress news inks are pseudoplastic but not viscoelastic at the shear rates shown in Figure 9. Polymer resins present in offset ink formulations render them viscoelastic. This can be measured under oscillatory shear in a rheometer such as the Mechanical Spectrometer:

$$\tau(t) = G' \gamma_0 \sin(\omega t) + \eta' \dot{\gamma}_0 \cos(\omega t) \quad (15)$$

where: $\tau(t)$ = shear stress

G' = elastic storage modulus

η' = dynamic viscosity

γ_0 = shear strain

$\dot{\gamma}_0$ = shear rate

G' is a measure of the storage of elastic energy and η' is a measure of the viscous dissipation of strain energy. These parameters are shown in Figure 19 as a function of the frequency of oscillation ω of the cone in the cone and plate fixture of the Mechanical Spectrometer for an offset news ink. It can be seen

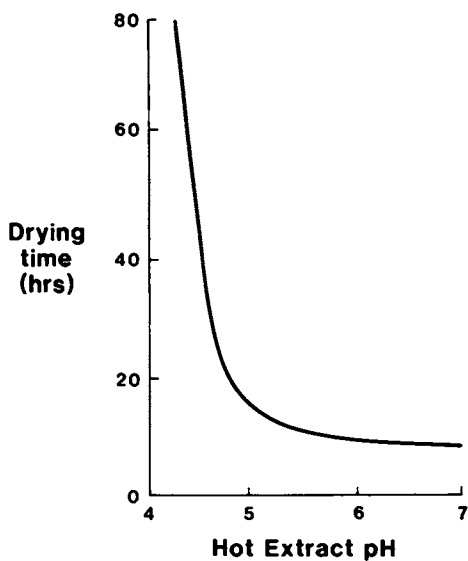


Figure 18. Effect of extractive pH of paper on drying time of a lithographic ink (in a 75% RH atmosphere) (20).

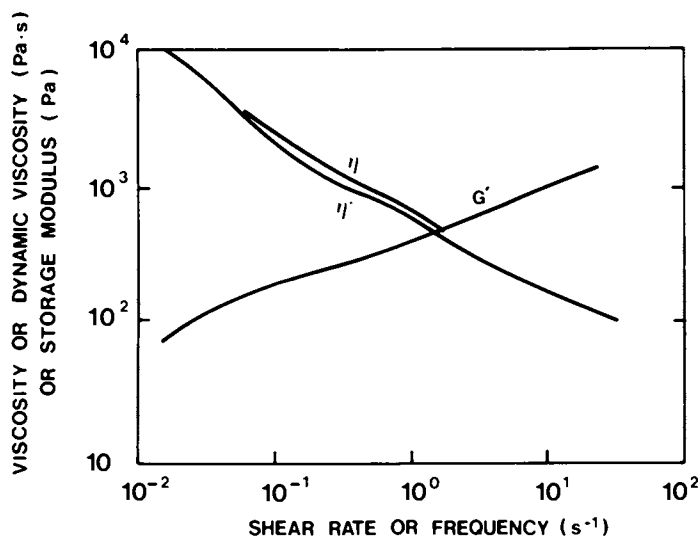


Figure 19. Rheological properties of a commercial lithographic offset news ink (viscosity η , dynamic viscosity η' , and elastic storage modulus G') as measured in a plate fixtures with a cone angle of $2^\circ 20'$ (22).

that the storage of elastic energy increases and the viscous dissipation decreases as the frequency of oscillation is increased. Thus at the shear rates encountered in printing, offset inks are likely to behave principally as elastic materials.

An adequate description of the rheology of sheet-fed offset inks²³ requires higher order (nonlinear) terms in addition to those in equation (15). Measurement of the normal forces may also be useful in elucidating ink rheology.

As mentioned previously, at very slow rates of film splitting a simple hydrodynamic model can be used to describe the separation force²⁵. The velocity of separation of the two surfaces multiplied by the viscosity of the fluid gives a reasonable indication of the separation force in this case. However, it should be borne in mind that even pure polymeric liquids such as the polyisobutene used by the paper industry to measure the surface strength, or picking resistance, of paper is non-Newtonian at high shear rates. As shown in Figure 20 it is difficult to decide the actual viscosity of polyisobutene during print simulation tests. More importantly, the velocity-viscosity product does not predict the separation force at the high rates of separation encountered in printing due to cavitation effects and complex flow behaviour in the ink filaments.

Elasticity at high shear rates is also bound to influence tack force in the nip of an offset press. Besides shear rate the elasticity is influenced by the molecular weight and molecular structure of the dissolved polymers, and interactions between the pigment particles, the vehicle, and the dissolved polymer molecules. Of particular interest is the effect of the molecular mobility of stiff-chain polymers such as polyindene on elasticity and tack force at the shear rates encountered in an offset printing nip.

Unfortunately, laboratory instruments such as the Inkometer and Tack-o-Scope do not measure tack force, but rather a complex combination of tack force, ink viscosity, and the rheological properties of the elastomeric covering on the measuring roller^{40 41}. Investigation of the origins of tack force is also hampered by a lack of knowledge surrounding the shear conditions in the printing nip, and measurements of elasticity and other rheological parameters may be misleading for the case of offset inks if the shear rates do not correspond to those in the printing nip. Kelhä et al.^{42 43} developed a parallel plate tackmeter in which the rate of acceleration of the separating plates was 50 m/s². While this is comparable to the rate of ink filament acceleration in a commercial press the ink did not undergo shearing as it would in a printing nip. However, they observed tack forces of about 5 mPa for linseed oil-carbon black offset inks having a film thickness of 5 μm . This tack force is slightly

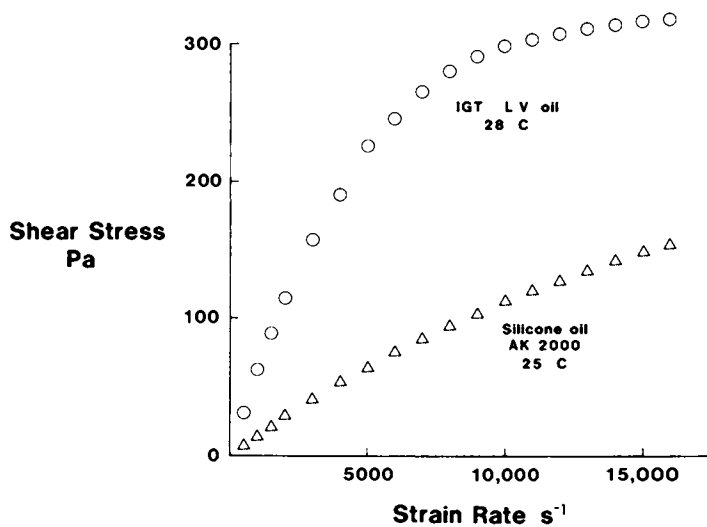


Figure 20. Shear stress developed in IGT polyisobutene pick test oil and a silicone oil as a function of shear rate in a Ferranti-Shirley cone and plate viscometer with a cone angle of 20'30" (22).

lower than the specific bond strength between fibres in paper but could well cause fibre removal by bond peeling.

Summary

Using a dynamic compression model for paper it is possible to calculate the void fraction and effective capillary radius of paper under printing compression. A simple Poiseuille model can then be used to make an estimate for the hydraulic impression of ink into interfibre capillaries during the passage of paper through the printing nip. The role of surface chemistry in the wetting of paper and adhesion of ink during the passage of paper through the printing nip is not yet clearly understood.

Calculation of the rate of capillary imbibition after the printing nip agrees well with the setting times for news inks and observations of opacity change in paper immediately after printing. Spreading appears to be the long-term mechanism by which ink vehicles migrate in paper.

In the case of offset lithography the wetting of the surface of paper and subsequent sorption of fountain solution is important for the avoidance of printing problems such as ink refusal in multicolor printing, linting and picking, and interference with ink drying mechanisms when residual acid in paper is solubilized.

Tack forces generated during ink film splitting are not well defined or easily measured with existing instrumentation. However, it is suggested that ink tack is related to ink elasticity, or more fundamentally, to molecular mobility of stiff chain polymer additives to lithographic inks.

Literature Cited

1. L.M. Lyne and V. Madsen, *Pulp Pap. Mag. Canada* 65, (12), T523 (1964).
2. L.O. Larsson and P.O. Trollsas, in *Paper in the Printing Process*, W.H. Banks, ed., Pergamon, Oxford, (1965) p. 57.
3. J-E. Levlin and L. Nordman, *ibid*, p. 33.
4. R. Chiodi and J. Silvy, in proceedings of Fourteenth EUCEPA Conference, Budapest, 1971; J. Silvy, C. Pannier and J. Veyre, in proceedings of Sixteenth EUCEPA Conference, Grenoble, 1976.
5. R.W. Bassemir, *American Ink Maker*, 59 (2), 33 (1981).

6. A. Surland, TAGA Proceedings, 1980, 222.
7. W.C. Walker and J.M. Fetsko, American Ink Maker 33 (12), 38 (1955).
8. P.J. Mangin, M.B. Lyne, D.H. Page and J.H. De Grâce, in Advances in Printing Science and Technology, V. 16, W.H. Banks, ed., in press.
9. S.M. Chapman, Pulp Pap. Mag. Canada, 48 (Convention Issue), 140 (1947).
10. J. Albrecht and M. Brune, in Recent Development in Graphic Arts Research, W.H. Banks, ed, Pergamon, Oxford (1971), p. 311.
11. W.C. Bliesner, Tappi 53 (10), 1871, (1970).
12. G. Blokhuis and A.E. Blogg, in Proceedings of the 12th International Conference of Printing Res. Inst., W.H. Banks, ed. IPC Science & Tech., (1974), p. 53.
13. M.B. Lyne, Tappi 59 (7), 102, (1976).
14. G. Larocque, P.P. Mag. Can., 52 (Convention Issue), 166 (1951).
15. A.J.C. Yule, A.J. Howe, and J.H. Altman, Tappi 50 (7), 337, (1967).
16. P. Oittinen, Advances in Printing Science and Technology, Vol. 16, W.H. Banks, ed. in press.
17. G.H. Dienes and H.F. Klemm, J. Appl, Phys. 17, 458 (1946).
18. J. Colley and J.D. Peel, Paper Tech., 13 (10), 350 (1972).
19. B. Hsu, Appl. Sci. Res. 10A, 277, (1961).
20. Pira Visual Aid Kit, The Research Association for the Paper and Board Printing and Packaging Industries, Surry, U.K.
21. J.H. De Grâce and P.J. Mangin, "A Mechanistic Approach to Ink Transfer through Simplified Models", Part I: "Model Substrates" and Part II: "Model Inks", to be submitted to Tappi.
22. J.S. Aspler, M.B. Lyne, J.M. Dealy and G.C. Pangalos, in Advances in Printing Science and Technology, Vol. 16, W.H. Banks ed., in press.

20. LYNE AND ASPLER *Ink-Paper Interactions* 419
23. P. Oittinen, D. Tech. Thesis, Technical University of Helsinki; Acta Polytechnica Scandinavia No. 131 (1976).
24. C.O. Rosted, J. Oil Col. Chem. Assoc. 55, 520 (1971).
25. A.C. Zettlemoyer, R.F. Scarr and W.D. Schaeffer TAGA Proceedings, Part A, 1957, 75.
26. L.O. Larsson and G. Sunnerberg, TAGA Proceedings, 1972, 403.
27. G.M. Dorris and D.G. Gray, J. Coll. Interface Sci. 71 (1) 93, (1979).
28. W.R. Haselton, Tappi, 37 (9) 404 (1954).
29. P. Luner and M. Sandell, J. Polym. Sci. Part C. 28, 115 (1969).
30. S. Lee and P. Luner, Tappi 55 (1), 116 (1972).
31. M.B. Lyne, in Handbook of Physical and Mechanical Testing of Paper and Paperboard, R.E. Mark, ed; Marcel Dekker, Inc., in press.
32. J.A. Bristow, Svensk Papperstidning, 70 (19), 623 (1967).
33. M.B. Lyne, in Fibre Water Interactions in Paper-Making, Tech. Div. B.P.B.I.F., London (1978), 641.
34. G. Suranyi, D.G. Gray, and D.A.I. Goring, Tappi 63 (4), 153 (1980).
35. S. Takeyama and D.G. Gray, Cellulose Chem. and Technol., submitted for publication.
36. R.W. Hoyland, in Fibre-Water Interactions in Paper-Making, Tech. Div. B.P.B.I.F., London (1978) p. 557.
37. U. Lindqvist, S. Karttunen and J. Virtanen, in Advances in Printing Science and Technology, Vol. 16, W.H. Banks ed., in press.
38. J.C. Miller and R.R. Myers, Trans. Soc. Rheol. II, 77 (1958).
39. R.D. Hoffman and R.R. Myers, Trans. Soc. Rheol. IV, 197 (1962).
40. L. Hellinckx and J. Mewis, Rheologica Acta 8, 519 (1969).

41. J. Mewis and F. Dobbels, *Ind. Eng. Chem. Prod. Res. Dev.*, 20 (3), 515 (1981).
42. V. Kelhä, M. Manninen, and P. Oittinen, *J. Oil & Col. Chem. Assoc.* 57 (6), 184 (1974).
43. V. Kelhä, M. Manninen, and P. Oittinen, *Tappi* 57 (4), 86 (1974).
44. P. Oittinen, personal communication.
45. J. Anhang, and D.G. Gray, *J. Appl. Polym. Sci.*, in press.
46. M.B. Lyne and J.S. Aspler, "Wetting and the Sorption of Water by Paper Under Dynamic Conditions", to be presented at the 1982 TAPPI Paper Physics Seminar, Pointe Claire, submitted to Tappi.
47. W.A. Zisman, in *Contact Angle Wettability and Adhesion*, ACS Advances in Chemistry Series no. 43, (164) p. 1.
48. M.B. Lyne and A. Parush, "The Print Quality of Offset and Letterpress Newsprint" given at the 1981 ANPA-CPPA conference on Newsprint in the Pressroom, submitted to *Pulp and Paper Mag. of Can.*
49. J.F. Oliver and S.G. Mason, in *Fundamental Properties of Paper Related to Its Uses*, Tech. Div. B.P.B.I.F., London (1976) p. 428.
50. R.W. Hoyland, P. Howarth and R. Field, in *Fundamental Properties Paper Related to Its Uses*, Tech. Div. B.P.B.I.F., London (1976) p. 464.

RECEIVED April 30, 1982

Surface Properties of Cellulose and Wood Fibers

DEREK G. GRAY

McGill University, Department of Chemistry, Montreal, Canada H3A 2A7

Two relatively new ways to study paper surfaces are reviewed. In the first method, the adsorption of hydrocarbon vapors on cellulose surfaces is measured by means of inverse gas chromatography. Adsorption isotherms, surface areas and surface free energies may be derived from the measurements. More significantly, the technique allows measurements at different relative humidities, and thus the effect of this important variable on surface areas and other surface properties may be investigated. An increase in relative humidity leads in general to a decrease in surface area and a decrease in the affinity of the paper surface for hydrocarbons. The second technique has proved of some value for the chemical analysis of paper surfaces, which may contain wood components such as lignin and low molecular weight organic extractives in addition to cellulose and related polysaccharides. The bulk composition of paper is readily determined, but analysis of the surface requires more effort. By combining ESCA measurements of the oxygen-carbon ratio of paper surfaces with solvent extraction of the samples, it is possible to estimate the amount of lignin and extractives at the paper surface. This information may be relevant to the wettability of the paper. Results of the ESCA analyses of mechanical and chemical pulp surfaces will be reviewed.

The surface properties of cellulose, wood fibre, and paper are of great importance in the production and utilization of paper and board. Phenomena as diverse as the formation of fibre-fibre bonds in papermaking and the ink-paper interaction during printing processes are certainly influenced by the surface properties of fibres and sheet. With the development of increasingly sophisti-

0097-6156/82/0200-0421\$06.00/0
© 1982 American Chemical Society

cated reprographic techniques, the surface properties of the receptor sheet may become more critical. Paper, still the most important reprographic substrate, is an exceedingly complex material. In addition to cellulose, its chemical constituents may include hemicellulose, lignin, and low molecular weight organic extractives. Each of the latter materials can vary widely in composition and abundance. Sheet composition is further complicated by the addition of flocculants, retention aids, and inorganic fillers during the sheetmaking process, and by subsequent sizing and coating procedures. The complex morphology of fibres and sheets means that the surface composition may be very different from the bulk composition. Obviously, a wide range of methods is required to determine the surface composition and properties of paper. In this summary, no attempt will be made to review the literature on the surface properties of paper. Discussion will be limited to two techniques, inverse gas chromatography (GC) and electron spectroscopy (ESCA), which are of value for some aspects of the surface characterization of fibres and paper.

Gas Chromatography

Although best known as an analytical technique, gas chromatography is also used to make physical measurements (1). Applications to polymeric substrates where the material under study is the stationary phase in the GC column have been reviewed (2, 3). GC methods have been used to measure the adsorption of non-swelling vapours on the surface of dry (4-8) and moist (9-12) cellulose. Adsorption isotherms, surface areas, isosteric heats and entropies of adsorption have been measured for a range of hydrocarbons and organic vapours. Perhaps the most useful aspect of the method is that the effect of relative humidity on surface properties may be investigated. The validity of the method as applied to surface area measurements is described in some detail below. Other applications of GC to cellulose surfaces are then summarized briefly.

Effect of Relative Humidity on the Surface Area of Paper.

Virtually all the physical and mechanical properties of fibres and paper vary strongly with moisture content, and it would be expected that surface properties should also be sensitive to relative humidity. Little work has been published on the effect of moisture on the surface properties of fibres and paper. As a starting point, it may be noted that the basic property of any surface is its surface area. How does the surface area of a fibre or paper sheet change with relative humidity?

In considering this question, the surface area must be clearly defined. We are concerned here not with the simple geometric area of a sheet of paper, but rather with the larger area of fibre surface and pores which are accessible to a gas-phase adsorbate. This is the area which may be measured by the standard nitrogen

sorption technique on dry fibres and sheets. However, measurements by nitrogen adsorption are not possible on sheets containing moisture (the measurements are made at very low temperatures, where water freezes) so an alternative way to measure the change in surface area is required. The method we use is to measure the surface adsorption of hydrocarbons at ambient temperatures by a gas chromatographic (GC) method. With care, GC measurements allow adsorption measurements to be made, even with less-volatile vapours on relatively low surface-area substrates.

We apply the GC method to measurements of the surface properties of cellulosic fibres and paper as follows:-

1. Fibres are packed directly into a chromatographic column. The packing density is low, to give as permeable a column as possible. Paper samples must first be cut into small pieces before packing.
2. A carrier gas such as nitrogen, containing a fixed proportion of water vapour, is passed through the column until the contents are equilibrated at the required relative humidity.
3. A small sample of a suitable hydrocarbon probe is injected into the moist carrier gas and its emergence from the column is measured with a flame ionization detector. The time required for the probe to pass through the column indicates the interaction between the probe and the column packing. By changing the size of the probe sample, a complete adsorption isotherm may be calculated from the GC data. A full description of the apparatus and theory is available (10).

The adsorption isotherms provide information about the surface properties of the fibres or paper in the column. For example, the surface area in the column may be deduced from the shape of the isotherm according to the Brunauer-Emmett-Teller theory for multilayer adsorption (13, 14). This theory gives the number of molecules, N_m , which forms a layer one molecule thick on the surface of the adsorbent. If the area, a_m , occupied by each vapour molecule adsorbed on the surface is known, then the total surface area, A , is simply given by

$$A = N_m \cdot a_m \quad (1)$$

Adsorption isotherms for n-alkanes on dry cellulose fibres and films obey the BET theory, and readily give values for monolayer coverage, N_m (4, 5, 6, 8). However, to estimate the surface areas, values for a_m are also required. At first, areas of the hydrocarbon molecules were estimated from the density of the liquid, assuming a spherical shape (4, 5). This is the same way that a_m is estimated for nitrogen in the classical surface area method. Different organic adsorbates on a given dry column packing gave roughly the same value for the surface area, A (long chain alcohols were an exception (5)), but the value measured with organic mole-

cules by GC was 10 - 20% less than the area measured by nitrogen adsorption at 77 K (4, 6). If the nitrogen adsorption method is assumed to be correct, then the actual area, a_m , occupied by the organic adsorbate molecule must be greater than that estimated theoretically assuming a spherical shape. In subsequent papers (6, 8), the area occupied by an adsorbate at monolayer coverage, a_m , on a dry cellulosic surface was taken as $a_m = A_n/N_m$, where N_m was given by the BET treatment of the adsorption isotherm and A_n was the area of the dry surface measured by nitrogen adsorption.

What happens when water vapour is introduced into the carrier gas? Water is of course adsorbed until the water content of the cellulosic material in the column is in equilibrium with the relative humidity of the carrier gas. An organic vapour is then injected into the carrier gas stream. The vapour must be virtually insoluble in water so that it interacts only with the external surface of the moist cellulosic column packing. (The surfaces of internal pores which are filled with water are not accessible to the vapour phase, and do not contribute to the interaction.) The equilibrium between the organic vapour and the surface is much more rapid than the equilibrium between water vapour and the cellulosic fibre, so the vapour injection should not perturb the water-cellulose equilibrium. The gas chromatographic retention times for hydrocarbons were observed to decrease with increasing moisture content in the column. This indicates that either the surface area or the affinity of the surface for hydrocarbons was decreasing, or both. To separate these two effects, the adsorption isotherms were fitted to the BET theory. With n-decane as adsorbate on cellulose fibres, preliminary experiments showed a marked decrease in monolayer coverage, N_m , between 10% and 80% RH (9). This indicates that either the surface area, A , decreases or the area occupied by a decane molecule, a_m , increases with increasing relative humidity. For samples which were exposed to moist carrier gas and then redried, the monolayer coverage of the redried samples decreased irreversibly. Because the measurements before and after exposure to moisture were made on dry surfaces, a_m was the same for each measurement and so a true decrease in surface area had occurred. This suggested that at least part of the change in N_m on wet surfaces was due to a real decrease in surface area. However, the large reversible decrease in surface area at higher relative humidities was (prematurely) attributed to changes in a_m (9).

The GC experiments were subsequently repeated, in more detail, on paper rather than on fibres (10). This circumvented possible artifacts due to the method of preparation of unbonded fibres. Two different vapours were employed. The changes in surface area, assuming a constant value of a_m equal to that of dry cellulose, are shown in Figure 1. From 0 to ~ 35% RH (points 1-5), the surface area decreases very slightly. A significant decrease of 20% occurs around 60% RH (point 6). To check if the change was irreversible, after two days at 60% RH, the paper was

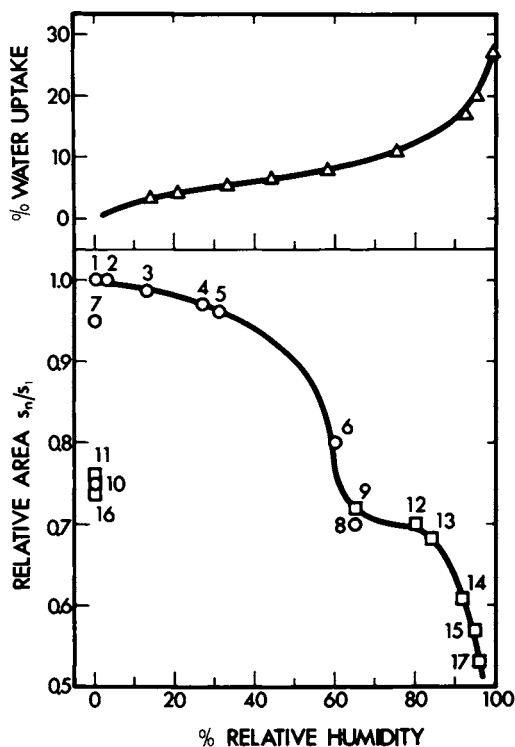


Figure 1. Water uptake and changes in relative surface areas of Whatman #1 filter paper as a function of relative humidity. The adsorbates are n-decane (\circ) and mesitylene (\square). The numbers beside the points indicate the order of the measurements. (Reproduced, with permission, from Ref. 10. Copyright 1981, Royal Society of Chemistry.)

dried (point 7) and the measured area was $1.14 \text{ m}^2\text{g}^{-1}$, only 5% less than the original dry sample but 15% greater than the area at 60% RH. The sample was re-exposed to 65% RH and the surface area (point 8) returned to a value 12% lower than at 60% RH.

The abrupt decrease in the region 50 → 65% RH may reflect a true change in the surface area of the paper or alternatively, a change in the area occupied by each decane molecule in the monolayer. To test the second possibility, we changed the probe to mesitylene. This vapour also has a low solubility in water but possesses a more rigid structure than decane, so that the molecular area is less likely to change drastically with humidity. At 65% RH, mesitylene gave excellent reproducibility in peak profiles. Within 2.3% (points 8 and 9), the same area was obtained with decane and mesitylene. Unless the two adsorbates alter their conformation or packing in a similar way on humid paper, the drop in surface area appears to be real. After four weeks at 65% RH, the sample was redried and the surface area determination was repeated twice using both solutes (points 10 and 11). The agreement between the two determinations was again better than 2%. The area of the dry paper was ~ 7% higher than at 65% RH but was 24% lower than the original dry sample and 20% lower than the first drying from 60% RH. The second drying suggests that the almost total reversibility observed on the first drying is lost when the paper is at $\text{RH} > 60\%$ or that the relaxation of the humid structure is time dependent.

Using mesitylene as the probe, the surface area remained almost constant between 65% and 85% RH (points 12 and 13), while over 85% RH (points 14 and 15) another significant loss of area was observed. Another drying (point 16) from 95% RH showed no further decrease in the surface area of the dry paper. A re-exposure at 96% RH (point 17) gave a further drop in area over that for 95% RH (point 15). The paper was then exposed to very high moisture contents (100 - 250 weight % water) by injecting liquid water into the column. The wet surface area, measured with n-decane as adsorbate (11) dropped to a very low value of about $0.03 \text{ m}^2/\text{g}$. This corresponds to the geometric surface area of the paper, and suggests that all the interfibre pores and rugosities have been filled by water.

Further evidence that the changes in surface area of paper and fibres with RH are real is provided by some experiments on regenerated cellulose film (12). This smooth uniform substrate gives a value for the surface area close to the geometric area of the film. The monolayer coverage as measured by the GC method remains virtually constant as the RH increases. Thus, the decrease observed on the paper surfaces is not due to changes in the area occupied by the adsorbate as the water content of the cellulose changes, because no such change was observed on the cellulose film. We conclude that the surface area of the pulp fibres and paper examined to date does in fact decrease with increasing relative humidity.

The sharp decrease in surface area at very high water contents is clearly attributable to the filling of pores in the fibre and sheet structure by liquid water. The reason for the decrease in surface area at lower relative humidities is less obvious. One may speculate that fibrillation occurs at the fibre-fibre bond during bond formation, because of the stresses induced by drying under tension. On subsequent re-exposure to a moist atmosphere, the hydrogen-bonded network may relax, and the fibrillated areas may collapse onto the fibre surfaces, causing the observed loss of surface area.

Adsorption Isotherms and Thermodynamics of Adsorption. The adsorption isotherms for non-swelling organic adsorbates on the surface of dry cellulose fibres (4, 5), papers (6), and films (8) are characterized as type II BET isotherms (13, 14), but with relatively small discontinuities at monolayer coverage, as expected for vapours with a low specific affinity for the substrate. It must be emphasized that there is no hysteresis in the adsorption isotherms on these non-porous low-surface area adsorbents. (In fact, the elution GC method used in this work cannot be applied to adsorption processes where hysteresis or other kinetic effects are operative (1)). The adsorption isotherms thus characterize the vapour-adsorbate equilibria for these systems, and the temperature dependence of the isotherm gives the (isosteric) heat of adsorption (14) as a function of surface coverage. For hydrocarbon vapours, the isosteric heat of adsorption decreased monotonically with coverage, and approached the value for the latent heat of condensation to the liquid hydrocarbon at coverages of about two monolayers (4, 5). However, normal alcohols showed a sharp maximum in the isosteric heats at coverages of about one third of a monolayer, indicating a more specific interaction with the cellulose surface (4, 5). On regenerated cellulose film, isotherm shape and isosteric heats (8) indicate that hydrocarbons interact even less specifically than on natural cellulose surfaces.

The adsorption isotherms for hydrocarbons on wet cellulose approach BET type III (14) in form as the relative humidity is increased (9), and the isosteric heats approach the heat of condensation for all surface coverages of hydrocarbon (11). Thus, water lowers the affinity of cellulose for hydrocarbons. This effect is independent of any changes in surface area with relative humidity, and is also observed on regenerated cellulose film (12). However, the thermodynamic data indicate that the surface does not behave as expected for pure water, even at very high water contents (11). In fact, the GC method has also been used to study adsorption of hydrocarbons on liquid water (15, 16). In this case, the interactions are very weak and the adsorption isotherm does not fit the BET theory, so that surface areas cannot be estimated directly (16).

Measurements at 'Zero Coverage'. In the methods described

above, the GC data are used to construct the adsorption isotherm. However, the sensitivity of the GC detector may allow measurements at very low vapour pressures, where the isotherm approaches linearity. In this 'zero coverage' region, the retention time for a single small injection may be used to calculate the limiting slope of the isotherm. This in turn is related to the free energy of adsorption, which characterizes directly the interaction between vapour and surface. This forms the basis of a new method (7) to characterize surfaces according to the differential free energy change associated with the adsorption from the vapour phase of a suitable 'probe', namely a $-\text{CH}_2-$ segment of the n-alkane chain, at effectively zero surface coverage. This quantity is readily related to measured quantities by:

$$\Delta G_{A,(\text{CH}_2)}^{\circ} = -RT \ln(t_R^{(n+1)}/t_R^{(n)}) \quad (2)$$

where $\Delta G_{A,(\text{CH}_2)}^{\circ}$ is the incremental standard free energy of adsorption per mole² of $-\text{CH}_2-$ group at zero surface coverage, R is the gas constant, T the absolute temperature, and $t_R^{(n+1)}$, $t_R^{(n)}$ are the corresponding peak net retention times. Measurements are made as follows. The film or paper must first be reduced to a form suitable for packing into a gas chromatographic column. It is cut into strips which are then passed through a cleaned paper tape punch. The perforated strips are discarded and the discs ("holes") are collected, carefully cleaned and dried, and then packed into the GC column. A series of hydrocarbons is injected into the carrier gas stream passing through the column, and the times $t_R^{(n)}$ and $t_R^{(n+1)}$ for n-alkanes with n and (n+1) carbon atoms, respectively, are measured. The measurements are made on a given column at constant temperature and carrier gas flow rate.

The quantity $\Delta G_{A,(\text{CH}_2)}^{\circ}$ is a direct measure of the interaction between the surface and a non-polar probe, and is thus analogous to the critical surface tension, γ_C , or the London non-polar component of the surface energy, γ_S^L (14), quantities derived from contact angle measurements which are often used to characterize surfaces. In fact, an empirical method for deriving γ_S^L from GC data has been proposed (7). Reasonable agreement between contact angle and GC measurements was observed for paper (7), cellulose film (8), and poly(ethylene terephthalate) film (17). The GC method thus may avoid some of the well-known drawbacks of the contact angle methods. However, it can only be applied to surfaces such as cellulose where bulk sorption of vapours is negligible in the time scale of the experiment.

ESCA of Paper and Fibre Surfaces

Characterization of paper and fibre surfaces by wetting or adsorption measurements gives useful information on physical properties averaged in some manner over the surface. To use this in-

formation effectively requires that the chemical composition of the surface be known. A variety of surface-specific spectroscopic techniques has been developed. Here, we consider applications of ESCA (Electron Spectroscopy for Chemical Analysis), otherwise known as XPS (X-ray Photoelectron Spectroscopy). This technique (18) allows elemental analysis of solid surfaces. The sample is irradiated with monochromatic X-rays, which cause the emission of photoelectrons from the inner-shell orbitals of atoms in the solid. The energies of the emitted photoelectrons, which are characteristic of the elements in the sample, are measured in an electron spectrometer. Areas of the order of a few square millimeters and depths of the order of 1 - 10 μm , depending on the element and matrix, are sampled. Chemical shifts in the measured electron binding energies provide information on the chemical bonding of the elements close to the surface. The ESCA technique has proved very useful in analysing the surface composition of polymeric materials (19), and in particular, of polymers with functionally modified surfaces (20). We wondered whether ESCA might give useful information about the surface composition of materials as complex and heterogeneous as wood pulp and paper.

ESCA Spectra of Cellulose and Lignin. The ESCA spectra for a pure cellulose paper, bleached kraft and sulphite pulps, and for some lignin samples gave encouraging results (21). The measured oxygen-carbon atom ratios for the cellulose and lignin samples were in good agreement with the bulk elemental analyses; there was no time-dependent degradation or surface contamination. Traces of chlorine were detected in the chemical pulp surface. The shapes of the carbon peaks was rationalized by assigning the carbon atoms in wood components to one of four classes:

- C₁; Carbon atoms bonded only to carbon and/or hydrogen
- C₂; Carbon atoms bonded to a single oxygen, other than a carbonyl oxygen
- C₃; Carbon atoms bonded to two non-carbonyl oxygens, or to a single carbonyl oxygen
- C₄; Carbon atoms bonded to a carbonyl and a non-carbonyl oxygen.

The electron binding energies associated with each class increase from class C₁ to C₄. The spectra for a filter paper (pure cellulose) and for a fibre sample containing hemicelluloses, lignin, and extractives are shown in Figure 2. The major peak for the pure cellulose corresponds to the five carbon atoms in each anhydroglucose unit which are bonded to a single oxygen atom, and the shoulder at high binding energy corresponds to the single carbon atom bonded to two oxygen atoms. The shoulder at low binding energy is attributed to class C₁ carbon atoms present as impurities or contaminants on the surface of the cellulose. This peak component is very much more pronounced for the sample of wood fibre (Figure 2), due to the presence of lignin and extractives at the fibre surface. Unlike cellulose, these wood components are rich

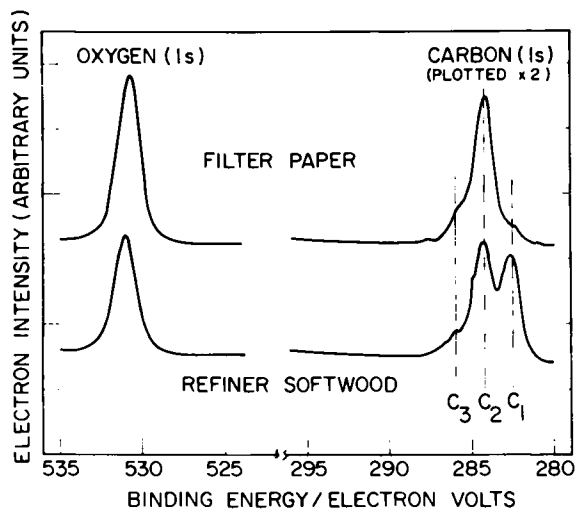


Figure 2. ESCA spectra for filter paper and for a handsheet of mechanically refined softwood pulp. The binding energies associated with classes C₁, C₂, and C₃ carbon atoms are indicated. Binding energies are not corrected for sample charging effects. (Reproduced, with permission, from Ref. 21. Copyright 1978, Cellulose Chemistry and Technology.)

in carbon atoms which are not bonded to oxygen. A semiquantitative method is available for deconvolution of the carbon ESCA peaks into component peaks (22), but it must be remembered that in a material as complex as wood, the component peaks represent not a single chemical bond type, but a mixture of similar but distinct chemical environments. For a pure filter paper, the ratio of carbon atoms of each class in the surface was measured to be $C_1:C_2:C_3 = 0.2:0.81:0.17$ compared to a theoretical value of $0:0.833:0.167$ for cellulose; a typical refiner mechanical pulp gave $C_1:C_2:C_3 = 0.36:0.54:0.10$ (22).

Estimation of Surface Lignin Content by ESCA. It is evident that lignin and extractives on the surface cause a marked change in the ESCA spectra. Mechanical pulps, containing almost all of the material in wood, are finding increasing use in pulp and paper products. A quantitative method to measure the amount of lignin and extractives in the surface of such pulps would be very useful. Our method is based on the relative size of the oxygen and carbon ESCA peaks, from which the relative numbers of oxygen and carbon atoms in the surface, N_O/N_C , can be determined. For a pure cellulose surface, $N_O/N_C = 5/6 = 0.83$, for lignin $N_O/N_C \sim 0.36$, and pure extractives have even lower values (e.g. $N_O/N_C = 0.10$ for abietic acid) based on the empirical formulae of these wood components. Experimental ESCA values are in fair agreement; $N_O/N_C = 0.81$ and 0.36 for a filter paper and a dioxane lignin preparation, respectively. Wood pulps give intermediate values for N_O/N_C . If the surface contains only lignin and cellulose, then obviously the ratio of these components in the surface of the fibres may be estimated from N_O/N_C . A range of different mechanical pulps was examined by this method. The samples were first extracted with organic solvents to remove low molecular weight components from the surface. The extraction caused a marked increase in N_O/N_C , indicating that significant quantities of extractives were present. The extracted pulps gave values for N_O/N_C of from 0.56 to 0.65 , which corresponded to surface compositions of from 30 to 45% by weight lignin, depending on the pulping process (23). Thus, the surface lignin composition of these pulps is only slightly higher than the bulk lignin. However, thermomechanical pulps prepared at an unusually high temperature did give very low values of N_O/N_C (23). Under such conditions, fibre separation occurs at relatively low energy inputs along the thermally-softened lignin-rich middle lamellae between the fibres. An extracted sample of one of these pulps gave a surface lignin content of 75% by weight (24).

Heating, exposure to the spectrometer environment, surface roughness, and variation in fines content caused no serious variation in the measured N_O/N_C values (23). However, the values of N_O/N_C were very sensitive to the extraction procedures. The method of extraction of mechanical pulp samples was, therefore, investigated (24), and acetone extraction, either in a Soxhlet condenser or by elution, was found to be satisfactory.

The surface composition of some sulphite pulps has also been examined (25). Results for the low-yield samples showed small amounts of surface lignin and extractives, and a trace of sulphur was also detected. However, a high-yield sample showed surprisingly low values for N_O/N_C , both before and after solvent extraction and even after a treatment with sodium methoxide. Assuming an appropriate empirical formula for the sulphite lignin, the amount of lignin in the surface, calculated from the ESCA value for N_O/N_C , was 17% by weight, compared to a bulk lignin content of 7% by weight. A method to estimate the surface lignin content based on the ESCA analysis for sulphur was also described. The sulphur signal was small and so the precision of the method was low, but a value of 16% by weight for the surface lignin was in good agreement with the value from the oxygen signal.

Other ESCA Applications. The ESCA method provides a semi-quantitative method to estimate surface lignin contents of extracted pulps. Extractives also exert a very marked effect on the surface properties of fibres and paper, so a direct method for estimating the amount of extractives on a paper surface is desirable. In an attempt to see if ESCA might work, we examined a model system composed of stearic acid chemisorbed on filter paper (26). The stearate ester on the paper surface was clearly evident from the ESCA results. The amount of stearate was estimated by treatment with sodium methoxide in methanol, followed by analysis of the liberated stearate by gas chromatography/mass spectrometry. Coverage was estimated to be about half a monolayer, but this was sufficient to render the paper hydrophobic. A simple model was developed to describe electron emission from a paper sheet partially coated with a thin hydrocarbon-rich layer. The calculated and observed values for N_O/N_C were brought into agreement for reasonable values of the model parameters, but the crudeness of the model and the lack of precision in the ESCA measurements detract from the significance of this agreement. The ESCA method does, however, give a rapid qualitative indication of the presence of extractives on the surface of fibres and paper.

Other published applications of ESCA include surface characterization of pulps for press-drying applications (27) and investigation of the chemical effects of corona discharge treatment on a pulp surface (28). The surface concentration of mesyl ester groups introduced on the surface of cellulose pulps was determined from the ESCA sulphur and carbon spectra (29). ESCA is also ideally suited for determining the presence of elements other than carbon and oxygen in the surface of paper samples. For example, the elements silicon, aluminum, and nitrogen, if present in sheet components such as fillers, coatings, sizes, retention aids, and drainage aids should be readily detected. Little work on these applications has been published.

Acknowledgments

The author thanks Dr. Gilles Dorris for his many contributions to this work, which was supported in part by grants from the Government of Quebec and the Natural Sciences and Engineering Research Council of Canada.

Literature Cited

1. Conder, J.R.; Young, C.L. "Physicochemical Measurements by Gas Chromatography"; Wiley: New York, 1979.
2. Braun, J.-M.; Guillet, J.E. Advances in Polymer Science 1976, 21, 108.
3. Gray, D.G. "Progress in Polymer Science"; Jenkins, A.D., Ed.; Pergamon: Oxford, 1977; Vol 5, p 1.
4. Mohlin, U.-B.; Gray, D.G. J. Colloid Interfac. Sci. 1974, 47, 747.
5. Tremaine, P.R.; Gray, D.G. J. Chem. Soc. Trans. Faraday Soc. I 1975, 71, 2170.
6. Dorris, G.M.; Gray, D.G. J. Colloid Interfac. Sci. 1979, 71, 93.
7. Dorris, G.M.; Gray, D.G. J. Colloid Interfac. Sci. 1980, 77, 353.
8. Katz, S.; Gray, D.G. J. Colloid Interfac. Sci. 1981, 82, 326.
9. Tremaine, P.R.; Mohlin, U.-B.; Gray, D.G. J. Colloid Interfac. Sci. 1977, 60, 548.
10. Dorris, G.M.; Gray, D.G. J. Chem. Soc. Trans. Faraday Soc. I 1981, 77, 713.
11. Dorris, G.M.; Gray, D.G. J. Chem. Soc. Trans. Faraday Soc. I 1981, 77, 725.
12. Katz, S.; Gray, D.G. J. Colloid Interfac. Sci. 1981, 82, 339.
13. Brunauer, S.; Emmett, P.H.; Teller, E. J. Amer. Chem. Soc. 1938, 60, 309.
14. Adamson, A.W. "Physical Chemistry of Surfaces"; Wiley: New York, 1976; 3rd ed.
15. Hartkopf, A.; Karger, B.L. Accounts Chem. Res. 1973, 6, 209.
16. Dorris, G.M.; Gray, D.G. J. Phys. Chem. In press.
17. Anhang, J.; Gray, D.G. J. Appl. Polym. Sci. In press.
18. Carlson, T.A. "Photoelectron and Auger Spectroscopy"; Plenum Press: New York, 1975.
19. See for example "Handbook of X-ray and Ultraviolet Photoelectron Spectroscopy"; Biggs, D., Ed.; Heyden: London, 1977; Chs 4 and 6.
20. See for example Clark, D.T. Paper in this symposium.
21. Dorris, G.M.; Gray, D.G. Cellulose Chem. Technol. 1978, 12, 9.
22. Gray, D.G. Cellulose Chem. Technol. 1978, 12, 735.
23. Dorris, G.M.; Gray, D.G. Cellulose Chem. Technol. 1978, 12, 721.

24. Katz, S.; Gray, D.G. Svensk Papperstidn. 1980, 83, 226.
25. Takeyama, S.; Gray, D.G. Trans. Tech. Sec. CPPA 1980, 6, TR61-4.
26. Takeyama, S.; Gray, D.G. Submitted to Cellulose Chem. Technol.
27. Horn, R.A. Tappi 1979, 62(7), 77.
28. Suranyi, G.; Gray, D.G.; Goring, D.A.I. Tappi 1980, 63(4), 153.
29. Sawartari, A. Mokuzai Gakkaishi 1979, 25(6), 442.

RECEIVED April 30, 1982

Wetting and Penetration of Paper Surfaces

J. F. OLIVER

Xerox Research Centre of Canada, Mississauga, Ontario, Canada L6J-5X6

High level image quality specifications demanded by non-impact technologies such as ink jet, electrophotography and thermography, pose new requirements in the printing substrate which for economic reasons, will continue to be predominantly paper-based. Traditional static methods for evaluating wetting and penetration behaviour are severely limited however because of the relative size of the liquid ink drops or dry toner particles and the inherent physicochemical complexity of paper structures. To avoid many of the pitfalls associated with static measurements a dynamic sorption apparatus has been developed to study spreading and penetration directly at fibre-level resolution. In this article sorption of an aqueous ink jet ink on a wide variety of commercial printing papers is reported. The ramifications of these experiments are discussed in the light of some existing theoretical models for liquid penetration and in terms of some structural aspects of paper substrates.

The porous nature of paper is of fundamental importance in determining its physical interaction with liquids. An extensive review and discussion of liquid penetration in paper has recently been covered in an excellent series of articles by Hoyland (1,2). Experimentally two major difficulties emerge which complicate interpretation of penetration data for aqueous liquids into paper: (i) unambiguous description of the porous structure; and (ii) the effect of fibre swelling on the pores. Moreover in reprographic technologies, where the relative size of paper fibres with respect to ink jet (IJ) drops or toner particles for example, are comparable, fibre interactions obviously play a more significant role on the resultant image quality, and thereby impose special demands upon structures with acceptable printing properties(3). Thus use of standard static test measurements of wetting and penetration of

0097-6156/82/0200-0435\$06.00/0
© 1982 American Chemical Society

macroscopic drops such as contact angle and size methods which are employed in conventional printing technology, are of limited value. To avoid these shortcomings we have developed a dynamic sorption apparatus capable of studying spreading and penetration of IJ drops directly at microscopic resolutions.

In this article we report some experimental studies on spreading and penetration of an aqueous IJ ink on a variety of commercial printing papers. The data are tested against existing simple theoretical models for liquid penetration in porous media. No attempt has been made to develop or employ more rigorous models.

Capillary and Diffusion Models For Porous Media

Penetration of a liquid flowing under its own capillary pressure in a horizontal capillary, or in general, where gravity can be neglected, is theoretically described (4) by the Lucas-Washburn equation

$$l = \left(\frac{r\gamma\cos\theta}{2\eta} \right)^{\frac{1}{2}} t^{\frac{1}{2}} \quad [1]$$

where l = penetration distance after time t , r = pore radius, γ = surface tension, θ = contact angle, and η = liquid viscosity. Alternatively for the purpose of these experiments it will be more convenient to employ the volume V , of liquid penetrating into the porous structure after time t . Thus from [1] it can be shown (4) that for capillaries so small that the external pressure is negligible in comparison to the capillary pressure

$$V = k' \left(\frac{\gamma\cos\theta}{\eta} \right)^{\frac{1}{2}} t^{\frac{1}{2}} \quad [2]$$

where k' is a constant depending on the pore structure of the particular system.

In the following experiments it is assumed that throughout penetration the unabsorbed liquid drop remaining on the surface maintains a circular contact line and spherical cap geometry. On this basis V can be calculated from the contact angle θ and base diameter of the drop a , according to Bikerman's (5) equation

$$V = \frac{\pi a(2 - 3\cos\theta + \cos^3\theta)}{24\sin^3\theta} \quad [3]$$

The Lucas-Washburn equation is the simplest equation to model the rate of capillary penetration into a porous material. It is derived from Poiseuille's law (4) for laminar flow of a Newtonian liquid through capillaries of circular cross-section by assuming that the pressure drop (ΔP) across the liquid-vapor interface is given by the Laplace-Young (6) equation. In practice, depending

upon the complexity of the porous system the effective pore radius r necessary to give the correct flow rate according to [1] can vary considerably from the average cross-section. To overcome this shortcoming several supposedly more realistic models have been proposed. Cheever (7) for example developed a model to describe flow of polymer liquids in porous substrates which is given by the equation

$$(R - R_0)^2 = \frac{2\gamma_{LV} d \cos \theta t}{3\eta} \quad [4]$$

where

R_0 = drop radius at zero time

R = drop radius at time t

d = half slit width of pores.

Gillespie (8) on the other hand developed an equation of the Lucas-Washburn type without specific reference to an explicit pore model on the basis of D'Arcy's law (6). Assuming that ΔP was constant Gillespie derived the following equation for two dimensional radial spreading of a liquid drop

$$R^2 (R^4 - R_0^4) = \frac{3\beta}{2} \left(\frac{3V}{2\pi h} \right)^2 t \quad [5]$$

where

R_0 , R = radius of stain at time zero and after spreading time t ,

h = substrate thickness,

and β is given by

$$\beta = \frac{bK_s \gamma \cos \theta}{C_s^3 \eta} \quad [6]$$

where

b = constant for the substrate,

C_s = liquid saturation concentration in the substrate,

K_s = corresponding substrate permeability at C_s .

Gillespie demonstrated the approximate validity of [5] for spreading of drops of non-polar liquids on filter paper. More recently Kissa (9) extended its application to the sorption of various alkanes on natural and synthetic fabrics. Rather than using drop radii Kissa measured drop areas which are more accurate particularly for spreading on anisotropic structures such as textiles or paper. On this basis [5] can be written in the general form

$$A = \sigma \left(\frac{\gamma}{\eta} \right)^u v^m t^n \quad [7]$$

where the exponents u , m and n are constant for a given substrate, and the capillary sorption coefficient σ , given by

$$\sigma = \frac{27\pi bK_s \cos\theta}{8h^2 C_s^3} \quad [8]$$

There have been a number of experimental studies (7,8,10-13) reported for porous surfaces in which liquid penetration is not consistent with [1], [2], [4] or [5], and values of the exponent n , for example in [7], are < 0.5 . For paper the Lucas-Washburn capillary model generally holds for penetration of non-swelling/non-interactive liquids such as oil-based printing inks and various organic solvents (1). With water and other polar liquids the situation is compounded by swelling and hence the validity of [1] becomes more questionable. Since the inter fibre voids are idealized as cylindrical capillaries having effective mean radii equal to r , and θ is assumed constant with time, this hardly seems surprising. However Everett et al (14) based on their experimental studies maintain that although [1] originates from a simple model it is not strictly necessary for the real pore system to resemble the model in order that Washburn kinetics are followed.

Alternatively an equation of the general form [1] can be obtained by treating penetration analogous to a molecular diffusion process (15,16). In this case the properties of the pore system and penetrating liquid are incorporated into a diffusion coefficient. However on the basis of experimental data obtained for one-dimensional flow in paper (17) there is still a need to develop more realistic models for the pore geometry. Despite this and primarily because swelling is a diffusion process, Hoyland (2) contends that aqueous liquids penetrate paper more by this process than by capillary action. Commencing with Fick's second law of diffusion which relates the diffusion coefficient D to a function of the concentration change of diffusing liquid in time t at any point x along the direction of diffusion:

$$\frac{\partial C}{\partial t} = D \frac{\partial^2 C}{\partial x^2} \quad [9]$$

Hoyland arrived at the following solution of [9], to describe penetration of an aqueous liquid by diffusion

$$F = \frac{m_t - m_0}{m_\infty - m_0} = \frac{2}{h} \left(\frac{D}{\pi} \right)^{1/2} \quad [10]$$

where

F = fraction of the amount of penetrant taken up in time t relative to the amount taken up at infinite time,

m_0, m_t, m_∞ = amount of penetrant present at time zero, t and ∞ ,

h = the initial thickness of paper.

The approximate validity of these two models will be examined where appropriate in the following experiments by analyzing the data with respect to [2], [4], [7], and [10].

Experimental Part

Apparatus. Spreading and penetration experiments of IJ drops were performed in a dynamic sorption apparatus (shown schematically in Figure 1) consisting of a drop-on-demand IJ printer (which typically ejected drops in the range 120-260 μ m diam. (18)), printing substrate sample holder and video system capable of simultaneously recording plan and profile viewing of an IJ drop from impact through to drying. Simultaneous recording of the contact line and drop profile down to fibre level resolution at \sim 30 fps was achieved by means of: two video cameras equipped with macro lenses; a screen splitter; synchronizing pulse generator; and video recorder. Interfacing the video recorder with an image analyzer enabled statistical analysis of the sorption of many drops.

The whole apparatus was mounted on a heavy metal block free of extraneous vibration and surrounded by a removable Lexan enclosure which permitted constant temperature and humidity control. The apparatus was located in a laboratory controlled at $23 \pm 1^\circ\text{C}$ and relative humidity of $72 \pm 2\%$. Temperature variations in the enclosure never exceeded $\pm 0.1^\circ\text{C}$ and the relative humidity never varied more than $\pm 0.5\%$ during a single experiment.

Procedure.

(a) Characterization of Paper Samples: All the paper samples investigated were subjected to CPPA or TAPPI standard test measurements. These included caliper, Sheffield roughness, Gurley porosity, and Cobb and Hercules size. For the Hercules test the actual ink jet ink was used as the reference liquid. In addition non-standard test measurements which included profilometry and dynamic ink absorption, were conducted on a Rank Taylor Talysurf profilometer (Model 5M) and Bristow absorption apparatus (19), respectively.

(b) Drop Formation: Narrow strips of the paper samples were cut from the center of an 8" x 11" sheet so that the machine direction was lengthwise and perpendicular to the camera optic axes when clamped (felt side toward jet) to the sample holder. Individual IJ drops were fired by single pulse activation at a pre-focussed area at least three drop diameters from the sample edge. Following drop sorption, which varied from near instantaneous to several minutes depending upon the grade of paper, the sample was moved approximately three drop diameters and firing of at least seven more drops repeated on adjacent unprinted areas.

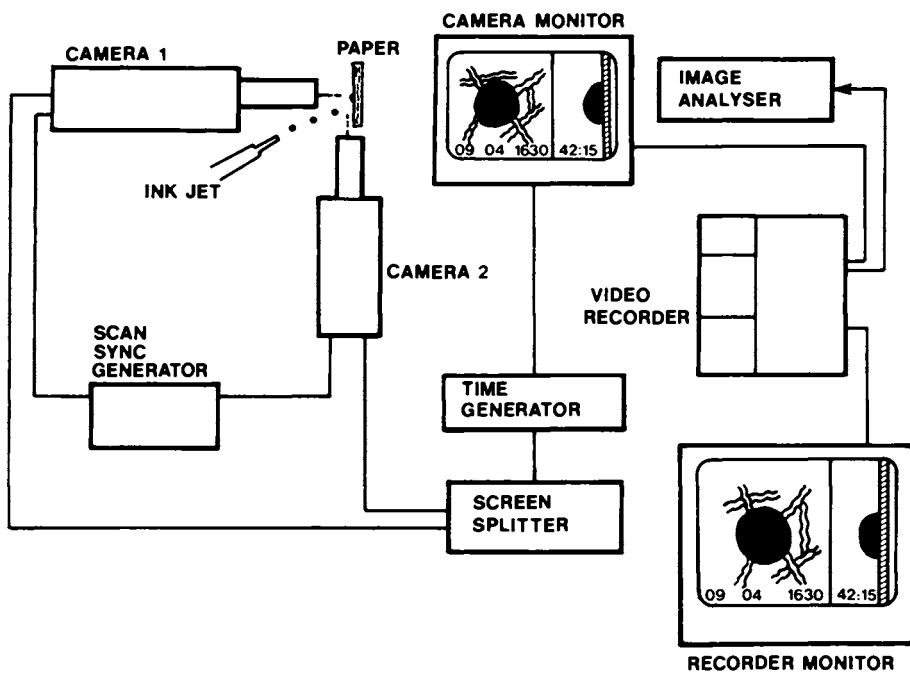


Figure 1. Schematic of dynamic sorption apparatus and recording system.

(c) Data Analysis: Frame by frame playback of video recordings of the drop contact line and profile history (3) were used to measure or calculate the following parameters: drying time (t_d), the time elapsed between the first video frame ($t_0 \sim 0.03$ sec) and complete disappearance of the drop meniscus beneath the paper surface; drop radius R_0 and R for an approximately circular drop after time t_0 and t respectively; drop area A_0 and A ; and contact angle θ_0 and θ after time t_0 and t . Also assuming that throughout penetration the unabsorbed liquid drop remaining on the surface maintains a circular contact line and spherical cap geometry, the volume V_t and V_p after time t and t_d was calculated from the contact angle θ and base diameter of the drop profile according to [3].

Materials. A variety of commercial uncoated and coated printing grade papers were selected for this study (see Table I). These papers were evaluated with an aqueous dye-based ink of surface tension (γ) approximately $60 \text{ mN}\cdot\text{m}^{-1}$.

Results and Discussion

Dynamic Sorption of Ink Jet Ink Drops on Commercial Papers. Drying times (t_d) and various parameters measured or derived from contact line spreading, profile development and penetration data for the various systems studied are summarized in Table I. A wide variation occurred in the values of t_d among the various papers studied. The maximum deviations in t_d based upon an analysis of many drops, indicated an appreciable variability for a given paper. However the consistency of the calculated penetration volume, V_p , for drops included in detailed contact line and profile analysis suggest that these deviations result from the structural variability in paper rather than drop-to-drop volume variations. This was substantiated by the marked variations in the final image shape observed among several drops printed on the same paper sample.

(a) Contact Line Development: Contact line spreading contours revealed the complexity of the surface and porous structure of uncoated and coated papers. With the exception of samples K and P, where rapid spreading occurs prior to the 'initial' period, the initial contours for all other samples remained near-circular and smooth. In part the latter results from the degree of sizing and is reflected by higher θ_0 values (see Table I). However even on these papers considerable deterioration in image quality subsequently ensues prior to, or after, t_d . In contrast the coated papers Y and C produced the highest quality images even with a lower surface tension ink.

The detailed history of contact line development and its implications with respect to the paper structure are reported elsewhere (3).

Table I. Drying times, initial apparent contact angles and calculated penetration parameters for single drops of an aqueous IJ ink on various commercial printing grade papers.

Ref.	PRINTING GRADE	t_d sec.	$n^{(b)}$	θ_o deg.	$v_p^{(e)}$ $\text{cm}^3 \times 10^{-5}$	$D^{(f)}$ $\text{m/sec} \times 10^{-10}$
K	ink jet (unsized)	0.02	0.22	40 ^d	a	a
H	newsprint	1.0	0.43	71.5	1.1	150
P	wet xerographic	4.0	0.15	32	1.3	2
J	rotogravure (coated)	6.4	0.14; 0.55	53	1.2	13
Y	offset (gloss coated)	20.0	0.20	49	2.6	a
V	wet xerographic (internally sized)	21.7	0.08	71	1.4	8
A	offset	43.7	0.08; 0.47	50	1.5	9
C	offset (coated)	81	0.10	57	1.7	0.4
F	dry xerographic	120	0.09; 0.50	73	1.8	0.8
Z	bond (100% rag content)	150	0.005	77	1.5	1

- (a) Not resolvable.
 (b) Exponent in Equation 7 derived from Figs. 2 and 3, which should equal 0.5 if Lucas-Washburn capillary model is valid. Double values for some papers refer to a second or third stage of area development, respectively.
 (d) Determined from high-speed cinematographic study (Ref. 18).
 (e) Calculated from [3].
 (f) Diffusion coefficient derived from Figs. 7 or 8 and calculated according to [10].

(b) Contact Area Development: Figures 2 and 3 show the contact area data plotted according to Eq. [7]. Apart from systems H and F the corresponding slope values (n) are $\ll 0.5$. Thus none of these systems exhibits penetration rates typical of the Lucas-Washburn model, but rather they show more prolonged spreading and complex behaviour. Systems A, F, and J however, which initially have very small slope values, show a more rapid stage of area development commencing close to t_d for which corresponding slope values are approximately 0.5.

Drop radii data determined in the machine (MD) and cross-machine (CMD) directions for system C were also plotted according to [4], [5] and [7]. In contrast to previous studies on porous surfaces (8, 12) the data plotted according to [5] (which has been omitted), only showed linear behaviour approaching t_d . This obvious difference in sorption behaviour is more apparent in Figure 4, which is plotted according to [4]. Two stages of spreading are apparent (i) initial region, $t < 1$ sec, in which $n > 0.5$, and (ii) second region, $t > 1$ sec, in which $n < 0.5$. Although there is a discrepancy between the MD and CMD data caused by the anisotropic nature of the coating, the derived values of n for the same sorption regions agree reasonably. The noticeably lower value of n (given in Table I) which is derived from Figure 3 on the basis of [7] is probably due to a combination of factors. Firstly insufficient area analysis was completed in the initial region thus values of n in Table I correspond to the second or third spreading regions. Secondly in the light of Figure 4 and drop axis ratio values, [4] must be regarded as approximate even for system C.

(c) Profile Development: Corresponding changes in drop profiles expressed in terms of contact angle, θ , for systems with $t_d < 22$ sec. and $t_d > 44$ sec. are shown in Figures 5 and 6 respectively. For the former systems, with the exception of V which is internally sized, a pronounced decrease in θ occurred within the initial 0.05 sec. Following this stage, θ decreased more slowly and approximately linearly with time. For systems with $t_d > 44$ sec the rate of decrease in θ remained approximately linear and constant throughout. The average rate of change of θ is thus mainly dependent upon θ_0 and t_d . With the exception of sized papers (i.e. F and Z), the relationship between θ_0 and t_d is quite inconsistent and obviously other structural factors must be implicated. It should be emphasized that for many papers the liquid drop contact line became increasingly anisotropic beyond the initial period, i.e. $t > 0.05$. Thus θ is increasingly dependent upon the direction of observation (20).

(d) Penetration: Calculated values of the final penetration volume, V_p , which is assumed equivalent to the initial drop volume calculated from [3] are also given in Table I. The curvilinear behaviour of plots of V_p vs $t^{1/2}$ indicated the inapplicability of [2] for both coated and uncoated papers. Alternatively Figures 7 and 8 show graphs of the same data plotted in terms of V_t/V_p

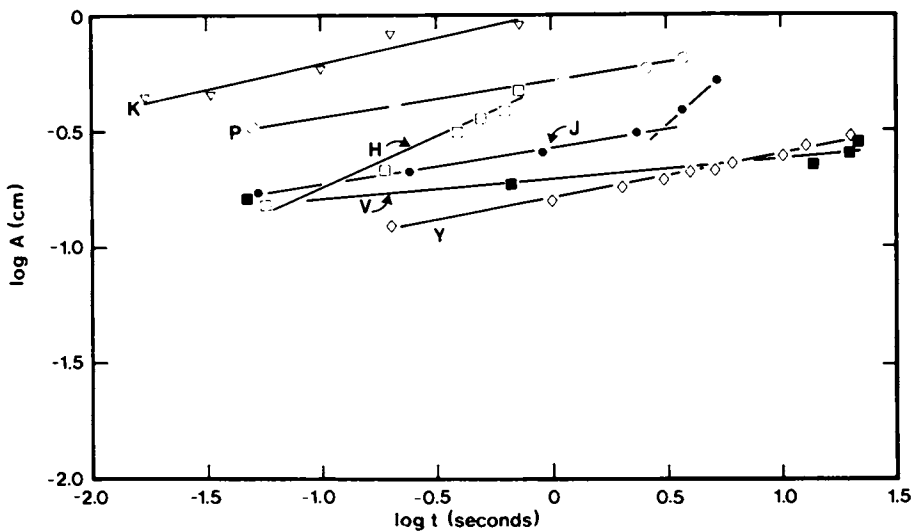


Figure 2. Drop area data plotted according to [7] for system with $t_d \leq 22$ s.

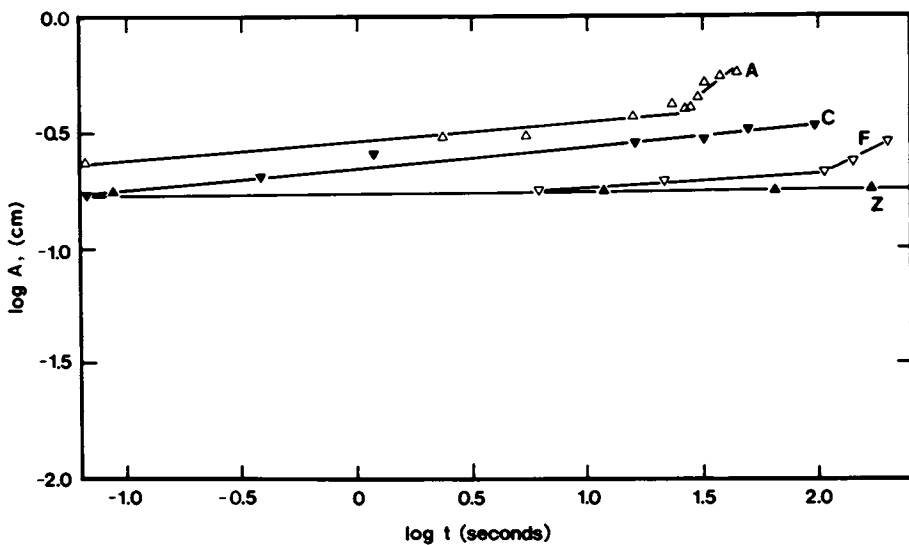


Figure 3. Drop area data plotted according to [7] for systems with $t_d \geq 44$ s.

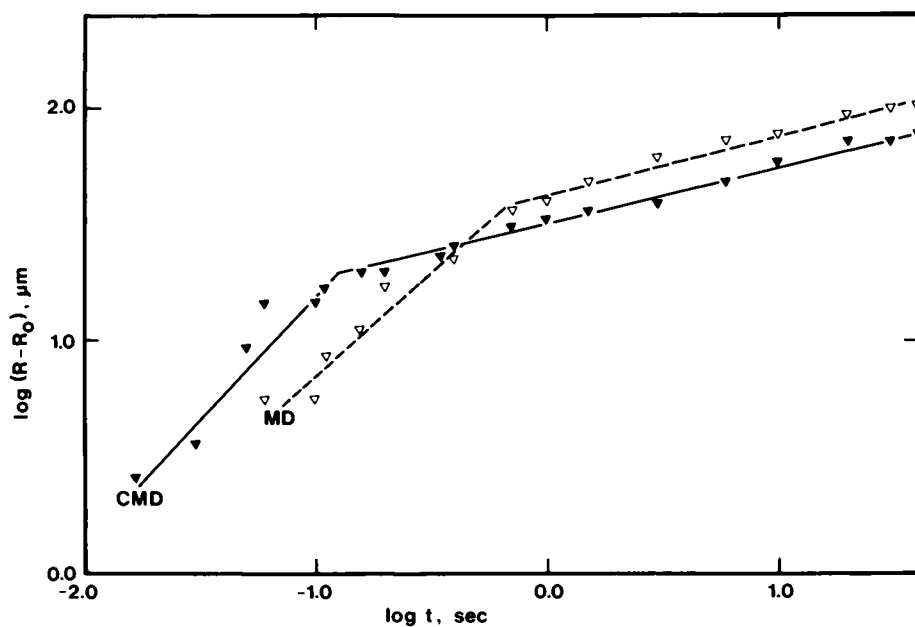


Figure 4. Radial spreading on coated paper (C) plotted according to [4].

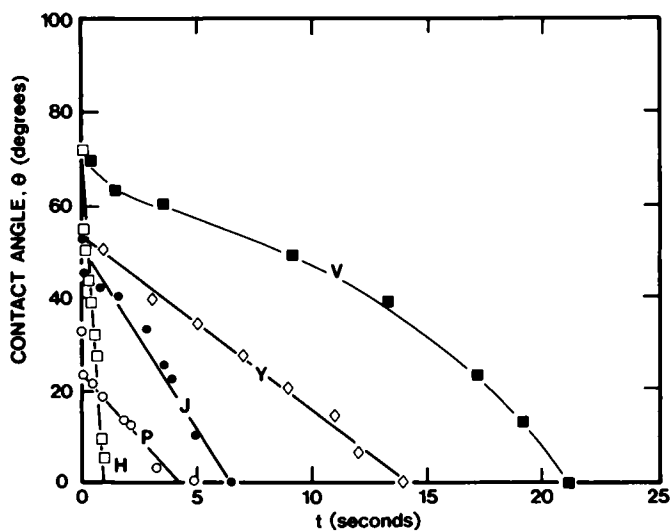


Figure 5. Apparent contact angle (θ) variations with time for systems with $t_d \leq 22$ s.

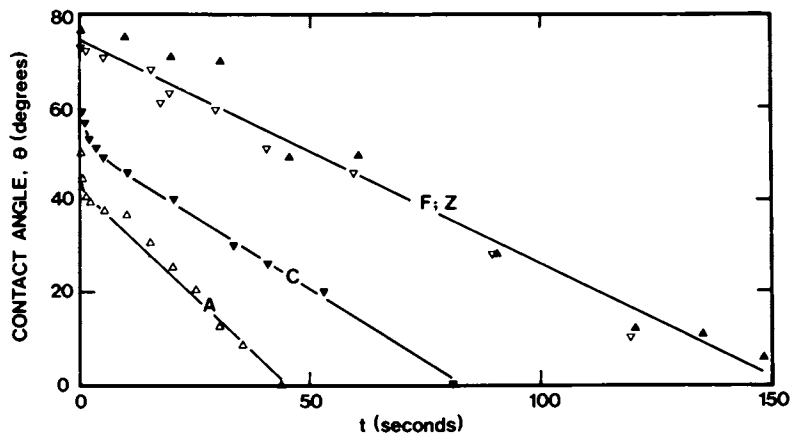


Figure 6. Apparent contact angle (θ) variations with time for systems with $t_d \geq 44$ s.

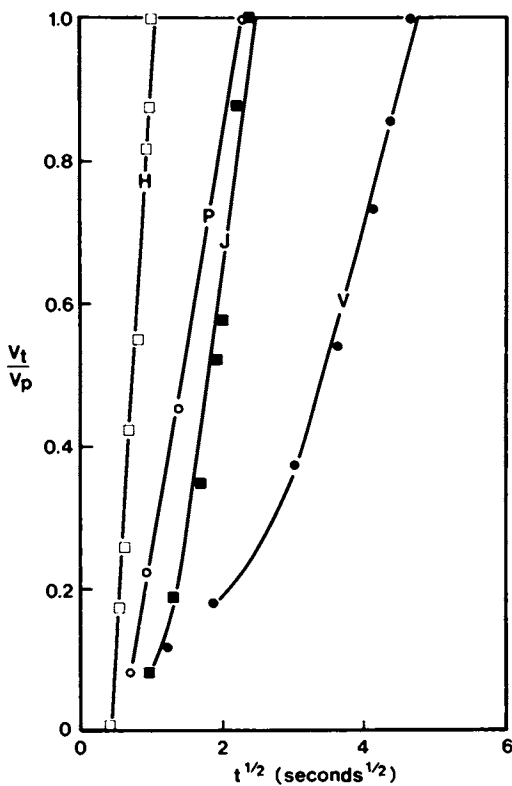


Figure 7. Volume data for systems with $t_d \leq 22$ s plotted according to Hoyland's diffusion equation [10].

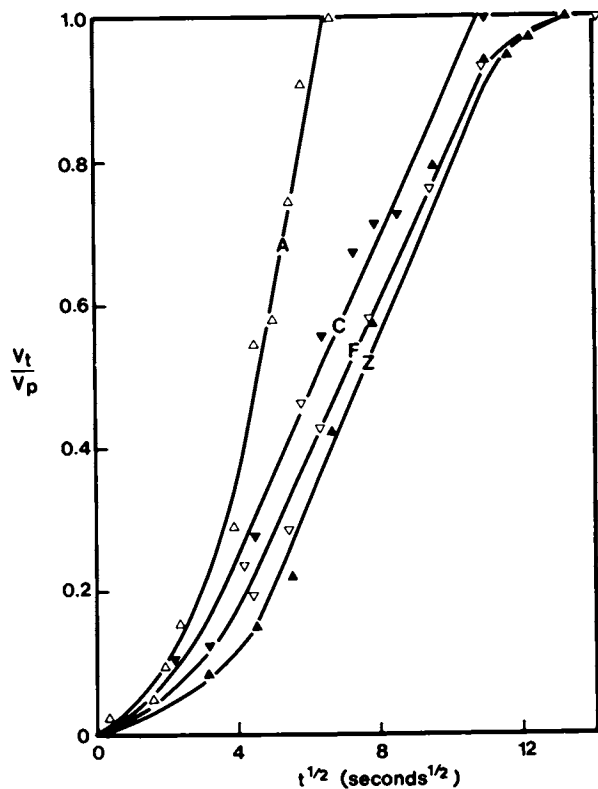


Figure 8. Volume data for systems with $t_d \leq 44$ s plotted according to Hoyalnd's diffusion equation [10].

American Chemical
Society Library
1155 16th St., N.W.

according to the diffusion equation [10]. The initial non-linear behaviour is partly as a result of the error involved in calculating small values of V , and probably, as suggested by Hoyland (2), because the diffusion coefficient, D for penetration of aqueous liquids is not constant at the commencement of swelling. Values of D derived from the remaining linear portions of the graph and calculated according to [10] are also given in Table I.

It should be emphasised that the assumptions invoked by [3] may be reasonable during the 'initial' stages, but in view of the anisotropic nature of both uncoated and to a lesser degree coated papers (3), its validity becomes more questionable as V_p increases. Also because several systems exhibited show-through prior to t_d , values of D in these experiments (which are based upon the caliper rather than the value of h at $t = \infty$) are subject to an additional error.

In addition to the volume data, it was also possible to observe and estimate transverse spreading velocity of the penetrating liquid front during the incipient stages (3). Preliminary observations demonstrate some profound differences in the porous nature of uncoated versus coated structures and in the relative capillary resistance with lateral and transverse spreading of inks with different surface tensions. One further important aspect involved with penetration, was that shortly before disappearance of the drop many paper samples became irreversibly swollen. The amount of swelling, expressed as the percentage increase in the original caliper was quite appreciable and ranged from ~ 5 to 25% for uncoated papers and ~ 5 to 10% for coated papers.

(e) Application of Capillary and Diffusion Models for Drop Sorption: Despite wide variability in spreading, penetration and image development, a consistent pattern of events emerge among the systems studied. Consequently one may employ a generalized mechanism of sorption to describe all these systems (3). Initially, significant lateral liquid drop spreading is in evidence for systems with low t_d values, but quickly diminishes as bulk capillary forces take effect. This is substantiated, at least for coated paper, by the initial value of $n > 0.5$, derived from Figure 4 based on [4]. As was noted by Cheever (7) during this stage the drop must be skimming over the surface and substrate penetration is negligible.

In the subsequent second and, in a few systems, third stage, liquid spreading terminates and penetration predominates. Papers with values of n (derived from Figures 2 or 3 and given in Table 1) which are < 0.5 indicate slower penetration than predicted by a simple capillary model. Frederick and Bobalek's (13) explanation for this deviation from theory is the irregularity of the spreading front as opposed to a discrete liquid edge assumed in Cheever's model. Rather, a selective filling process occurs in the spreading zone, i.e. filling of smaller, then larger, capillaries which is similar to the spreading behaviour described by Gillespie. A good example illustrating this type of behaviour is

revealed in studies on microspreading of liquids on grooved surfaces (21). Variations in groove dimensions and hence capillary pressure produce intermittent capillary movement in the grooves causing local protrusions in the contact line. Apart from the aforementioned, other factors contributing to this apparent increased porous resistance (or decreased liquid permeability) are the effect of : sharp fibre edges, pore tortuosity, build-up of air pressure particularly in 'dead-end' pores, breakdown in liquid supply to spreading front, and fibre swelling which tends to diminish the average pore size.

Finally increase in n shown by several systems during post-drying (3) (see Table I) stems from subterranean absorption processes e.g. interconnection of partially filled pores and localized surface fibre wicking. The values of n which in several cases are close to the theoretical value, 0.5, for a Lucas-Washburn type capillary model, suggest that the condition of flow through completely filled and interconnected capillaries to supply the spreading front, is ultimately attained. This final stage reflects lag in the equilibration of bulk and surface capillary forces.

Deviations between the experimental results and the modified Lucas-Washburn capillary models demonstrate the limitations of these theories for paper structures. Moreover, as discussed above, concentration gradients will likely exist within the penetration zone during ink jet printing so that ΔP , the capillary pressure, is no longer constant and hence [1] loses its validity. The inapplicability of [1] thus makes derivation of an effective pore radius, on the basis of [4] and Figure 4, dubious.

Alternatively on the basis of a diffusion type model, approximate values of the diffusion coefficient D , have been calculated for these systems. Values of D which fall in the range of 10^{-2} to 10^{-5} mm/sec are of the same order of magnitude as those obtained by Hoyland (2) for the penetration of various aqueous liquids in bleached softwood paper. Although Hoyland's diffusion model takes into consideration fibre swelling during penetration it still overlooks many of the aforementioned structural complications unique to paper.

Relationship Between Paper Structure and Ink Sorption.

Values of various physical test measurements used to characterise the different structures in terms of ink receptivity and image quality are given in Table II. The standard as well as non-standard physical test measurements, indicate a poor correlation between structural and sorptive properties of paper. At best methods such as Cobb size provide only a qualitative guide-line. The trend in porosity, roughness, and liquid absorption measurements, in terms of t_d is very inconsistent for most papers. Similarly Lyne (22) has found that Bendsten or Sheffield roughness tests do not correlate with perception of letterpress image uniformity, due to the relatively larger areas monitored by these

Table II. Standard and non-standard physical test measurements of various commercial grade printing papers (determined at 23°C and 50% relative humidity).

Ref.	Caliper μm	Sheffield Roughness Felt Wire	Gurley Porosity sec/100cm ³	Cobb Size g/m ²	Hercules Size sec.	Talysurf, R _a ^d μm	Bristow Absorption ^c			
							Absorption Coeff. ml/m ² /S ^{1/2}	Roughness Index ml/m ²		
A	107.5	151 ^a	164	11.4	55.3	29.6	3.7	8.5	7.6	b
C	71.3	35		1000+	61.4	29.4	5.6	5.4	1.7	
F	97.0	145	151	18.9	27.8	153.0	2.9	6.3	6.7	
P	77.5	77	80	662	56.6 ^b	2.3	4.5	10.7	6.8	b
V	83	52	53	262.9	25.3	8.8	12.6	10.1	4.9	
Z	102.5	157	161	14.4	26.0	443.5	3.7	-	-	
H	83.3	174	146	30.1	62.9 ^b	1.8	5.6	64.2	5.5	b
J	57.5	41	48	1000+	53.1 ^b	1.2	9.3	38.9	3.3	b
K	89.8	234	160	15.1	79.9 ^b	0.7	5.4	38.9	16.7	b
Y	116.3	18	26	1000+	32.3	441	1.8	-	-	

- a Twin wire paper, wire side #1.
 b Water completely soaked through sample.
 c See Ref. (19).
 d Trace 8mm long in CMD.

methods. Parker Print Surf roughness however was found to be superior, presumably because it is more sensitive in the size range of half-tone dots, which can be comparable to IJ drop images. For Talysurf roughness it is doubtful whether other parameters in addition to R_a (but not listed in Table II) such as bearing ratio, waviness, peak-to-valley height, etc. are of more significance. On the other hand the means of generating 3- rather than 2-dimensional profilograms with the Talysurf (23) would enable derivation of more meaningful distribution patterns of the actual drop contact area. Furthermore since all commercial papers are chemically heterogeneous, i.e. they consist of cellulose fibres with varying amounts of lignin, hemicellulose, organic and inorganic papermaking additives, and papermaker's aids, there is also an obvious need to map and quantify their surface chemical distribution.

The significance of the latter parameters can be realised if one considers the initial drop impact. In a fibrous structure such as paper a liquid is unable to discern differences in pore depth until entering the bulk structure. Prior to penetration, following dissipation of mechanical forces, drop wetting and spreading of an aqueous ink jet drop will be primarily determined by the combined effects of chemical heterogeneity and physical roughness. The combination of these effects can be approximated (24) in terms of Cassie and Baxter (25) and Shuttleworth and Bailey's (26) equations:

$$\cos\theta = f_1\cos\theta_e + f_2 \quad [11]$$

where θ refers to the apparent contact angle and θ_e the equilibrium contact angle and f_1 and f_2 to the solid-liquid area fractions (physical and/or chemical) respectively, and

$$\theta = \theta_e + \emptyset \quad [12]$$

where \emptyset refers to the fibre edge angle. It should be emphasized that on a porous surface such as paper, θ represents the resultant of surface and bulk capillary processes (27). Also the contact line and drop shape in the contact zone will be perturbed to an extent determined by the ratio of drop size to surface roughness (28).

Bearing these arguments in mind it is not surprising that values of θ_0 for most systems (see Table I) correlate poorly with data reported in Table II. Until more meaningful surface physicochemical data are available the interpretation, or application of contact angle measurements to develop sorptive models for paper, remains highly questionable.

Conclusion

A wide variation in the rate of absorption drying and image quality of an aqueous ink jet ink was apparent among the commer-

cial printing papers examined. Comparison of some of the sorption data with simple capillary and diffusion models reveal the present limitations of these theories when applied to paper structures. A more rigorous theoretical treatment of ink sorption in relation to the printing substrate requires further developments in characterizing the physicochemical properties of paper.

The dynamic sorption apparatus clearly demonstrates the advantages of performing dynamic rather than static measurements of spreading and penetration at microscopic resolutions on substrates as complex as paper. The ability to observe ink or toner/paper interactions in situ should be especially valuable for investigating other non-impact technologies.

Acknowledgments

The author is grateful for the assistance of R. Forsyth with the dynamic sorption apparatus, A. Jones for physical test data and Xerox Corporation for granting permission to publish this article. Thanks are also due to Dr. M.B. Lyne (PAPRICAN) for providing Bristow absorption data.

Literature Cited

1. Hoyland, R.W. and Field, R. Paper Tech. Ind. 1976, 17, 213; 216; 292; 304; and 1977, 18, 7.
2. Hoyland, R.W. "Fibre-Water Interactions in Papermaking"; Tech. Div. BPBIF, London, 1978, 557.
3. Oliver, J.F., paper presented at the Seventh Fundamental Research Symposium: 'The Role of Research in Papermaking', Tech. Div. BPBIF, Cambridge, UK, Sept. 1981.
4. Washburn, E.W. Phys. Rev. 2nd Series, 1921, 17, 273.
5. Bikerman, J.J. Ind. Eng. Chem. Anal. ed 1941, 13, 443.
6. Adamson, A.W. "Physical Chemistry of Surfaces", Interscience Pub., N.Y., 1967.
7. Cheever, G.D. "Interface Convers. Polym. Coatings", Proc. Symp. 1967. Ed. by P. Weiss, 150-81.
8. Gillespie, T. J. Colloid Interface Sci. 1959, 14, 123.
9. Kissa, E. ibid. 1981, 83, 265.
10. Greinacher, H. Z. Phys. Chem. 1959, 19, 101.
11. Mack, G.W. J. Oil Colour Chem. Ass. 1961, 44, 737.
12. Schickentanz, W. Powder Technol. 1974, 9, 49.
13. Frederick, W.J. and Bobalek, E.G. Ind. Eng. Chem. Fundam. 1975, 14, 40.
14. Everett, D.H.; Haynes, J.M.; R.J. Miller, "Fibre-Water Interactions in Papermaking", Tech. Div. BPBIF, London, 1978, 519.
15. Ruoff, A.L.; Prince, D.C.; Giddings, J.C.; Stewart, G.H. Koll. Zeit. 1959, 166, 144.
16. Rudd, D.F. J. Phys. Chem. 1060, 64, 1254.

17. Ruoff, A.L.; Stewart, G.H.; Giddings, J.C. Koll. Zeit. 1960, 173, 14.
18. Oliver, J.F., Forthcoming Publication.
19. Bristow, J.A. Svensk, Papperstidn. 1963, 70, 623.
20. Oliver, J.F.; Huh, C.; Mason, S.G. J. Adhesion, 1977, 8, 223.
21. Oliver, J.F.; Mason, S.G. J. Colloid Interface Sci. 1977, 60, 480.
22. Lyne, M.B., paper presented at the Seventh Fund'l Research Symposium: "The Role of Research in Papermaking", Tech. Div. BPBIF, Cambridge, UK, Sept. 1981.
23. Sayles, R.S.; Thomas, T.R. J. Phys. E: Sci. Instrum. 1976, 9, 855.
24. Oliver, J.F.; Huh, C.; Mason, S.G. Colloids and Surfaces, 1980, 1, 79.
25. Cassie, A.B.D.; Baxter, S. Trans. Farad. Soc. 1944, 40, 546.
26. Shuttleworth, R.; Bailey, G.L.J. Disc. Farad. Soc. 1948, 3, 16.
27. Oliver, J.F.; Mason, S.G., "Fundamental Properties of Paper Related to its Uses", Tech. Div. BPBIF, London, 1976, 428.
28. Huh, C.; Scriven, L.E. Symp: Contact Angle Phenom., ACS Mtg. LA, March 1971.

RECEIVED April 30, 1982

Surface Chemistry of Business Papers: Electron Spectroscopy for Chemical Analysis Studies

MICHAEL M. FARROW, ALLEN G. MILLER, and ANNE MARIE WALSH
IBM Corporation, Information Products Division, Boulder, CO 80302

A series of standard business paper specimens of controlled composition have been examined using ESCA (Electron Spectroscopy for Chemical Analysis). Samples of varying pulp composition, varying filler content, and those with and without both bulk and surface sizing are discussed. The performance differential of the various paper surfaces in the adhesion of thermally fused, xerographically toned images is addressed.

The performance of an electrographic copier is ultimately judged by the product it produces--that is, a photographic quality reproduction of the original document. In order to do this, plain-paper copiers transfer the electrostatically-produced toner image from the photoconductor to the paper. The image is then bonded to the paper with either pressure or heat or both. In those copiers using temperature/pressure fusing, the toner is a pigmented polymer chosen so that the polymer's glass transition temperature, T_g , can be conveniently achieved by the hot roll fuser. A series of polymers of this nature are those based on styrene and acrylates.

In some copiers, the residence time in the fuser and the temperature and pressure encountered are not sufficient to cause flow of the toner, and only sintering occurs. In these cases, the toner cannot interlock with the cellulose fibers and must rely on more subtle forms of bonding to the paper surface. This bonding is probably in the form of polar-polar interactions between the cellulose hydroxyl groups and the acrylate ester groups. This presents a problem since one of the requisites for a well-sized paper is that the internal sizing be of low surface energy to offer adequate resistance to water penetration.(1, 2) Although the surface sizing applied to seal in the fillers and produce a smooth surface texture(3) may provide a degree of relief from the low surface energy internal sizing, it often appears that complete coverage of the internal sizing does not occur.(4) As a

0097-6156/82/0200-0455\$06.00/0

© 1982 American Chemical Society

consequence, a lower degree of fusing occurs, and inadequate fusing quality results. Compounding this problem is the increasing use by paper mills of non-rosin sizes or modified sizes which, although more efficient in preventing the penetration of water, tend to produce a more uniform, low energy surface by coating even more of the hydroxyl units on the cellulose.(5) In order to enhance the performance of toner without sacrificing the durability and water penetration resistance of paper, it is necessary to understand that surface to which toner is expected to bond.

In a previous series of articles, Gray and his coworkers have investigated the surface of cellulose fibers, giving particular attention to mechanical pulps that had not been sized either internally or externally.(6, 7, 8) In this series of works, Gray and his coworkers were able to show the applicability of ESCA (Electron Spectroscopy for Chemical Analysis) to a cellulose surface and interpreted the peaks in terms of the chemical structure of the cellulose.(6) He demonstrated a remarkable variability in the oxygen to carbon ratio on the surface of a series of samples ranging from stone-ground wood, that is, merely abraded wood, to thermomechanically-prepared pulps in which the cellulose fibers are agitated under temperature and pressure.(7) He demonstrated that the oxygen to carbon ratio variations were accounted for by the presence of the lignin on the surface of some of the cellulose fibers. He also showed that the accuracy in measuring surface atomic ratios had an expected error of less than $\pm 10\%$ on the series of samples. Lastly, he indicated that deconvolution of the C 1s peak for cellulose and wood fibers gave reasonable accord with the expected stoichiometry of the constituents.(8) His analysis of the expected chemical shifts in the C 1s spectra formed the basis for the understanding of this work.(6, 7)

ESCA analysis by now is a familiar tool to those interested in the surface chemistry of samples. Developed in the 1960's by Siegbahn and coworkers in Sweden,(9, 10) ESCA provides information about the electronic structure and bonding of atoms on the surface of a sample. In order to obtain the electron binding energy spectrum of a sample, the sample is placed in an ultrahigh vacuum and irradiated with X-ray photons. Some of the photons cause ionization of inner-shell electrons of the atoms, and after impact of the photons, the electrons leave the surface with the kinetic energy equal to that of a photon minus the energy binding the electron in its orbit. The electron binding energies differ for every element, and thus, it is possible to determine which elements are present in a sample merely by measuring the kinetic energy of the emitted electrons.

Although the X-rays may penetrate the sample to the extent of several thousand angstroms, only those electrons emitted from the top 50 to 100 angstroms of the surface are able to escape inelastic collisions with other electrons and retain their

initial energy. Thus, only those constituents that truly are on the surface are sampled. The energy of the emitted electrons characterizes the elements present, and the intensity is proportional to their abundance. In addition to this information, additional data may be obtained about chemical bonding from the subtle shifts in the characteristic binding energy of the element. Extensive tabulations for a variety of elements are available to establish the exact chemical shifts in various compounds. (11, 12) One difficulty lies in the fact that frequently, the chemical shifts observed are smaller than the line width of the spectrometer. However, with an approximate knowledge of the chemistry involved, it is possible to deconvolute the peaks mathematically and arrive at a firm conclusion about the chemical species on the surface.

In addition to photoelectrons emitted from the sample, another class of electrons, Auger electrons, are also emitted with characteristic energies. These Auger electrons arise from the process which eliminates the very high energy state of the atom after photoionization. As the hole remaining in the core is deenergized by an outer-shell electron filling the hole, another outer shell electron, the Auger electron, is emitted with high energy. In the case of the Auger process, the kinetic energy of the electron is independent of the ionization source and is dependent only upon the binding energy to the element. Wagner et al. (13) have studied the chemical shift in the oxygen Auger lines and have shown that it is often greater than the chemical shift of the parent line, and therefore, very useful diagnostically.

In order to understand the surface to which toner in electrographic copiers is expected to bond and to provide information to assist in formulating optimum toners, a series of paper samples has been investigated. These samples range from raw, unbleached papers to finished, bond-quality paper. The goal of this study was to understand, step-by-step, what changes occur on the surface of cellulose fibers during the paper manufacturing process, and to provide a broad, general background in understanding the surface of finished business papers.

Experimental

Paper specimens were obtained from Mead Paper, Printing and Writing Paper Division (Chillicothe, Ohio 45601). Samples were identified as being free from other materials, i.e., no preservatives, slimicides, defoamers, etc. Internally-sized samples were sized by conventional alum/rosin sizing; surface-sized materials were prepared by an application of starch at the size press; and all the other samples were unsized. Whatman filter paper was extracted with a 68/32 mixture of chloroform/acetone to remove any organic binder from the fiber surface. The fiber composition of the Whatman filter paper was identified by optical microscopy as cotton. The sample identified as "No Sizing" was

also extracted for 24 hours in a Soxhlet extractor with acetone in order to remove any incidental hydrocarbon on the surface. All other samples were examined in an "As Received" condition.

All fuse grade samples were prepared using IBM Series III, Model 40 Copier, running at a fuser temperature of 170°C, a nip pressure of ~20kg/cm², and residence time of 18 msec. Evaluation of the fuse grade was by an abrasion method which is a modification of ASTM F362-79. The modified procedure uses a standard test pattern which is abraded with a Taber Abraser, and the change in reflectance of the abraded area is measured using a Gardner reflectometer.

All ESCA spectra were obtained using a Physical Electronics, Model 548, electron spectrometer operated under control of the MACS (Multiple Techniques Analytical Control System) computer (copyright Physical Electronics Industries). A magnesium x-ray anode was used supplying photons with an energy of 1253.6 eV. Survey spectra (1,000-0 eV) were collected on all specimens using the pass energy of 100 eV with 0.5 eV sampling. Survey spectra are typically collected at low resolution for a short period of time primarily to establish the overall elemental composition of the surface. Survey spectra are, in general, not precise enough to establish semi-quantitative analysis of the surface. More detailed surface information can be obtained by "multiplex" scans acquired by repetitively scanning narrow windows in the binding energy range over the elements of interest. These multiplex scans are taken at higher instrument resolution and for a sufficiently long period of time to generate a high signal to noise ratio. This is done automatically by the software program in association with an instrumental interface. Multiplex data were collected at a pass energy of 25 eV with 0.2 eV sampling over the appropriate binding energies for those elements detected in the survey spectra. The spectrometer was calibrated to the Au 4f 7/2 peak at 83.8 eV. At 25 eV pass energy, the Au 4f 7/2 has a full width at half maximum (FWHM) of 1.25 eV. Typical vacuum chamber pressure during analysis was approximately 5×10^{-9} torr. All samples were handled with standard surface analysis techniques to avoid surface contamination. Representative samples of each type of paper were removed from the center of the sheet to avoid any edge contamination due to previous handling.

The multiplex data consisted of several regions with overlapping peaks. The C 1s and O 1s regions were resolved using curve-fitting routines that were supplied with the MACS System. Before fitting, all data were treated with a three-point digital smoothing and corrected for inelastic back-scattering. From previous work on a polyethylene sample at similar instrument parameters, it has been established that the convolution of instrumental line width and natural line width of the carbon and oxygen 1s lines have FWHM of 1.6-1.8 eV, and the line shape can be fitted with a curve that ranges from 90% Gaussian, 10% Lorentzian to 100% Gaussian. Fitting was initially carried out with only

minimum restraints on binding energy and without correction for static charge. A second-pass fit was carried out, correcting for the static charging by shifting the low-energy C 1s peak (saturated hydrocarbon) to 284.6 ± 2 eV. Details of this fitting procedure will appear elsewhere, but in every case, satisfactory fitting was obtained using three species of carbon and two species of oxygen. The criteria for the satisfactory fit were: a) a minimum number of species, b) the difference between the computed curve and the data curve did not show unresolved features above the background noise level, and c) reasonable chemical correspondence between the sample and the chemical shifts of the resolved features.

Results and Discussion

The ESCA spectra for all paper samples are dominated by the O 1s line and C 1s lines, lying at about 535 eV and 285 eV respectively. Figure 1 is a survey spectrum for paper without sizing. In addition to the O 1s and C 1s lines, other features also visible are the oxygen Auger and carbon Auger lines lying at about 750 eV and 1000 eV respectively. The O 2s line at about 30 eV is also evident. The feature at approximately 200 eV is the chlorine 2p transition (arising from the bleaching operation on the paper). Some evidence of aluminum, presumably arising from contamination during the formation of the sheet, is visible at approximately 75 eV and at 120 eV. The intensity ratios appearing in the survey spectra are not directly proportional to the abundance of various elements on the surface since the photoelectron yield from the ESCA process varies from element to element. Figure 2 is a spectrum of a filled paper (unsized). In addition to the previously mentioned features, there now appear two lines from silicon lying at approximately 100 eV and 150 eV. Note that the ratio between carbon and oxygen is changed between the paper with no filler and the high filler content paper. Figure 3 is a survey spectrum of Mead 20 lb. bond paper. In comparison to the previous samples, the carbon to oxygen intensity ratio has changed and features from silicon are no longer visible, presumably as a consequence of an overlaying of starch surface sizing.

Figure 4 is the C 1s multiplex which has been shifted 3 eV and smoothed with a digital smoothing algorithm. The 3 eV shift is to accommodate the surface static charging caused by the photoemission of electrons. Figure 5 is the O 1s region treated in the same way. In addition to the smoothing, baseline corrections have been applied to remove the background noise level and to correct for inelastic electron scattering. Examination of Figure 4 shows that the C 1s line for paper without sizing is considerably greater in FWHM than the expected 1.6 eV. Both Linfors(14) and Wagner(15) have indicated that the FWHM and line shape should be approximately constant for the 1s response of a

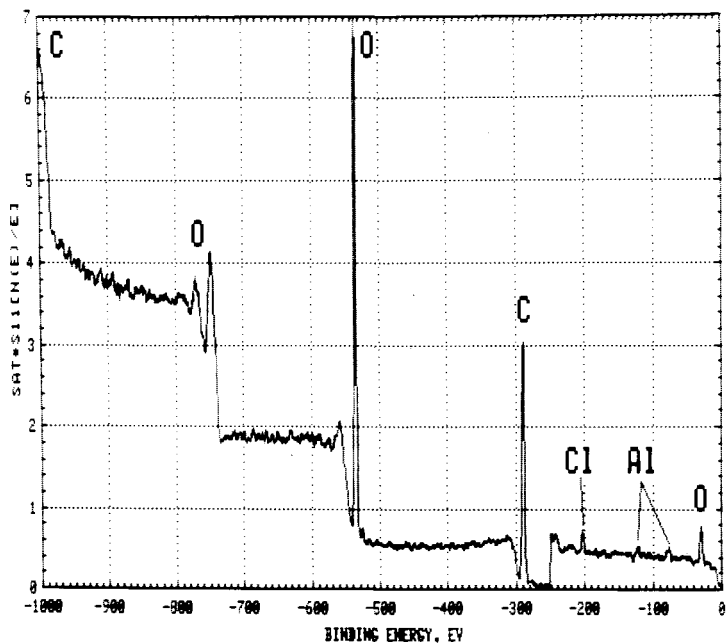


Figure 1. ESCA survey spectra of paper with no sizing and no filler.

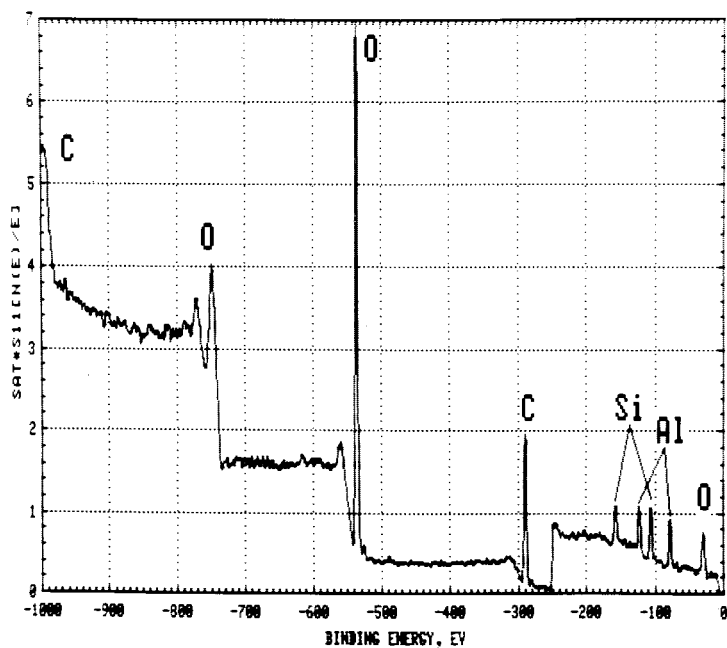


Figure 2. ESCA survey spectra of paper with high filler content and no sizing.

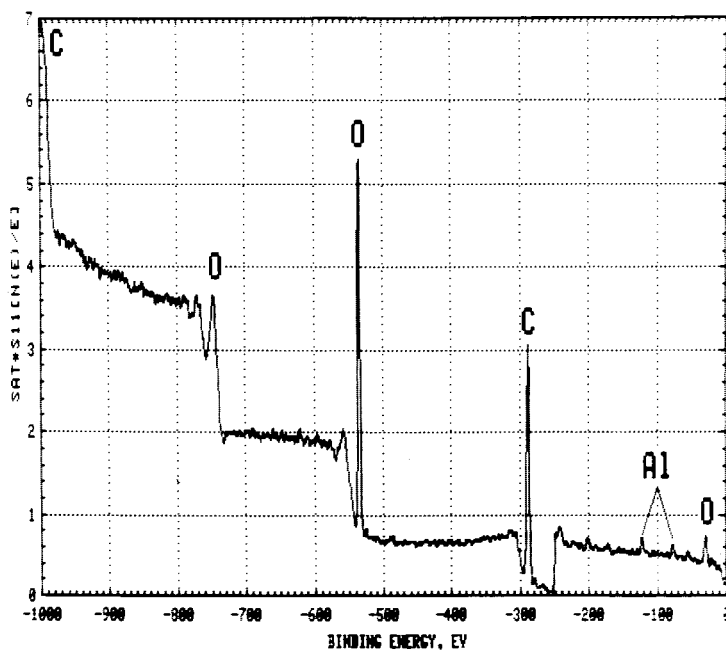


Figure 3. ESCA survey spectra of Mead 20 lb. bond paper.

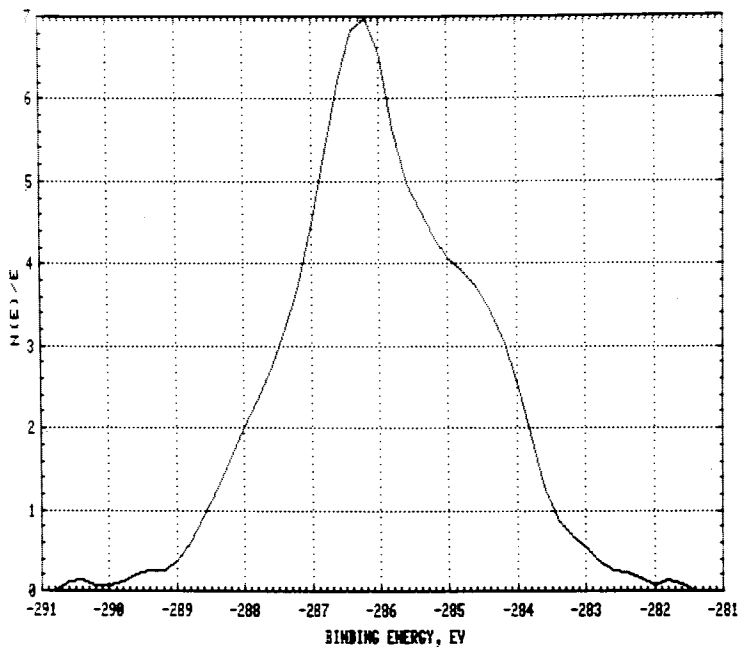


Figure 4. ESCA carbon 1s multiplex spectra for paper without sizing.

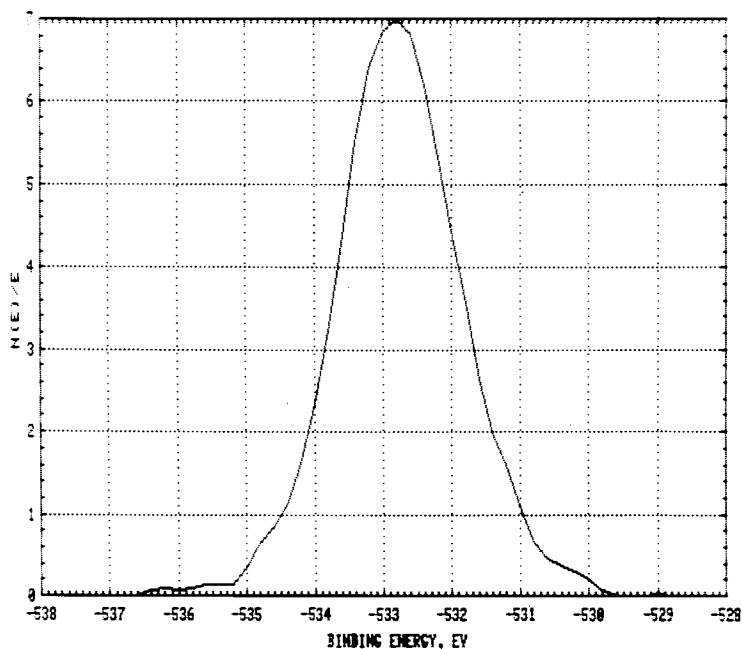


Figure 5. ESCA oxygen 1s multiplex spectra for paper without sizing.

given spectrometer for all elements from lithium through sodium. This is because the natural line width is narrower than the instrument response function and in general the line width and shape are a consequence of the convolution of the natural line width and the instrument response function. An examination of Figure 5 shows that the O 1s line also has a FWHM somewhat greater than 1.6 eV.

Once multiplex spectra have been collected, it is possible to compute a semi-quantitative surface composition. Using the MACS program software, which accounts for varying elemental sensitivities, and using peak intensity, all regions sampled in the multiplex spectra are ratioed to establish a surface composition. Of course, those regions not sampled in the multiplex spectra are not accounted for and the resulting semi-quantitative surface composition will not reflect their presence. In this study all elements detected by the survey scan were sampled by multiplex spectra.

A difficulty arises from the use of the MACS program in that the computed relative abundances of the elements are based on intensities only. Although a purely Gaussian line would have a peak height proportional to the area, any deviations from the purely Gaussian line would not be accommodated by this program. This is obviously the case of the C 1s region in which multiple species occur. For this study all semi-quantitative surface atomic concentrations were determined by the "Curve Fitting Package" (copyright Physical Electronics Industries) which allows semi-automatic computation of surface concentrations based on areas not on peak intensities. Table I lists the overall surface atomic concentrations of all the elements detected in the survey spectra for the samples. It is interesting to note that as the sample undergoes more and more preparation toward producing the finished sheet, relatively little change occurs in the oxygen to carbon ratio overall, until filler and sizing are added. Some aluminum contamination was found on all samples, probably deposited during the paper finishing operations.

Once the multiplex spectra have been collected and stored, it is possible to continue analysis using the curve fitting package. Gray et al(6, 7, 8) have shown that the surface of the cellulose fibers should be composed primarily of two carbon peaks: carbon bonded to hydroxyl (carbinol) and carbon singly bonded to two oxygens (acetal). In addition, most samples show the presence of carbon bonded only to other carbons and/or hydrogen. Wagner et al(13) have shown that the oxygen species in cellulose should be a single line at 532.5 eV. Table II lists the parameters and identification of the carbon and oxygen species used to fit this multiplex data.

The vendor supplied curve fitting package requires that the number of species be identified and ranges established for their intensity, binding energy, FWHM, and shape factors, and the values be initialized. Using a multi-dimensional grid search

TABLE I
Surface Atomic Concentrations for Paper Specimens

All specimens 50/50 hardwood/softwood except as noted

Sample	Elements (Atomic Concentration ¹ , %)				
	C	O	Al	Si	Cl
Whatman ²	55.3	44.7	-	-	-
No Sizing	57.4	41.4	0.9	-	(0.3) ³
Extracted ⁴ No Sizing	58.8	38.3	-	-	0.9
Unbleached	54.4	44.9	0.7	-	-
Bleached	56.1	42.9	1.0	-	-
Bleached Hardwood ⁵	57.9	40.6	1.5	-	-
Light Refining	60.3	38.8	1.0	-	-
Hard Refining	59.3	40.3	-	-	-
Low Filler	55.9	42.7	0.8	0.5	-
High Filler	43.5	50.9	3.3	2.3	-
Internal Sizing	78.0	19.5	2.4	-	-
Internal and Surface Sizing	73.6	25.2	1.2	-	-
Mead 20# Bond	67.2	25.9	4.4	-	0.5

¹ Using integrated areas and area sensitivity, MACS program.

² Cotton fibers extracted with 68/32 chloroform/acetone.

³ Noise level.

⁴ Extracted 24 hrs. with acetone.

⁵ 100% hardwood.

TABLE II
Species Assigned to Chemical Shifts

Binding energy, eV ¹	
C ₁ 284.5	Hydrocarbon, carbon bonded only to other carbon or hydrogen: (-CH-) 2
C ₂ 286.3	Carbon singly bonded to oxygen, other bonds to carbon and/or hydrogen: (-C-OH)
C ₃ 287.9	Carbon, doubly bonded to oxygen or singly bonded to two oxygens, acetal: (C=O or (-O-C-OR)
O ₁ 531.5	Incidental oxygen, inorganic oxygen.
O ₂ 532.8	Anhydroglucose oxygen, absorbed H ₂ O (C-O-H, C-O-C, H ₂ O)

¹ Average values, 12 samples, ±0.1 eV

routine, the deviation of the computed curve from the data curve is minimized. All parameters are allowed to vary within the predetermined limits and upon convergence of the error signal, iteration ceases. Figure 6 is an example of the computer fit of the C 1s region of paper without sizing. Fitting was carried out on all C 1s regions and O 1s regions shifted so that the C₁ species hydrocarbon, (carbon bonded to hydrogen and other carbons only) fell within 0.2 eV of 284.6 eV. Fairly narrow initial fitting parameters were used on the energy to correspond to C₁, C₂, and C₃ and the FWHM was restricted to 1.6-1.8 eV. The line shape factor, which can be varied from a 0-100% mix of Gaussian/Lorentzian was restricted between 80 and 100% Gaussian. Figure 7 shows the fit for the O 1s region in paper without sizing. An adequate fit could be obtained by using two species with the parameters as indicated in Table II. Once again, energies were restricted to a fairly narrow band corresponding to the expected chemistry. Line widths and shape factors were restrained in a manner similar to the carbon. Only the C 1s region and O 1s regions were fitted; all other regions were assumed to be single species as identified by the chemical shift. For example, the aluminum, corrected for static charging, was shifted in a manner to indicate aluminum oxide, and silicon when detected was found to be in the form of silicon dioxide.

Table III shows the results of the resolution of all carbon and oxygen species on the 13 samples studied. Values in the table are based on the overall atomic concentration of the two elements in the sample ratioed to the fractional area contribution of each component to the region. The expected error in the resolution result is anticipated to be less than 10% of the value of each species. Continued fitting of the data did not yield a significantly better result. Based on the Auger parameter listed in Table IV for all the samples, Wagner's measurement of the Auger parameter for cellulose,⁽¹³⁾ and Gray's work on cellulose fibers,^(6, 7, 8) it is possible to assign the prime constituent of all the samples as being anhydroglucose (cellulose or starch).

Cellulose is a polymer consisting of anhydroglucose units, (C₆H₁₀O₅). Since hydrogen is not detected in the ESCA experiment, the only species visible on a pure cellulose surface should be carbon and oxygen. All carbons are bonded to at least one oxygen, either in the form of carbinol or in the form of carbon singly bonded to two different oxygens (acetal). Therefore, the stoichiometric ratio of oxygen to carbon and carbinol to acetal are fixed by the anhydroglucose structures. These can be computed as O₂/C₁ + C₂ (oxygen to carbon) and C₂/C₃ (carbinol to acetal) which stoichiometrically are 5:6(0.833) and 5:1 respectively for anhydroglucose.

The results of the curve fitting as it relates to the anhydroglucose stoichiometry is listed in Table V. In order to provide reference to Gray's previous work,^(6, 7, 8) we have included a sample of Whatman filter paper. Although this material

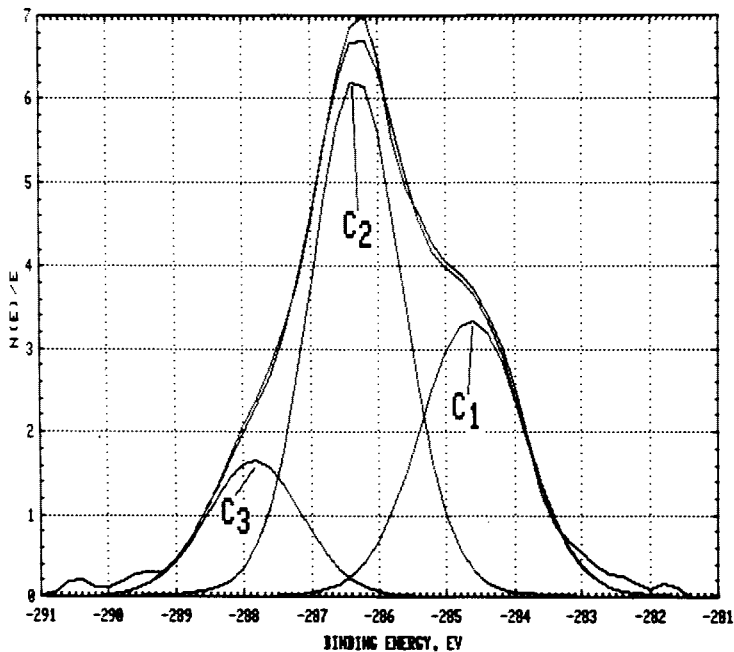


Figure 6. Curve fitting results for carbon 1s multiplex spectra of paper without sizing.

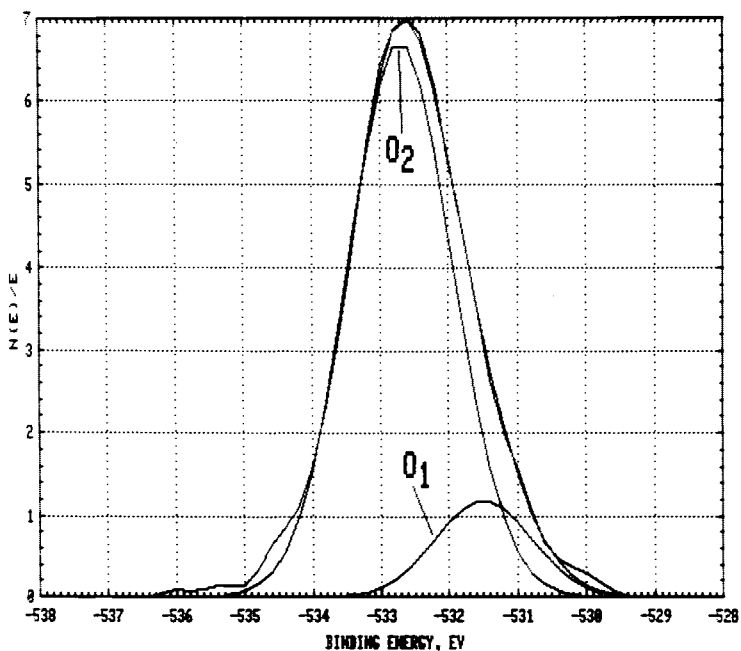


Figure 7. Curve fitting results for oxygen 1s multiplex spectra of paper without sizing.

TABLE III
Resolved Carbon and Oxygen Species

Sample ¹	Species (Overall % Surface Atomic Concentration)				
	C ₁	C ₂	C ₃	O ₁	O ₂
Whatman	6.0	42.0	7.3	2.9	41.8
No Sizing	18.5	30.8	8.1	5.1	33.2
Extracted No Sizing	8.4	39.3	11.2	5.1	35.2
Unbleached	14.8	32.8	6.8	6.9	38.0
Bleached	11.2	36.9	8.0	5.2	37.7
Bl. Hardwood	17.0	31.5	9.4	6.1	34.5
Light Refining	19.2	31.7	9.4	4.3	34.5
Hard Refining	13.7	37.9	7.7	9.8	30.5
Low Filler	12.3	33.3	10.3	9.1	33.6
High Filler	5.3	32.1	6.1	11.6	39.3
Internal Sizing	54.2	16.6	7.2	5.8	13.7
Internal and Surface Sizing	45.0	22.5	6.1	3.6	21.6
Mead 20# Bond	32.8	26.4	8.9	5.4	19.5

¹ Sample description as in Table I.

TABLE IV
Auger Parameter¹ and Static Charge²

Sample ³	α , eV	Static Charge, eV
Whatman	1041.9	3.3
No Sizing	1042.5	3.1
No Sizing, Extr.	1042.2	3.0
Unbleached	1042.5	2.7
Bleached	1042.1	2.7
Bleached Hardwood	1042.3	3.7
Light Refining	1042.1	3.6
Hard Refining	1041.8	3.8
Low Fill	1042.0	3.0
High Fill	1041.7	3.2
Internal Sizing	1042.1	2.5
Internal and Surface Sizing	1041.6	2.6
Mead 20# Bond	1041.4	2.6

¹ Kinetic energy of the oxygen KLL Auger transition plus the Binding Energy of the oxygen 1s electron, α .

² Referencing to 284.6 eV for carbon bonded to other carbon and to hydrogen only. Actual values were at greater binding energies than 284.6 eV.

³ Sample description as in Table I.

TABLE V
Species Ratios Based on Deconvolution Results

Sample ¹	$\frac{C_2}{C_3}$	$\frac{O_2}{C_2 + C_3}$
Theoretical Anhydroglucose	5	0.833
Whatman	5.8	0.848
No Sizing	3.8	0.933
No Sizing, Extr.	3.5	0.657
Unbleached	4.8	0.960
Bleached	4.6	0.840
Bleached Hardwood	3.4	0.844
Light Refining	3.4	0.839
Hard Refining	4.9	0.669
Low Filler	3.2	0.771
High Filler	5.3	1.03
Internal Sizing	2.3	0.576
Internal and Surface Sizing	3.7	0.755
Mead 20# Bond	2.9	0.569

¹ Sample description as in Table I.

is assumed to be standard cellulose, the ratio of C_2 to C_3 is well above the expected error. One possible interpretation of this variation, other than fitting errors, is that during the preparation of the cotton fibers to produce the filter paper, the fibers are acid washed to remove any residual inorganics. Such acid washing may be sufficient to cause depolymerization of the cellulose on the surface, producing a surface that is enriched in hydroxyl units. Other deviations from ideal stoichiometry seem to be related to the presence of hydrocarbon on the surface partially obscuring the anhydroglucose. This same effect seems to be responsible for the depression of the expected oxygen to carbon ratio ($O_2/C_1 + C_2$) to below normal stoichiometry. Other deviations from ideality, for example, the oxygen to carbon ratio in high filler paper, can be accounted for by the presence of adsorbed water on the filler material. This is possible since water oxygen has the same chemical shift as anhydroglucose oxygen and will be included in that area. Although no particular precautions were taken to dehydrate the samples before examination by ESCA, it is expected that at the very high vacuum conditions in the spectrometer, most non-bound water would be volatilized immediately.

Table VI lists the relationship between the sample preparation and the amount of hydrocarbon (C_1) on the surface. Obviously, those samples with internal sizing added have an elevated hydrocarbon content. It is this hydrocarbon, in the form of rosin and rosin salts, that imparts the low surface energy and resistance to water penetration to the paper. In other cases, the hydrocarbon is probably in the form of lignin remaining from the pulping operation or adventitious carbon simply from the handling of the sample.

Table VI also shows the relationship between the amount of hydrocarbon in the form of percent C_1 and the relative fuse grade. The number of samples in Table VI is reduced from previous tables since many of the papers, because of their properties, were unable to withstand the abrasive fuse grade testing. For example, the sample with high levels of filler separated rather easily and pulled fibers from the surface, invalidating the test procedure. Even without these samples, however, a clear relationship between the amount of hydrocarbon on the surface, either in the form of rosin and rosin salts or lignin, is clearly related to the adhesion of the toner polymers to the paper surface. A least square fit of these data has a (relatively low) correlation coefficient of 0.85, and a slope of -0.8. Although the relationship may not be a linear one, it is clearly reasonable to presume that higher quantities of hydrocarbon on the surface of paper do prevent adequate adhesion of toner. This result corresponds with the previous work done by Borch(16) and also with results presented elsewhere in this symposium volume.

TABLE VI

Sample	%C ₁	Relative Fuse Grade, %
No Sizing	18.5	100
Internal Sizing	54.2	57
Internal and Surface Sizing	45.0	77
Light Refining	19.2	76
Hard Refining	13.7	96
No Filler	~14	94
Mead 20# Bond	32.8	76

Conclusion

The surface of paper can be adequately represented as a combination of anhydroglucose and hydrocarbon from the rosin sizing and residual lignin. One intent of the paper manufacturing process is to remove lignin, which from an ESCA perspective appears primarily as hydrocarbon on the cellulose, and prepare a clean surface. The subsequent addition of sizing to prevent water penetration once again adds hydrocarbon to the surface. The internal sizing hydrocarbon is not necessarily totally obscured by the surface sizing. This latter result may partially respond to the question raised by Marten on "whether the starch film on the saturated surface is monomolecular layer or polymolecular. It is most likely that the surface is covered only patchwise by aggregates several molecules thick as suggested for other polymers".(17) Since ESCA cannot distinguish between starch and cellulose and since the sizing efficiency is considered to be fairly high in modern paper manufacturing, it is probable that the anhydroglucose units on the surface of finished paper are in the form of starch.

The demonstrated relationship between the presence of hydrocarbon and fuseability of toner to the paper is equally important to the paper manufacturers and to the toner/copier manufacturers. It is possible that modifications to the surface sizing process could provide better surfaces for toner adhesion.

Further work is underway to characterize finished papers, especially those sized with the alkaline sizing process. Such papers on initial examination do seem to have a greater amount of hydrocarbon on the surface and these sizing methods are thought to be more efficient and environmentally cleaner.(18) European and some domestic manufacturers have been using the alkaline sizing process and more are considering it. If the surface of alkaline sized paper is less polar, as found by Borch,(16) then even greater difficulties can be expected with the fusing of styrene/acrylate based toners.

Acknowledgments

The authors gratefully acknowledge the samples provided by Mr. Ivan E. Shaffer of Mead Paper Co., Chillicothe, OH. The discussions with Dr. Derik Gray of McGill University, Dr. Charles D. Wagner of Oakland, CA, Dr. Paul Lindfors of Physical Electronics Industries and especially Dr. Jens Borch of IBM, Tucson were particularly helpful.

Literature Cited

- 1 E. Strazdins, *Tappi*, 64, 31 (1981).
- 2 W. H. Griggs and B. W. Crouse, *Tappi*, 63, 49 (1980).
- 3 L. C. Coughlin, "Handbook of Pulp and Paper Technology", Von Nostrand Reinhold Co., New York, K. W. Britt, Ed. 1970, Chapter 5-4.
- 4 J. M. Gess, *Tappi*, 64, 35 (1981).
- 5 D. H. Dumas, *Tappi*, 64, 43 (1981).
- 6 G. M. Dorris and D. G. Gray, *Cellulose Chem. Technol.*, 12, 735 (1978).
- 7 G. M. Dorris and D. G. Gray, *Cellulose Chem. Technol.*, 12, 721 (1978).
- 8 D. G. Gray, *Cellulose Chem. Technol.*, 12, 735 (1978).
- 9 K. Siegbaum, C. Nordling, G. Johansson, J. Hedman, P. F. Hedman, K. Hamrin, U. Gelius, T. Bergmark, L. O. Werme, R. Manne and Y. Baer, "ESCA Applied to Free Molecules," North Holland, Amsterdam, 1969, Ch. 5.
- 10 K. Siegbaum, K. Hamrin, J. Hedman, G. Johansson, T. Bergmark, S.-E. Karlsson, I. Lindgren and B. Lindbert, "ESCA: Atomic, Molecular and Solid State Structure by Means of Electron Spectroscopy," Almquist and Wiksells, Uppsala, Sweden, 1967.
- 11 C. D. Wagner, W. M. Riggs, L. E. Davis, J. F. Moulder and G. E. Mullenberg (Ed.), "Handbook of X-ray Photoelectron Spectroscopy," Perkin-Elmer Corporation, Eden Prairie, Minn., 1976.
- 12 J. W. Robinson, Ed. "Handbook of Spectroscopy" Vol. I, CRC Press, Cleveland, OH., 1974.
- 13 C. D. Wagner, D. A. Zatko and R. H. Raymond, *Anal. Chem.*, 52, 1445 (1980).
- 14 P. A. Linfors, "Computer Curve Fitting of ESCA Data to Aid Interpretation," 3rd Symposium on Applied Surface Analysis, Dayton, OH., 1981.
- 15 C. D. Wagner, personal communication.
- 16 J. Borch, submitted to *Tappi*.
- 17 J. Marten, *Tappi*, 63, 87 (1980).
- 18 J. G. Penniman, *Paper Trade Journal*, Aug. 15, p. 34 (1981).

RECEIVED April 30, 1982

Effect of Paper Chemistry in Electrophotography

J. BORCH

IBM Corporation, General Products Division, Tucson, AZ 85744

The effect of paper chemistry on electrophotographic printing is reviewed. The requirements of this printing process are that the polymeric toner particles spread on and subsequently adhere to paper fibers in the sheet surface. Therefore, adequate image fix (fusing) is affected by paper chemistry through furnish composition and surface sizing treatment. Physically, the fusing process can be characterized as one where wetting and adhesion are being promoted by a relatively high surface energy of the paper. It is shown that commercially produced printing papers vary considerably in energetics due to the methods by which they are sized, either internally or at the size press. The effect of this on fuse fix and other important electrophotographic process characteristics (e.g. friction) is presented. The impact of the present trend in papermaking towards alkaline process using cellulose reactive sizes is analyzed.

In electrophotographic printing, image fix is obtained by the spreading of the molten polymeric toner on fiber surfaces and the subsequent adhesion of the glassy polymer to cellulose at points where adequate contact has been obtained. In contrast to other printing processes using liquid inks, no penetration into the fiber wall of the paper fibers occurs. Most electrophotographic printers and fast-speed copiers employ pressure assisted fusing where the heating process in some designs is assisted by preheating the paper on a metal platen before entrance into the fusing nip (1). The requirements to the paper substrate are then that

0097-6156/82/0200-0475\$06.00/0

© 1982 American Chemical Society

it must withstand both heat and pressure and provide an ideal surface for the spreading and the subsequent adhesion of the toner. Fuse quality depends on heat, pressure and time allowed for the fusing process to occur (machine speed). Both optical microscopy and scanning electron microscopy (Figures 1 and 2) demonstrate that toner spreading is rarely optimized for a wide variety of commercially available toner formulations. Sintered particles are well-defined without the film-like appearance that is characteristic of, for example, printing inks that show good affinity for the cellulosic fibers (good spreading and penetration). It has been demonstrated that the physical paper roughness may affect fuse grade in electrophotographic fuser designs (Figure 3)(2). It was speculated that the considerable variation for the smoother papers was due to differences in paper surface composition causing a variation in toner adhesion. The present study is an effort to describe variation in fusing due to paper chemistry and analyze the effect of paper on the spreading and subsequent adhesion of toner in the electrophotographic printing process.

Paper Wettability

Paper wettability by polystyrene based toner has been studied by Lee (3). Wax/polymer coating of paper and paperboard has been investigated by Swanson and Becher (4), Glossman (5), and more recently by Fredholm and Westfelt (6). In the coating studies it was believed that surface energetics of the paper structure played a fundamental role in the spreading process and subsequent adhesion of polymer to the paper surface.

Wetting Equilibrium Limited wettability of plane, smooth surfaces by non-swelling liquids can be analyzed using the Young-Dupré Equation (7):

$$W = \gamma(1 + \cos\theta_{\infty})$$

where W is the thermodynamic work of adhesion, γ is the liquid-vapor surface tension of the spreading liquid, and θ_{∞} is the steady-state contact angle attained when allowing sufficient time t for the spreading process ($t \rightarrow \infty$).

Dynamic Wettability In electrophotography, the toner spreading process has been characterized by the following 'shift factor' (3):

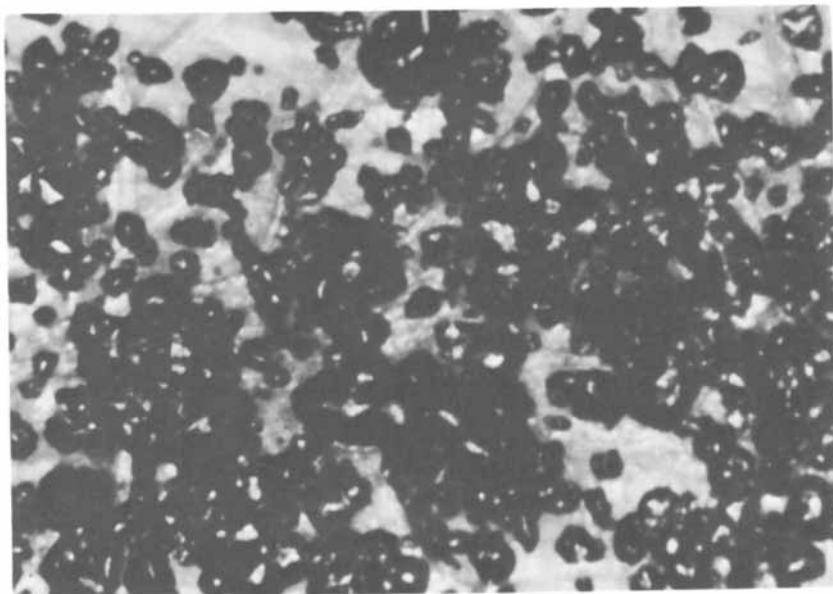


Figure 1. Electrophotographic fused image. Optical micrograph (133 \times).

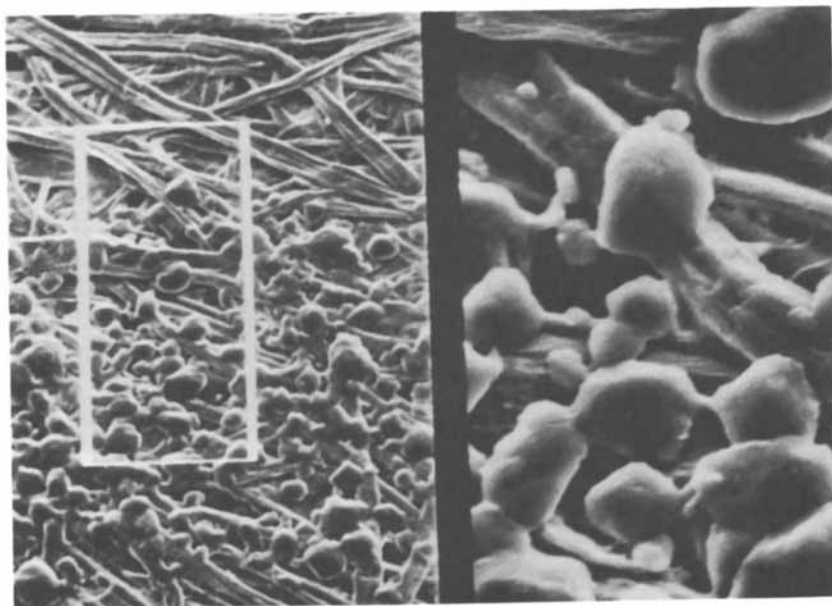


Figure 2. Electrophotographic fused image. Scanning electron micrograph (133 \times and 600 \times at part of framed area).

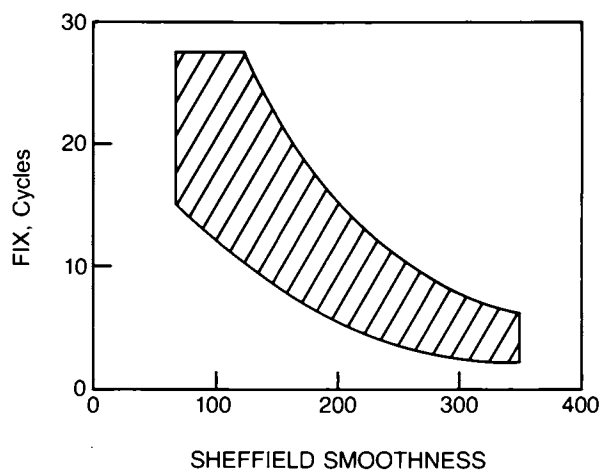


Figure 3. Sheffield smoothness vs. number of Taber abrasion cycles required to produce 20% image loss. (Reproduced, with permission, from Ref. 2. Copyright 1981, TAPPI.)

$$F = (\gamma \cos\theta)/(R\eta)$$

Here, the $\cos\theta$ term assumes dynamic values according to the spreading time allowed for the process. R is the initial drop radius and η is the polymer viscosity that is attained through the heating process.

Ideally, both equilibrium and dynamic wettability would appear controlled by surface energetics through the contact angle θ . High energy of the substrate would increase the wettability by lowering θ . Complete wetting would occur when $\theta_{\infty} = 0^{\circ}$. The general interpretation and measurement of 'surface energetics' have been discussed by Mittal (7). Procedures and experimental data applicable to cellulosic films and papers have been presented by Swanson (8).

Paper Surface Energetics Wettability of paper by low viscosity liquids is affected by additional effects due to the physical structure (porosity and roughness) and the chemical heterogeneity of the paper surface (swelling and possible chemical reaction). Drop spreading occurs rapidly and a steady-state contact angle is often not obtainable. In cases where contact angle procedure was successful and surface energetics were calculated on basis of angle measurements (8, 9, 10), energy values for pure cellulose would exceed 35-40 mN/m (Table I). A gas chromatographic procedure for energy determination confirmed the values obtained using contact angle analysis for cotton cellulose. Therefore, there is reason to believe that the cellulose substrate energy for both extrusion coating and electrophotographic fusing is higher than energy values for the molten polymers (polystyrene: $\gamma = 26-35$ mN/m (16)) and, given sufficient time, adequate wetting should occur due to an increase in the shift factor described above (3).

However, for the samples in Table I that are 'cellulosic', that is, containing organic additives either laboratory added (4) or present as constituents of commercially made papers (15), it is seen that energy values were found to be lowered into the range applicable to that of the molten polystyrene polymer. Effective wetting is no longer certain. So far, little attention has been paid to the effect of paper on the wettability by electrophotographic toners. This is possibly due to the overriding effect of toner viscosity and spreading time on the shift factor. Lee (3) analyzed the spreading process on only one paper for which surface energetics were not measured. Given the

TABLE I. SURFACE ENERGETICS OF
CELLULOSE FILMS AND PAPERS

<u>SAMPLE</u>	<u>SURFACE ENERGY</u> (mN/m)	<u>METHOD</u>	<u>REFERENCE</u>
REGENERATED CELLULOSE FILM	44	A	11
REGENERATED CELLULOSE FILMS	35.5-49.0	A	12
BLEACHED MITSCHERLICH HANDSHEETS AND KRAFT MACHINE MADE PAPER	25-60	A	4
PAPERBOARD	31-48	A	5
GLASSINE PAPER	35-36	A	5
CELLOPHANE	59	B	13
COTTON CELLULOSE	48	C	14
LIGNIFIED WOOD FIBER	37	C	14
ALKYL KETENE DIMER SIZED PAPER	21-33	B	15

Method A: Critical surface tension through Zisman
Contact Angle Procedure (9).

Method B: London dispersion force contribution through
Owens-Wendt Contact Angle Procedure (10).

Method C: London dispersion force contribution through
gas chromatographic analysis (14).

above general principles for wettability, it would appear realistic to consider the range of papers used for electrophotographic printing and expect that variation in paper nature will affect fuse grade through the influence of surface energetics on the spreading rate of the molten toner ($\cos\theta$ at t in the shift factor expression).

Paper Adhesion

In both extrusion coating and in electrophotographic printing, the end product is dependent on how well the polymer adheres to the paper surface. Swanson and Becher (4) found that polyethylene adhesion was strongly dependent upon the surface energetics of the paper (Figure 4). Glossman (5) encountered "poor" to "good" adhesion for a wax/polymer blend applied to substrates of surface energy increasing from 31 to 48 mN/m (Table III in Reference 5).

Toner-Paper Bonding Since variation in polyethylene-paper adhesion had been documented in extrusion coating studies (4, 6), it was decided to conduct similar experiments for polystyrene based toner and commercially available bond type printing papers. Polystyrene based toner was extruded into 0.5 mm diameter filament. Strips of paper were sandwiched together on a hot plate at fixed temperature for 1 minute using 4 mm length filament inbetween the paper pieces. Thereafter, the shear strength of the joint was measured in an Instron tensile tester by shearing the sandwich at 0.5 cm/min pulling speed as shown in Figure 5. Results demonstrated that both the adhesion force range and variability depended on paper brand for samples of papers of different grade and manufacture. Examples are shown in Figure 6.

Though it was recognized that such measurements were easily obscured by effects unrelated to failure at the toner-paper interface, the response to variations in sample preparation technique indicated that variability in paper nature overrode the error due to testing procedure. For example, an increase in the temperature at which the papers were fused (sandwiched together) provided a consistent increase in adhesive strength for both the "worst" and the "best" paper brand in Figure 6 as shown in Figure 7. A comparison between Figure 6 and Figure 7 shows that the strength variation due to paper brand was as significant as that due to temperature.

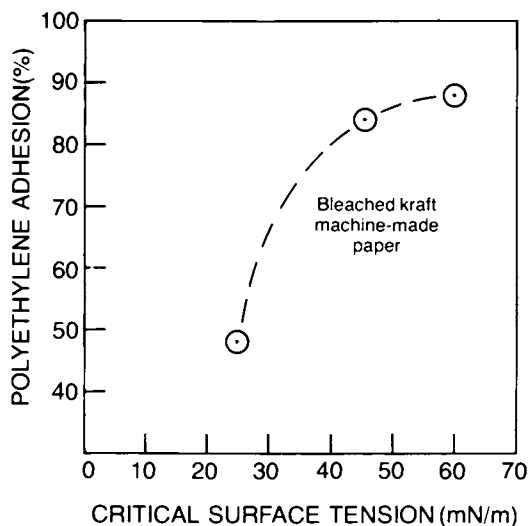


Figure 4. Polyethylene adhesion of machine made papers at different critical surface tension levels. (Reproduced, with permission, from Ref. 4. Copyright 1966, TAPPI.)

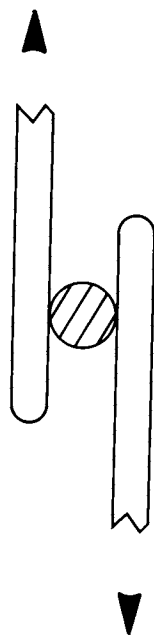


Figure 5. Laboratory shear testing. Extruded polymer filament bonded between paper strips is sheared in directions of arrows.

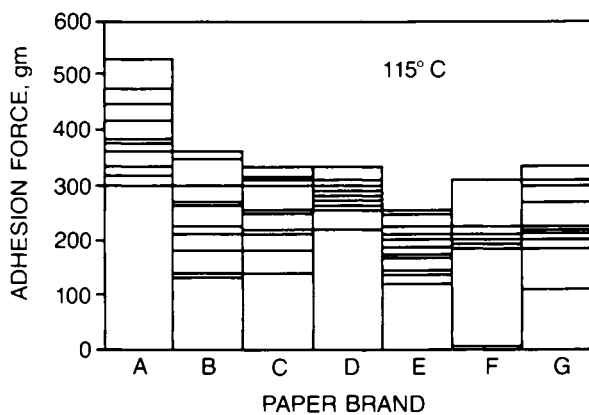


Figure 6. Adhesive strength comparison of laboratory fused paper brands (A-G). Ten measurements for each brand.

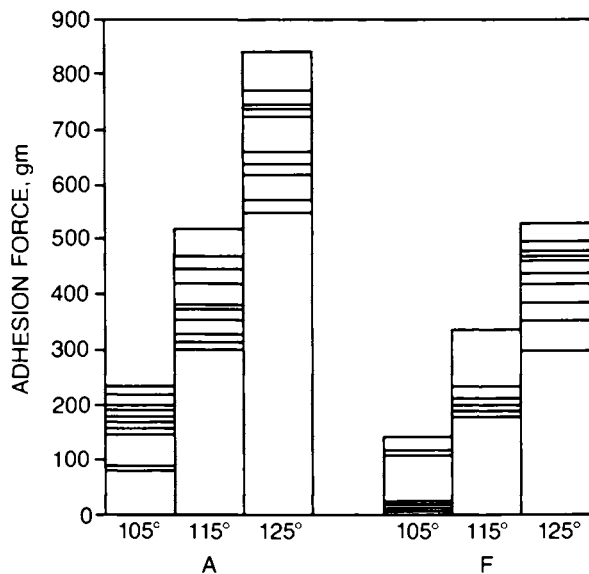


Figure 7. Adhesive strength comparison of "worst" and "best" paper brand in Figure 6 at different bonding temperatures. Ten measurements at each temperature for each brand.

Effect of Surface Energetics Data obtained using toner powder and a more complex laboratory fusing method (15) entirely corroborated the data obtained by Swanson and Becher for extrusion coated sheets (4)(Figure 8). Here, premeasured non-extruded toner powder was evenly distributed over a larger paper area to obtain a toner coverage that would simulate electrophotographic imaging more closely. The average adhesive strength at the highest sizing level was only half of that at the minimum sizing level. For all three samples, the surface energetics as measured by the Owens-Wendt procedure was in a range similar to that of the molten polystyrene based toner (16). The data shown in Figure 8 were obtained for papers sized with alkyl ketene dimer as described below. Normally, rosin and rosin-modified sized papers produced significantly higher adhesive strength levels (Table II). For rosin sized paper, as recently demonstrated by Farrow, Miller, and Walsh using ESCA technique (17), there is correlation between electrophotographic fuse grade and paper surface hydrocarbon content.

TABLE II. ADHESIVE STRENGTH OF PRINTING PAPERS TREATED WITH DIFFERENT SIZING AGENTS (from Borch, Reference 15)

<u>SOURCE</u>	<u>SIZE</u>	<u>ADHESIVE STRENGTH</u> (kPa)
A	ROSIN	40
B	ROSIN	31
C	MODIFIED ROSIN	29
D	ALKYL KETENE DIMER	13
E	ALKYL KETENE DIMER	24

How far this variability in toner adhesion on different papers is guided by surface energetics is not known at present. Both the degree of fiber wettability and the nature of toner-paper bonding should affect the adhesive strength. In a recent study of polyethylene bonding to different substrates Brewis and Briggs (18) came to the conclusion that several effects (wetting and forces due to both chemical interaction and intermolecular dispersion) determined bond strength. In a number of studies where complete wettability was claimed, maximum adhesive strength was obtained at equal surface energies of the two solid phases bonded together (7, 19, 20)(Figure 9). Here, surface energetics appear to be a useful bonding

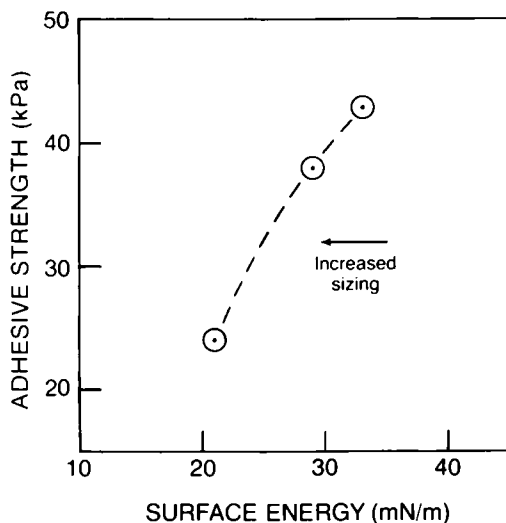


Figure 8. Toner adhesion of commercially made printing papers at different surface energy levels. (Reproduced, with permission, from Ref. 15. Copyright 1982, TAPPI.)

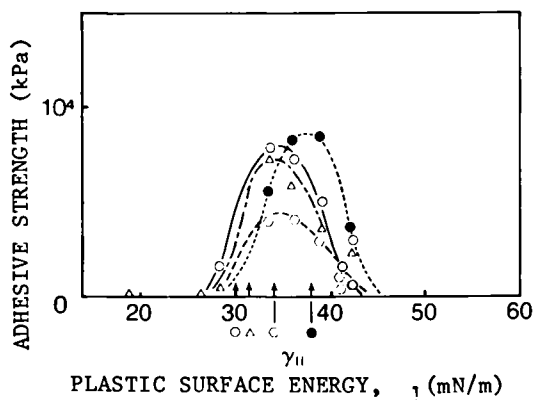


Figure 9. Adhesive strength of plastics bonded together by lacquers and resin. Maximum strength was obtained when the surface energy of the adhesive γ_{11} matched that of the plastic, γ_1 . (Reproduced, with permission, from Ref. 19. Copyright 1972.) Key: —○, PVC-PVA lacquer; ---●, polyurethane lacquer; ---△, alkyd resin lacquer; and ---○, alkyl phenol resin.

characteristic no matter what the details of the bonding process may be.

Electrophotographic Papermaking

Sizing Techniques Recently, the sizing of printing and writing papers has become more complex both with regard to chemistry and the techniques used in adding sizes. The traditional rosin-alum procedure has been challenged by several alternate methods using other chemicals developed due to cost saving incentives and a better understanding of the physical and chemical nature of the sizing process (21, 22, 23). For example, cellulose reactive sizes of the alkyl ketene dimer type react chemically with the cellulose fiber surface thereby creating increased liquid repellency at very low addition levels (22)(Figure 10). This sizing agent may be added either internally or at the size press. Unfortunately, the impact on electrophotographic fusing is substantial as shown in the previous section (Figure 8) where the adhesive strength was shown to decrease drastically at increased size level (15). It was found that a significant fraction of electrophotographic papers procured from non-domestic sources was alkaline made and synthetic sized. This would adversely affect the fuse grade of electrophotographic printers and copiers that rely on the available plain paper supply.

Fredholm and Westfelt (6) have shown that polyethylene to paper adhesion need not be compromised if action is taken to choose the proper substituents in the size chemical (Table III). Normally, commercially available dimers are supplied with straight chain alkyl substituents. Substitution by the phenyl or chlorophenyl group enhances the bonding ability of the fiber surfaces without appreciably affecting the sizing degree of the paper. Similar substitutions should benefit electrophotographic fusing.

TABLE III. POLYETHYLENE ADHESION OF SYNTHETIC SIZED PAPERS (from Fredholm and Westfelt, Reference 6)

<u>SIZING AGENT</u>	<u>PEELING WORK</u> (J/m ²)	<u>COBB VALUE</u> (g/m ²)
ALKYL	16	25
PHENYL	79	24
CHLOROPHENYL	92	25
NONE	101	120

Paper Friction In addition to the effect on toner fix, organic components in plain uncoated papers intended for electrophotography have other important characteristics that should be evaluated for proper machine performance. For example, chemical surface treatments tend to impact the friction characteristics. Synthetic sizes, when surface applied, may significantly decrease the overall paper-paper friction level (Figure 11), and the static friction peak or resistance towards initial movement is not developed (Figure 12).

Due to the adhesive nature of the friction process (24), it is to be expected that sizing treatments will influence friction levels through changes in surface energetics. Lee (25) has discussed the effect of surface energetics on polymer friction and also has presented correlation data between the friction coefficient and the surface tension of a number of polymers. Cherry (26) has reviewed the general role of surface energetics in processes involving polymer contact.

Alkaline Papermaking The present trend towards increased use of synthetic sizes is brought about by alkaline papermaking. Here, clay filler added to the paper furnish is substituted by calcium carbonate. In both cases the filler particles enhance the quality of the paper surface for conventional printing purposes, but the carbonate interferes less with fiber-fiber bonding thereby creating less sheet strength degradation. This allows the substitution of pulp fibers with associated savings in energy cost. Other benefits are: a more permanent and brighter paper, lower corrosion and cleaner operation of mill equipment, and increased production rate (27).

Though alkaline papers often are heavily filled (C in Table IV), physical sheet characteristics such as sheet porosity and felt/wire surface smoothness appear relatively unaffected (Columns 4 and 5 in Table IV). The sheet is perceived to be porous and uncoated though in fact the filler content on the felt side is appreciable (4.9 felt-to-wire weight ratio for 20.3% average ash for sample C) and is easily visible in the scanning electron microscope as shown in Figure 13). This pronounced "two-sidedness" is capable of generating significant difficulties in both handling and image characteristics when the paper is used for electrophotographic printing. For image fix, the added and usually overriding effect of the sizing treatment must be considered, and performance level is often best determined by trial printing.

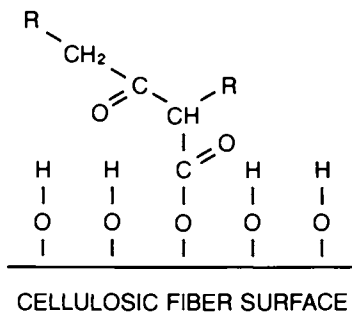


Figure 10. Alkyl ketene dimer size reaction product.

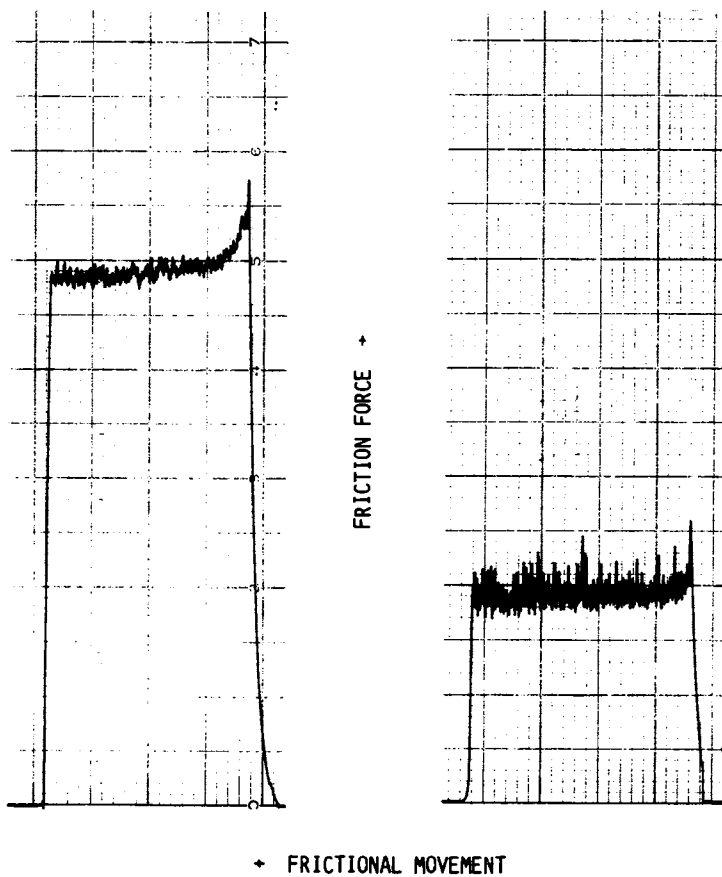


Figure 11. Examples of paper-paper friction traces for rosin sized (left) and synthetic sized (right).

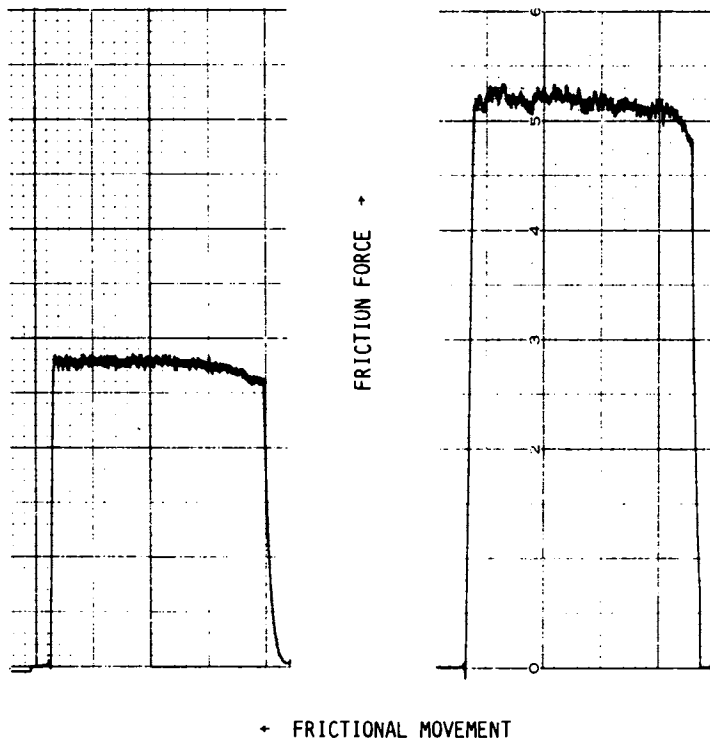


Figure 12. Paper-paper friction traces for synthetic sized sheets. Static friction peaks were not developed.

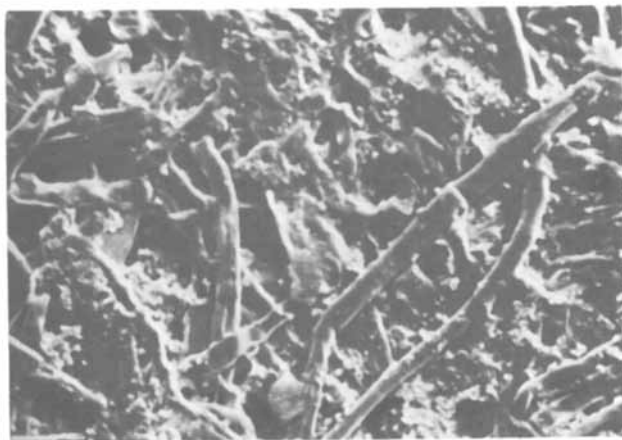


Figure 13. Felt side of carbonate filled paper (C in Table IV). Scanning electron micrograph (140 \times).

TABLE IV. EXAMPLES OF CARBONATE FILLED PAPER PROPERTIES

<u>SAMPLE</u>	<u>% FILLER</u>	<u>RATIO FELT TO WIRE*</u>	<u>SHEFFIELD SMOOTHNESS</u>	<u>SHEFFIELD POROSITY</u>
A	8.7	2.4	135/137	169
B	14.2	1.8	188/212	133
C	20.3	4.9	183/186	154

* obtained by SEM/EDAX count

Conclusions

Measurement of adhesive strength on laboratory fused papers showed variation due to paper grade. Chemical paper analysis and analogous studies of extrusion coated papers demonstrated that image fix in electrophotography is affected by paper chemistry and specifically by the sizing treatment. Wettability theory and experimental surface energetics measurements indicated that the fusing process is one where wetting and adhesion are being promoted at relatively high surface energy levels of the paper.

Synthetic paper sizing mainly associated with alkaline papermaking was found to severely affect electrophotographic fusing and influence other paper properties important to electrophotography (e.g. paper-paper friction). It is perceived that a greater variability in electrophotographic paper performance will be experienced due to future variability in papermaking procedures (alkaline vs. an acidic process).

Acknowledgments

The laboratory fusing method was developed on basis of procedures devised by L. Ho, IBM, Boulder. J. Witt and F. Rodgers, IBM, Tucson provided chemical paper analysis and fuse quality measurements.

Literature Cited

1. Brooms, K. D. IBM J. Res. Develop. 1978, 22 (1), 26.
2. Green, Jr., C. J. Tappi 1981, 64 (5), 79.
3. Lee, L. H. in Adhesion Science and Technology, Vol. 9B (Lee, L. H., Ed.); Plenum Press: N.Y., 1975; p 831.
4. Swanson, J. W.; Becher, J. J. Tappi 1966, 49, 198.

5. Glossman, N. Tappi 1967, 50 (5), 224.
6. Fredholm, B.; Westfelt, L. Svensk Papperstidn. 1979, 82 (7), 202.
7. Mittal, K. L. in Adhesion Science and Technology, Vol. 9A (Lee, L. H., Ed.); Plenum Press: N.Y., 1975; p 129.
8. Swanson, J. W. "Mechanisms of Paper Wetting, Dynamic Wettability"; Tappi 1981 Sizing Short Course; Chicago, 1981.
9. Zisman, W. A. Advan. Chem. Series No. 43; American Chemical Society: Washington, DC, 1964; chapter I.
10. Owens, D. K.; Wendt, R. C. J. Appl. Polymer Sci. 1969, 13, 1741.
11. Ray, B. R.; Anderson, J. R.; Scholz, J. J. J. Phys. Chem. 1958, 62, 1220.
12. Luner, P.; Sandell, M. J. Polymer Sci., Part C 1969, 28, 115.
13. Brown, P. F.; Swanson, J. W. Tappi 1971, 54 (12), 2012.
14. Dorris, G. M.; Gray, D. G. J. Coll. Interface Sci. 1979, 71 (1), 93.
15. Borch, J. Tappi, to be published.
16. Lau, W. W. Y.; Burns, C. M. J. Polymer Sci., Polymer Phys. 1974, 12, 431.
17. Farrow, M. M.; Miller, A. G.; Walsh, A. M. "ESCA Studies of the Surface Chemistry of Business Papers"; Colloids and Surfaces in Reprographic Technologies, ACS Symposium; N.Y., 1981.
18. Brewis, D. M.; Briggs, D. Polymer 1981, 22, 7.
19. Dyckerhoff, G. A.; Sell, P. J. Angew. Makromol. Chem. 1972, 21, 169.
20. Kitazaki, Y.; Hata, T. J. Adhesion 1972, 4, 123.
21. Davison, R. W. Tappi 1975, 58 (3), 48.
22. Strazdins, E. Tappi 1981, 64 (1), 31.
23. Dumas, D. H. Tappi 1981, 64 (1), 43.
24. Bayer, R. G.; Sirico, J. L. Wear 1971, 17, 269.
25. Lee, L. H. in Advances in Polymer Friction and Wear, Vol. 1 (Lee, L. H., Ed.); Plenum Press: N.Y., 1974.
26. Cherry, B. W. "Polymer Surfaces"; Cambridge University Press: Cambridge, 1981; chapter 6.
27. Dumas, D. H. "An Overview of Cellulose Reactive Sites"; Tappi 1981 Sizing Short Course; Chicago, 1981.

RECEIVED April 30, 1982

Electrical Conductivity of Paper: Measurement Methods and Charge Transport Mechanisms

JACK Y. JOSEFOWICZ

Arco Solar Industries, Limited Material Science Laboratory,
Calabasas, CA 91302

YVES DESLANDES

Xerox Research Centre of Canada, Mississauga, Ontario, Canada L5L-1J9

This paper describes some recently completed work on the electrical conductivity of paper. A reliable method of measuring bulk conductivity of paper, where the contact resistance is reduced to negligible values, has been developed. A study of the effect of some papermaking variables, such as the type of pulp, the degree of refining and the fiber orientation, on the bulk conductivity of paper is reported. Finally, an investigation has been made into the current transient phenomena exhibited by paper upon the application of an electric field. These transient currents were interpreted as the transport of ionic species within a water associated fibrous network making up the paper.

During recent years a host of new marking technologies have been developed which have put more stringent requirements on the properties of paper. Reprographic technologies utilize the electrical properties of paper in the process of producing an image. Electrical processes which take place both prior and during image formation include^(1,2): transport of ions through the water-containing fibrous network of the paper, charge exchange between the paper surface and a metallic backing electrode, charge exchange between toner or charged pigmented particles and the paper surface, as well as other electrical processes involving chemical reactions. These reactions depend on specific additives which are used in paper to modify physical and optical properties. Therefore the electrical characteristics of a specific paper are very important and in most cases directly account for the speed and image quality of a reprographic process. Producing paper which combines optimal physical, optical and electrical properties has proven to be a most difficult task. This is primarily due to the extremely complex structure of paper, which is composed of a random assembly of cellulosic fibers and chemical additives. A description of paper structure is given in the next section.

0097-6156/82/0200-0493\$10.50/0

© 1982 American Chemical Society

Interest in the study of the electrical properties of paper is certainly not new. More than half a century ago, Kujirai and Akahari⁽³⁾ showed that the resistance, through a paper sheet, falls with increasing humidity. They, along with other investigators^(4,5,6,7,8) found that the logarithm of the resistance is essentially a linear function of the relative humidity in the measuring environment. Furthermore, it was established that charge transport within paper is due primarily to ion migration.

In recent years, emerging reprographic technologies are forcing more attention to the understanding of charge transport phenomena in paper. An understanding of charge transport phenomena is very important to the continuing advancement of reprographics since there is an increasing emphasis being placed on high speed imaging. Studies of charge transport must first ensure that the experimental methods and test fixtures are available to provide reliable and reproducible data from which conclusions regarding the role of the paper may be drawn.

In this chapter, the authors describe some recently completed work on the electrical properties of paper. Emphasis has been placed on two main areas. The first is the development of methods and tools with which conductivity measurements can be made readily. The second is the correlation of structure and chemical content with conductivity measurements on a variety of different types of paper. The paper samples which we have studied include those produced in our laboratory as well as those obtained from commercial sources. As pointed out earlier, paper is an extremely complex system from an electrical standpoint and therefore, it is a great advantage, in the interpretation of experimental results, to have a knowledge of the precise manner by which a paper is produced.

Paper Structure and Chemistry

Paper can be generally described as a felted sheet of fibers formed by introducing a water suspension of fibers onto a fine screen. The water drains through the screen leaving behind a wet sheet of paper which is removed and dried. Additives can be introduced into the sheet which contribute desired properties to paper⁽⁹⁾. According to this definition, the final properties of a sheet of paper can be significantly affected by the following three factors: the nature of the fibers, the conditions by which the sheet is produced and the type and quantity of non-fibrous chemical additives. Although a detailed description of the structural characteristics of paper is not the intent of this work, it seems appropriate to briefly discuss these three variables in the following paragraphs because of their potential influence on electrical properties of paper. For a more complete description of paper structure and chemistry, the reader is referred to Brett⁽¹⁰⁾, and Casey⁽¹¹⁾.

Fibers. The morphology of a wood fiber is represented schematically in Figure 1. It consists of several layers of cell walls which contain aggregates of cellulosic chains called microfibrils which are embedded in a polymeric matrix composed of amorphous hemicelluloses, i.e. all types of polysaccharides other than cellulose, and of lignins⁽¹¹⁾ which are phenolic compounds acting as a glue between the wood components. The primary wall (PW) of the cell contains randomly organized cellulose

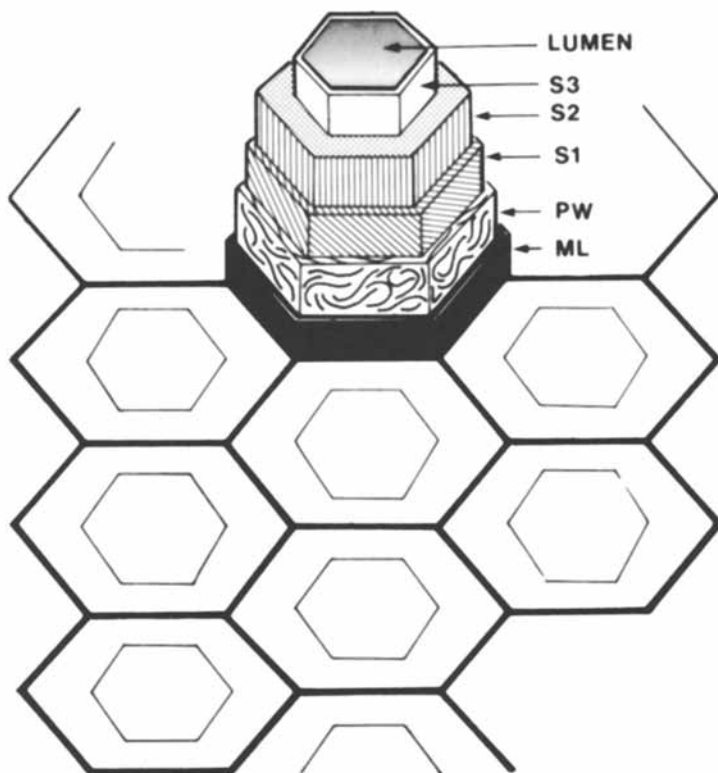


Figure 1. Schematic of a wood cell within a piece of wood.

microfibrils, embedded in a matrix of other polysaccharides. The secondary wall is divided into three layers: S_1 is the outer layer and contains a cross-hatch pattern of microfibrils, S_2 contains microfibrils oriented almost parallel to the fiber axis and S_3 surrounds the lumen which contains organic debris of the dead cell nuclei. S_2 is the thicker layer of the wood cell wall and accounts for the major part of the volume.

An important characteristic of these wood cells is the heterogeneous distribution of cellulose, hemicelluloses and lignins over the cell walls. For example, lignins are located mainly in the middle lamellae (ML) and glue the individual fibers together. A smaller quantity is also distributed throughout the secondary wall with a higher concentration in the S_3 layer.

Major differences are encountered between the fibers of the two main classes of wood, i.e. the gymnospermes (softwoods) and the angiospermes (hardwoods). The softwood fibers are usually longer than the hardwood fibers (see Figure 2) and although their composition in cellulose and lignin is approximately the same, the nature of their hemicellulose are different. Xylans are encountered in relatively high quantity in hardwoods, whereas glucomannans are the major hemicelluloses found in softwoods. It should also be mentioned that wood fibers are also characterized by a variability in structure encountered between species of the same class, different trees of a same species and even in different locations within the same tree.

In a wood fiber, the cellulose portion of the microfibrils is the only major component found in a crystalline state. A cellulose microfibril is a long thread-like aggregate of cellulose chains of about 200 Å wide and a few microns long. These constitute the basic elements of the fibers and are responsible for its rigidity. The cellulose microfibrils, however, are not totally crystalline but rather contain amorphous regions which are accessible to water molecules. Water does not penetrate the crystalline region. The total water content of a whole fiber and its distribution within the fiber is a function of: the relative amount of amorphous material, the presence of lignins, which are hydrophobic, and the presence of hemicelluloses which are hydrophilic. The total water content of a whole fiber will affect the conductivity by allowing an increased effective ionic mobility.

Papermaking Process. A wood fiber is subject to two treatments prior to the making of the sheet; these are pulping and bleaching. Pulping consists of separating the large aggregates of fibers into individual fibers. This can be achieved by mechanical or chemical treatments or by a combination of these. The bleaching treatment is usually performed using chlorine in order to remove the colored materials. These two processes remove a significant quantity of the lignins surrounding the individual fibers and also dissolve part of the accessible hemicelluloses.

At this point the fibers could be processed into a sheet of paper, but they are normally treated further in order to increase the mechanical properties of the sheet. Refining or "beating", consists of a mechanical treatment carried out in presence of

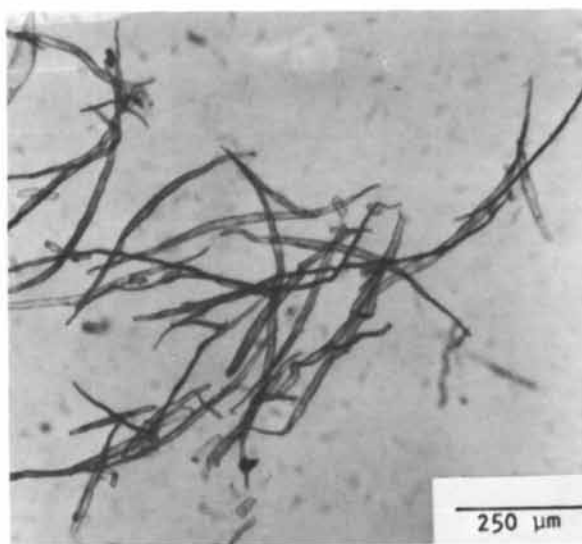
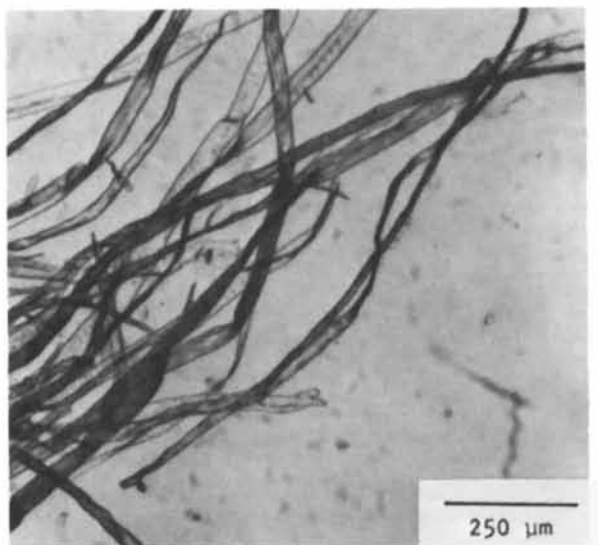


Figure 2. Photomicrographs of wood fibers of softwood pulp (top) and hardwood pulp (bottom).

water and involves passing the suspension of pulp fibers through a relatively narrow gap between a revolving rotor and a stationary stator. This treatment results in a fibrillation and a slitting of the fibers. Consequently the surface available for bonding increases and the rigidity of the fibers decreases. The fibers are then dispersed in water and the suspension is deposited on a moving screen. The newly formed sheet is then drained, pressed, dried, cut and packaged.

As water is removed during the formation process, surface tension creates a large force which compacts and draws the fibers together into more intimate contact. Hydrogen bond formation occurs between the hydroxyl groups of the cellulose chains of the fibers. These bonds are responsible for the internal strength of the paper. Other processing that occurs during the latter part of the papermaking process includes pressing and calendering the sheet and addition of sizing agents. These steps are performed to improve the physical or optical properties of paper and also affect the degree of the interfiber bonding.

An important consequence of the dynamic conditions used in the papermaking process is the introduction into the paper sheet of a three dimensional anisotropy. During the papermaking process as the fibers are much longer than the paper thickness, they undergo an in-plane orientation. Furthermore, the dynamic conditions cause the fibers to orient themselves, not only in the plane of the sheet, but also in the direction of the moving wire. This direction is called the Machine Direction (MD) and the direction perpendicular to it is the Cross-Direction (CD). Paper anisotropy is one of its more important characteristics, since it influences all its mechanical properties. A schematic illustration of the distribution of the fibers in a paper sheet is shown in Fig. 3. In this article, it will be demonstrated that, the anisotropy also influences the electrical conductivity of the paper.

Additives. There are many types of additives used by the papermaker to modify the physical and optical properties of the sheet. The most commonly used include kaolin and titanium dioxide for optical properties, starch for strength and rosin sizes for water repellency. All these materials can affect the electrical properties of the paper since they can eventually modify the nature of the interfiber contact as well as the fiber itself. These changes can influence the flow of charge through the sheet.

Additives can also be used to impart higher electrical conductivity to the sheet;⁽¹²⁾ for example, because of its ionic nature, NaCl is one effective additive. Recently, cationic polymers have replaced inorganic materials for the purpose of imparting higher conductivity to paper. These polymers have the advantage of stabilizing the conductivity over a wide range of relative humidity. These polymers are not conductive themselves, but rather are effective by keeping a higher water content inside the paper structure, hence increasing the mobility of the ions which are responsible for the electrical conductivity.

The Preparation of Paper

The method and ingredients used in preparing a paper are of critical importance to any study where structure, chemistry and



Figure 3. Cross-section microscope picture of a paper sheet showing the preferential orientation of the fibers. (Reproduced, with permission, from Ref. 17. Copyright 1981, American Institute of Physics.)

properties are being correlated. Commercial papers are usually processed using a Fourdrinier machine⁽¹⁰⁾ under conditions that cannot be reproduced in the laboratory. Therefore, in our study the two procedures listed below were used for the preparation of paper samples. These procedures allow for some control of the variables such as structure and chemistry during the paper forming process.

British Handsheet Machine. Preparation of samples using this method involves filtering a fibre suspension through a fine screen. The newly formed sheet is then pressed and dried. The disadvantage of this method is the lack of preferential orientation of the fibers in the sheet. Except for this drawback sheets can be prepared with well defined characteristics and are suitable for any study in which the preferential orientation of the fibers is not important.

Five different pulps were used in the preparation of paper sheets using the British Handsheet Machine. They are listed below:

- i) Q-90: Made by Domtar , Canada, from black spruce using the Kraft pulping process. The pulp is highly bleached, to over 90 brightness, and is used mainly in fine papers.
- ii) Q-30E: Made as above, from black spruce, but left unbleached. The pulp is specially washed to give a high resistivity for use in electrical grade papers.
- iii) Q-30C: Made as Q-30E except for the special washing. This pulp is used in regular commercial papers such as bag stock.
- iv) Seagull W: Made by Domtar, Canada from mixed hardwoods using the Kraft process. Pulp is highly bleached and is used mainly in fine papers.
- v) 503: Made by Buckeye Corporation from cotton linters. Has a brightness of over 90 and is used in many high quality rag papers.

80 g/m² handsheets made from pulps refined to different levels were made according to CPPA Standard C-4, using distilled water in the handsheet machine.

For studies relating to transient electrical conduction in paper, the following procedure was used to prepare the paper samples. Handsheets were prepared in a British Standard Handsheet Machine using softwood Kraft pulp, refined to 450 Canadian Standard Freeness, and at a basis weight of 80 g/m². Once dried, a section of that sheet was soaked in a 0.5 % NaCl solution, pressed and weighed. The concentration of NaCl in the dry sheet was 0.2% by weight calculated knowing the amount of the 0.5% solution retained in the sheet prior to drying. A third sample is a conductive sheet produced by the James River Paper

Co. It consists of a sheet of paper coated with an electroconductive resin.

Centrifugal Former. The use of a centrifugal former allows for the preparation of a sheet of paper that possesses a fiber orientation similar to the orientation present in commercial papers. With this apparatus, the fiber suspension is sprayed onto a fast rotating screen. The dynamic motion of the screen mimics the moving wire of the Fourdrinier machine and induces fiber orientation. In addition, by independently varying the flow of the fiber suspension and the speed of rotation of the screen, different degrees of fiber orientation can be obtained.

Paper samples were prepared, with basis weights of 60, 115 and 190 g/m², all with a 1:1 ratio by weight of softwood to hardwood pulp, in a centrifugal dynamic vertical sheet former (Allimand 38140 Rives, France). Each of the different basis weight samples was calendered at three different calendering levels of 250, 500 and 750 kN/m respectively. These paper samples were used in a study aimed at determining the influence of the surface morphology on measured electrical conductivity.

Electrical Conductivity: Methods and Experimental Techniques

Reproducible and accurate measurements of electrical conductivity of paper are of great importance in a number of technologies. Two commonly measured electrical parameters of paper are its surface and bulk conductivity. A method for measuring surface conductivity has been reported by Greisner⁽¹³⁾, and his recommendations were incorporated in D.C. surface conductivity measurements reported by Howlett and Landheer⁽¹⁴⁾. Bulk electrical conductivity has always been controversial for paper since the contact resistance at the paper-electrode interface can be much higher than the resistance of the paper itself. This neglect of contact resistance has produced many erroneous reports of bulk conductivity of paper.

In the following section, a new bulk conductivity cell is described that significantly reduces the contact resistance to a level where the measurements of paper bulk conductivity can be made with an accuracy that is limited primarily by the anisotropic structure of the paper itself. A small uncertainty in the measured conductivity arises from compaction (~10%) of the paper sample in the apparatus caused by the application of 13.8 MPa pressure to the stainless steel electrode system in the cell. This pressure is used to eliminate contact resistance. Despite this uncertainty, measurement errors in the new cell are significantly less than the spread in the conductivity values (~200%) determined at different points in a single paper sheet. The variability arises from inhomogeneities in the cellulose fiber network within the sheet.

To measure the surface resistivity of paper, a variant of a four-point probe method proposed by Cronch⁽¹⁵⁾ was used. This approach has proven to be reliable, avoiding the effects of contact resistance by employing an electrostatic voltmeter (utilizing contactless probes) to measure the surface potential of paper subject to a constant current.

As discussed above, processing the fibers introduces an anisotropy in the sheet even if one uses only pure cellulosic

fibers. The elementary fibers (15-50 μ m wide and 1-7 mm long)⁽¹⁰⁾ tend to orient themselves parallel to the XY plane. Moreover, during the formation of the paper sheet the fibers will also orient along the "machine direction" corresponding to the direction of the moving wire screen. Most commercial papers are anisotropic.

The orientation of cellulosic fibers has some effect on the conductivity of the paper. The conductivity in the XY plane of the sheet (surface conductivity parallel to most of the fibers) may be quite different from the conductivity along the Z direction (bulk conductivity perpendicular to the fibers). Comparison of surface and bulk conductivity for a given paper sheet can thus yield information which reflects the anisotropy in the structural morphology due to fiber orientation. Bulk conductivity measurements are also important since many paper sheets used in reprographic processes are composed of a conductive base sheet coated with a dielectric material⁽¹⁶⁾. One important specification for these types of papers is the value of the bulk conductivity of the base paper.

In-Situ Pressure Bulk Conductivity Cell. A cell specifically designed to measure the bulk conductivity of paper was recently described⁽¹⁷⁾. A cross-section view of the bulk conductivity cell is shown in Fig. 4. This cell was designed with the objective of simultaneously applying pressure to a set of optically polished stainless steel electrodes which are subject to an applied voltage. The current through the sample is measured allowing the bulk conductivity to be determined. A schematic diagram of the measuring circuit is shown in Fig. 5. The presence of the grounded guard ring electrode serves to eliminate the contribution of any surface current to the bulk conductivity measurement. A step function D.C. voltage, positive or negative, is applied (using a Fluke high voltage power supply) to the bottom electrode of the conductivity cell by way of a high voltage switch. The current passing through the paper sample is detected by a Keithley electrometer (Model 610CR). A record of the current transient may be obtained using a strip chart recorder. The bulk resistivity is determined using the relationship:

$$\rho_B = \frac{V \cdot A}{i \cdot t} \quad (1)$$

where

- V = the applied voltage
- A = cross-sectional area of the measuring electrode
- i = current flowing through the sample
- t = thickness of the sample measured after the

experiment.

As the electrical properties of paper are extremely sensitive to relative humidity, all measurements described in this article were performed in an environmental chamber where relative humidity and temperature could be controlled to within 1% and 0.5°C, respectively.

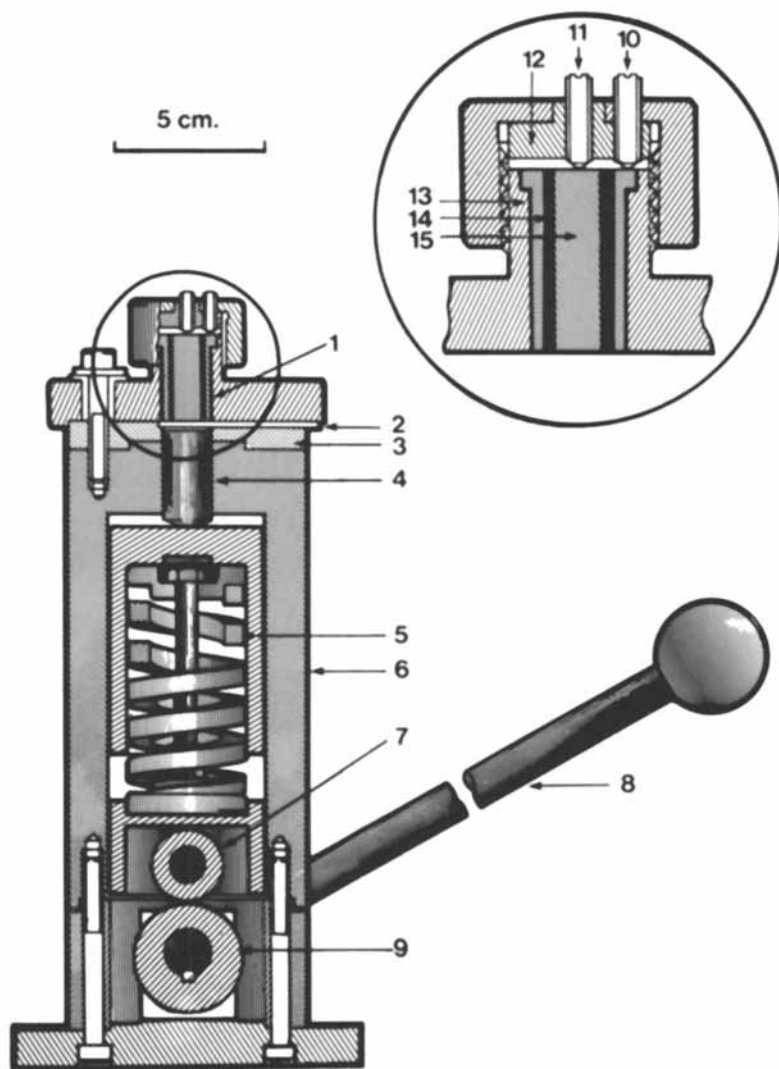


Figure 4. A cross-sectional view of the *in situ* pressure bulk conductivity cell.

Key: 1, guard ring optically polished stainless steel electrode; 2, slot in the Delrin gasket; 3, Delrin insulating gasket; 4, bottom optically polished stainless steel electrode; 5, pressurized coil spring module; 6, aluminum cell housing; 7, roller bearing; 8, lever arm; 9, rotating asymmetric cam; 10, ball bearing contact for guard ring electrode; 11, ball bearing contact for measuring electrode; 12, Delrin block; 13, guard ring portion of top electrode; 14, Delrin insulating collar; and 15, measuring portion of top electrode. (Reproduced, with permission, from Ref. 17. Copyright 1981, American Institute of Physics.)

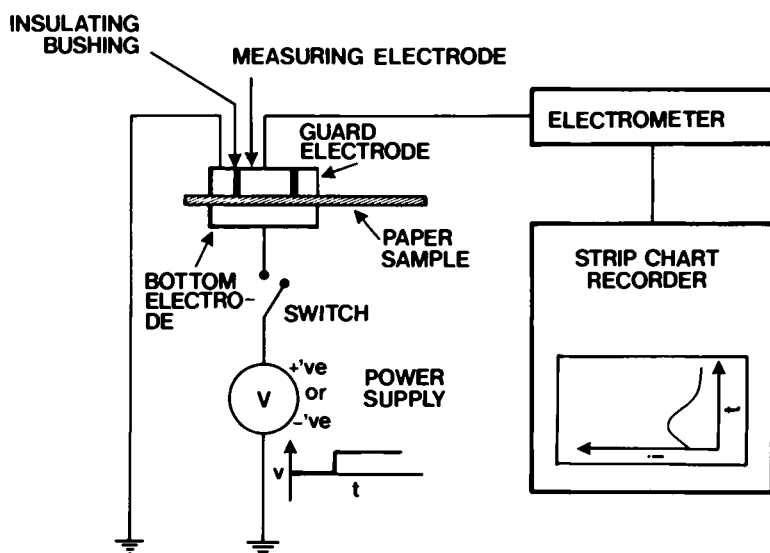


Figure 5. Schematic of the measuring circuit showing the guard ring stainless steel electrodes.

Two important requirements must be met by a technique designed to provide accurate measurements of the bulk conductivity of paper. First, the contact resistance between the electrode and the paper should be either known or negligible and, secondly, the paper should not be significantly modified by the technique used. The *in situ* pressure bulk conductivity cell satisfies these requirements, as will be shown in the following sections.

Surface Resistivity Experimental Set-Up. The surface resistivity was determined using a modified version of the standard 4-point probe method applied by Cronch⁽¹⁵⁾. A diagrammatic representation of the apparatus used for this measurement is shown in Fig. 6. A D.C. voltage is applied, using a constant current power supply (Hewlett Packard 6209B), to a 8 cm long by 5 cm wide paper sample. The voltage drop across a section of the paper strip, between the end electrodes, is determined using contactless electrostatic voltmeter (TREK, model 360). The voltmeter probes are mounted on a micrometer stage to facilitate precise positioning of the probes along the paper strip. Current flowing through the paper strip is measured using an electrometer (Keithley, 610CR). Surface resistivity is determined using the following expression:

$$\rho_s = \frac{\Delta V \cdot W}{i \cdot \Delta X} \quad (2)$$

where

- ΔV = difference in voltage measured by the two electrostatic voltmeter probes
 ΔX = distance between the electrostatic voltmeter probes
 W = width of the paper strip
 i = current flowing through the length of the paper strip.

Surface resistivity, ρ_s , and surface conductivity, σ_B , are related in the following way:

$$\rho_s = \frac{1}{\sigma_B} \quad (3)$$

In the same way bulk resistivity ρ_B , and bulk conductivity, σ_B , have the relation:

$$\rho_B = \frac{1}{\sigma_B} \quad (4)$$

Surface and bulk resistivities may also be related using the following expression:

$$\rho_B = \rho_s t \quad (5)$$

In applying eqn. 5 to paper, it should be pointed out that the thickness, t , does not necessarily represent the current-carrying region. The current may be restricted to localized regions through the thickness of the paper as a result of the fibrous or porous structure. Consequently, the relationship given in eqn. 5 should be considered only as an approximation when applied to paper.

Results and Discussion

In the section which follows, studies are described which focus on both, the development of reliable methods to evaluate the electrical properties of papers and the dependence of electrical properties on the specific structural and chemical properties of the paper. These properties include the type of pulp, the type and degree of refining, the degree of orientation of the fibers, the thickness of the paper and its degree of homogeneity, as well as the types of chemical additives. All of the above items have been found to influence the electrical properties of paper.

Steady State Electrical Measurements.

i) **Liquid Metal Electrodes:** In order to measure the bulk conductivity of paper by D.C. methods, the contact resistance must be eliminated as four-point probe methods are not practical. An investigation into the use of evaporated metal electrodes on both sides of a paper sample showed that this approach was unreliable. It was concluded that evaporated metal penetrates into the bulk of the paper. Recently, one of the authors reported⁽¹⁶⁾ that Ga-In liquid metal electrodes painted onto both sides of paper reduces the contact resistance to a negligibly small value. Another liquid metal, mercury, was found to be unsuitable because of its poor paper wetting properties. The Ga-In alloy, however, was found to be ideal. A cross-section electron micrograph of a sample painted with Ga-In showed that the eutectic alloy wetted the paper surface without penetrating into the cellulose structure. Use of Ga-In is somewhat untidy and time consuming but it has the advantage that paper samples with Ga-In electrodes can be placed in any cell with suitably flat electrodes, since only low electrode pressures are required to make good electrical contact.

Another method which the authors have developed uses the *in situ* pressure bulk conductivity cell⁽¹⁷⁾ described in this article. A direct comparison between these two approaches is given in the following sections.

All measurements reported in the next section were made using samples of conducting base paper obtained from the James River Paper Co. They were performed in an environmental chamber whose relative humidity and temperature were controlled to 50.5% and 73°F (~23°C), respectively. Paper samples equilibrated overnight in the chamber before use.

ii) ***In Situ* Pressure Bulk Conductivity:** Investigations were made to determine the applicability of the *in situ* pressure conductivity method to both conductive and non-conductive papers. The initial study described below was made using James River conductive base paper as used in dielectric papers. Figure 7 shows a plot of current vs time for one sample following application of a potential of 10V and a pressure of 2000 psi

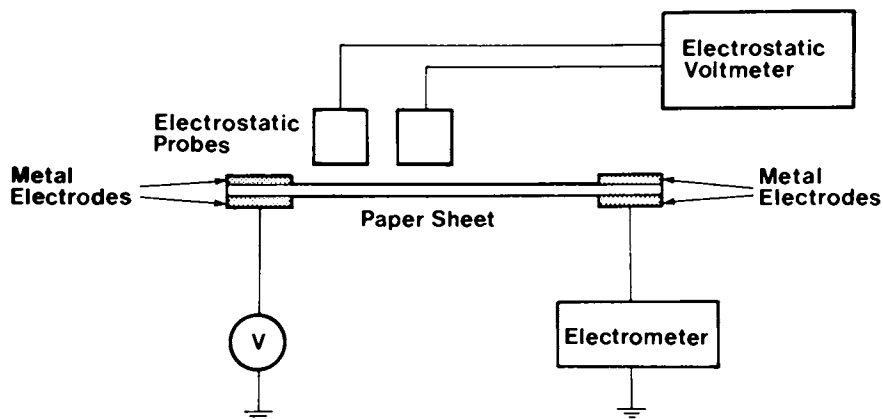


Figure 6. Schematic showing the experimental setup for the determination of the surface resistivity of paper.

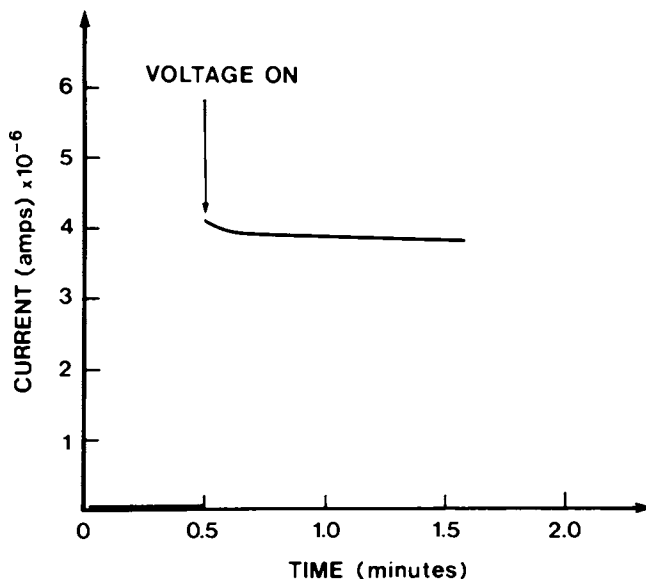


Figure 7. A transient current plot for James River conductive base paper using an applied voltage of 10V and a pressure of 2000 psi (13.8 MPa) at 50% RH. (Reproduced, with permission, from Ref. 16. Copyright 1981, TAPPI.)

(13.8 MPa). The current was relatively constant, this was typical for the results reported in this section. Conductivities were calculated from the current measured 12 seconds after the application of the voltage.

Shown in Figure 8 is a plot of conductivity as a function of the pressure applied to the paper samples. In the low-pressure range, up to approximately 5000 psi (34.5 MPa), the paper conductivity appears to increase linearly. Above 5000 psi (34.5 MPa), there is a distinct increase in the bulk conductivity, followed by another linear region which has a much steeper slope than the dependence found in the low-pressure region. A precise measurement of the paper thickness as a function of pressure⁽¹⁶⁾ showed that the paper sample starts with a thickness of 70 μm prior to the application of pressure and then decreases in thickness to 50 μm at 15,000 psi (103 MPa) in an essentially linear manner. The change in conductivity shown in Fig. 8 is most probably associated with the compression of the cellulose fiber network in the paper.

For the purpose of making relative measurements of the bulk conductivity in paper, a pressure of 2000 psi (13.8 MPa) was chosen. At that pressure, most paper samples typically compress 5 μm , from 70 μm to 65 μm ⁽¹⁶⁾. As can be concluded from the discussion below, the results of measurements at 2000 psi (13.8 MPa) are in good agreement with the Ga-In liquid alloy method. Samples were contacted on both sides with Ga-In over an area of 0.8 cm^2 and were placed in the pressure conductivity cell. A nominal pressure of 3.2 psi (22 kPa) was applied to the electrodes.

Figure 9 compares the two methods for making bulk conductivity measurements on conductive base paper: the pressurized stainless steel electrode method and the Ga-In eutectic liquid metal method. The conductivity is plotted as a function of voltage at 50% RH. For the stainless steel electrodes, at 2000 psi (13.8 MPa), the measured current is a superlinear function of voltage and a strong function of time⁽¹⁶⁾, up to a voltage of approximately 10V. With the Ga-In electrodes this effect is noticeable only for applied potentials up to approximately 3V. Between 10 and 50V, the bulk conductivity measured by both methods is essentially independent of voltage, and the current traces are reproducible and show no time dependence.

Measurements taken at 39% RH were similar to those shown at 50%, except for the expected lower values for bulk conductivity.

In the study described above, strong evidence was shown that for the case of James River conductive base paper, a pressure of 13.8 MPa applied to stainless steel electrodes was sufficient to effectively reduce contact resistance to negligibly small proportions. In the study described below the question as to whether the *in situ* pressure conductivity method would also be appropriate for different types of nonconductive papers which exhibit varied surface morphology is addressed. Consequently, paper samples were prepared, with basis weights of 60, 115, and 190 g/m^2 , all with a 1:1 ratio by weight of softwood-hardwood pulp, in a centrifugal dynamic vertical sheet former. Each of

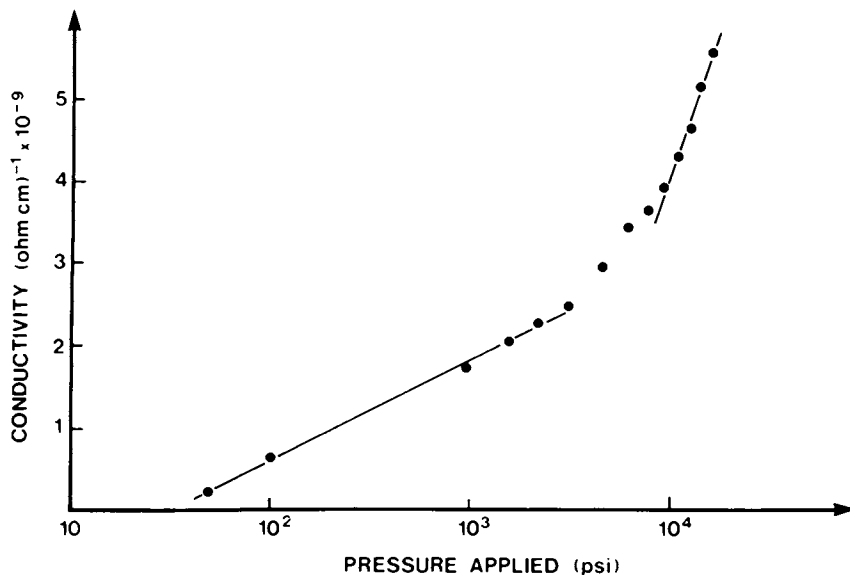


Figure 8. Bulk conductivity as a function of applied pressure for James River conductive paper, using 10V applied to the electrodes at 50% RH. (Reproduced, with permission, from Ref. 16. Copyright 1981, TAPPI.)

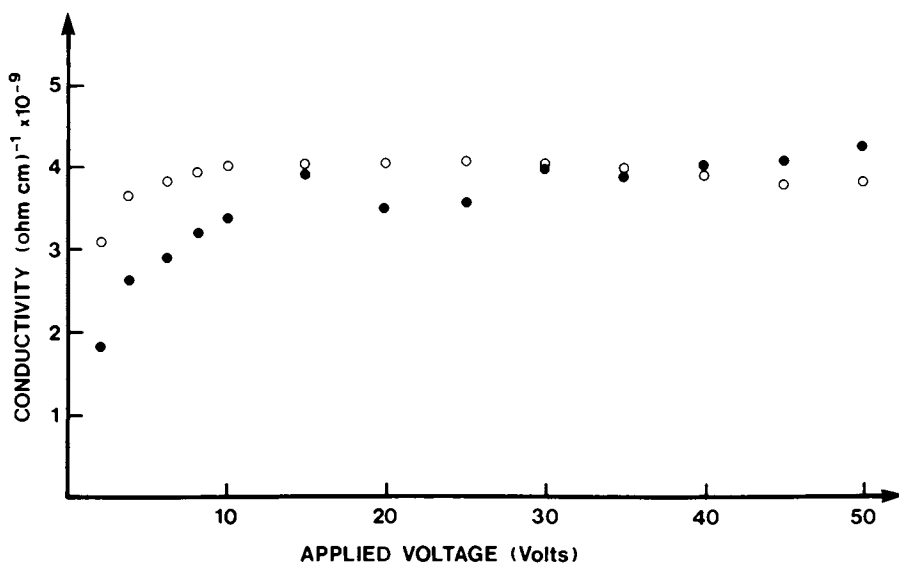


Figure 9. Bulk conductivity as a function of applied voltage for James River Paper using an electrode pressure of 2000 psi (13.8 MPa) at 50% RH. Key: ●, stainless steel electrodes; and ○, Ga-In liquid electrodes. (Reproduced, with permission, from Ref. 16. Copyright 1981, TAPPI.)

the different basis weight samples was calendered at three different levels: 250, 500 and 750 kN/m, respectively.

The bulk conductivity of these sheets was measured using the *in situ* pressure cell. Five measurements were obtained from different areas on each sheet and wide variations were observed for a given sheet as illustrated in Figs. 10, 11, and 12, corresponding to samples with basis weights of 60, 115, and 190 g/m², respectively. All the values obtained are reported for the twelve different sheets. Almost no difference in conductivity is observed for a given basis weight having different surface smoothness. The values for the uncalendered sample A in Fig. 10 are lower, but no explanation can be given for this result. The calendering treatment and consequently the surface smoothness does not seem to affect the conductivity of a given paper, when using an applied pressure of 13.8 MPa.

Surface profiles of both sides of a calendered and an uncalendered sheet were recorded with a Talysurf 5 instrument (Rank Taylor Hobson, England), and are reported in Fig. 13. The surface is different in each case, but the bulk conductivity is not significantly altered. The pressure applied to the electrodes within the cell has not changed the surface profile of the sheet for the calendered sample. Although a difference is observed for the uncalendered sample, the surface is not as smooth as that of the calendered sheet after pressure is applied.

From all these observations it is concluded that the contact resistance is not a function of the surface roughness when an applied pressure of 13.8 MPa is used. This indicates the possibility that the air gaps between the fibers and the electrode are contributing to the electrode surface area as a result of an electrical breakdown phenomenon. This hypothesis would lead to a very low contact resistance since almost all the electrode area would be effective whether the current is carried directly from the electrode to the paper fibers or through a conductive air gap.

A study, similar to that described above, was made to compare the results of using optically polished stainless steel electrodes under pressure with Gallium-Indium eutectic liquid electrodes in determining bulk conductivity of papers. The Ga-In alloy is believed to make intimate contact with the surface of the paper, thus significantly reducing the contact resistance. In Fig. 9, it was shown that optically polished stainless steel electrodes at 13.8 MPa pressure gave the same results that the Ga-In alloy when electric fields between 1.4×10^3 and 10^4 V/cm are used.

Similar experiments were performed to compare the determined conductivity for paper samples with different surface morphology. The conductivity measured with both types of electrodes were comparable. Also shown in Figs. 10, 11 and 12 are the conductivity values obtained with both the Ga-In electrodes as well as the stainless steel electrodes. The values for the Ga-In electrodes are slightly higher than those obtained with the stainless steel electrodes. The spread in the conductivity values for a given paper sample is also illustrated in sample C of each basis weight. Two important conclusions may be drawn from these results. Firstly, the spread in the values of the

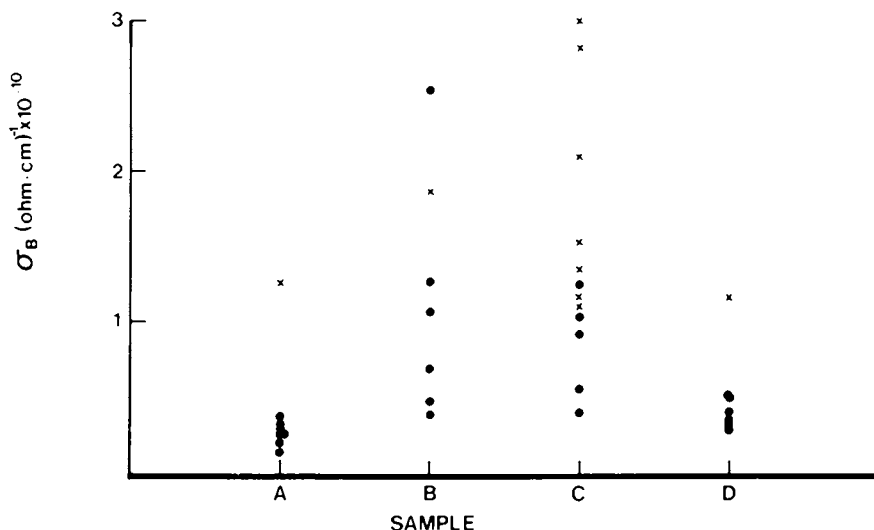


Figure 10. Conductivity values obtained for a sheet of paper with a basis weight of 60 g/m². For every weight four different calenderings were examined. Key: A, not calendered; B, 250 kN/m; C, 500 kN/m; D, 750 kN/m; ●, stainless steel electrodes. X, liquid Ga-In electrodes. Measurements were made at 50% relative humidity and 23°C. (Reproduced, with permission, from Ref. 17. Copyright 1981, American Institute of Physics.)

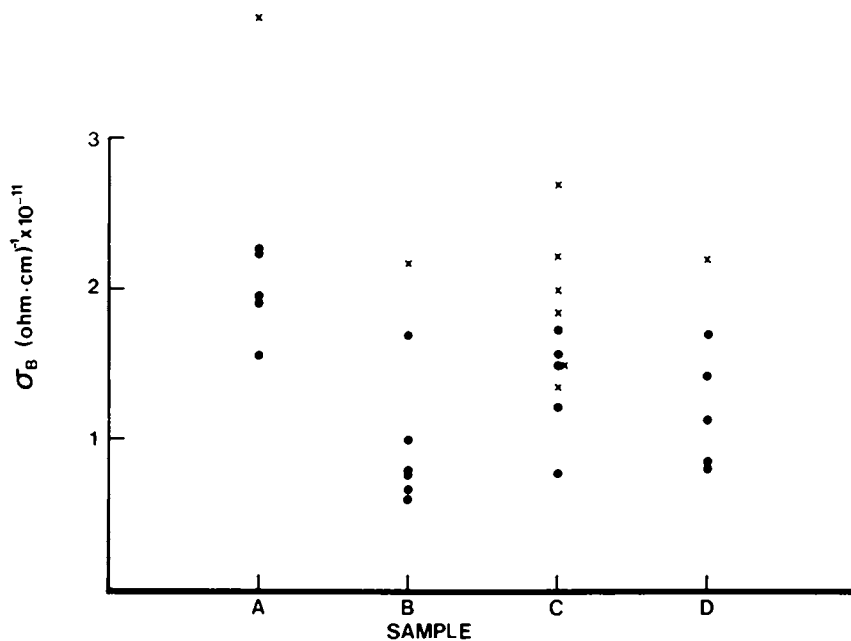


Figure 11. Same as Figure 10, but for paper with a basis weight of 115 g/m². (Reproduced, with permission, from Ref. 17. Copyright 1981, American Institute of Physics.)

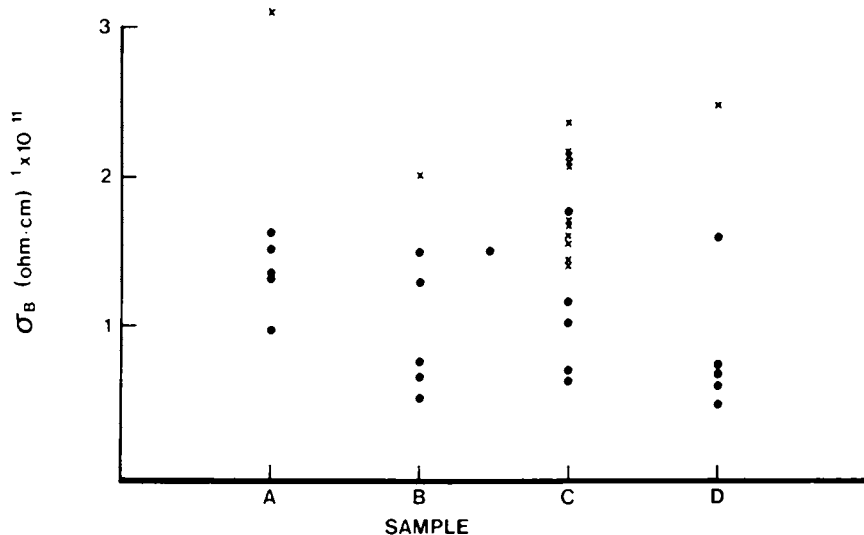


Figure 12. Same as Figure 10, but for paper with a basis weight of 190 g/m². (Reproduced, with permission, from Ref. 16. Copyright 1981, American Institute of Physics.)

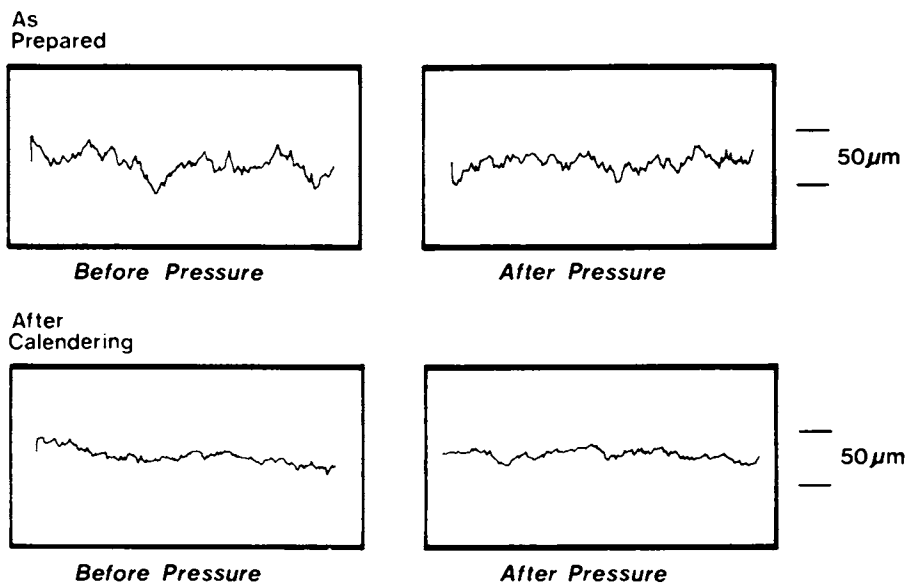


Figure 13. Surface profiles for a paper sheet with and without calendaring, and before and after pressure. (Reproduced, with permission, from Ref. 16. Copyright 1981, American Institute of Physics.)

conductivity as determined by both electrode systems is effectively the same. Extreme care was taken to ensure that all paper samples were handled in the same way. Consequently, we conclude that the spread in conductivity values for a given paper is due to the anisotropy associated with the cellulosic fiber network and that the contact resistance for all of these paper samples is essentially the same. A similar spread in the bulk conductivity was also measured for several different commercial nonconductive papers. Secondly, we conclude that the slightly higher conductivity values obtained with the Ga-In electrodes the liquid metal conforms to the surface morphology of the paper. Since the Ga-In fills all the indentations and crevasses associated with the cellulose fiber network at the paper surface, the effective electrode area is larger than the area which is defined by the optically polished surface of the stainless steel electrode. For this reason, the determined bulk conductivity is expected to be higher, in the case of Ga-In, by a factor which is proportional to the difference in the effective areas between the liquid metal and stainless steel electrodes.

iii) Bulk Conductivity of Papers With Different Thickness: One study which clearly determines the value of the contact resistance at the electrode-paper interface is based on the determination of bulk conductivity for a series of similar paper samples that have different thicknesses. Paper sheets were made from the same furnish, prepared under the same conditions, but having a different basis weight or thickness. Such paper samples should have the same contact resistance R_C ; the bulk resistance R_B would however be proportional to the paper sample thickness. The bulk and contact resistance are in series during an electrical measurement. Consequently, the total resistance, R , measured for a paper sample between a pair of electrodes is

$$\begin{aligned} R &= 2R_C + R_B \\ &= 2R_C + \frac{\rho_B t}{A} \end{aligned} \quad (6)$$

where ρ_B is the bulk resistivity, A is the electrode area, and t is the sample thickness. It can be seen from Eq. (6) that the value of the contact resistance can be determined from a plot of R vs t , where the slope of the straight line is ρ_B/A and the intercept corresponds to $2R_C$.

Paper samples with basis weights ranging from 31 to 315 g/m² were prepared with a 1:1 ratio by weight of softwood-hardwood pulp using the centrifugal machine. The sheets were all pressed at the same pressure and dried. Twelve measurements were taken on each sheet. A strip was cut and measurements were taken every 3/4 of an inch along the whole strip. All the measurements are reported in Fig. 14. The large spread in the resistance is again observed. Since this spread in the bulk resistance has been ascribed to, the anisotropy of the cellulosic fiber network making up the paper sheet (see discussion above), only the

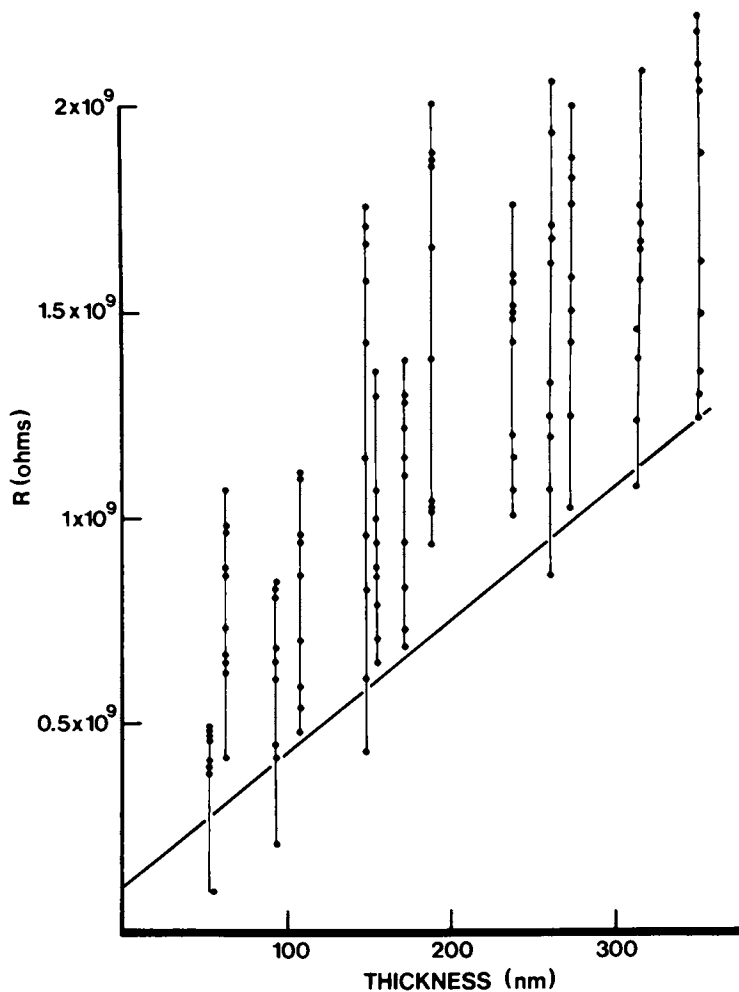


Figure 14. Resistance vs. thickness for a series of papers with different basis weight. The intercept of the minimum values gives the contact resistance and the slope is proportional to the resistivity of the paper. (Reproduced, with permission, from Ref. 16. Copyright 1981, American Institute of Physics.)

minimum values are considered when determining the intercept which defines the contact resistance. As can be seen from Fig. 15, the intercept associated with a least squares fit through the minimum points associated with the different paper samples, has the value $1.05 \times 10^8 \Omega$. Consequently, it may be concluded that the contact resistance is a negligibly small value compared with both the absolute bulk resistance of the paper samples, as well as being negligible with respect to the spread resistance values obtained for all the samples measured.

iv) Effect of Pressure on Nonconductive Papers It has been shown that in order to eliminate contact resistance during a measurement of paper conductivity, it is necessary to apply a relatively high pressure to the stainless steel electrode system. The application of pressure, however, may change the paper structure and consequently may result in a change in the bulk conductivity. To clarify the effect of pressure on paper conductivity, Ga-In was used to measure the conductivity of the calendered paper (see Sec. ii) with a nominal pressure applied (the weight of the lever arm) and at 13.8 MPa pressure.

Table I lists the conductivities obtained with the stainless steel electrodes and the Ga-In electrode, at 13.8 MPa pressure, as well as Ga-In without pressure. It is clear, from the Ga-In results, that the effect of pressure accounts for a 20% increase in conductivity. The value obtained from the stainless steel electrode under pressure is lower than that obtained with Ga-In without pressure, this being the result of the difference in the electrode areas, as discussed earlier. Furthermore, the table of results clearly shows that the effect of surface smoothness, as a result of the different calendering pressures, has no significant effect on the measured bulk conductivity for the case of the stainless steel electrodes with 13.8 MPa pressure.

v) Effect of Pulp Type and the Degree of Refining: Pulp type and the degree of refining are both basic factors which affect the physical properties of paper. A study was made to determine how strongly they affect the electrical properties of paper. Summarized in Table II, are the values of bulk conductivities, σ_B , measured at 50% relative humidity and 73°F for handsheets made from the five different pulps described earlier; Q-90, Seagull-W, Q-30E, Q-30C and 503. In Fig. 15, the results of measurements are shown for the bulk conductivity of these pulps as a function of the degree of refining. The degree of refining is defined as the inverse of the Canadian Standard Freeness value (CSF). It is observed that all the pulps show an increase in bulk conductivity as the degree of refining is increased. There appears to be a significant increase in conductivity initially as the degree of refining is increased. This is followed by a region where the conductivity levels off and is only slightly affected by the degree of refining.

The increase in conductivity can be explained in terms of an initial significant increase in the number of contacting points between fibers. The refining process, which causes shearing and slitting of the fibers, increases the specific area of the fibers and the number of interfiber contacts that can serve as

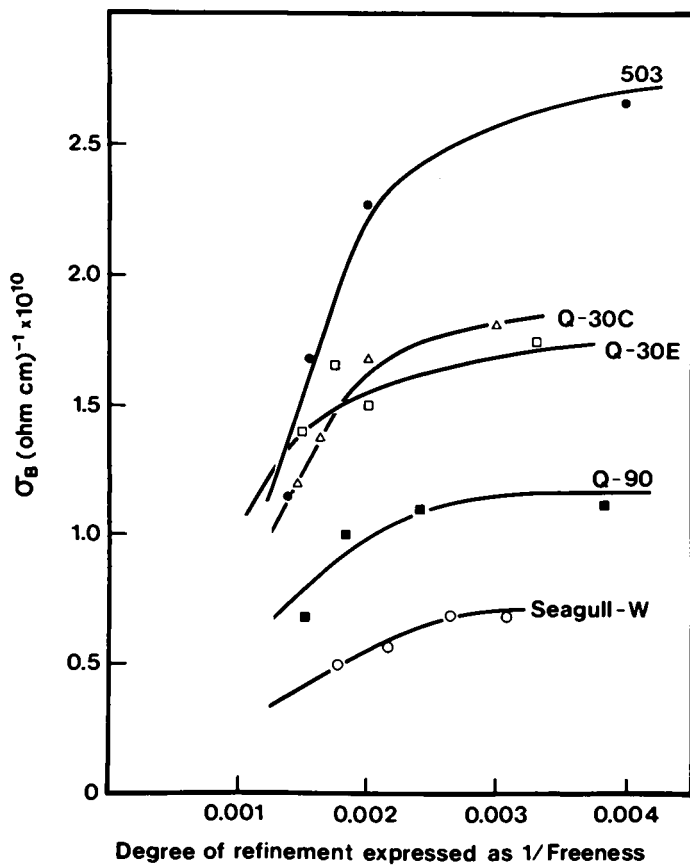


Figure 15. Bulk conductivity, σ_B , vs. the degree of refining. Because the Canadian Standard Freeness (CSF) value decreases as the degree of refining increases, the reciprocal of the CSF value was taken to be the quantity representing the degree of refining.

Table I Conductivity of paper with different basis weights and calendering.

		CONDUCTIVITY $10^{-11} \times (\text{ohm-cm})^{-1}$			
Basis Weight (g/m^2)	Calendering (gauge Pressure) bars	Stainless Steel (115 bar)	Ga-In (no pressure)	Ga-In (115 bar)	
A00	190	0	2.0	4.3	4.2
A20	190	1.4	1.0	1.9	2.1
A40	190	2.8	1.4	1.7	2.2
A60	190	4.2	1.2	1.7	2.2
B00	115	0	1.4	2.61	3.1
B20	115	1.4	0.9	1.6	2.0
B40	115	2.8	1.1	1.4	1.9
B60	115	4.2	0.85	2.0	2.5
C00	60	0	3.5	9.7	1.2
C20	60	1.4	11.	16.	1.8
C40	60	2.8	8.4	12.	1.5
C60	60	4.2	4	9.9	1.1

Table II Bulk conductivity at 50% RH as a function of the degree of freeness for handsheets prepared with different pulps, using distilled water.

Sample	Freeness (CFS)	Moisture Content (%)	σ_b (ohm-cm) ⁻¹ x 10 ⁻¹⁰
Q-90-0-D	661	5.8	.67
Q-90-2500-D	547	6.4	1.0
Q-90-6000-D	415	6.1	1.2
Q-90-11500-D	261	6.4	1.2
Seagull-W-0-D	563	6.7	.50
Seagull-W-2000-D	464	8.2	.56
Seagull-W-6000-D	379	8.6	.67
Seagull-W-9000-D	324	8.1	.67
Q-30E-0-D	681	7.0	1.4
Q-30E-3000-D	586	6.7	1.7
Q-30E-6000-D	494	6.3	1.5
Q-30E-12000-D	302	5.6	1.7
Q-30C-0-D	686	8.0	1.2
Q-30C-3000-D	600	6.3	1.4
Q-30C-6000-D	502	5.4	1.7
Q-30C-12000-D	301	5.3	1.8
503-0-D	729	5.8	1.2
503-3000-D	641	4.6	1.7
503-6000-D	491	3.8	2.3
503-12000-D	245	2.4	2.7

conduction pathways for charge carriers. Charge carriers, which are restricted to move along the water associated pathways of the fibers and fibrils, now find many more conductive pathways through which they can travel. This would result in the effective increase of the bulk conductivity. Beyond a certain degree of refining the conductivity no longer increases at the initial rate, which seems to indicate that beyond a certain degree of refining there is no significant increase in the bonded area of the paper.

In Fig. 15, it is seen that the sheet made of cotton linters is more conductive than the other sheets. The sheet made with "Seagull W" hardwood pulp is the least conductive while the three other pulps have intermediate conductivity values. This behaviour seems to be related to the size of the different types of fibers used to make the sheets. As mentioned previously, hardwood fibers are shorter than softwood fibers, and consequently, there are more interfiber contacts in the sheets made of hardwood fiber. The surface area of a contact is very important to the conductivity. There may be a constrictive effect due to smaller surface at these contacts which results in a restricted flow of ions through the paper, and therefore a lower conductivity. Cotton linters are chemically different and longer than wood fibers and the sheet made of these fibers is more conductive. The difference between the three softwood pulps is probably related to a different chemical composition of its fibers.

From these results, it may be concluded that the degree of refining has a relatively small effect on the bulk conductivity of paper. A small change in the electrical properties is also observed for different pulp types in paper. These variations are not significant when compared with the variations resulting from a change in relative water content. For cellulose the conductivity increases with water content by a factor of 10^{14} from 0% to 20% water content⁽⁸⁾.

Transient Conduction in Fibrous Materials and Paper. In this section a study is presented which focusses on transient ionic currents in paper and fibrous materials. The phenomenon that we observed in the case of paper samples closely resembles the transient phenomena observed and reported for dissociating species in dielectric fluids⁽¹⁸⁾. For the case of paper, the conductive medium is the water network associated with the fibrous cellulose structure. The ionic species can be transported through this structure by applying an electric field.

The measurement of charge transport phenomena within cellulose fiber structures was performed according to the following sequence. The sample was introduced between the stainless steel electrodes of the *in situ* pressure bulk conductivity cell and a pressure of 11.6 MPa was applied. A step function D.C. voltage (rise time of 1 msec) either positive or negative was initially applied to the sample for a period of 120 seconds. This was followed by the application of a D.C. voltage of the same magnitude but of opposite polarity. Successive transient current experiments on the same samples, where the electric field is monotonically increased, were performed by alternating the voltage polarity between experiments.

An example of such a series of transient experiments for a sample of paper without conductive additives (softwood Kraft pulp, 450 CSF, 80 g/m² basis weight, Sample 1), is shown in Fig. 16. This series of transient currents represents the electric field dependence of charge transport associated with mobile ions within the water associated with the fibrous network of the paper. The initial transient current, labeled (a), corresponds to the first application of an electric field ($E = 2.5 \times 10^3$ Volts/cm) to the new sample. After reversing the polarity of the power supply an electric field of the same magnitude is applied to the sample which leads to the transient current shown by label (b) in Fig. 16. (N.B. the scale of the ordinate is different for Fig. 16 (a)). Again reversing the polarity of the voltage and maintaining the same value of the electric field leads to the transient current labeled (c). Subsequent experiments, where the magnitude of the electric field was monotonically increased but where the polarity of the power supply was first positive and then negative, results in the transient current pairs (d) and (e), (f) and (g), and (h) and (i), respectively.

These results appear to be similar to the transient conduction phenomenon observed in dielectric fluids containing dissociated species or ionisable small molecules⁽¹⁸⁾. As in those cases, the initial application of a step function D.C. voltage to the virgin sample results in a dispersive transient current, depicted by label (a) in Figure 16. This seems to suggest displacement of the positive and negative ionic species, which are initially randomly distributed, to their respective oppositely charged electrodes. Such a process, requires ionic transport through the H₂O network within the fibrous structure of the paper. After approximately 120 seconds, the transient current reaches a steady state value which may be associated with charge injection at the electrodes. Reversing the polarity of the applied voltage, (maintaining its magnitude), resulted in the transient current, label (b) in Fig. 16. A transient current with a well defined peak now appears. Maintaining the same voltage magnitude but again reversing the polarity, results in the transient current shown in (c), which is simply an inversion of the transient (b) in Fig. 16. Continuing along these same lines of experiments, using positive and negative polarities for a given voltage, pairs of transient currents are obtained for increasing applied electric fields as shown in labels (d) and (e), (f) and (g), and (h) and (i), respectively.

As the applied electric field was increasing, two interesting phenomena were observed in the transient current. First, the transient current peak shows an electric field dependence. Secondly, at $E = 2 \times 10^4$ Volts/cm, and above, two distinctly different peaks can be distinguished in the transient currents which have a different field dependence of both the current amplitude and the current peak time.

Shown in Fig. 17 is a plot of the inverse of the transient current peak time, $1/t_p$, versus the applied voltage, V , for the two peaks of the undoped pulp sample containing no additives (Sample 1) and the pulp sample doped with 0.2% NaCl (Kraft pulp, NaCl 0.2% by weight, Sample 2). A similar plot for the

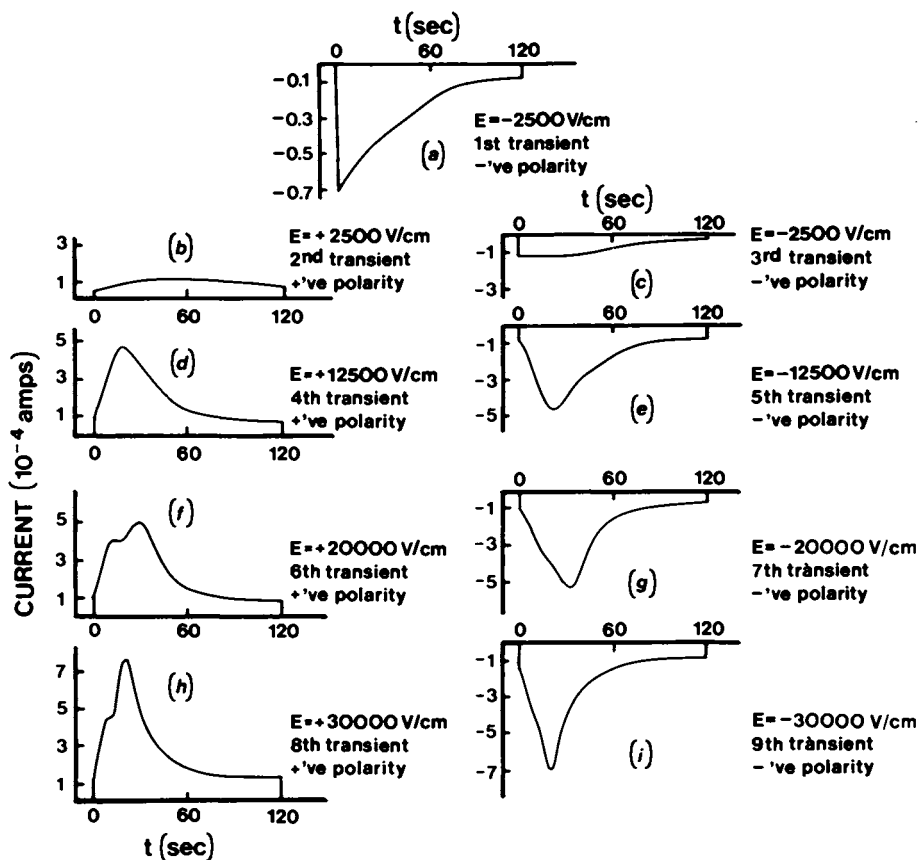


Figure 16. Transient currents for an undoped pulp sample for varied, increasing applied electric field and alternating polarity. (The scale of the ordinate is different for (a)).

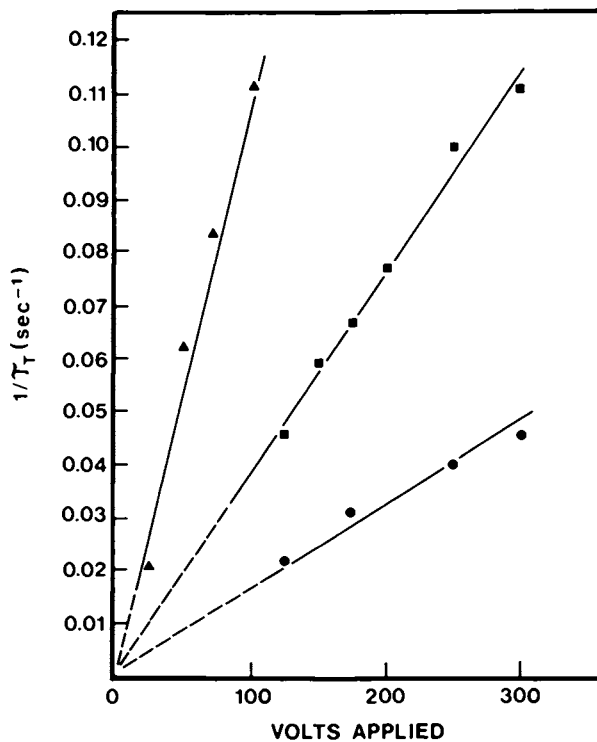


Figure 17. Plot of the inverse of the transient current peak time vs. the applied voltage for the paper sample doped with 0.2% NaCl (Sample 2) and for two peaks observed in the undoped paper sample (Sample 1). Key: \blacktriangle , paper doped with NaCl; \blacksquare , plain paper—second peak; and \bullet , plain paper—first peak.

conductive base paper (James River conductive base paper, Sample 3) is shown in Fig. 18. The two papers (three peaks) in Fig. 17 exhibit a linear relationship between $1/\tau_1$ and the applied voltage, V . The results for the conductive base sheet are not as straightforward. The plot of $1/\tau_1$ versus V for this paper (see Fig. 18) shows a nonlinear dependence as opposed to the other paper samples. The conductive base paper sample which was at 50% relative humidity during the experiment had a significantly greater peak time than the other samples which were held at 80% RH. This may be the result of the lower volume content of water at lower RH as well as the possible influence of the conductive polymer resin within the water network of the fibrous structure.

The observed transient current results described above do not have a straightforward interpretation. From the magnitude of the transient current shown in Figure 16, it can be determined that the number of ions transported during the measurement correspond to approximately 10^{-2} coulombs of charge. If this charge is distributed on the electrode, it gives rise to a space-charge field of $\approx 10^9$ V/cm, which is orders of magnitude higher than the applied electric field used in this study. On the other hand, the linear dependence of $1/\tau_1$ versus applied voltage (for undoped pulp), as well as the reproducible and reversible features of the transient current, seem to suggest a classical "time of flight" behaviour. Another possibility is that the transient current phenomena observed is due to the effect of electrochemistry. However, the latter seems unlikely since the transient currents are reversible when voltage polarity is changed. This would require the unlikely occurrence of reversible electrochemical reactions at the electrodes.

There is presently not enough information to conclusively interpret the experimental observation. Nevertheless, the authors favor a "time of flight" approach to the transient currents. Clearly, this is not consistent with an assumption that enormous space charge fields are developed in the paper during the ionic transport process. However, there is the possibility that space charges may be compensated for by the presence of numerous charged groups which are present all along the backbone of the polymer chains making up the wood fibers. Two observations support this. As already pointed out, the dependence of $1/\tau_1$ versus applied voltage is linear. Secondly, for the case of undoped pulp the current peak versus applied voltage is also linear. Acknowledging that this data is not conclusive the authors have nevertheless applied a "time of flight" interpretation to the transient current. The results of this approach which is described below appear to be in good agreement with previous reports of O'Sullivan⁽⁴⁻⁷⁾.

In table 3, the voltage dependence of the transient current peak, the peak current magnitude, and the calculated mobilities associated with the current peak times for all the paper samples studied. The mobility was determined using the standard equation:

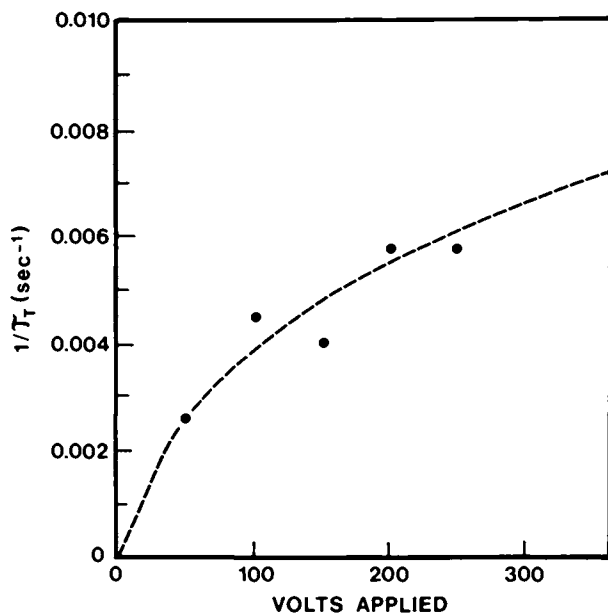


Figure 18. Plot of the inverse of the transient current peak time vs. the applied voltage for the conductive base sheet.

TABLE III ELECTRICAL PARAMETERS OF THE DIFFERENT PAPER SAMPLES

SAMPLE	Voltage (Volt)	Peak Time (Sec)	Peak Current (10^{-4} amp)	Mobility (μ) ($10^{-8}\text{cm}^2\text{V}^{-1}\text{s}^{-1}$)
<hr/>				
Plain Paper				
80% RH 1st Peak	125	22	4.7	3.6
	150	17	4.9	3.9
	175	15	4.1	3.8
	200	13	3.9	3.8
	250	10	4.1	4.0
	300	9	4.2	3.7
2nd Peak	125	46	2.8	1.7
	150	40	2.8	1.7
	175	32	4.6	1.8
	200	30	4.9	1.7
	250	25	6.5	1.6
	300	22	7.5	1.5
Paper Doped with Salt				
80% RH	25	48	15	8.3
	50	16	19	11.1
	75	12	21	9.5
	100	9	18	11.1
	125	8	22	10.0
Conductive Base Paper	50	375	0.4	0.30
50% RH	100	225	1.2	0.25
	150	250	1.0	0.15
	200	175	1.5	0.16
	250	175	1.2	0.13

$$\mu = \frac{d^2}{V \tau_t} \quad (7)$$

where d is the sample thickness, τ_t is the transient current peak time or time of flight. The ionic mobility determined using equation (7) is in agreement with the ionic mobility reported by O'Sullivan^(4,7) in cellulosic sheets, where the transport of ionic species was detected using various indicators. He reported that the ionic mobility of the potassium ion in a salt impregnated cellulose sheet at 10% water content, was $\mu = 1.7 \times 10^{-8} \text{ cm}^2 \text{ v}^{-1} \text{ sec}^{-1}$.

As can be seen in the table, the mobility is reasonably constant as a function of voltage for the undoped paper and the paper doped with NaCl. Some variability can be noted in the conductive base sheet paper; however this is more likely to be due to sample variability than intrinsic electric field dependence of mobility, since as previously noted, every electric field measurement in that case was performed on a fresh sample. In the case of pure paper doped with 0.2% NaCl, it may be suggested that the dominant charge transporting species are Na^{\oplus} and Cl^{\ominus} and that their respective mobilities are similar since only one peak is observed. In the case of undoped plain paper significantly different mobilities are observed for at least two different ionic species that may be other than Na^{\oplus} or Cl^{\ominus} . However, the presence of high salt content in the plain paper sample doped with 0.2% NaCl may lead to a significantly higher water content which may account for the higher mobility of Na^{\oplus} and Cl^{\ominus} , and consequently does not rule out one or both of these ions being associated with one of the transient current peaks in the pure plain paper sample.

A study was made of how the current peak magnitude varies as a function of the applied voltage. The results for an undoped pulp sample is shown in Fig. 19. This is the sample which exhibited two distinct transient current peaks. The voltage dependence of the initial current peak increases linearly with the applied voltage up until 150 volts, after which no further increase occurs with an increase in the voltage. In contrast the second current peak magnitude remains a linear function of voltage right up to 300 volts. This result may be due to the ionic species associated with the first current peak is being depleted at the electrode surface beyond approximately 125 volts. This depletion phenomena was always found to be associated with the anode as seen by a deterioration of the stainless steel electrode surface. Consequently, one possible explanation may be that this ionic species is anionic and that it takes part in an redox reaction with the electrodes. This anion is most likely Cl^{\ominus} or OH^{\ominus} . The same phenomenon is also observed for the other samples and the same conclusions may be drawn.

Ion Diffusion in Paper. Using the "time of flight" model, it has been found that the mobility of the ionic species is approximately 4 orders of magnitude lower in these systems than for the case in normal aqueous systems. Based on this result, an

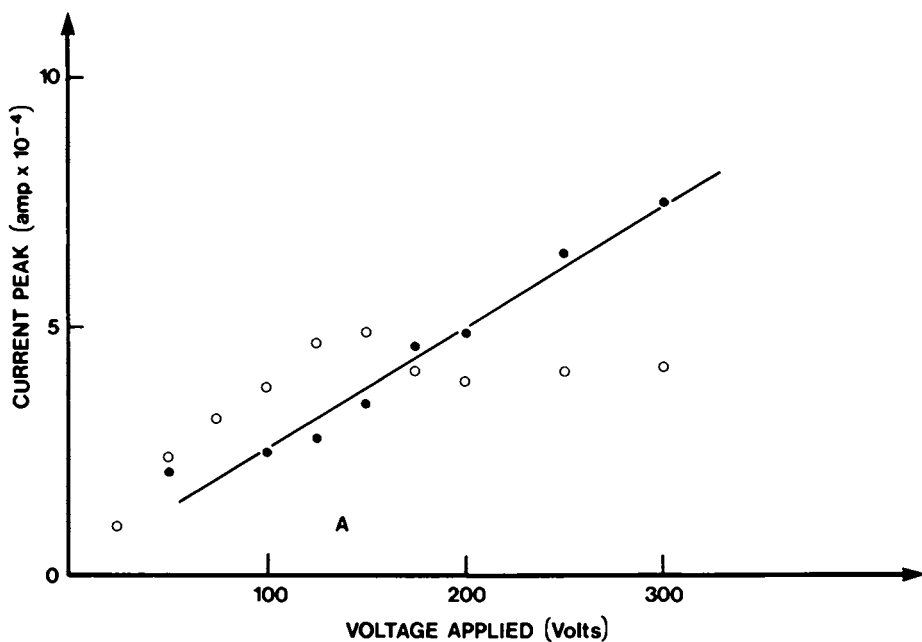


Figure 19. The transient current peak plotted against applied voltage for the pure paper sample. Key: ○, initial current peak; and ●, second current peak.

estimate was made of the diffusion coefficient (D) of the ionic species within the water containing fibrous structures.

The diffusion coefficient is given by the well known Einstein relation;

$$D = \frac{K T}{f} \quad (8)$$

where K is the Boltzman constant, T is the temperature and f the friction coefficient of the ionic species. If the results of the previous section are valid, the friction coefficient f may be determined according to;

$$f = \frac{e Z}{\mu} \quad (9)$$

where e is the charge of the electron and Z is taken as 1 assuming univalent ions. Taking the mobility $\mu = 1.7 \times 10^{-8} \text{ cm}^2 \text{ V}^{-1} \text{ sec}^{-1}$ for the 2nd peak observed at 200V of the plain paper sample, one finds $D \approx 4 \times 10^{-10} \text{ cm}^2 \text{ sec}^{-1}$.

The above value of the diffusion coefficient is approximately 5 orders of magnitude lower than the case for ions diffusing in a pure aqueous system. Although the diffusion coefficient appears to be extremely low, this is not a surprising result in view of the complex structure and low water content associated with the cellulose fiber network. More specifically, the small amount of water present in the fibrous network restricts the transport of the ions through the random spacial distribution of the fibers making up the paper. There is also the opportunity for the ions to be trapped by the ionized groups chemically fixed on the polysaccharide chains or lignin molecules, both of them being the major constituents of wood fibers.

In summary, the results which are presented in this section suggest that the charge transport of ions within paper and paper-like structures is essentially the same as that of the transport properties associated with aqueous electrolyte systems. Furthermore, the transient current behaviour which has been observed in these fibrous cellulosic systems show characteristics similar to the ionic transient current conduction exhibited in both dielectric fluids and aqueous ionic systems.

Summary

This article has addressed a number of issues relating to the electrical properties of paper or fibrous structures. It was shown that reliable measurement methods are now available for estimating both the bulk and surface conductivities of paper. In the case of the bulk conductivity, a new *in situ* pressure conductivity cell was described which significantly reduces contact resistance. The surface conductivity can be determined by the application of a modified four-point probe method first used on paper by Cronch⁽¹⁵⁾. It was shown that the degree of refining has a small effect on the bulk conductivity of paper. The type of pulp in paper also has an effect on paper conductivity. However both effects are negligible when compared to the effect of the relative humidity. Furthermore, chemical additives can completely dominate other paper variables in

controlling the electrical conductivity. The orientation of the fibers within the paper strongly effects the conductivity. For this reason, in a paper where fibers are oriented in the plane of the sheet, surface conductivity is several hundred times higher than bulk conductivity. It was concluded that ions are transported through paper by means of a water associated fibrous network. The mobility and diffusion of ions in paper is severely restricted, compared to a water solution, due to the limited degree of freedom imposed by the fibrous network. The mobility and diffusion coefficient for ions appears to be 4 or 5 orders of magnitude lower in paper at 50% relative humidity when compared with ions in a water solution.

The above studies are only just a beginning of a probe of the details important to the electrical conductivity in paper. It is hoped that further work in this area will lead to a better understanding of the electrical properties of paper.

Literature Cited

1. Brodie, I.; Dahlquist, J.A., and Sher, A., J. Appl. Phys., 39, 1618-1624 (1968).
2. Hartmann, G.C; Marks, L.M. and Yang, C.C., J. Appl. Phys., 47, 5409 (1976).
3. Kujiari and Akahari, Sci. Papers Inst. Phys. Chem. Res. (Tokyo). I, 94 (1923).
4. O'Sullivan, J.B., J. Text. Inst., 38, T271-T284 (1947).
5. O'Sullivan, J.B., J. Text. Inst., 38, T285-T290 (1947).
6. O'Sullivan, J.B., J. Text. Inst., 38, T291-T297 (1947).
7. O'Sullivan, J.B., J. Text. Inst., 38, T298-T306 (1947).
8. Algie, J.E. "D.C. Conduction in Keratin and Cellulose", Applied Fiber Science, Vol. 2, Chap. 5, edited by F. Happey, Academic Press, London 1979.
9. Browning, B.L. "Analysis of Paper", Dekker, New York 1977.
10. Britt, K.W. editor, "Handbook of Pulp and Paper Technology", 2nd ed., Van Nostrand/Reinhold, New York 1970.
11. Casey, J.P. editor, "Pulp and Paper Chemistry and Chemical Technology", Vol. I, II, & III 3rd ed., John Wiley and Sons, New York 1980.
12. Dolinski, R.J. and Dean, W.R. Chemtech, May 1971, pp. 304-309.
13. Greismer, J.J. TAPPI Conference Papers - Reprography, 1976, pp. 71-83.

14. Howlett, W.H. and Landheer, D. Proceedings from Testing, Printing, and Reprography Conference, Rochester, New York, 1979.
15. Cronch, R.D., "Novel Methods of Measuring the Basic Resistivity of Electrographic Papers," in "1979 Printing Reprography Testing Conference Proceedings", TAPPI, Atlanta, 1979, p. 89.
16. Josefowicz, J.Y. and Landheer, D. TAPPI, 64, 116 (1981).
17. Josefowicz, J.Y.; Anczurowski, E.A.; Jones, A.Y. and Deslandes, Y. Rev. Sci. Instrum., 52, 926-932 (1981).
18. Novotny, V. and Hopper, M.A. J. Electrochemical Society, 126, 925-929, (1979).

RECEIVED June 3, 1982

Color Ink Jet Printing: Materials Parameters

A. B. JAFFE, E. W. LUTTMAN, and W. CROOKS

IBM ISD Advanced Technology, San Jose, CA 95125

High quality color reproduction is now obtainable by ink jet printing and will be illustrated. Once the printing parameters are selected, the quality achieved in the color reproduction depends strongly on the materials parameters of the system. Ink-paper interactions, ink formulation, and paper surface preparation all contribute to the quality of the resulting print. Archivality of the print is controlled by the lightfastness of the dye, the pH of the ink, and of the waterfastness achieved.

Conventional color reproduction involves many forms of printing processes which strive to reproduce a color original. These can be either photographic or mechanical printing processes, depending on the number of copies to be made and the quality desired. Each one of the many mechanical processes has a unique set of requirements including equipment, inks, paper, and copy preparation that gives reproduction of differing quality and cost. For a small number of copies, photographic reproduction is the only present practical cost effective solution. Mechanical reproduction (e.g. letterpress, rotogravure, etc.) requires color separations to be made for each of the primary printing colors plus black. Even with the most modern technology, this is very time consuming and expensive, and for these reasons is only used for multiple copies.

Ink jet printing has the inherent capability to displace many of the mechanical processes since it is an electronic technology. Data can be printed from any digitized source such as a scanner or a computer such that plates are not necessary for multi-color printing. This makes it equally easy for single or multiple copies with no variation of quality.

Since ink jet technology has not yet been used for high quality color reproduction, the objectives of this process must be considered in terms of the materials limitations of ink jet printing. When a color reproduction is made by a mechanical process, much time is spent matching different dyes and papers with the desired effect wanted. After the materials decision is made,

0097-6156/82/0200-0531\$06.00/0
© 1982 American Chemical Society

printing then begins. With ink jet printing, many trials cannot be run before the printing begins or any advantage this technology holds would be lost. Reasonable quality print must be possible at the first attempt. This paper will discuss the parameters of the dye in the ink and the paper on which it is printed that limits the color capabilities of ink jet printing.

Ink

The basic requirements of an ink for ink-jet printing are numerous and sometimes contradictory. In order to be jetted properly, the ink must have the correct physical properties of viscosity, specific gravity, surface tension, conductivity, and pH. It should have compatibility with all machine parts to which it comes in contact, low corrosion, low particulate contamination, no biological growth, long shelf life, and no chemical hazards. Once it is on the paper, it should have good print quality and should be archival. The ink is composed of many materials in order to satisfy all these requirements but the only concerns of this report are those factors which affect the reproduction of color. Although the colorants in conventional inks has traditionally been pigments, insoluble particulate matter in the ink is totally unacceptable for jetted inks due to the possibility of clogging of the small orifices. The nozzles in this study are .75 mil in diameter. The inks, in order to fulfill the operating parameters of the ink jet process, are water based and therefore water soluble dyes are the chosen colorants. Unfortunately, this makes the print susceptible to problems of water-fastness after it is printed.

A recent study by Ohta (1) of dyes used in photography has indicated the important parameters of a set of dyes for subtractive color reproduction are:

- 1) Peak Wavelength
- 2) Breadth of the Absorption Peak
- 3) Unwanted Secondary Absorptions

In order to reproduce a large color gamut (this can be thought as the number of colors that can be reproduced by a set of three primary inks), these dyes must be chosen in a set that contains three peak wavelengths that corresponds to the colors cyan, magenta, and yellow. There is a large range of each of these colors which are acceptable and the size of the color gamut must be used to insure that one set of inks is the best match for most color reproduction. This entails the good reproduction of reds, blues, and greens, as well as a large color gamut. These properties of a set of inks depend only on the absorption wavelength of the dyes chosen.

Once a dye has been chosen, there is little that can be done to control its spectroscopic properties except those affected by concentration. The example in Figure 1 shows the spectroscopic changes that can accompany concentration variations of a dye. The optical density does not necessarily increase at the wavelength of interest as the concentration of the dye is increased. Not only does Acid Violet 19 exhibit a large increase in the width of the peak as

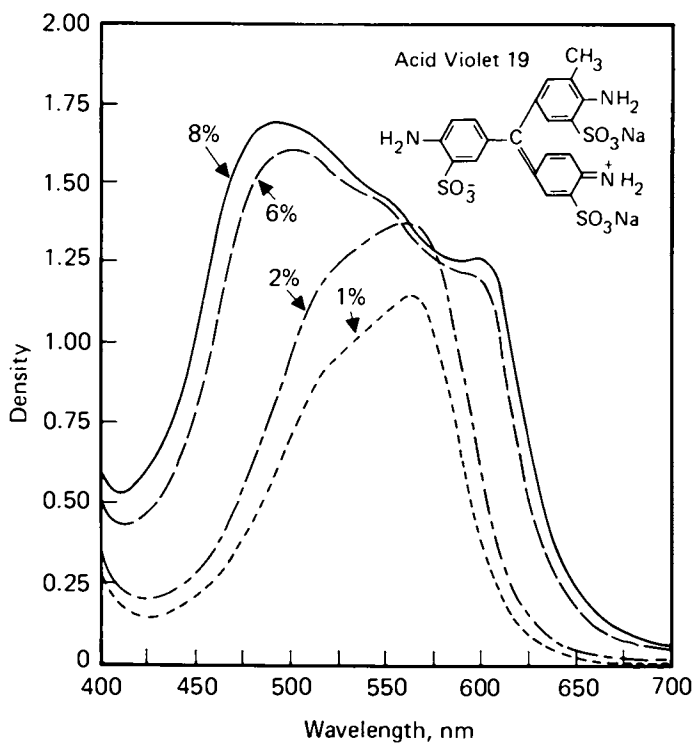


Figure 1. Spectral changes of Acid Violet 19 when the concentration is varied from 1% to 8%.

the concentration is increased, but , more importantly, there is a shift in the wavelength of the principal absorption. This shift affects the hue of the desired color and the broadening of the peak affects both the saturation and lightness. The perceived colors at higher concentration are darker, have shifted their hues, and are 'dirty'. In this case, the shift in principal wavelength can be attributed to the formation of a dimeric species (2) which absorbs light very strongly. Not all dyes behave in this manner, but the use of water based systems does increase the possibility of this happening. Since many water soluble dyes are primarily composed of hydrophobic, organic molecules which have a few specific sites for water solubilization, as the concentration of the dye is increased to the levels needed for an ink, dimerization can occur. Any dye that is being considered for a subtractive set of inks must be carefully screened to examine the change in spectroscopic parameters in the concentration range of interest.

Since many water-soluble dyes are pH indicators, this becomes an important parameter to consider when formulating an ink. For a continuous ink jet system in which the unused ink supply is recirculated back to the main ink supply and reconstituted, controlling the pH becomes a serious problem. Acid Violet 14 (figure 2) shows a strong dependence of the peak wavelength of absorption as the pH is varied. For a practical ink, a dye such as that in Figure 3 is more suitable as it does not vary greatly over a wide pH range. If the pH drifts, shifts in optical density will be noticeable to the eye in the color reproduction.

Although lightfastness of any dye does not immediately affect the color capabilities of an ink, the long range potential of the color can be severely restricted. Any dye that would be considered for an ink should have sufficient archival properties to sustain an image after exposure to light. Figures 4, 5, and 6 show three dyes with varying lightfastness capabilities. Patent Blue A would not be very useful since it is totally decomposed by exposure to 40 hours in a fadeometer. The other dyes are more resistant to fading and could be considered practical in an ink.

Paper

Important parameters affecting the quality of any printing process involving the deposition of ink onto a surface are the properties of the ink and the properties of the surface to which the ink is applied. A paper, or a paper modified surface, is the most common surface on which inks are deposited. Most printing papers have been formulated to accept ink which are not water-based and to resist the penetration of water. To obtain high quality images from water-based inks applied by ink jet, it is necessary that the printing surface has properties which allow controlled penetration of the water based inks. This is complicated by the fact that the drying of the ink is accomplished by absorption into the paper. Instead of spreading on the paper in a regular fashion, the ink can

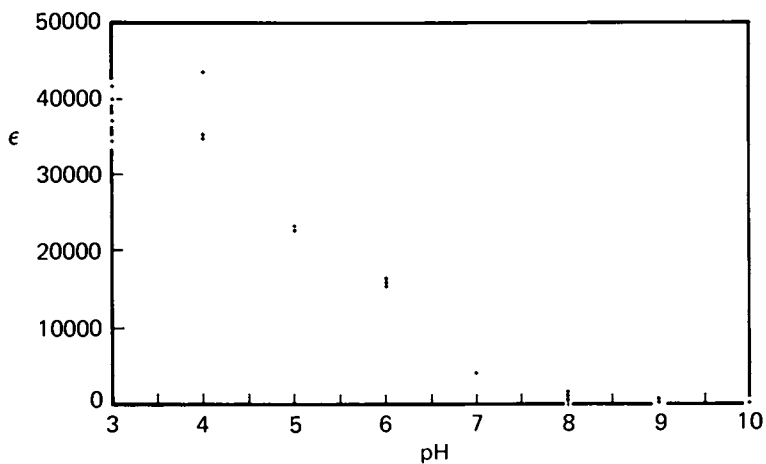


Figure 2. Variation of the extinction coefficient of Acid Violet 19 at the peak wavelength of absorption with pH.

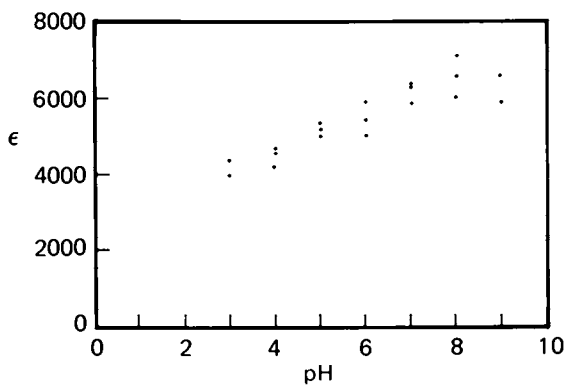


Figure 3. Variation of the extinction coefficient of Dye A at the peak wavelength of absorption with pH.

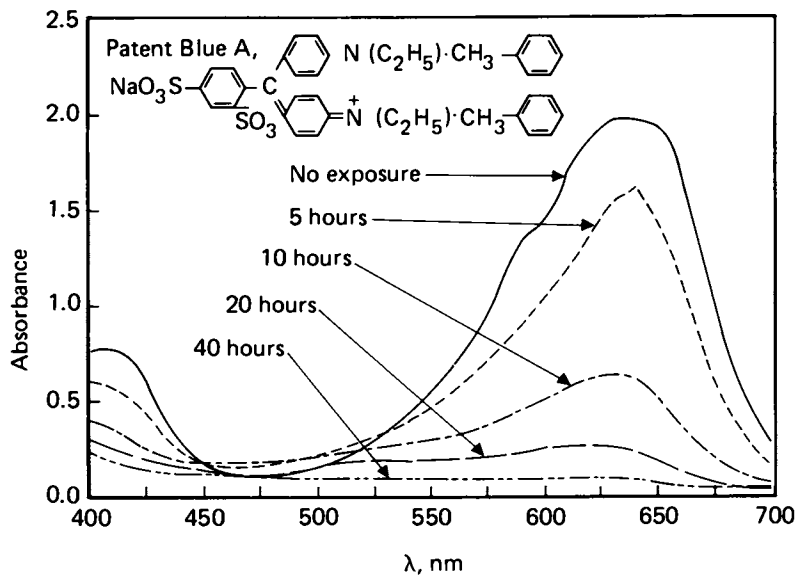


Figure 4. Lightfastness behavior of Patent Blue A as exposed to an Atlas Fadeometer.

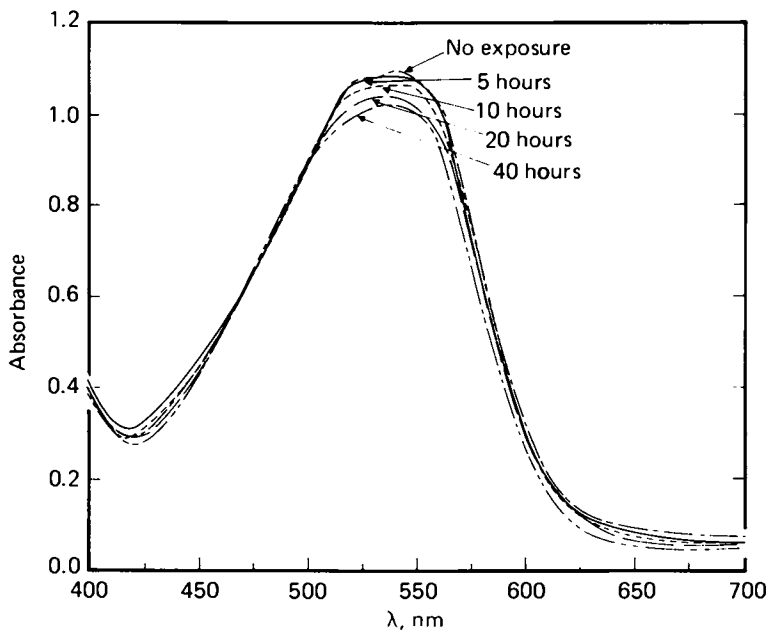


Figure 5. Lightfastness behavior of Dye A as exposed to an Atlas Fadeometer.

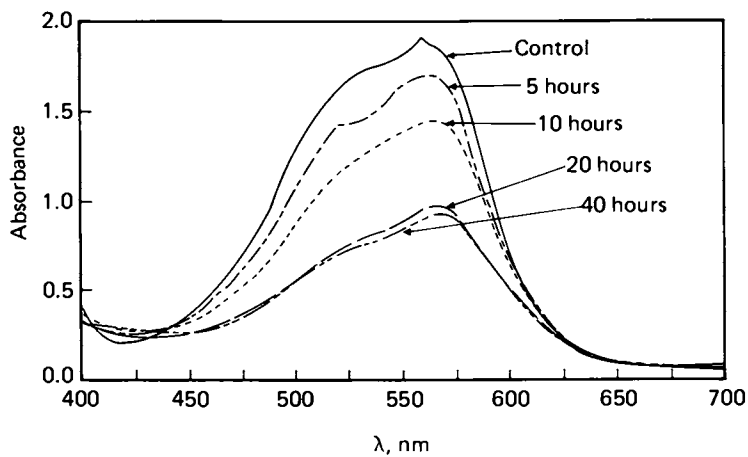


Figure 6. Lightfastness behavior of Acid Violet 19 as exposed to an Atlas Fadeometer.

travel in a cellulose fiber. This causes a problem in which the drop spreads out in an irregular shape which is called feathering. The print quality is degraded. If the ink penetration is controlled, then spots of specific dimensions can be printed. The spot diameter is related not only to the paper surface characteristics such as its water absorptivity and surface smoothness, but also to the ink jet nozzle diameter, ink pressure and the physical properties of the ink.

To obtain optimum color quality or maximum color gamut, an opaque paper with a white, bright surface is required. Bond paper, which has a rough surface, absorbs the ink into the bulk. The resulting diffuse reflection from the fiber/air interface limits the maximum optical density obtainable (Figure 7). This is due to the fact that the eye receives white light from the source that has not been through the ink layer. Furthermore, because of the uncontrolled absorption of the ink into the paper, ink spreading or feathering occurs and resolution is adversely affected. In Figure 8, the SEM shows the drop shape irregularity on bond paper.

If a coating such as polyvinyl alcohol is applied to the paper, the water-based inks remain on the surface after printing. The first surface reflection becomes specular (Figure 7) and results in increased optical density and better saturation. The light going through the ink layer also must be reflected from the paper base. Very high quality reproduction can be obtained if a commercially manufactured photobase paper is used. (3) The barium sulfate coating on this paper is extremely smooth and has high optical reflectivity. A polyvinyl alcohol coating is applied on top to ensure that the water-based inks remain on the surface. Figure 9 shows the excellent drop formation on this type of paper.

Conclusion

High quality color printing has been achieved using digitized ink jet printing at a resolution up to 189 drops/cm. Materials parameters of importance are paper surface preparation and inks. Excellent quality has been obtained on poly vinyl alcohol coated photographic base paper with a careful choice of dyes and dye concentration. When dyes with appropriate spectral properties have been selected, then the dye concentration levels must be chosen in which dye aggregation effects are minimized. The necessity of using dyes which are relatively insensitive to pH changes has also been discussed. Dyes must also be selected to have maximum fastness to light if archival properties are required.

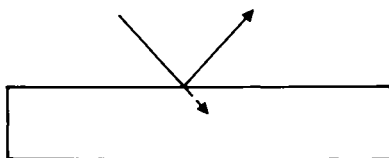
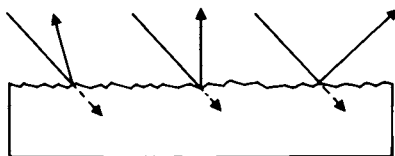
Specular**Diffuse**

Figure 7. Specular and diffuse first surface reflections.

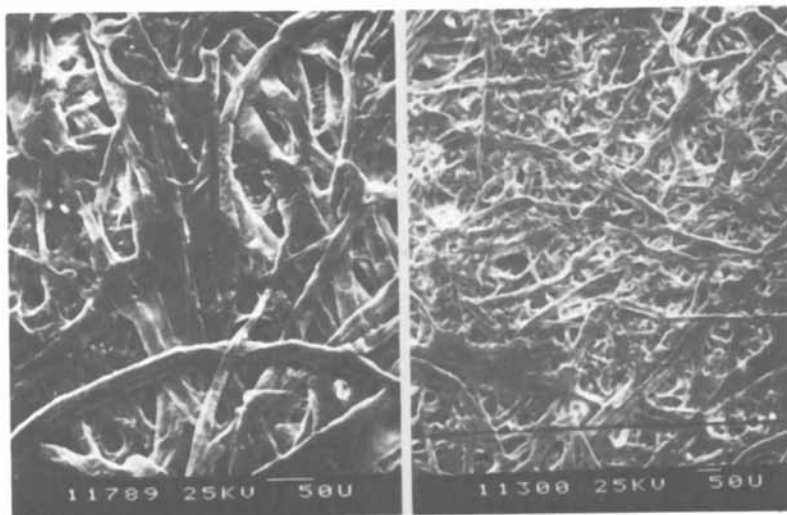


Figure 8. Scanning Electron Micrograph of bond paper with and without a drop of ink.

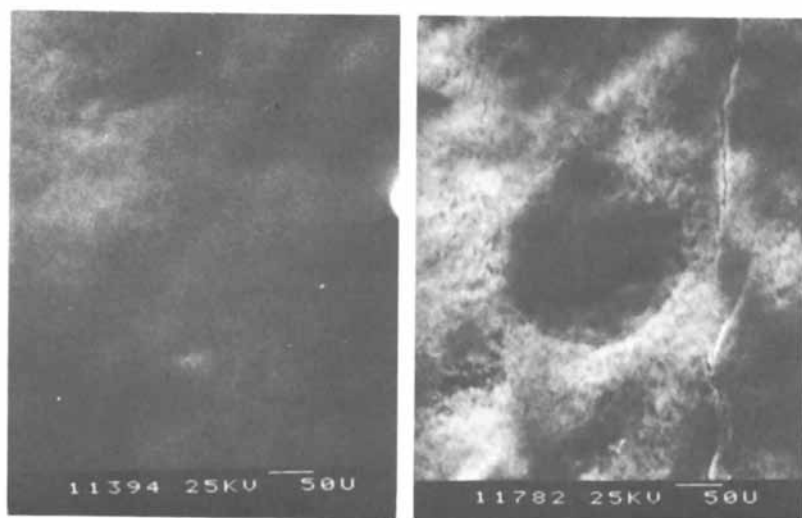


Figure 9. Scanning Electron Micrograph of polyvinyl alcohol coated barytes photobase paper with and without ink.

Acknowledgments

The authors would like to thank J.P. Montoya, T. Niweigha, and G.S. Keller.

Literature Cited

1. N. Ohta: 'Color Reproduction in Reflection-Type Color Prints', J. Appl. Photog. Eng., 2, 75-81, (1976)
2. E. Coates: 'Aggregation of Dyes in Aqueous Solutions', J. Soc. Dye Color., 355 - 368, (1969)
3. This paper was obtained from Schoeller Technical Papers, Inc., Pulaski, New York.

RECEIVED June 18, 1982

Magnetic Ink for Magnetic Ink Jet Printing

ZLATA KOVAC and CARLOS J. SAMBUCETTI

IBM, T. J. Watson Research Center, Yorktown Heights, NY 10598

This work will describe a series of magnetic colloidal systems that were specifically developed for an application in ink jet printing technology. This application imposes a certain set of requirements such as: particle size $100 \pm 50 \text{ \AA}$, magnetic moment of 25 emu/g or 35%w Fe_3O_4 in colloidal dispersion, viscosity of 8-10 cps, non-toxic aqueous system, shelf life of a few years, freeze-thaw stability, fast drying (2 msec) and high optical density of magnetic ink on various papers. Experimental details of Fe_3O_4 precipitation, choice of surfactants and additives used to give above properties of colloidal printing inks will be given in detail.

Colloidal dispersions of ferromagnetic materials such as Fe, Co, Ni and their alloys, or ferrites in a liquid carrier are fluids with ferromagnetic properties; they are often referred to as ferrofluids.¹ Due to their magnetic properties, such colloidal dispersions have been used to reveal the structure of magnetic materials,² to separate materials such as oil spills from water,³ or to make zero-leak high speed seals and self-lubricating bearings.⁴ Furthermore, precise magnetic controllability of such fluids makes them useful in ink jet printing.⁵⁻⁷ The basic concept in ink jet printing consists of an ink being supplied under pressure through a nozzle or an orifice. The ink jet is periodically interrupted to produce droplets, which impinge upon a sheet of moving paper. For printing purposes, it is necessary that drops be uniform in size, equally spaced from each other, and be formed at a high rate ($\sim 10^7$ /sec). The drops from the ink jet can be electrostatically charged and deflected to form a dot on a paper as described by Sweet⁸ and later reviewed in a paper by Kamphoefner. If a

0097-6156/82/0200-0543\$06.00/0

© 1982 American Chemical Society

magnetic ink is used, then printing is achieved by selection and deflection of the droplets using a magnetic field gradient.

The objective of this work was to develop a magnetic ink which could be used in magnetic ink jets for printing experiments.

Kaiser¹¹ and Miskisczy,¹⁰ using Pappel's grinding technique, prepared a stable colloidal suspension of magnetic particles of 100Å diameter in kerosene, fluorocarbons and water, using oleic acid as a stabilizing agent. Using this technique, the highest concentration they achieved was 13% by volume of Fe_3O_4 in kerosene and ~3% by volume in water. Reamers and Khalafalla¹² precipitated Fe_3O_4 from an aqueous solution of ferric and ferrous ions with NH_4OH and then coated Fe_3O_4 particles in situ with ammonium oleate. Addition of kerosene to this mixture with heating and stirring resulted in phase separation and formation of a stable colloidal dispersion of an oleate-coated magnetic particles-in-kerosene phase and a soluble ammonium salt-in-water phase. The concentration of Fe_3O_4 which they obtained in kerosene was the same as the Kaiser obtained by grinding.

Kerosene-based ferrofluid is unsatisfactory when used in an ink, due to spreading of ink drops on paper. In addition, a high concentration of magnetic particles in the dispersing medium is desired for magnetic ink jet printing, since each drop of an ink is addressed according to its magnetic moment. Water-based inks are used in electrostatic ink jet printing due to their low viscosity, non-toxic and non-flammable nature.¹³ Due to the above facts, it becomes clear that water-based inks having high magnetic moments are desirable for magnetic ink jet printing.

WATER-BASED INKS FOR INK JET

Figure 1 illustrates the principles of printing with a Magnetic Ink Jet, showing the sequences of ink drop generation, deflection, and placement on paper. In this technology the fluid itself possesses an inherent magnetic moment so that droplets of the ink can be subjected to magnetic field gradients to deflect and position these droplets on paper according to prearranged patterns. (Figure 1) As metals and metal oxides are not water soluble and soluble metal compounds which exhibit ferromagnetism have very low magnetic susceptibility, the ink is made of a dispersion of particles. Therefore, the magnetic jet uses an heterogeneous system: an aqueous magnetic colloid. For this particular kind of colloid, the essential parameters to consider on the particles are: magnetic moment, particle size, electrical charge and chemical stability. The use of colloids in which the nuclei are made of materials of high magnetic moment, such as Fe, Co, Ni have been considered.

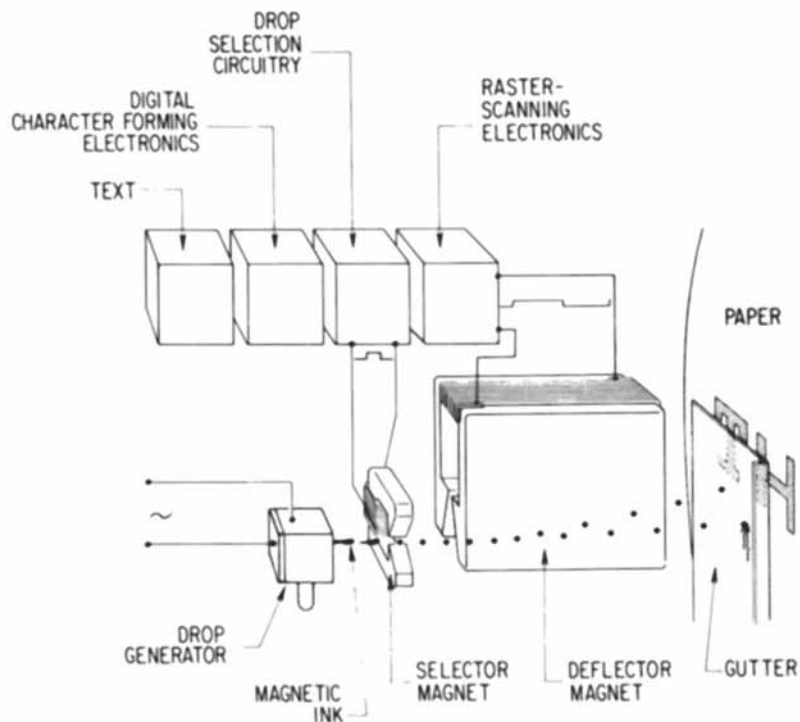


Figure 1. Magnetic Ink Jet System. Drops of ink are steered by non-uniform magnetic fields. Deflection in the horizontal plane selects the drops for printing, vertical deflection by the deflector magnet controls placement of drops on paper.

However, particles of ferromagnetics, when sufficiently small, are of single domain character and possess an intrinsic permanent magnetic dipole moment μ such that

$$2\mu^2/a^3 = \frac{Ms^2 a^3 \pi}{18} \quad (1)$$

where μ magnetic dipole moment, M_s saturation magnetization, a particle radius. At a certain particle size the in-line dipole-dipole interaction energy becomes greater than the thermal energy and the particles tend to agglomerate in linear chains. For example, for Co, at particle size greater than 50\AA the interaction energy overcomes KT . Furthermore, systems containing Fe or Ni as nuclei, present problems in chemical stability due to oxidation and hydrolysis in aqueous solutions. The magnetic colloids considered here have been synthetically prepared by precipitation of magnetite (Fe_3O_4) and dispersion in aqueous media. In this type of aqueous colloids stabilization is mainly due to formation of electrostatic double layer. This stability of these heterogeneous aqueous systems is governed by the overall energy of interaction E between particles, which can generally be expressed as

$$E = \underbrace{K_1 e^{-\psi a}}_{\substack{\text{electrostatic} \\ \text{double layer} \\ \text{repulsion}}} - \left[\underbrace{K_2 a^3 X^{-3}}_{\substack{\text{magnetic} \\ \text{attraction}}} + \underbrace{K_3 X^{-6}}_{\substack{\text{Van der Waals} \\ \text{attraction}}} \right] \quad (2)$$

where K_1 , K_2 , K_3 are constants, a is particle radius, X interparticle distance, and ψ the electrokinetic potential which is a function of the charge of the double layer around the particles. The higher the value of $K_1 e^{-\psi a}$, the more stable the system is. The electrostatic mechanism was established by attaching to the particles various charged surfactants which give the particles different values of ψ (Zeta potential) and determining suspension stability by ultracentrifugation.

In addition, referring to Eq 2, the stability of the suspended particles is enhanced by forces of repulsion due to (a) steric hindrance or entropic repulsion, and (b) hydration or in general solvation of adsorbed surfactant molecules. The latter two effects (although difficult to treat mathematically) are known to combine in some aqueous systems creating repulsive forces and an energy barrier which stabilizes the magnetic colloids even in the absence of large electric repulsive fields. For example, stable inks have been made using only uncharged non-ionic surfactants and highly hydrated polyoxyethylenated surfactant layers.

Figures 2 and 3 show typical results of calculations of total energy of interaction E , for Fe_3O_4 particles of 100\AA and 200\AA diameter respectively. The energy is normalized over thermal energy KT . Values of E greater than $10KT$ indicate a stable system (1). The abscissa is the ratio ($S = R/r$) between the interparticle distance R and the radius of the particles r . The electrostatic repulsion force was calculated using the expression of Verwey and Overbeek 15, using a constant $K = 10^6 \text{\AA}$ as the constant Hückel parameter and varying the zeta potential ψ . The force of attraction by Van der Waals energy was derived using the Hamaker expression for spheres of arbitrary dimensions, with a constant $A = 10^{-12}$. For the magnetic attraction forces for oleate covered Fe_3O_4 particles with ~12% oleate an experimentally obtained value of $M_s = 2430$ gauss was used rather than the theoretical value for bulk materials. The surface layer of Fe_3O_4 does not contribute to the magnetic properties of the particles, so the saturation magnetization of the particle is less than that of the bulk Fe_3O_4 . Furthermore, precipitated Fe_3O_4 contains around 12% H_2O , which further contributes to a lower value of M_s for particles than for bulk Fe_3O_4 , which is 4500 gauss.

From the above figures, it can be concluded that it is possible to obtain a stable dispersion of Fe_3O_4 particles in water when $\psi \geq 60$ mV and when $r < 200\text{\AA}$. The particles should be prevented from "touching" each other in order that agglomeration does not occur in the presence of a magnetic field. As can be seen from Figure 3, a slow coagulation of the particles may start when $r \geq \sim 200\text{\AA}$. Thus, according to the above calculations, the precipitated magnetite particles with radius less than 200\AA , with zeta potential equal to or greater than 60 mV and with a coating of a thickness of $\sim 20\text{\AA}$, should yield a stable colloid with or without the presence of a magnetic field.

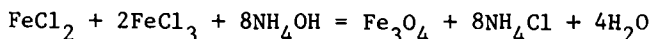
EXPERIMENTAL

As was mentioned in the previous section, the key problems making magnetic ink are:

- (i) Formation of small ($r = 25\text{-}150\text{\AA}$) particles of high saturation magnetization.
- (ii) Formation of a stable colloidal dispersion of these particles water.
- (iii) Modifications of this colloidal system to obtain a printing ink.

(i) Formation of Fe_3O_4 particles

Magnetic particles of the above dimensions can be prepared by chemical precipitation according to:



American Chemical
Society Library
1155 16th St., N.W.

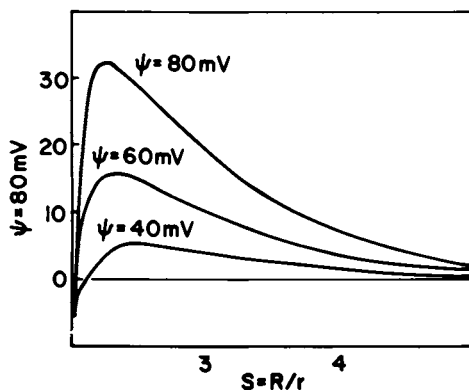
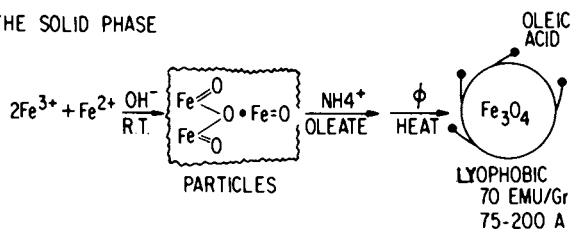


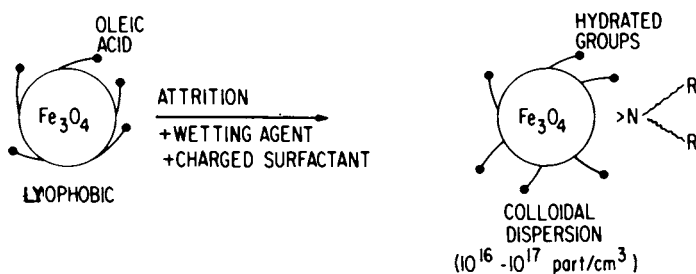
Figure 2. Energies of interaction between two magnetite particles as a function of their separation. Conditions: $r, 100\text{\AA}$; and $\kappa, 1 \times 10^6$.

FLUID SYNTHESIS

A) THE SOLID PHASE



B) THE MAGNETIC FLUID



C) CONVERSION FLUID INTO INK

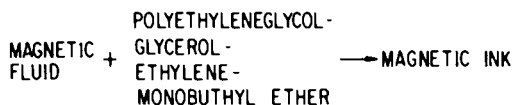


Figure 3. Schematic of the three principal steps in the preparation of magnetic ink for ink jet printing.

When precipitation is carried out from a concentrated solution, in an ultrasonic bath, at room temperature or below, the diameter of the particles formed is 50-250Å.

Ferrous and ferric chloride were separately dissolved in deionized water, then mixed together so that the final solution contained 0.47 M/l Fe^{3+} and 0.27 M/l Fe^{2+} ions. Precipitation with NH_4OH was carried out in an ultrasonic bath and with a mechanical stirrer. The highest magnetic moment of dry Fe_3O_4 was obtained when the ratio of $\text{Fe}^{3+}/\text{Fe}^{2+}$ ions in solution was 1.74 and at pH = 9.5, in agreement with Reimers et al.

In order to prevent the close approach of the particles and thus their agglomeration, after the precipitation was completed (i.e., after the slurry had completely turned black), the Fe_3O_4 particles were coated in situ with ammonium oleate solution in an ultrasonic bath.

It should be pointed out that the role of the oleate is not unique for coating Fe_3O_4 particles. Other long chain organic anions capable of forming insoluble iron salts around Fe_3O_4 particles, such as sodium lauryl sulfate, were also successfully used.

The amount of oleate added was between 9 and 15%, based on the weight of Fe_3O_4 formed. Using 20.5Å^2 /oleate ion and $r = 55\text{Å}$ for an average Fe_3O_4 particle, then the above amounts correspond to a coverage of 0.4 to 0.6 fraction of a monolayer. A subsequent heating of the slurry to 100°C resulted in an increase of the magnetic moment and fast settling of the particles due to formation of water insoluble iron soap around them. Magnetite is then washed from NH_4Cl by decantation. After rinsing, coated Fe_3O_4 particles are separated from excess water in a centrifuge (3000 rpm).

A typical size distribution of the particles (as analyzed by TEM and micrographs printed at 200,000 magnification) is given in Table I.

Table I

Number of particles:	2	19	39	20	12	3	3	1	1
Maximum dia Å	50	75	100	125	150	175	200	225	250

Mean: $113 \pm 36\text{Å}$

The saturation magnetization of the dry powder varied between 66-76 emu/g depending upon the amount of oleate added.

(ii) Formation of colloidal dispersion

Coated magnetite particles have to be wetted in order to disperse them in water. Alkylaryl polyether alcohols with 10-15 moles of ethylene oxide are adsorbed on oleate coated Fe_3O_4 particles and thus make them wettable. Triton N-101 (Rohm and Hass), which is polyoxyethylenated nonylphenol

with 9-10 moles ethylene oxide is a very effective wetting agent. It is interesting to mention that Triton N-101 does not adsorb on "bare" Fe_3O_4 , but only on coated particles. This adsorption probably takes place with the hydrocarbon end of the Triton molecule toward the oleate, and the ethylene oxide groups toward water. The amount of non-ionic surfactant adsorbed was 10-20% based on the stoichiometric amount of magnetite formed.

Figure 3 illustrates the different steps of the process for the synthesis of these fluids. The result of Step A is a liophobic system obtained by chemisorption and this system is stable in non polar solvents but incompatible with aqueous solutions. To produce the water base ink, Step B is necessary where physical absorption of the secondary surfactant occurs on the hydrocarbon side of the chemisorbed oleic acid molecules creating a "double surfactant layer" around the particles. This model is in agreement with the one proposed by Rosenweigh and Shimoisaka.

Colloidal stability was achieved by adsorption of a cationic surfactant such as amines or quaternary ammonium compounds on the oleate-coated particles. Mono or dialkyl quaternary ammonium compounds with an alkyl chain of between 6 and 18C atoms give magnetite particles a large positive zeta potential (~ 70 mV). An ethoxylated quaternary ammonium compound (such as Ethoquad 0/12 - Armak Chem Div) can also be used as a dispersing agent. The amount of cationic surfactant was 2-6% based on Fe_3O_4 . It should be pointed out that the amount of surfactants used affect the ink yield (i.e., the amount of Fe_3O_4 transferred into a dispersion) and the viscosity. For a given concentration, or, more accurately, for a given surface area of Fe_3O_4 particles in a system, there is a minimum in the viscosity-concentration of the surfactant curve. When the ratio (surfactant/ Fe_3O_4) is small, the interaction between particles gives rise to high viscosity or even to gel formation. On the other hand, when this ratio is large, i.e., when the product of surfactant molecules or ions and their adsorbing area exceeds available Fe_3O_4 area, then micelle formation takes place. This condition gives rise to an increase in viscosity.

Mixing of water and wet Fe_3O_4 with cationic and non-ionic surfactants can be carried out in a blender (for 5-10 minutes) or in a ball type mill (attritor) for ~ 2 h. After mixing, the dispersion is heated in a hot water bath for 3 hours at 90-95°C. This "digestion" enhances the ink yield and colloidal stability (measured in a centrifuge at 16000 rpm). Undispersed Fe_3O_4 and surfactants are separated from the magnetic ink in the centrifuge (2h at 3000 rpm).

Example 18. The hydrates, 378g $\text{FeCl}_3 \cdot 6\text{H}_2\text{O}$ and 160g $\text{FeCl}_2 \cdot 4\text{H}_2\text{O}$ were separately dissolved in deionized water

stirring and in an ultrasonic bath. When the slurry turned black, a solution containing between 16-25g oleic acid and 15cc-NH₄OH in 250cc H₂O was slowly added (~30 minutes). The slurry was kept in the ultrasonic bath for another 20-30 minutes, then heated to the boiling point. The particles were allowed to settle and then rinsed with hot deionized water a few times. The excess water from the particles was removed in a centrifuge.

Wet magnetic pigment after centrifugation was mixed with some 70-100g water, 30g Triton N-101 (Rohm and Hass), and 7g Arquad 2HT-75 (75% active; Armak Chem Div) which is dimethyl dialkyl quaternary ammonium chloride and the alkyl groups are 24% hexadecyl, 75% octadecyl and 1% octadecenyl. Arquad 2HT-75 can be replaced with 10g Ethoquad O/12 (Armak Chem Div) which is monoalkyl (octadecenyl) monomethyl quaternary chloride with two moles of ethylene oxide. After thorough mixing of magnetic particles with the surfactants in an attritor (ball mill type) for 2 hours, the mixture was heated in a water bath at 90-95°C for 3 hours, then allowed to cool down. Undispersed particles were separated from the magnetic fluid in a centrifuge (2h at 3000 rpm). The magnetic fluid thus obtained has a magnetic moment between 24-28 emu/g (34-40% W Fe₃O₄). Brookfield viscosity at 60 rpm was 11-17 cp, pH, 6-7 and surface tension was 28-30 dynes/cm. Viscosity of these fluids is non-Newtonian. The sedimentation velocity in the centrifuge (at 16000 rpm) was found to be between 0.4 and 2 x 10⁻¹¹ sec⁻¹ or calculated terminal velocity in a gravitation field between 0.1 and 1 cm/year. Circulation of an ink through a magnetic ink jet printer in the presence of a magnetic field did not show agglomeration.

Literature Cited

1. Neuringer, J. L. and Rosensweig, R. E., *Phys Fluids* **7**, 1927 (1964).
2. Bitter, F., *Phys Rev* **41**, 507 (1932).
3. Kaiser, R., U.S. Patent 3,700,595.
4. Moskowitz, R., *Mechanical Engineering*, Feb 1975, p 30.
5. Johnson, Jr., C. E., U.S. Patent 3,510,878.
6. Kazan, B., U. S. Patent 3,287,734.
7. Fan, G. J. and Toupin, R. A., U.S. Patent 3,805,272.
8. Sweet, R. G., *Rev Sci Instr* **36**, 131, (1965).
9. Kamphoefner, F. J., *IEEE Trans on Elect Devices* ED-19, 584, (1972).
10. Kaiser, R. and Miskolczy, G., *J. Appl Phys* **41**, 1064 (1970).
11. Pappel, S. S., and Faber, Jr., O. C., NASA-TN-D, 3288 (1966).
12. Reimers, G. W. and Khalafalla, S. A., *Nat Tech Inf Serv Doc No. MIN-1645*, Dept of Interior, July 1972.

13. Ashley, C. T., Edds, K. E., and Elbert, D. L., IBM J. Res and Dev 21, 69 (1977).
14. Derjaguin, B. V., and Landau, L. D., Acta Physicochim. USSR 14, 633 (1941).
15. Verwey, E. J. W., and Overbeek, J. Th. G., "Theory of the Stability of Lyophobic Colloids," Elsevier, Amsterdam 1948.
16. Brown, Jr., W. F., "Magnetostatic Principles in Ferromagnetism," Intersci Publ Inc., New York, 1962.
17. Hamaker, H. C., Physika 4, 1058 (1937).
18. Kovac, Z. and Gardineer, B., U.S. Patent 3,990, 981.
19. Sambucetti, C. J., and Kovac Z., U.S. Patent 4,107,063.
20. Rosensweigh, R. L., Advances in Electronics and Elechtron Physics, Vol 48, Academz Inz p 103-199 - (1979).

RECEIVED June 18, 1982

Kinetics of Formation, Magnetic Moment, and Stability of Colloidal Magnetite

MARIA RONAY

IBM, Thomas J. Watson Research Center, Yorktown Heights, NY 10598

The transformation of the jointly precipitated mixture of ferrous and ferric hydroxides to colloidal magnetite of 50-100 Å diameter was studied by the continuous measurement of the magnetic moment. At large excess of ammonia magnetite forms at a fast rate by grain boundary nucleation and the transformation is complete. At small excess ammonia transformation is slow, diffusion controlled and incomplete. Magnetite produced in a magnetic field gradient has a saturation moment, 96.5 emu/g, that is larger than when produced without a magnetic field, 92 emu/g. In the course of the spontaneous oxidation of magnetite to γ -Fe₂O₃ the magnetic moment of the particles changes linearly with the Fe²⁺/Fe³⁺ ratio between that of pure magnetite and pure γ -Fe₂O₃. Implications to magnetic inkjet printing are discussed.

Magnetite belongs to the family of ferrites with a spinel structure, described by the general formula MeFe₂O₄, where Me represents a divalent metal ion. In the case of magnetite the divalent ion is iron. Natural magnetite exhibits a wide variation in composition; ideally it contains Fe²⁺ and Fe³⁺ in the ratio 0.5. The smallest cell of the spinel lattice that has cubic symmetry contains eight "molecules" of MeFe₂O₄. The relatively large oxygen ions form an f.c.c. lattice. In this cubic close-packed structure two kinds of interstitial sites occur, the tetrahedral and the octahedral sites. Of the 64 tetrahedral and 32 octahedral sites only 8 and 16 respectively are occupied by metal ions (called A and B sites). In normal spinels the eight divalent ions occupy

the eight available tetrahedral sites and the sixteen trivalent ions the sixteen octahedral sites. In magnetite, which is an inverse spinel, the bivalent iron ions together with half of the trivalent iron ions are distributed at random over the octahedral sites, the other half of the trivalent ions occupying the tetrahedral sites giving $(\text{Fe}^{3+}[\text{Fe}^{2+}\text{Fe}^{3+}]\text{O}_4)$ (1).

Because of the relative magnitudes of the exchange interactions one may expect the spins of the A and B ions in ferrites with spinel structure to be oppositely oriented, so that when $T = 0$, there will be two saturated and oppositely magnetized sublattices present. The resulting magnetization is thus the difference between the magnetization of the octahedral lattice (B) and that of the tetrahedral lattice (A). This was first postulated by Néel (2). For magnetite the resultant moment is that of the ferrous ion, which at $T = 0$ is predicted to be 4 Bohr magnetons.

Synthetic magnetite was made by Lefort (3) by wet chemical reaction already in 1852. A solution containing ferrous and ferric sulphates in a proportion 1:2, poured into a boiling solution of NaOH, gives a near colloidal precipitate. Krause and Tulecki (4) in 1931 precipitated magnetite at 18°C by adding ammonia to a mixed solution of ferrous and ferric chlorides yielding colloidal magnetite. Magnetite can also be produced by the partial oxidation of ferrous hydroxide; this reaction however leads to magnetite crystals that are larger than colloidal (5)

Owing to the brilliant black color of magnetite a process similar to the above one was patented in 1905 for producing printing ink (6), but it was not until the seventies with the invention of the magnetic inkjet printer that a printing process depended on the magnetic properties of the ink.

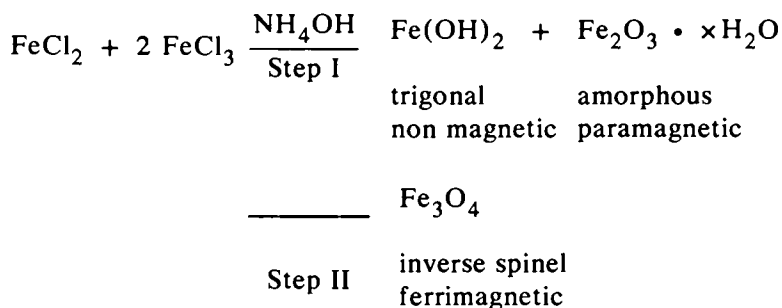
A magnetic inkjet printer (7) uses a continuous high speed capillary jet of a magnetic fluid. By direct periodic magnetic excitation uniform drops are generated from the jet. To create characters, single drops are magnetically selected, deflected in one direction and recirculated. The remaining drops are magnetically deflected in a direction orthogonal to the first, while the paper moves perpendicular to the direction of drop deflection.

The magnetic fluid to be used in inkjet printing should exhibit a fast magnetization in response to an applied magnetic field and a rapid decay of the resultant moment upon removal of the field, as well as a high saturation magnetization. Also, the magnetic particles ought to be very small and monodispersed in order to go through a nozzle of about

50 μm diameter. Beyond the magnetic requirements, an ink for inkjet printing must fulfill a number of other requirements such as, an aiming stability (i.e. the jet direction should not "wander") and the nozzle should not become clogged, both of which are related to agglomeration. Requirements for inks for an electrostatic inkjet printer are given in reference 8, most of which are relevant to magnetic inks as well.

Pure bulk natural magnetite has a saturation moment of 92 emu/g and its color is brilliant black. It can be synthesized in colloidal size, which makes it the first candidate for the pigment of magnetic inkjet ink. The question arises: Are the magnetic properties of the synthetic colloid the same as those of natural bulk magnetite? In the author's laboratory, magnetic inks were produced by precipitating magnetite from a mixture of ferrous and ferric chlorides with ammonia and coating the particles immediately with ammonium oleate to prevent agglomeration, while colloidal stability was achieved by the adsorption of a cationic surfactant such as amines or quaternary ammonium compounds on oleate coated particles (9). The question arises whether the magnetic moment of the particles develops before it is coated with surfactant. If not, will it fully develop after it is coated with surfactant? To answer these questions the kinetics of the magnetite formation need to be known. Also the reliable operation of a magnetic inkjet printer puts great demands on the magnetic and chemical stability of the ink. The aim of the work to be reported here was the study of the kinetics of formation and of the magnetic moment and stability of colloidal magnetite. The main results of this study have been disclosed (10).

Since magnetite precipitated at or below room temperature with ammonia from a solution of a mixture of ferrous and ferric chlorides has the smallest particle size, this is the reaction we studied. The reaction takes place in two steps:



Step I is the joint precipitation of an intimate mixture of $\text{Fe}(\text{OH})_2$ and $\text{Fe}_2\text{O}_3 \cdot x \text{H}_2\text{O}$ by chemical reaction which takes place instantaneously. This product *in statu nascendi* has practically no magnetic moment. (The paramagnetic susceptibility of $\text{Fe}_2\text{O}_3 \cdot x \text{H}_2\text{O}$ produced as given is $X_g = 60 - 80 \cdot 10^{-6}$ emu/g). The second step is the transformation of $\text{Fe}(\text{OH})_2$ and $\text{Fe}_2\text{O}_3 \cdot x \text{H}_2\text{O}$ to magnetite. Because the transformation product is magnetic, the transformation can be followed by the continuous measurement of the magnetic moment. It will be shown that the time dependence of this transformation and the extent to which it takes place depends on the amount of ammonia added in Step I.

Experimental conditions

The chemical reaction. Baker analyzed reagents were dissolved in distilled and demineralized water of 0.18 M Ω resistivity. The alkyl benzene sulphonate concentration indicative of the surfactant content was less than 0.001/10⁶. Since ferrous ions oxidize readily to ferric ions, to counteract this the quantity of ferric chloride to be used in the reaction was less than equivalent. Reimers and Khalafalla (11) found that the saturation magnetization of magnetite prepared by this reaction was the highest when the initial ratio of $\text{Fe}^{3+}/\text{Fe}^{2+}$ was 1.75 instead of the stoichiometric 2, and this was the ratio we used. Typically 4 g of $\text{FeCl}_2 \cdot 4 \text{H}_2\text{O}$ and 9.45 g $\text{FeCl}_3 \cdot 6 \text{H}_2\text{O}$ were dissolved in 125 ml water and cooled to +10°C. Separately 18.66 g NH_4OH (58%) were dissolved in 75 ml water and cooled to +10°C. This amount of ammonia is four times the equivalent amount, designated 4E, required for the amounts of ferrous and ferric salts. Reactions were also made in which 3E, 2.75E, 2.4E and 2E ammonia was used. In some of the reactions the ammonia was added at a slow rate (15 ml/min), in others at a quick rate (3 ml/sec) under continuous manual stirring. In one reaction together with the ammonia 0.1E oleic acid was added, in another 0.1E Ethomeen C-25 was added to the ferrous and ferric solution. Ethomeen C-25 (Armour Industrial Chemical Co.) is a (15) polyoxyethylene-dodecyl (coconut oil) amine and is a cationic surfactant. After the desired amount of ammonia was added at the desired rate, a sample was taken from the suspension into a preweighted plastic vial for the measurement of the magnetic moment. During the measurement the vial was closed and its total weight determined after the measurement.

The measurement of the magnetic moment. A force type measurement was used to determine the magnetic moment following the design of Bozorth and Williams (12) in which strain gauges are used to detect the displacement. In the instrument the sample is contained in a small balancing coil on the end of a phenolic sample rod. The sample holder is placed between the poles of an electromagnet. In this instrument the horizontal deflection of the sample bends a thin vane to which the sample rod is attached. Four strain gauges are mounted on the flexible vane in Wheatstone bridge arrangement, two on either side of the vane. The measurement procedure involves returning the sample holder to zero position by a current in the balancing coil; this nullifies the sample moment. The current in this coil is a direct measure of the magnetic moment. The unbalanced condition is detected by an amplifier. The magnetic moment σ of a sample was calculated by the formula $\sigma = i \cdot 0.0349/w$ emu/g, where i is the balancing current in amperes and w is the weight of the sample in grams (total weight - vial weight). The constant 0.0349 is determined by calibrating the instrument with nickel. When the magnetic moment of the suspension was measured as a function of time to follow the transformation to magnetite, the measurement was made in a magnetic field of 13K Oe. Since the suspension contained magnetite, water, excess ammonia in varying amounts, and a side product of the reaction NH_4Cl , the magnetic moment of the suspension was multiplied by a factor consisting of the ratio of the total weight of reagents over the theoretical Fe_3O_4 yield of the reaction, both in grams. The theoretical yield of the reaction is 4.246 g.

When the magnetic moment of a magnetite powder or suspension was measured as a reaction product and the time dependence was not a concern, the magnetic moment was measured in the magnetic fields $H = 2, 4, 6, 8, 10, 12$ and 13K Oe and the measured values were plotted against $1/H$ and extrapolated to infinite field ($1/H = 0$) to get the value for the saturation magnetization denoted σ_s .

Chemical reaction in a magnetic field. When ferrous and ferric chloride solutions are reacted with ammonia, the side product of this reaction is NH_4Cl in water. It is difficult to separate this from the magnetite particles due to their colloidal size. In order to make the transformation to magnetite complete as well as to facilitate the removal of NH_4Cl , the precipitation from the ferrous and ferric solution with ammonia, both the transformation to magnetite as well as the decantation, was made in a magnetic field gradient. The aim was to make magnetite with the highest possible magnetic moment. The magnetic

field gradient was produced by putting two wedges made of steel between the poles of a large electromagnet. The opening of the wedges was 36° . The gradient of magnetic field inside the opening was 2K Oe/cm. A wedge shaped reaction vessel to fit the opening was made of quartz. The ratio and dilution of the ferrous and ferric salts was the same as given previously. In every reaction 4E ammonia was added also in the dilution given. The ferrous and ferric solutions were cooled to $+10^\circ\text{C}$ and placed in the magnetic field. The ammonia solution was added at the slow rate applying careful manual stirring. When the stirring stopped, the black precipitate settled to the bottom of the wedge. After time was allowed for the transformation to take place, determined from the kinetic studies, the clear solution from the top was sucked off with a syringe. Washing took place by manual stirring with the wash fluid while the magnetic field was turned off. Subsequently the magnetic field was turned on, the precipitate settled, and the wash fluid sucked off with a syringe. Washing was repeated three times. The magnetic moment and the $\text{Fe}^{2+}/\text{Fe}^{3+}$ ratio of the suspension were determined immediately.

Chemical analysis Chemical analyses on suspension or powder samples were performed by a volumetric method (0.05 normal potassium dichromate) following dissolution in hydrochloric acid. The ferrous (Fe^{2+}) content was determined directly. The ferric (Fe^{3+}) content was analyzed via the Zimmermann-Reinhardt (SnCl_2 reduction) technique, which gives the total iron. Subtraction of the Fe^{2+} gives the desired Fe^{3+} value. The $\text{Fe}^{2+}/\text{Fe}^{3+}$ ratio was determined with an accuracy of ± 0.01 . The accuracy of the determination of the total iron was $\pm 0.5\%$ of the result. Chloride content was determined by Volhard titration with an accuracy of $\pm 5\%$ of the result. Nitrogen content was analyzed with the Nessler method with a relative accuracy of $\pm 15\%$.

Structure analysis. The particles were suspended in alcohol and put on a carbon substrate. They were examined in a Philips 301 electron microscope. Bright field, dark field and interference image micrographs on a high resolution stage were taken as well as transmission electron diffraction patterns. The lattice parameter of powders was determined by X-ray diffraction using Cu K_α radiation.

Results and interpretation

Kinetics of magnetite formation. After the chemical reaction was performed with the amount of ammonia and at the rate indicated, the magnetic moment of the suspension was measured continuously in order to follow the time dependence of the transformation to magnetite. It was found that the rate of transformation and the extent of transformation as indicated by the final moment is greatly influenced by the amount of ammonia and the rate it was added in Step I. Examples of the transformations are shown in Figure 1. It is to be seen that the more ammonia is added in Step I, the faster the transformation takes place. Surfactants lower somewhat the rate of transformation. The final moments achieved under the various conditions are given in Table I. These numbers show the extent to which the transformation took place, since their calculation was based on the assumption that the transformation took place to completion. These are not precise, absolute values and, since they were measured at only one field strength, they do not give the (larger) value of saturation magnetization. Such values will be given in the next section. Table I. shows that the magnetic moment at the end of the transformation is about 90 emu/g when the ammonia was between 2.4–4 equivalent and was added slowly. The same amount of ammonia added quickly produced a final moment of around 82 emu/g. When the ammonia is 2E and is added slowly, the final moment is 67 emu/g. The same ammonia added quickly produces the lowest final moment of about 60 emu/g. Similar low moment is achieved if, with the same rate and same total amount of ammonia, the ferrous and ferric hydroxides are precipitated separately and mixed together subsequently. While the presence of 0.1E Ethomeen C-25 does not affect the final moment, 0.1E oleic acid added together with 3E ammonia at a quick rate results in a final moment of 76 emu/g, compared to 82 emu/g resulting from the same reaction without oleic acid. It has been reported that the moment of $\sim 100\text{\AA}$ diameter NiFe_2O_4 particles decreases when coated with oleic acid (13). Continued investigation has demonstrated that the apparent moment decrease is due to strong pinning of the spins of those ferrite cations that are bonded to the organic molecules. (14).

The experimental determination of the magnetic moment as a function of time enables us to find the ζ - t relations, where $\zeta = V^B/V$ is the volume fraction transformed at time t . Avrami (15) proposed that for a three-dimensional nucleation and growth process we should use the general relation

$$\zeta = 1 - \exp(-kt^n) \quad (1)$$

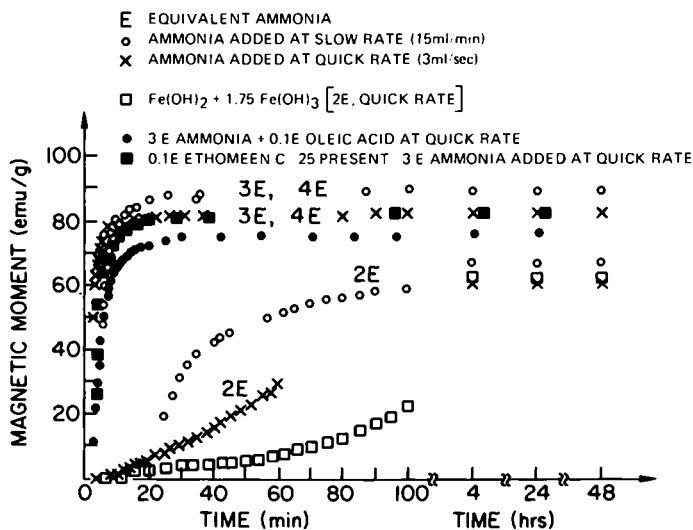


Figure 1. Transformation of the jointly precipitated ferrous and ferric hydroxides to magnetite for different amounts of ammonia added at different rates in Step 1. Also shown is the effect of surfactants and the transformation of separately pre-precipitated and subsequently mixed hydroxides.

Table I.

The magnetic moment of magnetite
at the end of transformation.

Sample	ammonia equivalent	rate added	σ emu/g
M25M	4	slow	89.68
M26M	4	quick	81.6
M23M	3	slow	88.3
M22M	3	quick	81.9
M29M	3	quick Ethomeen	82.27
M28M	3	quick oleic	75.9
M34M	2.75	slow	90.2
M33M	2.75	quick	82.4
M32M	2.4	slow	88.96
M35M	2.4	quick	81.2
M20M	2	slow	67.16
M21M	2	quick	60.52
M30M	2	quick hydroxides	62.5

where k is the rate constant and $3 < n < 4$. This should cover all cases in which ${}^{\vee}I$, the nucleation rate per unit volume, is some decreasing function of time up to the limit when ${}^{\vee}I$ is constant ($n=4$). The exponential growth law summarized in Eq. (1) is valid for linear growth under most circumstances and approximately valid for the early stages of diffusion controlled growth. Plotting $\log \log [1/(1 - \zeta)]$ against $\log t$, the slope of the line gives n . The value of n is indicative of the kinetic process (16). The existence of a straight line relationship might be thought to imply random volume nucleation since the kinetic law of a transformation nucleated on grain boundary surfaces, grain edges or corners can not be expressed in the simple form of Eq. (1). We will see that this is not so. We plotted the results of a few of the kinetic investigations in the form described above. ζ was taken as the ratio of the magnetic moment at time t over the final magnetic moment, and t was given in seconds. Figure 2 shows $\log \log [1/(1 - \zeta)]$ as a function of $\log t$ for the transformations where 2.75E, or 3E ammonia was added at a slow rate as well as for transformations where 3E and 4E ammonia were added at a quick rate. In the two former cases the plot consists of two straight lines of slopes four and one, with an intermediate region over which the slope decreases. In the 3E Q case a disappearing slope 4 is indicated by a single point, and in the case of 4E Q slope 4 disappears completely and only slope 1 is recorded. Figure 3 shows the transformation when 3E ammonia is added at a quick rate, but in the presence of 0.1E Ethomeen C-25, or added together with 0.1E oleic acid. Since surfactants lower the rate of transformation, here the plot clearly shows the two straight lines of slope four and one.

Consider that nucleation is on grain boundary surfaces (16). When the kinetic parameter $a^B = ({}^B I u^2)^{1/3} t$, where ${}^B I$ is nucleation rate per unit area of grain boundary and u is the growth velocity, is very small, the kinetic law approaches the limiting form

$$\zeta = 1 - \exp(-\pi {}^{\vee} I^B u^3 t^4 / 3) \quad (2)$$

where ${}^{\vee} I^B$ is the grain boundary nucleation rate per unit volume. This expression is identical with Eq. (1), so that ζ depends only on the nucleation rate per unit volume, irrespective of where the nuclei are formed. When a^B is very large, the kinetic law has another limiting form

$$\zeta = 1 - \exp(-2 {}^{\vee} O^B u t) \quad (3)$$

where ${}^{\vee} O^B$ is the grain boundary area per unit volume. The $\log \log [1/(1 - \zeta)]$ versus $\log t$ plot thus consists of two straight lines of slopes

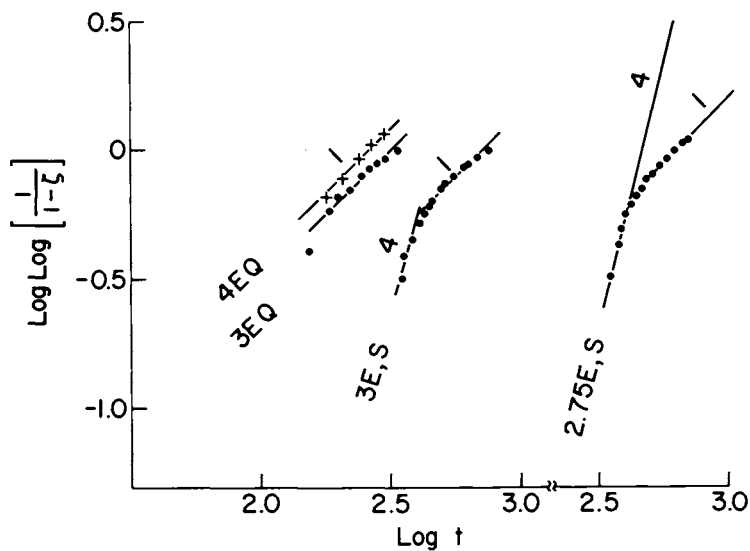


Figure 2. $\text{Log Log} [1/(1 - \zeta)]$ as a function of $\text{log } t$ for transformations where 2.75E and 3E ammonia was added at a slow rate (S), and where 3E and 4E ammonia was added at a quick rate (Q).

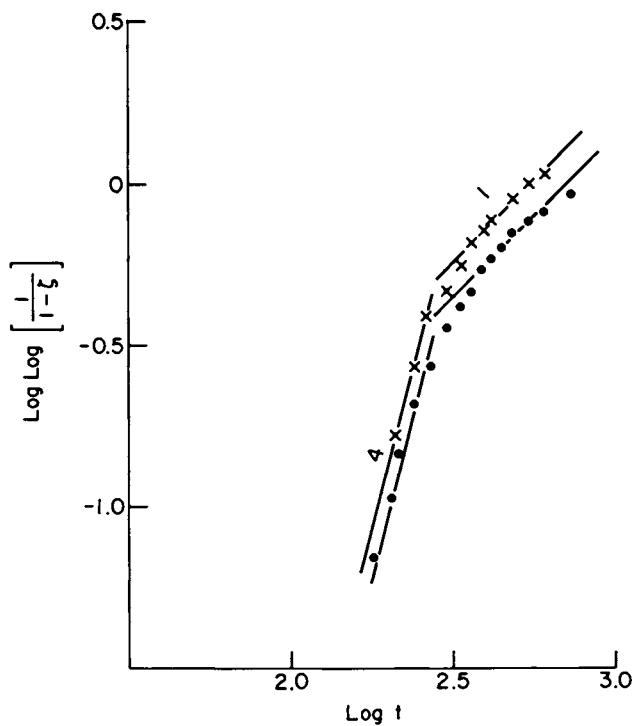


Figure 3. $\text{Log Log } [1/(1 - \zeta)]$ as a function of $\text{log } t$ when 3E ammonia is added in the presence of 0.1E Ethomeen C-25 (\times), or added together with 0.1E oleic acid (\bullet), both at a quick rate.

four and one; such is the plot for all grain boundary nucleated reactions. The physical explanation for the change in the slope was termed by Cahn "site saturation" (16). We cannot expect that the change in slope can always be observed. It is probable that the whole observable range of reaction will correspond to one or other of the straight line regions even when nucleation is confined to the grain boundaries. Site saturation will be observed if it occurs when $\zeta \approx 0.5$. It was shown (16) that site saturation occurs at half reaction when

$$v_I^B \approx 6 \times 10^3 u / (L^B)^4 \quad (4)$$

where L^B is the mean grain diameter. For values of v_I^B smaller than some value near that given by this equation, saturation of nucleation sites will not occur until a late stage of the reaction, and the kinetics are equivalent to those of random volume nucleation. For larger values of v_I^B , saturation occurs early in the reaction. Only for a small critical range, where the condition in Eq. (4) holds almost exactly, should the change be discernible on a $\log \log [1/(1 - \zeta)]$ versus $\log t$ plot.

Figure 4 shows this plot for the transformation when the ferrous and ferric hydroxides were precipitated separately by the quick addition of the sum of 2E ammonia and mixed together subsequently. The plot consists of two straight lines of slopes 1 and 2.5. When 2E ammonia was added to the mixture of ferrous and ferric solutions quickly the slopes were 1 followed by 1.85; when added slowly, the slopes were 1 and 1.82. Slope 1 indicates grain boundary nucleation after saturation. Slopes between 1.5 and 2.5 are indicative of diffusion controlled growth from small dimensions (16). Note that the curve for 2E Q seems to begin with a larger slope.

When the reaction takes place with a large excess of ammonia, 2.75E or greater, and the slopes 4 followed by 1 indicate grain boundary nucleation, a possible mechanism for magnetite formation is that the boundary surface of the ferric hydroxide reacts with Fe^{2+} ions in solution. There are two arguments supporting this mechanism. It is known that $\text{Fe}(\text{OH})_2$ is soluble in excess ammonia in the presence of ammonium salts, so there is a supply of Fe^{2+} in solution. The other argument is based on Figure 5 which shows the change in pH of the ferrous and ferric solution upon the addition of ammonia at 10°C . The isoelectric point of $\text{Fe}(\text{OH})_3$ is at $\text{pH} \approx 7.7$ (Reference 4). The pH at 2.75E ammonia is 9.2 and at 4E ammonia 9.6. As the charge on the $\text{Fe}(\text{OH})_3$ particles becomes more negative with increasing pH, more positive Fe^{2+} ions may be adsorbed.

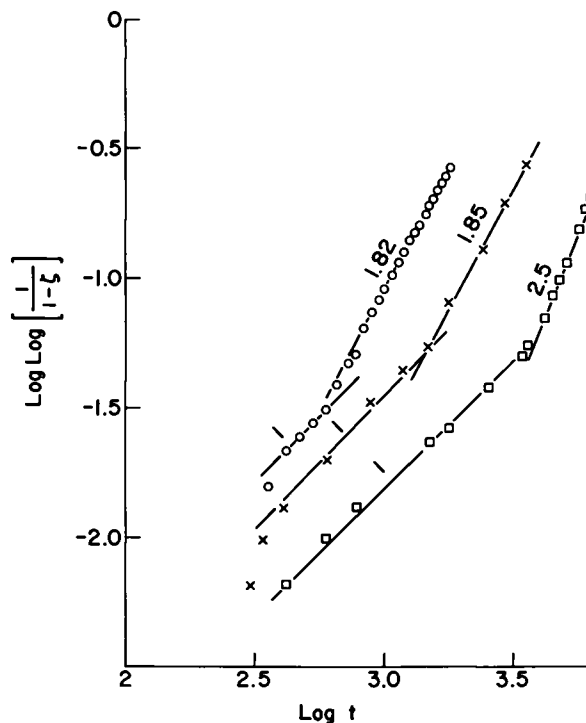


Figure 4. $\text{Log Log} [1/(1 - \zeta)]$ as a function of $\log t$ when ferrous and ferric hydroxides were precipitated separately and mixed together subsequently, also when 2E ammonia was added to the mixture of ferrous and ferric solutions quickly and slowly. Key: \square , hydroxides; \circ , slow; and \times , quick.

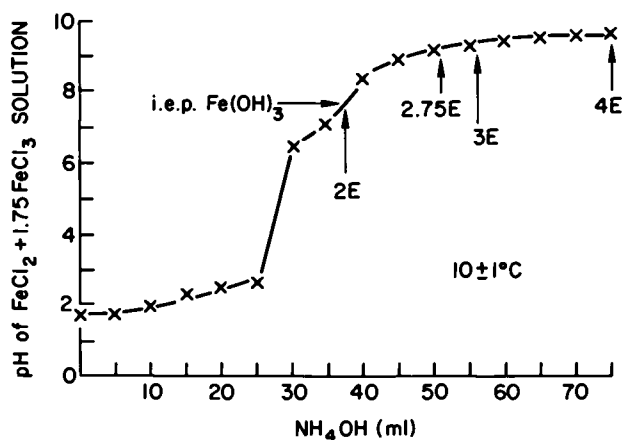


Figure 5. Change in pH of the ferrous and ferric solution upon the addition of ammonia at 10°C . The isoelectric point (i.e.p.) of $\text{Fe}(\text{OH})_3$ is at $\text{pH} \approx 7.7$.

When 2E ammonia was used in the reaction or pre-precipitated (with the sum of 2E ammonia) ferrous and ferric hydroxides were mixed, the slopes were 1 followed by 1.8–2.5 indicating grain boundary nucleation after saturation followed by diffusion controlled growth. In this case magnetite probably nucleates at the boundary between solid ferrous and ferric hydroxide particles and grows by the counterdiffusion of Fe^{2+} and Fe^{3+} cations similarly to its formation in sintering (Wagner mechanism 17). As shown in Figure 5 at 2E ammonia, the pH is 7.5, about the same as the isoelectric point of $\text{Fe}(\text{OH})_3$. Few Fe^{2+} ions would adsorb, but the electrostatic repulsion between the primary particles is small and the particles can interact.

Magnetic moment and stability of magnetite. Magnetite was made and washed in a magnetic field gradient as described in the experimental section. The current proportional to the saturation magnetization of the suspension was determined immediately, as well as the $\text{Fe}^{2+}/\text{Fe}^{3+}$ ratio. After the measurement of the current the vial containing the suspension was placed with its cover open in a vacuum desiccator. After the suspension dried to a powder the current proportional to the powder's saturation magnetization was measured. This current was less than the previous one indicating that the magnetic moment decreased in the course of drying. The $\text{Fe}^{2+}/\text{Fe}^{3+}$ ratio of the dry powder was determined immediately together with total iron, chloride ion and nitrogen content. From these data it was possible to estimate the magnetic moment of magnetite when it was freshly formed and in suspension form. In the formula for the calculation of the saturation moment the current applied for the fresh suspension was used. This, however, was divided by the corrected weight of the powder. The correction took place as follows: First the weight of the powder was reduced by the chloride content (which was on the order of 0.3–0.5%) and with 0.5% of its weight to account for adsorbed humidity. The nitrogen content of the powder was negligible. In the course of drying, the $\text{Fe}^{2+}/\text{Fe}^{3+}$ ratio changed dramatically. If for example this ratio was 0.50 in the suspension, it became 0.31 in the powder. The reason for this change was that part of the magnetite oxidized to maghemite, $\gamma - \text{Fe}_2\text{O}_3$. Upon such oxidation the molecular weight of Fe_3O_4 , $M_1 = 231.55$, becomes larger by $1/2 \text{ O}$, which makes it $M_2 = 239.55$. Denoting the ratio $\text{Fe}^{2+}/\text{Fe}^{3+}$ in the powder r_p and in the suspension r_s ,

the factor to correct the weight of the powder is given as

$$f = \frac{2r_p \times 231.55 + 2(1-r_p) \times 239.5}{2r_s \times 231.55 + 2(1-r_s) \times 239.55}$$

After the corrections for chloride and humidity were made, the weight of the powder was multiplied by this factor.

When magnetite was produced in the magnetic field gradient and washed with water three times, the $\text{Fe}^{2+}/\text{Fe}^{3+}$ ratio was 0.50 ± 0.01 in the suspension, and the saturation moment of magnetite in the suspension was 96.5 emu/g. When magnetite was produced without the magnetic field gradient, the $\text{Fe}^{2+}/\text{Fe}^{3+}$ ratio was again 0.50 ± 0.01 , but the saturation moment was 91.45 emu/g in accordance with the accepted value of 92.0 emu/g. Producing magnetite in a magnetic field gradient thus increases the magnetic moment. The value 96.5 emu/g is the highest ever reported for magnetite. The freshly made suspension was frozen and its saturation moment measured at 250K, 77.2K and 4.2K. The saturation moment was 11% higher at 4.2K and 9.3% higher at 77.2 K than it was at 250K. Neglecting the moment change between R.T. and 250K, the saturation moment of magnetite at 4.2K is 107.1 emu/g if made in a magnetic field gradient.

In the following we made magnetite in the magnetic field gradient, but varied the $\text{Fe}^{2+}/\text{Fe}^{3+}$ ratio. This ratio could be increased to 0.52 or 0.55 by using various dilute solutions of $\text{FeCl}_2 \cdot 4\text{H}_2\text{O}$ for washing instead of pure water. Magnetite with a ratio < 0.50 was made from suspensions with an initial 0.50 ratio by simply letting them stand for various lengths of time in suspension form, or drying them to powder, or a combination of these. The results are given in Figure 6. It shows that the maximum saturation moment is at exactly 0.50 ferrous to ferric ratio corresponding to pure magnetite and its value is 96.5 emu/g. This experiment was repeated four times. The figure shows that in the course of oxidation the magnetic moment of the particles changes linearly with the ferrous to ferric ratio between that of pure magnetite, $\sigma = 96.5$ emu/g, $\text{Fe}^{2+}/\text{Fe}^{3+} = 0.50$ and that of pure maghemite, $\sigma = 73.5$ emu/g, $\text{Fe}^{2+}/\text{Fe}^{3+} = 0$. It is interesting to note that in seven months the particles did not oxidize completely to maghemite, and 17% of the magnetite ($\text{Fe}^{2+}/\text{Fe}^{3+} = 0.085$) was still preserved.

The ease of oxidation is explainable in view of the fact that maghemite has the same spinel lattice as magnetite, but has no divalent ions; two thirds of the octahedral B sites vacated by the divalent iron

ions are occupied by Fe^{3+} ions, the other third remains vacant. The oxidation is accompanied by a small volume decrease. Another contributing factor to the ease of oxidation is the large surface area these particles exhibit. The lattice parameters of two powders with $\text{Fe}^{2+}/\text{Fe}^{3+}$ ratios 0.14 and 0.31 were determined by X-ray diffraction and are marked with crosses in Figure 6. The lattice parameters marked with circles are the standard ones for the pure compounds. It seems that the lattice parameter also changes linearly with the ferrous to ferric ratio.

Particle size. Particle size was determined using transmission electronmicroscopy on samples made in the magnetic field and precipitated with 4E ammonia at a slow rate. Figure 7a shows the particles in bright field and Figure 7b in dark field, both in a magnification of 98,000X. The particle size is in the range of 50–100 Å. Figure 8 shows an interference image micrograph of the same particles using a high resolution stage. The magnification of this picture is 500,000X. The picture shows that the particles are rather perfect. The lattice planes of the magnetite show little evidence for the presence of imperfections or inhomogeneous strain.

The particle size after precipitation in the magnetic field with 3E ammonia is the same as when precipitated with 4E ammonia. Figure 9a shows particles precipitated with 3E ammonia at a quick rate, Figure 9b with 3E ammonia at a slow rate. Figure 9c shows particles precipitated with 2E ammonia at a quick rate and Figure 9d with 2E ammonia at a slow rate. The particles precipitated with 2E ammonia are somewhat larger than those precipitated with 3E and 4E ammonia. The magnetite particles produced by adding ammonia at a fast rate are smaller and more uniform in size than particles produced by adding ammonia at a slow rate. All the pictures shown refer to particles produced in the magnetic field gradient. When the particles are produced without a magnetic field, the size of particles is the same as when the reaction and transformation takes place within the magnetic field gradient. The diffraction pattern of the freshly made magnetite particles in which the $\text{Fe}^{2+}/\text{Fe}^{3+}$ ratio was 0.50 was identical with Fe_3O_4 .

Discussion

The saturation moment of magnetite which was made in a magnetic field gradient is approximately 107.1 emu/g at 4.2K. The relation

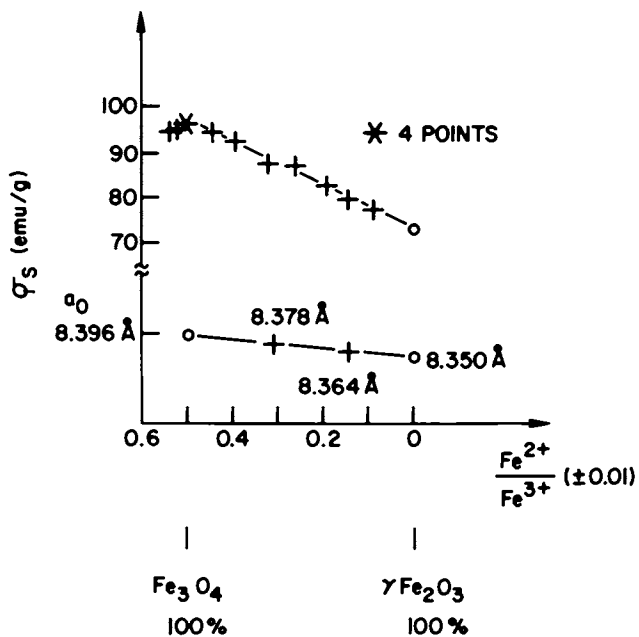


Figure 6. The magnetic moment and lattice parameter as a function of Fe^{2+}/Fe^{3+} ratio.

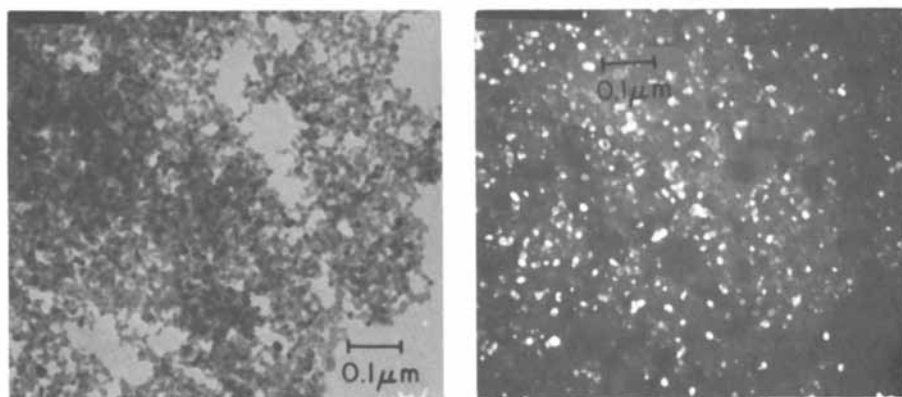


Figure 7. Magnetite particles made with 4E ammonia at a slow rate in the magnetic field gradient, bright field (left) and dark field (right) (68,600 \times).

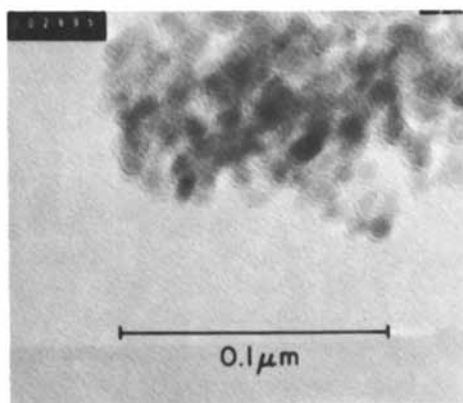


Figure 8. Interference image micrograph of magnetite particles made as in Figure 7 (350,000 \times).

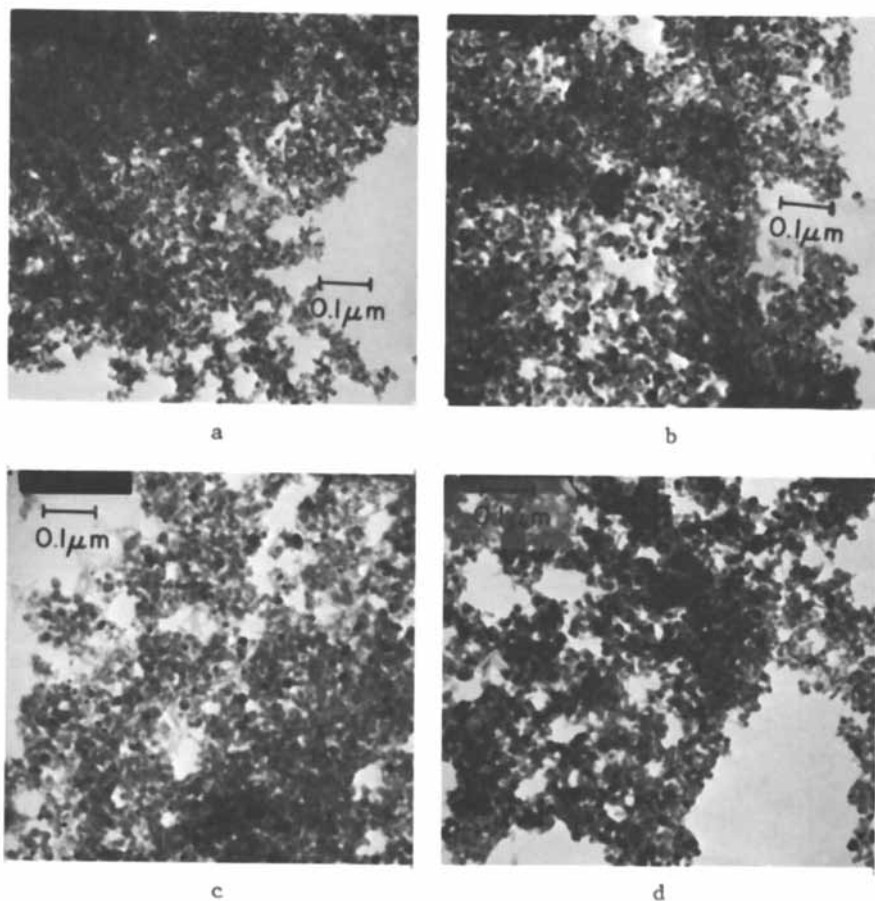


Figure 9. Magnetite particles made with 3E ammonia at a quick rate (a), with 3E ammonia at a slow rate (b), with 2E ammonia at a quick rate (c), and with 2E ammonia at a slow rate (d) (68,600 \times).

between σ at 0 K and the number of Bohr magnetons n_B per molecule Fe_3O_4 is given by

$$n_B = \frac{M}{N \cdot \mu_B} \sigma = \frac{231.55}{5585} 107.1 = 4.44$$

where M is the molecular weight of Fe_3O_4 , N is Avogadro number and μ_B is the magnetic moment of the electron called the Bohr magneton. Substituting the relevant quantities, the saturation magnetization of a Fe_3O_4 molecule at 0 K is 4.44 Bohr magnetons if it was made in a magnetic field gradient. The possible cause for deviation from the theoretical value of 4, which takes only the spin moment into account, is that when magnetite is not made in a magnetic field the orbital moment of the Fe^{2+} ion is "quenched" by the crystalline field. In the presence of a magnetic field, the crystal field is not able to remove the orbital degeneracy, and the orbital moment is of the same order of magnitude as the spin moment. Similarly to magnetic annealing, the effect of a magnetic field applied *in statu nascendi* is permanent.

In the following we discuss the implications of our study to magnetic inks and magnetic inkjet printing. The study of the kinetics of magnetite formation showed that in the case of a large excess of ammonia, which is required to make the transformation complete, oleic acid indeed has to be added very quickly to the suspension if the particles are to be surrounded with a surfactant before the magnetic moment develops. The investigation also showed that the presence of 0.1E oleic acid or Ethomeen C-25 does not affect the mechanism of transformation.

The oxidation of magnetite to maghemite may however have profound consequences on the stability and reliability of magnetic inks for inkjet printing. Welo and Baudisch (18) had already found in 1925 that synthetic Fe_3O_4 particles as well as their magnetic oxidation product $\gamma - \text{Fe}_2\text{O}_3$ are very active catalysts of oxidation. Many substances were oxidized by H_2O_2 only in the presence of these particles. This finding can be explained by the $\gamma - \text{Fe}_2\text{O}_3$ being a p-type oxide and of great surface area. Other p-type oxides (Cu_2O , CoO , NiO) are known to be the most active catalysts of oxidation.

Metal soaps, particularly oleates, are used as driers in the paint, printing ink and linoleum industries to accelerate the change of a liquid oil to an elastic solid by oxidation and polymerization reactions. It has been long established that the metal cation of the metallic soap is responsible for the catalytic activity, and iron soaps are among the most effective. Magnetic inks containing $\text{Fe}_3\text{O}_4 + \gamma - \text{Fe}_2\text{O}_3$ particles

partially coated with oleic acid as well as some iron oleate thus contain powerful catalysts of oxidation and polymerization. When a few drops of dilute H_2O_2 solution is added to oleate-based magnetic inks, they respond with violent and long-lasting gas formation and dry subsequently to a gum-like tough substance. Even though this is a harsh test, the ink in the course of inkjet printing is kept under high pressure in the container and is intermittently thoroughly exposed, in the form of small drops, to air. The possibility of oxidation and polymerization during the repeated recirculation of the ink is there. Even if the degree of such reactions is small and takes place mainly at micelles which are preferred sites of oxidation and polymerization (19), even small and loose agglomerates can cause a wandering of a jet by their radial migration. They can also deposit inside the nozzle causing first a change in the direction of the jet and later the clogging of the nozzle.

To avoid agglomeration, one possibility is to use a saturated fatty acid instead of oleic acid. Also, the use of such surface-active agents that are both oxidation inhibitors and form micelles only at concentrations larger than the ones used is recommended. Examples of such surfactants are the polyoxyethylene fatty amines. Since the critical concentration for micelle formation increases with decreasing alkyl- and increasing ethylene oxide chain length, short alkyl and long polyoxyethylene chains are favorable, such as Ethomeen C-25.

An open question remains whether natural magnetite and a magnetic fluid made of finely ground natural magnetite is not more stable than synthetic colloidal magnetite. Welo and Baudisch (20) reported that the complete oxidation of natural magnetite (size not known) to $\gamma - \text{Fe}_2\text{O}_3$ takes place at a much higher temperature (about 800°C) than the oxidation of synthetic magnetite (about 220°C).

Conclusion

The transformation of the jointly precipitated (Step I) mixture of ferrous and ferric hydroxides to magnetite (Step II) was studied by the continuous measurement of the magnetic moment. It was found that at large excess ammonia, added in Step I, magnetite forms at a fast rate and the transformation is complete. At small excess ammonia the transformation is slow and incomplete. The application of Avrami's theory to the data indicated grain boundary nucleation in the former case and grain boundary nucleation after saturation followed by diffusion controlled growth in the latter case. Mechanisms are proposed for both cases.

It was found that magnetite produced in a magnetic field gradient has a saturation moment, 96.5 emu/g, that is larger than when produced without a magnetic field, 92 emu/g. The saturation moment of a magnetite molecule made in a magnetic field gradient is 4.44 Bohr magnetons at 0 K, instead of the theoretically predicted 4. An explanation for the increase in moment is offered.

The magnetite particle size is in the range 50–100 Å, and the particles are of great perfection. Particle size depends only weakly on the variables investigated in this paper.

In the course of the spontaneous oxidation of magnetite to γ - Fe_2O_3 , the magnetic moment of the particles changes linearly with the $\text{Fe}^{2+}/\text{Fe}^{3+}$ ratio between that of pure magnetite and pure γ - Fe_2O_3 .

Since magnetite, γ - Fe_2O_3 and iron oleate are all powerful catalysts of oxidation, agglomeration due to oxidation and polymerization may take place in magnetic inks based on oleate coated magnetite particles. This may cause aiming instability or clogging if such inks are used in magnetic inkjet printers.

Acknowledgments

I am grateful to P. Chaudhari for drawing my attention to Avrami's theory, indebted to B. L. Gilbert for the chemical analyses, S. Herd for the electron-microscopy, J. W. Mitchell for the use of the magnetometer and H. R. Lilienthal for the low temperature measurements.

Literature Cited

1. Smit, J and Wijn, H. P. J. "Ferrites"; John Wiley and Sons: New York, 1959, p 141.
2. Néel, L. *Ann. de Phys.* 1948, 3, 137-198.
3. Lefort, *Compt. Rend. Acad.* 1852, XXXIV, 488.
4. Krause, A.; Tulecki, J. *Zeit. Anorg. Chem.* 1931, 195, 228.
5. Baudisch; Mayer, *Biochem. Z.* 1920, CVii, 1.
6. Fireman, Peter, U.S. Patent 189,944, Dec. 13, 1905.
7. Fan, G.; Toupin, R. A., U.S. Patent 3,805,272, April 16, 1974.
8. Ashley, C. T.; Edds, K. E.; Elbert, D. L., *IBM J. Res. Develop.* 1977, 21, 69.
9. Kovac, Z.; Sambucetti, C., this meeting. Magnetic inks for magnetic inkjet printing.

10. Ronay, M., IBM Technical Disclosure Bulletin, 1976, 19, 2753-2759, *ibid.* 2760-2763, *ibid.* 1976, 18, 3490-3491.
11. Reimers, G. W.; Khalafalla, S. E., Bureau of Mines Innovative Processes in Extractive Metallurgy Program Technical Progress Report – 59. September 1972. U.S. Department of the Interior.
12. Bozorth, R. M.; Williams, H. J., Phys. Rev. 1956, 103, 572.
13. Berkowitz, A. E.; Lahut, J.A., AIP Conf. Proc. 1973, 10, 966.
14. Berkowitz, A. E.; Lahut, J. A.; Jacobs, I. S.; Levinson, L. M., Phys. Rev. Lett. 1975, 34, 594.
15. Avrami, M. J. Chem. Phys. 1939, 7, 1103; *ibid.* 1940, 8, 212; *ibid.* 1941, 9, 177.
16. Christian, J. W. "The Theory of Transformations in Metals and Alloys," Second edition, Part I; Pergamon Press: Oxford, etc., 1975; p 525-542.
17. Wagner, C., Z. Phys. Chem. 1936, , B34, 309.
18. Welo, L. A.; Baudisch, O., Journal of Biological Chemistry, 1925, LXV, 215.
19. Harkins, W. D., J. Amer. Chem. Soc. 1947, 69, 1428.
20. Welo, L. A.; Baudisch, O., Phil. Mag. S.6. 1925, 50, 399.

RECEIVED April 30, 1982

INDEX

- A**
- Absorbed dye 12*f*
 spectroscopic observations 9–12
 surface coverage 13
- Acetic anhydride 317
- Acid–base transitions, bromocresol
 green 202
- Acid–base transitions, bromothymol
 blue 202
- Acid Violet 14 534
- Acid Violet 19 532
 lightfastness 537*f*
 pH effect 535*f*
 spectral changes 533*f*
- Acidic surfaces 152
- Acidity transfer 219
- Adatoms 124
- Additives in paper formation 498
- Adherants, classification 157
- Adhesion 372
 closest-range forces 161
 photochemical dissipation 372
 thermodynamic work 476
 van der Waals forces 158, 160*f*
 viscosity effects 400
- Adhesion dissipation,
 mechanism 372, 375–377
- Adhesive bond, permanent,
 formation rate 164
- Adhesive failure, nonuniform 400
- Adhesive strength 483*f*, 485*f*
 bonding temperature effect 483*f*
 sizing agent effect 484*t*
- Adsorption entropies, measurement 422
- Adsorption isotherm(s) 285, 424, 427
 cellulose fibers 427
 measurement 422
- Adsorption thermodynamics 427
- AES—*See* Auger spectroscopy
- Aggregate
 energy shift calculation 19
 excited-state interaction 18*f*
 spectral shifts 15
- Aggregate structure, spectroscopic
 observations 15
- Alkaline papermaking 487
- Alkyl ketene dimer 486
- Alois Senefelder 327
- α -Alumina 200
 acidity 207*f*
 acidity alteration 211*f*
 appearance of acid groups 210
 Black Pearls L contact 206
 electrophoretic mobility 214*f*, 215*f*
 intrinsic acidity 206
- α -Alumina catalyst 202
 surface group density 203
- Alumina surface,
 dehydroxylated 200
 α -alumina titers 206
- Alumina-silica catalyst 202
 acidity 205*f*
 surface group density 203
- Aluminum atoms, heat treatment 200
- Aluminum contamination 459, 463
- Ammonia 553, 556
- Ammonium oleate 555
- Amorphous selenium 143, 144*f*
- Angiospermes 496
- Anhydroglucose 471
- Aqueous liquid, penetration 438
- Arachidic acid 95, 121
- Auger electron(s) 457
- Auger electron emission 457
- Auger parameter 469*t*
- Auger spectroscopy 63
- B**
- Bar pattern 269*f*
- Bar spacing 268
- Bar target 266
- Barium sulfate 538
- Basic particles 319*f*
- Basic sulfonates 308
- Basic surfaces 152
- Beating 496
- Beer's Law, integral variation 14
- Behenic acid 106, 108
- Bentonite 317, 319*f*
- Benzene 202, 213
- Bikerman's equation 436
- Binary mixtures, particle
 interactions 197–221
- Binding energy 465*t*
- Bipolar conduction 290*f*
- Bistable behavior 102, 104

- Bistable photochromic system,
energy transfer 100-104
- Black Pearls L 202, 205f, 207f, 220
- α -alumina contact 206
- contact potential difference 217
- electrophoretic mobility 214f, 215f
- titration 208f
- toluene extraction 206
- Black toner 147
- Bleaching 496
- Blocking 161
- Boltzmann's constant 252
- Bond paper, electron spectroscopy
spectra 461f
- BPL—See Black Pearls L
- Bristow's instrument, dynamic wetting 408f
- British Handsheet Machine 500
- Bromocresol green, acid-base
transitions 202
- Bromothymol blue, acid-base
transitions 202
- Bulk conductivity 502, 505, 509f
- measurements
- gallium-indium eutectic liquid
 metal method 508
- stainless steel electrode method 508
- of paper 510, 518f
- paper thickness effect 513-515
- pulp effect 518f
- refining effect 516f
- Bulk conductivity cell 501
- in situ pressure 502-505, 503f
- Bulk diffusion 402
- Bulk electrical conductivity 501
- Bulk resistivity
- Business paper 505
- carbon species 468f
- electron spectroscopy spectra 459
- high filler, electron spectroscopy
 spectra 460f
- hydrocarbon content 471
- oxygen species 468f
- surface atomic concentration 464f
- surface chemistry 455-473
- unsized
- electron spectroscopy spectra 460f
- fitting 466
- n*-Butylamine 202
- C**
- Cadmium sulfide, effective contact 145
- Calcium carbonate 317, 319f, 487
- Calcium oxide 317
- Capillary imbibition 402, 403
- Capillary sorption 410
- Capillary sorption coefficient 438
- Carbon absorption 244
- surface species effect 241
- Carbon black 185, 197-221, 291
- absorbance spectra 243f
- acidity 239
- adsorbed polymer ions 312
- air atmosphere 238f
- back titration 226
- carboxyl group 239
- chemical activity 198
- computer dried 242f
- desorption mechanism 235
- evolved gases 226
- heat treated 235-237
- inert atmosphere 236f
- interparticle scattering 231
- IR spectroscopy 227
- mixture with white solid acids—
 See Binary mixtures
- moisture removal 228
- resolved spectra 232f, 233f, 236f, 238f
- selective neutralization 237-241, 242f
- sodium bicarbonate neutralization 238f
- sodium carbonate neutralization 240f
- sodium carbonate titration 239
- spectral features 231
- sulfur impurities 241
- surface acid groups 199
- surface characteristics 245f
- surface chemical structure 198
- surface oxides 225
- thermogravimetric analysis 236f
- vibrational species 237
- volatile content 226
- weight change 235
- Carbon black absorption 230f, 232f
- potassium bromide disc effects 234f
- Carbon black functional group(s)
 Fourier transform IR
 characterization 225-245
- oxygen 229f
- phenolic-OH group 241
- Carbon black suspensions in
 mineral oil 308
- Carbon compounds 227
- Carbon 1s multiplex spectra,
 curve fitting 467f
- Carbonate filled paper 489f
- properties 490
- Carboxylic acid 235
- Carboxylic acid band 237
- Carboxylic acid groups 372
- Carrier cores 151
- Cavitation 400, 412, 413
- CCA—See Charge control agent
- Cellulose 404, 466, 496
- capillary sorption 410

- Cellulose—*Continued*
- conductivity 519
 - electron spectroscopy 429–431
 - energy values 479
 - surface properties 421–432
 - wetting delay 410
- Cellulose fiber 463
- network
 - anisotropy 513
 - diffusion coefficient 528
 - orientation 502
 - structures, charge transport phenomena 519
 - Cellulose films, surface energetics 480*t*
 - Cellulose microfibrils 496
 - Cellulose paper, wetting delay 407
 - Cellulosic material, water absorption 424
 - Centrifugal former 501, 502
 - Cesium iodide 228
 - Charge carriers 519
 - Charge control agent 322
 - Charge exchange 151–155
 - Charge transfer 213, 219, 259
 - electronic 219
 - kinetic motion 260
 - Charge transport 250–251, 367, 369
 - contactive 257
 - convective 257
 - current 258*f*
 - Charge transport experiments 249–264
 - Charge transport phenomena 494
 - measurement 519
 - Charging 145
 - Charging electrode, stainless steel 186*f*
 - Chemical indicator adsorption 201
 - Chemisorbed oxygen, removal 202
 - Chlorinated polyvinylchloride, zeta potentials 319*f*, 321*t*
 - Chromophores, two-dimensional, copying 104
 - Cleaning 157–161
 - Close-packed monolayers 8
 - Closest-range forces 161
 - Coalescence 130
 - Coated magnetite, dispersion in water 549
 - Coated paper 389, 396
 - drop spreading 445*f*
 - ink 389
 - print density 370*f*
 - surface hardness 364
 - Coating resins 374*t*
 - Coatings 322
 - Cobalt 546
 - Color ink jet printing 531–540
 - Colloid
 - description 282
 - extent of double layers 284
- Colloid—*Continued*
- intermediate conductivity, adsorption isotherms 298
 - mobility 284
 - nonaqueous 281–304
 - characterization 282–285
 - mobility measurement 283
 - properties, intermediate
 - conductivity 295–299
 - Colloidal charges, measurement 284
 - Colloidal magnetite 553–575
 - Colloidal particles, characterization 284
 - Colloids with physically adsorbed surfactant 285
 - Color quality, paper effect 538
 - Color reproduction 531
 - dye parameters 532
 - ink 532
 - paper 534, 538
 - pH effect 534
 - Commercial paper
 - dynamic sorption of ink 441–449
 - physical test measurements 450*t*
 - processing 500
 - Colorants 532
 - Complete condensation 131
 - Composite powders
 - charge levels 187*f*
 - contact charging 183–196
 - preparation 185
 - Conductive base paper, bulk
 - conductivity measurements 508
 - Conductive base paper, transient
 - current plot 507*f*
 - Conductive polymer resin 523
 - Conductivity cell 503*f*
 - bulk 501
 - Conductivity
 - basis weight effect 511*f*
 - contact surface area 519
 - fiber size effect 519
 - water content effect 496
 - Contact, optical 392
 - Contact angle 479
 - measurements 329, 331
 - Contact area 184
 - Contact area development 443
 - Contact charge exchange 213, 220
 - Contact charging, carbon black
 - effects 189, 194*f*
 - Contact charging, dispersion
 - effect 191, 193*f*
 - Contact electrification—*See* Contact charging
 - Contact fraction, paper smoothness
 - effect 393*f*
 - Contact line development 441

Contact potential	226	Developer materials	151
Contact potential difference	216-218	Diamond stylus, engraved	362f
Black Pearls L	217	Dichloromethane	317, 318, 319f
carbon black preparation	216-217	Dielectric, charge exchange	152, 153f
Graphon	217-218	Dielectric polarization	282
Contact resistance	510, 515	Dielectric properties	143
Contactive charge transport	257	Dielectrophoresis	282
Continuous process precipitation	82	3,3'-Diethyl-9-methyl thiocarbo- cyanine bromide, double-banded absorption	41f
Contrast function	268-273	Diffusion coefficient	528
Contrast transfer function	265, 272f	Dimer aggregate, adsorption dipoles	17f
equation	270	Dimers	95
limiting resolution	270	Dimethyl dialkyl quaternary ammonium chloride	551
model	270	dinonylnaphthalene sulfonates	308
Convective charge transport	257	<i>N,N'</i> -Dioctadecyl-indocarbocyanine	100
Copy, separation	105	<i>N,N'</i> -Dioctadecyl- <i>p</i> -phenylenedi- amine	119
Copy monolayer, separation	108	Dioxane	317, 319f
Corona charge, negative	143	Dispersants, acidity	309
Corona charging	143, 144f	Dispersants, basicity	309
Cotton fiber, preparation	471	DLVO theory	312
Cotton linters	519	Donor-sensitizer-acceptor system, radical obtained	119
CPD— <i>See</i> Contact potential difference		Donor-sensitizer-acceptor system supersensitization	119-121
CPVC— <i>See</i> Post-chlorinated polyvinylchloride		Doping	155
Creep compression	395	Double kink	60
Critical growth rate	88	Double-jet method	82
Critical size	84	Double-jet precipitation, nucleation stage	82-88
Cross-direction	498	Double-jet precipitation, stable nuclei	82
Crystal, critical size	84	Driographic plate	342
CTF— <i>See</i> Contrast transfer function		Driography	356
Current, charge transport	258f	Drop area	444f
Cyanine dye	6, 12f	Drop formation	439
absorption	9	Drop penetration	443
epitaxial contact	9	Drop profiles	443
monolayer, spectra	114f	Drop sorption	448
oxidation reactions	36	Drop spreading	437, 479
spectra	114f	Dry inks	335
structures	7f	Dry lubricants	158
Cyanine dye-arachidate matrix	104	Dry model systems, charge exchange	152
Cyanine dye-arachidate monolayer	96	Dry silicone roll	163
Cyanine dye-arachidic acid	97f	Dry transfer xerography	140-147
Cyanine sensitizer, monolayer assembly	114f	Drying inks	389
D			
Dampening system, isopropanol	349	Dye	
Debye length, calculation	313	energy level(s)	74f
Deconvolution, species ratios	470t	effects	75
Density values, measurement	273	light-induced electron spin resonance signals	72
Deposit morphology	132	molecular structure	73f
deposition rate effect	127f	pH effect	535f
temperature effect	127f	water based systems	532, 534
Deryagin equation	313	Dye aggregate-viologen system	118f
Desensitization	77	Dye chromophores	95
Desorption	124	Dye positive holes, formation	75
mechanisms	235		
Developer compositions	165		

- Dynamic sorption apparatus 440f
 Dynamic water absorption 409f
 Dynamic wettability 476
- E**
- Elasticity 415
 Electric charging of particles
 acidic dispersants 309
 basic dispersants 309
 mechanism 307-323
 Electrical conductivity 501
 Electrical conductivity of paper 493-529
 steady-state electrical measure-
 ments 506-519
 Electrical double layer 291
 Electrical plateout 292
 Electrical processes, image formation 493
 Electron-adduct radical 116, 118f
 stabilization 116
 supersensitization 120f
 Electrodeposition tests 308-312
 results 310r
 Electrohydrodynamics 286-291, 290f
 Electron graphic copiers, toner bonding 457
 Electron injection 6
 Electron scanning microscopy 284
 Electron spectroscopy 456, 457
 cellulose 429-431
 extractives on paper 432
 lignin 429-431
 mechanical pulps 430f
 multiplex data 458
 multiplex spectra 463, 462f
 species assigned to chemical shifts 465t
 stearate ester on paper 432
 surface lignin content 431
 wood pulps 430f
 Electron spin resonance, light-
 induced, exposure effect 77
 Electron spin resonance of silver
 bromide microcrystals 71-80
 Electron spin resonance signals,
 light-induced, decay curves 76f
 Electron spin resonance signals,
 light-induced, decay time 76f
 Electron transfer reactions, photo-
 induced 112
 Electron transfer 96
 in monolayer organizes 93-109
 photoinduced 96-100
 sensitizer acceptor system 113, 119
 Electron transfer reactions,
 photoinduced 112
 Electron transmission microscopy 284
 Electron trapping 60
 Electronic charge transfer 219
 Electrophoresis 317
 Electrophoretic displays 300
 Electrophoretic liquid
 development 165-168
 interfaces 167
 Electrophoretic mobility 210-216
 α -alumina 214f
 Black Pearls L 214f, 215f
 characterization by single value 212
 Graphon 214f, 215f
 sample preparation 210
 Electrophotographic fusing, cellulose
 substrate energy 479
 Electrophotographic paper-
 making 486-490
 paper friction 487
 sizing techniques 486
 Electrophotographic printing, paper
 adhesion effects 481-486
 Electrophotography, interfacial
 role 139-174
 Electrophotography, paper chemistry
 effect 475-490
 Electrostatic assist
 dot skipping 360f
 ink meniscus 366f
 roll coverings 369
 side effects 369
 Electrostatic assist process 359, 364
 Electrostatic assist units, power
 supply voltages 367
 Electrostatic charge generation 308-316
 Electrostatic charging mechanism,
 basic dispersants 311f
 Electrostatic force 158
 Electrostatic image,
 development 301f, 302, 303f
 Electrostatic latent image,
 development 147
 Electrostatic stabilizer 295
 Electrostatically assisted ink
 transfer 359-370
 Emulsification rate curves 334, 335, 337f
 Emulsified inks, shortness ratios 342
 Emulsion grain, dye adsorption effect 75
 Energy transfer 96-100, 101f, 103f
 bistable photochromic system 100-104
 Entropic stabilization 167
 Epitaxial attachment 19, 20, 42
 Epitaxial hypothesis 30
 ESCA—See Electron spectroscopy
 ESA process—See Electrostatic assist
 process
 2-Ethyl-1,3-hexanediol 356
 9-Ethyl dye aggregate, silver
 bromide 28f, 29f
 Excitation 98
 Extinction coefficient 535f

- Extrusion coating, cellulose substrate energy 479
- Extrusion coating, paper adhesion effects 481-486
- F**
- Fast development 300
- Feathering 538
- Fe₃O₄—*See* Magnetite
- Ferranti-Shirley cone 416f
- Ferric chloride 549
- Ferrofluid, kerosene-based 544
- Ferromagnetic materials, colloidal dispersion 543
- Ferromagnetic particles 546
- Ferrous chloride 549
- Fiber(s)
- orientation 499f
- surface chromatography, inverse gas chromatography 422-428
- zero surface coverage 428
- Fiber slitting 515
- Fiber surfaces, electron spectroscopy 428-432
- Fibrous materials, transient conduction 519-526
- Filled paper 459
- Film deposition
- conditions 125f
- coverage 132
- experimental 131, 132
- number density 133f
- process 124
- radium 133f
- temperature effect 124
- Film growth, impingement rate 125f
- Film morphology, coalescence 130
- Film morphology, growth 128, 129f, 131
- Film splitting 413
- cavitation 412
- separation force 415
- Final copy, removal 157
- Flocculation, stabilization 307
- Fluid ink, deformation 392
- Fluorescence quenching 98
- Fluorocarbon powder 158
- Fluoropolymer 163
- Fountain solution 353, 389
- dynamic wetting 405-411
- retraction 355
- Fourier transform IR characterization, carboxylic acid band 237
- Fraction ink transfer 391f, 393f
- Frangung mode 380
- Free ink film, splitting 391f
- Free ink film split 398-402
- Friction coefficient 528
- Fusing temperature 164
- FTIR—*See* Fourier transform IR characterization
- Fuse grade, hydrocarbon effect 472f
- Fuse grade, paper roughness effect 476
- Fuse quality 476
- Fused image 477f
- Fusing, bond strength 484
- Fusion 475, 477f
- G**
- Gallium-Indium liquid metal electrode(s) 506, 508
- Gas chromatography, inverse 421, 422-428
- Gelatin 8
- Gliding phase transition 27
- Glucmannans 496
- Gold latensification 46
- Gold sensitization 46
- Granularity 265, 268, 276f
- Graphon 202, 220
- alterations
- contact potential difference 217-218
- electrophoretic mobility 213, 214f, 215f, 216
- Gravure, image carrier 361
- Gravure cylinder 362f, 364
- Gravure printed midtone 365f
- Gravure printing, electrostatically assisted ink transfer 359-370
- Gravure printing nip, charge distribution 365f
- Gravure printing nip, ink deformation 365f
- Gravure printing unit 363f
- Growth, crowding factor 90
- Growth rate 88
- Gymnospermes 496
- Gypsum 10, 42
- H**
- Halftone dot reproduction 394
- Handsheet Machine, British 500
- Hardwood 496
- Hardwood pulp 497f
- Heat of adsorption, isosteric 427
- Hemicellulose 496
- Herringbone aggregates, spectra 25f
- Heat treated carbon blacks 235-237
- Hole injection 171f
- Horizontal contacting method 106
- Hot roll fusing 161, 162f
- electrical power 163
- Hydroxyethers 354
- I**
- Image bonding 455
- Image development, particle charge 302

- Image development, particle/ionic mobility effect 302
- Image differentiation 355
- Image fix 475, 486
- See also* Fusing
- bond strength 484
- two sidedness 487
- Image fixing 161-164
- interfaces 161
- Image formation 134
- electrical processes 493
- Image generation 371-380
- Image quality 265
- Image quality parameters 268
- Image transfer 140, 155-157
- corona-assisted 156f
- humidity effects 155
- paper properties 155
- role of silica 159f
- Imaging performance 379, 380
- Imaging technology 134
- monolayer particle array 134
- Immobilization, letterpress printing 394-398
- In situ measurements, optical technique 284
- In situ pressure bulk 503f
- In situ pressure bulk conductivity cell 502-505
- Inductive charging 249
- Inert matrix 95
- Information storage 94
- Information transfer monolayer manipulation 104, 107f
- Ink 361
- lateral spreading 394
- letterpress 386
- pH effect 534
- press ready 361
- volume resistivities 369f
- water wetting 348
- Ink absorption, and ink impression 387f
- Ink bulging 364
- curvature 366f
- Ink drop, contact angle variations 445f, 446f
- Ink drying, pH effect 412
- Ink drying, solvent evaporation 389
- Ink emulsification, rate determination 332
- Ink emulsification tests 332-334
- single point test methods 334
- Ink emulsion rheology 334-342
- Ink film, filamentation 400
- Ink film, splitting, tack forces 412
- Ink film thickness 390
- Ink holdout 398
- Ink jet ink drop(s)
- contact angle 442t, 451
- contact area development 443
- Ink jet ink drop(s)—*Continued*
- drying time 442t
- dynamic sorption 441-449
- penetration 443
- penetration parameters 442t
- profile development 443
- Ink jet print, magnetic 554
- Ink jet printing 532
- advantage 531
- color 531-540
- ferromagnetic materials 543
- magnetic 543-551
- paper 534, 538
- Ink jet system, magnetic 545f
- Ink jetting, requirements 532
- Ink-paper contact 392, 394
- Ink-paper interactions 385-417
- Ink properties 532
- Ink rheology 398
- Ink rheology and tack force 413
- Ink runnability 327
- Ink setting mechanisms 403
- Ink sorption, and paper structure 449
- Ink transfer 353, 391f
- capillary imbibition 396
- electrostatically assisted 359-370
- fractional 391f, 393f
- influences 390
- paper smoothness 398
- Ink transfer process 364
- Ink vehicle, migration 402
- Ink vehicle, penetration 403
- Ink water interaction 332
- Ink and water mixing 348, 349
- Ink wetting, by water 347
- Inorganic pigments in polymer solutions, zeta potentials 316-322
- Interaction(s)
- ink-paper 385-417
- particle-particle, evaluation 285
- particle-wall, evaluation 285
- particle-wall, force 295
- surfactant and surface 377
- Interaction mechanisms 219
- surface groups 219
- Interfaces 139-174
- carrier and toner 151
- Interfacial surfactant, RAIR spectroscopy 379
- Interfacial surfactant activity, ESCA analysis 377, 379t
- Intermediate conductivity colloid, adsorption isotherms 298
- Intermediate conductivity colloid properties 295-299
- Intermediate conductivity nonaqueous colloids 286, 287f
- Internal sizing 455, 471

Interparticle scattering	231	Letterpress ink	386
Inverse gas chromatography	422-428	transfer	399f
measurements	421	viscosity	401f
Ion diffusion in paper	526, 528	Letterpress printing	386, 390-405
Ionic characteristics	292	fractional coverage calculation	392
Ionic concentrations	284	free ink film split	398-402
Ionic mobility	523, 526	immobilization	394-398
of potassium ion	526	ink-paper contact	392, 394
Ionic species, diffusion coefficient	528	post-transfer phenomena	402-405
Iron	546, 553	pressure	396
Iron hydrogen precipitation,		Light-induced electron spin resonance,	
rate effect	566f	exposure effect	77
Isoexposure curves	48, 50f	Light-induced electron spin resonance	
Isopropanol	349	signals, decay	76f
advantages	349	Light absorption studies	36
effects	351f	Lignin	404, 421, 496
in lithography	349	electron spectroscopy	429-431
role	352-355	Lignin content, surface, electron	
Isosteric heat, measurement	422	spectroscopy	431
Isosteric heat of adsorption	427	Limiting resolution	270
		Liquid development	300, 302
		disadvantages	302
		electrophoretic	165-168
		Liquid immersion development	165
		advantages	165
		counter ions	167
		equipment	166f
		Liquid metal electrode, gallium-	
		indium	506, 508
		Lithographic ink(s)	348
		apparent viscosities	338f
		dot resolution ratings	341f
		dot sharpness	341f
		press performance	342
		printed star targets	341f
		rheological measurements	334
		shortness ratio	340f
		viscosity	335
		yield stress	339f
		Lithographic ink drying, pH effect	414f
		Lithographic fountain solution	353
		dynamic surface tension	
		measurements	329
		Lithographic offset news ink,	
		rheological properties	414f
		Lithographic printing	327
		fountain solution application	410
		pH effect on ink drying	412
		tack forces and ink film splitting	412
		Lithographic process	327-344
		emulsification rate curves	337f
		ink emulsification tests	332-334
		ink emulsion rheology	334-342
		ink film on image area	330f
		plate image area	330f
		polar component of image area	332
		used plate surface energies	332
K			
Kaolin	317, 319f		
Kerosene-based ferrofluid	544		
Kinetic charge transport, apparatus	255f		
Kinetic resistivity	254-260		
apparatus	254		
developer rotation speed	257		
Kinetically enhanced conductivity	249		
Kink, double	60		
Kink, single	60		
Kink site, positive	45		
Krupp's centrifuge technique	158		
L			
Lactones	239		
Laser-doppler spectroscopy	213		
Latensification, density increase	52f		
Latent image	44, 51		
desensitization effect	77		
electrophoretic development	300		
fast development	300		
liquid development	301f		
oxidation	47		
surface electrochemical properties	47		
Latent image fading	79f		
Latent image formation	46		
Latent sub-image	46		
buffer treatment	49f		
control cycle	48		
isoexposure curves	50f		
latensification effect	52		
redox properties	47		
Lateral spreading of ink	394		
calculation	394		

- Lithographic process—
Continued
 virgin ink surface energies 331*t*
 virgin plate surface energies 331*t*
- Lithography
 isopropanol 349, 352–355
 with isopropanol substitutes 355
 simplified 352
 and surface chemistry 327–344
 surface chemistry control 347–357
 viscous flow 348
 without isopropanol 353–355
- Low conductivity 286
- Low conductivity colloid
 electrical transient 294*f*
 mobility distribution 294*f*
 optical transient 294*f*
- Low conductivity nonaqueous
 colloids 287*f*
- Low energy electron diffraction 6
- Lubrication oil dispersants, electro-
 static charge generation 308–316
- Lucas–Washburn equation 436
- M**
- Machine Direction 498
- Maghemite 568, 573
- Magnetic bristles, conduction 150
- Magnetic brush development 150
- Magnetic colloids 546
- Magnetic field, Brookfield viscosity 551
- Magnetic field, surface tension 551
- Magnetic field lines 251*f*
- Magnetic ink
 oleate-based 574
 preparation 548*f*
 preparation problems 547
 requirements 554, 555
- Magnetic ink jet printing 543–551
 printer 554
- Magnetic ink jet system 545*f*
- Magnetic jet 544
- Magnetic moment, measurement 557
- Magnetite 546
 agglomeration prevention 574
 Bohr magnetons 573
 chemical analysis 558
 coated, dispersion in water 549
 colloidal 553–575
 colloidal stability 550, 555
 ease of oxidation 569
- Magnetite
 formation
 in excess ammonia 565
 iron effects 570*f*
 kinetics 559
- Magnetite—*Continued*
 in a magnetic field 568, 571*f*
 mechanism 565
 nucleation rate 562
 pH effect 566*f*
 presence of ammonia, with
 oleic acid 564*f*
 interaction energies 548*f*
 magnetic attraction forces 547
 magnetic moment 555, 561*t*
 measurement 557
 magnetization 554
 mixing with water 550
 oxidation 573
 particle size 569
 ammonia effect 569
 particles 572*f*
 precipitated with iron chlorides 555, 557
 preparation 549, 556
 ammonia addition 556
 preventing particle agglomeration 549
 saturation magnetization 573
 saturation moment 555, 565
 stable dispersion 547
 structure 553
 structure analysis 558
 surface layer 547
 synthetic 554
 transformation 560*f*, 563*f*
 transformation rate 559
 ammonia effect 559
 surfactants effect 559
- Matrix monolayer, rigidity 105
- Mechanical integrity 145
- Mechanical pulps, electron
 spectroscopy 430*f*
- Mechanical pulps, surface lignin
 content 431
- Mercury 506
- Merocyanine 102
- Merocyanine dye 12*f*
- Mesitylene 426
- Metal soaps 573
- Metal–metal contact charging 189
- Methacrylates 308
- Methyl ethyl ketone 317
- Micellar dispersants 308
 electrostatic energy barrier 315*f*
- Microelectrophoresis 282
- Mineral oil, carbon black
 suspensions 308
- Mineral oil, wetting delay 407
- Mobility measurement 282, 283
- Mock substrate, silver bromide 35*f*
- Mock substrate, sodium chloride 33, 34
- Moisture proofing 145
- Molecular assemblies 93

- Molecular organization, requirements 93, 94
- Monocomponent developer 251f
resistance 253f
- Monocomponent development 250-252
shell rotational velocity 263f
- Monocomponent development process, toner 249
- Monocomponent toner(s)
charge transfer 259
charge transport 249-264
kinetic resistivity 254-260
resistivity differences 252
static resistivity 252-254
transient current 262f
- Monolayer manipulation, information transfer 104, 107f
- Monolayer matrix, modification 95
- Monolayer organizes 93-109, 111-121
air-water interface 94
construction 94-96
electron transfer 99f
information 94
mobility 102
photoinduced electron transfer 111-121
solution 94
transfer 97f
- Monolayer particle arrays 123-134
imaging technology 134
- Monolayer transfer 97f, 106
- Monolayers, close-packed 8
- Monolayers, separation 108
- Monomeric dye, absorption strength 14
- Multilayer photoconductors 143, 145
- Mylar 398
- N**
- Na₂CO₃—*See* Sodium carbonate
- Negative corona charge 143, 144f
- Negative kink, silver adsorption 63
- Neutral polymers 167
- Neutralization, toner and photo-receptor charge 158, 159f
- Newsprint, wettability 409f
- Newtonian fluid, film splitting 388f
- Nickel 546
- Nip capacitance 368f
- Nitrobenzene 317
- 2-Nitrobenzyl protecting groups 375
- Noise spectrum, particle distribution effect 277
- Nonaqueous colloid 281-304
applications 300-303
autocorrelation function 293f
characterization 282-285
charge control adsorption isotherm 296f
electrical plateout 292
- Nonaqueous colloid—*Continued*
electrohydrodynamic effects 288
intermediate conductivity 286, 287f
ionic characteristics 292
low conductivity 287f
mobility 291
mobility measurement 283
monolayer coverage properties 295
particle mobility 297f, 298
 electric field effect 299f
particle size, charge control agent effect 297f
unipolar conduction 288
- Nonaqueous dispersions
electrodeposition tests 309
flocculation rate 314
- Nonaqueous electrophoresis, effects 286
- Nonaqueous electrophoresis, space charge limited 288
- Nonaqueous liquids, electric charging of particles 307-323
- Nondrying inks 389
- Nonepitaxial attachment 42
- Nonfoaming surfactant 354
- Nonuniform adhesive failure 400
- Nucleation 82-88, 562
reactant addition rate effect 84, 85f
silver concentration effect 86, 87f
solubility effect 86, 89f
temperature effect 86, 89f
- Nucleation rate, kinetic law 562
- Nucleation region 82
- Nucleation sites 400
- O**
- n*-Octadecane 44
- Offset ink 412, 415
interfacial tension 329
pigment content 412
polymer resins 413
- Offset lithography 389, 405-417
dynamic wetting by fountain solution 405-411
- Oil dispersions, electrostatically stabilized 312
- Oil sludges 316
- Oil viscosity 400
- Oleate-based magnetic inks, hydrogen peroxide addition 574
- Oleates 573
- Optical contact 392
- Optical density 397f
- Optical density traces 274f
- Optical latensification 46
speed gain 53
- Optical sweepout transients 292

- Optical technique,
 crossbeam velocimetry 283
- Optical technique, transient 283
- Optical transient technique 283
- sweepout mode 283
- transit mode 283
- Organic media, electrostatic effect 307
- Organic pigment generators 146*f*
- Oxygens 1s multiplex spectra,
 curve fitting 467*f*
- Oxygen/carbon ratio, depression 471
- P**
- Packing studies 36
- PAPE—*See* Photoactive pigment
 electrophotography
- Paper 386, 422
- adhesion 481–486
- Auger parameter 469*t*
- bulk conductivity 502, 510, 518*t*
- pulp effect 518*t*
- business, surface atomic
 concentration 464*t*
- surface chemistry 455–473
- carbonate filled, properties 490
- charge transport 494
- commercial, dynamic sorption
 of ink 441–449
- physical test measurements 450*t*
- conductive base, bulk conductivity
 measurements 508
- contact resistance 515
- dynamic compressibility 394
- electrical conductivity 493–529
- steady-state electrical
 measurements 506–519
- electrical parameters 525*t*
- electrical properties
 pulp type effect 515–519
- refining effect 515–519
- fatty acids effect 410
- fiber anisotropy 513
- fiber distribution 498
- fiber orientation 502
- final properties 494
- ion diffusion 526, 528
- ionic mobility 523, 526
- liquid sorption measurement 405
- liquid transfer 407, 408*f*
- opacity 404
- self stripping 157, 159*f*
- shear testing 482*f*
- static charge 469*t*
- surface 473
- surface area, humidity effects 425*f*
- surface characterization, inverse
 gas chromatography 422–428
- Paper—*Continued*
- surface free parking 404
- surface profiles 512*f*
- surface resistivity 501, 505, 507*f*
- total resistance 513
- transient conduction 519–526
- transient current 527*f*
- water based inks 534, 539*f*
- zero surface coverage 428
- Paper adhesion
- polyethylene 486
- surface energetics effect 484
- Paper compression 395
- equation 395
- basis weight effect 517*t*
- calendering 517*t*
- cellulosic fiber orientation 502
- pressure effects 515
- Paper formation 498–501
- additives 498
- British Handsheet Machine 500
- centrifugal former 501
- Paper friction 487
- Paper sample, characterization 439
- Paper stripping 164, 166*f*
- Paper structure 494–501
- fibers 494–496
- and ink sorption 449
- Paper surface(s)
- electron spectroscopy 428–432
- penetration 435
- wetting 435
- Paper surface area 422
- humidity effects 422–427
- increasing relative humidity 424
- Paper surface energetics 479
- Paper wettability 476–481
- dynamic 476
- electrophotography 476
- paper adhesion effects 481–486
- wetting equilibrium 476
- Papermaking process 496, 498
- hydrogen bond formation 498
- surface tension 498
- three-dimensional anisotropy 498
- Paper–paper friction 488*f*, 489*f*
- Particle, suspended, electrostatic
 charges 307
- Particle charge density 216
- Particle contaminant removal 300
- Particle growth, spherical 129*f*
- Particle migration 135*f*
- Particle mobility, contact-induced
 shift 216
- Particle mobility, determination 292
- Particle–particle interactions
 evaluation 285
- Particle–wall interaction, force 295

Particle-wall interactions, evaluation	285	Pigment-binder composites	145-147
Patent Blue A	534	mechanical integrity	145
lightfastness	536f	Pigment concentration	403
Peel-developed construction,		Pigment dispersion, photoconductive	145
mechanics	372	Pigment-to-polymer adhesion,	
Peel-developed imaging system,		enhancement	317
interactions	378f	Pigments in organic polymer solutions,	
Peel development		applications	322
complementary images	373f	Planographic printing system	342, 343
peel apart construction	373f	Plate, used, surface energies	332f
photolabile blocking groups	371-380	Polarization	37
surfactant activity	377	Polarized aggregate spectra	39-42
surfactant data	376f	Polycarbonate	317
surfactant and surface interaction	377	basic oxygens	318
surfactant testing	375	zeta-potential	319f, 320f
Penetration experiments, apparatus	439	Polychrome photoelectrophoresis	173f
Penetration experiments, method	439, 441	Polyethylene	486
Percolation theory	254	Polyethylene adhesion, surface	
Petroleum sulfonates	308	tension effects	482f
Photoactive pigment electro-		Polyethylene film, charging	184
photography	168	Polyethylene terephthalate	372
Photobase paper	538	Polymer liquid flow, porous media	437
polyvinyl alcohol coated	540f	Polymer resin(s)	413
Photochemical dissipation of		conductive	523
adhesion	372	Polymeric coatings	372
Photochromic system, molecular		Polymeric dispersants	308
environment control	102	electrostatic energy barrier	315f
Photoconductive pigment dispersions	145	role	316
Photoconductor, multilayer	143, 145	Polymeric powders	
Photoconductor, single layer	143	charge levels	187f
Photoconductor drum	140	contact charging	183-196
Photodischarge	145	preparation	185
Photoelectrophoresis	168-171	Polymeric silicones	356
color reproduction	172	Polymethylmethacrylate	317
image initiation	172	dispersions, zeta potentials	321f
interfaces	170	Polyoxyethylenated nonylphenol	549
polychrome	173f	Polyoxethylene glycols	354
Photoelectrophoretic imaging		Polystyrene based toner	476, 481
configuration	169	Polyvinyl alcohol	538, 540f
Photographic emulsions	81	Porous media	
Photographic phenomena, electron		aqueous liquid penetration	438
spin resonance correlation	75, 77	capillary models	436
Photoinduced electron transfer	96-100	capillary sorption coefficient	438
reactions	112	diffusion coefficient	438
supersensitization	111-121	diffusion models	436
Photoinduced redox reaction	112	oil-based printing inks	438
Photoinitiated electron transfer	101f	polymer liquid flow	437
Photoisomerization reactions	100, 102	swelling	438
Photoliberation of surfactants	375	water sorption analysis	441
Photon transfer in monolayer		Post-chlorinated polyvinylchloride	
organizates	93-109	(CPVC)	317
Photo-oxidation	98	Positive kink site	45
Photoreceptor, charging	142	Post-transfer phenomena	402-405
Photoreceptor, interface	142	Potassium bromide	228
Photoreduction	98	Potassium ion, ionic mobility	526
Photosensitized absorption	117f	Powder adherants, classification	157-158
Phthalocyanine, effective contact	145	Precipitation, silver halide	81-91
Phthalocyanine, energy levels	171f	Press ready ink	361

- Print density 405, 406f
 Printing compression, effective
 capillary radius 395
 Printing compression, void
 fraction 395
 Printing nip 386
 Propanol solutions, surface tensions 350f
 Pseudoindole carbocyanine 22f, 23
 Pulp(s)
 mechanical, surface lignin content 431
 sulphite, lignin content 432
 transient current 521f, 522f
 wood, surface lignin content 431
 Pulping 496
- Q**
- Quasielastic-light scattering
 velocimetry 284
 Quenching 116
 Quinone 239
- R**
- Refining 496
 Refining process effects 515
 Residual charge reduction 157
 Resin 380
 Resistance
 basis weight effect 514f
 thickness effect 514f
 total, paper 513
 Resolving power 265
 Reversible photoisomerization 107f
 Roll coverings 369
 Rotogravure 361
- S**
- Saturation magnetization 559
 Scatterers 284
 Scumming 161
 Selective neutralization, sodium
 carbonate 239
 Selenium
 amorphous 143, 144f
 deposition 126
 particles 127f
 Self stripping paper 157, 159f
 Selwyn granularity coefficient 268
 Senefelder, Alois 327
 Sensitizer-acceptor system,
 electron transfer 113, 119
 Set off 405, 406f
 Shear testing, paper 482f
 Shearing 515
 Sheffield smoothness 478f
 Shift factor 479
 Shortness ratios, viscosities 342
 Show-through 405, 406f
 Show-through penetration 448
 Signal amplification 96-100, 101f
 Signal transduction 100-104
 Silica 159f
 Silica-alumina 200
 formation 200
 Silica-alumina catalyst 202
 acidity 205f
 surface group density 203
 Silicon oxides 377
 Silicon rubber 163
 Silicone, polymeric 356
 Silver, binding energy 63f
 Silver bromide 3
 behavior 4-5
 crystal morphology 86
 5,5'-disubstituted dye structure 26f
 9-ethyl dye aggregate 28f, 29f
 Langmuir isotherm 35f
 mock substrate 35f
 See also Sodium chloride
 multilayer coverage 33
 1,1',3,3'-tetraethyl-5,5',6,6'-tetra-
 chlorobenzimidazolocarbo-
 cyanine iodide dyeing 32f
 Silver bromide crystal 83f
 facial form 5
 surface ions 5
 Silver bromide dispersions, absorption
 spectra 23, 24f
 Silver bromide dispersions, cubic
 adsorption 23
 Silver bromide emulsions 78f
 light-induced electron spin
 resonance 74f
 rhodium(III) effect 78f
 stannous chloride effects 78f
 Silver bromide growth rates 91f
 Silver bromide microcrystals, electron
 spin resonance 71-80
 Silver bromide models 61f
 Silver bromide photography, single
 side dyeing 38f
 Silver bromide photolysis 61f
 mechanism 60
 Silver bromide-dye aggregate, electrical
 neutrality 31
 Silver bromide-gelatin dispersions,
 reflection spectra 21f, 22f
 Silver cluster(s)
 chlorine exposure 66
 chloroform chemisorption 66f
 chloroform exposure 64, 65f
 electron affinity 60, 62f
 electron trapping 60
 evaporated on carbon 65f
 halogen deposition 64

Silver cluster(s)—		Spiropyran	102
<i>Continued</i>		Spreading	402
ionization potential	60, 62 <i>f</i>	Spreading experiments, apparatus	439
Silver cluster growth, charge effects	63	Spreading experiments, method	439, 441
Silver halide colloid formation	81–91	Stabilization, electrostatic contri-	
Silver halide crowded system	91 <i>f</i>	bution	313
Silver halide photography		Stainless steel	508
light sensitivity	3–58	charging electrode	186 <i>f</i>
optical observations	10	electrodes	504 <i>f</i> , 510
single crystal method	10	Stannous chloride	77
Silver halide photography, surface		Static charge	469 <i>t</i>
effects	3–58	Static resistivity	252–254
Silver halide precipitation	81–91	Steady-state electrical measurement	
continuous process method	82, 83 <i>f</i>	bulk conductivity of papers, paper	
double-jet method	82, 83 <i>f</i>	thickness effect	513–515
growth stage	88–90	in situ pressure bulk	
nucleation stage	82–88	conductivity	506–513
single-jet method	81, 82, 83 <i>f</i>	liquid metal electrodes	506
Silver halide surface, epitaxial		pulp type effect	515–519
contact	9	refining effect	515–519
Silver ions, mass spectrometry	45	Stearate wax dispensers	158
Silver orbital interaction	68	Steric stabilizer	295
Silver particles	59–68	Stripping	157
Single chromophores, preferential		Styrene copolymer particles, carbon	
orientation	106	black on surface	189, 189 <i>f</i> , 190 <i>f</i>
Single kink	60	Styrene- <i>n</i> -butyl methacrylate,	
Single layer photoconductor	143	dispersion with carbon black	192 <i>f</i>
Single-jet method	81, 82	Subsurface growth, model	128–131
Sintering forces	161	Subsurface particles	132 <i>t</i>
Site saturation	565	average radius	132 <i>t</i>
Sizing techniques, alkyl ketene		number density	132 <i>t</i>
dimer	486	Subsurface particulate deposit	126, 127 <i>f</i>
Sizing techniques, rosin-alum		conditions	126, 127 <i>f</i>
procedure	486	growth	128, 131
Skipped dots	361	Sulfite pulps, lignin content	432
Sludges	316	Sulfonates	308
Society of Photographic Scientists		Sulfones	231
and Engineers, emblem	5, 7 <i>f</i>	Sulfur sensitization	46
Sodium carbonate	239	Supersaturation ratio	82, 85 <i>f</i>
Sodium chloride	10, 33, 34, 498, 526	solid-phase nucleation effect	82
Sodium lauryl sulfate	549	Supersensitization	111, 112
Softwood	496	donor sensitizer–acceptor	
fibers	496	system	119–121
Softwood pulp	497 <i>f</i>	Supersensitizer, mechanism	112
Solar energy conversion	93	Surface acid group distributions	203, 204 <i>f</i>
Solid acidities	209 <i>f</i>	α -alumina catalyst	204 <i>f</i>
Space charge	286–291	Al–Si catalyst	204 <i>f</i>
conditions	288, 291	Surface acid groups, strengths	201
factor	302	Surface acid groups, water effects	202
fields	523	Surface area, paper	422–427
Space charge limited	288	humidity effects	425 <i>f</i>
Space charge limited conditions	289 <i>f</i>	Surface characterization of paper,	
Space charge parameter	288	inverse gas chromatography	422–428
Sparking, gap width breakdown		Surface chemistry of business	
field	368 <i>f</i>	papers	455–473
Spatial frequency	271 <i>f</i>	Surface chemistry and	
analysis	265–278	lithography	327–344, 347–357
Spectroscopic dimers, formation	104		

- Surface chromatography of fibers,
 inverse gas chromatography 422-428
- Surface conductivity 505
- measurement 501
- Surface groups
- chemical indicator adsorption 201
- interaction mechanisms 219
- selective neutralization 237
- Surface group concentration,
 measurement 201
- Surface group titration 201-210
- chemical indicator adsorption 201
- procedure 203
- Surface lignin content, electron
 spectroscopy 431
- Surface profiles 510
- calendering 512f
- Surface resistivity, equation 505
- Surface resistivity, measurement 505
- Surface resistivity of paper 501, 507f
- Surface science, tools 6-14
- Surface states, alteration 155
- Surface tension 352, 402
- Surfactant(s), photoliberation 375
- Surfactant activity, interfacial,
 ESCA analysis 377, 379
- Surfactant testing 375
- Suspended particles, electrostatic
 charges 307
- Suspended particles, stability 546
- Swelling 438
- Synthetic magnetite 554
- Synthetic sizes 487
- Synthetic sizing 489f
- T**
- Tack force, and ink rheology 413
- Tack force measurement 415
- Teflon fiber brushes 158
- 1,1',3,3'-Tetraethyl-5,5',6,6'-tetra-
 chlorobenzimidazolocarbo-
 cya-
 nine iodide dye, silver bromide 32f
- Tetrahydrofuran (THF) 317
- Thermodynamic work of adhesion 476
- Thermodynamics of adsorption 427
- Thermogravimetric analysis,
 carbon black 236f
- THF—*See* Tetrahydrofuran
- Thiacarbocyanine, transition energy 18f
- Thiopyrylium-polycarbonate complex
 effective contact 145
- Thio-indigo derivatives 102
- Three-dimensional anisotropy 498
- Titration, surface group 201-210
- chemical indicator adsorption 201
- Toner 252
- bulk resistivity 253f
- Toner—*Continued*
- charging 150
- composition 147
- current density 252
- developer shell rotational speed
 effect 256f
- voltage effects 254
- Toner adhesion, surface energy effect 485f
- Toner bonding 456
- Toner brush, charge 250
- Toner charging 251f
- Toner contact site, capacitance 259
- Toner deposit 274f
- characterization 265
- composition 266
- granularity 268
- preparation 266
- Toner deposition, maximizing 250
- Toner-developer-gold plate 261f
- Toner image 269f
- density fluctuations 273
- noise 273-277
- Toner-paper bonding 481
- temperature effect 481
- Toner-paper interface, critical
 surface tension 164
- Toner particle size
 distribution 265, 267f, 278f
- measurement 265-278
- Toner particles, charge acquisition 257
- Toner particles, optical density 270
- Toner and photoreceptor charge,
 neutralization 158, 159f
- Toner powder, transient current
 measurement 261f
- Toner release, electric fields 150
- Toner spreading, shift factor 476, 479
- Toner transfer 157
- Transient absorption 100
- optical density 100
- Transient current 262f, 520
- plot 509f
- pulp 521f, 522f
- voltage effects 262f
- Transition density 16
- Transition dipole 16
- Transition energy, thiacarbo-
 cya-
 nine 18f
- Tribo charging 152, 154f
- Tribo series 184
- Triboelectric charging 226
- Triboelectrification—*See* Contact
 charging
- Tri-hexyl benzene sulfonates 308
- Triton N-101 549, 550
- Twisted molecules 9
- Two-component magnetic brush 147, 149f
- Two-dimensional chromophores,
 copying 104

- Two-dimensional viologen concentration 115f
- Two-sidedness 48f
- U**
- Uncoated paper 389
- surface hardness 364
- Unipolar conduction 290f
- threshold voltage 288
- Unsize paper 459
- UV photoemission spectroscopy 59
- V**
- Vapor deposition 123-134
- conventional 123
- Vapor-adsorbate equilibria 427
- Van der Waals force 158
- Viologen 113
- quenching action 113, 115f
- Viologen concentration, two-dimensional 115f
- Viologen molecule, spacing 115f
- Viologen radical, detection 98
- Virgin ink, surface energies 331t
- Virgin plate, surface energies 331t
- Virgin plate, water vapor adsorption 331
- Void fraction 395
- Volatile content 226, 235
- W**
- Walker-Fetsko ink transfer equation 390
- Water adsorption, dynamic 409f
- Water-based inks 544
- magnetic 544
- Water-dispersible gums 353
- Water and ink mixing 348, 349
- Water soluble dyes 532, 534
- Water surface tension, isopropanol concentration effect 411f
- Water surface tension, surfactant concentration effect 411
- Water wetting, by ink 348
- Waterless lithography 342, 343
- definition 342
- silicone oil additive 343
- Weak acids 353
- Wetting, paper surface roughness effects 407
- Wetting, viscosity effects 400
- Wetting action 348
- Wetting delay 407
- Wetting equilibrium 476
- Wetting time, solvent extraction of fatty acids effects 410
- Whiskering 369
- White solid acidity, alterations 206
- White solid acids 197-221
- mixture with carbon black—
 See Binary mixtures
- White solid activation 202
- White solid catalyst, indicators 201
- White solids 202
- Wiener spectrum 278f
- equation 273
- model first approximation 275
- toner samples 274f, 276f
- Wood fiber 497f
- cellulose portion 496
- characterization 496
- morphology 494, 495f
- primary wall 494, 496
- secondary wall 496
- surface properties 421-432
- Wood pulps, electron spectroscopy 430f
- Wood pulps, surface lignin content 431
- Work function, insulating powders 217
- X**
- Xerographic copier 141f
- process steps 140
- Xerographic developer 151
- Xerographic photoreceptor 142
- Xerographic process 147-165
- development 147-151
- toner viewpoint 147, 148f
- Xerography, dry transfer 140-147
- XPS—*See* Electron spectroscopy
- X-Ray photoelectron spectroscopy—
 See Electron spectroscopy
- Y**
- Yule-Neilsen effect 394
- Z**
- Zero coverage, measurements 427
- Zero surface coverage, measurements 428
- Zeta potential 291, 546
- polycarbonate concentration effect 310t, 320
- Zinc oxide 145, 147
- adsorption 148f
- effective contact 145